# BIOMASS GRANULAR FEEDING FOR GASIFICATION AND COMBUSTION

by

**Jianjun Dai**

B. A. Sc. Tianjin University, Tianjin, China, 1993
M. A. Sc. Tianjin University, Tianjin, China, 1996

A THESIS SUBMITTED IN PARTIAL FULFILMENT OF
THE REQUIREMENTS FOR THE DEGREE OF

DOCTOR OF PHILOSOPHY

in

THE FACULTY OF GRADUATE STUDIES

(Chemical and Biological Engineering)

THE UNIVERSITY OF BRITISH COLUMBIA

May 2007

# ABSTRACT

Successful feeding is critical to biomass utilization processes, but is difficult due to the heterogeneity, peculiar physical characteristics and moisture content of the biomass particles. The objectives of this project were to define what limits screw feeding in terms of the mechanisms of blockage and to examine the effects of key properties like mean particle size, size distribution, shape, moisture content (10-60%), density and compressibility on screw feeding of biomass. Wood pellets, ground wood pellets, sawdust, hog fuel, ground hog fuel and wood shavings were used in a screw feeder/lock hopper system previously employed to feed biomass to a circulating fluidized-bed gasifier. Three hopper levels (0.3, 0.45, 0.6 m), five casing configurations (common straight, tapered and extended sections) and two screws with different configurations were investigated. Experimental results showed that large particles, wide size distributions, irregular shapes, rough particle surfaces, large bulk densities and high moisture contents, as well as higher hopper levels and special casing configurations, generally led to large torque requirements for screw feeding. The "choke section" and seal plug play important roles in determining torque requirements for biomass fuels. The unique characteristics of biomass and system requirements of biomass processes create special challenges for biomass feeding.

A fundamental study on a Particulate Flow Loop was also conducted to investigate the probability of blockage/bridging as a function of particle size, shape, density, hardness, flexibility and compressibility. Experimental results showed that large particle size, irregular shape, and large ratio of particle to constriction dimension can all increase the blockage tendency. Reynolds number based on water mean velocity and hydraulic diameter of duct,

constriction dimensions and shape, particle density, particle hardness, flexibility and compressibility are also important factors affecting blockage probability.

The present study developed a new theoretical model with consideration of compression, aimed to understand the mechanism of biomass screw feeding and to predict torque requirements to turn the screw feeder instead of being blocked. Boundaries around the bulk material within a pocket were considered, and forces acting on these surfaces were analyzed. Two parameters are employed in this model to describe stress in screw pockets in the hopper and to analyze compression in the choke section. The model extends previous models by considering effects of all boundaries on torque, and allowing for compression in the choke section. The torque requirement is approximately proportional to the vertical stress exerted on the hopper outlet by the bulk material in the hopper and to the third power of the screw diameter based on the theoretical analysis. This indicates that large screws and high feed loads require large torque. The starting torque and volumetric efficiency of screw feeding with consideration of compression in the choke section were also estimated with reasonable success based on this model.

Special casing configurations (e.g. tapered and extended sections) are also considered in the model, leading to better understanding of blockage in the choke section and approximate prediction of torque requirements for screw feeders of special casing configurations. The choke section length, screw and casing configurations were closely related to plug formation and plug sealing of the reactor, while also affecting the torque requirements.

The new theoretical model successfully predicted torque requirements and efficiencies for both compressible and incompressible materials for certain screw configuration. The present experiments and model are expected to be very useful for biomass utilization.

# TABLE OF CONTENTS

# LIST OF TABLES

# LIST OF FIGURES

# ACKNOWLEDGMENT

I am most grateful to my supervisor, Dr. John R. Grace. This thesis would have been inconceivable without his support, guidance and encouragement. He has helped in every possible way: lecturing my courses, leading discussion, proofreading the thesis and improving its quality both scientifically and editorially, and offering financial support.

I am also grateful to the National Research Council of Canada (in particular, Dr. M. Sayed) and Natural Sciences and Engineering Research Council of Canada for providing funding for this project.

Many thanks are given to Drs. Richard J. Kerekes and Paul McFarlane for kindly being members of my supervising committee.

Special thanks are given to Mr. Horace Lam, Mr. David Adam and Mrs. Chee Chen in the Stores for helping me with all kinds of procurement, and to Mr. Peter Roberts, Mr. Doug Yuen, Mr. Graham Liebelt, Tim Paterson, and Mr. Alex Thng in the workshop for making a number of components and control panels. My fellow graduate students and all of my friends have made my program a completely pleasant experience.

I would also like to thank AXTON Incorporated and Sunrise Manufacturing for fabricating the screw and tapered sections. Thanks, also, to the Centre for Advanced Wood Processing at UBC, for generously providing wood shavings for use in the experimental study.

Finally, I am deeply indebted to my wife Jing Li and my parents, as well as my sisters, for their consistent backing and encouragement, which have been a steady source of pleasure and inspiration.

# CHAPTER 1. INTRODUCTION

## 1.1 Biomass and Biomass Feeding

Interest in biomass feedstocks to produce heat, power, liquid fuels and hydrogen, as well as to reduce greenhouse gas emissions, is increasing in Canada and worldwide in recent decades. The biomass share of current world energy consumption is 14%, with 4% in North America, 38% on average in developing countries, and 85% in the least developed ones (Hall and Rosillo-Calle, 1998).

Biomass includes all matter that can be derived, directly or indirectly, from plant photosynthesis. It is organic matter, as well as a renewable energy source, which could replace some fossil fuels. Biomass feedstocks are potentially available in five categories: mill wastes, urban wastes, forest residues, agricultural residues, and energy crops. 50% of the biomass globally available is woody, whereas 20-40% is grassy (ECN, 2004).

The chemical composition and physical properties of feedstocks influence the design of gasifiers/combustors, as well as the composition of the product gas and downstream cleanup requirements. In general, fuels with high inherent energy content, high carbon-to-nitrogen ratio, relatively little sulfur, low ash content, regular particle shapes, small particle sizes, narrow particle size distribution, low moisture content < 55% (wet basis), suitable bulk density, and low contaminant concentrations are preferred as raw materials. Biomass fuel particles tend to be unusual, varying greatly in size and shape. Some are wet, leading to sticking. They also tend to be compressible and pliable (e.g. sawdust, hog fuel, straw, rice hull, sugar cane, bagasse and grass). Some are easily fractured (e.g. wood pellets, walnut shells, other hard and brittle husks),

while others may be stringy and very resilient (e.g. grass, straw, hay, cotton stalks, corn stover, wood chips and wood shavings). Demolition woods (either pure or mixed with other materials such as sewage sludge and paper sludge) have also been used for gasification (van der Drift, 2001).

Biomass processes, including direct combustion, gasification and pyrolysis, have been under development for many years in various countries. A critical problem is how to feed biomass into the reactors. Frequently the solids feeding devices become blocked and do not provide uniform and continuous flow of the feedstock materials required for the process. Fuel feeding problems often impede smooth operation in industry. Feeding is made more difficult by a number of factors. Improperly sized particles, excessive moisture content and an insufficient or excessive pressure differential between the feed vessel and reactor, as well as poor design of feeders, can all lead to feeding failures. If the reactor operates at high-pressure and/or high temperature, there are additional challenges in establishing reliable feeding (Elliott, 1989; FBT, 1994; Cuenca and Anthony, 1995; Cummer and Brown, 2002).

Feeding method choices are closely related to the above characteristics of biomass feedstocks. Wood pellets tend to be denser than normal biomass feedstocks, and to have volume-equivalent diameters from 8 to 16 mm. Typical bulk densities are of the order of 750 $kg/m^3$, and final moisture content is typically ~8%. These characteristics are generally suitable for gasification or other processes that require uniform and smooth feeding, but at a cost. In general, particle size, size distribution, shape, surface texture (e.g. smooth, rough or sharp edges), density, moisture content, compressibility and other properties (e.g. strength of large particles, time consolidation, etc.) should be considered when choosing the feeding method. Bulk flow properties (e.g. cohesion strength, internal and wall friction), which can be used to characterize the flowability of biomass fuels, are closely related to the physical properties.

Biomass feeding systems typically consist of two parts: fuel transport from storage to the conveying line, and injection into the reactor. Special attention is paid in this thesis to the latter, i.e. injection into the reactor, since this directly affects the reactor performance and plays a major role in achieving continuous, reliable and efficient operation of the reactor. Biomass feeding systems vary greatly depending on fuel properties and the entire system requirements. For example, several conveyors and feeders, as well as storage vessels, may be connected together in order to implement smooth feeding (Wilén and Rautalin, 1993; Koch, et al, 1996; Cummer and Brown, 2002; Aldred et al., 2003). The feeding systems considered in the present study exclude drying and sizing units.

In biomass energy processes, several kinds of feeders and their combinations have been reported including hopper or lock hopper systems, screw feeders, rotary valves, piston feeders and pneumatic feeders. These feeders have been developed for a variety of solids, and they have limitations in handling certain types of biomass and/or operating in conjunction with pressurized reactors. These feeders require careful design to handle heterogeneous and fibrous biomass feedstocks. Some screw or piston-type plug feeders, commonly used to feed coal or in the pulp and paper industry, have been tested with biomass (Bundalli et al., 1986; Ghaly et al., 1989; Wilén and Rautalin, 1993; Nelson, 1994; Babu, 1995; Gabra et al., 1998; Cummer and Brown, 2002; Li et al, 2004). The flow patterns developed by a screw feeder coupled to a hopper have been studied extensively (Bates, 1969; Bates, 1986; Haaker et al., 1993; Bates, 2000). The mechanics and transport function of screw feeders have also been investigated in some detail (Metcalf, 1966; Roberts, 1996; Yu and Arnold, 1996; Yu and Arnold, 1997). The motion of particles in screw feeders has been simulated by a Discrete Element Method. Mixing and transportation of particles inside the screw feeder have also been analyzed (Tanida et al., 1998).

Kinetics and reaction chemistry have received much attention in previous research work on combustion and gasification. On the other hand, not enough research on biomass feeding systems has been carried out, and little detailed information has been published, partly because of patent protection. The wide variations in feeder characteristics and in the physical properties of biomass materials make research on biomass feeding complex, with general rules difficult to formulate.

## 1.2 Scope of This Study

Hoppers and screw feeders are among the most widely used feeders for biomass processes. Screw feeders share similarities with rotary valve feeders in lateral motion and with piston feeders in axial motion of bulk materials. Research on screw feeders could also assist in understanding the basic principles and operation of rotary valve feeders and piston feeders, which are also commonly used in the biomass industries.

The present study focuses on screw feeding of biomass fuels, largely ignored in previous research. The objectives are to define what limits screw feeding in terms of the mechanisms of blockage and to examine the effects of key properties like mean particle size, size distribution, shape, moisture content (10-80%) (CIWMB, 2007), density and compressibility on screw feeding of biomass.

Chapter 2 provides an overview of current research efforts, as well as a critical review of biomass feeding for combustion and gasification. This background knowledge helps provide an understanding of biomass properties, hopper flow, screw feeding and existing feeding problems. This leads to a statement of the objectives of this thesis.

In order to further understand blockage mechanism and effects of particle size, shape and compressibility on particle flow through constrictions, a Particulate Flow Loop was assembled,

providing qualitative information in Chapter 3. This Chapter provides introduction, experimental set-up, experimental results and analysis of pressure drop required to break up the blockage. This Chapter aims at deepening understanding of effects of particle size, shape, density, stiffness and compressibility on blockage and particle flow through constrictions.

The next part of the thesis presents a study of the feeding system of UBC's existing Circulating Fluidized Bed Gasifier. In Chapter 4, we introduce the experimental system, biomass materials, and experimental methods and procedure for biomass feeding systems employed in the present study. Chapter 5 reports and discusses the experimental results and summarizes the findings. Chapter 6 provides a model to predict torque requirements and efficiency for biomass screw feeding and compares the predictions with the experimental results of the previous Chapter.

Finally, in Chapter 7, a brief summary of conclusions is given, together with recommendations for biomass feeding and for future work.

# CHAPTER 2. BACKGROUND

## 2.1 Biomass Properties

Biomass properties, including chemical and physical properties as shown in Table 2-1, influence feeder design and reactor performance.

### 2.1.1 Physical properties

Diverse biomass feedstocks have been tested for different biomass processes for centuries, especially in recent decades with market potential and technological reliability indicated in Figure 2-1. From this figure, one can see that woody biomass, short-rotation forest (SRF) and refuse-derived fuel (RDF) have relatively high market potential and overall technological reliability, while the market potential and technological reliability of sludge, straw and grasses are relatively low due to their low energy density and peculiar properties. Biomass fuels fall into three categories according to their size and states: granular material (typically > 0.5 mm, see Chapter 3), powder (typically < 0.5 mm) and slurry. Granular materials differ significantly from powders in flow properties. Biomass varies greatly in size, shape, density and compressibility, with moisture content as high as 80% (CIWMB, 2007), and it may even be in sludge or slurry form. Although biomass particles are usually between 0.5 and 50 mm in volume-equivalent diameter for gasification and combustion processes, fine biomass materials, such as fine sawdust, are also common.

Slurries (e.g. sludge and wastes plus water, or mixtures of oil and finely ground biomass) have also been used for gasification. Solids loading, viscosity, stability and heating value are important factors for slurries as fuels (Furimsky, 1998; Agarwal and Agarwal, 1999; DOE, 2001; Henrich and Weirich, 2004). Fuel preparation and feeding problems often impede smooth

operation in biomass industries. Biomass physical properties play a major role in these problems. The influences of these properties need to be understood before designing and operating feeding systems.

Table 2-1. Main physical and chemical properties of biomass fuels compared with bituminous coal [1]

| Proximate analysis | Biomass | Bituminous coal |
|---|---|---|
| Fixed carbon (db [2]) ASTM D-3172 | 17-23 % for woody biomass (e.g. black locust, sycamore, eucalyptus, hybrid poplar). 12-23 % for herbaceous biomass (e.g. wheat straw, bagasse, switch grass and corn stover). | 45 % (typical value) |
| Volatile matter (db) ASTM D-3175 | 77-83 % for woody biomass. 69-82 % for herbaceous biomass. | 35 % (typical value) |
| Ash content (db) ASTM E-1755-95 | < 2.5 % for woody biomass. Generally 2-14 % for herbaceous (19-23 % for rice hull, 9-11 % for wheat straw, 9-14 % for corn stover, 2-10 % for bagasse, 0.8-2.5 % for bamboo, 1.5-4.5 % for miscanthus) (CSIRO, 2002; EERE, 2006). | 1-12 % |
| Moisture content (wet basis) | 30-60 % for woody biomass. 8-30 % for herbaceous biomass. | 2-15 % |
| **Ultimate analysis** | | |
| Carbon (db) | 49-55 % for woody biomass. 43-49 % for herbaceous biomass. | 66 % |
| Hydrogen (db) | 5-7 % for woody and herbaceous biomass. | 4.4 % |
| Oxygen (db) | 35-45 % for woody and herbaceous biomass. | 5.7 % |
| Nitrogen content (db) ASTM D-537 | < 0.7 % for woody biomass. 0.2-1.54 % for herbaceous biomass. | 1.4 % |
| Sulphur content (db) ASTM D-4239 | < 0.07 % for woody biomass. 0.07-0.16 % for herbaceous biomass. | 0.5-1.5 % |
| Chlorine content (db) | < 0.1 % for woody biomass. 0.07-0.18 % for herbaceous (e.g. straw and grass). | 0.1 % |
| Potassium content (db) | < 0.04 % for woody biomass. < 1 % for herbaceous biomass. | 0.06-0.15 % |
| Bulk density ($kg/m^3$) | 100 - 700 for herbaceous and woody biomass (700-900 for densified pellets) | 850-1200 |
| HHV moisture free (MJ/kg) ASTM D-2015 | 14-19 MJ/kg (air dry) for herbaceous biomass 15-20 MJ/kg (air dry) for woody biomass | 28 |

Notes:
(1) All data are average or typical values and are mainly based on North America and European Countries. Data are from Hislop and Hall, 1996; Bridgwater, 2002; Ayhan, 2002, CSIRO, 2002; and Henrich and Weirich, 2004; EERE, 2006.
(2) db denotes dry basis.

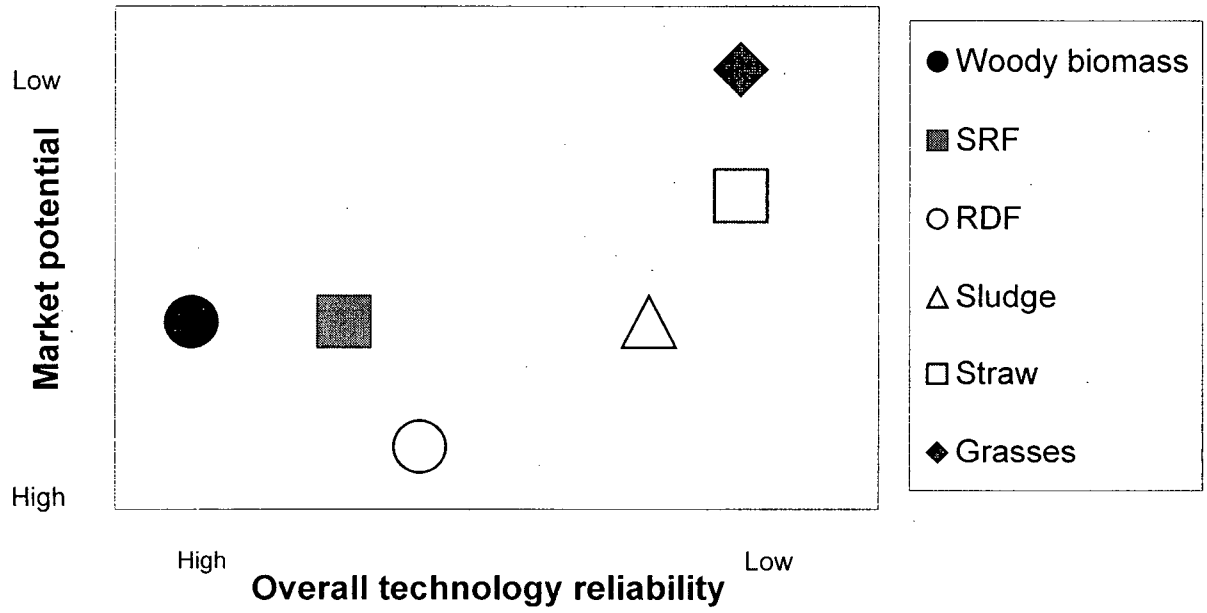


Figure 2-1. Status of feedstock technology reliability and market potential. (Bridgwater, 2002)

2.1.1.1 Particle size distribution

Particle size generally refers to the average volume-equivalent diameter of a particle. Biomass fuels rarely consist of particles of a given size. Thus to specify a fuel system, it is necessary to define not only a mean size, but also the relative numbers or masses of particles of different size, i.e. the size distribution. Sieving is the most commonly used method for size distribution analysis. Other technologies are also available (e.g. based on laser diffraction), especially for fine particles. In sieving, longer sieving times lead to more particles falling through sieves due to irregularity and compressibility of biomass particles. So longer sieving times result in smaller mean sizes and finer size distributions. For convenience and comparison, a fixed time is usually adopted, e.g. 20 minutes is a suitable sieving time for most fuels.

Different types of reactors have different fuel size requirements. Particles of uniform size are generally preferred to reduce the blockage tendency in feeders and to improve the

performance of the reactor (e.g. pressure drop and product gas quality). Oversize particles, especially those with high density and strength, are more likely to block the feeding system and to cause problems when the particles are fluidized. Too fine particles (e.g. those with diameters < 100 μm) can also lead to increased blockage propensity in the feeding system due to large cohesion and adhesion forces, as well as to elutriation in fluidized beds. It is generally important to remove oversize (e.g. > 50 mm) material, especially cube-shape particles of size > 6 mm, as these can increase the chances of bridging or blockage in fuel feeders. Excessive fine material (e.g. particles < 38 μm) is less of a problem, but the proportion should be limited to 10% of the fuel by mass in order to maintain reliable and stable operation of the reactor (McLellan, 2000). Requirements of fuel size and size distribution are determined by feeder configurations and reactor characteristics.

2.1.1.2 Irregular particle shapes and surfaces

Particle shape plays an important role in determining flow properties. Most particles encountered in practice are irregular in shape. Irregular shapes increase the tendency to bridge over openings. For example, a high proportion of hook-shaped or long and thin particles increases the tendency for a material to bridge (Mattsson, 1990/1997; Klausner, 2001; Mattsson and Kofman, 2001; Mattsson and Kofman, 2002). It is almost impossible to describe complex shapes by a single shape factor (Clift et al., 1978; Ming et al., 1986). Of the many possible shape factors, the most common are volumetric shape factor, sphericity and aspect ratio. The lack of suitable methods for measuring and characterizing particle shapes and the roughness of particle surfaces makes it difficult to quantitatively study their effects on flow properties of biomass. Image processing is a convenient technique for determining the shape of irregular particles.

2.1.1.3 Moisture content

Moisture content, the mass of water associated with the material per unit mass of dry or wet material, is one of the most important fuel characteristics. It usually refers to inherent moisture plus surface moisture. The moisture content of raw materials can be as high as 80% (*wet basis*). As the moisture content of a solid increases, so does its cohesive strength. Increasing moisture content usually accentuates the tendency to bridge and block in biomass feeding systems, especially for long and thin particles (Mattsson, 1990; Mattsson, 1997; Cuenca and Anthony, 1995; Mattsson and Kofman, 2001; Mattsson and Kofman, 2002). Excessive fuel moisture can also cause corrosion of processing equipment. On the other hand, fuels which are too dry have larger permeability and increase the possibility of backflow of gases and bed materials. In addition, the energy required for drying *may* greatly reduce the net energy generated from biomass processes. Moisture content of 10-20% (wet basis) is suitable for most biomass processes. More moisture reduces the efficiency for combustion systems, but it can lead to better carbon conversions, lower tar emissions, lower heating values of the product gas and lower cold gas efficiencies for gasification systems (FBT, 1994; Hughes and Larson, 1998; van der Drift et al., 2000).

Woody biomass is a hygroscopic material. Its moisture content is a dynamic property which changes with environmental conditions. The equilibrium moisture content (EMC) is affected more by variations in relative humidity (RH) than temperature. Small particles with large surface areas exposed to air respond very quickly to changes of RH. Other biomass materials have similar responses to RH changes. Although some researchers have proposed that moisture content be defined on an ash-free basis rather than based on total mass (Asadullah et al., 2003), moisture content is generally expressed on a wet basis. This is the convention in the present study, except where otherwise specified. Moisture contents were obtained from weight loss after

drying the fuel samples at 105°C for 5-72 hours, depending on biomass characteristics and requirements of the energy process. An understanding of moisture content, including its changes with time and environmental conditions, is necessary to estimate the flow properties and to design effective feeding systems.

2.1.1.4 Bulk and particle densities

Loose bulk density is the overall density of loose material, including inter-particle spaces (interstices). It is measured simply by pouring a quantity of particles into a graduated cylinder whose diameter is much larger than the particle diameter. The weight and volume occupied by particles determine the bulk density. Oven-dry bulk density and wet bulk density at different moisture contents may be reported. Apparent particle density (called solid density in some literature) is defined as the density of the particles, including the voids inside individual particles. It can be approximately measured and calculated according to procedures of the loose bulk density, except that the volume is compacted with the aid of mechanical pressure up to 0.5-1 MPa, or many (e.g. >1000) taps by mechanical tapping devices (Abdullah et al., 2003; Fitzpatrick et al., 2004). Pycnometry, a common technique for determining skeleton density, is based on gas displacement principles, and is sometimes also used to estimate particle density. From the bulk and particle density, voidage (volume fraction of inter-particle interstices) can be obtained readily since $\rho_b = \rho_p(1-\varepsilon)$. Bulk density is not only a function of the material density, but also of how tightly the material is packed. The density can also be altered by deterioration of the biomass particles. Bulk density is important when discussing biomass transportation and feeding, since it directly affects the flow properties of biomass, as well as transportation costs. To obtain a mechanically stable plug with a suitable low gas permeability, the plug should have a bulk density in the range from 1300-1500 kg/m$^3$, depending on the texture of biomass and the flow requirements (Koch, 2002; TK Energi, 2006).

2.1.1.5 Compressibility and compaction ratios

Compressibility is the relationship of the bulk density and consolidation pressure acting on the bulk material, which can be expressed by $\rho_b = a(1+\sigma)^b$ or $\rho_b = a(\sigma+b)^c$, where $\rho_b$ is bulk density, $\sigma$ is the consolidation stress acting on bulk solid, and $a$, $b$ and $c$ are constants (Arnold et al., 1980; Marinelli, 2000). Compressibility is the reciprocal of the bulk modulus, and is expressed by $(\Delta V/V)/\Delta P$, where $P$ is the consolidation pressure and $V$ is volume of materials (Beer et al., 2002). Compressibility is affected by moisture content, particle size, elasticity and temperature (Marinelli, 2000). The bulk density increases as the bulk material is subjected to increasing pressure or solids loading. More details of compressibility are provided in Chapter 6. The compaction ratio (CR) is defined as ratio of compacted density to loose bulk density or loose volume to compacted volume (Briggs, 1994; Marinelli, 2000; Marinelli, 2004). Compressibility is an important factor affecting biomass flow properties. Greater compressibility augments the resistance to bulk motion, i.e. contributes to low flowability. Hard robust particles tend to be incompressible, generally leading to low resistance to flow. However, they can be easily blocked if the outlet dimensions are not large enough relative to the particle dimensions.

2.1.1.6 Contaminants

The contaminant level is not a true material property, but it is included in this section since it can significantly affect the flow of biomass. Major contaminants in biomass fuels include stones, dirt, metals, paints, wood preservatives, and other non-combustible or hard materials intermixed with, or embedded in, biomass during collection and transportation. Contaminants should be eliminated, or at least minimized, since they can cause serious wear and stoppage in feeding, as well as severe problems in reactor performance. Ferrous metals can be removed with a magnet, with various types available. Detectors can tell the presence of non-ferrous metals and

stop the conveyor. The metal can then be identified and removed manually. Various types of equipment are available for removing stones and dirt from biomass feedstocks. The absence of stones and other debris is generally contractually dictated by the fuel suppliers.

As mentioned above, bridging and blockage in biomass feeding systems are mainly attributed to particle mean size and size distribution, low bulk density, irregular shape and cohesive/adhesive characteristics. Too large and too fine particles should be avoided since they may cause feeding stoppage and adversely affect reactor performance. Fluffy low-density materials, such as straw, bagasse and rice husks, present extreme difficulties in feeding, especially for fluidized bed and entrained flow reactors. Pelletizing and briquetting can change these physical properties and improve biomass flowability, but require extra costs. Wood pellets are denser than normal biomass feedstocks, with typical size 8-16 mm in volume-equivalent diameter. Bulk densities are usually of order 750 $kg/m^3$, and the final moisture content is typically 8% (wet basis). RDF (refuse derived fuel) pellets are also produced to suit both moving bed and fluidized bed gasifiers, promoting smooth feeding and favorable performance (Hislop and Hall, 1996). High-density materials of large size (e.g. > 50 mm wood blocks) are also difficult to feed.

Although other physical properties, such as particle surface roughness, hardness and strength, are hard to measure, they are also important parameters that affect flow properties.

### 2.1.2 Flow properties

Particle physical properties commonly measured are particle size, size distribution, moisture content, bulk density, particle density and compressibility. Particle shape and surface characteristics can be analyzed by image processing. These properties depend on the state of the material as determined by its stress history and the current stress acting on the bulk. The stress is strongly affected by environmental conditions (RH, temperature, vibration, external pressure

and microbial activity). Physical properties (as well as chemical properties) tend to change with time (e.g. due to consolidation) for any particular biomass, and special attention is required when measuring these properties. There are no direct widely-used correlations that allow these variables to be used to calculate flow properties.

At least four flow properties need to be measured to estimate the flowability (see Table 2-2 and Chapter 4). They are flow-function, cohesion strength, internal friction and wall friction. Flow- function is a plot of the unconfined yield strength of the bulk solid versus major consolidating stress (see Figure 2-2), and represents the strength developed within a bulk solid when consolidated, which must be overcome in making the bulk solid flow. The unconfined yield strength is the major consolidating stress that causes the material to yield in shear. A flow-function lying towards the bottom of the graph represents easy flow, whereas moving upwards in an anticlockwise direction in the graph indicates more difficult flow. The flow index in Table 2-2 is defined as the inverse of the slope of the flow-function. Jenike (1964) used the flow index to classify flowability, with higher values representing easier flow. This was extended by Tomas and Schubert (1979) as shown in Table 2-2. Bulk density, as well as compressibility, should also be considered for hopper design. These properties are typically measured and quantified using shear cell techniques depending on ISO, ASTM or EFCE standards (Arnold et al., 1980; Bates, 2000; Fitzpatrick et al, 2004; Jenike and Johanson, 2006). Analysis of flowability and physical properties can assist in the design of an effective feeder for biomass feeding. Chemical constituents and thermal properties of various biomass fuels have been reported in the literature (e.g. Li et al., 2004). and on-line databases (e.g. EERE, 2006).

Table 2-2. Jenike classification of flowability by flow index [1]

| Flowability | Hardened | Very Cohesive | Cohesive | Easy flow | Free flowing |
|---|---|---|---|---|---|
| Flow index | < 1 | < 2 | < 4 | < 10 | > 10 |

(1) Data from Jenike (1964), Tomas and Schubert (1979) and Fitzpatrick et al. (2004).

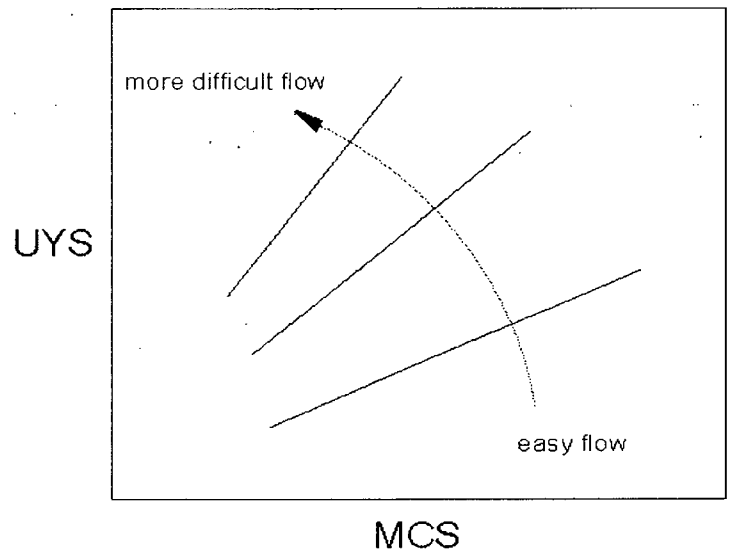


Figure 2-2. Flow-functions: easy flow versus difficult flow. (UYS is unconfined yield Strength and MCS is major consolidating stress).

## 2.2 Biomass Feeding Systems

### 2.2.1 Review of biomass feeding

An ideal feeding system provides smooth and continuous feeding with accurate control of the feed rate (e.g. coefficient of variation < 5% based on 1 sample taken over a 1 min interval). The system should be relatively insensitive to variations of fuel size, shape and moisture content, and it must maintain sufficient pressurization to prevent backflow of gases and bed material. Although a variety of biomass feeders have been designed and tested for biomass energy processes in Canada, Europe and the US, most of these feeders have encountered problems and may not be reliable, efficient or economical, particularly for herbaceous feedstocks and pressurized systems (Babu, 1995).

The feeding technique for biomass fuels depends on fuel properties, the type of reactor, throughput requirements and the operating conditions (e.g. pressure and temperature). Details of

reported feeders are summarized in Tables 2-3 to 2-5. Some feeders may work for specific conditions and have been developed in an ad hoc fashion, but most have limitations, such as being fuel-specific, suffer from pressure seal failure, or encounter bridging or blockages, inaccuracy, complex design and operation, noise, high cost or inability to survive due to wear in long-term service. Dust explosion may be a hazard with decreasing particle size due to spontaneous ignition of dust, especially for pressurized processes. Pyrolysis in the feeding system may also cause severe problems (e.g. tar accumulation in feeders) (Babu, 1995). The operating pressure varies greatly among gasifiers and combustors, from slightly negative pressure or virtually atmospheric to pressures greater than 100 bar (i.e. >10 MPa). Feeding devices for pressurized reactors often function well at atmospheric pressure with little or no modification (Reed, 1981; Babu, 1995; Cummer and Brown, 2002). It is pertinent to classify feeding systems based on their pressure limitations, i.e. low pressure (< 100 $kPa_g$), medium pressure (< 300 $kPa_g$), high pressure (< 1000 $kPa_g$) (Marcus, et al, 1990). If the feeding system operates at pressures above 1000 $kPa_g$, it may be termed extra-high-pressure and special attention is required. Note that the classification of feeders in terms of pressure differs from that of gasifiers or combustors, which may be categorized according to ASME Boiler and Pressure Vessel Codes. Feeders operating at relatively high pressure (e.g. > 2 $bar_a$) are more difficult to design and operate than those intended for normal pressure operation.

There is no universal choice of feeder due to the wide variety of equipment choices and biomass properties. For difficult-to-handle materials, the number of options is reduced. In biomass gasification and combustion processes, several kinds of feeders or their combinations have been reported in previous research and industrial applications. They include hopper or lock hopper systems, screw feeders (including single screw and twin screw feeders, etc.), rotary valve feeders, piston feeders, belt feeders, vibratory feeders, reciprocating pan feeders, rotary

Table 2-3. Typical biomass gasification projects and their feeding systems

| Project information | Fuels and gasifying agents | Design parameters | Main feeders | Supplementary comments | Source |
|---|---|---|---|---|---|
| Amer, ACFBG, 600$MW_e$ and 350 $MW_{th}$ for the entire boiler system (Netherlands) | Demolition wood; Air blown. | Atmospheric pressure 800-950 $^0$C | Silos and screw feeders. (Bottom feeding) | ACFBG for demolition wood produces gas which can be burned in coal boilers; Co-firing. | Willeboer, 1998 |
| ARBRE, ACFBG BIGCC, 8 -10 $MW_e$ (Yorkshire, UK) | Wood chips from forestry residues and from short rotation coppices; Air blown. | Atmospheric pressure Typically 850 $^0$C | Silos, screw feeders and rotary valve feeders. (Bottom feeding) | TPS gasification process | Babu, 1995; Pitcher et al., 1998 |
| BIG/GT project ACFBG 30 $MW_e$ (Bahia, Brazil) | Wood chips from eucalyptus plantation; Air-blown. | Atmospheric pressure Typically 850 $^0$C | Silos, screw feeders and rotary valve feeders. (Bottom feeding) | TPS gasification process | Babu, 1995; Waldheim and Carpentieri, 2001. |
| Värnamo Project/Bioflow PCFBG, IGCC, 6 $MW_e$ and 9 $MW_{th}$ (Sweden) | Wood chips, forest residues, sawdust and bark pellets, willow, straw and refuse-derived fuel (RDF) of a defined size distribution; MC [(1)]: 10 – 20%; Air-blown. | Pressure: 20 - 22 bar 950 – 1000°C | Silos, lock hopper and screw feeders (Bottom feeding) | Modifications had to be made to the fuel feed system. Plant shut-down Oct. 1999. Foster Wheeler technology. | Kwant, 2001 |
| BIOSYN, PBFBG, (Canada) | Sludge, RDF, rubber residues (containing 5 – 15 % Kevlar), and granulated polyethylene and propylene residues; Size: < 50 mm, MC: < 20%; Air or oxygen blown. | Pressure: 1.6 MPa; Temperature: 800-900°C | Sunds plug screw feeders. | Large ball valve was installed between reactor and feeder, BIOSYN process | Wilén and Rautalin, 1993; Kwant, 2001 |
| ACFBG, IGCC, 6.7 MWe (30 $MW_{fuel}$) (Chianti, Italy) | Refuse-derived fuel (RDF) Pellets; Air-blown; | Atmospheric pressure Typically 850 $^0$C | Storage silos, screw feeders, twin-screw feeders, bucket conveyors, feed hoppers and rotary valve feeders. (Bottom feeding) | TPS gasification process | Waldheim and Carpentieri, 2001; Granatstein, 2002. |

| Project information | Fuels and gasifying agents | Design parameters | Main feeders | Supplementary comments | Source |
|---|---|---|---|---|---|
| BioCoComb,<br>CFBG,<br>3.5 $MW_e$ (10 $MW_{th}$)<br>(Zeltweg, Austria) | Wet wood chips, bark and sawdust with MC up to 70%;<br>Size: < 30 X 30 X 100 mm;<br>Air-blown. | Atmospheric pressure<br>Typically 850 $^0$C. | Hoppers, weighing belt conveyors, screw feeders and rotary valves with purging mechanism; reverse control to prevent blockage<br>(bottom feeding) | Product gas is directly fed into pulverised coal (PC) boiler, co-fired with a PC boiler | Mory and Zotter, 1998;<br>Granatstein, 2002. |
| Hawaii PDU and BGF project, PFBG,<br>5 $MW_e$<br>(Hawaii, USA) | Wood chips, whole tree chips, barks, refuse-derived fuel, paper mill sludge, alfalfa stems and bagasse,<br>MC: <20 %,<br>Oxygen/air and steam blown. | 0.6-2.14 MPa;<br>750-980 ° C. | Hopper and lock hopper systems, screw feeders<br>(Bottom feeding) | Had to operate at reduced capacity and pressure. Feed system did not perform consistently and was modified with addition of lock hopper (bottom feeding).<br>RENUGAS process. | Lau, 1998. |
| Lahti project,<br>ACFBG,<br>60-70 $MW_{th}$<br>(Lahti, Finland) | Sawdust, wood chips and recycled refuse fuels with MC up to 20-60 %;<br>Air-blown. | Atmospheric pressure<br>800-1000 ° C. | Chain conveyors, belt conveyors, silos and screw feeders<br>(bottom feeding). | Excellent performance reported, produced fuel gas co-fired with a PC boiler.<br>Foster Wheeler technology. | Nieminen and Kivela, 1998. |
| Small-scale demonstration plant, fixed bed gasifier (downdraft),<br>75 kWth,<br>(Technical University of Denmark, Denmark) | Wood chips from beech,<br>Air blown. | Atmospheric pressure<br>< 1100–1200 ° C | Hopper and lock hopper system, screw feeders.<br>Feeding system worked well during the test, with only one stop, caused by blockage by a large piece of wood. | Gasifier was controlled by a PLC. The only essential parameter, which was not adjusted automatically, was the fuel-feeding rate. Two-stage gasifier with pyrolysis and char gasification in separate reactors | Henriksen et al, 2005 |
| Lab-scale dual-bed gasifier.<br>(Bangladesh and Japan) | Jute stick, bagasse, rice straw, and cedar sawdust, Size: 0.1–0.3 mm, MC: 4-10 %. Oxygen blown. | Atmospheric pressure<br>550–650 ° C. | Hopper and lock hopper system, vibrating feeder with $N_2$ flow.<br>Feeding fluctuation. | Dual-bed gasifier composed of two fluidized-bed sections (top feeding). | Asadullah et al, 2004. |
| 1.5 MWth (PFBG)<br>(Netherlands)<br>10–50 kWth<br>(DWSA system)<br>(Netherlands) | Coal, German brown coal (BC), and wood;<br>Air blown (DWSA)<br>Air/steam-blown (PFBG) | 0.12-1.6 MPa;<br>750-1000 ° C. | Belt conveyors, hopper and lock hopper system, rotary valve feeders, screw feeders and pneumatic feeding. | Bottom feeding from bottom plate and central nozzle or at the bottom just above the distributor by a screw feeder. | Jong et al, 2003 |

| Project information | Fuels and gasifying agents | Design parameters | Main feeders | Supplementary comments | Source |
|---|---|---|---|---|---|
| Pulverised-coal CHP-unit (79 $MW_e$ and124 $MW_{th}$), Entrained flow, (Vantaa, Finland) | Pine sawdust (< 10 mm, MC: 50-65%), coal (< 2 mm, MC: 9-13%). Sawdust needs to be dried. | Pressure: 180 bar; Temperature: not specified | Hoppers, belt conveyers, bucket chargers and pneumatic injectors | Co-firing of biomass and coal | Savolainen, 2003 |
| ACFBG, 500 $KW_{th}$, (BIVKIN, Netherlands) | Demolition wood (both pure and mixed with sewage sludge and paper sludge), verge grass, railroad ties, cacao shells and different woody fuels. Railroad ties contained very little heavy metals. Air-blown. | Atmospheric pressure 850 $^0$C | Fuel bunkers, rotary valve feeders, screw feeders. (Bottom feeding). | Initially, feeding problems often impeded smooth operation. Application of various feeding systems for various fuel mixtures. | van der Drift et al., 2001 |
| Cyclone gasifier and combustor (Two-stage) (Sweden) | Bagasse, cane trash and their pellets; Air or steam injection | Atmospheric pressure Ambient temperature for tests | Storage bin, screw conveyer, feed bin with two twin-screw feeders in bottom; pneumatic injector (Top feeding) | | Gabra et al., 1998. |
| ABFBG, (Iowa State University, USA) | Biomass fuels, Air/steam blown. | Atmospheric pressure 649 – 900 °C | Feed hopper, metering screw feeder, rotary valve feeder, screw injector feeder, purge air or nitrogen to prevent backflow of producer gas and bed materials. | Bottom feeding | Pletka et al, 1998 |
| Entrained flow gasifier, 130 MW(th), (SVZ, German) | Various waste slurries (e.g. char/pyrolysis oil slurry from short straw chops or wood sawdust) | 20 bar and 1200°C | Pump | | Henrich and Weirich, 2004 |
| Pilot scale CFBC, 0.3 MWth. Co-combustion of coal and biomass in CFB boiler (USA) | Pine bark < 30 mm; | Atmospheric pressure 800-900 °C | Hoppers and screw feeders. (Bottom feeding) | Biomass and coal are fed simultaneously to a third screw feeder leading to boiler. Rotation speed of this screw is kept constant and high. | Bahillo et al., 2003 |

Notes: (1) MC stands for moisture content, wet basis unless otherwise specified.

Table 2-4. Summary of fuels requirements and feeders by reactor type (combustion systems)[1]

| System | Fixed or moving bed combustors (Grate firing) | | | Suspension combustion system | Fluidized bed combustors (BFBC and CFBC) | |
|---|---|---|---|---|---|---|
| | Pile burners (wet cells) | Underscrew | Thin-pile spreader-Stoker | Cyclonic or air spreader stoker | AFBC | PFBC |
| Particle size | Generally < 500 mm (typically < 300 mm), and not too fine, depending on grate openings and feeder dimensions | Generally < 50 mm (typically 6-38 mm), non-stringy, not too large or too fine, depending on the auger size. | Generally 6-50 mm, depending on grate openings and feeder dimensions | Generally < 6 mm, not too fine, non-stringy | Generally < 500 mm for BFBC (typically < 50 mm for BFBC and CFBC), non-stringy, not too fine, depending on feed system | Generally < 500 mm for BFBC (typically < 50 mm for BFBC and CFBC), non-stringy, not too fine, depending on feeding system |
| Moisture content (wet basis) | < 65 % | < 40 % (typically 10-30 %) | 10-50 % | < 15 % (typically < 10 %) | < 60 % | < 60 % |
| Main feeders | Hoppers or lock hoppers, rotary valves, screw feeders, piston feeders | Screw feeders | Spreader stokers | Pneumatic feeding and/or spreader stokers | Hoppers or lock hoppers, rotary valves, screw feeders, pneumatic feeders, piston feeders | Lock hoppers, rotary valves, screw feeders, pneumatic feeders, piston feeders, can be used in series for better seal |
| Feeding positions | Mostly over-bed except underfeed stokers | Over-bed | Over-bed | Over-bed | Over-bed, under-bed or in-bed | Over-bed, under-bed or in-bed |
| Main feeding problems (Please also see Table 5) | Bridging and blockage, tar accumulation, dust explosion, feed rate fluctuations, poor gas and fuel distribution in the bed | Blockage, insufficient or excess biomass, poor gas and fuel distribution in bed, through-screw is better for ash removal | Blockage, insufficient or excess biomass, poor gas and fuel distribution in the bed | Blockage, insufficient or excess biomass, poor gas and fuel distribution in the bed | Bridging and blockage, tar accumulation in the fed line, dust explosion, feed rate fluctuations, poor gas and fuel distribution in the bed, seal | Bridging and blockage, tar accumulation in the fed line, dust explosion, feed rate fluctuations, poor gas and fuel distribution in the bed, pressure seal and leakage |

Notes: (1) Data from Quaak et al., 1999; Badger, 2002; Agarwal and Agarwal, 1999.

Table 2-5. Summary of fuels requirements and feeders by reactor type (gasification system) [1]

| System | Fixed bed or moving bed gasifiers | | | Fluidized bed gasifiers (BFBG and CFBG) | |
|---|---|---|---|---|---|
| | Downdraft | Updraft | Open-core | AFBG | PFBG |
| Scale range | Generally 0.01–10 $MW_{th}$ | Generally 2–12 $MW_{th}$ | Generally 2–12 $MW_{th}$ | Typically 2-50 $MW_{th}$ for BFBG; 8-150 $MW_{th}$ for CFBG | Typically > 80 $MW_{th}$ |
| Particle size | Generally 20-100 mm, depending on grate openings and feeder dimensions, as well as different reaction characteristics | Generally 5-100 mm, depending on grate openings and feeder dimensions, as well as different reaction characteristics | Generally 1-5 mm, depending on grate openings and feeder dimensions, as well as different reaction characteristics, especially suitable for low bulk density fuels (e.g. rice husks) | Generally 6-50 mm, not too fine or too stringy, depending on feeder and reaction characteristics. Relatively fine fuel sizes are preferred compared to FBC. | Generally 6-50 mm, not too fine or too stringy, depending on feeder and reaction characteristics, more flexible than BFBG, Relatively fine fuel sizes preferred compared to FBC. |
| Moisture content (wet basis) | < 25 % (typically < 12 %) | < 60 % (typically < 40 %) | < 15 % (typically 7-15 %) | < 65 % (typically 10-60 %) | < 65 % (typically 10-60 %) |
| Main feeders | Hoppers or lock hoppers, rotary valves, screw feeders, piston feeders | Hoppers or lock hoppers, rotary valves, screw feeders, piston feeders | Hoppers or lock hoppers, rotary valves, screw feeders, piston feeders, pneumatic feeders | Hoppers or lock hoppers, rotary valves, screw feeders, piston feeders, pneumatic feeders | Hoppers or lock hoppers, rotary valves, screw feeders, piston feeders, pneumatic feeders, in series for better seal |
| Feeding positions | Over-bed (top) | Over-bed (top) | Over-bed (top) | Over-bed, under-bed or in-bed | Over-bed, under-bed or in-bed |
| Main feeding problems | Bridging and blockage, tar accumulation, dust explosion, insufficient or excess biomass, poor gas and fuel distribution in bed | Bridging and blockage, tar accumulation, dust explosion, insufficient or excess biomass, poor gas and fuel distribution in bed | Bridging and blockage, tar accumulation, dust explosion, insufficient or excess biomass, poor gas and fuel distribution in bed | Bridging and blockage, tar accumulation in feed line, dust explosion, feed rate fluctuations, seal, poor gas and fuel distribution in bed | Bridging and blockage, tar accumulation in feed line, dust explosion, feed rate fluctuations, poor gas and fuel distribution in bed, pressure seal and leakage |

Notes: (1) Data from Quaak et al., 1999; Badger, 2002; Agarwal and Agarwal, 1999.

table feeders, pumps and pneumatic feeding systems, as shown in Table 2-6 (Reed, 1981; Bundalli et al., 1983; Bundalli et al., 1985; Bundalli et al., 1986; Ghaly, 1989; Wilén and Rautalin, 1993; Cuenca and Anthony, 1995; Babu, 1995; Gabra et al., 1998; Cummer and Brown, 2002; Henrich and Weirich, 2004; van der Drift et al., 2004). Most of these feeders can inject biomass directly into the reactor, whereas others (e.g. belt feeders) are generally not used for direct feeding. Pumps used for feeding in the coal and concrete industries, have also been tested with biomass (typically for biomass slurries), including feeding to pressurized vessels (Wilén and Rautalin, 1993; UONDEERC and GEI, 2001; Henrich and Weirich, 2004). Lock hoppers and piston feeders are common when there is significant pressurization and the need for a seal in the feeding system, whereas screw feeders, rotary valves and pneumatic feeders have considerable ability to seal and resist modest backpressures. For slurry feeding, pumps can feed and resist backpressure from the reactor. These feeders can provide feed rate control and injection into the reactor, and they are often used in combination rather than separately, especially for continuous operation. More detailed information about feeder types, their applications, properties and costs have been given by Rautalian and Wilén (1992) and Wilén and Rautalin (1993). These feeders have been developed for handling a variety of solids, but they have certain limitations in handling biomass with peculiar physical and chemical properties and/or operating in conjunction with pressurized and/or high temperature reactors. Therefore these feeders need be modified for handling heterogeneous and fibrous herbaceous biomass feedstocks (Babu, 1995).

There is no ideal feeding system for all applications. The chance of problems is ~80% for biomass feeding systems according to industrial experience, the highest risk rating in entire biomass reactor systems. Similar probability of problems occurs for fuel gas clean-up systems (van der Drift et al., 2000). With any feeding system, the feed line temperature and pressure, as

Table 2-6. Main feeders used in biomass industry [1]

| Feeder type | Pressure range | Volumetric capability | Main fuel requirements | Main advantages | Main problems |
|---|---|---|---|---|---|
| Hopper or Lock-hopper | <3.5Mpa$_a$ | 0.1-32000 kg/h | Size: smaller than outlet width, typically the maximum particle size < 1/5 outlet width; Moisture [2]: < 50 %. | Simple construction; compatibility with other feeding mechanisms; low energy consumption, cost effective. | Bridging; ratholes; flushing; aeration failure; pressure seal failure; incorrect choices of construction materials; linings cracked. |
| Screw feeder | <1.5 Mpa$_a$ | Single screw feeder: $1 \times 10^{-4}$ -56 m$^3$/h Twin screw feeder: $2 \times 10^{-4}$ -40 m$^3$/h | Size: smaller than clearance (typically < 1/5 clearance) or two-thirds of minimum pitch, generally < 50 mm; Moisture: < 60 %. | Volumetric feeding; suitable for cohesive and adhesive materials, especially for multi-screws; flexible arrangement; low energy consumption, cost effective. | Sticking on flights, shafts and casing surfaces; blockage; pressure seal failure; mechanical wear; particle attrition; short distance (typically < 6 m); fabrication and installation tolerance |
| Rotary valve | < 1.5 Mpa$_a$ | 0.01-566 m$^3$/h | Size: depending on valve configuration and dimension; Moisture: < 60 %. | Positive displacement; suitable for cohesive and adhesive fuels; low energy consumption and cost effective. | Sticking in pockets and on casing surfaces; jamming; carryover; mechanical wear; particle attrition; seal failure; fabrication and installation tolerance |
| Piston feeder | <15 Mpa$_a$ | 11-115 m$^3$/h | Size: wide range; Moisture: wide range; | Positive displacement; suitable for cohesive and adhesive fuels. | Gas leakage; intermittent feeding; mechanical wear; high energy consumption; fabrication tolerance; installation errors |
| Pneumatic feeder | Not available | Not available | Size: 0.02-50 mm, typically < 6 mm; Moisture: < 15 % (typically < 10 %) | Long distance transport (up to 150 m); flexible arrangement (e.g. vertical, horizontal or inclined); drying during transport; low capital cost. | Strict fuel requirement; gas and dust leakage; blockage; wear; intermittent feeding; high energy consumption; nozzle design failure; fabrication tolerance. |
| Weigh-belt feeder | Atmospheric | 22 kg/h-2500 t/h | Size: wide range; Moisture: wide range; | Suitable for cohesive and adhesive fuels with wide size and moisture range; low energy consumption and cost effective. | Mechanical wear; limited to 15° incline; light dry particles are easily blown off; not suitable for feeding fuels into pressurized reactors. |
| Pump | < 35 Mpa$_a$ | Not available | Slurry | Can feed fuels to high pressure . | Wear; leakage; corrosion |

Notes: (1) Data from Wilson and Dunnington, 1991; Wilson, 1998; Cummer and Brown, 2002; Badger, 2002; Hao et al., 2003.
(2) Wet basis for moisture content, unless otherwise specified.

well as the feed hopper level and other flow conditions (e.g. rotation speeds and torque readings if screw feeders are used), should be monitored to facilitate corrective measures (manual or automatic) to ensure safety and smooth feeding. Such measures might include pressurizing the feed line with air or inert gases to prevent reverse flow, providing agitation or starting spare feeding systems to ensure continuous feeding. For overall plant safety, reliable shut-off should be provided to isolate feed bins and hoppers from reactors. Biomass gasifiers are more difficult to operate and require more sophisticated instrumentation and controls than combustors. Instrumentation and control systems for fuel handling and feeding vary from plant to plant depending on operating policies.

2.2.2 Hopper or locker hopper systems

One of the most common devices for feeding solid fuel directly or indirectly into a reactor is a hopper or lock hopper system. One prominent design of the lock hopper system developed by Thomas R. Miles Consulting Engineers (Cummer and Brown, 2002) is shown in Figure 2-3.

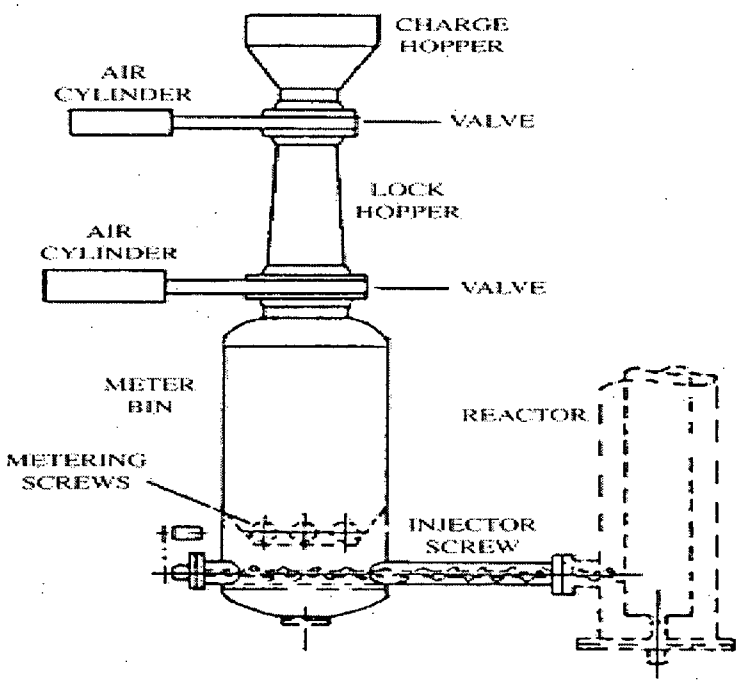


Figure 2-3. Lock hopper feeding system. (Reproduced with permission: Thomas R. Miles Consulting Engineers.) (feed rate: 5 t/h of biomass; reactor pressure: 10–25 bar)

There are many types of hoppers in industrial applications, mainly conical hoppers and wedge-shaped hoppers. A hopper has a converging sloping lower section, typically attached to the bottom of a silo. The hopper flow mainly depends on gravity, but may be assisted by mechanical means inside the hopper (e.g. stirrers) and rotating extractors (e.g. rotary valves and screw feeders). As solids flow from a hopper, the boundaries between flowing and non-flowing regions define the flow patterns. There are three common patterns, internal flow (i.e. funnel flow or core flow), mass flow and expanded flow. For internal flow, solids travel to the outlet through a channel within a stagnant region of solids. The stagnant materials may form a stable rathole. In addition, fine powders can become aerated and flush uncontrollably when bridges or ratholes collapse (Jenike, 1964; Thomson, 1997; van der Kooi, 1997). Internal flow hoppers have variable flow rates, depending on the material properties, hopper configurations, fill level in the hopper and operating conditions. On the other hand, internal flow diminishes the wear to the hopper wall surface, and the reduced investment and maintenance costs make internal flow hoppers attractive in many cases. Mass flow hoppers deliver uniform flow at the outlet and the flow rate is easy to regulate. Erratic flow, channeling, flooding and stagnant regions are avoided, and particle segregation is minimized. Flow of bulk solids in the hopper can also provide a gas seal. Some wear-resistant linings can be used on the inside surface of the hopper. The term "expanded flow" describes flow in a vessel that combines an internal flow converging hopper with a mass flow hopper attached below it. For biomass processes, mass flow hoppers are generally preferred, but it is impossible to avoid internal flow completely due to low bulk density, irregular shape and cohesion of biomass. Internal flow hoppers are common in biomass processes, especially when the flowability of the biomass fuels is poor.

The main problems for hopper flow are formation of bridges (i.e. arching) and ratholes. These problems are especially common for biomass fuels. There are two basic types of bridges:

cohesive and mechanical bridges, formed by different bridging mechanisms. A rathole is a stable void that develops through a mass of static bulk material.

Some hoppers are fitted with discharge aids such as vibrators, air bladders, air injection, fluidizing pads, hopper inserts and various mechanical agitators. Passive flow aids (e.g. special hopper design and fixed inserts) are generally preferred over active aids (e.g. vibrators and agitators), since the latter have large uncertainties in promoting biomass flow and need more maintenance (Marcus et al, 1990; Thomson, 1997; Wilson, 1998). Tests are essential before choosing discharge aids to promote uniform flow in the hopper and in the discharger. For example, vibrators may not work well for wet biomass and fine powders due to high adhesion to the wall surfaces, as well as increased cohesion (Joppich and Salman, 1999).

For a lock hopper system, the lock hopper is used as an air lock or lock vessel to receive biomass at atmospheric pressure and, after pressurization, to discharge biomass under gravity into a feed vessel, i.e. lower hopper. A pinch valve may be installed as the lock hopper discharge valve. The lower hopper operates at almost constant pressure, slightly above that of the reactor, to prevent reverse flow of hot gases and bed materials from the reactor to the feeding system (Marcus et al, 1990; Cuenca and Anthony, 1995; Li et al., 2004).

Lock hoppers work best at < 3.5 MPa. Air injection and pressurizing the hopper by air or inert gases (e.g. nitrogen) can effectively promote hopper flow and prevent backflow (Wilén and Rautalin, 1993; Pletka et al., 1998; Li et al., 2004; Cummer and Brown, 2002; Eriksson et al, 2004). Industrial experience, as well as some research facilities, have widely employed these methods, with a pressure differential of 0.5-20 kPa between the feed hopper and reactor (e.g. McLendona, 2004). Too small a pressure differential cannot effectively improve hopper flow and resist backpressure. Too large a pressure differential increases the feed rate of biomass unpredictably and interferes with reactor performance, while also expending energy and

increasing the difficulties in hopper design and operations. The pressure differential range depends on fuel properties, hopper configurations and reactor requirements.

Hopper flows have been subjected to modeling for many years. Most studies assume perfect spherical particles (elastic or plastic), but non-spherical particles have also been considered (Favier et al., 2001; Cleary and Sawley, 2002). So far no papers explicitly model biomass flow in hoppers due to the complex and unusual properties of biomass particles. Many experimental studies have focused on hopper flow in recent decades, including biomass hopper flow and bridging tendency. The tendency to bridge across openings is mainly a function of particle shape, mean size, size distribution, moisture content, compressibility, particle surface characteristics (e.g. roughness, hardness), and bed depth above the opening. Particles interact with each other in a complex manner resulting in interlocking and interior friction. Increasing the bed depth above the opening increases the tendency to bridge, particularly for fuels containing long thin particles. Wood chips have a relatively low tendency to bridge compared to grass and straw due to their relatively large bulk density, lower compressibility and greater hardness. Changing the particle size or mixing different fuel feedstocks can change the bridging tendency. For example, mixing wood chips into straw and reed canary grass may reduce the tendency of the latter to bridge. Fuels have been compared to roughly determine the relative likelihood of bridging (Bundalli et al., 1983; Bundalli et al., 1985; Bundalli et al., 1986; Mattsson, 1990; Mattsson, 1997; Klausner, 2001; Mattsson and Kofman, 2001/2002/2003; Jensen et al., 2004; Fitzpatrick et al., 2004). Drying and sizing, as well as suitable design of hoppers, can reduce hopper flow problems.

Hopper performance is closely related to the geometric characteristics and dimensions of the hopper (e.g. cone or wedge angle, and outlet dimensions), as well as vessel pressure and filling fraction. Jenike's mathematical methodology is the engineering standard practice for

designing a hopper in terms of calculating the minimum hopper angle and opening size for mass flow (Jenike, 1964; Fitzpatrick et al., 2004). Values of effective angle of internal friction and angle of wall friction are used to calculate the hopper angle and hopper opening size (Jenike, 1964; Fitzpatrick et al., 2004). Jenike's design principle has seldom been used for small hoppers, although it is widely used for designing large hoppers (Bates, 2000). Results from small hoppers are valuable, but special attention must be taken when using these data to design large hoppers. Typically shear cell techniques (e.g. Jenike shear tester and ring shear tester) are used for hopper design. The physical properties and flow properties which need to be considered and measured in hopper design include bulk density, compressibility, cohesion, internal and wall friction, and flow-function. These parameters are in turn affected by particle size, size distribution, particle shape, moisture content and particle surface characteristics. Hopper type, geometric shape and dimensions, as well as the hopper pressure, fill level and refilling procedures, are other factors which can affect design and performance, especially for mass flow hoppers (Jenike, 1964; Arnold et al., 1980; Bundalli and Martinez, 1982; Bundalli et al., 1983/1985/1986; Bates, 1986; van der Kooi, 1997; Fitzpatrick et al., 2004). In addition, hopper outlet shape and dimensions, as well as cone or wedge angle, are very critical to hopper performance. Once the radial stress field in hoppers is formed after initiation of feeding, the outlet plays a major role in hopper transport capacity no matter what mechanical or pneumatic aids are used in the hopper. The outlet width should not be too wide or too narrow compared to the screw diameter if a screw feeder is used as the discharge device. Too narrow outlets can cause bridging and blockage, while too wide an opening causes large stress at the hopper outlet for given bulk solid and hopper level, leading to large power consumption or large blockage possibility. Outlets which are too wide tend to cause dead zones in the corner. The critical arching span for many biomass fuels in a conventional

converging flow hopper is very large if no aids (e.g. inserts, mechanical aids, air injection) are employed.

Despite its great value, the classical Jenike method only covers conical and V-shaped hoppers and does not apply to discharging devices. Arnold et al. (1980) gave a more practical presentation on hopper design. A comprehensive approach to the design of an effective hopper demands not only an understanding of flow mechanics in different flow channels, but of interfacing considerations with available feeding devices (e.g. screw feeder), as well as inserts, mechanical aids and air injection characteristics. Hopper operating pressure is important, but is ignored in almost all previous research. For example, for wedge-shaped hoppers, special care should be taken when the hopper operates at high pressure since the wedge-shape is not well suited to pressure vessels. Higher hopper levels generally lead to higher vertical stress at the hopper outlet and increase higher fullness of screw pockets, tending to increase the feeder load and transport capacity of screw feeding. Hopper level is supposed to have insignificant effects on feeder load beyond a certain height above the outlet of the hopper (e.g. 2 times hopper outlet width) (Arnold, 1980; Nelson, 1996). The hopper can be refilled manually or automatically. Refilling can be activated automatically when a minimum level is reached. Refilling affects hopper performance, as well as discharger performance.

Linings are sometimes used to promote hopper flow, thermal insulation, or for improved wear, erosion and corrosion resistance. These linings include high-molecular-weight polymers, glass-coated steel, various epoxy paints, Teflon, smooth stainless steel, or other refractory linings (e.g. silica ceramic and aluminum oxide). Abrasion-resistant plates and replaceable metal liners are also used for hoppers (Ondik et al., 1982; Bundalli et al., 1986; Thomson, 1997).

When a screw feeder with constant pitch, shaft and screw diameters is combined with the hopper, the screw tends to withdraw material only from the rear (i.e. the upstream end of the

screw), as shown in Figure 2-4. At the front of the hopper, biomass particles are pushed against the front wall, resulting in severe compaction. More uniform withdrawal of biomass particles from the full length of the opening is highly desirable. Several methods have been proposed to restrict flow at the rear, while, at the same time, improving motion at the front of the hopper. For example, internals (e.g. stirrers) can be installed in the hopper, or the transport capability in the screw feeding direction can be increased (e.g. by increasing the pitch, increasing screw diameter or reducing shaft diameter along the screw), but these measures may complicate fabrication, operation and maintenance or risk pressure seal failure. Such measures may not work, especially for herbaceous biomass of low bulk density and for pressurized operations. Pressurizing the hopper has been widely used to promote hopper flow and resist backflow from the reactor in biomass processes.

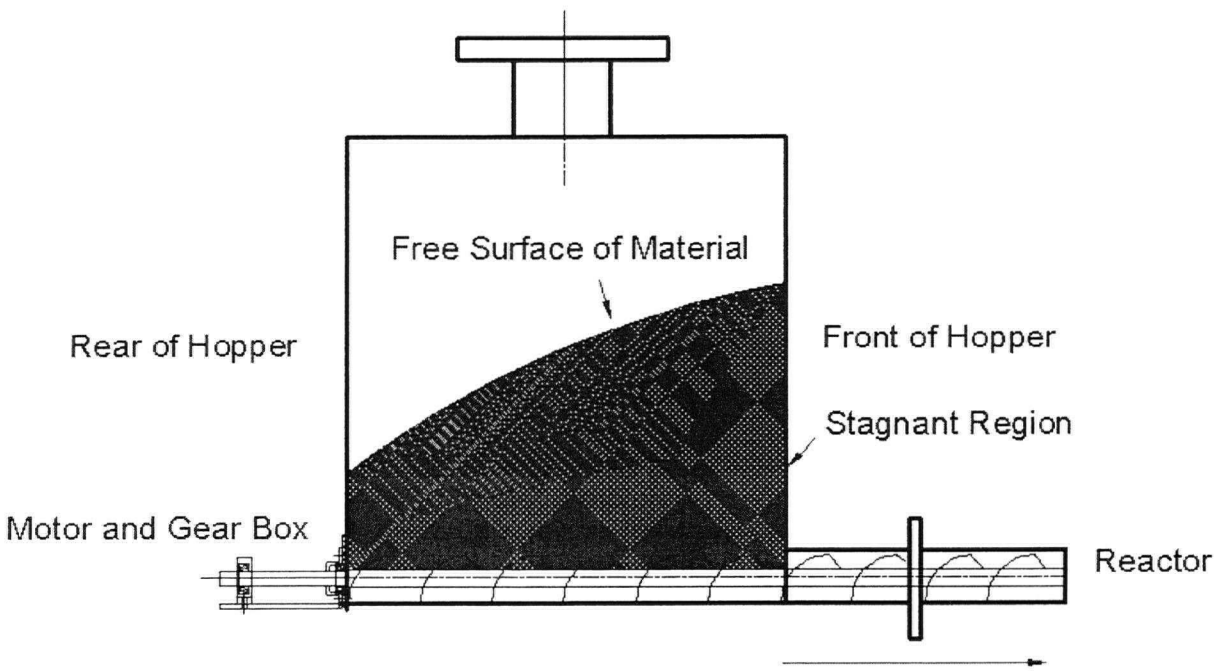


Figure 2-4. Non-uniform flow in hopper.

The huge size of industrial hoppers leads to difficulties in manufacturing (e.g. weld techniques) and installations besides the special hopper design. Lock hoppers have high pressures and pressure fluctuations, while temperature is normally < 420° C. Temperature-resistant pressure vessel steels with good mechanical properties (e.g. strength, toughness, fatigue and stress rupture), are leading candidates for construction materials for hoppers and lock hoppers (Ondik et al., 1982). A reliable and economical hopper-feeder system for biomass may be achieved by a converging flow hopper, an effective extractor and mechanical or pneumatic aids. Correct hopper profile and bed height of material on the feeder are essential for satisfactory performance. Hopper level is best determined by non-intrusive measurements (e.g. ultrasonic, radioactive, radar or laser level detectors).

### 2.2.3 Screw feeders

#### 2.2.3.1 Operating principles

Screw feeders are common feeding devices which can deliver bulk solids over a wide range of feed rates. Single and twin-screw feeders are common types for biomass feeding.

Screw feeders are volumetric devices. The volume delivered depends on the screw flight diameter and shaft diameter, pitch (distance between adjacent flights) and fullness (degree of fill) (Bell, 2003). In theory, the volumetric capacity is linearly proportional to the screw rotational speeds, and most published results show that the power requirements are also proportional to speed within the limits of normal operation (up to about 10 rpm) (Carleton et al, 1969; Wilson, 1998). If the solids entering the screw are compressible (like most biomass fuels), the mass delivered per unit time may not be proportional to rotation speed. The velocity of the solid material as it is conveyed is a vector having an angle to the direction of rotation. As the screw rotates, bulk solids move in a helical path of direction opposite to that of the screw (Bates, 1969; Bates, 2000). Volumetric efficiency is defined (Roberts, 1996) as ratio of volumetric flow rate

to maximum theoretical throughput with screw feeder completely full and particles moving at the feeder speed without slip and/or rotational motion as described in Chapter 6. The frictional effects of the solids on the screw flights and adjacent casing, together with the configuration of the screw itself and material properties, determine the efficiency. Higher filling fraction and less slip lead to higher efficiency. The efficiency decreases as the clearance between the discharge casing surface and screw flight tips increases (Roberts, 1996; Bell et al., 2003). Feed rate fluctuations, variability (i.e. coefficient of variation) and linearity are commonly used to describe the accuracy and stability of screw feeding (Joppich and Salman, 1999; Bell et al., 2003).

2.2.3.2 Main problems and solutions

When biomass is fed into a reactor, especially a pressurized reactor, the screw compresses the feedstock into a compact plug. Compaction of the plug is usually aided by tapering the feed channel or gradually reducing the pitch of the screw as it nears the reactor as shown in Figure 2-5.

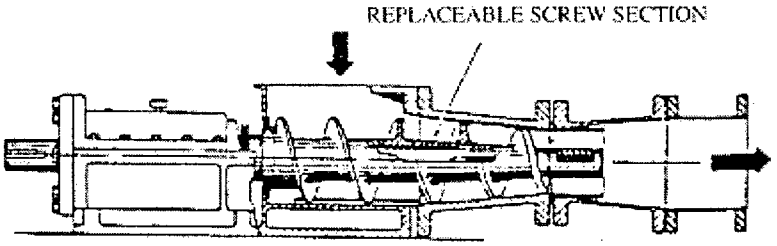


Figure 2-5. Screw feeder for wood chips.
(Cummer and Brown, 2002)

The feed plug then forms a barrier, preventing backflow of gases and reactor material. A backpressure adjuster (hydraulically adjustable throttle) can be employed to regulate the strength of the plug formed in the feeder and also its pressure sealing against backpressure. Owing to the conical shape of the backpressure adjuster, which also breaks extrudates, no

extrudate breaker is required in the reactor when feeding biomass. Sweden and Canada have employed this kind of screw feeder or its modified version in the pulp and biomass industries (Wilén and Rautalin, 1993; Cummer and Brown, 2002). When reducing pitch screws are used, the short pitch may more easily bridge in the screw pockets, especially for cohesive and/or adhesive materials, decreasing the transport capacity of the screw. Compression of biomass to form a seal plug in the screw casing only by reducing the pitch is not always effective and reliable, due to various properties of solid fuels (e.g. compressibility, permeability, cohesion and adhesion) and operating conditions (e.g. filling fraction of screw pockets, dilation of solids, screw vibration).

Attention must be given to both pitch and hopper design to make the compression and seal plug in the screw feeder effective and reliable. Even so, pressurization of the feed hopper is also advisable. For tapered feed channels, Bates (2003) advised that the screw should terminate before the casing so that the material is pushed forward within a confined channel. However, he did not advise converging the delivery pipe to increase the seal pressure, although this is used in the biomass industries. There are several other choices for the feed channel, such as a pipe with a converging part and enlarged mouth (similar to a venturi tube). Other screw geometries have also been recommended for hopper-screw feeders to form a seal plug or to increase the transport capacity in the feeding direction (e.g. increasing pitch, variable shaft diameter, and variable screw flight diameter). The challenge lies in maintaining both uniform flow and the pressure seal. Bundalli et al (1986) and Nelson (1996) found that variable pitch screws appear to have little benefit in achieving uniform flow along the full length of the opening for biomass (e.g. hog fuel and wood chips). Nelson (1996) also introduced multiple screw feeders (screw rotation speed 1-6 rpm) with tapered shaft diameter to successfully feed wood chips, hogged bark and other wood refuse to a power boiler.

Further experiments for different kinds of screws and channel geometries have shown promise, especially for combinations of different screw configurations. However, modifying screw or channel geometries are likely to increase manufacturing difficulties and costs. Other methods of promoting flow in hopper-screw feeders include various inserts and mechanical agitators, air injection and aeration, linings of the hopper surface and pressurization of the hopper (Bundalli et al, 1986; Nelson, 1996). A system for feeding bagasse to a fluidized bed gasifier, with a plug screw feeder followed by a shredding conveyer, has also been tested (Turn, 1977).

Screw feeders are commonly combined with a hopper or lock hopper system, rotary valve feeders, piston feeders or pneumatic feeding, as well as pressurization inside the feed line. In the UBC CFB plant gasifier (Li et al., 2004)(see Chapter 4), a lock hopper and a hopper-screw feeder were combined, and pressurized air was introduced into the feed hopper to assist feeding biomass into the pressurized circulating fluidized bed gasifier

The main problems of screw feeders are slippage, blockage and feed rate fluctuations. Lack of flow is usually caused by a bridge or a rathole in the hopper if the motor drive works well. Blockage is related to overload of materials, as well as fuel properties (e.g. large particles with large density and high strength, cohesive or adhesive particles). Cyclic variations due to angular position of screw flight rotation, intermittent bridging in the hopper, solids build-up on the screw and blockage in the screw feeder, as well as under- powered drive, may all cause feed rate fluctuations. As a rule, the clearance should exceed the particle size to prevent interlocking of particles between the screw flight tips and the channel, especially for relatively strong particles (e.g. wood chips), although backpressure may also prevent the particles from moving forward.

Special attention must be paid when using screw feeders on cohesive or adhesive fuels (e.g. $< 100$ μm in size or moisture content $> 50\%$) due to cohesive or adhesive build-up and blockage.

Most common feeders shear material from a head load (e.g. hopper load), which can lead to compaction. Such compaction should be avoided or at least minimized. Fibrous materials (e.g. wood wastes and chips) are especially prone to compaction and plugging. In addition, particle attrition and mechanical wear can lead to a higher fraction of fines, which can also cause blockage in the screw feeder and elutriation of small particles in fluidized bed reactors. Reversing screw rotation may help to break blockages. Care is needed that the drive power is large enough to feed fuels and that the screw feeder is strong enough to resist the reversing axial forces required to disrupt the blockage.

A brush-like device can be placed at the outlet of the screw feeder to help homogenize the flow and disperse the solids evenly in the reactor. It has also been suggested (e.g. Bates, 2003) that the delivery pipe be chamfered at an inclination less steep than the angle of repose of the biomass. This allows the advancing plug to shield the total inner surface of the screw casing, thereby avoiding accumulated build-up which obstructs the discharge. The disadvantage is that the discharge pipe protruding inside can interfere with the flow in the reactor. Moreover, the delivery pipe may encounter high temperature, severe abrasion and corrosion. A vibrator has also been tested to homogenize screw feeding of wood powders with mean size 0.368 mm and moisture content < 10% (Joppich and Salman, 1999). Caution must be exercised when using vibrators and agitators to stimulate flow of cohesive or adhesive fuels (e.g. too fine or too wet), since this can cause undue compaction, aggravating the problem.

For cohesive materials that tend to arch across the hopper outlet, it is desirable to have as wide a slot as possible. A pair of screws installed side-by-side provide the same slot width as a single screw of twice the diameter. However, the volumetric capacity of the twin screw is one-half that of one single larger screw. An even more pronounced effect is seen when three or more parallel screws replace a single larger screw. However, these arrangements are relatively rare in

the biomass industry. For multiple screw feeders (e.g. twin screw feeders), intermesh or non-intermesh, as well as the rotation direction (e.g. upward or downward relative to the casing), spacing of the non-intermesh screws, and clearance between the screw and the casing, are all important. Generally intermesh twin screws, with screws of opposite hand and counter-rotating, are used for cohesive material since they can prevent arching and self-clean one another (Wilson, 1996). The principal drawbacks of multiple screws are the increased cost and mechanical complexity of the drive train. Nelson (1996), Bates (2000) and Arnold (2003) provide more information regarding multi-screw feeders.

To prevent reactions in the feed line, measures should be taken to prevent the system from reaching temperatures at which pyrolysis commences. Inert gases (e.g. nitrogen) are often used to provide pressurization seal to the reactor and prevent reactions in the feed line. A large ball valve can be installed between the reactor and feeder for safety (Cummer and Brown, 2002).

Minor manufacturing eccentricities, shaft deflection and imperfect fabrication tolerances often result in poor flow, increased power consumption, and excessive compaction of material within the screw, especially for variable-pitch and tapered-shaft screws. Special operator attention is needed when feeding to gasification and combustion reactors. The feeding system can be controlled separately, or by a central control system. Torquemeters, revolution counters, zero speed switches and level detectors are among the simplest instruments to monitor and adjust hopper-screw feeding systems. Whatever control system is used, it should be able to detect flow problems (e.g. no flow, reduced or zero screw speed, or significant torque fluctuations) and take corrective measures (e.g. reversing the motor for several seconds, starting mechanical or pneumatic aids, pressurizing gases in the hopper, starting spare feeding systems or stopping the drive and shutting down the plant). The control system is essential for

continuous and reliable operation of the entire system, as well as for safety and minimizing operator attention.

2.2.3.3 Design guidelines

Screw designs depend on fuel properties, various feeder combinations and system requirements. The principles of screw feeders design are to ensure feeding capacity and uniform flow without bridging, ratholes and blockage and to prevent backflow of gases and bed materials from the reactor. The shaft and flights must be able to endure the torsional and bending loads, as well as the axial force. The parameters needed to design screw feeders are bulk density, compressibility, cohesion strength, internal and wall friction (Jenike, 1964; Bates, 1969; Bates, 1986; Carson, 1987; Maton, 1994; Yu and Arnold, 1996; Yu and Arnold, 1997; Bates, 2000).

Short pitch screws (pitch less than screw diameter) are generally recommended for inclined conveyors and screw feeders due to increased mixing, reduced dilation of the solids and higher filling fraction (Tsai, 1994; Maton, 1994). The minimum ratio of pitch to the screw diameter should exceed 0.25 to ensure reliable operation (Haaker et al., 1994). Pitch, screw flight diameter, shaft diameter, flight thickness and clearance determine the effective spaces for particle movement and therefore affect feeding capacity. Both too large or too small a pitch can decrease the feeding capacity. There should be an optimal pitch corresponding to the maximum feeding capacity for any screw feeder. 1-25 mm is a reasonable range for clearance depending on screw configurations, with standard clearance for most materials being ½" (12.7 mm). Too large a clearance causes efficiency loss, while too small clearances tend to cause particle jamming and severe mechanical wear. Too large flight thickness and too large ratio of shaft diameter to flight diameter may decrease transport capacity and cause a loss in efficiency. Too thin flights or ratios of shaft diameter to flight diameter which are too small may lead to

manufacturing difficulties and insufficient strength. For variable pitch screws, special attention must be given to the pitch nearest the outlet end of the hopper (i.e. start of the choke section), as well as the pitch at the discharge end, since they play a major role in determining the transport capacity of the feeder.

Screw feeders are well suited for hoppers with elongated rectangular outlets. The screw feeder design must be coordinated with the hopper design, so that bulk solids do not arch or rathole across the hopper outlet. Constant-pitch screws are generally not suited to rectangular hopper outlets as they only withdraw material from approximately one pitch length near the rear of the hopper (Figure 2-4). Increasing pitch, tapered shaft (reducing shaft diameter) and tapered screw diameter (i.e. increasing flight diameter) are commonly used to increase the screw capacity in the screw feeding direction. Obtaining sealed plugs is usually accomplished by reducing pitch, reducing screw diameter, missing flights in one section for plug formation, or tapering the feed channel. U-shaped, instead of V-shaped, troughs promote flow from the hopper outlet into the screw pockets and prevent fuels from accumulating on the hopper walls (Carson, 1987; Bates, 2000). The hopper outlet length is generally ~3-9 times the outlet width, while the length of the choke section in the hopper-screw feeder is at least one pitch (Bates, 1969) or twice standard pitch (CEMA, 1980; Yu and Arnold, 1997). A longer choke section may improve the pressure seal at the expense of power consumption. Special screws (e.g. ribbon and coreless screws) are recommended to transport cohesive materials, but may not be good for metering and direct injection of biomass into the reactor. Twin-screw or multi-screw feeders can be designed according to fuels properties and outlet width. For more information on design of screw feeders see Carson (1987), Maton (1994), Van der Kooi (1997), Bortolamasi and Fottner (2001) and Bell et al. (2003).

The effect of rotation speed of screw feeders has received limited attention for biomass. 15-100 rpm, and typically < 70 rpm, are usually recommended (CEMA, 1980; Carson, 1987; Bates, 2000; Arnold, 2003). For free flowing materials, slow screw speeds tend to cause high efficiency and feeding irregularity, whereas relatively high speeds reduce fluctuations, but also decrease efficiency, as well as enhancing wear and particle attrition. Owing to the poor flowability of biomass and plug seal inside the screw feeder, relatively slow screw speeds (e.g. 2-40 rpm) are preferred although higher screw speeds have also been reported (Pletka et al., 1998; Bahillo et al., 2003). Slow speeds increase mixing inside the feeder (Tsai, 1994). On the other hand, screw feeders with a cantilever structure, common in feeding biomass into reactors, may shake or vibrate when the rotational speed is increased. Shaking or vibrating may cause erratic flow, as well as mechanical wear and other operating problems. Some experiments have indicated that higher screw speeds reduce the blockage tendency inside the screw feeder, possibly because of higher dilation at relatively high screw speed and intense interlocking of particles at lower speeds, as well as blockage break-up due to significant shaking or vibration at higher speeds (Rautenbach. and Schumacher, 1987).

Most commercially available screw feeders are < 1 m in diameter, typically < 0.6 m. Oversized screws, while providing an extra margin of capacity, may lead to large feed rate variability, difficulties in manufacturing, installation and maintenance, and uneven distribution of fuels in the reactor. Multiple point feeding should be considered in such cases. One can choose larger screw feeders with fewer feed points, or smaller screw feeders and more feed points. The choice depends on the scale and type of the reaction system, reactor type and material properties. Standard screw feeders (with. pitch equal to flight diameter) should be considered first. Modification (e.g. variable pitch, shaft, screw diameter, or tapered feed channel) may be unavoidable for biomass applications.

Although screw conveyors with up to 45% fill and no feed rate control can be more than 50 m long, screw feeders have much shorter length, especially for cantilever structures. Intermediate bearings are needed if the screw feeder is too long. In general, screw feeders shorter than 6 m long work well, without too much deflection for cantilever structure, including inclined cases (Bates, 2000). Cantilever-mounted screw feeders have the advantages of flexible design, fabrication, installation and maintenance over screw feeders with bearings at both ends or intermediate bearings. They allow easy-clean, direct end outlet configurations, simple direct-acting cut-off valves, and plug seals to prevent pressure differentials, high temperature and reactions in the feed line. Screw feeders are usually horizontal. Inclined screw feeders (typically with inclination to the horizontal $< 15^{o}$) are sometimes used to overcome headroom problems.

The maximum design temperature for industrial screw feeders is generally about $550^{o}$C, whereas for biomass gasification and combustion, the reactor temperature can be $\sim 1000^{o}$ C. Sometimes the screw is water-cooled to prevent biomass devolatilization, and formation of char and tar. Caution is needed in the choice of construction materials. Mechanical wear and corrosion of the screw and housing are among the concerns. Stainless steel and carbon steel are used for most industrial applications. For biomass, stainless steel (usually SS 310 or SS 316) is preferred for long-term operation. The housing surfaces can be coated with liner (e.g. epoxy, ceramic or aluminum oxide) to prevent wear, corrosion and /or high temperature. Wear-resistant steel coating is also employed on key flight areas. As a rule, a relatively smooth screw finish and a relatively rough trough or casing finish are used to reduce particle rotation and to increase the efficiency.

Scale-up of a screw feeder is generally based on semi-empirical methods or on experimental studies using dynamic similarity. The motor must be large enough to allow the screw feeder to start up. Analytical formulae in the form of Equation 5-128 (Roberts, 1996) and

semi-empirical formulae (e.g. CEMA formulae) are commonly used to calculate the power requirement, but they may differ by as much as 30-40 % from experimental results. Note that Roberts (1996) adopted three empirical pressure ratios, as shown in Figure 5-6, to calculate the axial force and ignored the choke section. In fact, all such equations neglect the choke section and starting torque, which is also important in industrial practice and is typically several times (at least 1.5-2 times) larger than the operating torque due to the higher initial shear strength of confined bulk solids, particularly for firm granular materials (e.g. wood pellets) or very cohesive/adhesive fuels (Bates, 2000; Bortolamasi and Fottner, 2001). However, in some cases the starting torque is almost the same as the operating torque (Carson, 1987). However, it is advisable to choose a motor large enough (e.g. to work in the range of 30-75 % of its nominal capacity) to allow for normal start-up.

Torque is primarily a function of the geometric characteristics of the screw and hopper, and fuel flow properties (e.g. internal and wall friction angle). The screw speed has little effect on torque except for fuels with large shear strength. The vertical stress at the hopper outlet for initial and flow conditions can be estimated based on approaches recommended by Jenike (1964/1977) and Arnold et al. (1980). For plug screw feeder design and selection, power and torque requirements should be calculated with special attention since a large proportion of the feeder power is needed to compact the materials. The mechanics and power requirements of screw feeders have been analyzed (Metcalf, 1966; Carson, 1987; Roberts, 1996; Yu and Arnold, 1997; Bortolamasi and Fottner, 2001). Screw feeders work at combined torsional and bending loading, usually with torsion as the governing load. Imperfect design and fabrication tolerance, as well as manufacturing eccentricities or material deficiencies, often cause service failure (Aghdam, 2002; Sattarifar, 2002; Sattarifar, 2003).

## 2.3 Some Related Problems in Biomass Properties and Feeding

### 2.3.1 Effects of biomass physical properties on feeding and fluidization

Generally all physical properties, as well as chemical properties, affect feeding. Particle size and shape should meet requirements of feeding systems and reaction. Too large or too fine particles present difficulties in feeding (e.g. bridging and blockage) and reactor operations, affecting reliability and efficiency. Large particles with irregular shape, such as long and thin particles, tend to cause mechanical bridging in the feeder, as well as channeling in fluidized bed reactors. Fine particles tend to cause more elutriation in the reactor and larger tendency to bridge and block in the feeding system due to cohesion and adhesion effects, especially for particle sizes < 100 μm. High moisture content promotes cohesion and adhesion, which may cause problems in the feed line, including bridging and blockage. Pelletizing and briquetting often improve flow properties of biomass, making it easier to feed. In addition, Pelletizing some biomass feedstocks (e.g. bagasse and cane trash) and then grinding the pellets to powder can lead to easier feeding compared to crushed bagasse and cane trash, although Pelletizing and grinding pellets increases costs and reduces overall energy efficiency, mainly because Pelletizing and grinding lead to harder particles, higher bulk density, reduced sliver-shape effects and larger particles.

### 2.3.2 Effects of feeding rate and feeding fluctuations

Fluctuations in the fuel feed rate may affect the operation of the entire biomass plant. Feeding problems cause immediate change in the air/fuel ratio, triggering temperature excursions. Bed agglomeration and sub-optimal carbon conversion can be attributed, at least in part, to feeding problems. Too large feeding fluctuations may disturb the reactor operation and cause fluctuations of the fuel gas constituents (e.g. CO, $H_2$ and $CO_2$, etc.) (Asadullah et al., 2003). Typically fluctuations should be limited to within ± 15% (Gabra et al., 1998). The

possibility of bridging and blockage, including intermittent stoppage, must be minimized to ensure smooth and efficient feeding. Monitoring the feed line is essential to take immediate measures in time to handle the problems.

2.3.3 Effects of feeding positions

Biomass feedstock can be fed above, below, or directly into fluidized bed reactors. As a rule, large particles with large particle density are introduced from the top, whereas small particles with relatively low particle density are fed under-bed or by in-bed methods. Under-bed and in-bed feeding provide longer residence times promoting high gasification or combustion conversions. But pre-crushing and drying are then needed to make sure that the particle size is small enough (e.g. < 6 mm) and that the moisture content is no higher than 15% (typically < 10%). Screw feeders, rotary valves and piston feeders, temperature-resistant or with a cooling system, can also be used for under-bed and in-bed feeding. In smaller reactors, fuels can enter the reactor through sidewalls, while for large units, nozzles for fuel injection can be arranged uniformly on the air distributor. In coal feeding to fluidized bed reactors, one injection point is needed for each 1-1.5 $m^2$ of bed surface (Oka, 2003). Erosion and corrosion of pipelines for pneumatic conveying can be severe. Moreover, pressure sealing is more difficult for under-bed and in-bed feeding to prevent backflow of gases and bed materials from the reactor. Despite deficiencies, pneumatic in-bed conveying may be the best way to feed fine biomass (Oka, 2003).

Over-bed feeding is often accomplished by gravity from elevated hoppers with the aid of a screw feeder, rotary valve, piston feeder or pneumatic feeder, all of which also act as seal devices to prevent backflow of gases and bed materials into the feeder hopper. Over-bed feeding reduces complexity, but may allow the feedstock to become entrained without reacting and yield lower carbon conversion (van den Enden and Lora, 2004). One such feed point is needed for every 3-4 $m^2$ of bed surface according to experience from the coal industry (Oka, 2003).

Studies comparing top feeding with bottom feeding of a gasifier have shown differences in product distribution (Corella et al., 1988; Vriesman, 2000). However, comparison is difficult since other reactor-specific parameters can also influence the results. From the gasification experiments of Vriesman (2000), the position of the feeding points affects conversion of fuel-N to ammonia and CO levels. Top feeding leads to a lower conversion of fuel-N to ammonia and a higher percentage of product CO. No significant differences in carbon conversion to tar were found for top and bottom feeding.

2.3.4. Multi-point feeding and spare feeders

When the diameter of the reactor is relatively small, it is relatively easy to distribute the particles inside the reactor. However, large size fluidized beds in commercial power production may not achieve good mixing of fuel within the bed. Poor mixing of fuel yields uneven combustion or gasification. In such cases, multiple inlets are required (Cummer and Brown, 2002; Oka, 2002).

Each gasifier or combustor is usually served by several feeders or feed lines that enable full feeding capacity to be maintained in the event of a blockage and allow routine maintenance on one of the units at a time (McLellan, 2000). This also limits the dimensions for screws and feed channels to meet feed capacity requirements. Feed rates can be adjusted by screw rotation speeds or turning on/off some feed points for multi-point feeding.

2.3.5 Pressurization in feeding system

One function of biomass feeding systems is to provide reliable seals to prevent backflow of gases and bed materials, as discussed above. Seal failure may cause serious problems, such as gasification or pyrolysis in the feed line, feed stoppage, or dust explosions. A mechanically stable plug with a suitable low gas permeability can help resist backpressure. Typically if the leakage velocity of gases from the reactor is lower than the plug velocity towards the reactor,

the feed line can be successfully isolated from the reactor. Piston and screw feeders are often used to form a seal plug inside the feeder to prevent backflow. Other feeders, such as lock hoppers, rotary valves and pumps, can also provide effective seals. Even so, air or inert gases (e.g. nitrogen) are often used to pressurize feeders to minimize gas leakage and ensure sufficient pressure seal to the reactor, especially for pressurized processes.

### 2.3.6 Feeding for co-combustion and co-gasification systems

There is increasing interest in co-combustion of two or more fuels. For example, one can co-fire biomass and coal in existing boilers, or gasify biomass in a separate gasifier and burn the syngas with coal in a boiler. Co-gasification of various biomass feedstocks, particularly wastes and coals, is also promising.

Efforts are being made to develop technologies to co-feed various biomass fuels, particularly with wastes and coals, or fuels and sorbents (DOE, 2001). Co-feeding different biomasses may cause rapid changes in the feed line, as well as the reactor, making control difficult. Even biomass sources differing only in moisture content can cause significant variations in operating conditions and cause control problems. Fuel characteristic variations must be mitigated by blending before co-feeding (Tillman, 2000; Badger, 2002). As a result, separate feeding system may be used to increase reliability and fuel flexibility. Fuel processing, tar formation, ash slagging, catalyst deactivation, emissions, and boiler tube corrosion associated with co-firing are major barriers to co-combustion and co-gasification systems (Green et al., 1991; EERC, 2000; Bahillo et al., 2003; Savolainen, 2003).

## 2.4 Summary and Objectives for This Project

In this chapter key biomass properties and biomass feeding techniques for combustion and gasification are presented.

Biomass is organic matter with potential for renewable energy applications. Biomass feedstocks are potentially available as mill wastes, urban wastes, forest residues, agricultural residues and energy crops and roughly fall into three forms according to their size and states: granular material (typically > 0.5 mm), powder (typically < 0.5 mm) and slurry. Biomass tends to have peculiar physical properties and various chemical properties. Properties may change with time and environmental conditions. Cohesion, internal and wall friction, bulk density and compressibility all affect flow.

Smooth feeding is essential for biomass conversion processes. Reliable, efficient and economical feeding systems suitable for a wide range of biomass fuels are required for biomass utilization. Biomass feeding plays a critical role in continuous and reliable operations of reactor systems. Hopper or lock hopper systems, screw feeders (including single screw and twin screw feeders, etc.), rotary valve feeders, piston feeders, pumps and pneumatic feeding systems are the main feeders used for biomass. They may appear together, rather than separately, especially for continuous operations and pressurized processes, to ensure smooth, reliable and efficient feeding and pressure seals. Bridging, ratholes, blockage, seal failure, feeding fluctuations, reaction in the feed line, mechanical wear and corrosion are major problems for biomass feeders. Pressurization of feeders can promote and prevent backpressure. Monitoring and excellent control systems are essential for safety and reliable operations.

Lock hopper and piston feeders are mainly used for significant pressurization, while other feeders, such as screw feeders, rotary valve feeders and pneumatic feeders feed biomass into reactors, with considerable ability to resist backpressure. Pumps are mainly used for slurry feeding, with excellent ability to overcome backpressure. Feeding rate and fluctuations influence reactor performance. Feeding methods and feeding location depend on biomass properties and system requirements. Multi-point feeding and spare feed lines may be necessary

for large-scale biomass plants. Slurry feeding has some advantages over dry feeding. Co-feeding of different fuels or materials is also of increasing interest.

Not enough research has been done on biomass feeding systems, and little detailed information has been published. Varieties of feeders and materials make it difficult to formulate general rules. Hoppers and screw feeders are among the most widely used feeders for biomass processes. Screw feeders share similarities with rotary valve feeders in lateral motion and with piston feeders in axial motion of bulk materials.

Although screw feeders have been studied extensively, screw feeding of biomass and the effects of the choke section, as well as variations of the screw casing and seal plug examination, have been ignored in previous research. No reports of previous detailed experiments with respect to biomass feeding could be found, making the present study unique.

The present study focuses primarily on screw feeding of biomass materials. The objectives of the present work are to determine experimentally and also by modeling:

(1) Mechanisms of blockage;

(2) Effects of mean particle size, size distribution, shape, moisture content (10-60%), bulk density and compressibility on screw feeding of biomass;

(3) The importance of the choke section on torque requirements and transport functions in screw feeding of biomass;

(4) The influence of casing variations (e.g. tapered section and extended section) on torque requirements, blockage and seal plug formation;

(5) Prediction of the efficiency of screw feeding of biomass.

(6) The effects of pressurization of the hopper on torque requirements and feeder performance.

# CHAPTER 3. PARTICULATE FLOW LOOP

## 3.1 Introduction

The Particulate Flow Loop was designed and fabricated to investigate the fundamentals of the movement of clusters of particles of different well-characterized shapes through narrow gaps or constrictions as they are conveyed by water. The work undertaken in this equipment was intended to provide background information and a better understanding of key hydrodynamic multiphase flow factors which cause, or contribute to, stalling and blockage in particulate feeding systems such as those used for the feeding of biomass.

### 3.1.1 Flow in a rectangular duct

Experimental study and modeling of flow, both laminar and turbulent, in rectangular ducts of different aspect ratios have been widely conducted in past decades (Han, 1960; Hartnett et al., 1962; Goldstein and Kreid, 1967; Sparrow et al., 1967; Fleming and Sparrow, 1969; Beavers et al, 1970; Launder and Ying, 1972; Gessner, 1973; Melling and Whitelaw, 1976; Gessner and Po, 1976; Gessner and Emery, 1981; Su and Friedrich, 1994; Islam et al., 2002). The local flow structure in a rectangular duct may be dominated by traverse flow, commonly known as secondary flow (Gessner and Emery, 1981). This secondary motion can be caused by different mechanisms and strongly depends on the Reynolds number and aspect ratio of the cross-section. Secondary flow not only causes a reduction of the volumetric flow rate for a given pressure drop, but it also causes the axial velocity field to be distorted. Furthermore, the secondary motion produces an increase in wall shear stress towards the corner. A clear understanding of the evolution and consequences of secondary flow in ducts in its fully developed state is quite important. Little is known about the structure of internal turbulent flows, even in straight ducts

(Su and Friedrich, 1994). Various turbulence models have been developed and tested for turbulent flow in rectangular ducts of different aspect ratios.

The entrance length, $L_e$, where fully developed flow is achieved is commonly expressed in terms of the dimensionless downstream position, $L_e/(D_H \,\mathrm{Re})$, at which $U_c/U_{cfd}$ along the axis reaches 0.99 (McComas, 1967; Goldstein and Kreid, 1967, Garg, 1985), where $D_H$ is the hydraulic diameter of the duct and Re is the Reynolds number based on $D_H$ and the mean fluid velocity, while $U_c$ and $U_{cfd}$ are the local centreline fluid velocity and fully developed centreline fluid velocity, respectively. Generally, $L_e/D_H \approx 0.0567\,\mathrm{Re}$, and $L_e/D_H \approx 0.693\,\mathrm{Re}^{0.25}$ for laminar and turbulent flow, respectively (Brodkey and Hershey, 1988). At similar Reynolds numbers, the development length for turbulent flow is less than for laminar flow. A number of researchers have determined the entrance length for both laminar and turbulent flow in circular and rectangular ducts (Klein, 1981; Su and Friedrich, 1994). Han (1960) gave a dimensionless entrance length of 0.066 for a 2:1 ratio rectangular duct and 0.0427 for a 4:1 ratio rectangular duct for incompressible laminar flow. Goldstein and Kreid (1967) investigated laminar flow development in a square duct using Laser Doppler Velocimetry and reported measured and predicted dimensionless entrance lengths of 0.09 and 0.0752, respectively. Sparrow et al (1967) performed experiments on laminar flow to obtain a dimensionless entrance length of 0.08 for a 5:1 duct and concluded that hydrodynamic development in a 2:1 duct was somewhat slower than in a 5:1 duct, whereas Fleming and Sparrow (1969) obtained approximately 0.07 for 2:1 duct and 0.052 for 5:1 duct for the dimensionless entrance length of laminar flow. Wiginton and Dalton (1970) recommended a dimensionless entrance length of 0.08 for incompressible laminar flow for a rectangular duct. Garg (1985) found dimensionless entrance lengths for laminar flow of 0.0734, 0.075, 0.0533 for square, 2:1 and 5:1 ducts, respectively.

Gessner and Emery (1981) suggested that fully developed flow for turbulent flow occurred beyond $L_e / D_H = 120$. Klein (1981) found that the length required for full flow development in a pipe may exceed 140 pipe diameters. According to these viewpoints, fully developed flow has rarely been achieved.

Although the solution to laminar fully developed flow through a round pipe is the well-known parabolic profile, the corresponding analytical solution for flow through a channel of rectangular cross-section is less well known. McComas (1967) and Nguyen and Wereley (2002) provided experiments for fully developed laminar flow through a rectangular duct. Sufficiently far from the wall, the analytical solution in the short-side direction converges to the well-known parabolic profile for flow between infinite parallel plates. In the long-side direction, the flow profile is unusual in that it has a very steep velocity gradient near the wall, which reaches a constant value away from the wall.

Experimental research and numerical prediction of turbulent flow and turbulence-induced secondary flow have also been widely conducted (Launder and Ying, 1972; Gessner, 1973; Melling and Whitelaw, 1976; Gessner and Emery, 1981; Su and Friedrich, 1994; Eggels et al, 1994). Kim et al (1987) applied Direct Numerical Simulation (DNS) to investigate fully developed turbulent flow between two parallel plates at a Reynolds number based on mean centreline velocity and channel half-width of 3300. The general characteristics of turbulent statistics showed good agreement with experimental results of Eckelmann (1974) and Kreplin and Eckelmann (1979), except in the wall layer. A similar DNS was performed at a larger Reynolds number of 7900. Several other direct simulations of wall-bounded turbulent flows have been reported (Spalart, 1988; Lyons et al, 1991; Gavrilakis, 1992; Kristoffersen and Andersson, 1993). These computations all considered turbulent flow in a geometry with a rectangular cross-section or over a flat plate. Flows in cylindrical cross-section geometries differ

from those in ducts of rectangular cross-sections (Patel and Head, 1969; Eggels, et al, 1994). Generally, $U_{cfd}/U_m$ in cylindrical pipes exceeds that in channel flow. Despite the fact that square duct flow shows a secondary flow pattern, Gavrilakis (1992) reported $U_{cfd}/U_m$=1.33, in very close agreement with pipe flow predictions of Eggels, et al (1994), whereas Kim et al (1987) recommended $U_{cfd}/U_m$=1.16 for turbulent plane channel flow. This illustrates that additional wall friction at the side-walls of the pipe/square duct causes the mean flow to differ from plane channel flow. An abrupt entrance caused transition to turbulence at a Reynolds number of approximately 2000, whereas with a smooth entrance, transition Reynolds numbers were as high as 7,000 (Hartnett et al., 1962). Eckert and Irvine (1957) and Hartnett (1962) recommended critical Reynolds numbers of 4300, 2200, 6000 for rectangular ducts of aspect ratio 1:1 (smooth entrance), 1:1 (abrupt entrance), and 3:1 (smooth entrance), respectively. Re=6000 is taken as the transition Reynolds number for the rectangular duct of aspect ratio of (2.68:1) in the present study. A measure of flow development is the blockage factor, defined by the ratio of the centreline velocity to the mean velocity (i.e. $B = 1 - U_m/U_c$) (Sovran and Klomp, 1967; Klein, 1981). Based on the experimental data of Carpinlioglu and Gundogdu (1998), the entrance length for two-phase particulate flow decreases as Re increases.

3.1.2 Flow past obstacles and through nozzles

Circular and non-circular (e.g. rectangular) jets have been studied experimentally and theoretically for both single and multiphase flows (Leschziner and Rodi, 1981; Ogg, 1983; Nadeau et al., 1991; Miller et al., 1995; Ye et al., 1995; Tazibt et al., 1996; Ye and Kovacevic, 1999; Rembold et al., 2002; Eskin and Kalman, 2002; Uchiyama and Naruse, 2003). This previous work mainly focused on jet velocity profile, turbulence, particle motion, and cavitation. Nozzle configuration and nozzle design have also been investigated (Garrison and Byers, 1980;

Eisert and Dennenloehr, 1981; Li et al., 1995; Gotoh et al., 2000; Kwon, 2002). Flow past obstacles is also widely investigated, concentrating on velocity and pressure fields, turbulence and flow characteristics (Shieh, 1980; Islam et al., 2002). A survey of related literature indicates that nozzle or jet flow, and flow over obstacles are complex, especially for multiphase flow. The basic parameters influencing the flow are Reynolds number and turbulence, fluid properties, particles properties (e.g. size, shape and density), particle loading, obstacle or constriction dimensions and shape, and flow direction. Particles may block constrictions, due to particle-particle/particle-wall/particle-turbulence interactions. Like the blockage factor defined for turbulent pipe flow, a blockage index is defined in the present investigation of the blockage probability of particles in constrictions. No previous record of this could be found in previous studies.

### 3.1.3 Saltation, suspension and surface creep

Bagnold (1941) defined three transport modes for sand particles: saltation, suspension and surface creep. The term "saltation" denotes particles being picked up and displaced by the fluid. Due to the gravity, the particles return to the bed surface when they collide with other particles, exchanging mass, momentum, and energy with the bed. Due to collisions, some particles are ejected or rebound away from the bed with a lift-off velocity (Zheng et al., 2005). Saltation depends on how particles ejected into the flow are accelerated, and how, on impact with the bed, collisions lead to ejection of other particles into the flow stream (Anderson 1989; Nishimura and Hunt, 2000). The fluid threshold velocity (velocity that must be exceeded for saltation to be initiated) is generally thought to be greater than the impact threshold (fluid velocity that must be exceeded for saltation to be maintained). At higher fluid speeds, particles are transported upwards by turbulent eddies and by this means can be transported far downwind. This is the

process of suspension. Surface creep (also called reptation) describes particles making short hops, and rolling and jostling along the surface.

Saltation is the principal transport mechanism of wind-blown sand particles, accounting for 75% of total sand transport. Particle saltation has received considerable attention, and several researchers have investigated the trajectories of saltating particles. Most previous studies have obtained trajectory data by photography (White and Schulz, 1977; Willetts and Rice, 1985; Nalpanis et al., 1993; Zhang et al., 2006). Despite the considerable work, the mechanism by which particles leave the surface and the velocities of saltating particles are still not well understood. The saltation of sand particles in air has been shown to be a stochastic process. The ejection process, i.e. particles rebounding or not, angle of ejection and velocity of ejection, are all stochastic (Zhang, 2006). The forces acting on a single saltating particle include lift (Magnus force associated with particle rotation and Saffman force due to shear), drag, gravity, etc. (Saffman, 1965; White and Schulz, 1977). The relative influences of these forces depend on the environmental conditions, complicating numerical prediction. In addition, the effect of the size, shape and density of particles on saltation, complex interactions among the particles, and turbulent fluid flow are not clearly understood. As a result, an accurate theoretical model of the saltation process has not yet been developed (White and Tsoar, 1998; Zhang et al., 2006; Herrmann et al., 2006).

For fibres in the suspensions, a complication is that fibers do not always move affinely with the fluid, but rather aggregate (Mason, 1950; Kerekes et al. 1985; Kerekes and Schell, 1992; Schmid et al., 2000). Much is known about the motion of isolated fibers in low Reynolds number flow. Forgacs and Mason (1959) and Goldsmith and Mason (1967) have theoretically and experimentally investigated the flow induced deformation of single fibers in simple shear flow. Less is known about the processes by which fibers flocculate. Mason (1950) postulated

that flocculation is a dynamic equilibrium process, with fibers continuously entering and leaving flocs, both rates being equal at steady state. Kerekes (1995) has identified dimensionless groups that help predict flocculation in specific experiments.

Particle-turbulence interactions, particle-particle/particle-wall interactions and collisions, and particle motion, have also been widely investigated in previous research (Fukagata et al., 1998; Huber and Sommerfeld, 1998; Li et al., 1999; Hagiwara et al., 2002).

Figure 3-1 gives key details for the two main experimental systems utilized in the current project: a Particulate Flow Loop and a Biomass Feeding System, in terms of the fluids and particles investigated, the relative particle concentrations, and the principal forces acting on the particles as they travel through the two devices. The key factors which can lead to blockage and the main factors influencing blockage are also listed.

Possible modes of blockage are identified in Table 3-1, together with a "Blockage Index" used below to categorize the frequency and seriousness of blockages or partial blockages.

The principal objectives of the particulate flow loop were to:

(1) Demonstrate how blockage/bridging occurs.

(2) Perform experiments to measure the probability of blockage/bridging as a function of particle size, shape, density and compressibility.

Table 3-1. Proposed characterization of blockage type for Particulate Flow Loop

| **Blockage Type** | Particulate Flow Loop | Blockage Index |
|---|---|---|
| 1 | Stable blockage | 1 |
| 2 | Unstable blockage, blockage breaks up on its own within 5 s without intervention from the operator. | 0.5 |
| 3 | No blockage | 0 |

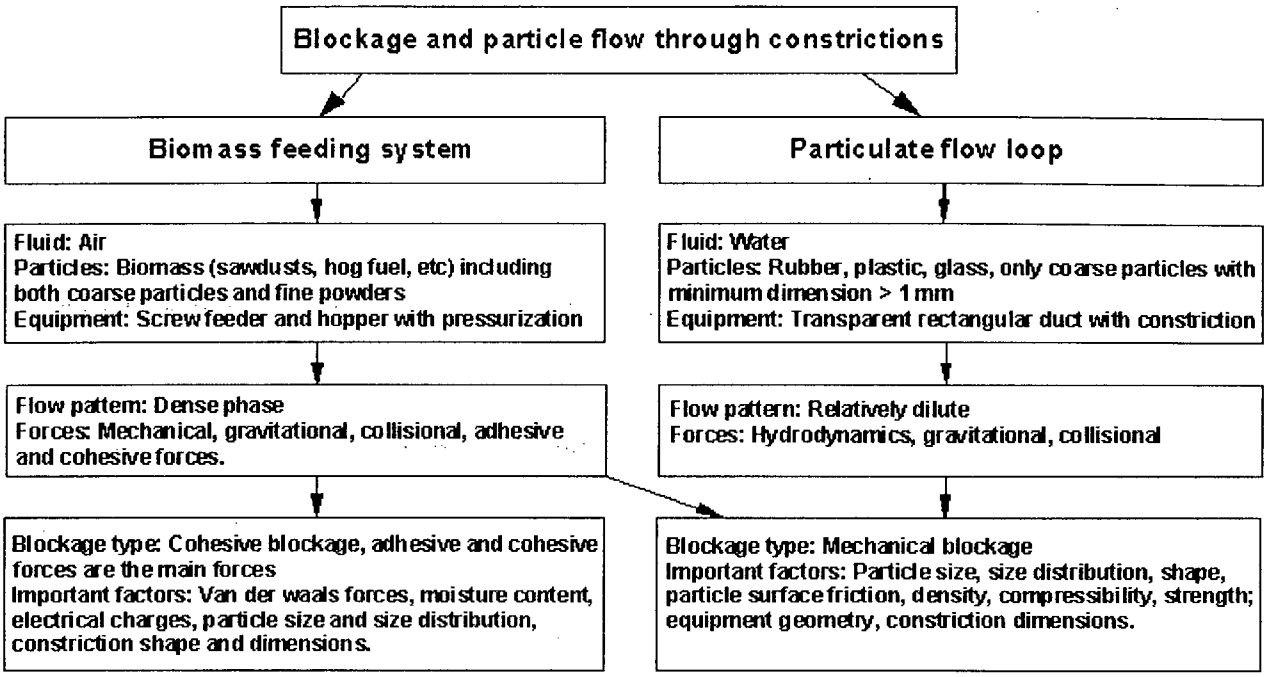


Figure 3-1. Schematic of Biomass Granular Feeding Study

Table 3-2. Reynolds number and water mean velocity for experimental tests in Particulate Flow Loop

| Water mean velocity, $U_m$ (m/s) | Reynolds number, Re, based on water mean velocity and hydraulic diameter of duct | Reynolds number, $Re_h$, based on water mean velocity and half-height of duct |
|---|---|---|
| 0.02 | 730 | 650 |
| 0.04 | 1450 | 1300 |
| 0.06 | 2200 | 1960 |
| 0.08 | 2900 | 2610 |
| 0.1 | 3600 | 3260 |
| 0.2 | 7300 | 6520 |
| 0.3 | 10900 | 9780 |
| 0.4 | 14500 | 13000 |
| 0.5 | 18100 | 16300 |
| 0.6 | 21800 | 19600 |
| 0.7 | 25400 | 22800 |
| 0.8 | 29000 | 26100 |
| 0.9 | 32600 | 29400 |
| 1 | 36000 | 32600 |
| 1.1 | 39900 | 35900 |
| 1.2 | 43500 | 39100 |

## 3.2 Experimental Set-up and Methodology

The test section is a rectangular duct (25.4 mm (wide) x 66 mm (high) x 600 mm (long)) with interchangeable narrow gaps of different shapes (ramp, circular, and rectangular constrictions). Upstream of the test section, there is a rectangular duct of length 5.18 m to ensure that the flow of the water and particles is fully developed before reaching the constriction. The Reynolds number based on the mean velocity of the conveying water and hydraulic diameter ($D_H$ = 0.0367 m) of the rectangular duct ranged from ~730 to 44,000, as shown in Table 3-2. The corresponding mean velocity of the water was 0.02-1.2 m/s. From previous work, the maximum development length for laminar flow in rectangular duct is $L_e/(D_H \mathrm{Re}) = 0.09$ (Goldstein and Kreid, 1967), whereas the development length is 140 times the hydraulic diameter for turbulent duct flow (Klein, 1981). Hence fully developed flow was achieved for turbulent flow ($\mathrm{Re} > 6000$) in the rectangular duct in the present study. When $\mathrm{Re} < 2000$, fully developed laminar flow could be achieved. For $2000 < \mathrm{Re} < 6000$, the flow was unable to reach the fully developed state. A screen with 0.71 mm openings is installed upstream to prevent particles from entering the pump (Model: LEESON 62RS1C-3.5, head: 15.2 m, capacity: 0.001 $m^3/s$). To ensure higher water flow rates and pressure, pressurized water (<83 $PSI_g$, <0.005 $m^3/s$) was introduced into the flow loop as shown in Figures 3-2 and 3-3. The rectangular duct is horizontal (confirmed with a level) with its centreline 39 mm above the laboratory floor. A plastic tank of capacity 300 litres containing a baffle separating the return flow region from the outlet region, is installed 2.64 m above the ground. Three vent holes on the upper plate of the duct (50, 350 and 1380 mm in front of the test section) are connected to plastic tubes to disengage air bubbles to ensure that only water and particles (two phases) pass through the constriction. Rubber and plastic particles (dimensions: 2 to 50 mm, density: 860-2100 $kg/m^3$) of different shapes (spheres, cylinders, disks and cuboids) were employed in the

experiments, with water as the conveying fluid. Water absorption of all particles was very low (typically < 1 wt% over 24 hours, and < 0.03 w% within 24 hours for PTFE and polyethylene particles). Therefore, change of physical properties (e.g. density) of all particles during flow is neglected. Photos of the various particles are provided in Figure 3-4. Physical properties appear in Table 3-3. Shore A durometer measurements (see Table 3-3) indicate that rubber particles with durometer 40-70 in the present study had significant compressibility. These rubber particles could experience elastic deformation. The particle density was obtained by putting a known mass of particles into a graduated cylinder with water (for particles with densities greater than that of water) or alcohol (for particles with densities are less than for water and greater than for alcohol). By keeping the liquid volume at certain value (e.g. 500 ml) before and after the particles are added to the graduated cylinder and measuring the corresponding mass, the particle volume and hence particle density, were obtained.

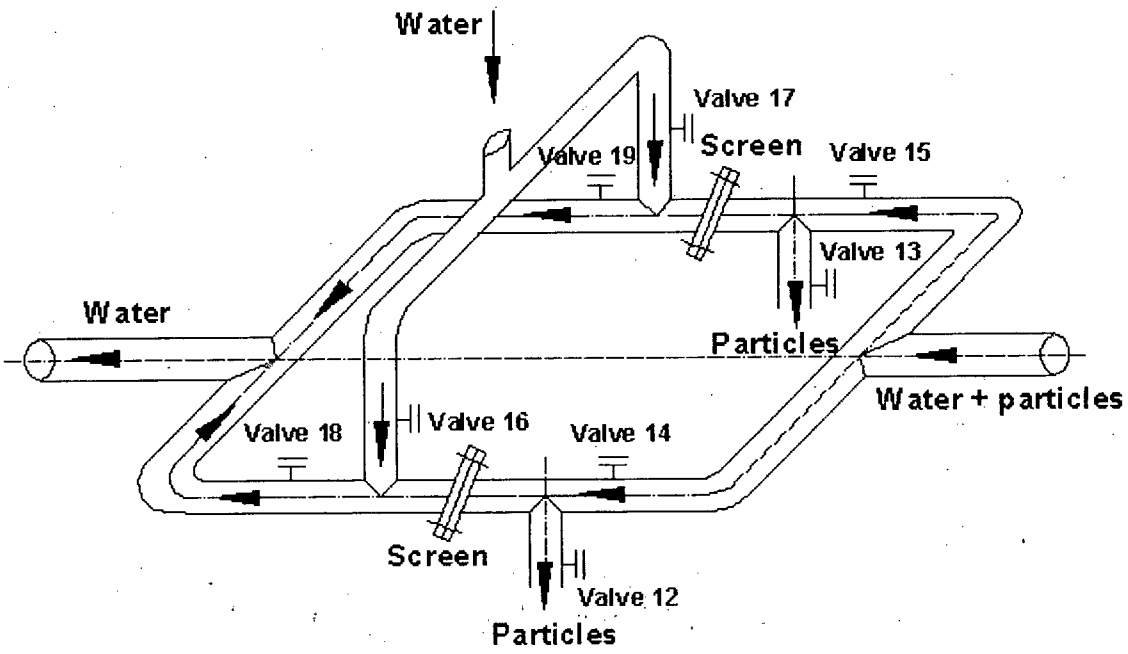


Figure 3-2-1. Schematic of filter and particle recycle

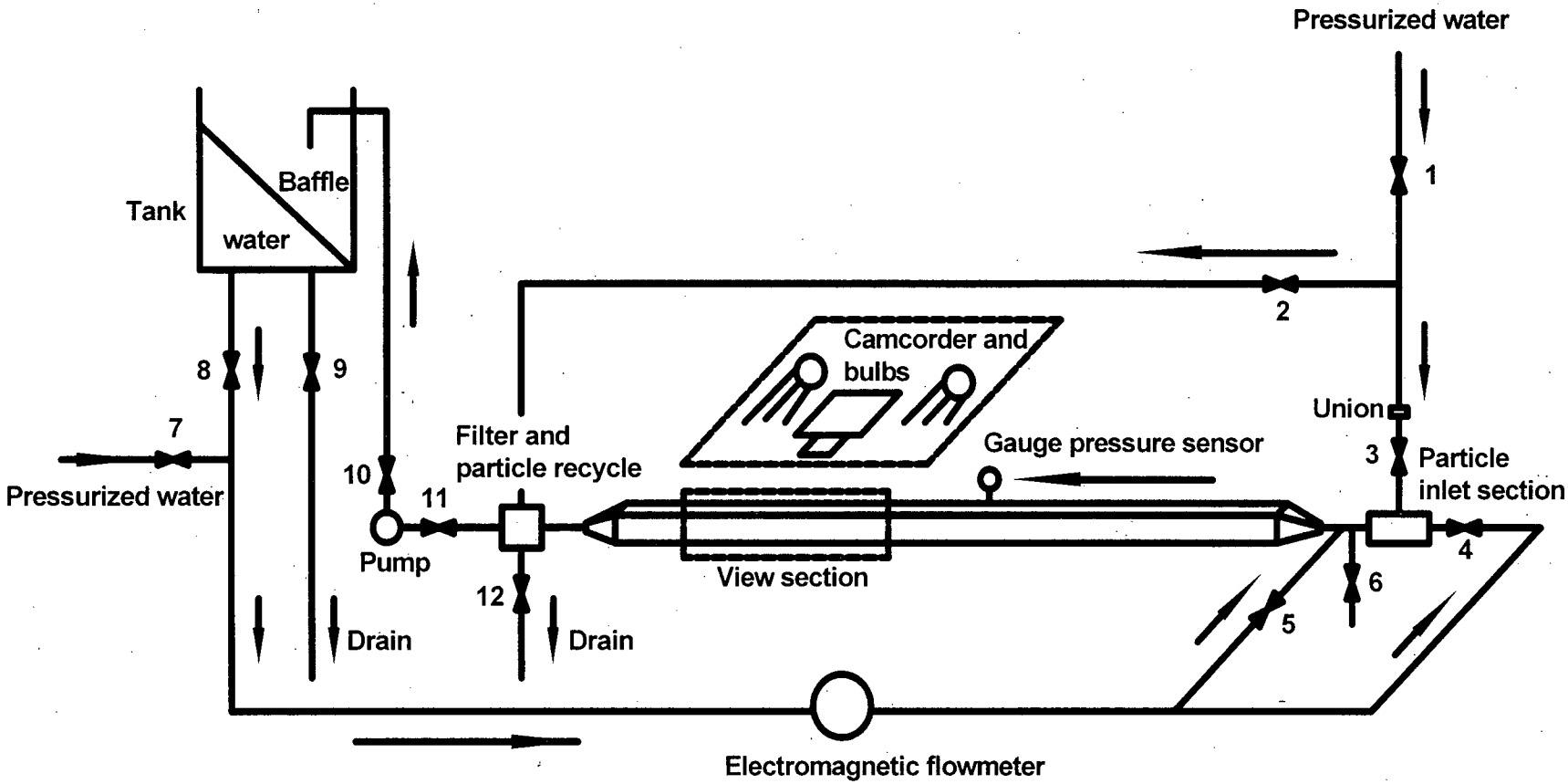


Figure 3-2-2. Schematic of Particulate Flow Loop

Figure 3-2. Schematic of Particulate Flow Loop and filter and particle recycle system

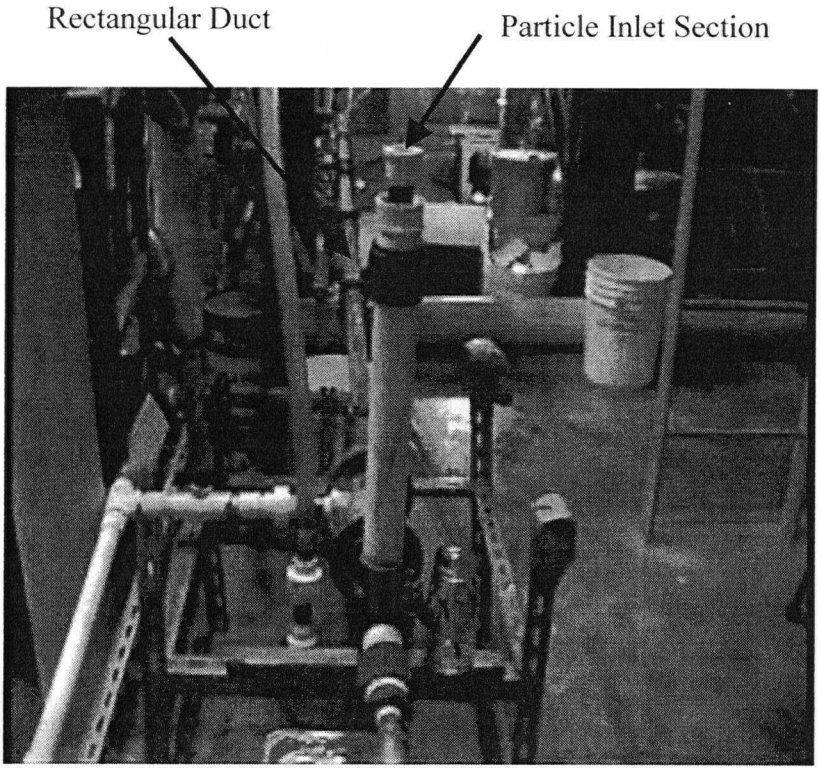


Figure 3-3. Photo of Particulate Flow Loop

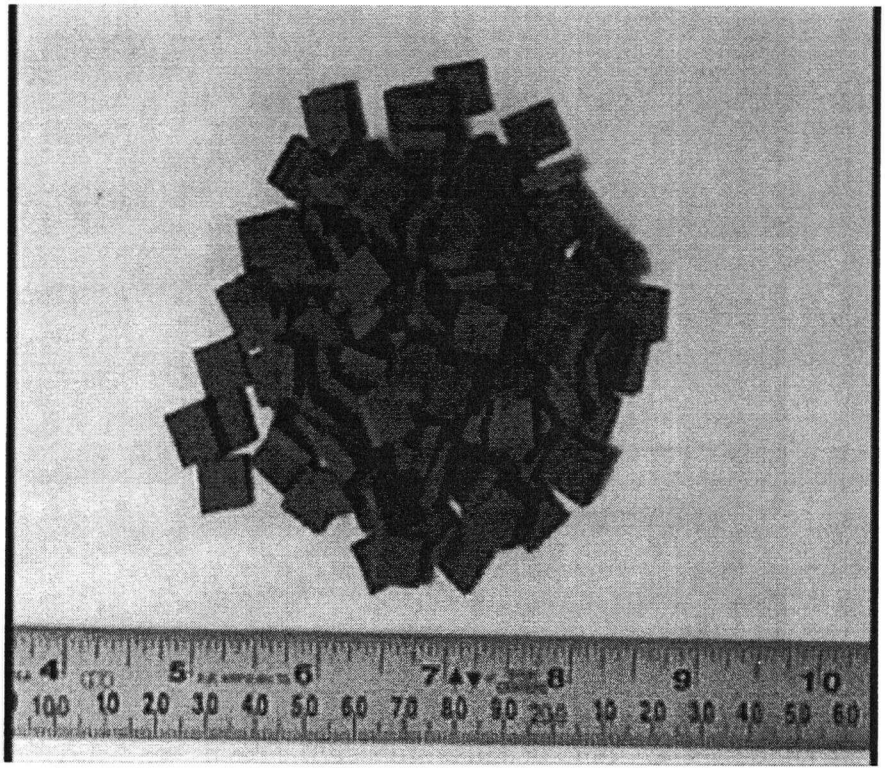

Figure 3-4-1. Photo of silicon-rubber70-cuboid-1 particles (7x7x3 mm)

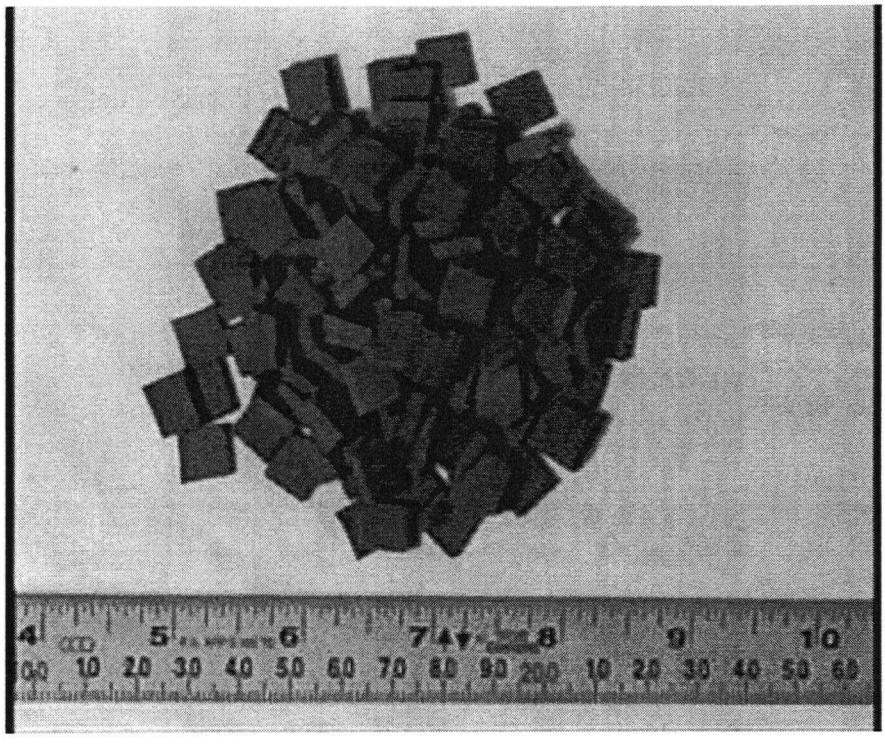

Figure 3-4-2. Photo of silicon-rubber70-cuboid-2 particles (9x9x3 mm)

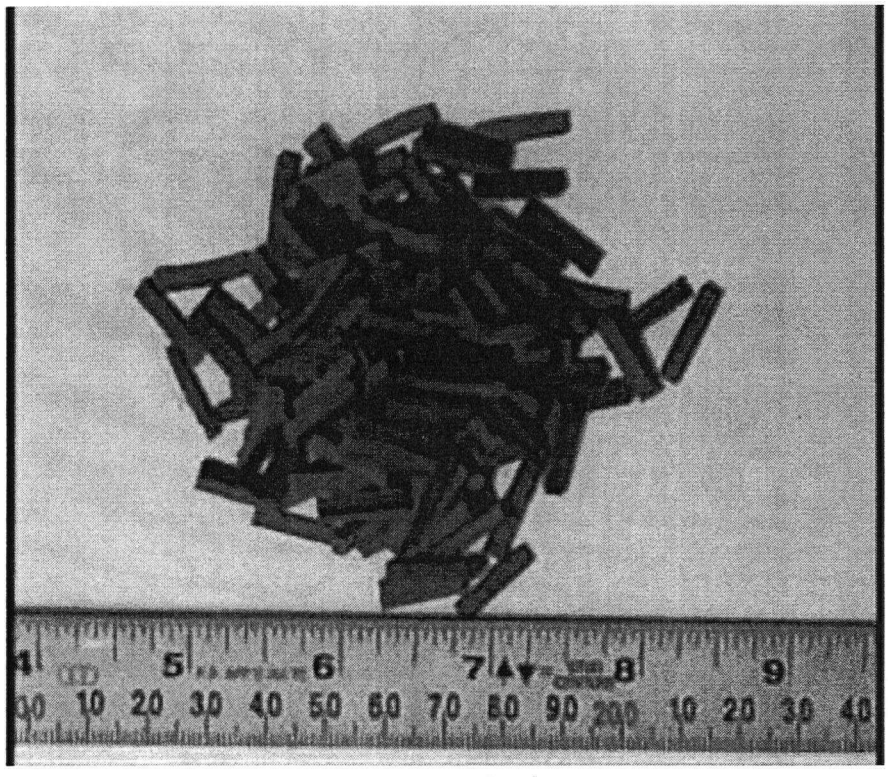

Figure 3-4-3. Photo of silicon-rubber70-cuboid-3 particles (15x5x3 mm)

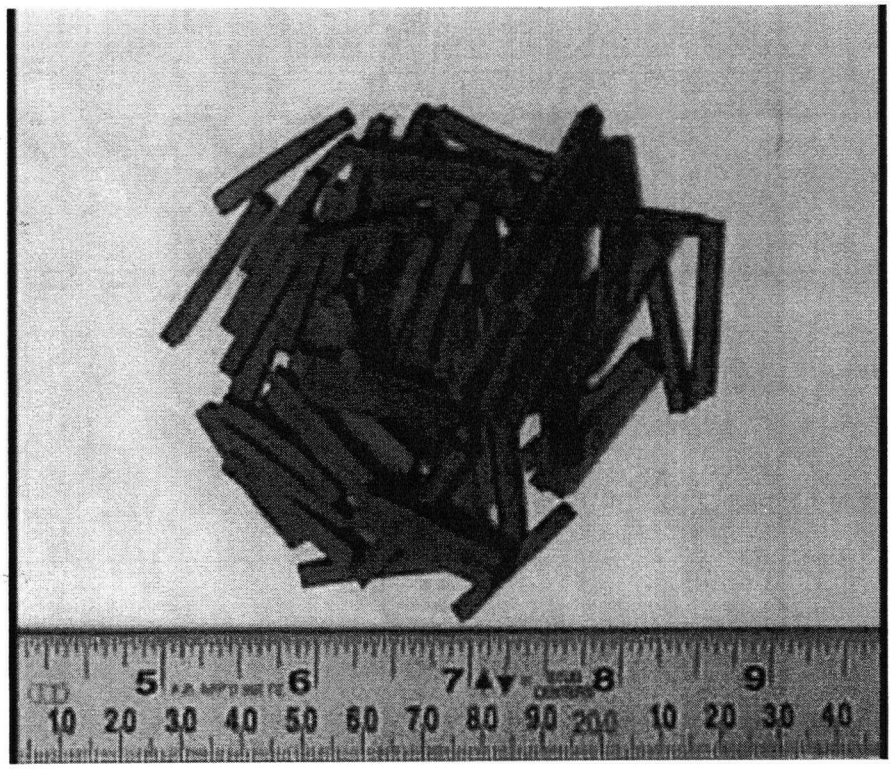

Figure 3-4-4. Photo of silicon-rubber70-cuboid-4 particles (25x3x3 mm)

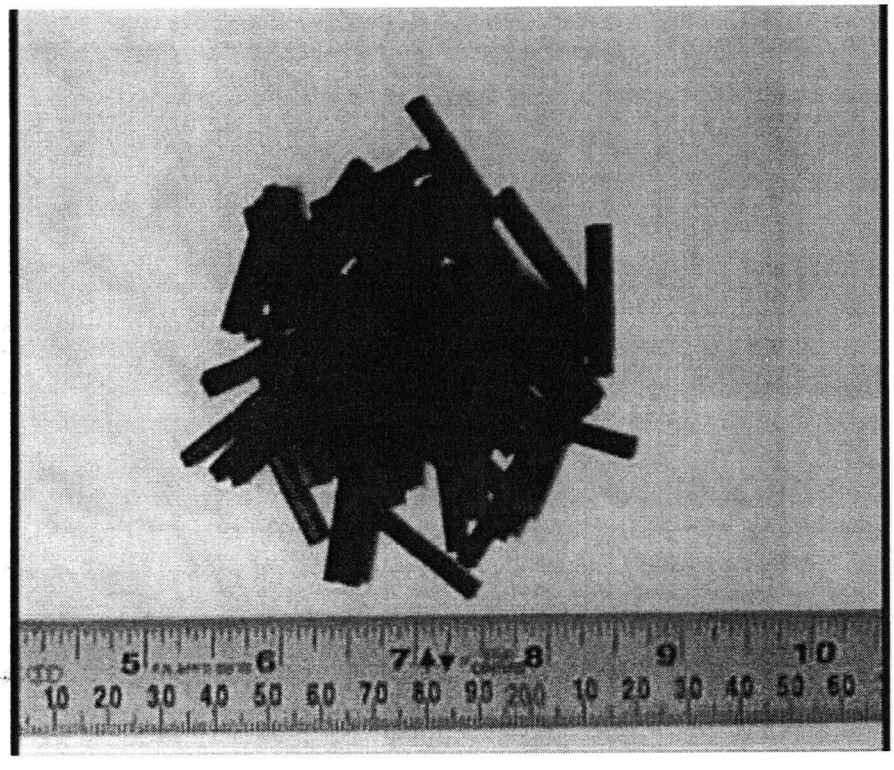

Figure 3-4-5. Photo of neo-rubber60-cuboid-4 particles (25x3x3 mm)

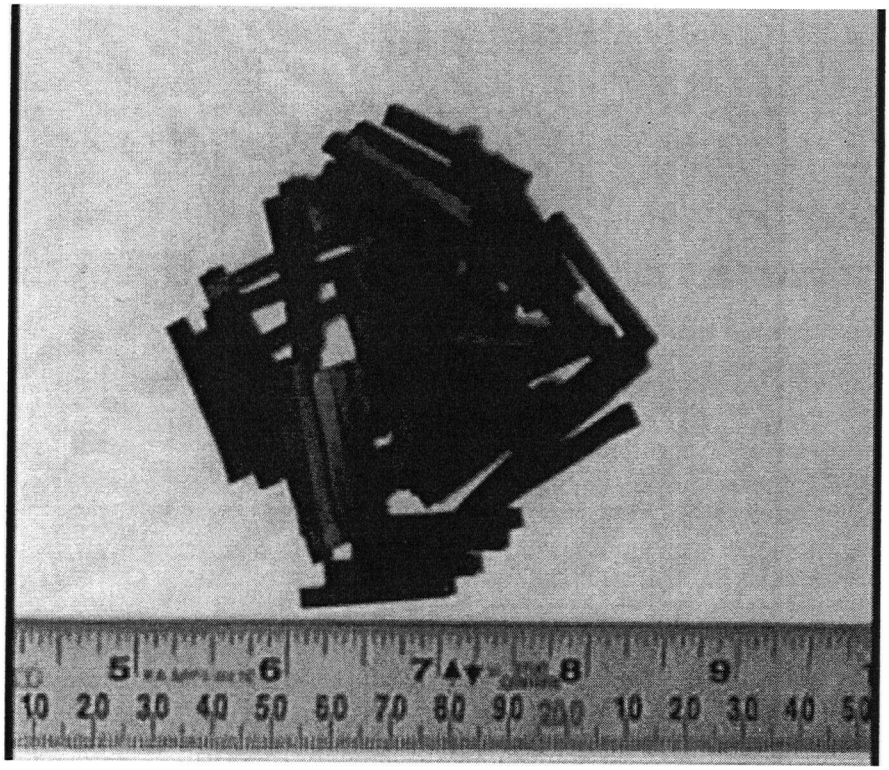

Figure 3-4-6. Photo of neo-rubber40-cuboid-4 particles (25x3x3 mm)

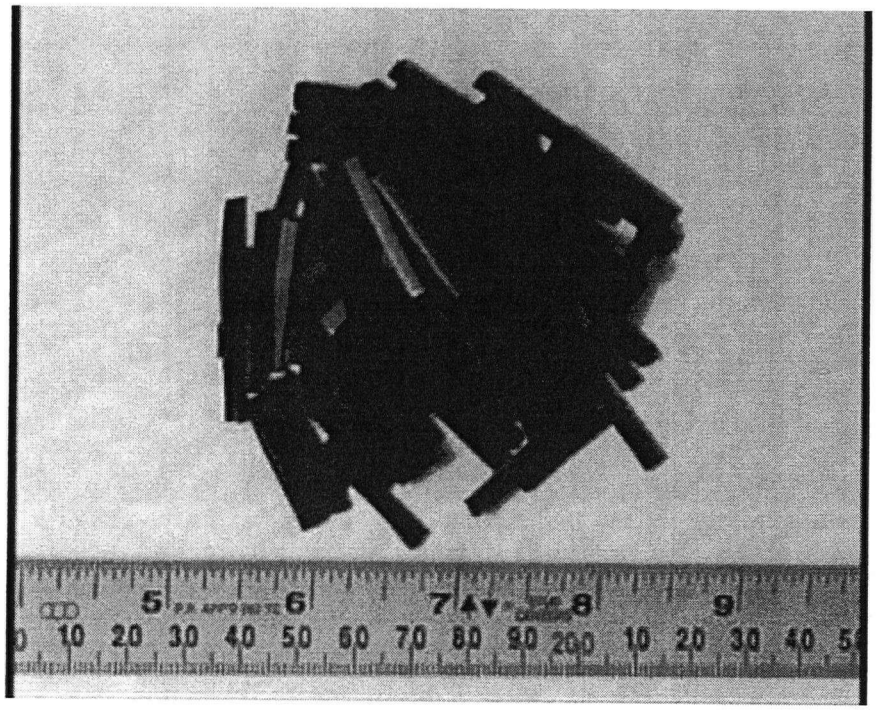

Figure 3-4-7. Photo of nitril-rubber60-cuboid-4 particles (25x3x3 mm)

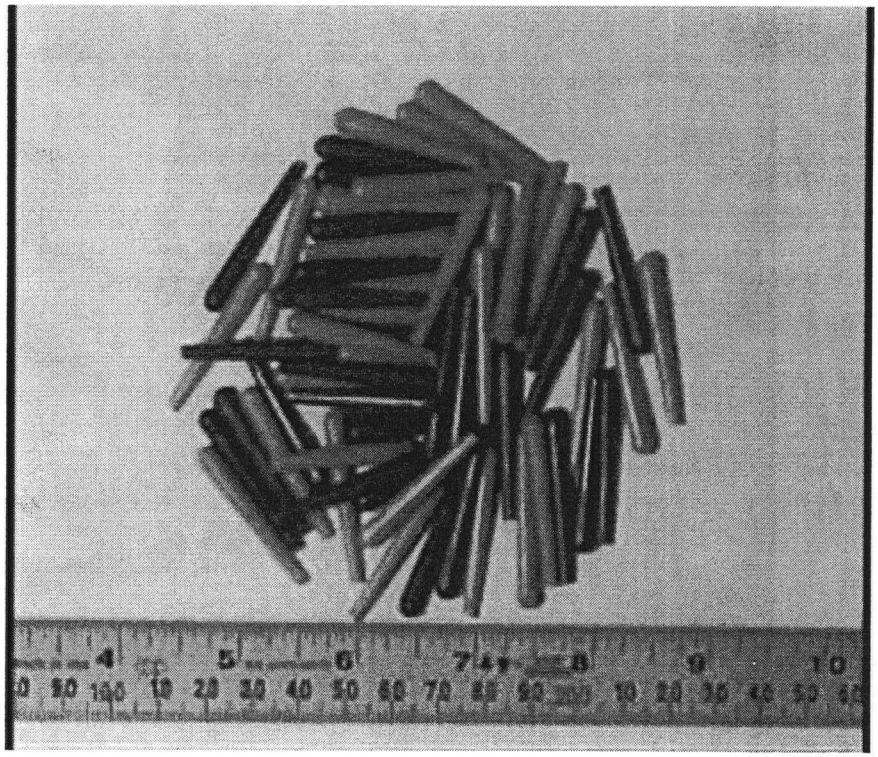

Figure 3-4-8. Photo of ABS-cone-1 particles

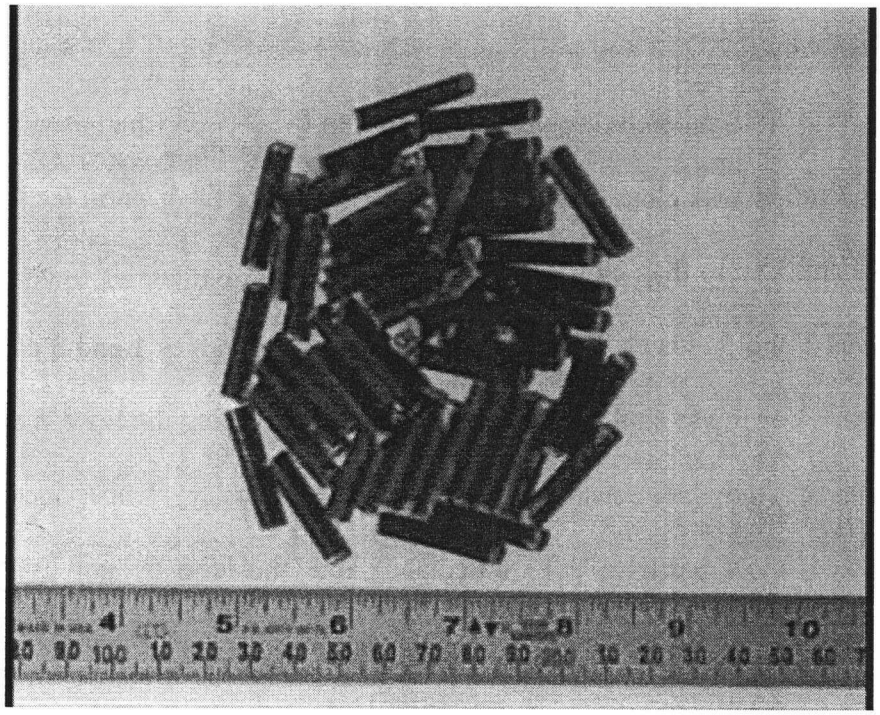

Figure 3-4-9. Photo of PTFE-rod-2 particles

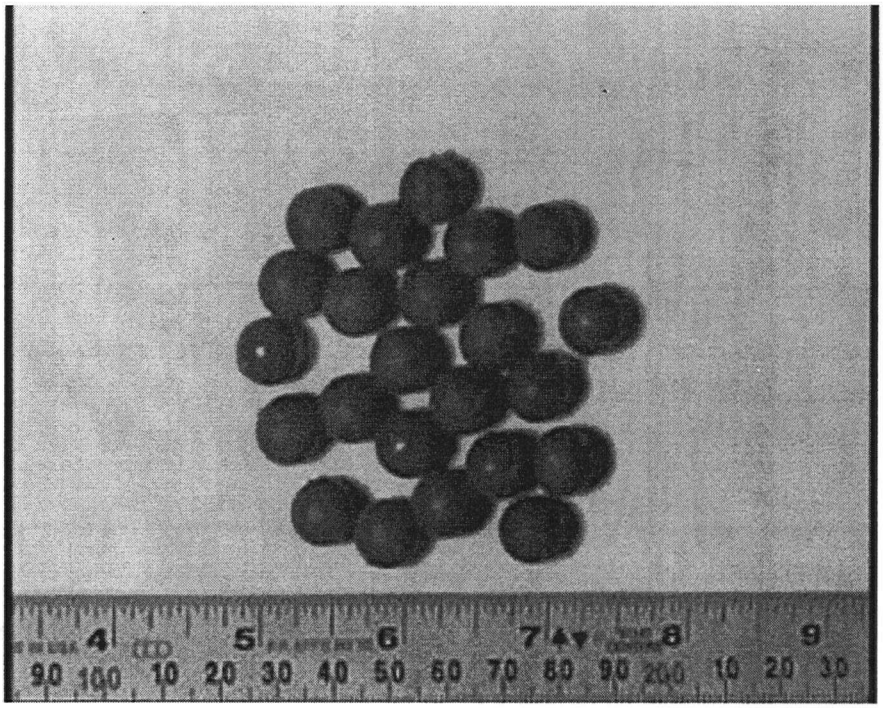


Figure 3-4-10. Photos of polyethylene-red-1 and polyethylene-red-2 spheres

Figure 3-4. Photos of main particles used in the present study

When valves 1, 2, 3 and 4 in Figure 3-2 were closed and valve 5 was opened, a number of particles (e.g. 200) entered through the union into the section (diameter: 51 mm) above valve 3. When the union was closed tightly and valve 3 was opened, particles fell into the flow loop. Valves 3 and 5 were then closed and valve 4 opened. Alternatively valves 1, 3 and 4 were open and valves 2 and 5 closed. The pressurized water from valves 1 and 3 carried particles into the loop. Valve 1 or 3 was shut off within 3 s to avoid disturbing the flow in the duct. Most particles in the present study had densities greater than that of water. Hence, once valve 3 in Figure 3-2 was opened, most particles fell immediately into the loop by gravity. However, there were commonly still 5-15% particles of irregular shape deposited along the duct, from the particle inlet section to the constriction, due to corners and irregular particle shapes. Therefore, slightly more particles were put into the particle inlet section than desired to ensure the expected number

Table 3-3. Sequences of particles in Particulate Flow Loop

| Particle type | Particle density ($kg/m^3$) | Shape | Dimensions (mm) | $D_v$ [1] (mm) | $D_s$ [2] (mm) | Sphericity | Aspect ratio [3] | Durometer [4] (Shore A) |
|---|---|---|---|---|---|---|---|---|
| Neo-rubber60-cuboid-0 [5] | 1445 | Cuboid | 5(l) x 5(w) x3 (h) | 5.23 | 2.96 | 0.78 | 1.7 | 60 |
| Neo-rubber60-cuboid-1 | 1445 | Cuboid | 7(l) x 7(w) x3 (h) | 6.55 | 3.81 | 0.74 | 2.3 | 60 |
| Neo-rubber60-cuboid-2 | 1445 | Cuboid | 9(l) x 9(w) x3 (h) | 7.74 | 4.64 | 0.7 | 3 | 60 |
| Neo-rubber60-cuboid-3 | 1445 | Cuboid | 15(l) x 5(w) x3 (h) | 7.55 | 4.64 | 0.66 | 5 | 60 |
| Neo-rubber60-cuboid-4 | 1445 | Cuboid | 25(l) x 3(w) x3 (h) | 7.55 | 5.03 | 0.56 | 8.3 | 60 |
| Neo-rubber40-cuboid-1 | 1080 | Cuboid | 5(l) x 5(w) x3 (h) | 5.23 | 2.96 | 0.78 | 1.7 | 40 |
| Neo-rubber40-cuboid-2 | 1080 | Cuboid | 9(l) x 9(w) x3 (h) | 7.74 | 4.64 | 0.7 | 3 | 40 |
| Neo-rubber40-cuboid-3 | 1080 | Cuboid | 15(l) x 5(w) x3 (h) | 7.55 | 4.64 | 0.66 | 5 | 40 |
| Neo-rubber40-cuboid-4 | 1080 | Cuboid | 25(l) x 3(w) x3 (h) | 7.55 | 5.03 | 0.56 | 8.3 | 40 |
| Nitril-rubber60-cuboid-1 | 1517 | Cuboid | 5(l) x 5(w) x3 (h) | 5.23 | 2.96 | 0.78 | 1.7 | 60 |
| Nitril-rubber60-cuboid-2 | 1517 | Cuboid | 7(l) x 7(w) x3 (h) | 6.55 | 3.81 | 0.74 | 2.3 | 60 |
| Nitril-rubber60-cuboid-3 | 1517 | Cuboid | 9(l) x 9(w) x3 (h) | 7.74 | 4.64 | 0.7 | 3 | 60 |
| Nitril-rubber60-cuboid-4 | 1517 | Cuboid | 25(l) x 3(w) x3 (h) | 7.55 | 5.03 | 0.56 | 8.3 | 60 |
| Silicon-rubber70-cuboid-0 | 1610 | Cuboid | 5(l) x 5(w) x3 (h) | 5.23 | 2.96 | 0.78 | 1.7 | 70 |
| Silicon-rubber70-cuboid-1 | 1610 | Cuboid | 7(l) x 7(w) x3 (h) | 6.55 | 3.81 | 0.74 | 2.3 | 70 |

| Particle type | Particle density ($kg/m^3$) | Shape | Dimensions (mm) | $D_v$ [1] (mm) | $D_s$ [2] (mm) | Sphericity | Aspect ratio [3] | Durometer [4] (Shore A) |
|---|---|---|---|---|---|---|---|---|
| Silicon-rubber70-cuboid-2 | 1610 | Cuboid | 9(l) x 9(w) x3 (h) | 7.74 | 4.64 | 0.7 | 3 | 70 |
| Silicon-rubber70-cuboid-3 | 1610 | Cuboid | 15(l) x 5(w) x3 (h) | 7.55 | 4.64 | 0.66 | 5 | 70 |
| Silicon-rubber70-cuboid-4 | 1610 | Cuboid | 25(l) x 3(w) x3 (h) | 7.55 | 5.03 | 0.56 | 8.3 | 70 |
| ABS-Cone-1 | 1020 | Cone | $\phi$ 5-$\phi$ 3 x 33 | 9.3 | 5.9 | 0.62 | 8.3 | 100 |
| PTFE-Rod-1 | 2040 | Cylinder | $\phi$ 5 x 10 | 7.2 | 3.7 | 0.83 | 2 | 100 |
| PTFE-Rod-2 | 2040 | Cylinder | $\phi$ 5 x 25 | 9.8 | 5.7 | 0.7 | 5 | 100 |
| Polyethylene-red-1 | 1019 | Sphere | $\phi$ 11.5 | 11.5 | 11.5 | 1.0 | 1 | 100 |
| Polyethylene-red-2 | 926 | Sphere | $\phi$ 11.5 | 11.5 | 11.5 | 1.0 | 1 | 100 |
| Polyethylene-yellow-1 | 866 | Sphere | $\phi$ 6.4 | 6.4 | 6.4 | 1.0 | 1 | 100 |

Notes: (1) Diameter of sphere of equivalent volume.

(2) Diameter of sphere of equivalent surface area.

(3) Ratio of maximum to minimum dimension.

(4) Shore Hardness, using either the Shore A or Shore D scale, is the preferred method for characterizing the hardness of rubbers/elastomers and is also commonly used for 'softer' plastics. The Shore A scale is used for 'softer' rubbers, while the Shore D scale is used for 'harder' ones. The shore A hardness is the relative hardness of elastic materials such as rubber or soft plastics. It is determined with an instrument called a Shore A durometer. If the indenter completely penetrates the sample, a reading of 0 is obtained, and if no penetration occurs, a reading of 100 results. The reading is dimensionless. High values correspond to high hardness. The hardness of relatively hard plastic particles in present study is approximately equal to 100.

(5) Neo denotes neoprene rubber.

of particles passing through the constriction. All particles were re-used after being recovered from the filter system. Swarms of particles were investigated to elucidate the influence of particle interactions with each other and with the gaps.

Table 3-4. Main specifications of digital video camcorder

| Item | Comments |
|---|---|
| Model | Canon xL1 |
| Frames per second | Set at 30 |
| Image size | 720 x 480 pixel image is obtained |
| Tape format | Videocassettes bearing the MiniDV mark |
| Lens mount | XL interchangeable lens system (16x zoom (supplied): f/1.6-2.6, 5.5-88 mm) |
| Focusing system | TTL autofocus, manual focusing possible |
| Minimum focusing distance | 20 mm on maximum wide angle; telephoto end: 1 m |
| Maximum shutter speed | 1/15,000 second |
| Recommended illumination | More than 100 lux |
| Filter diameter | 72 mm (XL lens) |
| Viewfinder | 18 mm, colour LCD (approx. 180,000 pixels) |

Five differential pressure transmitters (Endress+Hauser, Deltabar S PMD 230, -0.25~0.25 $mH_2O$) were installed to measure the pressure variation along the test section. An electromagnetic flowmeter (Endress+Hauser, promag 33) measured the mean velocity of the water. The flow visualization system included a digital video camcorder (Canon xL1), whose details are listed in Table 3-4), as well as a mirror and three 100 W lamps. The camcorder was connected to the serial port of a computer (Pentium III, 601 MHz, 128 MB of RAM). Information from every frame, including the time, was stored on the hard disk. During visualization, the laboratory lights were turned off so that the surroundings were dark. The three light bulbs were adjusted to a suitable brightness to give clear pictures on the viewfinder. A

shutter speed of 1/1000 s was employed. The camcorder was used not only to capture images of particles blockage, but also to record particle trajectories. It captured simultaneous images from the front and top surfaces of the test section, aided by a mirror fixed at 45° to the horizontal to provide a top view. The video camcorder, electromagnetic flowmeter and all pressure sensors were connected to the data acquisition system.

Particle velocities were determined by timing the passage of particles between grid lines inscribed on the test section. The refractive index, $n$, (relative to air at 20°C and 101.3 kPa for a wavelength of 589.3 nm) of Plexiglas is 1.491, while that of water is 1.332. Since the camcorder was directly in front of, and at some distance from, the area of interest, the difference in refractive indices between the water and Plexiglas was neglected. The flow pattern data were stored on videotape for later analysis. With image analysis software (Ulead, Pinnacle Systems DV300-Adobe Premiere LE 4.2, Adobe Photoshop 6.0 and Matlab 6.1), the data were transferred to digital values, which could be handled by the computer. Image analysis involved:

(1) Grabbing a frame from the videotape and digitizing;

(2) Minimization of background noise;

(3) Sharpening of images;

(4) Correcting the dimensions with the aid of the grid lines on the test section, and identifying the relationship between the pixel dimensions in the images and actual dimensions;

(5) Identifying the threshold (starting point) of particle motion.

(6) Identifying the edge of the particles in the images and finding the x, y and z coordinates of the particle centroid;

(7) Computing of the particle position and velocity at each time step (1/30 s); the number density and volume fraction of particles in each zone of an image could also be calculated.

The particle number density is the number of particles per unit volume of the test section 0.28 (L) x 0.0254 (W) x 0.066 (H) m just upstream of the constriction, whereas the volume fraction of particles is the total particle volume divided by the volume of the test section just upstream of the constriction. From image analysis, the number of particles entering and leaving the test section in each frame can be counted, so that the number of particles in the test section can be calculated. The volume of particles in the test section can be obtained from the number of particles because the volume of every particle is known. The volume of clusters in the test section is also based on particle number analysis.

A schematic of the experimental flow loop appears in Figure 3-2. Drawings of the ramp, circular and rectangular test sections are included in Figures 3-5 to 3-8 and Table 3-5. The surface of all blocks, including ramp, rectangular and circular blocks, were made smooth (roughness < 0.05 mm) during fabrication.

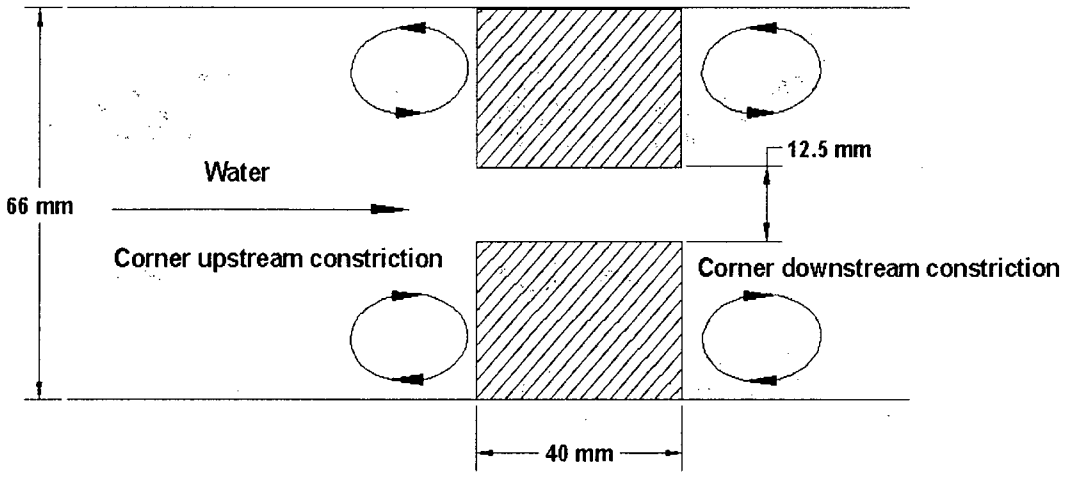


Figure 3-5. Rectangular constriction-1 with 25.4 (W) x 12.5 (H) mm gap

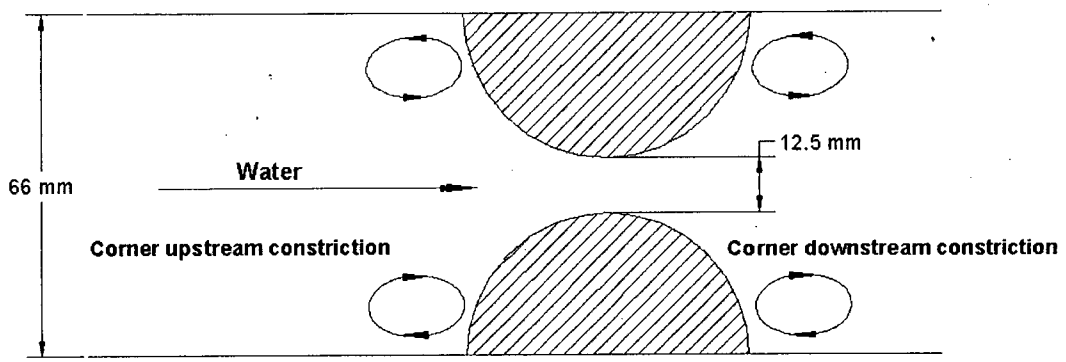


Figure 3-6. Circular constriction-1 with 25.4 (W) x 12.5 (H) mm gap

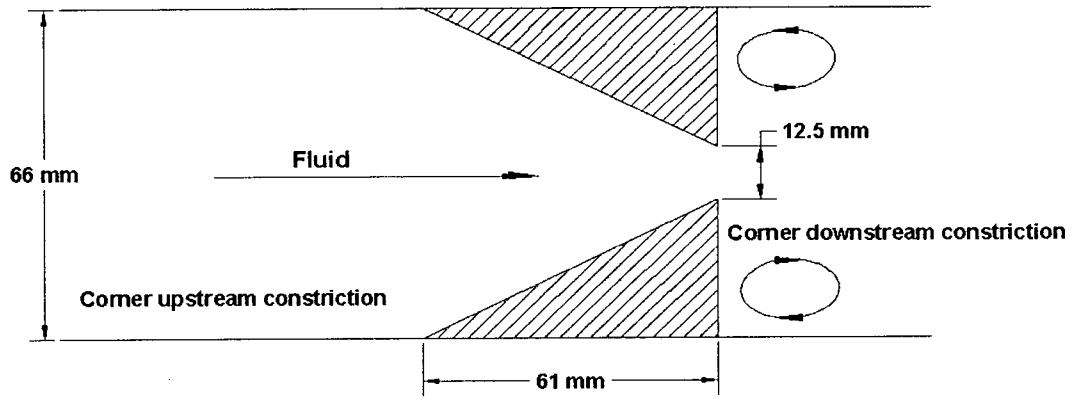


Figure 3-7. Ramp constriction-1 with 25.4 (W) x 12.5 (H) mm gap

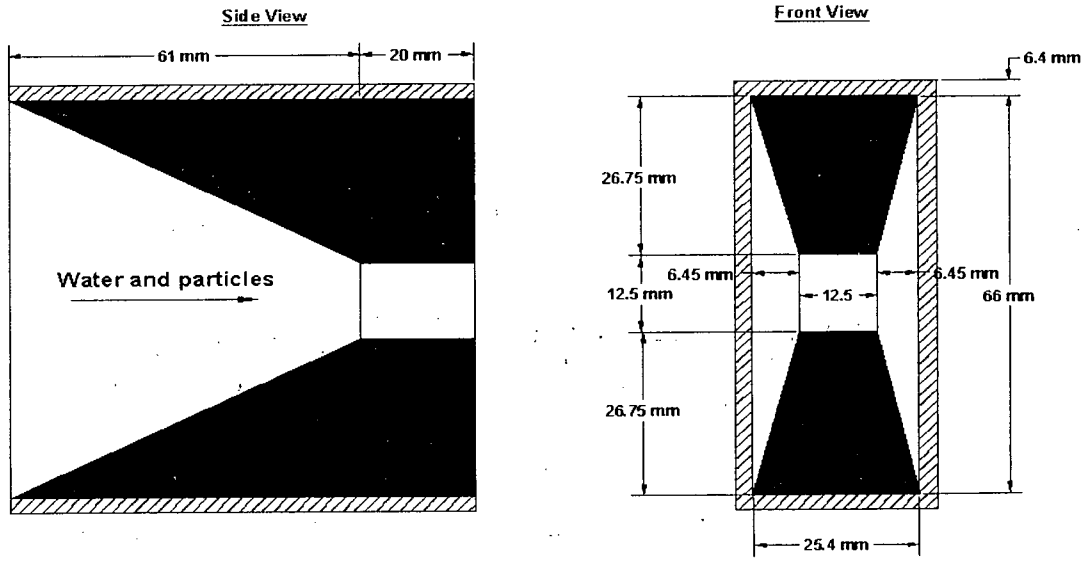


Figure 3-8. Ramp constriction-4 with 12.5 (W) x 12.5 (H) mm gap

Table 3-5. Configurations of various constrictions

| Constriction No. | Block Dimensions [1] | Minimum Gap Dimensions [2] | Constriction Shape |
|---|---|---|---|
| Ramp Constriction –1<br>(Gap between two wedges) | Length: 61 mm<br>Maximum Height: 26.8 mm<br>Width: 25.4 mm<br>Angle: 23.9 ° | Height: 12.5 mm<br>Width: 25.4 mm | 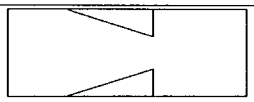 |
| Ramp Constriction –2<br>(Gap between two wedges) | Length: 71 mm<br>Maximum Height: 23.6 mm<br>Width: 25.4 mm<br>Angle: 18.4 ° | Height: 18.8 mm<br>Width: 25.4 mm | 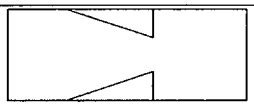 |
| Ramp Constriction –3<br>(Gap between two wedges) | Length: 61 mm<br>Maximum Height: 20.3 mm<br>Width: 25.4 mm<br>Angle: 18.4° | Height: 25.4 mm<br>Width: 25.4 mm | 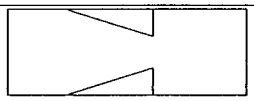 |
| Ramp Constriction –4<br>(3 dimensional wedge gap) | Length: 61 mm;<br>Maximum Height: 23.6 mm<br>Width: 25.4 mm<br>Angle: 18.4 ° | Height: 12.5 mm<br>Width: 12.5 mm [3] | 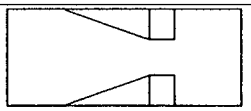 |
| Circular Constriction –1<br>(Gap between two half-cylinders) | Diameter: 26.8 mm<br>Width: 25.4 mm | Maximum Height: 12.5 mm<br>Width: 25.4 mm | 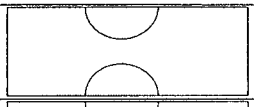 |
| Circular Constriction –2<br>(Gap between two half-cylinders) | Diameter: 20.3 mm<br>Width: 25.4 mm | Maximum Height: 25.4 mm<br>Width: 25.4 mm | 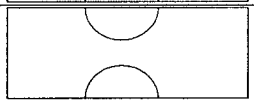 |
| Rectangular Constriction –1<br>(Gap between two rectangular blocks) | Length: 40 mm<br>Height: 26.8 mm<br>Width: 25.4 mm | Height: 12.5 mm<br>Width: 25.4 mm | 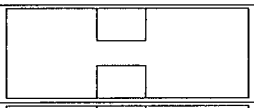 |
| Rectangular Constriction –2<br>(Gap between two rectangular blocks) | Length: 40 mm<br>Height: 20.3 mm<br>Width: 25.4 mm | Height: 25.4 mm<br>Width: 25.4 mm | 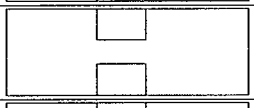 |
| Rectangular Constriction –3<br>(Gap between two rectangular blocks) | Length: 20 mm<br>Height: 26.8 mm<br>Width: 25.4 mm | Height: 12.5 mm<br>Width: 25.4 mm | 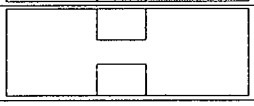 |

Notes: (1)(2) Length is the dimension in the streamwise direction; height is dimension in vertical direction (at right angles to the flow direction); width is dimension in spanwise direction.

(3) See Figure 3-8 to see how thinner width was achieved.

## 3.3 Experimental Results and Discussion

### 3.3.1 Observations of particle-liquid flows

The trajectories and velocities of small numbers of particles passing through the constrictions were visualized. Spherical particles of low density (e.g. polyethylene-yellow-1 in Table 3-3) were easily transported and were unlikely to block the constriction. These particles were transported along at the top of the duct due to buoyancy and lift forces, and there were always some particles trapped by bubbles sticking to the inner wall of the duct. When many particles passed through the constriction, particle-particle interactions became more important. Five polyethylene-red-2 particles (see Table 3-3) were tested in the present study. If these particles were very close to each other, they clearly interacted and experienced behaviour similar to what has been called "drifting", "kissing" and "tumbling" in the literature (Fortes et al., 1987; Hu et al., 2004) when passing through the constrictions. The wake produced by one particle can have an important effect on the motion of a nearby particle, even when the two particles do not collide with each other.

Small particles with density close to that of water (e.g. polyethylene-yellow-1) or denser than water (e.g. glass beads of 2 mm diameter), were easily trapped in the vortex behind the constriction. The motion of particles downstream of the constriction depends on many factors, such as fluid velocity, upstream turbulence level, constriction dimensions and shape, particle properties (e.g. density, dimensions and shape). Particles near the wall beyond the constriction risk being captured by the vortex. Some particles (e.g. polyethylene-red-2 and polyethylene-yellow-1) experienced a relatively stationary state for ~3-4 s near the wall downstream of the

constriction before being trapped by the vortex or travelling downstream. Fluid velocity and turbulence level upstream of the constriction, constriction configurations and particle properties together determine whether or not the particles proceed directly downstream. Larger particles with density greater than that of water were not readily trapped by the vortex because of their larger dimension and increased inertia. These particles were also more likely to collide with the block surface. Such collisions led to much more rotation, at the same time causing abrupt changes in particle trajectory and velocity. The larger or heavier the particle, the greater the chance of it colliding with the wall surface because of inertial effects.

When $U_m$ < 0.35 m/s, non-spherical particles of density greater than that of water (e.g. Silicon-rubber70-cuboid-0, in Table 3-3) were difficult to transport in the duct because of sedimentation. For 0.35< $U_m$ <0.55 m/s, non-spherical particles were easier to move (creep and saltation), with some piling upstream of the constriction and others passing through the gap almost one by one. Blockage was unlikely for this case. For 0.55< $U_m$ < 1.2 m/s, more and more heavier non-spherical particles were transported and lifted vigorously (saltation and suspension), increasing the probability of different particles passing through the constriction simultaneously, thereby increasing the probability of blockage. For the conditions of the present study, 3 to 10 non-spherical particles were sufficient to block the constriction if the ratio of particle maximum dimension to constriction minimum dimension > 0.4. On the other hand, as $U_m$ increased, blockage was less likely to occur and was more readily broken up, especially for small-particle-blockage in the constriction, because of the increased particle inertia, increased drag and increased pressure gradient immediately upstream of the constriction. The blockage

probability depended on the interactions of the fluid, particles and constriction. Re>29,000 or a water mean velocity > 0.8 m/s was required for PTFE-Rod-02 particles to move forward smoothly along the bottom of the duct (similar to creep). These particles were also more likely to block the constriction at high Re.

Ramp constriction–3 was relatively easy for particles to pass through because of its smooth profile and large gap dimensions, while the other constrictions (e.g. rectangular constriction–1 and ramp constriction–4) created a challenge because of their steep slope and small gap dimensions, and the vortex formed immediately downstream of the constriction.

In the runs described below, all experiments were performed at least 20 times for the same particles and same experimental conditions. The blockage index (see Table 3-1) is the average weighted value. The particle number density and volume fraction are important factors affecting blockage in the constriction. They were not identical in each test, even when the same particles and experimental conditions were employed. On the other hand, the differences were small for the same experimental procedures (e.g. particle injection method) with the same particles and same experimental conditions. Particle number densities were in the range 8000 to $4x10^5/m^3$, while particle volume fractions ranged from 0.001 to 0.1.

### 3.3.2 Effect of aspect ratio on blockage for cuboidal particles

These tests involved particles of Silicon-rubber70-cuboid-2, Silicon-rubber70-cuboid-3, Silicon-rubber70-cuboid-4, Neo-rubber40-cuboid-4 and Neo-rubber60-cuboid-4. 200 particles were released each time. The duct Reynolds number was Re=29700 with the water mean velocity being 0.8 m/s and rectangular constriction-1 (25.4 (W) x 12.5 (H) x 40 (L) mm). All of

these particles were cuboids, with almost the same equivalent volume diameter (7.74 mm for 9 x 9 x 3 mm, and 7.55 mm for both the 15 x 5 x 3 and 25 x 3 x 3 mm particles). The maximum dimensions of some particles (e.g. 15 x 5 x 3 and 25 x 3 x 3 mm particles) exceeded the minimum gap dimension (i.e. 12.5 mm).

The experiments indicated that cuboidal silicon-rubber particles of large aspect ratio (e.g. 8.3 for 25 x 3 x 3 mm Silicon-rubber70-cuboid-4 particles) were not easily transported by water. Some particles always deposited in the duct or blocked the gap instead of passing through the constriction. They were more likely to block compared to particles of smaller aspect ratio (silicon-rubber70-cuboid-3 15 x 5 x 3 mm particles). On the other hand, particles of smaller aspect ratios (e.g. 9 x 9 x 3 mm silicon-rubber70-cuboid-2 particles) were generally harder to transport than those of larger aspect ratio (e.g. 15 x 5 x 3 mm silicon-rubber70-cuboid-3 particles) as shown in Figures 3-9 and 3-10. It seems that there should be an optimum aspect ratio for particles with the same or similar equivalent volume diameter to reduce the blockage tendency. 7 x 7 x 3 mm silicon rubber particles of 70 durometer did not block the rectangular constriction, although some of these particles always deposited immediately upstream of the constriction. Irregular-shape particles readily deposited along the duct, low water mean velocities (e.g. $< 0.6$ m/s) were unable to transport these particles. Hence higher water mean velocities were employed ($> 0.8$ m/s) to avoid deposition. Even so, a small number of particles deposited along the duct, especially in front of the constrictions. If blockage occurred in the constriction, as shown in Figure 3-11, the particles retained in front of the constriction were counted. Upstream deposition is not considered to constitute blockage. Figure 3-12 also shows

the effects of particle size and shape on blockage, demonstrating that larger particles of more irregular shapes (larger aspect ratios and smaller sphericity) are generally more likely to become lodged in a given constriction.

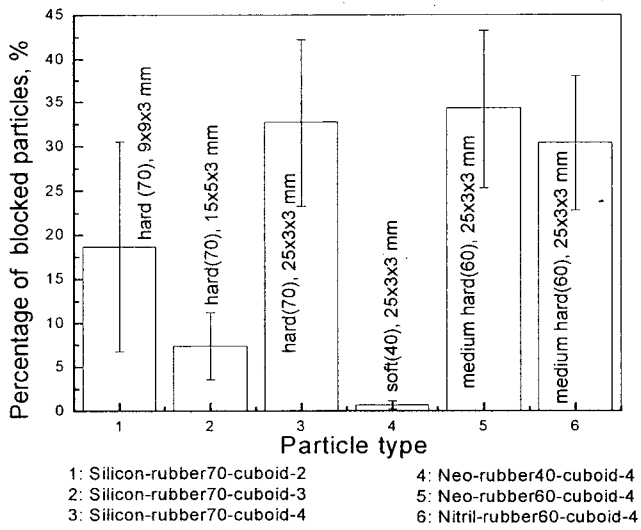


Figure 3-9. Percentage of blocked particles of hardness 40, 60, 70. (200 particles released each time, Re= 29700, rectangular constriction-1). Bars show 95% confidence intervals. For properties of particles and constrictions, see Tables 3-3 and 3-5.

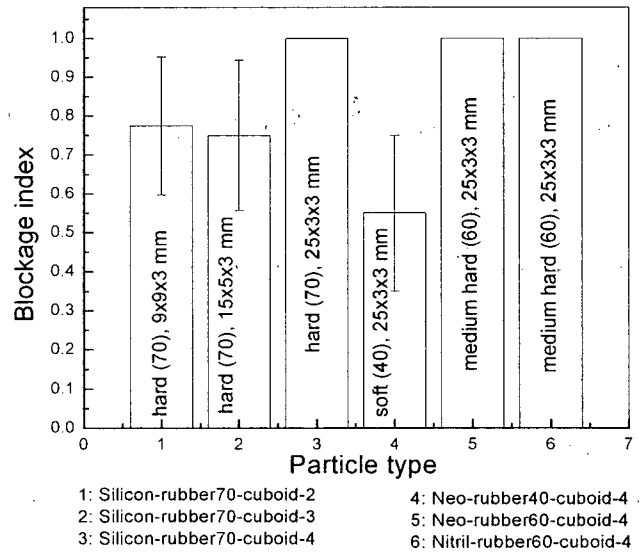


Figure 3-10. Blockage index comparison for different particles of hardness 40, 60 and 70. (200 particles released each time, Re= 29700, rectangular constriction-1). ). Bars show 95% confidence intervals. For properties of particles and constriction, see Tables 3-3 and 3-5.

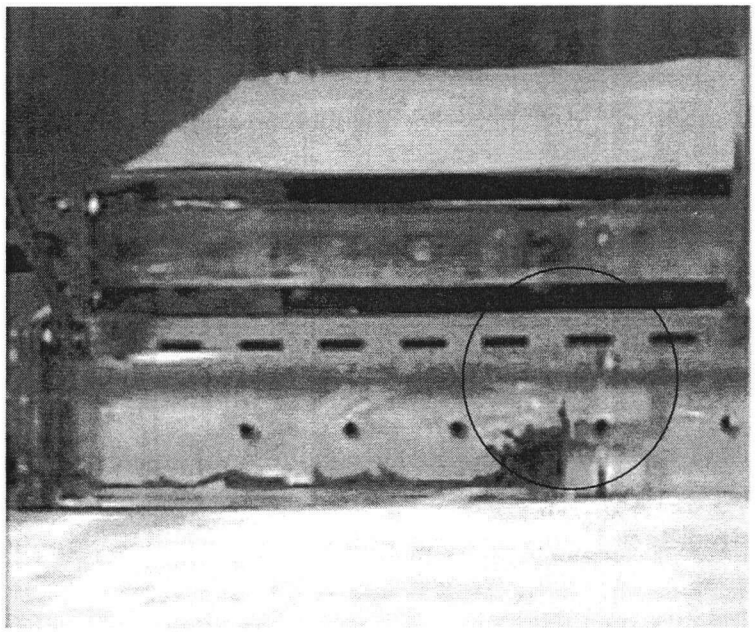

Figure 3-11. Particles (Silicon-rubber70-cuboid-4) blocked in Rectangular constriction-1

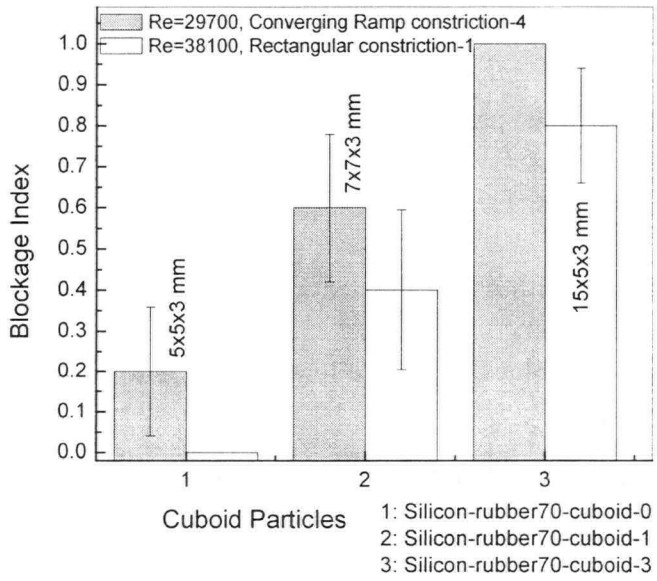


Figure 3-12. Effect of particle size and shape on blockage. (Injected particles each time=400, 200, 200 for Silicon-rubber70-cuboid-0,1,3). Bars show 95% confidence intervals. At $< 0.13$ level, the differences of the population means differ significantly from the test difference (Null Hypothesis: difference of two population means is 0), two samples t test. For properties of particles and constrictions, see Tables 3-3 and 3-5.

### 3.3.3 Effect of particle density on blockage

Neo-rubber60-cuboid-4 and Nitril-rubber60-cuboid-4 have slightly different particle densities, as shown in Table 3-3. This did not appear to cause an appreciable difference in blockage index or in deposition upstream of the constriction as shown in Figures 3-9 and 3-10. Denser particles are expected to deposit more easily than light ones for the same geometry and dimensions, and the same experimental conditions. Particles of density less than water (e.g. polyethylene-red-2 and polyethylene-yellow-1 particles) were transported readily, with no deposition along the duct. However, they were more likely to be trapped in the corners upstream and downstream of the constriction. Moreover, lower density corresponded to greater flexibility, making it easier for particles to adjust their orientations, velocities and positions, thereby reducing the probability of blockage. The blockage of particles of density less than that of water was not investigated in the present study.

### 3.3.4 Effect of particle stiffness on blockage

Neoprene rubber with 40 durometer was easily transported through the gap due to its low particle density. Stable blockages were less likely for soft rubber particles due to their softness (i.e. low bending/flexural strength), large compressibility (as defined in Chapters 2 and 6), and large flexibility (discussed below in this Chapter) than for relatively hard particles, as shown in Figures 3-9 and 3-10. Particle number density and solid volume fraction of particles in the above tests are shown in Table 3-6.

Table 3-6. Particle number density and solid volume fraction of particles [1]

| | PND (1/mm3) and SVF (2) | Lower limit | Upper limit | Mean | Passing time (3) (s) |
|---|---|---|---|---|---|
| Silicon-rubber70-cuboid-1 (7x7x3mm) | PND (mm-3) | 1.28E-05 | 2.56E-04 | 1.34E-04 | 5-9 |
| | SVF (-) | 1.88E-03 | 3.76E-02 | 1.97E-02 | 5-9 |
| Silicon-rubber70-cuboid-2 (9x9x3mm) | PND (mm-3) | 1.28E-05 | 2.56E-04 | 1.34E-04 | 7-11 |
| | SVF (-) | 3.11E-03 | 6.21E-02 | 3.26E-02 | 7-11 |
| Silicon-rubber70-cuboid-3 (15x5x3mm) | PND (mm-3) | 1.28E-05 | 2.56E-04 | 1.34E-04 | 6-10 |
| | SVF (-) | 2.88E-03 | 5.75E-02 | 3.02E-02 | 6-10 |
| Silicon-rubber70-cuboid-4 (25x3x3mm) | PND (mm-3) | 8.52E-06 | 1.28E-04 | 6.83E-05 | 8-16 |
| | SVF (-) | 1.92E-03 | 2.88E02 | 1.44E+02 | 8-16 |
| Neo-rubber40-cuboid-4 (25x3x3mm) | PND (mm-3) | 8.52E-06 | 1.07E-04 | 5.78E-05 | 5-7 |
| | SVF (-) | 1.92E-3 | 2.4E-02 | 1.30E-02 | 5-7 |
| Neo-rubber60-cuboid-4 (25x3x3mm) | PND (mm-3) | 8.52E-06 | 1.28E-04 | 6.83E-05 | 6-10 |
| | SVF (-) | 1.92E-3 | 2.88E-02 | 1.54E-02 | 6-10 |
| Nitril-rubber60-cuboid-4 (25x3x3mm) | PND (mm-3) | 8.52E-06 | 1.28E-04 | 6.83E-05 | 6-10 |
| | SVF (-) | 1.92E-3 | 2.88E-02 | 1.54E-02 | 6-10 |

Notes: (1) Number of particles released every time = 200, Re= 29700.

(2) PND denotes particle number density ($mm^{-3}$), SVF denotes solid volume fraction.

(3) Time for all particles to pass through the view section (as shown in Figure 3-19 below).

### 3.3.5 Effect of constriction type and dimensions on blockage

To investigate the influence of constriction type, clusters of 160 conical ABS-cone-1 particles were released with Re=38,100 ($U_m$=1.05 m/s) to reach ramp constriction-4 (12.5 (W) x 12.5 (H) mm) and rectangular constriction-1 (25.4 (W) x 12.5 (H) mm). Experiments were also conducted with the same two constrictions with the release of 220 silicon-rubber-cuboid-0 particles.

The smaller converging constriction showed a greater tendency to block than the larger rectangular constriction, as shown in Figure 3-13. For Ramp-constriction-4, the smaller dimension in the spanwise direction than for Rectangular constriction-1 led to more particle collisions with each other and with the gap, enhancing the probability of blockage.

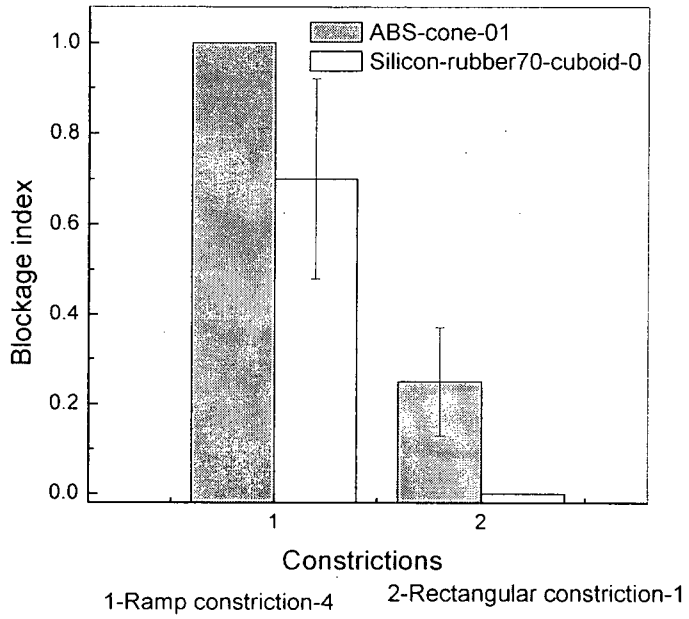


Figure 3-13. Effects of constriction type and dimensions on blockage for Re=38100 for 160 and 220 injected particles for ABS and silicon particles, respectively. Bars show 95% confidence intervals. At the 0.001 level, the differences of the population means differ significantly from the test difference (Null Hypothesis: difference of two population means is 0), two samples t test. For properties of particles and constrictions, see Tables 3-3 and 3-5.

Ramp constriction-1 and Rectangular constriction-1 had the same minimum gap dimension, i.e. 25.4(W) x 12.5(H) mm. 200 Neo-rubber60-cuboid-4 particles of dimensions 25 x 3 x 3 mm were released into the water flow at Re=29,700 ( $U_m$ =0.8 m/s). The maximum particle dimension (25 mm) exceeded the minimum dimension of the gap (12.5 mm). Due to the abrupt change of the dimension of rectangular constriction-1, water and particles also abruptly changed their velocities and directions of motion, promoting collisions with the wall and with each other, thereby increasing likelihood of blockage. The smooth convergence of ramp-constriction-1 reduced the probability of particle collisions and also provided more space for particles to migrate and disentangle before reaching the minimum cross section of the gap (see Figure 3-14).

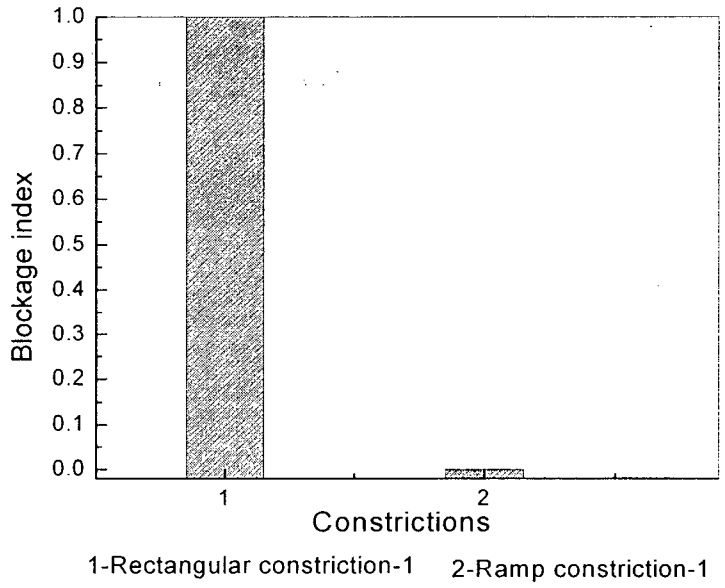


Figure 3-14. Constriction type and dimension effect on blockage for Re= 29700.(200 Neo-rubber60-cuboid-4 particles injected each time). For properties of particles and constrictions, see Tables 3-3 and 3-5.

3.3.6 Effect of Reynolds number on blockage

The effect of water velocity and Reynolds number over limited ranges can be seen by comparing results for conical ABS-01 and cuboidal silicon-rubber70-cuboid-3 particles with the rectangular (abrupt) and ramp constrictions. Figure 3-15 indicates that a larger Reynolds number (i.e. greater water mean velocity) generally caused more blockage. This appears to be because higher Reynolds number tends to cause more particles to pass through the constriction simultaneously, increasing the probability of particle collisions with each other and with the gap, in turn increasing the probability of jamming and blockage. For the Reynolds number range covered in the present study, smaller Reynolds numbers led to deposition along the duct, whereas larger Reynolds numbers increased the blockage tendency for the range covered.

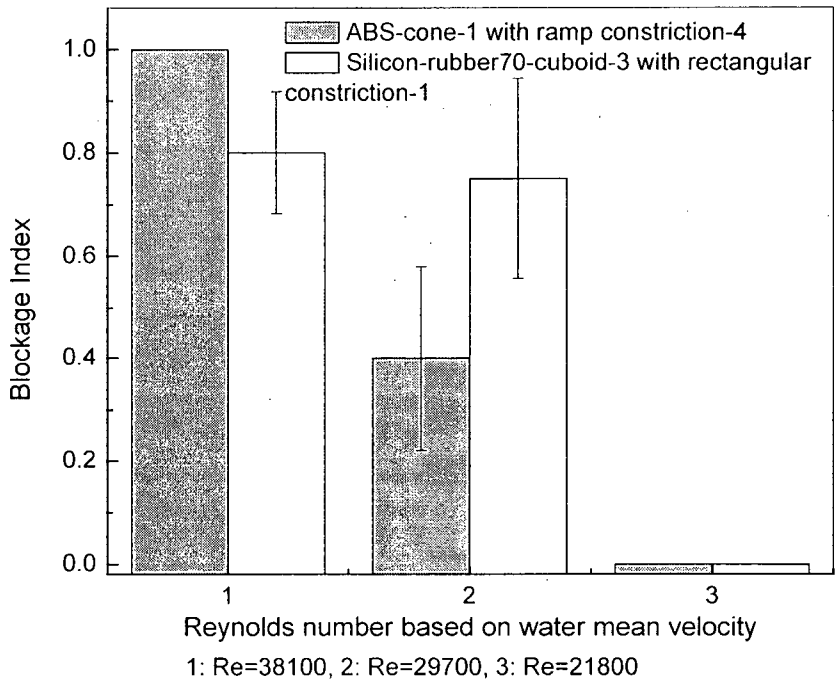


Figure 3-15 Effect of Reynolds number on blockage for release of 160 and 200 particles. (ABS and silicon rubber, respectively). Bars show 95% confidence intervals. At the 0.05 level, the differences of the population means differ significantly from the test difference (Null Hypothesis: difference of two population means is 0), two samples t test. For properties of particles and constrictions, see Tables 3-3 and 3-5.

### 3.3.7 Effect of ratio of maximum particle dimension to minimum gap dimension

Tests were carried out for particles of Silicon-rubber70-cuboid-0, -1 and -3, with release each time of 400, 200 and 200 particles, respectively. With rectangular constriction-1 (25.4 (W) x 12.5 (H) x 40 (L) mm) and ramp constriction-4 (12.5(W) x 12.5 (H) mm), Figure 3-16 shows that larger ratios of maximum particle dimension to minimum constriction dimension reduced the ability of particles to pass through the constriction, especially for ramp constriction-4, which did not provide as much space as rectangular contriction-1 for particles to migrate in the spanwise direction. As expected, larger particle size increased the propensity to block.

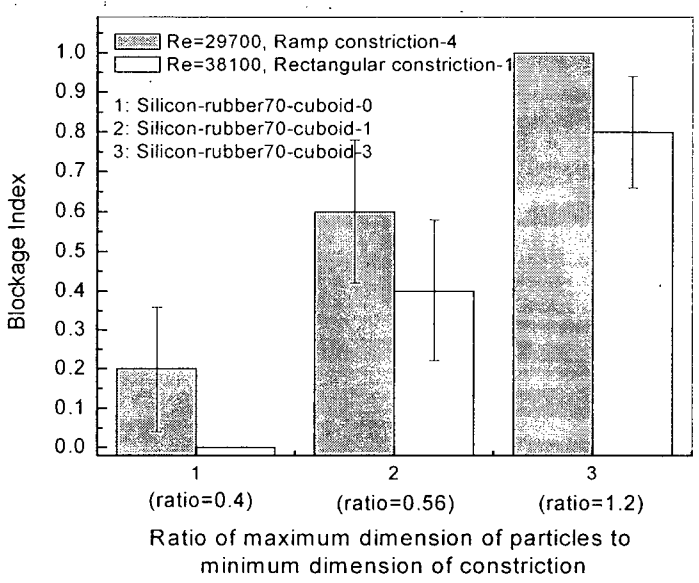


Figure 3-16. Effect of ratio of maximum particle dimension to minimum constriction dimension on blockage for cuboidal rubber particles of different sizes. (Number of particles released each time=400, 200, 200 for silicon-rubber70-cuboid-0, 1, 3, respectively). Bars show 95% confidence intervals. At < 0.09 level, the differences of the population means differ significantly (Null Hypothesis: difference of two population means is 0), two samples t test. For properties of particles and constrictions, see Tables 3-3 and 3-5.

### 3.3.8 Effect of particle compressibility and flexibility on blockage

To investigate the influence of particle compressibility and flexibility, 160 conical ABS-cone-1 and cuboidal Silicon-rubber70-cuboid-3 particles were released each time with Re=29,700 ($U_m$=0.8 m/s) to reach ramp constriction-4 (12.5 (W) x 12.5 (H) mm).

As mentioned above, when these particles collided with each other and with the gap, they tended to stick together due to compressibility and to increase the blockage probability. Neoprene rubber particles with 40 durometer were more easily transported along the duct due to their low density, and blockages were more easily dislodged due to their softness, flexibility (discussed below), and large compressibility than relatively hard particles, as shown in Figures

3-9 and 3-10. Particles with low bending/flexural strengths and low particle densities passed more easily through constrictions, and when they did block, the jam was more likely to break up. Compressible particles with relatively higher bending strengths and greater particle densities (e.g. silicon rubber particles with 70 durometer) caused more stable blockages. Incompressible particles of relatively low density (e.g. ABS-cone-1) were more likely to pass through constrictions over a certain Re range (e.g. 26,000<Re<38,000 in the present study). Increased Re and intensive particle collisions increased the probability of blockage.

Flexibility, F, is defined as the reciprocal of fibre stiffness in bending, S, which is the product of elastic modulus, E, and the area moment of inertia, $I$, of the fibre (Kumar, 1990). This can also be used to quantify the ability for particles to pass through a constriction. Thus

$$F = \frac{1}{S} = \frac{1}{EI} \tag{3-1}$$

The elastic modulus $E$ is defined by

$$\sigma = E\varepsilon \tag{3-2}$$

where $\sigma$ and $\varepsilon$ are the stress and strain, respectively.

Compressibility is inversely proportional to elastic modulus (i.e. $E$), which indicates that large compressibility leads to large flexibility for equal area moments of inertia. The larger the flexibility, the easier it is for particles to pass through constrictions. We see that soft rubber (e.g. 40 durometer) has a small $E$ relative to hard rubber (e.g. 70 durometer). For cuboid particles, the mass moment of inertia ($I_h$) and area moment of inertia ($I_w$) are given, respectively, by

$$I_h = \frac{1}{12} m(w^2 + l^2), \qquad I_w = \frac{wl^3}{12} \tag{3-3}$$

where $m$ is the particle mass, and $h$, $w$, and $l$ are the height, width and length of the cuboidal particle. $I_h$ is the mass moment of inertia about the axis in the $h$ direction which passes through the particle centroid. Mass moment of inertia is the rotational analogue to mass. Large mass and particle dimensions lead to large mass moments of inertia. We assume that the object has uniform density. The larger the area moment of inertia, the less the particle will bend.

From the particle flexibility point of view,

(1) For the same rubber, smaller particles lead to smaller area moments of inertia and greater flexibility, as indicated in Figures 3-9 and 3-10.

(2) For the same particle dimensions, softer particles (e.g. 40 durometer), smaller $E$ leads to larger flexibility causing the behaviour indicated in Figures 3-9 and 3-10.

(3) For particles of different materials, flexibility is a trade-off between area moment of inertia, elastic modulus and other particle properties (see below), as indicated in Figure 3-17. ABS-cone-1 and Silicon-rubber70-cuboid-3 have similar dimensions and shapes, but the latter have greater density and smaller elastic modulus. The larger density tends to increase the mass moment of inertia, whereas the smaller elastic modulus increases the flexibility. From Figure 3-17, the Silicon-rubber70-cuboid-3 particles demonstrated a larger blockage tendency than ABS-cone-1. The Silicon-rubber70-cuboid-3 particles bent more easily than the ABS-cone-1 particles, so that the former should pass through the constrictions more easily than the latter. However, the experimental results did not agree with this prediction. Note that silicon-rubber70-cuboid-3 particles with significant compressibility tend to stick together after collision with each other and/or with the wall. The resulting "agglomerate" could not be as readily broken up by

hydrodynamic forces as for the soft rubbers (e.g. 40 durometer), leading to enhanced blockage. Another major reason for the larger blockage tendency for the Silicon-rubber70-cuboid-3 particles was their large particle density, which increases the mass moment of inertia, reducing flexibility. ABS-cone-1 particles can easily adjust their orientation, position and velocity, while silicon-rubber70-cuboid-3 particles cannot adapt to fluid acceleration as easily as the ABS-cone-1 particles, thereby increasing the blockage probability. In fact, the ABS-cone-1 particles distributed across the cross-section of the duct more uniformly than the silicon-rubber70-cuboid-3 particles due to the effects of particle density as they approached the constrictions. The former underwent intense particle collision with each other and with the wall, increasing the probability of stall.

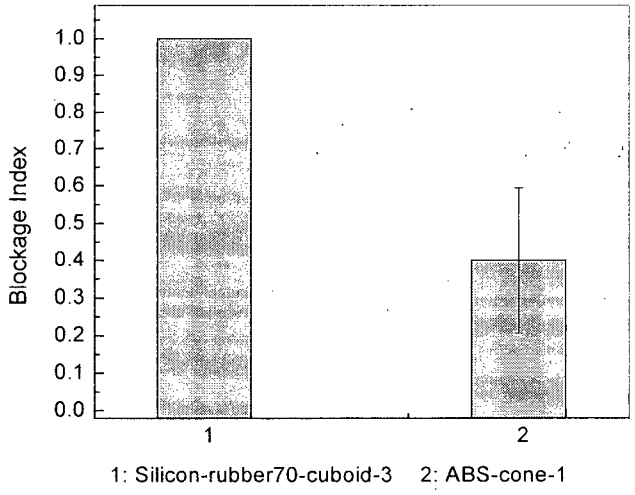


Figure 3-17. Effect of compressibility of particles on blockage for 160 ABS and rubber particles. Re= 29700, ramp constriction-4). Bars show 95% confidence intervals. At the 0.001 level, the differences of the population means differ significantly (Null Hypothesis: difference of two population means is 0), two samples t test. For properties of particles and constrictions, see Tables 3-3 and 3-5.

### 3.4 Horizontal Motion of a Neutrally Buoyant Spherical Particle

Particle motion in the vicinity of a constriction is complex, especially for irregular particles. Motion depends on the fluid velocity, upstream turbulence level, constriction dimensions and shape, particle density, particle dimensions and particle shape. Since particle motion is mainly in the streamwise direction, a single neutrally buoyant polyethylene-red-1 spherical particle (see properties in Table 3-3) was employed to investigate the horizontal motion. Vertical motion and rotation of the particle are difficult to analyze. Particles of density greater than water experienced complicated changes in position, velocity and orientation. Abrupt changes in direction, velocity and orientation caused inter-particle or particle-wall collisions, leading to more blockage.

The neutrally buoyant spherical polyethylene-red-1 particle was prepared by first drilling a small hole (1 mm diameter) radially into a polyethylene-red-2 particle to a depth slightly beyond the centre. Metal bead(s) or wires were then inserted into the hole and pushed to the centre. The hole was then plugged with glue (silicon sealant of density slightly less than that of water) so that the surface of the glue was flush with the particle surface as shown in Figure 3-18. The resulting particle then had virtually the same density as water (i.e. $\rho_p$=1019 vs $\rho_w$=998 kg/m$^3$).

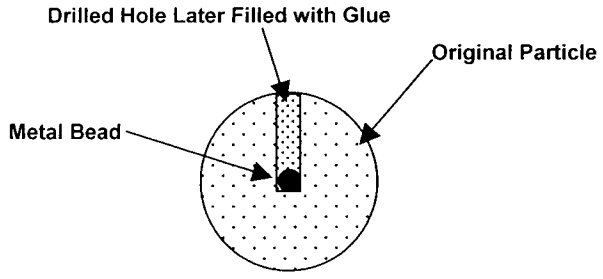


Figure 3-18. Production of neutrally buoyant spherical particle

In these tests, ramp constriction–3 was first employed (see Table 3-5). The length of the ramp in the streamwise direction was 61 mm, while the maximum height of each ramp block was 20.3 mm, and the width in the spanwise direction was 25.4 mm for a minimum gap dimension of 25.4 x 25.4 mm. The mean water velocity was 0.243 m/s, giving a Reynolds number based on hydraulic diameter of the duct of 8900, indicating that the flow was turbulent.

It was assumed that:

- The neutrally buoyant particle moved along the centreline of the test section. Only the horizontal direction is considered. Drag, added mass and fluid acceleration are taken into account, whereas the effects of gravity, buoyancy, lift and the Basset history term are ignored. The centreline water velocity is considered to be the local fluid velocity affecting the particle.
- The centreline water velocity upstream of the test section was obtained from previous study as discussed below.
- The centreline water velocity distribution is estimated from the pressure distribution along the constriction by the Navier-Stokes equation with viscous effects neglected.
- The coordinates are shown in Figure 3-19. The origin, point O, is at the geometric centre of the duct cross-section. The horizontal coordinate x is positive in the streamwise direction, while vertical coordinate y is positive in the upward direction; z is the spanwise direction as shown.
- The temperature is constant at 20 $^{o}$C.

### 3.4.1 Centreline water velocity

It is reasonable to use the arithmetic mean ratio of $U_{cfd}/U_{m}$ provided by Gavrilakis (1992) and Kim et al (1987), i.e. $U_{cfd}/U_{m}$=1.25, as the ratio of the centreline velocity to mean velocity

for turbulent flow through a rectangular duct (aspect ratio $\beta$=0.38) in the present study. Note that this is much less that the ratio of 1.92 obtained for steady fully developed laminar rectangular/square duct flow from the relationship given by McComas (1967). Hence, the centreline water velocity upstream of the test section is $U_c = U_{cfd}$ =0.243 x 1.25= 0.3 m/s.

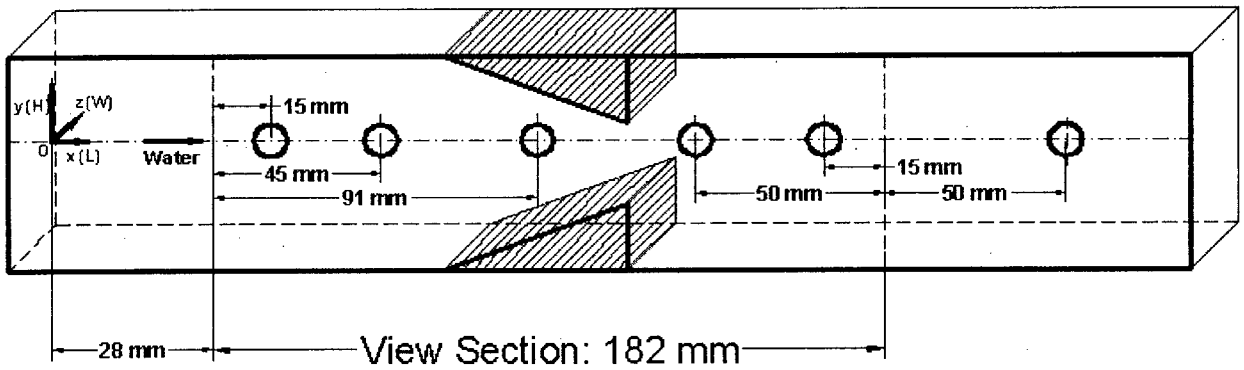


Figure 3-19. Schematic of view section with ramp constriction-3

The continuity and momentum equations (2-D) of the incompressible Newtonian fluid are (Hu, 1996; Marghzar et al., 2003):

$$\frac{\partial U_i}{\partial x_i} = 0 \qquad \text{(Continuity equation)} \tag{3-4}$$

$$\rho_f \frac{\partial U_i}{\partial t} + \rho_f \frac{\partial (U_i U_j)}{\partial x_j} = -\rho_f g \frac{\partial h}{\partial x_i} - \frac{\partial P}{\partial x_i} + \mu_f \frac{\partial}{\partial x_j}\left(\frac{\partial U_i}{\partial x_j} + \frac{\partial U_j}{\partial x_i}\right)$$

(Momentum conservation equation) (3-5)

In two-dimensions, Equation 3-5 gives

$$\rho_f\left(\frac{\partial U_x}{\partial t} + U_x \frac{\partial U_x}{\partial x} + U_y \frac{\partial U_x}{\partial y}\right) = -\frac{\partial P}{\partial x} + \mu_f\left(\frac{\partial U_x^2}{\partial x^2} + \frac{\partial U_x^2}{\partial y^2}\right) - \rho_f g \frac{\partial h}{\partial x} \tag{3-6}$$

In the vicinity of duct centreline, viscous effects can be neglected. Steady state is assumed for the centreline water velocity. The gradient of $U_x$ in the y-direction can be neglected due to the symmetry at the centreline of the duct. Gravity is also ignored in the horizontal duct flow. Hence, Equation 3-6 can be approximated by

$$\rho_f U_x \frac{\partial U_x}{\partial x} = -\frac{\partial P}{\partial x} \tag{3-7}$$

Hence, the centreline water velocity profile through the constrictions can be estimated by Equation 3-7 from the measured static pressure approaching the constriction, as in Table 3-7.

Table 3-7. Static pressure and corresponding calculated centreline water velocity along streamwise direction for ramp constriction–3 (see Table 3-5)

| x-coordinate of particles (m) * (see Figure 3-19) | Static Pressure (Pa (g)) | Centreline water velocity (m/s) |
|---|---|---|
| 0 | 5800 | 0.305 |
| 0.043 | 5790 | 0.337 |
| 0.119 | 5738 | 0.466 |
| 0.159 (throat) | 5585 | 0.723 |
| 0.194 | 5546 | 0.776 |
| 0.26 | 5617 | 0.678 |

* Ramp constriction position is from 0.089 to 0.15 m, with 0.15 m corresponding to the throat.

The Saffman lift force is negligible at very small shear rates (e.g. in the vicinity of centreline) or very low $Re_p$. When the particle is small or the spin velocity low (e.g. near the vicinity of centreline), the Magnus lift force is negligible (Fan and Zhu, 1998). At very low particle Reynolds numbers, particle motion is governed by the BBO (Basset, Boussinesq and Oseen) equation (Rudinger, 1969; Soo, 1990; Fan and Zhu, 1998; Massoudi, 2003),

$$\frac{\pi d_p^3}{6}\rho_p\frac{du_p}{dt}=C_D\frac{\rho_f|U_f-u_p|(U_f-u_p)A_p}{2}-\frac{\pi d_p^3}{6}\nabla P+\frac{1}{2}\frac{\pi d_p^3}{6}\rho_f\left(\frac{dU_f}{dt}-\frac{du_p}{dt}\right)+$$
$$\frac{3}{2}d_p^2\sqrt{\pi\rho_f\mu_f}\int_{t_0}^{t}\frac{\frac{dU_f}{dt'}-\frac{du_p}{dt'}}{\sqrt{t-t'}}dt'-\rho_p g \qquad (3\text{-}8)$$

The left-hand side represents the inertia. The right side sums the forces on the particle, the first term being the drag force, the second the effect of the pressure gradient and the third the force required to accelerate the added mass. The integral Basset history term accounts for deviation of the flow around the particle from undisturbed steady flow. The final term is gravity.

Beyond the Stokes regime, the effect of convective acceleration of the fluid surrounding the particle is important and the BBO equation must be modified. The modified equation with the history term neglected takes the form (Odar and Hamilton, 1964; Hansell et al., 1992):

$$\frac{du_p}{dt}=\frac{3}{4}\frac{C_D\rho_f|U_f-u_p|(U_f-u_p)}{d_p\rho_p}+\frac{1}{2}\frac{\rho_f}{\rho_p}\left(\frac{dU_f}{dt}-\frac{du_p}{dt}\right)+\frac{\rho_f}{\rho_p}\frac{dU_f}{dt}+(\frac{\rho_f}{\rho_p}-1)g \qquad (3\text{-}9)$$

Table 3-7 and Figure 3-20 show the calculated centreline water velocity profile through ramp constriction-3. Based on fourth order polynomial curve fitting to the calculated centreline water velocities, the centreline water velocity can be expressed by

$$U_c=-828.3x^4+267.79x^3-9.77x^2+0.41x+0.31 \qquad (3\text{-}10)$$

with $R^2=0.98$ and a standard deviation of 0.07 m/s, respectively.

3.4.2 Particle velocity in horizontal direction

Measured particle velocities in the streamwise direction appear in Table 3-8.

From Equation 3-10, the change of centreline velocity following the fluid is

$$\frac{dU_c}{dt} = (-3313.2x^3 + 803.37x^2 - 19.54x + 0.41)U_c \tag{3-11}$$

The following equations can then be obtained to predict particle velocity:

$$\frac{du_p}{dt} = \frac{3}{4}\frac{C_{D,wall}\rho_w|U_c - u_p|(U_c - u_p)}{d_p\rho_p} + \frac{\Delta_A}{2}\frac{\rho_w}{\rho_p}\left(\frac{dU_c}{dt} - \frac{du_p}{dt}\right) + \frac{\rho_w}{\rho_p}\frac{dU_c}{dt} \tag{3-12}$$

$$C_D = \frac{21}{\mathrm{Re}_p} + \frac{6}{\mathrm{Re}_p^{0.5}} + 0.28 \quad (0.1 < \mathrm{Re}_p < 4000) \text{ (Clift et al., 1978)} \tag{3-13}$$

$$K_F = \frac{1}{1 - 1.6(d_p / D_H)^{1.6}} \quad (d_p \le 0.6D_H) \text{ (Clift et al., 1978)} \tag{3-14}$$

$$C_{D,wall} = C_D K_F \quad \text{(Clift et al., 1978)} \tag{3-15}$$

Boundary conditions: $x(0) = 0.0331$ m, $U_c(0) = 0.337$ m/s, $u_p = 0.297$ m/s.

Here we assume an added mass coefficient of $\Delta_A = 1$.

The particle Reynolds number based on $(U_c - u_p)$ at $t = 0$ is

$$\mathrm{Re}_p = \frac{d_p(U_c - u_p)\rho_w}{\mu_w} = \frac{0.0115 \times (0.337 - 0.297) \times 998}{0.001} = 460 < 1000 \tag{3-16}$$

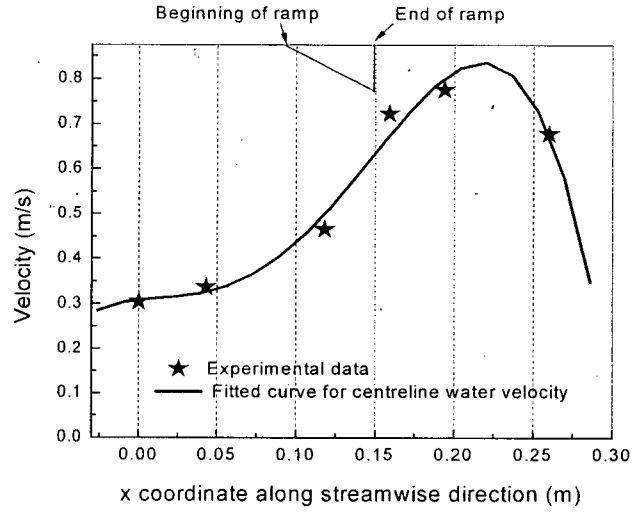


Figure 3-20. Centreline water velocity along streamwise direction for a neutrally buoyant spherical polyethylene-red-1 particle. (ramp constriction-3 position is 0.09-0.15 m)

Table 3-8. Measured positions and velocities in horizontal direction for neutrally buoyant polyethylene-red-1 particle

| Time (s) | Velocity at each time step (m/s) | Position along streamwise direction at each time step (m) |
|---|---|---|
| 0 | 0.297 | 0.033 |
| 0.033 | 0.296 | 0.043 |
| 0.067 | 0.305 | 0.053 |
| 0.100 | 0.311 | 0.063 |
| 0.133 | 0.311 | 0.073 |
| 0.167 | 0.337 | 0.084 |
| 0.200 | 0.359 | 0.095 |
| 0.233 | 0.397 | 0.107 |
| 0.267 | 0.470 | 0.120 |
| 0.300 | 0.651 | 0.136 |
| 0.333 | 0.802 | 0.158 |
| 0.367 | 0.732 | 0.184 |
| 0.400 | 0.546 | 0.209 |
| 0.433 | 0.394 | 0.227 |
| 0.467 | 0.286 | 0.240 |
| 0.500 | 0.413 | 0.250 |
| 0.533 | 0.489 | 0.263 |
| 0.567 | 0.467 | 0.280 |

$\mathrm{Re}_p$ varies as the flow develops and is in the range of 270 to 460 in the above-mentioned calculation with Equations 3-13 to 3-15 used to calculate the drag coefficient.

The Reynolds number based on the water mean velocity upstream of the constriction and hydraulic diameter of the duct is

$$\mathrm{Re} = \frac{D_H U_m \rho_w}{\mu_w} = \frac{0.0367 \times 0.243 \times 998}{0.001} = 8900 \qquad (3\text{-}17)$$

Since $\mathrm{Re} > 6000$, the flow is in the turbulent regime, as considered above.

The fourth-order Runge-Kutta method with variable stepsize was used to solve the three ordinary differential equations, $dx/dt = U_c$ plus Equations 3-11 and 3-12 (see Appendix A). From Figure 3-21, we see that agreement between calculated horizontal particle velocities and

the experimental results is only fair. The deviation is mainly attributed to particle motion in the vertical and spanwise directions, inaccurate centreline velocity prediction, neglect of some terms (e.g. lift and Basset history forces) and only the horizontal direction being considered. Investigation of the horizontal particle velocity could help to understand the particle behaviour while passing through constrictions. Blockage in the constrictions is mainly attributed to particle behaviour, especially particle collisions with each other and with the wall. Further work is needed for particle collisions in both dilute and dense flow.

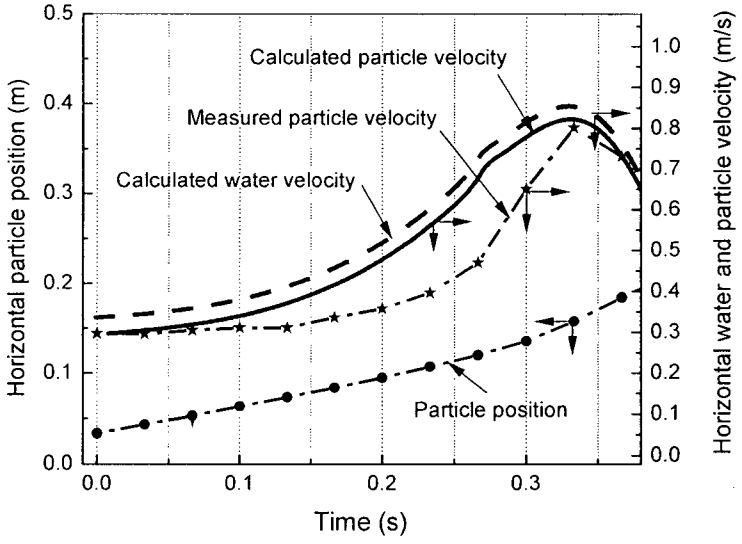


Figure 3-21. Horizontal particle position vs time and comparison of calculated and measured particle velocities in horizontal direction for a neutrally buoyant spherical polyethylene-red-1 particle passing through ramp constriction-3 (see Table 3-5). (0.17-0.32 s corresponds to the constriction)

## 3.5 Estimation of Pressure Drop for Blockage

For the rectangular (abrupt) constrictions investigated in the present study (see Table 3-5), blockage only occurred at the entrance of the constriction (zone 1 in Figure 3-22) when particles moved and collided with each other and with the wall, eventually leading to blockage. For the

dilute water-particle flows, no blockage was observed inside the rectangular constriction (zone 2 in Figure 3-22). For converging ramp constrictions, the particles blocked inside the ramp, as indicated schematically in Figure 3-23. No stable blockages were observed in circular constrictions (see Table 3-5) since particles slipped relatively easily through the gap due to the smooth profile of the circular semi-cylinders.

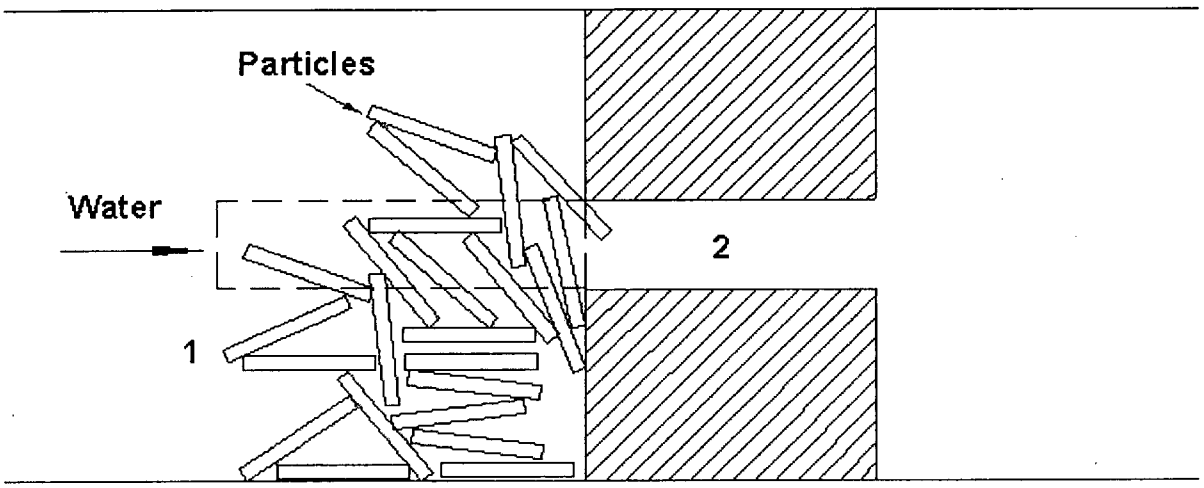


Figure 3-22. Schematic of blockage in rectangular (abrupt) constriction

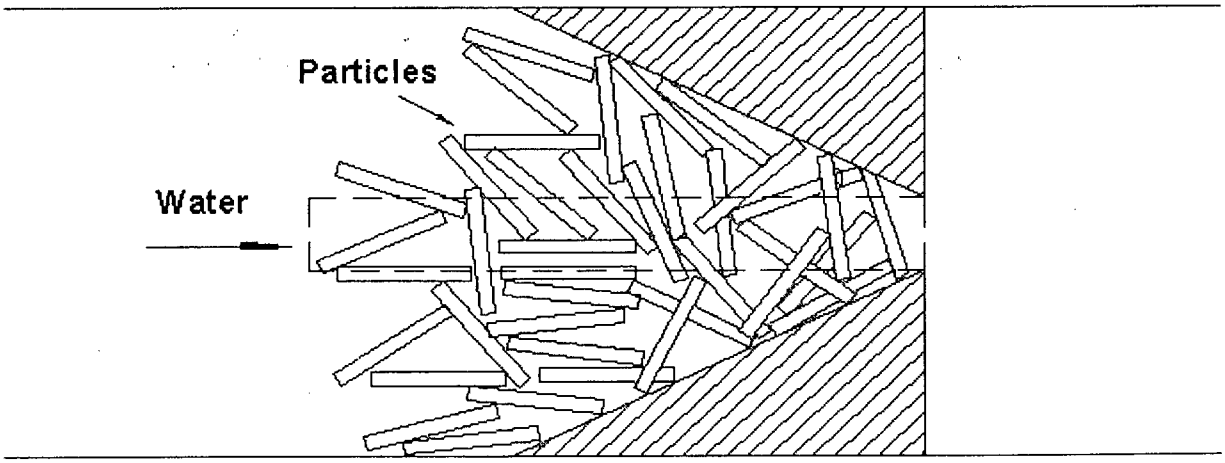


Figure 3-23. Schematic of blockage in converging ramp constriction

From Figures 3-22 and 3-23, imagine that a blockage can only be broken from the rectangular region shown by a dashed line in both figures. Particles inside the rectangle are influenced by fluid and particles around the dashed boundary. A rectangular control surface is considered as shown in Figure 3-24, where the surface represents the real wall or interlocked particles surrounding the rectangular control volume.

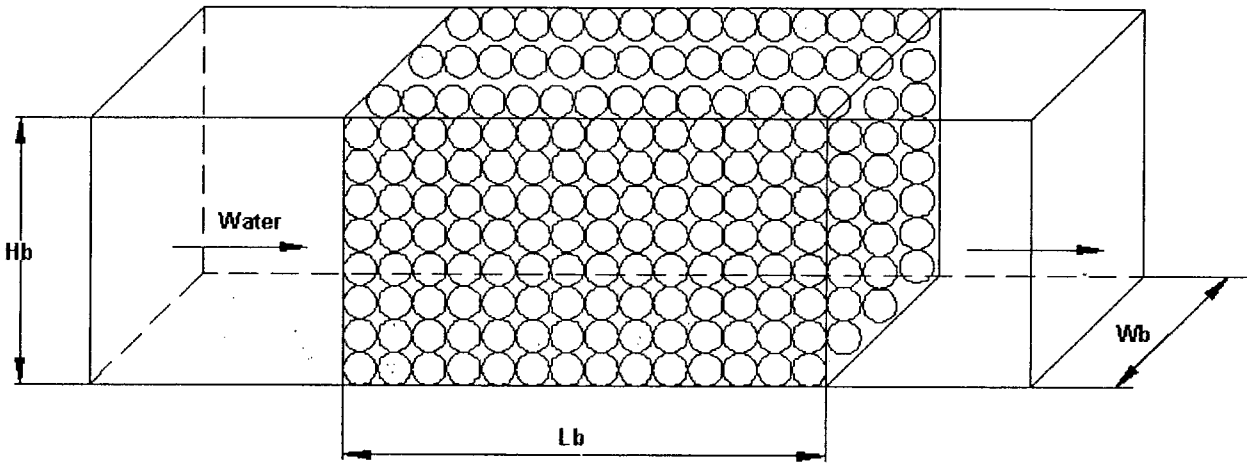


Figure 3-24. Schematic of blockage in constriction. ($L_b$, $W_b$, $H_b$ are length, width, height of blockage bed, respectively)

To estimate the pressure drop through the blockage, the following assumptions are made:

(1) Horizontal packed bed;

(2) Gravity is neglected;

(3) Particles pack uniformly giving rise to continuous flow channels;

(4) Flow inside the horizontal bed is at intermediate Reynolds number (typically $10<Re_p<1000$ ) or in turbulent flow.

The Ergun equation (Ergun, 1952; Nemec and Levec, 2005; Keyser et al., 2006) can be written as:

$$\frac{\Delta P}{L_b} = A\frac{\mu_f U_0 (1-\varepsilon)^2}{\phi_s^2 d_v^2 \varepsilon^3} + B\frac{\rho_f U_0^2 (1-\varepsilon)}{\phi_s d_v \varepsilon^3} \tag{3-18}$$

where

A= Blake–Kozeny–Carman constant, typically =150;

B= Burke–Plummer constant, typically= 1.75.

$d_{sv}$ = Equivalent surface-volume diameter of particle, m.

$d_v$ = Equivalent volume diameter of particle, m.

$L_b$ = Length of blockage bed, m.

$S_p$ = Particle surface area, $m^2$.

$U_0$ = Superficial velocity of water, m/s.

$V_p$ = Particle volume, $m^3$.

$\Delta P$ = Pressure drop, Pa.

$\mu_f$ = Dynamic viscosity of water, = 0.001 Pa.s at 20 °C.

$\varepsilon$ = Void fraction of blockage bed, -.

$\phi_s = 6V_p/(d_v S_p) = d_{sv}/d_v$, sphericity, -.

For cylindrical particles, Nemec and Levec (2005) recommend

$$A = \frac{150}{\phi_s^{3/2}}, \qquad B = \frac{1.75}{\phi_s^{4/3}} \tag{3-19}$$

Since cylindrical particles are reasonably similar to cuboidal particles (maximum aspect ratio much greater than 1) in shape, Equation 3-19 was employed to calculate A and B. A void

fraction of 0.5 was assumed for all irregular particles, and the absolute water velocity, $U_i$, inside the horizontal blockage bed (formed by the "log-jammed particles") was calculated from

$$U_i = U_0 / \varepsilon \tag{3-20}$$

The particle Reynolds number based on the hydraulic diameter of the flow channel can be expressed by

$$\mathrm{Re}_p = D_h U_i \rho_f / \mu_f \tag{3-21}$$

where $D_h$ is the hydraulic diameter expressed by

$$D_h = 4 \times V_w / S_w \tag{3-22}$$

$V_w$ is the volume available for flow, and $S_w$ is the wetted surface area.

For a packed bed of spherical particles,

$$D_h = 4 \times \frac{\frac{\pi}{6} d_{sv}^3 \varepsilon}{(1-\varepsilon)\pi d_{sv}^2} = \frac{2\varepsilon \times d_{sv}}{3(1-\varepsilon)} \tag{3-23}$$

so that

$$\mathrm{Re}_p = \frac{2}{3} \frac{d_{sv} U_0 \rho_f}{\mu_f (1-\varepsilon)} \tag{3-24}$$

Equation 3-24 can also be replaced by

$$\mathrm{Re}_p = \frac{d_{sv} U_0 \rho_f}{\mu_f (1-\varepsilon)} = \frac{\phi_s d_v U_0 \rho_f}{\mu_f (1-\varepsilon)} \tag{3-25}$$

Particle Reynolds numbers calculated from Equation 3-25 are listed in Table 3-9. For the superficial velocities in the present study, the particle Reynolds number was in the range of 1,900-12,960 if particles inside the horizontal blockage bed are assumed to be stationary. When blockage occurred, the static pressure upstream of the blockage increased abruptly. This excess

pressure was released either by opening the by-pass valve 6 (see Figure 3-2) or by collapse of the blockage bed. Figure 3-25 indicates that the higher the superficial velocity of the water, the larger the pressure drop across a horizontal blockage bed of given length. The larger pressure drop of silicon-rubber70-cuboid-4 (right-hand column) is mainly attributed to the extreme particle shape (small sphericity). Different sphericity also may lead to different void fractions. Generally, the more non-spherical (i.e. small sphericity) the particle, the larger the void fraction (Nemec and Levec, 2005), whereas a void fraction of 0.5 is assumed throughout the above analysis. The friction between particles and wall, as well as the interlocking characteristics and bending strength of particles, determines whether or not the blockage can be broken.

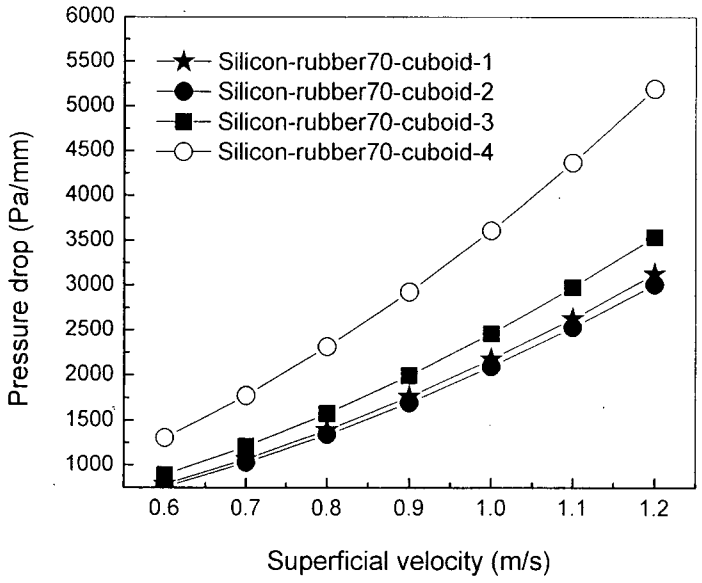


Figure 3-25. Effect of superficial velocity of water on predicted pressure drop per unit length of horizontal blockage bed. (For Reynolds numbers, see Table 3-9. For properties of particles see Table 3-3).

Table 3-9. Calculated particle Reynolds numbers (void fraction=0.5) for cuboids

| $U_o$ | $U_i$ | $Re_p$ | | | |
|---|---|---|---|---|---|
| | | 7x7x3 mm | 9x9x3 mm | 15x5x3 mm | 25x3x3 mm |
| 0.2 | 0.4 | 1932 | 2172 | 1992 | 1692 |
| 0.3 | 0.6 | 2904 | 3252 | 2988 | 2532 |
| 0.4 | 0.8 | 3876 | 4332 | 3984 | 3384 |
| 0.5 | 1 | 4848 | 5424 | 4980 | 4224 |
| 0.6 | 1.2 | 5820 | 6504 | 5976 | 5076 |
| 0.7 | 1.4 | 6792 | 7584 | 6972 | 5916 |
| 0.8 | 1.6 | 7752 | 8664 | 7968 | 6768 |
| 0.9 | 1.8 | 8724 | 9756 | 8976 | 7608 |
| 1 | 2 | 9696 | 10836 | 9972 | 8460 |
| 1.1 | 2.2 | 10668 | 11916 | 10968 | 9300 |
| 1.2 | 2.4 | 11628 | 12960 | 11964 | 10152 |

From the dimensions of the constrictions most subject to blockage in Table 3-5, we assume $W_b = 0.0254\,\text{m}$ and $H_b = 0.0125\,\text{m}$ in Figure 3-24. In order to break the blockage,

$$\frac{\Delta P}{L_b} \times W_b \times H_b \geq \tau_s \times 2(W_b + H_b) \tag{3-26}$$

where $\tau_s$ is the average shear stress on the boundary of the blockage bed and $\tau_s < \tau_c$, where $\tau_c$ is the critical shear stress on the boundary, calculated via.

$$\tau_c = \frac{\Delta P}{2L_b(W + H_b)} \times W_b \times H_b \tag{3-27}$$

Calculated shear stresses, plotted in Figure 3-26, are in the range of 350-22,000 Pa, depending on the superficial water velocity, particle properties and packing characteristics of the blockage bed. When the average shear stress at the boundary is less than the critical shear stress, the blockage tends to collapse. Note that the average shear stress may be generated either by particle-wall friction or interlocking of particles at the boundary of the horizontal blockage. As the superficial water velocity increases, the blockage bed becomes more and more compact (i.e.

void fraction decreases), increasing the shear stress required to break the blockage. Hydrodynamic forces cannot break up all blockages, especially when the blockage is tight. Mechanical means may then be required to force the particles through the constriction, as discussed in Chapters 4 to 6. Due to the effect of gravity, the packing of particles with $\rho_p \neq \rho_w$ tends to be non-uniform. For $\rho_p > \rho_w$, the upper part of the blockage bed is more easily broken.

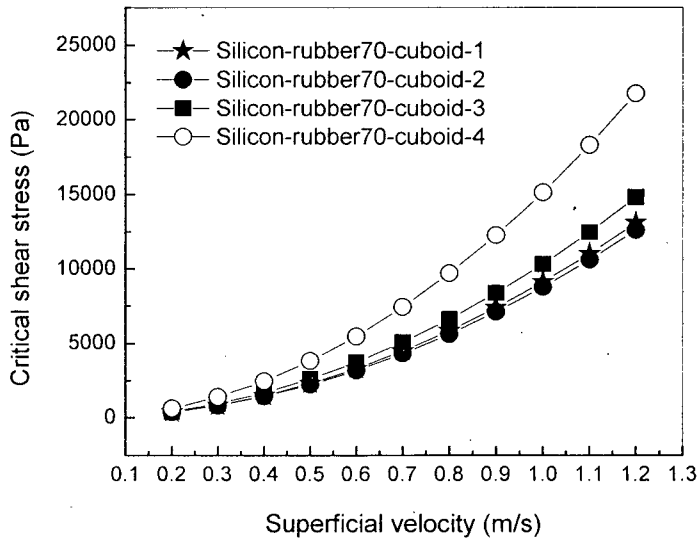


Figure 3-26. Effects of superficial velocity of water on critical shear stress at boundary of horizontal blockage bed. (For Reynolds numbers, see Table 3-9. For properties of particles, see Table 3-3).

## 3.6 Conclusions

(1) Spherical particles of small size and low density (e.g. polyethylene-yellow-1 in Table 3-3) were easily transported and were unlikely to block constrictions, while irregular rubber and plastic particles of density greater than water were difficult to convey. With increasing water mean velocity, particles experienced creep, saltation and suspension.

(2) Large particles of high aspect ratio and density higher than water were difficult to transport. These particles were also more likely to block the constriction at high Re.

(3) The maximum particle dimension does not solely determine whether or not blockage occurs when the minimum dimension of the particles is less than the maximum gap dimension. However, large particles were more likely to cause blockage, and a lower particle concentration was required to block a constriction for larger than for smaller particles.

(4) Nearly neutrally buoyant conical particles (e.g. ABS-Cone-1) were more likely to block a constriction at a high water mean velocity. This appears to be mainly because of the unbalanced shape, intense fluid-particle and particle-particle interactions, and a large ratio of maximum particle dimension to minimum constriction dimension.

(5) Particles with some compressibility (e.g. Silicon-rubber70-cuboid particles) were more likely to block constrictions than hard particles (e.g. PTFE-Rod particles), mainly because compressible particles tended to jam together instead of separating after colliding. However, soft particles (e.g. Neo-rubber40-cuboids) did not form stable blockages due to their low hardness, low bending strength and high flexibility.

(6) Reynolds number affects particle motion and blockage tendency. At small water mean velocity, non-spherical particles of density greater than that of water were difficult to transport because of sedimentation. As the water mean velocity increased, non-spherical particles were easier to transport (via creep or saltation), with some piling upstream of the constriction and others passing through the gap almost one by one. Blockage was unlikely for this case. For higher water mean velocities, more and more heavier non-spherical particles were transported

and lifted vigorously, increasing the probability of different particles passing through the constriction simultaneously, thereby augmenting the probability of blockage. For the conditions of the present study, 3 to 10 non-spherical particles were sufficient to block the constriction if the ratio of particle maximum dimension to constriction minimum dimension > 0.4. As Um increased, blockage was less likely to occur and more readily broken, especially for small-particle-blockages, because of increased drag and increased pressure gradient immediately upstream of the constriction. The blockage probability depends on the interactions among the fluid, particles and constriction.

(7) Ramp constriction-4 (see Table 3-5) with a square gap (12.5 (W) x 12.5 (H) mm) in the middle was more likely to cause blockage than a rectangular constriction-1 (25.4 (W) x 12.5 (H) mm). This is because the latter provides more space for particles to disperse laterally, reducing the probability of blockage.

(8) Flow properties of the water upstream of the constriction, constriction configurations and particle properties (dimensions, shape, density, etc.) determined whether or not particles proceed directly downstream. Large particles denser than water were not readily trapped by the vortex immediately downstream of the constriction, especially at larger Re, because of their dimensions and inertia.

(9) Particles of larger densities and dimensions were more likely to collide with the block surface and with each other. Such collisions led to more rotation, causing abrupt changes in particle trajectories and velocities. The larger or heavier the particles, the greater the chance of them colliding with the wall and with each other because of inertial effects. Preliminary

observations show that understanding the motion of a single particle is helpful to understand the motion of swarms of particles. However, blockage is related to swarms of particles and cannot occur without particle-particle and particle-wall interactions.

(10) The pressure drop needed to break a blockage was predicted based on horizontal packed bed assumption using a modified Ergun equation, to help understand the mechanism of blockage.

# CHAPTER 4. PILOT STUDY OF BIOMASS FEEDING: EXPERIMENTAL SETUP AND METHODOLOGY

This chapter introduces the experimental set-up and methodology for the biomass feeding system. It also gives the properties of the biomass fuels tested. This work utilizes a screw feeder/ lock-hopper system previously fabricated and commissioned to feed sawdust to a circulating fluidized bed gasifier (Li et al, 2004). The feeding system was decoupled from the gasifier for the current experiments. Experiments were then undertaken to investigate the influence on biomass screw feeding of such particle properties as moisture content and heterogeneity

## 4.1 Material Properties of Interest

### 4.1.1 Bulk density

Bulk density is the overall mass of loose material per total unit volume including interstices. For biomass feedstocks, both oven-dry bulk density and wet bulk density due to different moisture content are commonly employed. It is measured simply by weighing a certain quantity of sample of particles after pouring into a cylinder, i.e.

$$\rho_b = \frac{M_1 - M_2}{V} \tag{4-1}$$

where $M_1$ and $M_2$ are the masses of filled and empty cylinders and V is the occupied internal volume of the cylinder which had a height of 0.12 m and a diameter of 0.1 m in the present study. The bulk solids were poured into the cylinder from a height of 0.2 m measured from the bottom of cylinder, and the top surface were gently flattened after gently shaking the cylinder.

4.1.2 Particle density

Apparent particle density (sometimes called solid density) is the density of particles, including any voids inside the particle, but excluding interstices between particles. It can be estimated by the same procedures as for the loose bulk density except that the volume is compacted with the aid of mechanical pressure up to 0.5-1 MPa. In our case, the material was poured into a mold and manually compressed to 0.5 MPa by mechanical pressure.

4.1.3 Voidage

Particles rest on each other due to gravity to form a packed bed in the hopper. A certain volume of space between the particles remains unoccupied depending on particle density, particle shape and packing characteristics. The interstitial spaces are called voids. The volume fraction occupied by voids, called voidage, is related to particle and bulk density by:

$$\varepsilon = 1 - \frac{\rho_b}{\rho_p} \tag{4-2}$$

4.1.4 Compressibility and compaction ratios

Compressibility and compaction ratios are important concepts for biomass fuels. See Chapter 2 and Chapter 6 for more details.

4.1.5 Angle of friction and friction coefficient

Friction is a measure of the resistance to the movement of one object in relation to another surface with which it is in contact. We can measure the friction in terms of a coefficient of friction, defined as the ratio of the force needed to move two objects in contact with one another and the normal force holding the two objects together. The arc tangent of the coefficient of friction is called the friction angle. For most material combinations, the static friction is higher than the kinetic or dynamic friction. To determine the former in this work, a spring balance connected to a block of the material (of depth 0.12 m in an open-at-both-ends cylinder of 0.1 m

diameter) was pulled in a horizontal direction as it sat on a surface, slowly increasing the force until the block began to slide, ensuring that the spring balance was parallel to the surface. The reading on the spring balance scale when the block begins to slide is a measure of the static friction force required to initiate motion, whereas the reading when the block slides at constant speed is employed to calculate the dynamic coefficient of friction and hence the angle of kinetic friction. The angle of kinetic friction and the kinetic friction coefficient are used in the present study.

4.1.6 Internal friction angle and coefficient of internal friction

Internal friction is a measure of the force required to cause particles to slide over each other. The internal friction angle is measured by building a flat-topped pile of the bulk material, with one side of the pile resting against the vertical face of a rigid block. To measure the internal friction coefficient, the block is pushed forward slightly into the pile and the position where shearing occurs at the top of the pile is noted. This is assumed to represent the upper limit of a shear plane extending upward from the foot of the block. The inclination of such a plane to the horizontal should be $45^o - \delta/2$, where $\delta$ is the angle of internal friction. This method was recommended by Metcalf (1966). Some researchers instead use the angle of repose or the "reclaim surface angle" to estimate the angle of internal friction angle. The latter is the angle with the horizontal of the shear plane when material is withdrawn through a horizontal slot. Note that the angle of internal friction may not be single-valued, and it can be time- and velocity-dependent. The Metcalf (1966) method was adopted due to its simplicity in the present study and the measured angle of internal friction is assumed to be the effective angle of internal friction.

### 4.1.7 Flowability

Flowability, simply defined as the ability of bulk solids to flow, is an important concept for bulk materials. Jenike (1964) suggested a flow index (see Table 2-2) to quantify flowability, while others have proposed other tests. For the definition of flow-function and flow index see Chapter 2. Mohr-Coulomb model is also used to address flowability, leading to two measurable parameters (cohesion and internal friction angle) and two derived parameters (unconfined yield strength and major consolidation stress). Flowability relies on a combination of material physical properties that affect material flow and equipment for storing, feeding and handling the material (Prescott and Barnum, 2000; Fitzpatrick et al., 2004).

### 4.1.8 Granular materials

Granular materials are collections of discrete and macroscopic solid particles and are defined in different ways. Granular materials do not quite fit any of the usual phases of matter: solid, liquid, or gas. The lower size limit of granular material were set at 1 μm (Duran, 2000), whereas Richards (1966), and Chattopadhyay et al. (1994) recommend lower and upper size limits of 0.42 mm and 3.35 (or 6) mm, respectively. Granular materials are generally defined as $> 0.5$ mm and $< 12.5$ or 25 mm in size for industrial applications (Link Belt Co., 1959; IS-8730, 1978; CEMA-550, 1980; Chattopadhyay et al., 1994), while particles smaller than 0.5 mm are considered to constitute powders. Granular materials differ significantly from powders in flow properties. Biomass particles are unusual granular materials, varying greatly in size and shape, compressibility and pliability, with moisture content as high as 60%. Although biomass particles are usually between 0.5 and 15 mm in equivalent diameter for gasification and combustion applications, biomass powders are also quite common.

## 4.2 Experimental Set up and Methodology

Schematics of the biomass feeding systems used in the experiments (including the upper hopper, lower hopper and screw feeder) appear in Figures 4-1 and 4-2. The dimensions of the hopper-screw feeder are given in Table 4-1. Two screws were employed in the present study as shown in Figure 4-3. Before commencing feeding, biomass fuels (e.g. wood pellets, hog fuel and sawdust) were added to the lower hopper and the surface leveled from above. The air inlet to the hopper is at the front of the hopper lid. This was connected to the building air supply via a pressure regulator and a flow meter in order to pressurize the hopper.

Table 4-1. Hopper and screw dimensions

| | Parameters of screw configuration | | Screw-1 | Screw-2 |
|---|---|---|---|---|
| Screw | Screw length | Feed hopper length, $L_h$ | 910 mm | 910 mm |
| | | Choke section length, $L_c$ | 610 mm | 610 mm |
| | Screw diameter, $D_o$ | | 100;90;80 (1) mm | 80 mm |
| | Shaft or core diameter, $D_c$ | | 30 mm | Variable (2) |
| | Pitch, $P$ | | 100 mm | Variable (2) |
| | $P / D_o$ | | 1 | Variable |
| | Clearance, $c$ | | 1;6;11 (1) mm | 11 mm |
| | Flight thickness, $\gamma$ | | 6.35 mm | 6.35 mm |
| | Average helix angle of screw with vertical | | 14 ° | Variable |
| | Material | | 316 SS | Carbon steel |
| Trough | Inside diameter, $D_t$ | | 102 mm | |
| | Material | | Carbon steel | |
| | Transparent test section | | Cast acrylic tube | |
| Hopper | Type | | Wedge-shaped | |
| | Length | | 910 mm | |
| | Height | | 910 mm | |
| | Angle of hopper wall with horizontal | | 70 ° | |
| | Material | | Carbon steel | |

Notes: (1) Screw diameter 100 mm for length of 800 mm, then 90 mm for length of 300 mm, and finally 80 mm for length of 420 mm.
(2) $P$ =40 mm, $D_c$ =56 mm for first 100 mm length; $P$ =56 mm, $D_c$ =43 mm for next 310 mm length; then $P$ =71 mm, $D_c$ =30.5 mm for 310 mm length; then $P$ =80 mm, $D_c$ =20.3 mm for length of 495 mm; $P$ =70 mm, $D_c$ =20.3 mm for final 305 mm length.

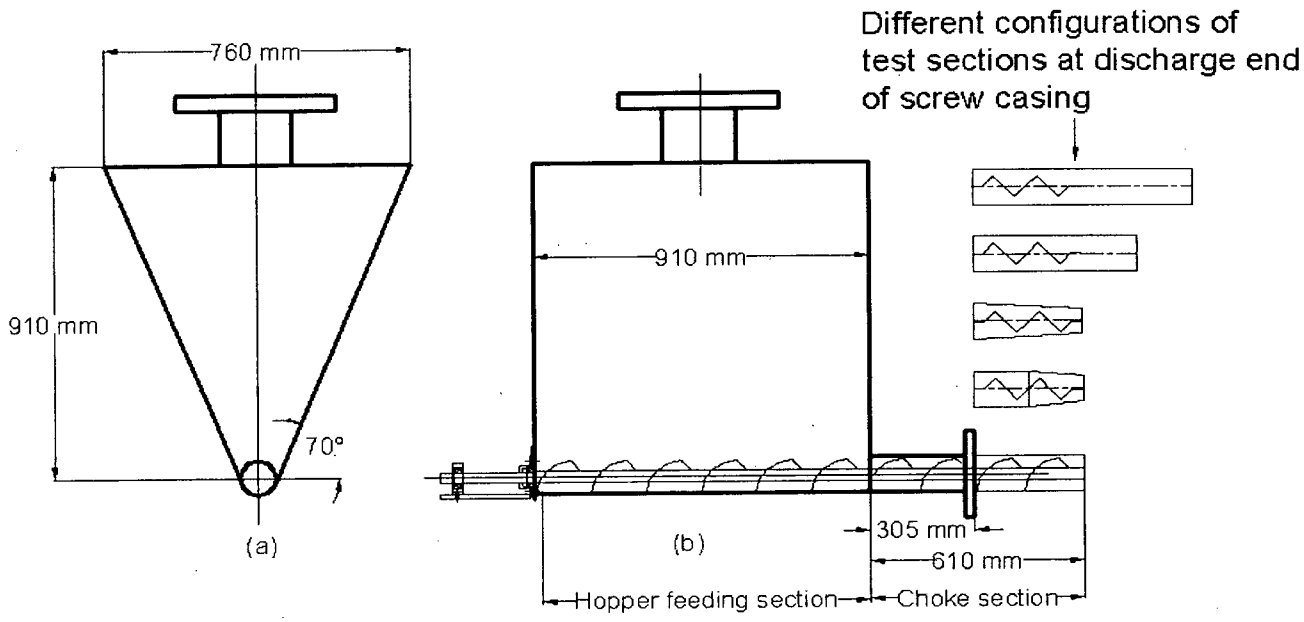


Figure 4-1. Schematic of lower hopper and screw feeder: (a) Front view of lower hopper; (b) Side view of lower hopper and screw feeder

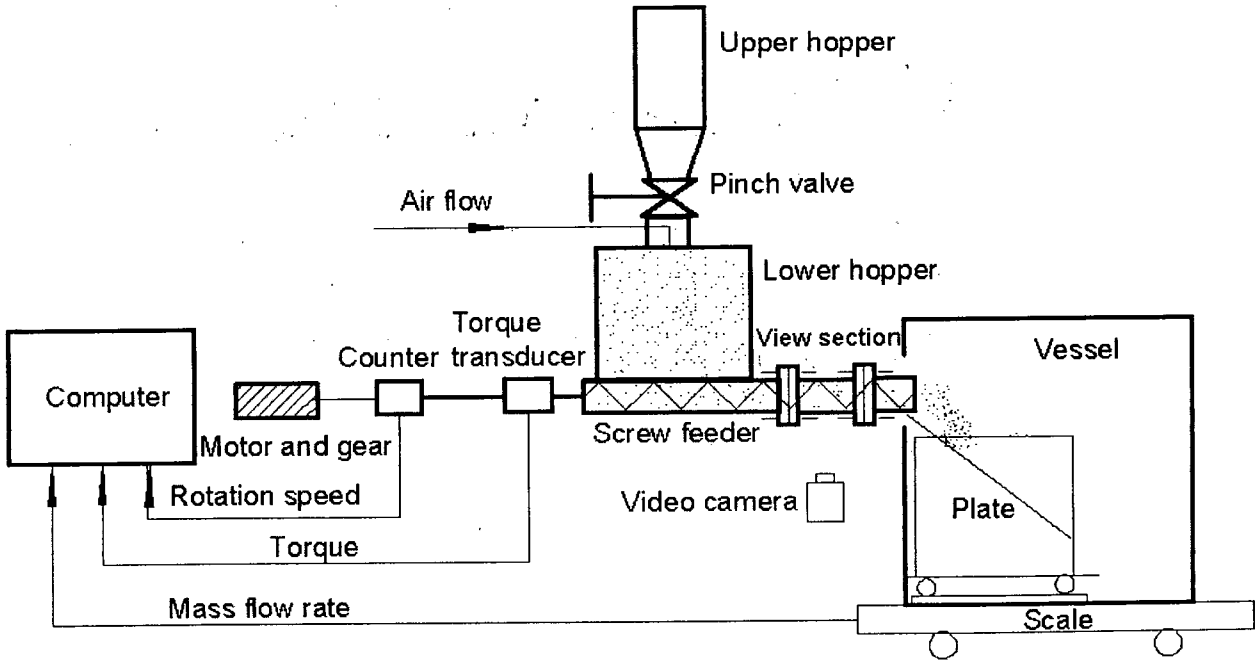


Figure 4-2. Schematic of biomass feeding system

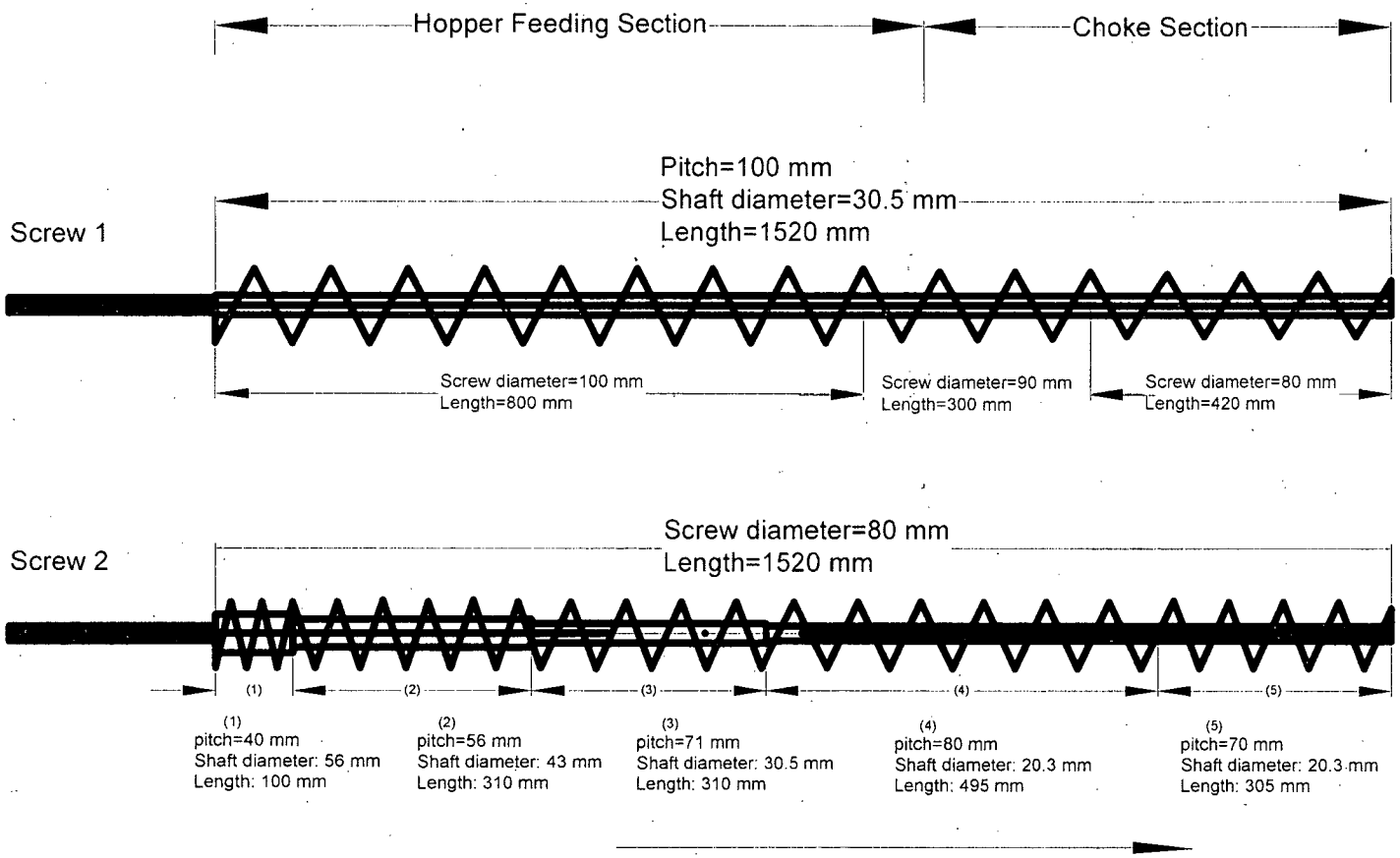


Figure 4-3. Configuration of test screws

A variable-speed DC motor (0.56 kW, Baldor CDP 3440) adjusted the rotational speed of the screw. A φ102 (ID) x 305 mm long cast acrylic tube was installed between the lower hopper and receiving vessel. The transparency of the tube allowed the mode of flow through the screw feeder to be visualized. Different test section configurations were available as shown in Figure 4-1. A video camcorder (see Table 3-4) captured images of particles interacting with each other and with the inside wall of the transparent tube, as well as with the screw flights. The observed particle trajectories are helpful to understand the flow of particles inside the screw feeder and the mechanisms of blockage.

A scale (Model: CARDINAL EF 100) with a digital weight indicator (see Table 4-2) was connected to a serial port of the computer for continuous measurement of the weight of material fed, with a time interval of 2 s between weight measurements.

Table 4-2. Main specifications of scale system

| Items | Models | Specifications | Supplier |
|---|---|---|---|
| Scale | CARDINAL EF 100 | 50 kg. x 0.02 kg.<br>0.46 x 0.46 m base,<br>Stainless Steel | B.C. Scale Co. Ltd. |
| Indicator | IQ plus 355 | RS232 and analogue output (0-10 VDC) | B.C. Scale Co. Ltd. |

A torquemeter with a counter (Model: MCRT28004T 5-3) with Model 721 Mechanical Power Instrument (see Table 4-3) was installed between the DC motor gear reducer and the lower hopper to measure the torque and rotational speed of the screw during feeding. Blockages could be detected by changes in torque and rotational speed. All data were stored in the hard disk of the data acquisition computer for later analysis. The experimental work began with relatively coarse materials of spheroidal shape, such as polyethylene particles, then progressed

to less regular materials such as wood pellets, and finally to materials of low bulk density, wide size distribution and significant compressibility, such as sawdust, hog fuel and wood shavings. All experiments were performed 2-5 times in order to determine the repeatability and range of flow rates and torque values for a given material and given set of experimental conditions. The work in this thesis does not emphasize hopper flows, which have been widely studied, but rather the transport of particles through the screw feeder.

The fill level in the feed hopper declines during each trial unless the hopper is periodically refilled. The draw-down pattern is not uniform for common screws with constant pitch, core shaft and screw diameter. On the other hand, refilling the hopper momentarily disturbs the feeder operation.

Table 4-3. Main specifications of torque measurement system

| Items | Models | Specifications | Supplier |
|---|---|---|---|
| Torquemeter | MCRT28004T 5-3; Rotary, inline, shaft-style, transformer-coupled, Frequency output sensor | Capacity: ± 565 N.m, 2 times safety overload for stall<br>Accuracy (% of full scale): ≤ ± 0.1%<br>Output (nominal): 1.5 mV/V | Instronics Inc. (produced by S. Himmelstein and Company) |
| Mechanical Power Instrument | 721 | RS232 serial interface<br>Sampling frequency: 36 Hz | Instronics Inc. (produced by S. Himmelstein and Company) |

Flow rates given here were obtained by calculating the average flow rate during the first two minutes after stable feeding was established. Feed rates and torque readings for a given material and the same experimental conditions were then averaged. Standard deviation and error bars are used in later analysis in Chapter 6. Repeatability, sometimes referred to as equipment variation, is the ability of the measurement system to provide consistent readings when used by a single

operator. Reproducibility, sometimes called appraiser variation, is the ability for multiple operators to achieve consistent results. Repeatability is analyzed for flow rates and torque reading in Chapter 6.

When blockage occurred and could not be broken, the materials were removed from the hopper manually before performing the next run. Three initial hopper levels were tested in the present experiments: a high (0.60 m), medium (0.45 m) and low level (0.30 m).

## 4.3 Material Preparation and Properties

The present study employed polyethylene particles, wood pellets, sawdust, hog fuel and wood shavings as biomass materials. (The polyethylene particles provided a reference case for comparison with the less regular biomass particles). The wood pellets were supplied by FireMaster Ltd and were thoroughly dry when received. The ground wood pellets were collected from those fed through the screw feeder and sieved into ground wood pellets-1 and 2. The sawdust was obtained by spraying water onto the wood pellets, causing the pellets to disintegrate into the original sawdust which had been used to form the pellets in the first place. The hog fuel came from previous work in our laboratory. Ground hog fuel was obtained from another researcher who had been using them for feeding a combustor. The wood shavings were provided by the Wood Processing Center of UBC from planar shavings.

The main physical properties of the materials tested are listed in Table 4-4. All measurements were carried out at room temperature (20°C) and atmospheric pressure. Material size distributions appear in Appendix B. Moisture contents were obtained from the weight loss after drying samples at 105°C for 5 hours. The particle mean diameters and size distributions shown in Figure 4-4 were determined by sieve analysis (RX-29, W.S. Tyler), with a sieving time of 10 minutes (see Table B-1). In all cases, the particles were mixed well before sampling

and five separate samples were analyzed in order to obtain average and representative values. A Sauter mean particle diameter was employed, defined as

$$d_m = \frac{1}{\sum x_i / d_i} \tag{4-4}$$

where $x_i$ is the mass fraction of particles of mean diameter $d_i$. The wood pellets were approximately cylindrical and almost uniform in size (average dimensions: ϕ 6.5 mm x 15 mm) except for some fines. Fines were removed by sieving through a 4.75 mm opening screen. Some grinding of the wood pellets by the screw feeder occurred in our experiments. Therefore wood pellets were only reused after removal of generated fines by again sieving through a screen with 4.75 mm openings. When the dimensions of wood pellets were observed to have changed significantly, they were replaced by new pellets to ensure a uniform size of the wood pellets during the experiments. Photos of the main materials in the present study appear in Figures 4-5 to 4-12, while the relations of bulk density and consolidating pressure on these materials are shown in Figure 4-13 (discussed in Chapter 6).

As shown in Figure 4-4, only sawdust-1 and wood pellets-2 are normal distribution at 0.05 level, the distribution of other materials are not normal at 0.05 level.

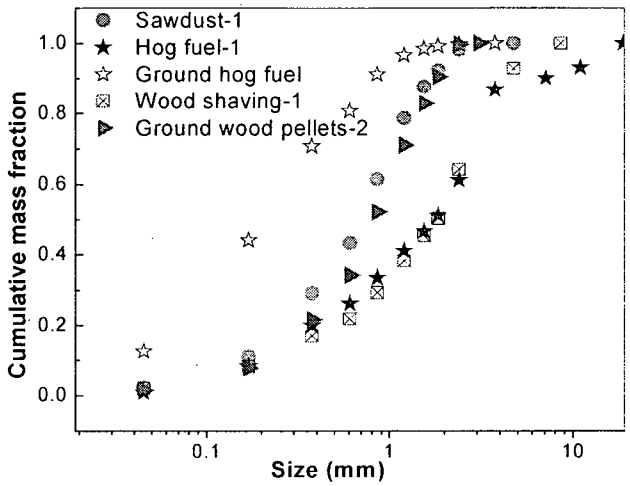


Figure 4-4. Particle size distributions of biomass fuels as initially fed

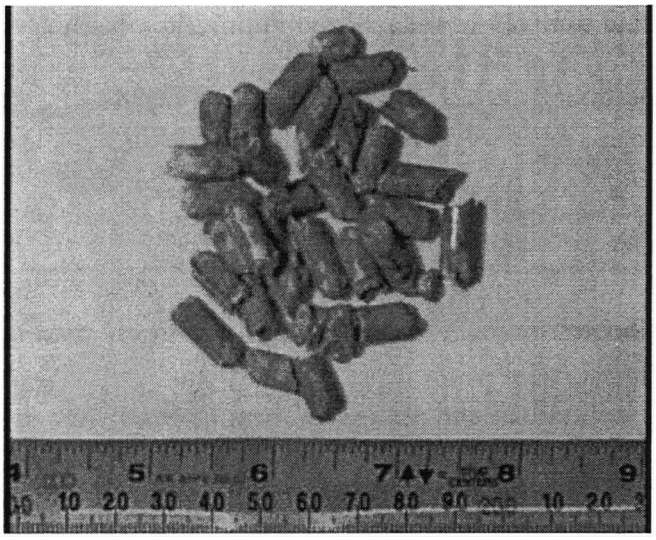

Figure 4-5. Photo of wood pellets

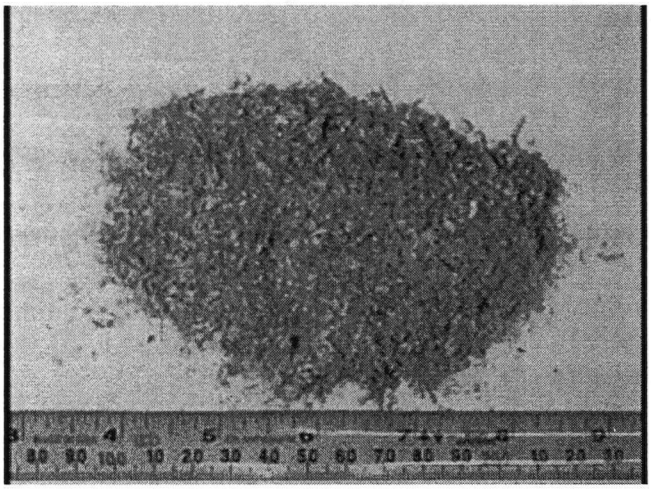

Figure 4-6. Photo of sawdust-1

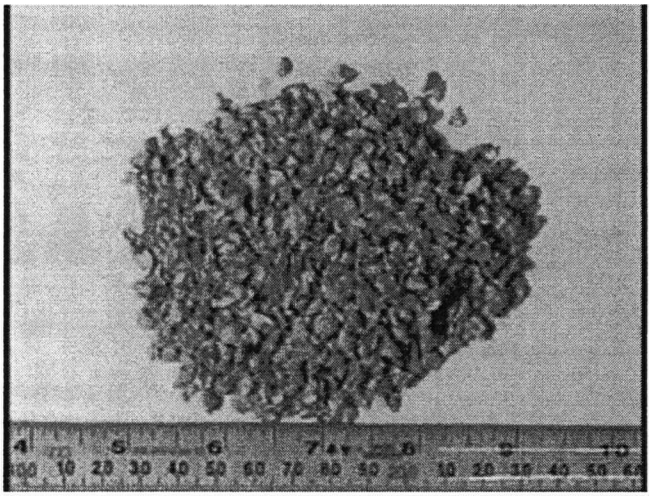

Figure 4-7. Photo of ground wood pellets-1

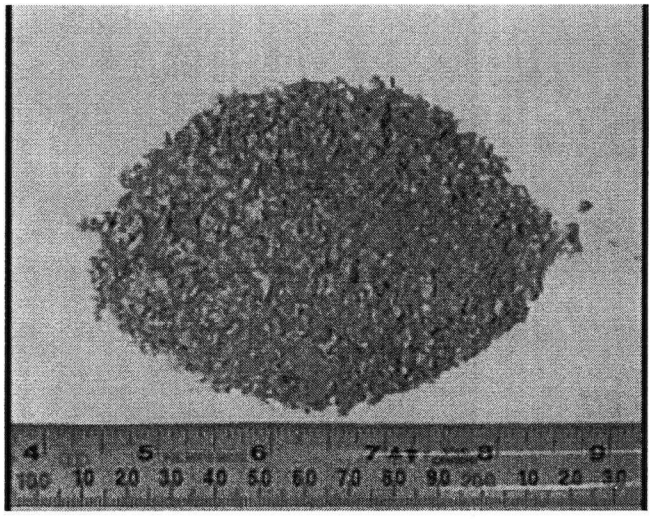

Figure 4-8. Photo of ground wood pellets-2

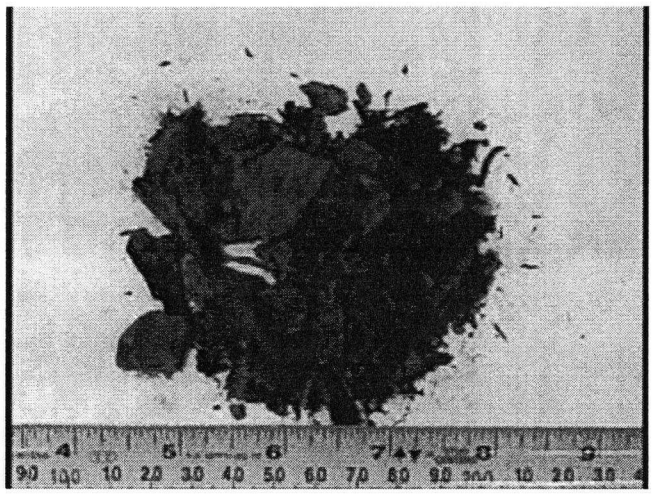

Figure 4-9. Photo of hog fuel-1

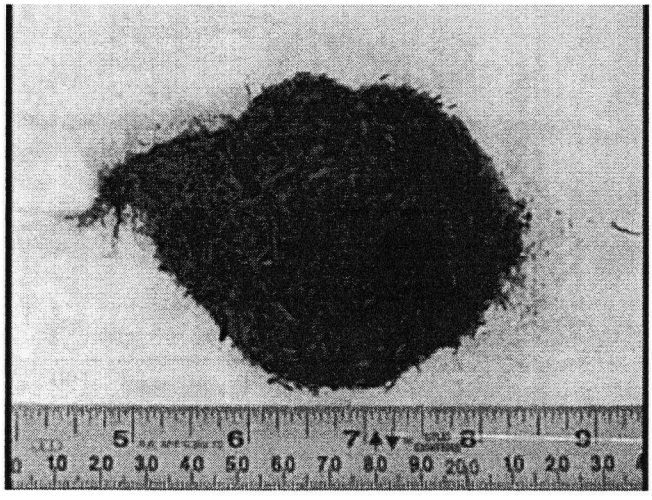

Figure 4-10. Photo of ground hog fuel

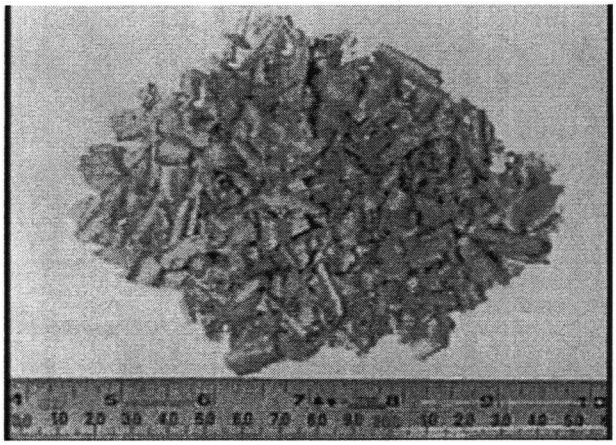

Figure 4-11. Photo of wood shavings

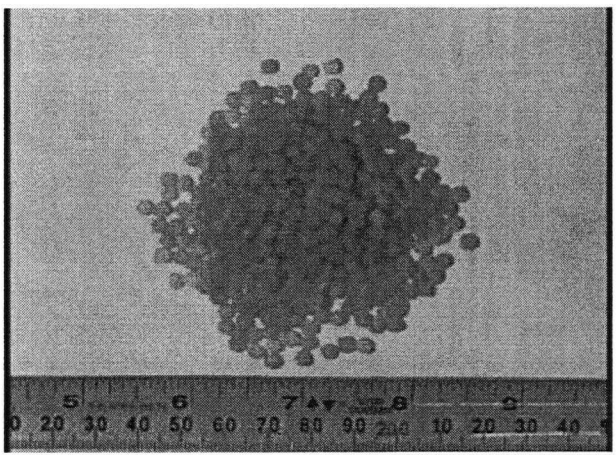

Figure 4-12. Photo of polyethylene particles

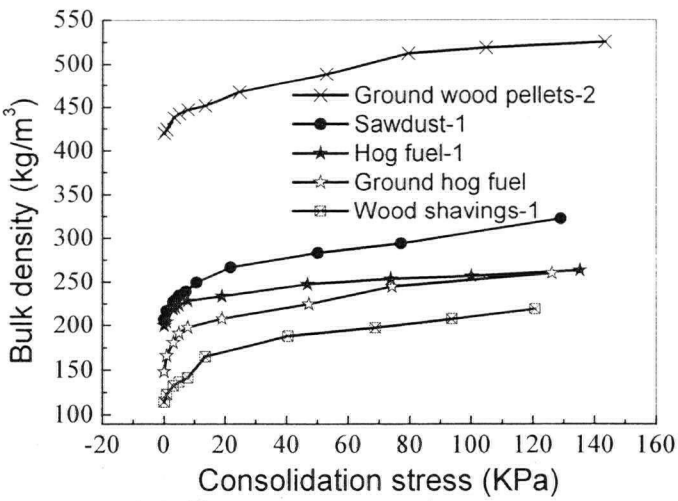


Figure 4-13. Relations between bulk density and consolidating pressure

Table 4-4. Hydrodynamic properties of materials in the present study

| Type | Mean diameter[1] (mm) | Size range (mm) | Bulk density ($kg/m^3$) | Particle density ($kg/m^3$) | Moisture (wet basis) [2] | Shape |
|---|---|---|---|---|---|---|
| Polyethylene particles | 4 | 3.0-5.0 | 610 | 908 | dry | Spheroid |
| Wood pellets | 9.8 | 8.0-11.6 | 630 | 1200 [3] | 8% | Cylinder |
| Ground wood pellets-1 | 4.05 | 3.35-4.75 | 485 | 1200 | 8% | Cylinder, cone, disk |
| Ground wood pellets-2 | 0.55 | 100% < 3.35, 98.5 % > 0.09 | 423 | 1200 | 8% | Cylinder, cone, disk |
| Sawdust-1 | 0.45 | 100% <6.73, 96 % (0.09 to 2.8) | 210 | 370 | 14% | Irregular |
| Sawdust-2 | 0.45 | 100% <6.73, 96 % (0.09 to 2.8) | 330 | 550 | 40% | Irregular |
| Sawdust-3 | 0.45 | 100% <6.73, 96 % (0.09 to 2.8) | 440 | 688 | 60% | Irregular |
| Hog fuel-1 | 0.72 | 100% < 25, 90 % (0.09 to 9.5) | 200 | 360 | 11% | Irregular |
| Hog fuel-2 | 0.72 | 100% < 25, 90 % (0.09 to 9.5) | 310 | 490 | 40% | Irregular |
| Hog fuel-3 | 0.72 | 100% < 25, 90 % (0.09 to 9.5) | 322 | 510 | 60% | Irregular |
| Ground hog fuel | 0.18 | 100% <4.75, 98.7 % (0.09 to 2.8) | 150 | 330 | 14% | Irregular |
| Wood shavings-1 | 0.67 | 100% <12.5, 91 % (0.09 to 6.73) | 110 | 300 | 10% | Irregular |
| Wood shavings-2 | 0.67 | 100% <12.5, 91 % (0.09 to 6.73) | 156 | 380 | 40% | Irregular |
| Wood shavings-3 | 0.67 | 100% <12.5, 91 % (0.09 to 6.73) | 188 | 430 | 60% | Irregular |

Notes: (1) Sauter mean particle diameters, except for the first two which are volume-equivalent diameters;

(2) Measured after drying at 105°C for 5 h.

(3) Mass divided by volume, with volume calculated from the measured dimensions of wood pellets. Arithmetic mean density was used from 5 measurements.

# CHAPTER 5. PILOT STUDY: EXPERIMENTAL RESULTS

This chapter presents results from the pilot experimental study of biomass feeding. The effects of mean particle size (0.5-15 mm), size distribution, shape, moisture content (10-60%), density and biomass compressibility on screw feeding are examined. Screw and casing configurations, as well as pressurization of the hopper, are also investigated.

## 5.1 Experimental Results and Discussion

### 5.1.1 Feed rate and variability

Figures 5-1 and 5-2 indicate that the mass and volumetric flow rates are linearly proportional to screw rotational speeds, as expected. The standard deviation of the flow rate divided by the mean provides a percentage value (i.e. coefficient of variation), which can be used to describe the variability of feeding. This value is affected significantly by several factors, including the time interval and degree of fill of the screw pockets.

The time interval to acquire each weight data point in the present study was 2 s. The flow rate and coefficient of variation were calculated for the first two minutes after establishing stable feeding. In this interval, no stable bridge formed in the hopper, so that bridging could be neglected during this period. All materials in the present study provide lower volumetric feed rates than the theoretical volumetric capacity of the screw feeder, as shown in Figure 5-2. Reduced filling fraction and unavoidable rotation of the particles both result in decreased volumetric efficiency, defined as the true volumetric flow rate divided by the theoretical volumetric flow rate. Hog fuel (11% moisture) and wood shavings-1 (10% moisture) had somewhat higher volumetric efficiencies than the polyethylene particles, wood pellets and

ground wood pellets due to their greater compressibility. The bulk density of compressible materials (e.g. hog fuel, sawdust) did not change much after they passed through the screw feeder. However, these materials were compressed inside the screw feeder, making their bulk density a little larger than in the loose state. This allowed the screw feeders to deliver more mass flow for compressible materials. Hog fuel-1 and wood shavings-1 also had slightly larger volumetric flow rates than sawdust-1 (14% moisture) at the same screw speed. Their wide size distributions are expected to be the main reason since fines can fill the spaces between larger particles, effectively increasing the mass and volumetric flow rates. Polyethylene particles provide volumetric flow rates similar to those of sawdust-1 and ground wood pellets at the same screw speed, despite differences in particle shape and surface roughness. The relatively low volumetric efficiency for the wood pellets can be attributed to their larger mean size, cylindrical shape, and rougher surfaces.

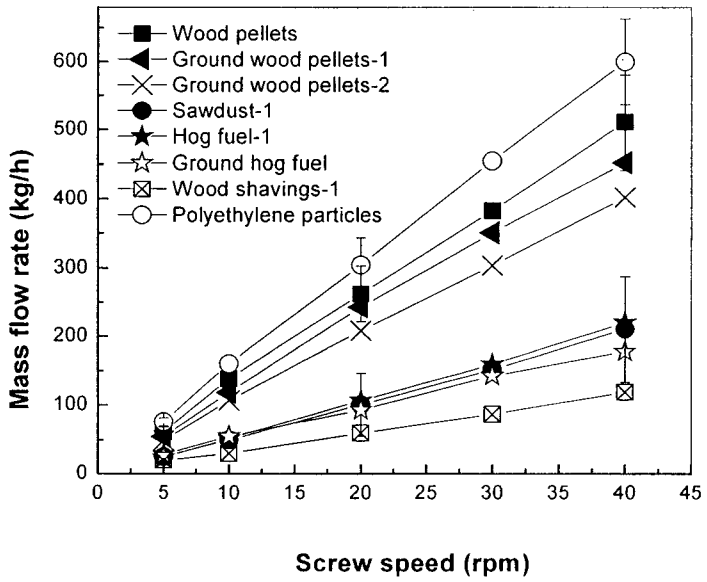


Figure 5-1. Relationship between mass flow rate and screw speed for screw-1 for different biomass materials with initial hopper level=0.30m. For properties of the biomass materials, see Table 4-4.

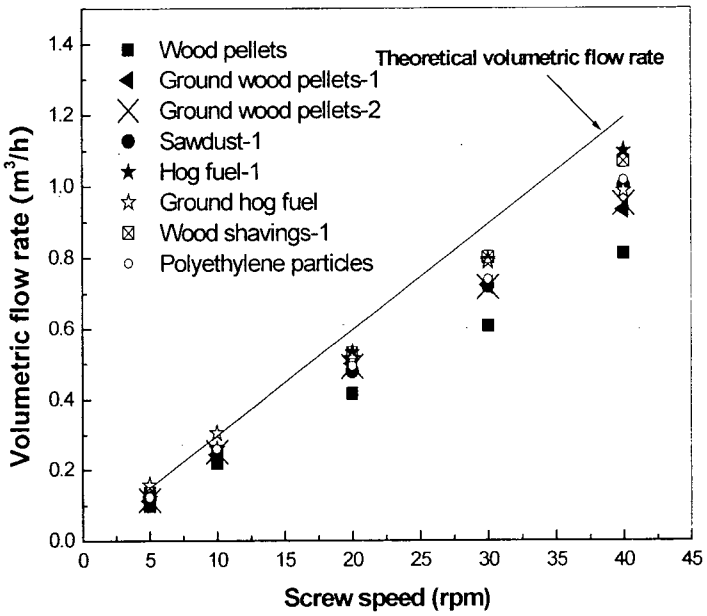


Figure 5-2. Relationship between volumetric flow rate and screw speed for screw-1 with different biomass materials and initial hopper level=0.30 m. For properties of the biomass materials, see Table 4-4.

The hopper level (i.e. distance from axis of screw to leveled free surface of bulk solid in the hopper) affects the flow rate, although the effect is relatively small as shown in Figure 5-3. A higher hopper level provides larger feeder load and increases the vertical stress on the screw feeder, increasing the fullness of the screw pockets and promoting bulk solids flow. For polyethylene particles, a larger hopper level led to larger flow rate for levels < 0.4 m due to greater filling of the screw pockets caused by higher vertical stress inside the hopper. For hopper levels > 0.4 m, the mass flow rate did not change significantly, and could even decrease with increasing hopper level. Higher hopper levels can increase the fullness of the screw pockets and hence the feeding efficiency, but excessive hopper levels give no further gain. The active stress field is replaced by a passive stress field in the hopper once feeding has been initiated, inhibiting hopper flow and reducing the influence of hopper level (Arnold et al., 1980). In general, higher feeder loads require larger torque for feeding if no bridging occurs, or if bridging

in the hopper is insignificant. No obvious bridging in the hopper nor blockage inside the screw feeder was found for the sawdust with 14% moisture content (wet basis) (hopper level < 0.7 m), nor for the polyethylene particles (hopper level < 0.60 m) during the present tests. The loose bulk density was used to calculate the volumetric flow rate at different hopper levels for sawdust-1.

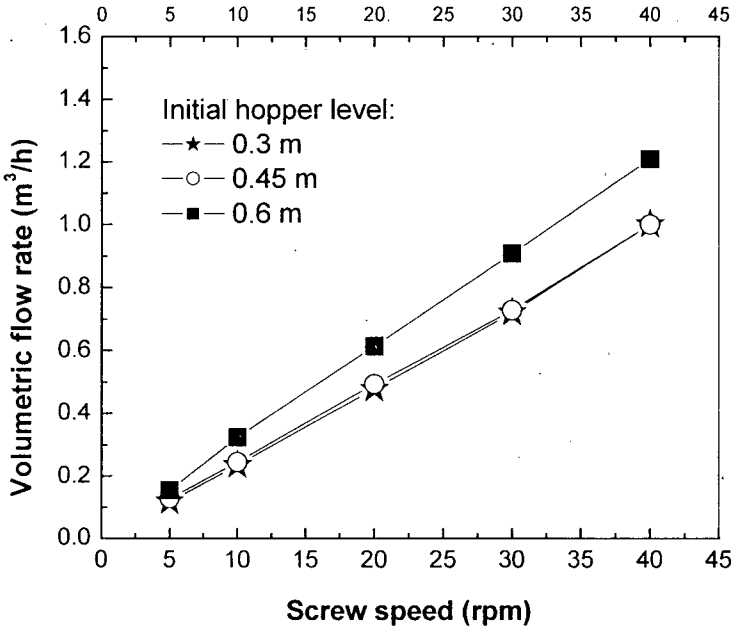


Figure 5-3. Hopper level effects on volumetric flow rate for sawdust-1 and screw-1. For properties of the biomass material, see Table 4-4.

Moisture content also affects flow rate. Higher moisture content is more likely to cause bridging or rat-holes in the hopper, leading to reduced mass and volumetric flow rates for screw feeding. Sawdust of higher moisture content shows lower volumetric efficiencies (see section 6.2) than one of lower moisture content, as shown in Figure 5-4, although their mass flow rates are almost the same for a given screw speed. Sawdusts of high moisture content (e.g. 40% or 60 %, wet basis), especially after 24 hours of consolidation, easily bridged in the hopper due to increased cohesion, as well as increased wall and internal friction, especially for higher hopper

levels (e.g. > 0.2 m). Erratic flow of sawdusts of 60% moisture content (wet basis) indicated momentary bridging. The arches or bridges in the hopper had to be broken for the sawdust to fall into the screw pockets, whereas no blockages could be observed inside the screw feeder in the present study. However, loud "screeching" could be heard from time to time due to the pressure and friction of the sawdust on the screw surface and casing wall surface. Note that loose bulk densities were used in the calcilation of volumetric flow rates for each sawdust.

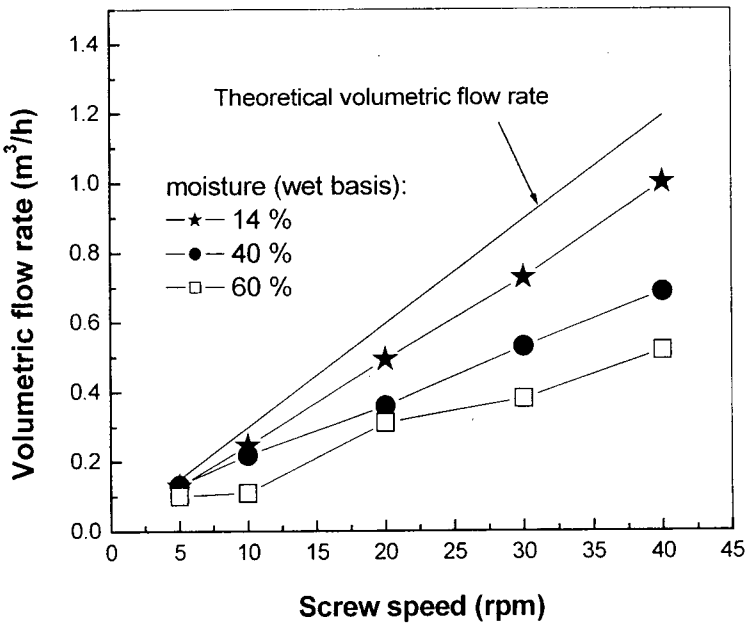


Figure 5-4. Effects of moisture content on volumetric flow rate for sawdust and screw-1. For properties of the biomass materials, see Table 4-4.

As indicated in Figure 5-5, larger screw speeds generally led to lower coefficients of variation, although higher screw speeds also caused lower volumetric efficiencies (as defined in sections 5.1.1 and 6.2). The large coefficient of variation of ground hog fuel may be attributed to intermittent bridge in the hopper due to its fibrous shape and poor flowability. Figure 5-6 presents the fluctuations of the flow rate at a rotational speed of 5 rpm, with the deviations from the mean mass flow rate plotted versus time. This figure shows typical cyclic characteristics of

screw feeding. The peaks occurred at a frequency corresponding to the rotational speed of the screw feeder.

5.1.2 Blockage tests and analysis

Two regions could be identified along the screw for the present hopper-screw feeder (Figures 4-1 and 4-2): a hopper feeding section and a choke section.

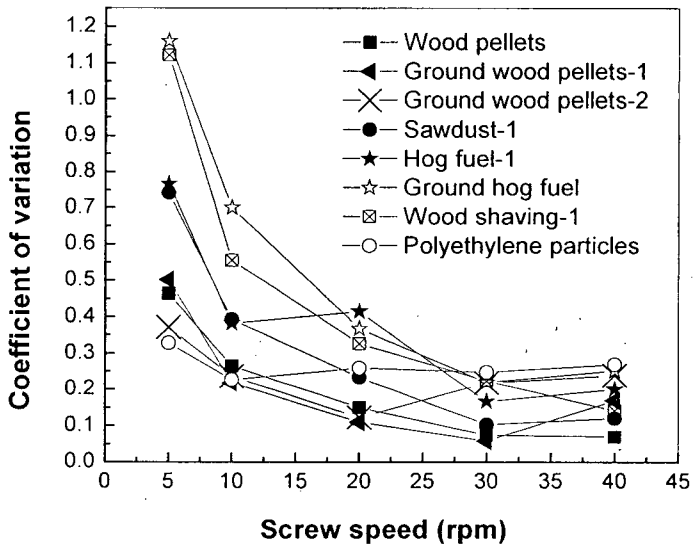


Figure 5-5. Dependence of coefficient of variation on screw speed for screw-1. For properties of the biomass materials, see Table 4-4.

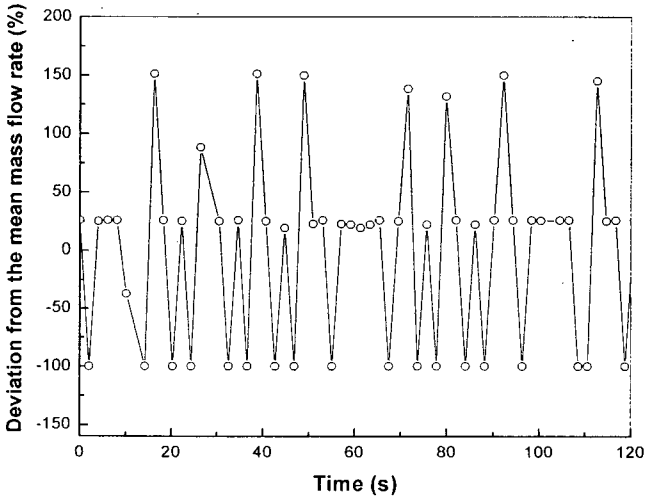


Figure 5-6. Fluctuations of flow rate at a rotational speed of 5 rpm for sawdust-1 and screw-1 at initial hopper level=0.45 m (mass flow rate: 27 kg/h). For properties of the biomass material, see Table 4-4.

Higher hopper levels could trigger blockages, depending on the particle properties and equipment configuration. The hopper used here was wedge-shaped, as shown in Figure 4-1, which is better able than a cone-shaped hopper to prevent bridging (Marinelli, 1999, Fitzpatrick et al., 2004). For wood pellets of uniform size (average dimension of single particle: φ 6.5 (D) x 15 (L) mm), blockage inside the screw feeder tended to occur when the hopper level exceeded 0.35 m. When the feeder load was large enough (e.g. hopper level > 0.4 m), the screw feeder blocked almost immediately after it was started. Furthermore, the blockages could not be broken up by reversing or by restarting the motor. To recover, it was necessary to remove the wood pellets from the hopper manually. On the other hand, blockages could be broken up without intervention within 6 s, or by reversing or restarting the motor for hopper levels <0.4 m. Compared to the polyethylene particles, which did not block the screw for hopper levels up to 0.60 m, wood pellets blocked more easily. This is mainly attributed to their poor flowability caused by larger particle size (mean diameter = 9.8 mm), more irregular shapes (cylindrical), and rougher surfaces. The screeching due to the friction of the pellets on the screw and casing surfaces could often be heard when feeding wood pellets.

Wood pellets containing some fines (see Table 5-1) were found to block more readily than wood pellets of uniform size. However, blockage was broken up relatively easily for these materials, without too much intervention. Wood pellets of relatively uniform size were provided by sieving wood pellets on each occasion, using a screen with 4.75 mm openings. New wood pellets were employed for further experiments as soon as some of the pellets were observed to have lost their original dimensions and shape. Our experiments suggest that 12-16% (mass) of the wood pellets are ground into particles smaller than 4.75 mm, including 6-9% (mass) of particles smaller than 3.35 mm, for each screw speed.

Table 5-1. Size distribution of wood pellets containing some fines

| Diameter range $d_p$ (mm) | Mass ($kg$) | Mass fraction ($x_i$) |
|---|---|---|
| 0-0.25 | 0.72 | 0.016 |
| 0.25-0.5 | 0.72 | 0.016 |
| 0.5-1 | 0.72 | 0.016 |
| 1-2 | 0.72 | 0.016 |
| 2-3.35 | 0.72 | 0.016 |
| 3.35-4.75 | 2.7 | 0.06 |
| 4.75-19 | 38.7 | 0.86 |
| | Total mass: 45 kg | |

The time at which the first blockage occurs provides an indication of how easily blockage occurs for a given material under different experimental conditions. Although the first blockage time should be measured many times (e.g. 20 times) for the same operating conditions, three runs for each screw speed gave preliminary results and trends. Higher screw speeds led to quicker blockage after the motor is started, but more fuel was delivered to the receiving vessel for higher screw speeds before blockage occurred. Experiments indicated that somewhat higher screw speeds (e.g. >30 rpm) reduced the tendency to block inside the screw feeder compared to slower speeds (e.g. 5 rpm) for relatively incompressible particles (e.g. wood pellets and polyethylene particles). However, when blockage occurred at the higher screw speeds, the blockage was harder to break up. The level of stress in the hopper section directly above the screw is influenced by the screw speed. With increasing screw speed, and consequently increasing flow rate, the porosity of the bulk material slightly increased near the screw. In other words, materials in the vicinity of the screw in the hopper section are dilated as a result of increasing screw speed. Even minimal increases of the material porosity, however, cause a

distinct decrease of the stress level at the hopper outlet (Rautenbach and Schumacher, 1987), also leading to a decrease in torque requirements as discussed below. For fine particles inside the bulk material, even slight increase of the inter-particle distance cause a drastic decrease of the van der Waals interactions, also contributing to reduced blockage tendency for higher screw speeds. Furthermore, the screw feeder may shake or vibrate during feeding due to its cantilever structure, minor manufacturing eccentricities and imperfect fabrication. Shaking or vibrating may cause erratic flow, as well as mechanical wear and other operating problems. The higher the screw speed, the more the screw shakes or vibrates, and the more the screw dilates the materials inside the screw feeder. This may partly explain why high screw speeds led to fewer blockages and why blockages at high screw speeds were difficult to break up. No clear relationship between screw speed and blockage tendency was found for compressible fuels, probably due to the interlocking characteristics of compressible materials.

A small favourable pressure drop (0.02 bar) from the hopper to the downstream vessel led to an increase in mass flow rate and a reduction in the tendency to block, as indicated in Figure 5-7.

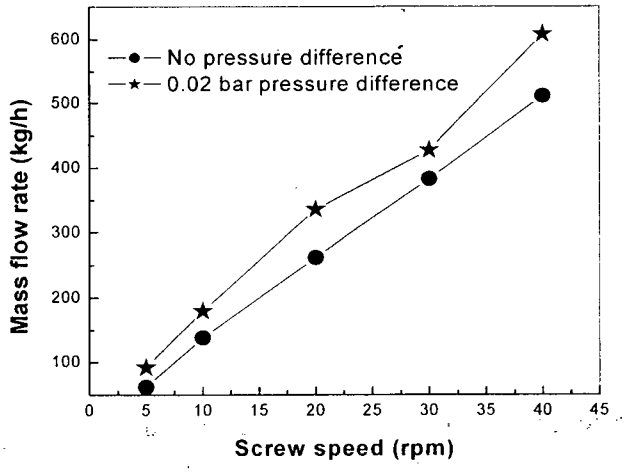


Figure 5-7. Effect of screw speed and difference in pressure between hopper and receiver on mass flow rate for wood pellets and screw-1 at initial hopper level=0.30 m. For properties of the biomass material, see Table 4-4.

When the hopper was at a somewhat higher pressure than the receiving container, the particles (e.g. ground wood pellets) in the upper part of the screw pockets were mainly transported by air, reducing the filling fraction and blockage tendency inside the screw feeder, whereas particles in the lower part of screw pockets were mainly transported by the screw flights.

Feeder loads in the hopper put vertical stress on the screw, causing friction between the screw and bulk solids in the hopper. This is the source of the first resistance for the screw to rotate and push particles forward. We call this region the hopper feeding section. When particles enter the choke section, their movement is controlled by screw rotation and the casing as indicated in Figure 5-8. The screw flights press and shear particles, making them rotate and move forward. There are significant normal pressure and shear stresses on the wall surfaces, including casing surfaces and screw flight surfaces. If the flowability of the particles is adequate for screw feeding (e.g. for low bulk density, spherical particle shape and smooth particle surfaces), the pressure and friction can be accommodated. However, materials that do not flow readily (e.g. those with for large bulk density, irregular shapes and rough surfaces), the screw flights must be able to push the particles forward, overcoming the normal and shear resistance, or the particles stay in place and do not move. When the power and torque delivered by the motor are large enough, the materials can be transported inside the screw feeder relatively smoothly. However, if the power and torque are too small, the particles cannot gain enough energy, momentum and friction from the screw surfaces to advance. For this case, blockage, possibly irreversible, may occur. When the power and torque provided by the motor are similar to those needed by particles to move forward, blockage may occur. This may break up without intervention, be resolved by reversing or restarting the motor, or be irreversible. If the screw speed does not change much, but the mass flow rate decreases, bridging or rat-holing may occur

in the hopper. When the screw slows down and the torque increases due to high resistance, blockage may occur inside the screw feeder. Screw speed reduction or fluctuations in torque readings provide good warning indicators of impending blockage.

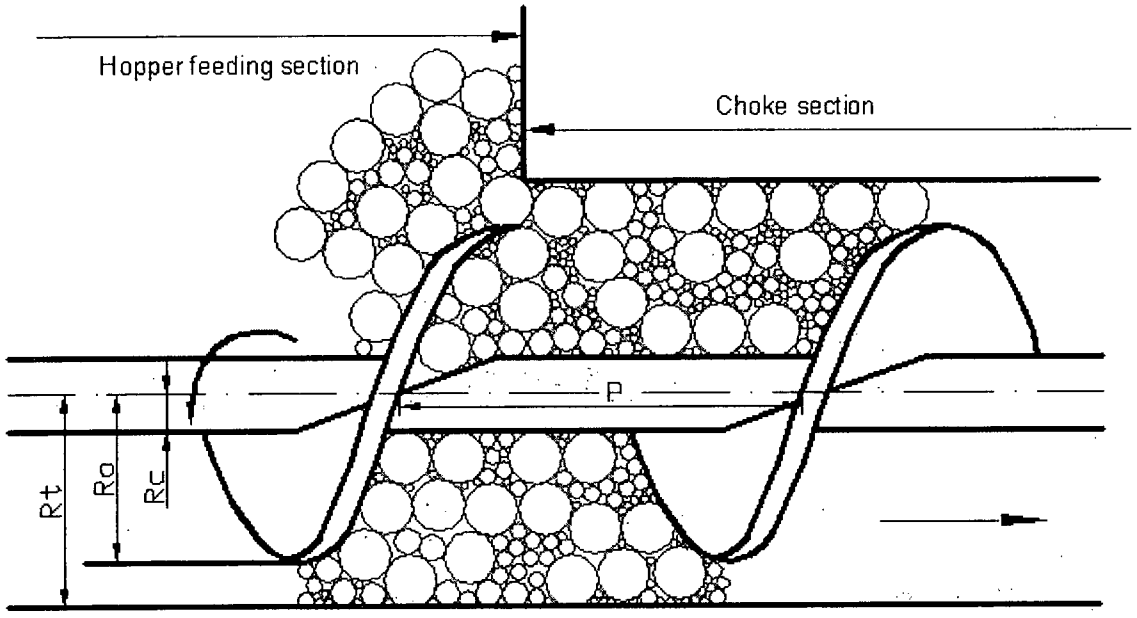


Figure 5-8. Schematic of particle motion at entrance of choke section.

The particles inside the screw pockets (spaces between the screw flights and core shaft surface) are transported by friction and pressure provided by the screw surfaces. Particles at the front (discharge end) of the hopper cannot enter the screw pockets because the pockets are already filled by particles from the back of the hopper. Hence particles at the front of the hopper pile against its front wall, forming a so-called stagnant region, as indicated in Figure 2-4.

Experimental observations indicate that if the stagnant region cannot be broken up and the hopper is refilled, particles from the back of the hopper are transported first just as before, and the strength of the stagnant region at the front of the hopper increases (dead zone), especially for cohesive and adhesive materials. This kind of flow pattern belongs to "funnel" or "rat-hole"

flow, a "first in, last out" pattern which should be avoided in hopper-screw feed systems (Marinelli, 1999). The stagnant region tends to cause blockage inside the hopper, as well as potential blockage in the screw feeder. The interface between the hopper and choke sections is a special region, from which particles are transported into a limited casing space. Some particles build up in a stack outside since not all particles can enter the casing smoothly. Observations suggest that wood pellets at the front of the hopper pile up as a result of the periodic screw motion, making the screw expend larger torque and require more power to continue feeding. The stagnant region limits the screw feeding. Furthermore, once the material in the stagnant region collapses due to external forces, the screw may shear and press the materials from the stagnant region, which may, by this time, be strong and hard due to consolidation and other factors (such as temperature). In general, non-uniform draw-down in the hopper leads to larger torque and power requirements for screw feeding compared to uniform draw-down. Different screw configurations (e.g. variable pitch, screw diameter and core shaft diameter) and various mechanical aids may assist in achieving uniform draw-down. For biomass feeding, uniform draw-down and smooth feeding are even harder to realize due to the peculiar particle properties.

### 5.1.3 Torque analysis

Increases in torque and power requirements were found to signify a larger blockage tendency for a given biomass and given feeder configuration. Starting torque and operating torque are used in analyzing screw feeders (Bortolamasi and Fottner, 2001). Average torque is determined under relatively steady state conditions after feeding is initiated. Maximum torque, a critical parameter for biomass feeding, is the largest torque recorded during feeding. If the screw feeder is unable to provide this torque, blockage may occur at any time. Starting torque is the largest torque, experienced at the onset of feeding, as shown in Table 5-2. For all materials tested in the present study, the screw speed increased from zero to the final speeds (e.g. 5 and 40

rpm) within 1 s once feeding commenced. Hence the screw speed increased instantly when the screw feeder was started. The sampling frequency for torque and screw speed measurements was 36 Hz. We take the time corresponding to the first non-zero screw speed as 1/36 s; hence the time corresponding to the adjacent zero screw speed is 0, as shown in Appendix G. We can see from Table 5-2 that compressible materials spend more time after the feeding commences to reach the starting torque for given screw speed. These torques are related to the blockage tendency. The larger they are, the more difficult it is to transport these materials.

Table 5-2. Time corresponding to starting torque (unit: s)

| Bulk solids | Time corresponding to starting torque | | | | |
|---|---|---|---|---|---|
| | 5 rpm | 10 rpm | 20 rpm | 30 rpm | 40 rpm |
| Wood pellets | 2.1-3.2 | 1.4-1.6 | 0.8-1.8 | 0.6-1 | 0.8-0.9 |
| Ground wood pellets-1 | 3.2-3.9 | 2.4-3.7 | 1.3-1.7 | 1-1.3 | 0.8-1.1 |
| Ground wood pellets-2 | 5.9-6.1 | 3.4-4.7 | 1.8-2.1 | 1.2-2.1 | 0.9-1.1 |
| Sawdust-1 | 7.1-7.9 | 3.7-4.8 | 2-2.4 | 1.9-2.2 | 1.5-1.6 |
| Hog fuel-1 | 2.7-5.3 | 2.1-2.7 | 1.3-1.6 | 1.2-1.4 | 1.1-1.2 |
| Ground hog fuel | 3.3-7.3 | 3.2-3.8 | 1.5-2 | 1.4-1.9 | 1.3-1.6 |
| Wood shavings-1 | 2.3-6 | 1.8-2 | 1.4-1.6 | 1.2-1.3 | 1-1.1 |
| Polyethylene particles | 2.3-2.5 | 1.5-1.9 | 0.8-1 | 0.5-0.6 | 0.6-0.8 |

Experiments were repeated 2-5 times in order to obtain a range of torque values and to provide a better sense of the errors for each material. With no feeder load inside the hopper, the screw feeder was found to run smoothly, with some torque spikes, depending on the screw speed (e.g. see Figure 5-9). The same was true for screw feeding with a limited feeder load (see Figure 5-10). Both figures show typical characteristics of screw feeding: counting the torque peaks during a 1-minute interval gives a number equal to the rotational speed of the screw. For example, a 5 rpm screw speed was found to produce 5 peaks per minute, implying that there is a direct relation between screw speed and the frequency of torque fluctuations. The fluctuations are due to cyclic characteristics of screw feeding and inherent features (e.g. slight eccentricities from manufacturing and/or installation). When biomass is transported into the choke section,

the required torque increases. The choke section plays a critical role in biomass feeding. Generally the length of the choke section is at least one pitch (Bates, 1969) or twice the standard pitch (CEMA, 1980; Yu and Arnold, 1997). For biomass feeding, the choke section may be longer, e.g. 6-10 times the pitch, in order to promote plug formation and prevent backflow of hot gases and bed materials from the reactor (Li et al., 2004). This causes the torque reading to increase gradually after initiating feeding. When the biomass was distributed relatively evenly in the hopper and choke section, the torque was also observed to be relatively stable. From this relatively stable stage, average torque requirements could be obtained. Since the screw in our study was a common screw with a constant pitch, constant core shaft diameter and constant screw diameter in the hopper section, the draw-down pattern was not uniform. Instead a stagnant region formed at the front of the hopper, whereas the back end tended to be empty after some time as shown in Figure 2-4. The total feeder load also decreased as feeding continued (without refilling). Furthermore, the passive stress field became important after feeding commenced. All of these factors led to a decrease in the torque reading after a relatively stable stage of torque readings. The torque fluctuated significantly during feeding, probably because of intermittent bridging in the hopper and complex dilation and compression inside the choke section. Screw speeds also fluctuated due to torque fluctuations, with the screw speed decreasing as the torque reading increased and increasing as the torque decreased. Stopping and restarting the screw feeder did not affect the torque reading significantly (see Figure 5-10).

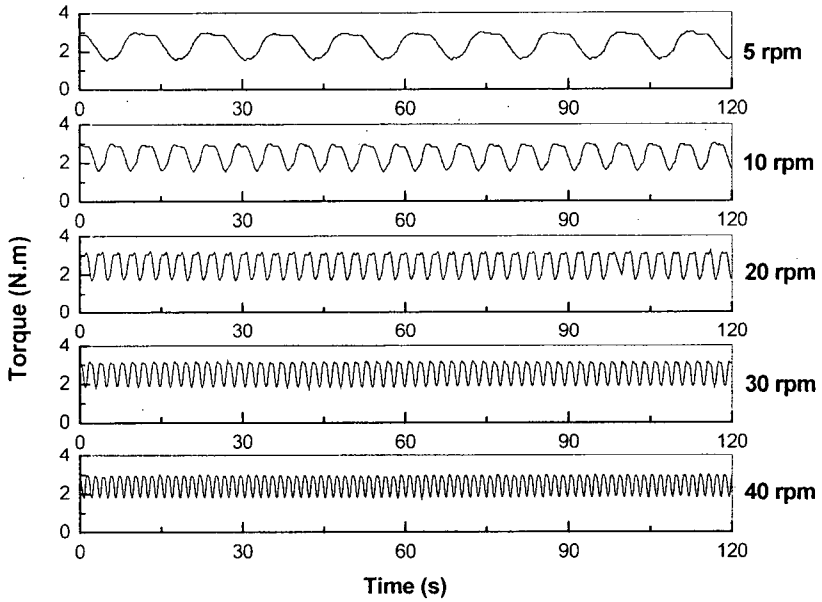


Figure 5-9. Torque vs time for screw feeder with no solids present

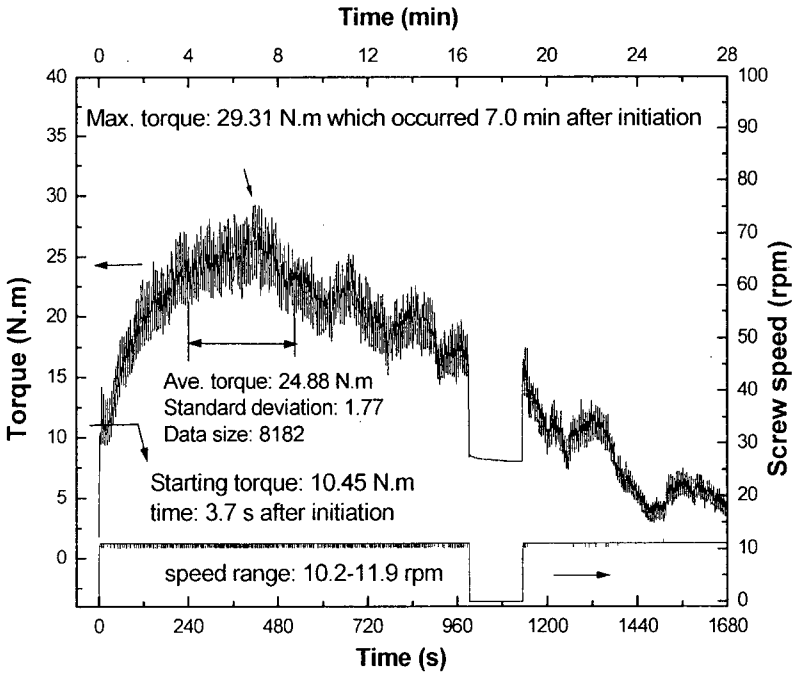


Figure 5-10. Torque vs time for screw feeder at 10 rpm for sawdust-1 and screw-1 at initial hopper level=0.45 m. For properties of the biomass material, see Table 4-4.

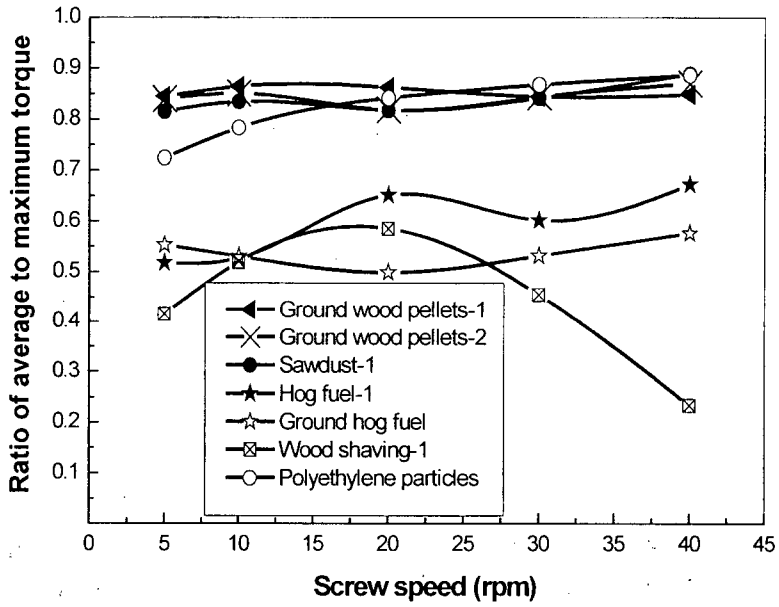


Figure 5-11. Ratio of average to maximum torque for various materials and screw-1 at different screw speeds (initial hopper level=0.45 m). For properties of the biomass, see Table 4-4.

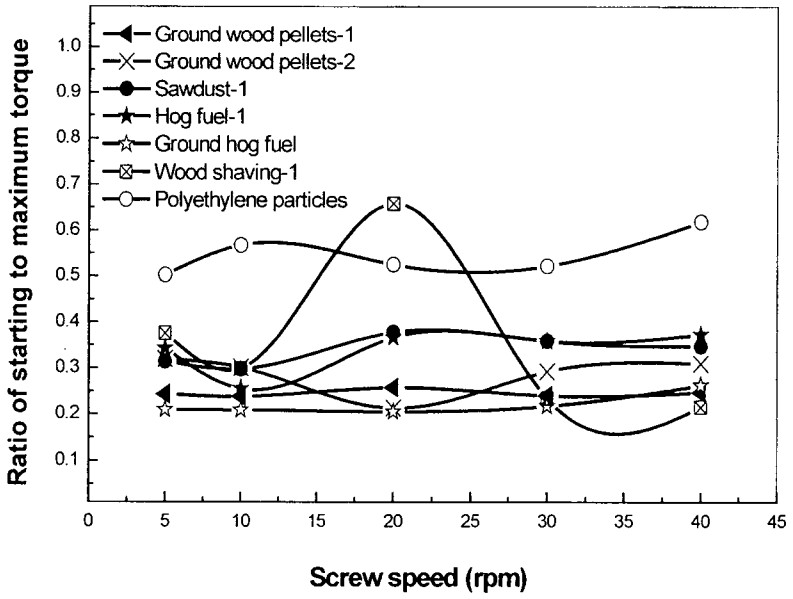


Figure 5-12. Ratio of starting to maximum torque for various materials and screw-1 at different screw speeds (initial hopper level=0.45 m). For properties of the biomass, see Table 4-4.

Ratios of average-to-maximum torque and starting-to-maximum torque are plotted in Figures 5-11 and 5-12. The former ratio reflects, to some extent, the fluctuation of torque reading during feeding. This ratio is in the range of 0.25-0.70 for hog fuel, ground hog fuel and wood shavings, and 0.75-0.90 for the other materials tested. The smaller range is mainly attributed to the wider size distribution and more irregular shape of hog fuel, ground hog fuel and wood shavings relative to the other materials. The ratio of starting-to-maximum torque represents the percentage of starting torque in the actual torque requirement during feeding (i.e. maximum torque). The smaller this ratio, the less important the starting torque and the more important the choke section in determining the total torque. In this work, all materials except polyethylene were found to have a ratio in the range of 0.2 to 0.5, whereas polyethylene particles gave ratios of 0.5 to 0.6. These values indicate that the starting torque of all fuels was manageable relative to the overall torque requirements. Smaller ratios were mostly found for the low bulk density materials, especially biomass fuels, and in the long choke section for biomass screw feeding. The longer the choke section, the greater its influence in determining the total torque requirements in biomass screw feeding.

Average torques are plotted in Figures 5-13 to 5-15. From these figures, it is seen that larger mean particle size, more irregular shape and higher bulk density (e.g. wood pellets and ground wood pellets) lead to higher torque (see also Table 4-4). Large standard deviations of average torque for ground wood pellets-2 are probably mainly due to their wide size distribution and relatively large density. It should be noted that larger particle mean size and wider particle size distributions cause larger maximum torque and starting torque for hog fuel-1 than for sawdust-1, while the larger bulk density of sawdust-1 may contribute to its somewhat higher average torque relative to hog fuel-1 (see Table 4-4). For wood shavings-1, the size distribution and particle strength cover wider ranges compared to the other materials, especially the latter (see Table 4-4).

Some particles in wood shavings are harder and have larger strengths due to the manufacturing process, making the standard deviation of the maximum torque second only to that of wood pellets. The smaller torque requirements of polyethylene particles are mainly attributed to their regular shape and smooth surfaces. Torque requirements are determined by material properties and equipment configurations, whereas feeder configurations vary greatly depending on the material properties and different applications. Biomass feeders differ significantly from feeders used for other materials (e.g. screw configurations and the choke section length), so that torque measurements in the present study cannot be readily compared with results from other facilities using different materials.

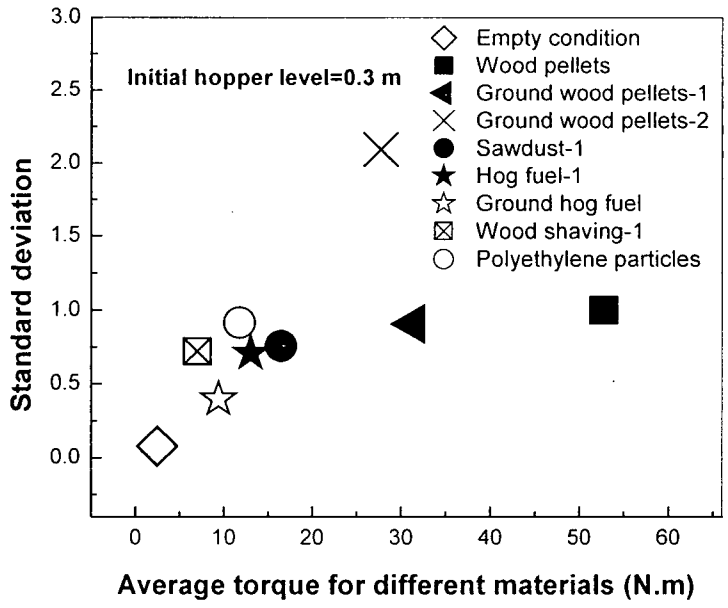


Figure 5-13. Variability of torque, expressed as standard deviation vs average torque for different materials and screw-1 with initial hopper level=0.30 m. For properties of the biomass materials, see Table 4-4.

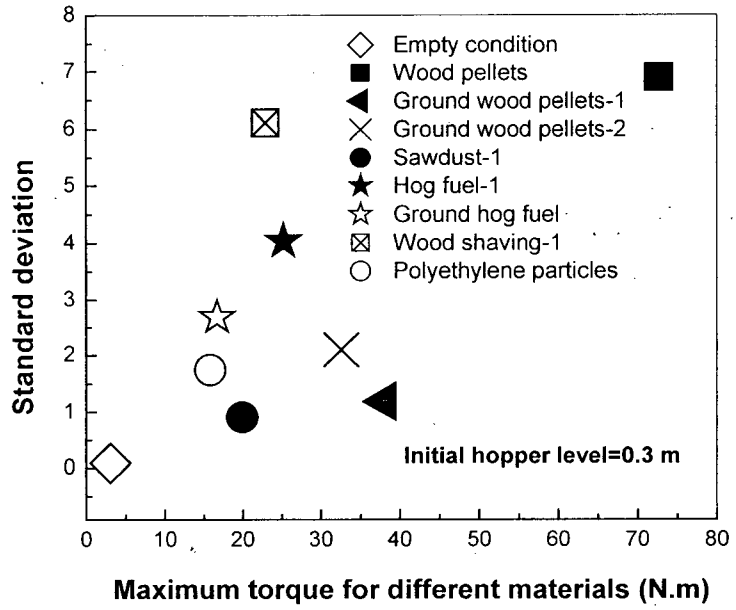


Figure 5-14. Variability of torque, expressed as standard deviation vs maximum torque for different materials and screw-1 with initial hopper level=0.30 m. For properties of the biomass materials, see Table 4-4.

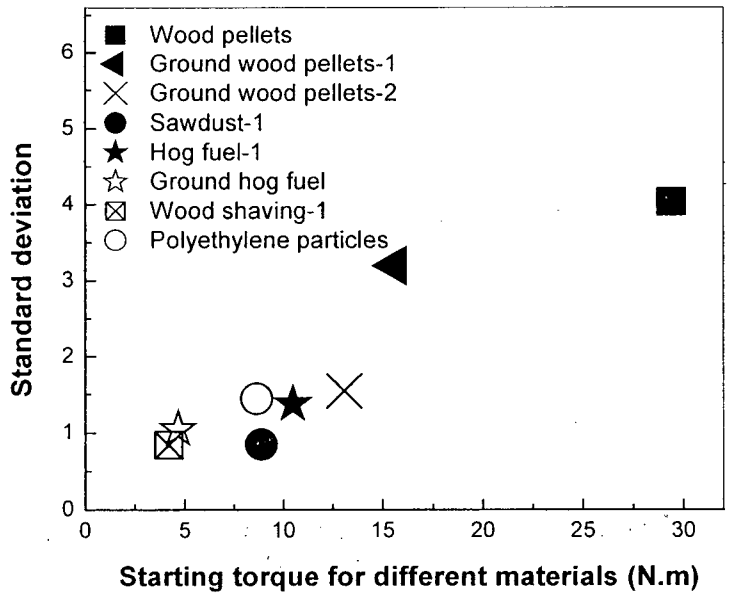


Figure 5-15. Standard deviation vs starting torque for different materials and screw-1 with initial hopper level=0.30 m. For properties of the biomass materials, see Table 4-4.

5.1.3.1 Effect of particle size

Wood pellets, ground wood pellets-1 (3.35-4.75 mm) and ground wood pellets-2 (< 3.35 mm) are all irregular in shape with similar bulk density, particle strength and surface roughness. Wood pellets were relatively smooth compared to the ground wood pellets. Their differences in torque requirements are mainly attributable to differences in mean size. Figures 5-16 to 5-18 show that larger particles require more torque (maximum, average and starting torque). Furthermore, ground wood pellets-2 only contain 1.5% fines (< 0.09 mm), suggesting that the effect of fines is limited. This can be confirmed by experimental results. Ground wood pellets-2 have relatively low torque requirements compared to ground wood pellets-1, indicating that fines have negligible effect on torque. Fines increase the fullness of screw pockets and cohesive strength, tending to cause larger torque requirements, as indicated in Section 5.1.2. Maximum torque is an indicator of the instantaneous blockage potential during screw feeding. If the feeder cannot provide the maximum torque, the screw stalls, at least temporarily. Note that the maximum torque decreases as screw speed increases for wood pellets, as shown in Figure 5-17. Hence the blockage tendency was found to decrease as the screw speed increased, as mentioned above. This may be partly because of higher dilation of bulk materials at higher screw speeds and intense interlocking of particles at relatively low speeds, as well as blockage break-up due to shaking or vibration at the higher screw speeds.

5.1.3.2 Effect of particle shape

Since Ground wood pellets-1 and polyethylene particles have similar mean sizes and size ranges, particle shape and surface roughness are the main reasons for their different torque requirements. Figure 5-19 shows that particles of more irregular shape (e.g. cylindrical or conical) need much more torque to feed, presumably due to poorer flowability. The maximum torque requirement for ground wood pellets-1 was almost independent of screw speed, whereas

that of the polyethylene particles was somewhat dependent on screw speed. For the wood pellets, the faster the screw rotated, the less the maximum torque requirement. Interlocking of ground wood pellets appears to be much more intense than for wood pellets and polyethylene particles due to their relatively small size, rough particle surfaces and high compressibility. Vibration of the screw and dilation of ground wood pellets inside the screw feeder are offset by intense interlocking of particles (even at relatively high screw speeds). As a result, high speeds cannot significantly reduce the required maximum torque for ground wood pellets-1. The maximum torque requirements for compressible materials (e.g. sawdust, hog fuel and wood shavings) appear to have been independent of screw speed in the present study. As in a previous study (Rautenbach and Schumacher, 1987), both the average torque and starting torque were nearly independent of screw speed for both compressible and incompressible materials.

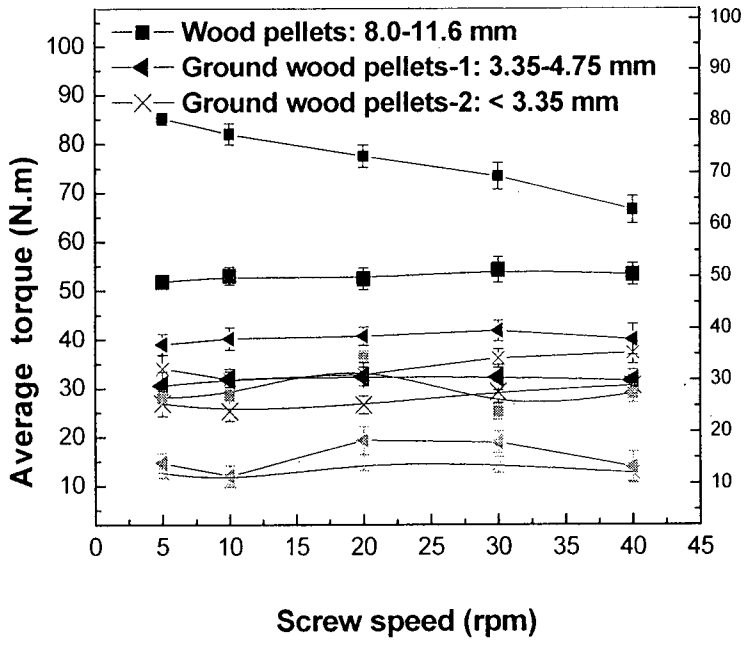


Figure 5-16. Effects of screw speed and particle size on average torque for screw-1 for wood pellets and ground wood pellets with initial hopper level=0.30 m. For properties of the biomass materials, see Table 4-4.

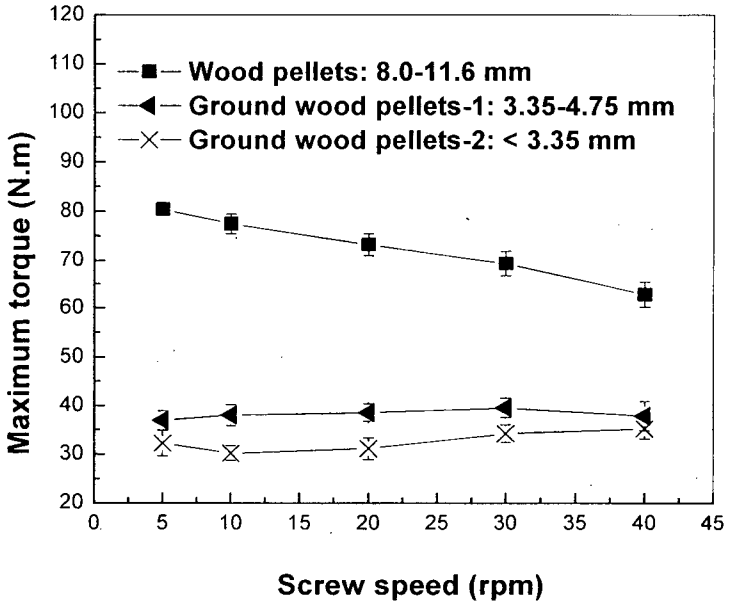


Figure 5-17. Effects of screw speed and particle size on maximum torque for screw-1 for wood pellets and ground wood pellets with initial hopper level=0.30 m. For properties of the biomass materials, see Table 4-4.

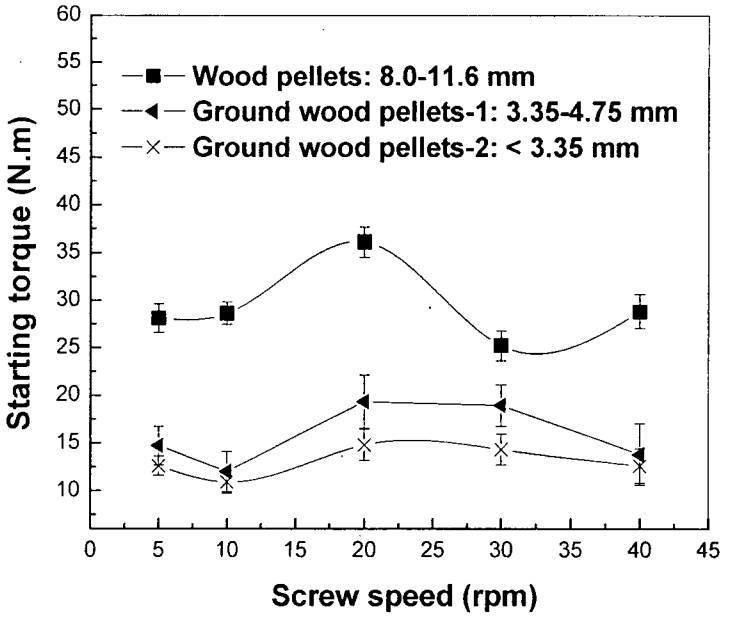


Figure 5-18. Effects of screw speed and particle size on starting torque for screw-1 for wood pellets and ground wood pellets with initial hopper level=0.30 m. For properties of the biomass materials, see Table 4-4.

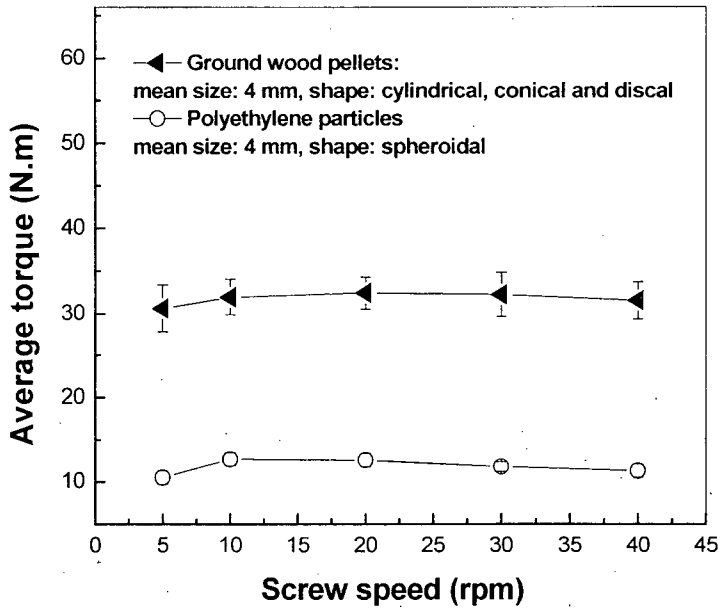


Figure 5-19. Effects of particle shape and screw speed on average torque for screw-1 for polyethylene particles and ground wood pellets-1 with initial hopper level=0.30 m. For properties of the materials, see Table 4-4

5.1.3.3 Effect of moisture content

Sawdust-1 (14% moisture) and sawdust-3 (60% moisture) were employed to investigate the effects of moisture content. The bridging of wet sawdust in the hopper was severe, whereas the tendency to block inside the screw casing decreased since the pockets were nearly empty. Any bridge in the hopper needs to be broken to allow the wet sawdust to enter the screw casing. Sawdust-3 had a lower average torque than sawdust-1, but sawdust-3 had higher maximum and starting torques than sawdust-1 (see Figure 5-20). This indicates that wet sawdust is more likely to block inside the screw feeder if no bridging occurs inside the hopper. Furthermore, both maximum and average torques decreased as the screw speed increased for wet sawdust (60% moisture) due to increased bridging in the hopper and reduced fullness inside the screw feeder as the screw speed increased. There was no obvious relationship between starting torque and screw speeds for sawdust-3. For sawdust-1 (14% moisture), none of the recorded torque

values (maximum, average or starting) changed significantly as the screw speed varied. The same held approximately also for other dry biomass fuels (e.g. hog fuel, ground wood pellets and wood shavings). For wet biomass (e.g. 40% and 60% moisture-content sawdusts), the flow rates and torque requirements could vary considerably, depending on the bridging conditions inside the hopper. Wood shavings-1 (10% moisture), wood shavings-2 (40% moisture) and wood shavings-3 (60% moisture) were also compared in the present study. The torque requirements of wood shavings do not seem to have depended significantly on the moisture content. This is probably due to their wide size distribution, wide range of particle strengths and low bulk densities.

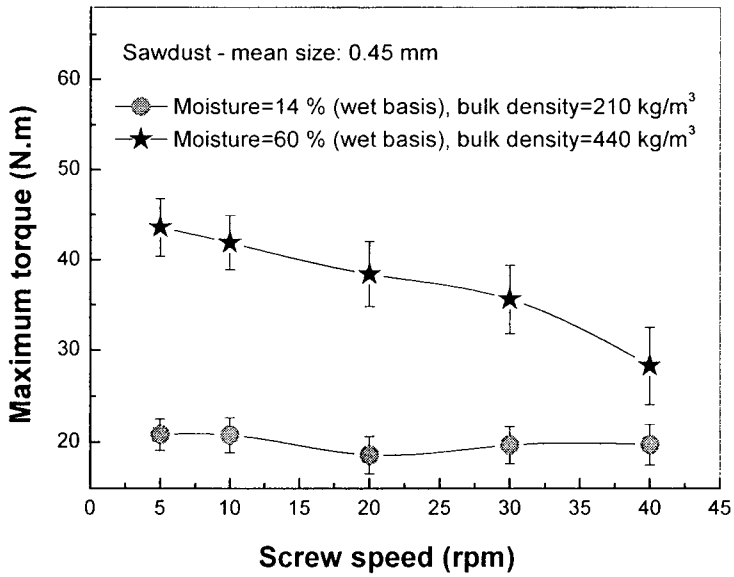


Figure 5-20. Effects of moisture content and screw speed on maximum torque for screw-1 for sawdust-1 and sawdust-3 with initial hopper level=0.30 m. For properties of the biomass materials, see Table 4-4.

Hog fuel was stored in garbage cans at 30% moisture content (wet basis) at a temperature of 20 °C. The garbage cans were covered by the lids, but not perfectly sealed. After two months, the moisture content fell to 14-28% (wet basis), varying according to depth. When these hog

fuel particles with non-uniform moisture content were added to the hopper, a large torque requirement could be observed as shown in Figure 5-21 for a rotational speed of 5 rpm. The compacting and non-uniform moisture content, major characteristics of biomass fuels after time consolidation, appear to have been the main reasons for the large torque requirements. After the hog fuel was loosened and air-dried on a wood plate for three weeks, its moisture content fell to 11%, and the resulting hog fuel was relatively easy to feed with low torque requirements. Keeping this hog fuel with 11% moisture content in the hopper for two days did not cause significant differences in torque compared to feeding immediately after filling.

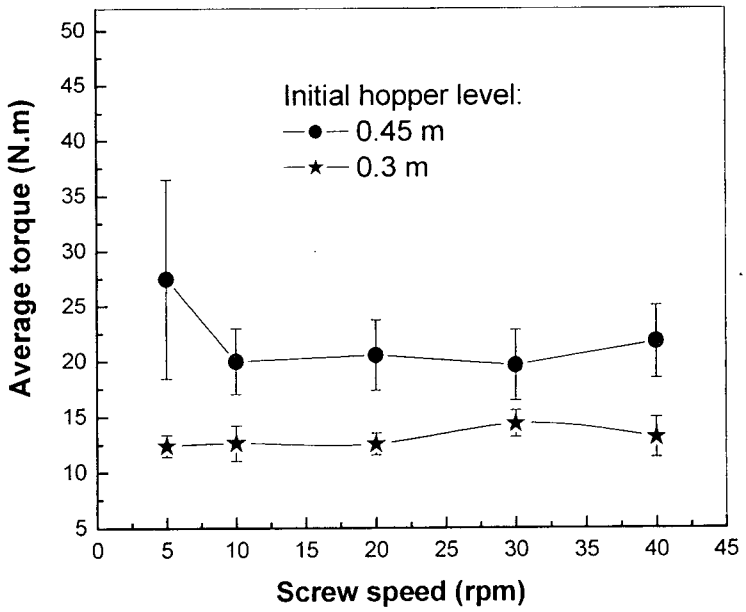


Figure 5-21. Effects of hopper level and screw speed on average torque for hog fuel-1 and screw 1. For properties of the biomass material, see Table 4-4.

5.1.3.4 Effect of hopper level

Hopper level affects feeder load through the passive stress field after the hopper flow begins (Arnold et al., 1980). In this work, the hopper level was found to play an important role for hard and heavy particles on the torque requirements. For compressible light bulk materials

(e.g. sawdust, hog fuel and wood shavings), especially for higher moisture contents, an increase in hopper level could increase the feeder load, as well as increasing the bridging tendency in the hopper. From Figures 5-21 to 5-23, a higher hopper level led to larger average and maximum torques. The starting torque seems to have been independent of screw speeds and hopper levels for sawdust-1 (14% moisture) and hog fuel-1 (11% moisture), indicating again that the choke section plays an important role in torque requirements. For hopper levels < 0.5 m (e.g. 0.30 and 0.45 m), average torque and maximum torque were both independent of screw speeds, but when there was more material in the hopper (e.g. a depth of 0.60 m), the torque increased as the screw speed increased, although the increase was small. This may be partly because higher hopper levels increased the degree of fill of the screw pockets, leading to intense compression and dilation inside the screw pockets, with compaction dominant due to compressibility and intense interlocking of particles as the screw speed increased, causing larger average and maximum torque (see Figure 5-22). Incompressible particles (e.g. polyethylene particles and wood pellets) generally needed less torque to be fed at relatively high screw speeds due to dilation of bulk solids, vibration of the screw, and reduced interlocking. Note that the effect of screw speed on torque requirements was again relatively small for both compressible and incompressible materials.

5.1.3.5 Effect of choke section length

Stress in the choke section is particularly difficult to analyze due to the complicated compression and dilation conditions inside the casing. So far, no satisfactory analysis is available for this section. Normally the length of the choke section is twice the pitch of the screw, but for biomass feeding, due to the need to form a plug seal to prevent backflow of hot gases and bed materials from the reactor, the choke section may be longer (Li et al., 2004).

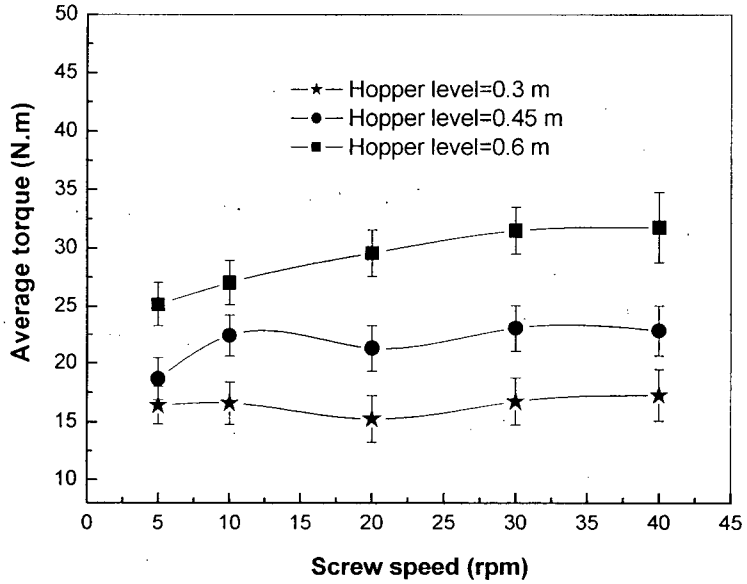


Figure 5-22. Effects of hopper level and screw speed on average torque for sawdust-1 and screw-1.For properties of the biomass material, see Table 4-4.

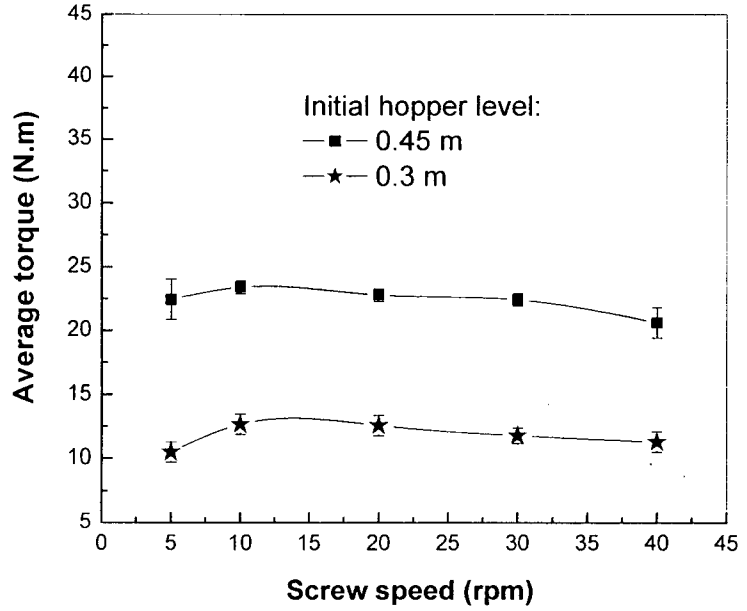


Figure 5-23. Effects of hopper level and screw speed on average torque for polyethylene particles and screw-1.For properties of the material, see Table 4-4.

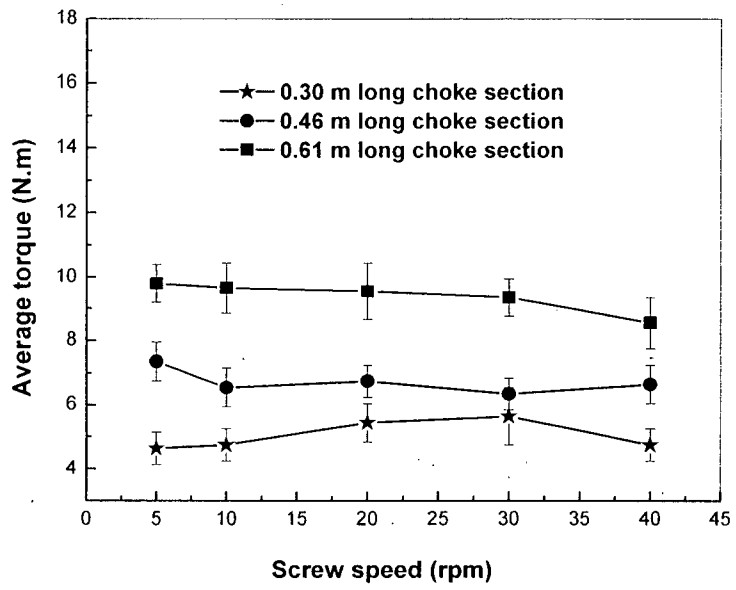


Figure 5-24. Effects of choke section length and screw speed on average torque for screw-1 for wood shavings-3 with initial hopper level=0.45 m. For properties of the biomass materials, see Table 4-4.

The choke section plays an important role in screw feeding and reactor operations, as well as in determining the torque and power requirements. Five different lengths of choke section were tested, 0.30 m, 0.46 m, 0.61 m, 0.76 m and 0.91 m, with the 0.61 m choke section as the base value in the present study since the length of the screw outside the hopper is 0.61 m (Table 4-1 and Figure 4-2). From Figure 5-24, it is clear that a longer choke section led to larger torque requirements. For wood shavings-3 (60% moisture), 0.76 m and 0.91 m long choke sections (i.e. extending 0.15 m and 0.30 m long beyond the screw), both tended to cause stoppage of the screw feeder. A plug formed inside the extended section with a plug density in the range of 220-320 kg/m$^3$, whereas the plug density in the screw region was 190-220 kg/m$^3$ for wet wood shavings (60% moisture). For ground hog fuel, the plug density inside the extended section ranged from 200 to 280 kg/m$^3$, whereas the plug density in the screw region of the choke section was 180-260 kg/m$^3$. To obtain a mechanically stable plug with a suitable low gas permeability,

plugs should have a bulk density from 1300 to 1500 kg/m$^3$ (similar to particle density of wood pellets), depending on the biomass texture and operating requirements (TK Energi, 2006). Special screw and casing configurations, as well as large torque and power, are needed to form such dense plug seals. Hoppers are also commonly pressurized to prevent backflow from the reactor, especially when plug sealing is unstable and unreliable. Plug formation inside the extended section is expected to play a significant role in blocking and stopping the screw feeder since no blockage occurred when there was no extension beyond the end of the screw. For extended sections, sawdust-1 (14% moisture) was much more likely to cause stoppage of the screw feeder than hog fuel-1 or ground hog fuel.

Large mean size and wide size distribution of the hog fuel appeared to hinder plug formation inside the extended section, especially for the 0.15 m long extension, compared to sawdust-1. This is mainly because a larger particles tend to give a larger void fraction, providing more room for particle motion and readjustment inside the extended section, thereby reducing interlocking of particles and decreasing the probability of blockage. This indicates that uniform particle size and small voidages are preferred for forming plugs inside the extended section, even inside the screw casing. Blockage occurred for both 0.15 m and 0.30 m extended sections for sawdust-1, whereas only the 0.30 m extension caused blockage for hog fuel-1. Experiments with ground hog fuel indicated that the 0.15 m extended section may or may not lead to blockage and stoppage of the screw feeder, depending on the flow conditions inside the hopper and screw feeder, whereas the 0.30 m extension made ground hog fuel form a tight plug inside the extended section, contributing in a major way to blockage and stoppage of the feeder. Ground hog fuel bridged relatively easily in the hopper due to its fibrous cylindrical shape and low bulk density, reducing the fullness of the screw pockets. This was likely the main reason why ground hog fuel passed through the 0.15 m extended section more easily than sawdust-1.

5.1.3.6 Effect of casing configuration

The choke section effects on torque requirements depended not only on the length of the casing, but also on the screw length and casing configuration. Different casing test sections were tested in the present study, with straight test section (cast acrylic), and 0.15 m and 0.30 m long tapered converging sections (carbon steel) (see Figure 4-1) with 2.6° and 1.2° half-taper angles, respectively. Experimental results are plotted in Figure 5-25. The 0.30 m tapered section was the most difficult of the three, needing more torque to feed for the biomass materials tested. On the other hand, plug seals were better than for the other two configurations. Large mean particle size and wide size distribution of hog fuel-1 caused it to be more prone to blockage in the tapered section. Large hog fuel particles played an important role in setting the torque requirements and in triggering blockage inside the tapered sections. For ground hog fuel, the fibrous cylindrical shape, as well as the poor flowability, caused blockage to occur more frequently in the tapered sections than for sawdust-1. Relatively uniform particle size, regular shapes and large compressibility of sawdust-1 (14% moisture) are likely the main factors explaining why sawdust-1 passed through the tapered sections more easily than hog fuel-1 and ground hog fuel. For the ground hog fuel (14% moisture) and wood shavings (10, 40 and 60% moisture), the plug density formed in the taper section were both in the range of 150-300 kg/m$^3$, depending on the compression conditions.

5.1.3.7 Refilling

Refilling is essential for continuous industrial processes. To investigate the effect of refilling without consideration of bridging or rat-holes in the hopper, 3.5 kg ground hog fuel (14% moisture) was first put into the hopper, with the top surface flat (0.15 m hopper level), and then the screw feeder was started. When the hopper was empty, the fed ground hog fuel was returned to the hopper while the screw was still turning.

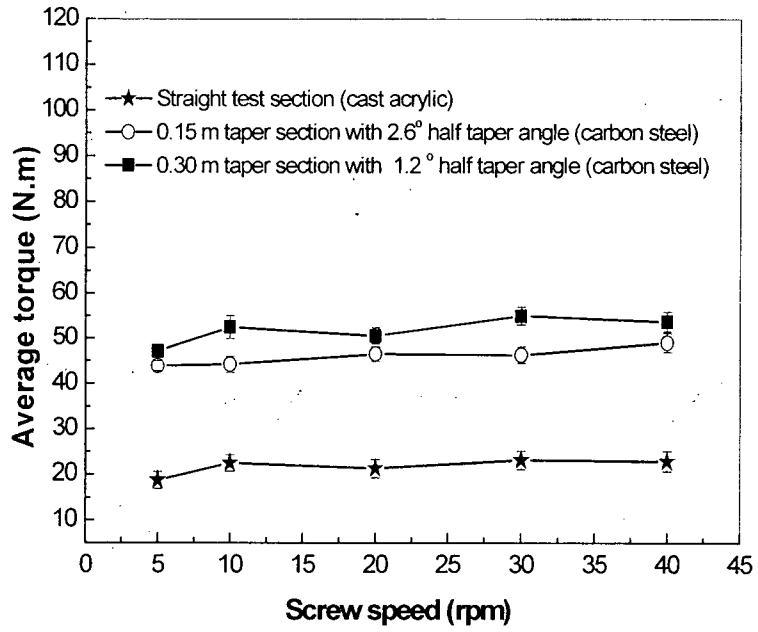


Figure 5-25. Effects of casing configuration on average torque for sawdust-1 and screw-1 with initial hopper level=0.45 m. For properties of the biomass materials, see Table 4-4.

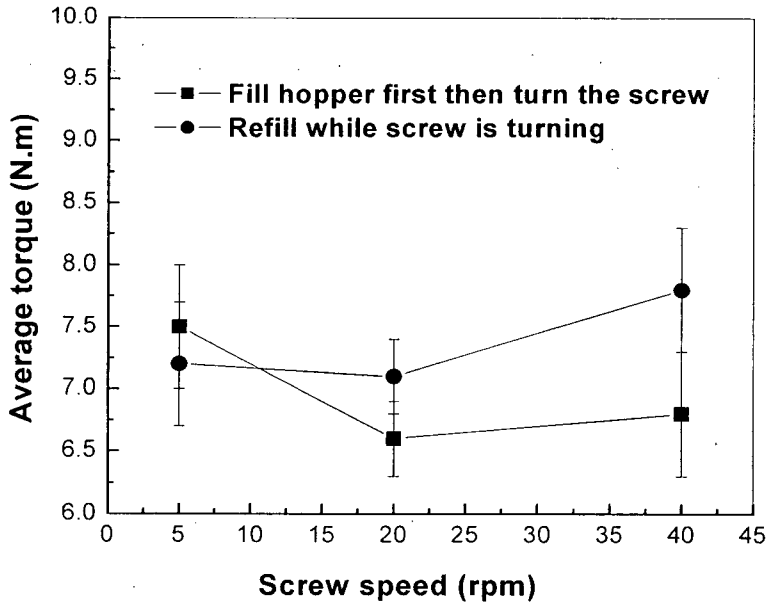


Figure 5-26. Effects of mode of filling on average torque for ground hog fuel (3.5 kg) and screw-1. For properties of the biomass material, see Table 4-4.

The refill material was added to the middle of the hopper (not leveled). As shown in Figure 5-26, these experiments did not show much difference in torque requirements. Refilling was tested for all materials while feeding continued, i.e. while the screw continued to turn, with a maximum refilling mass of 10 kg. Although there seemed to be some torque peaks during refilling, especially for the denser materials (e.g. wood pellets and polyethylene particles), it was unclear whether or not these peaks were caused by the refilling. For heavy particles and a large steep hopper, a large refilling "dump" can cause larger fluctuations of torque readings and feed rates. Ideally refilling should occur continuously, maintaining a nearly constant hopper level. In this case, there should be no interruption to feeding, especially for biomass of low bulk density.

5.1.3.8 Pressurization

Experiments were conducted to test the influence of pressurizing the hopper for screw-1. Pressurization of the hopper relative to the receiving vessel reduced torque requirements and increased the flow rate, as shown in Figures 5-27 to 5-32. The permeability of biomass and flow conditions inside the hopper and the screw casing affected the pressurization. The larger the permeability and the more non-uniform flow in the hopper and in the screw casing, the easier it is for air to flow through the screw casing to the reactor, tending to equalize the pressure levels on the two sides. Ground wood pellets were better than wood pellets from a pressure-seal point of view, and ground wood pellets were more amenable to formation of a plug seal than wood pellets. Pressurization and air flow in the hopper can help break up bridges inside the hopper, especially for light feedstocks (e.g. wood shavings and ground hog fuel). Air flow can help break up the stagnant region that can form at the front of the hopper. From observations, small pressurization and low air flow rates did not affect screw feeding significantly when there was an effective pressure seal. Hence, little or no pressurization and small forward gas flow rates are preferred for biomass feeding, especially when the plug seal inside the screw casing works well.

0.5-20 kPa is the recommended pressure drop from the feed hopper to the reactor (e.g. McLendona, 2004). In the present system, the hopper was not designed for significant pressurization, and so the maximum absolute pressure in the hopper was limited to 110 kPa, whereas the pressure of the outlet of the screw feeder was atmospheric. A pressure drop of 0.3-10 kPa and air flux < 0.7 m/s (based on cross-sectional area between shaft and casing surface at entrance of choke section) worked best in the present study. Higher pressure differentials and larger air flow rates not only lead to larger energy consumption, but may also interrupt the reactor operations.

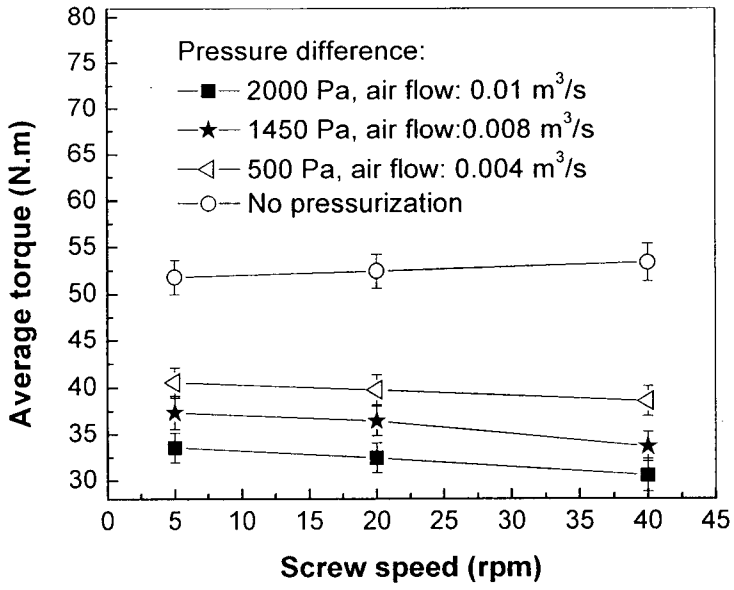


Figure 5-27. Effects of pressure difference between hopper and receiving vessel on average torque for wood pellets and screw-1 with initial hopper level=0.30 m. For properties of the biomass materials, see Table 4-4.

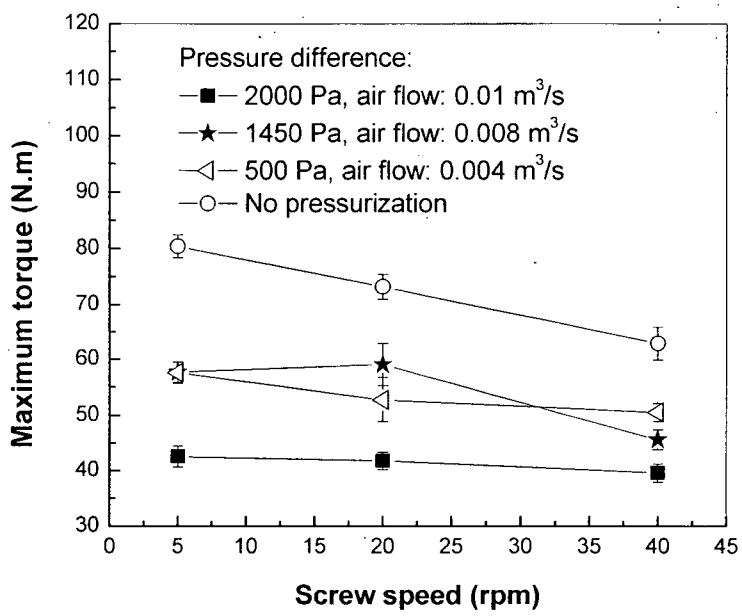


Figure 5-28. Effects of pressure difference between hopper and receiving vessel on maximum torque for wood pellets and screw-1 with initial hopper level=0.30 m. For properties of the biomass materials, see Table 4-4.

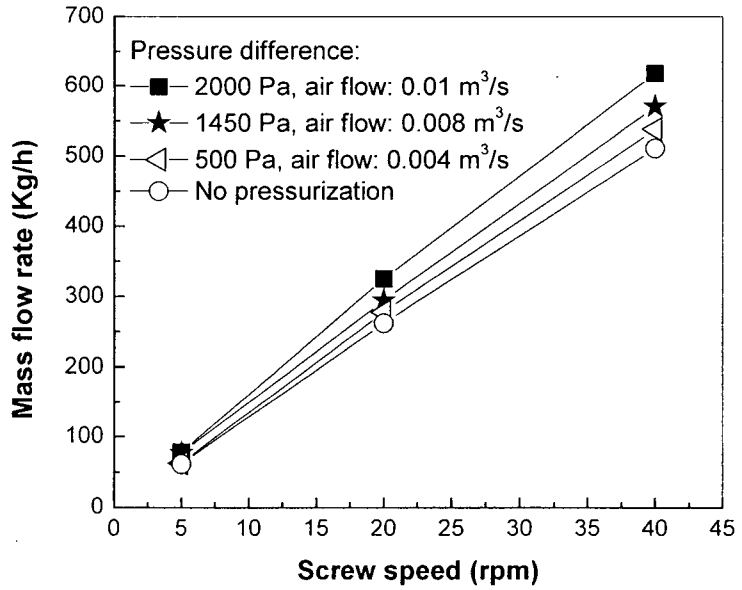


Figure 5-29. Effects of pressure difference between hopper and receiving vessel on mass flow rate of wood pellets for screw-1 with initial hopper level=0.30 m. For properties of the biomass materials, see Table 4-4.

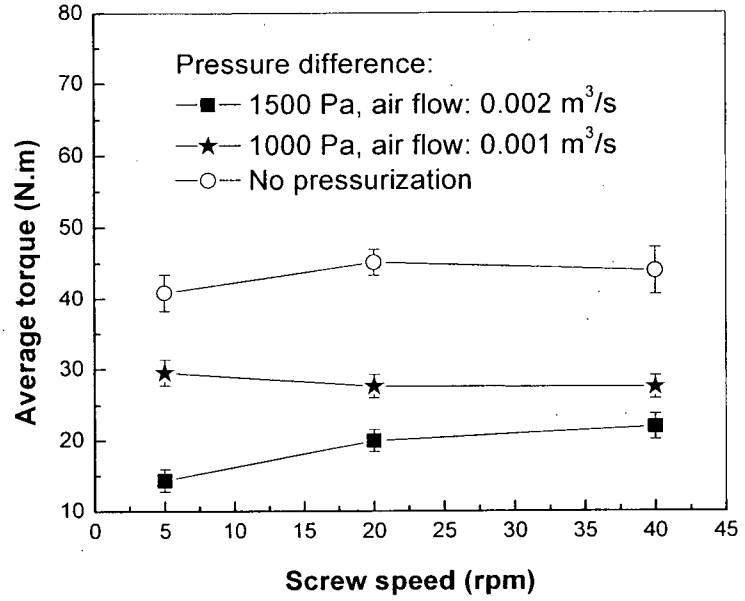


Figure 5-30. Effects of pressure difference between hopper and receiving vessel on average torque for ground wood pellets-2 and screw-1 with initial hopper level=0.45 m. For properties of the biomass materials, see Table 4-4.

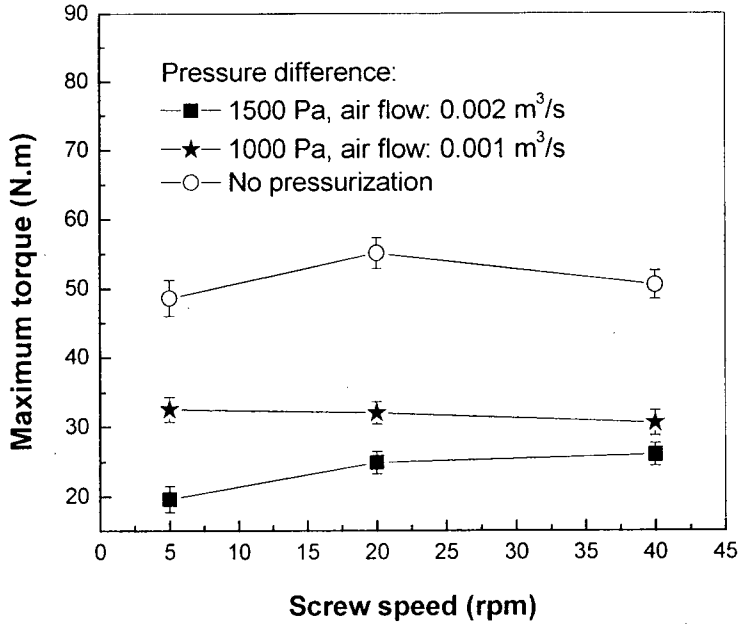


Figure 5-31. Effects of pressure difference between hopper and receiving vessel on maximum torque for ground wood pellets-2 and screw-1 with initial hopper level=0.45 m. For properties of the biomass materials, see Table 4-4.

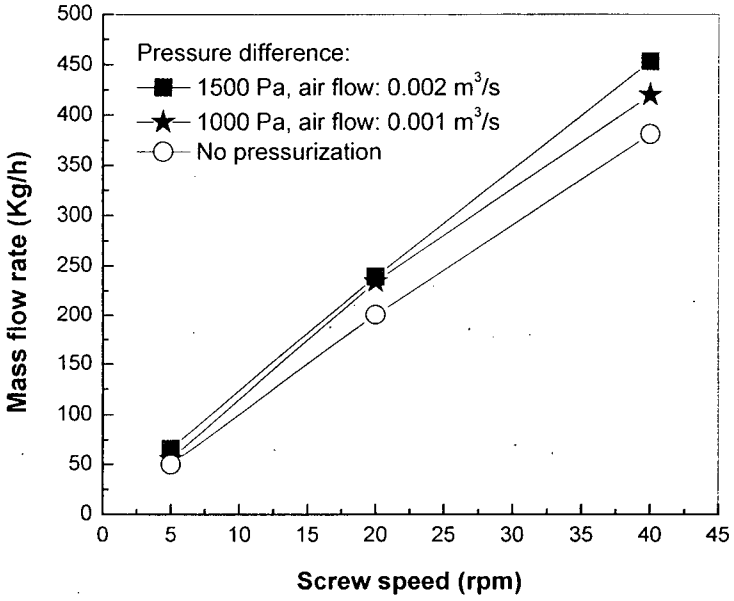


Figure 5-32. Effects of pressure difference between hopper and receiving vessel on mass flow rate of ground wood pellets-2 for screw-1 with initial hopper level=0.45 m. For properties of the biomass materials, see Table 4-4.

5.1.3.9 Effect of screw configurations

Two different screw geometries, screw-1 and screw-2, shown in Figure 4-3, were compared in the present study. Figures 5-33 to 5-35 indicate that screw-2 reduced the torque requirements. The reason is mainly because screw-2 provides a relatively uniform flow in the hopper due to its increased capacity along the length of the screw, as well as a larger clearance between the flight tips and the casing surface due to the reduced screw diameter compared to screw-1. The reduced torque requirements were, however, accompanied by a decrease in efficiency as shown in Figures 5-36 and 5-37. A tapered or extended section beyond the screw can be employed to form seal plugs in order to prevent backflow of gases and bed materials from the reactor.

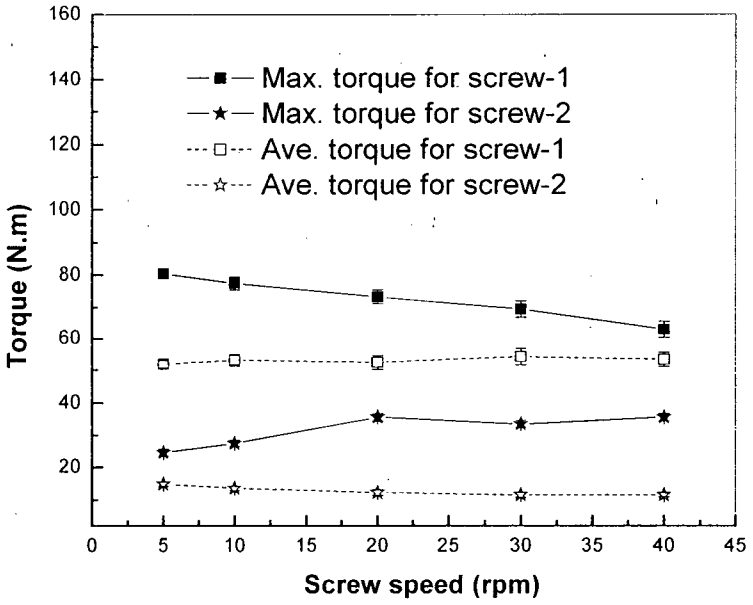


Figure 5-33. Effects of screw configurations on torque requirements for wood pellets with initial hopper level=0.30 m. For properties of the biomass materials, see Table 4-4.

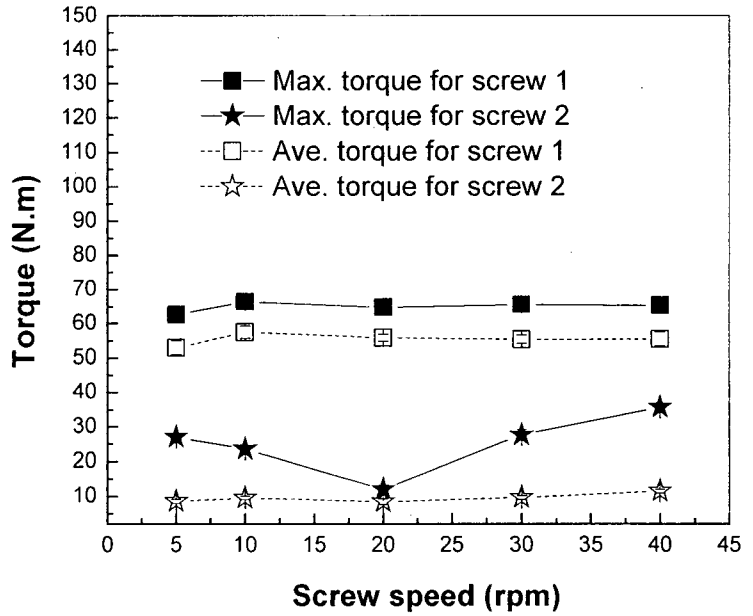


Figure 5-34. Effects of screw configurations on torque requirements for ground wood pellets-1 with initial hopper level=0.45 m. For properties of the biomass materials, see Table 4-4.

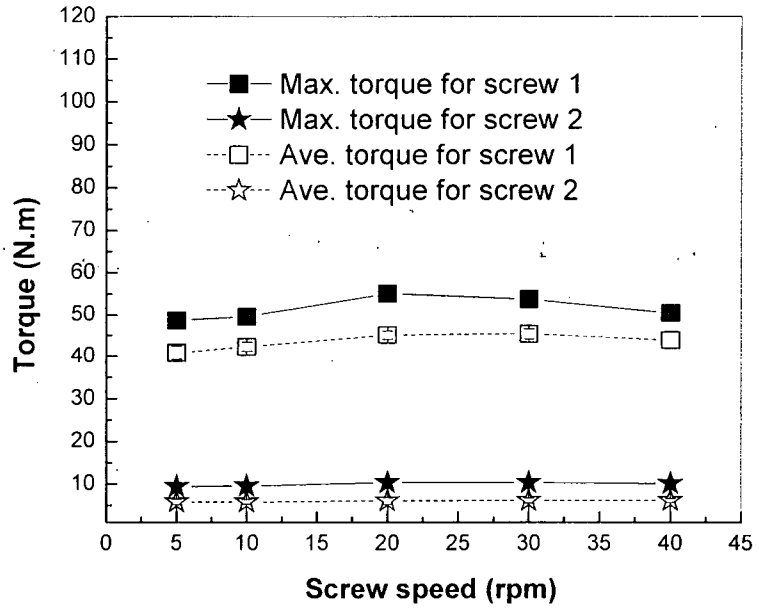


Figure 5-35. Effects of screw configurations on torque requirements for ground wood pellets-2 with initial hopper level=0.45 m. For properties of the biomass materials, see Table 4-4.

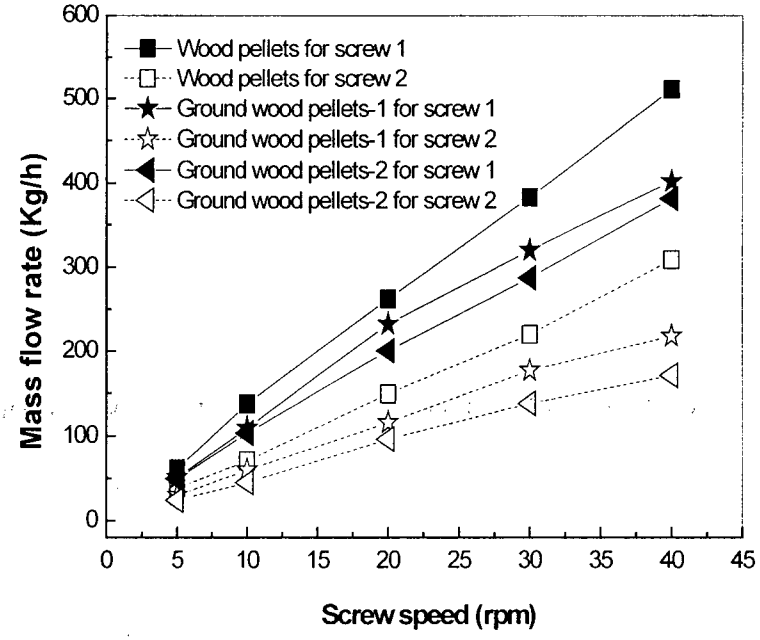


Figure 5-36. Effects of screw configurations on mass flow rate for wood pellets (hopper level=0.30 m) and ground wood pellets (hopper level=0.45 m). For properties of the biomass materials, see Table 4-4.

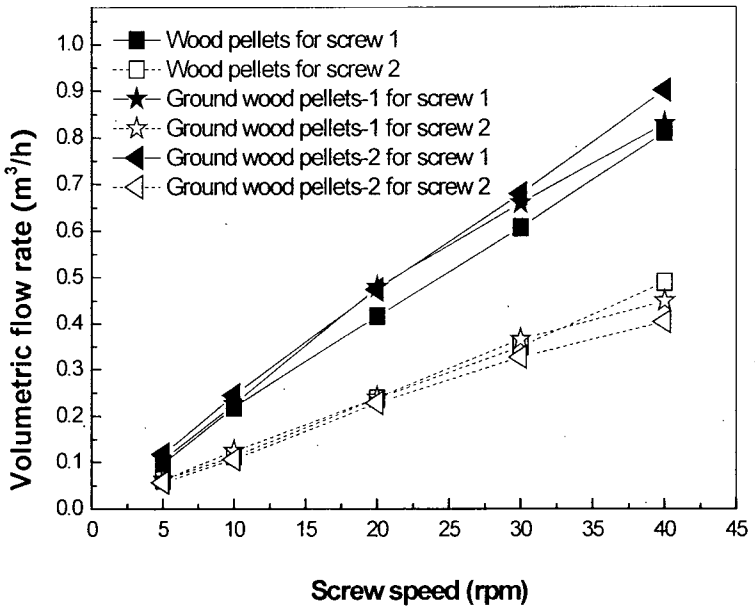


Figure 5-37. Effects of screw configurations on volumetric flow rate for wood pellets (hopper level=0.30 m) and ground wood pellets (hopper level=0.45 m). For properties of the biomass materials, see Table 4-4.

## 5.2 Summary

(1) The level of solids in the hopper is an important factor affecting blockage inside screw feeders. For wood pellets of uniform size, when the hopper level exceeded 0.35 m, blockage could occur, whereas no blockage occurred for hopper levels less than 0.30 m. For a hopper level exceeding 0.4 m, blockage occurred almost immediately after starting the screw feeder. This blockage was irreversible and could not be broken up by reversing or restarting the motor. Spheroidal polyethylene particles never blocked for hopper levels < 0.60 m due to their regular shape and smooth surfaces.

(2) Larger particles, more irregular particle shapes, rougher particle surfaces and larger bulk densities increased the tendency to block in the hopper-screw feeder. The torque required to

feed wood pellets was larger than for ground wood pellets due mainly to different sizes of the pellets.

(3) Irregular particle shapes and rougher particle surfaces made ground wood pellets-1 more difficult to feed than polyethylene particles.

(4) Particle size distribution plays a significant role in determining bulk flow. Wood pellets containing some fines blocked more frequently than wood pellets of uniform size. This is contrary to fluidization where fines promote better fluidization characteristics. Wider size distribution, especially large particles, required larger torque for hog fuel-1 compared to ground hog fuel and sawdust-1.

(5) High moisture content (e.g. 40 and 60%) caused larger cohesion and adhesion, making biomass fuels more likely to bridge in the hopper. Intermittent bridging in the hopper reduced the volumetric flow rate for wet biomass fuels. Wet biomass generally needed much more torque to achieve blockage-free feeding than dry biomass.

(6) Higher compressibility led to higher volumetric flow rates for screw feeding than for incompressible materials. Compressible biomass fuels passed through tapered sections more readily than incompressible materials. Plug formation inside the screw casing was also facilitated by increased compressibility, especially inside the extended "choke" section beyond the screw.

(7) The choke section played an important role in biomass feeding. The choke section length and casing configurations (e.g. tapered and extended sections) were closely related to plug formation and plug sealing of the reactor, while also affecting the torque requirements.

(8) Pressurizing the hopper slightly relative to the receiving vessel generally increased the feed rate and decreased the torque requirements, while also preventing backflow of gases and bed materials.

(9) More compact materials (i.e. larger bulk density) and non-uniform moisture content tend to increase the torque requirements for feeding.

(10) Careful refilling does not disrupt feeding, especially for biomass fuels of low bulk density.

(11) Large clearance and increasing capacity along the length of screw-2 led to reduced torque requirements. Small clearance caused larger torque requirements and a greater blockage tendency, as well as better plug sealing, for screw-1.

(12) For biomass feeding, the choke section may be longer, e.g. up to 6-10 times the pitch, in order to promote plug formation and prevent backflow of hot gases and bed materials from the reactor. Maximum torque, rather than starting torque, is critical to screw feeders with long choke sections.

(13) Torque requirements were nearly independent of screw speeds, both for compressible and incompressible solid materials.

# CHAPTER 6. MODELING OF BIOMASS FEEDING

## 6.1 Introduction

The flow patterns developed by a screw feeder connected to a hopper have been studied extensively in previous work, with particular reference to the volumetric capacity, mechanics and torque characteristics. Metcalf (1966) analyzed the mechanics of a screw feeder, especially the delivery rate and the torque required to feed various coals. The resulting model assumed a rigid plug of bulk materials in the screw pockets moving helically at an angle to the screw axis. Some materials may move in this manner, especially those with large internal friction angles, but observations indicate that shear and velocity gradients exist within screw feeders for most materials. Burkhardt (1967) conducted experiments on the effects of pitch (i.e. distance between adjacent screw flights), radial clearance, hopper exposure and hopper level on the performance of screw feeders. Carleton et al. (1969) discussed the performance of screw conveyors and screw feeders based on experiments focused on the effects of screw geometry, speed, fill level and material properties. Bates (1969) provided detailed analysis of mechanics and entrained patterns of screw feeders, especially combinations of screw feeders and hoppers. Rautenbach and Schumacher (1987) derived a relevant set of dimensional parameters by dimensional analysis to calculate the power consumption and transport capacity. Two geometrically similar screws were compared for scale-up experiments.

Several analyses have focused on flow in screw feeders. The geometry appears in Figure 6-1. Roberts (1991;1992), Roberts and Manjunath (1994), and Roberts (1996) analyzed the volumetric characteristics and mechanics of screw feeders in relation to the bulk solid draw-down characteristics of the feed hopper. Distribution of throughput along screw and uniform

draw-down patterns were investigated. It was assumed that the force exerted on the screw flights is distributed uniformly along the whole screw length, with three empirical ratios ($K_1$, $K_2$ and $K_3$ in the hopper section, see Figure 6-1) to determine the required torque. Yu and Arnold (1995; 1996) estimated the volumetric capacity and efficiency of screw feeders. They proposed an equivalent helix angle for screw flights and an equivalent helix angle for material motion. The effects of screw parameters (e.g. ratio of pitch to screw diameter) and clearance on the volumetric efficiency and volumetric capacity were also investigated. Yu and Arnold (1996) conducted experiments on flow in a wedge-shaped hopper. Different screw configurations and limitations of some methods of increasing the screw capacity were investigated.

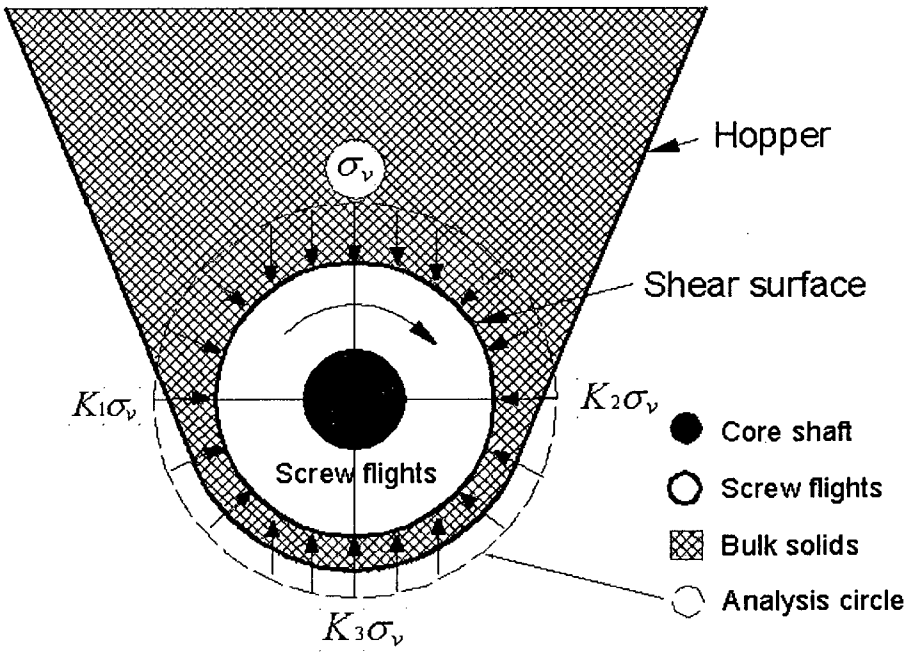


Figure 6-1. Stress around boundary in hopper section; ($\sigma_v$ is the vertical stress exerted by bulk solids at the hopper outlet).

Yu and Arnold (1997) proposed a theoretical model for torque requirements for single screw feeders. They assumed that the load imposed on a screw feeder by the bulk solids in the hopper is determined by the major consolidation stress. Considering the bulk material boundary

in a pocket between adjacent flights, forces are imposed on five surfaces (see five labels in Figure 6-2) With boundary conditions applying to the bulk material moving within screw flights, two basic regions were specified in the hopper section: an upper region in which a "shear surface" is assumed, representing the interface between bulk material surrounding the screw and bulk material propelled by the screw, and a lower region in which bulk material moves within a limited space. In the choke section, a rigid upper casing surface was assumed to limit the screw flight space, instead of a shear surface. The motion of particles in screw feeders was simulated by a Discrete Element Method, to analyze mixing and transportation of the particles inside a screw feeder (Tanida et al., 1998). Background information on screw feeders was given by Bates (2000) and Bell (2003). Most analyses of the torque characteristics of screw feeders have been based on flow conditions, rather than an initial filling condition. Screw feeding of biomass and the effects of the choke section on screw feeding have been ignored in previous research.

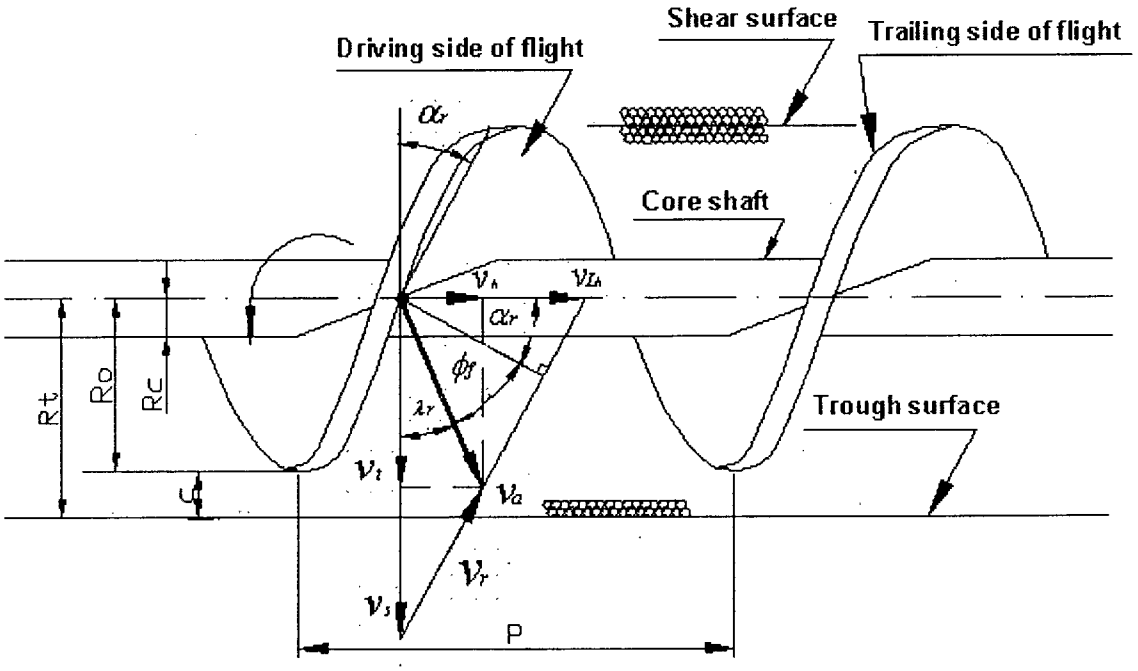


Figure 6-2. Five boundary surfaces for a material element in a pocket.

Schematics of our biomass feeding systems (including upper hopper, lower hopper and screw feeder) appear in Figures 4-2 and 4-3. The dimensions of the hopper-screw feeder are provided in Table 4-1. Biomass fuels (e.g. wood pellets, hog fuel and sawdusts) were added to the lower hopper and the surface flattened. The current model is intended to delineate what limits screw feeding in terms of the mechanisms of blockage and to predict torque requirements for biomass screw feeding. It extends previous models by considering effects of all boundaries (driving side, trailing side, core shaft and flight tips) on torque, and allowing for compression in the choke section, as well as in the hopper section. Unlike previous models, the choke section, whether straight or tapered, is explicitly included in this model. Predictions are compared with the experimental results presented in the previous chapter. Temperature variation and thermal effects are neglected in the present study.

## 6.2 Estimation of Volumetric and Mass Flow Rates

Screw feeders are volumetric devices (see Chapter 2). The velocity of a particulate material as it is conveyed by a screw feeder is a vector having an angle to the direction of rotation (see Figure 6-2). As the screw rotates, particles move in helical paths of direction opposite to that of the screw. Friction between the solids and screw flights/casing surface, together with the configuration of the screw itself, determines the efficiency of the screw feeder. The efficiency decreases as the clearance between the discharge casing surface and screw flight tips expands. In a screw feeder, an auger tends to compress the feedstock into a compact plug. The compression of the plug is aided by tapering (converging) the feed channel or gradually reducing the pitch of the screw as the feed material approaches the outlet.

The volumetric flow rate is predicted by Haaker et al. (1993), Yu and Arnold (1996), and Roberts (1996). The feeder volumetric flow rate is calculated based on screw and casing dimensions (see Figure 6-2) at the entrance to the choke section in the present study.

$$V = \pi\eta_v (P - \gamma)\left[(R_o^2 - R_c^2) + (1-k)(2cR_o + c^2)\right] \times \frac{f}{60} \tag{6-1}$$

where

$c$ = Clearance between screw flight tips and trough or casing inside surface, m.

$f$ = Rotational speed of screw feeder, rpm.

$k$ = Coefficient, $0 \le k \le 1$, accounting for a possible dead layer of material between the screw flights and the trough or casing wall. $k = 0$ indicates full wall slip with no dead layer; $k = 1$ indicates an annular layer in the choke section with the material shearing at the flight radius. $k$ needs to be fitted by experiments or based on experience.

$P$ = Pitch of screw, m.

$R_o$ = Screw flight radius, m.

$R_c$ = Core shaft radius, m.

$V$ =Volumetric flow rate, $m^3/s$.

$V_{TM}$ = Maximum theoretical throughput with screw feeder completely full and particles moving at the feeder speed without slip and/or rotational motion.

$\gamma$ = Thickness of screw flight, m.

$\eta_v$ = Volumetric efficiency, $\eta_v = V / V_{TM}$, dimensionless.

In practice, the actual volumetric flow, $V$, is less than $V_{TM}$ for several reasons:

(1) The axial velocity of particles is less than the ideal or optimum velocity owing to the rotary motion imparted by the screw.

(2) Slip may occur in the clearance space between the screw and casing.

(3) The filling fraction of screw pockets decreases as rotational speed increases.

The corresponding mass flow rate $M$ is obtained by multiplying by the bulk density, $\rho_b$, at the hopper outlet (i.e. interface between hopper and screw).

$$M = \rho_b V = \pi \eta_v (P - \gamma)\left[(R_o^2 - R_c^2) + (1-k)(2cR_o + c^2)\right]\rho_b \times \frac{f}{60} \tag{6-2}$$

The thickness of the screw flight is usually neglected in predicting the flow rate.

Typically the mass flow rate is employed to identify the transport capacity of screw feeders, especially for feeding into reactors. Since most biomass materials are compressible, their bulk density varies according to the compaction ratio. Inside the screw feeder, the bulk density is expected to depend on the radial and axial positions due to complicated dilation and compression conditions. The bulk density in the choke section is generally employed in estimating the mass flow rate. The loose bulk density can only be used if there is insignificant compression of the biomass in the hopper and screw feeder.

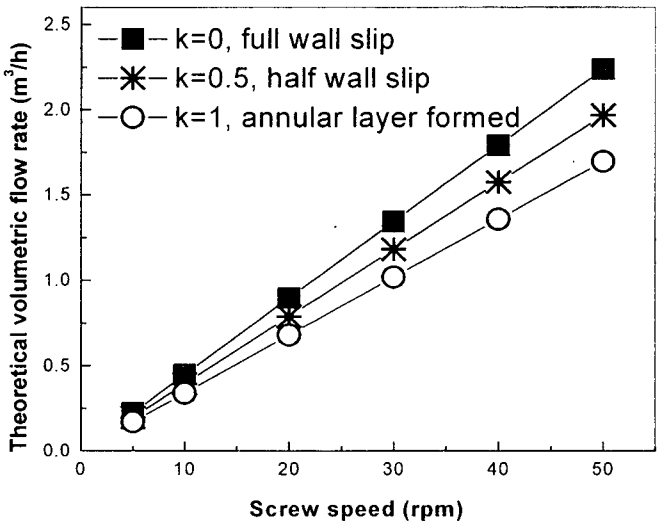


Figure 6-3. Theoretical volumetric flow rate prediction neglecting particle properties.

Different $k$ values lead to different flowrate predictions. However, the differences are not very great as shown in Figure 6-3. In the present study, it is assumed that $k = 1$, i.e. the clearance effect on the flow rate is neglected. For one revolution, the axial movement of each flight is $P$. Thus, the volumetric efficiency of screw feeder can be estimated from the geometry shown in Figure 6-4 (Yu and Arnold, 1997):

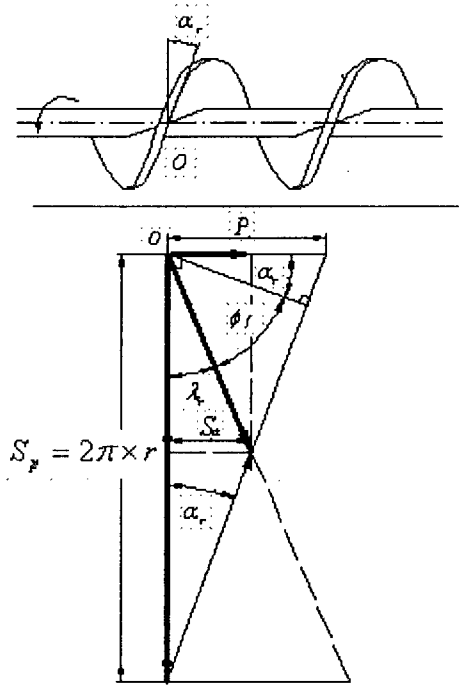


Figure 6-4. Velocity and displacement diagram for element at screw radius $r$.

$$\eta_v = \frac{S_a}{P} = \frac{S_a \cot \alpha_r}{S_p} \tag{6-3}$$

$$\frac{S_a}{S_p} = \frac{\tan \lambda_r}{1 + \tan \lambda_r \cot \alpha_r} \tag{6-4}$$

$$\frac{S_a}{P} = \frac{\tan \lambda_r}{\tan \alpha_r + \tan \lambda_r} \tag{6-5}$$

Hence the volumetric efficiency can be expressed by

$$\eta_{vr} = \frac{\tan \lambda_r}{\tan \alpha_r + \tan \lambda_r} \tag{6-6}$$

where

$\alpha_r$ = Flight helical angle at screw radius $r$, radians.

$\phi_f$ = Wall friction angle between bulk solids and flight surfaces, radians.

Here we make use of the relationship $\alpha_r + \lambda_r + \phi_f = 90^o$, as shown in Figure 6-4.

Because the flight face varies in helix angle ($\alpha_r$) from a minimum at the outside radius to a maximum at the core shaft, the bulk volume transported per revolution within a pocket can be estimated from the following equation, given by Haaker et al. (1993), Roberts and Manjunath (1994), and Yu and Arnold (1996):

$$\eta_v = \frac{2}{R_o^2 - R_c^2} \int_{R_c}^{R_o} \frac{\tan \lambda_r}{\tan \alpha_r + \tan \lambda_r} r dr \tag{6-7}$$

From Figure 6-4, the following expressions exist at $r$:

$$\tan \alpha_r = \frac{P}{S_p} = \frac{P}{2\pi \times r} \tag{6-8}$$

$$\tan \lambda_r = \tan(\frac{\pi}{2} - \alpha_r - \phi_f) = \cot(\alpha_r + \phi_f) = \frac{1 - \tan \alpha_r \tan \phi_f}{\tan \alpha_r + \tan \phi_f} = \frac{2\pi \times r - P \tan \phi_f}{P + 2\pi \times r \tan \phi_f} \tag{6-9}$$

Substituting Equations 6-8 and 6-9 into Equation 6-6 gives:

$$\eta_{vr} = \frac{\tan \lambda_r}{\tan \alpha_r + \tan \lambda_r} = 1 - \frac{1 + 2\pi \tan \phi_f \frac{r}{P}}{1 + 4\pi^2 (\frac{r}{P})^2} \tag{6-10}$$

The volumetric efficiency can be expressed as

$$\eta_v = \frac{2P^2}{R_o^2 - R_c^2} \int_{R_c/P}^{R_o/P} (1 - \frac{1 + 2\pi \tan \phi_f (r/P)}{1 + 4\pi^2 (r/P)^2})(r/P) d(r/P) \tag{6-11}$$

Equation 6-11 is exactly the same as obtained by Robert and Manjunath (1994), and Yu and Arnold (1996). Equation 6-11 can be solved either analytically or numerically.

Several other theories have also led to estimates of the volumetric efficiency:

(1) Haaker et al. (1993) proposed a method based on the plug flow of bulk solids. It is assumed that the internal friction of bulk solids is great enough to prevent internal shear. The helical angle of the outer radius of the flight ($\alpha_o$) is then utilized, giving

$$\tan\alpha_o = \frac{P}{2\pi R_o} \tag{6-12}$$

$$\lambda_o = 90^o - \alpha_o - \phi_f \tag{6-13}$$

$$\eta_v = \frac{\tan\lambda_o}{\tan\alpha_o + \tan\lambda_o} \tag{6-14}$$

(2) Bates (1969) proposed a mean radius, $R_m$, obtained from:

$$\pi R_o^2 - \pi R_m^2 = \pi R_m^2 - \pi R_c^2 \tag{6-15}$$

so that

$$R_m = \sqrt{\frac{R_o^2 + R_c^2}{2}} \tag{6-16}$$

A mean helical angle, $\alpha_m$, can then be calculated from:

$$\tan\alpha_m = \frac{P}{2\pi R_m} \tag{6-17}$$

Hence the volumetric efficiency can be obtained from:

$$\eta_v = \frac{\tan\lambda_m}{\tan\alpha_m + \tan\lambda_m} \tag{6-18}$$

where

$$\lambda_m = 90^o - \alpha_m - \phi_f \tag{6-19}$$

(3) Roberts and Manjunath (1994) assumed an average radius expressed by:

$$R_{av} = \frac{R_o + R_c}{2} \tag{6-20}$$

The volumetric efficiency is then given by

$$\eta_v = 1 - \frac{1 + 2\pi \tan\phi_f \dfrac{R_{av}}{P}}{1 + 4\pi^2 (\dfrac{R_{av}}{P})^2} \tag{6-21}$$

Equation 6-21 is exactly the same as Equation 6-10 except that an average radius replaces $r$.

Equation 6-11 provides a slightly smaller prediction than other methods, as indicated in Figure 6-5. For compressible materials (e.g. sawdusts and hog fuel), the volumetric flow rate tends to be larger than for incompressible materials if the compression inside the choke section is significant and the loose bulk density is assumed for materials leaving the screw feeder. In the present study, the theoretical prediction of volumetric efficiency is based on Equation 6-11, with modification due to compression of biomass inside the coke section, as discussed below.

## 6.3 Mechanics, Torque and Power Analysis for Hopper-Screw Feeders

There are two main regions for the screw feeder, the hopper feeding section and choke (or conveying) section as shown in Figure 4-1. The analysis presented below considers both sections.

Once flow is initiated, active stress fields change to passive or arched stress fields inside the hopper as shown in Figure 6-6. Initial filling and flow conditions lead to different vertical forces acting on screw surfaces at the hopper outlet, causing different mechanics and torque for screw feeders. For the initial condition, we focus on the hopper feeding section, since there is no flow in the choke section in this initial static state.

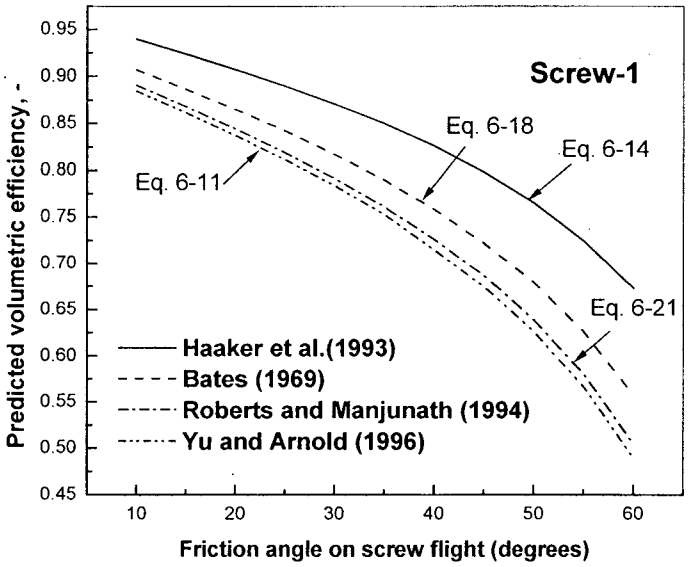


Figure 6-5. Prediction of volumetric efficiency (For screw configurations, see Figure 4-3).

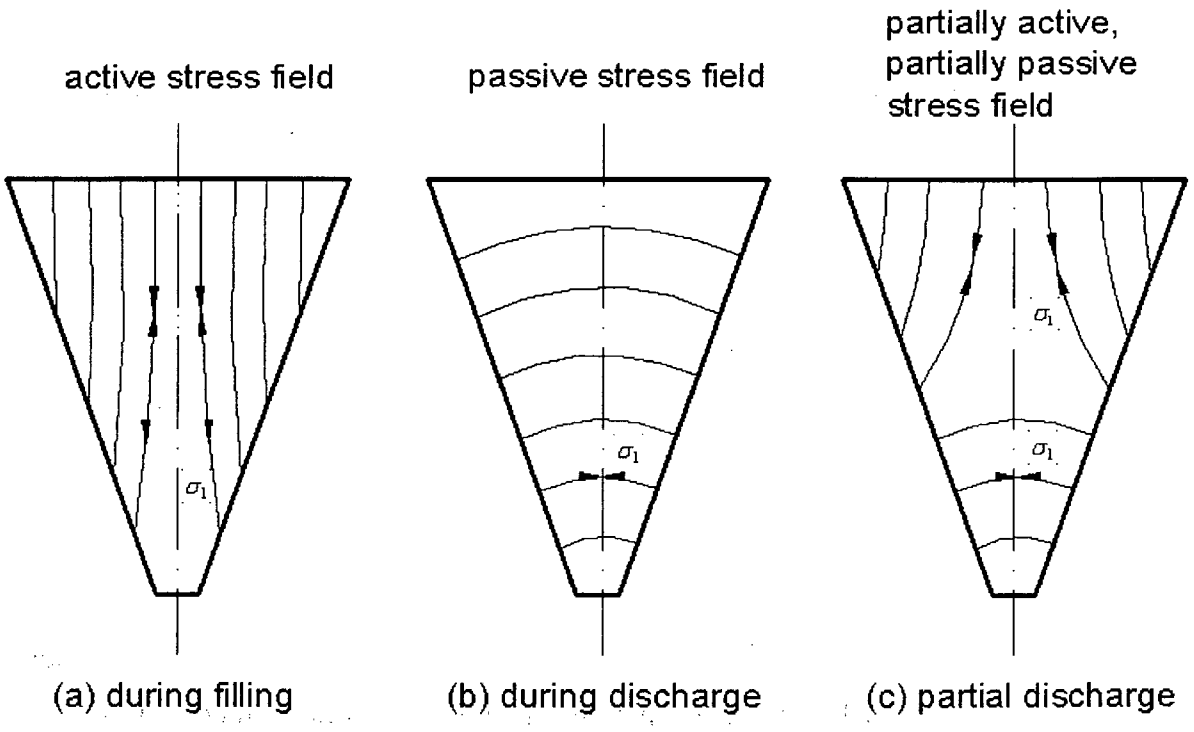


Figure 6-6. Directions of major principal stress in a hopper during filling and discharge (Arnold et al., 1980; Tardos, 1999).

6.3.1 Estimation of feeder load for initial filling and flow conditions

The theoretical prediction for a mass flow hopper requires consideration of both initial and flow consolidation stresses acting on the bulk solids. Following the approach adopted by Mclean and Arnold (1979), the feeder load $Q_v$ and vertical stress $\sigma_v$ acting on the outlet of a mass flow hopper are given by

$$Q_v = q\rho_b g L_h^{1-m} B^{2+m} \tag{6-22}$$

$$\sigma_v = \frac{q\rho_b g L_h^{1-m} B^{2+m}}{L_h B} = q\rho_b g L_h^{-m} B^{1+m} \tag{6-23}$$

where

$B$ = Hopper outlet width or diameter, m.

$g$ = Acceleration of gravity, m/s$^2$

$L_h$ = Hopper outlet length, m.

m= Hopper shape factor; m=1 for axisymmetric flow or a conical hopper; m=0 for plane flow or a wedge-shaped hopper, dimensionless

$Q_v$ = Feeder load exerted by bulk solids at hopper outlet, N.

$q$ = Dimensionless surcharge factor, dimensionless

$\sigma_v$ = Vertical stress exerted by bulk solids at hopper outlet as shown in Figure 6-1, Pa.

$\rho_b$ = Bulk density of solids in hopper, kg/m$^3$

We assume that the feeder load is distributed uniformly over the whole area of the hopper outlet, both initially and subsequently during flow.

For the wedge-shaped hopper in the present study, Equations 6-22 and 6-23 become

$$Q_v = q\rho_b g L_h B^2 \tag{6-24}$$

$$\sigma_v = q\rho_b gB \tag{6-25}$$

6.3.1.1 Initial filling condition

An active state stress is assumed as the initial filling conditions. The feeder load at the outlet is considered to be given by the weight of the material in the hopper section, plus the surcharge (i.e. $Q_c$, see Figure 6-7) at the transition of the vertical section and the hopper (if applicable), minus the vertical wall support. The original method of Jenike (1977) was employed by McLean and Arnold (1979), Arnold et al. (1980) and Manjunnath and Roberts (1986) for the initial stress in the hopper. The resulting dimensionless initial surcharge factor is given by

$$q_i = (\frac{\pi}{2})^m \frac{1}{2(m+1)\tan\alpha}\left\{\frac{D}{B} + \frac{2Q_c \tan\alpha}{A_c \rho_b gD} - 1\right\} \tag{6-26}$$

where

$A_c$ = Cross-sectional area of vertical section of bin, $m^2$.

$D$ = Width of long rectangular vertical section of bin or solid surface width in hopper, m

m = 0 for plane flow or wedge-shaped hoppers, or 1 for axisymmetric or conical hoppers.

$Q_c$ = Surcharge force at transition between vertical section and hopper (see Figure 6-7), N.

$\alpha$ = Hopper half-angle, radians.

$D$ in the denominator of the middle term of the section within the bracket was replaced by the hopper outlet width $B$ by Manjunnath and Roberts (1986), leading to

$$q_i = (\frac{\pi}{2})^m \frac{1}{2(m+1)\tan\alpha}\left\{\frac{D}{B} + \frac{2Q_c \tan\alpha}{A_c \rho_b gB} - 1\right\} \tag{6-27}$$

Since there was no surcharge force above the hopper (i.e. the hopper was never full, see Figure 6-7), then $Q_c / A_c = 0$ in our case. Also the hopper was wedge-shaped in the present study. Hence both Equations 6-26 and 6-27 simplify to

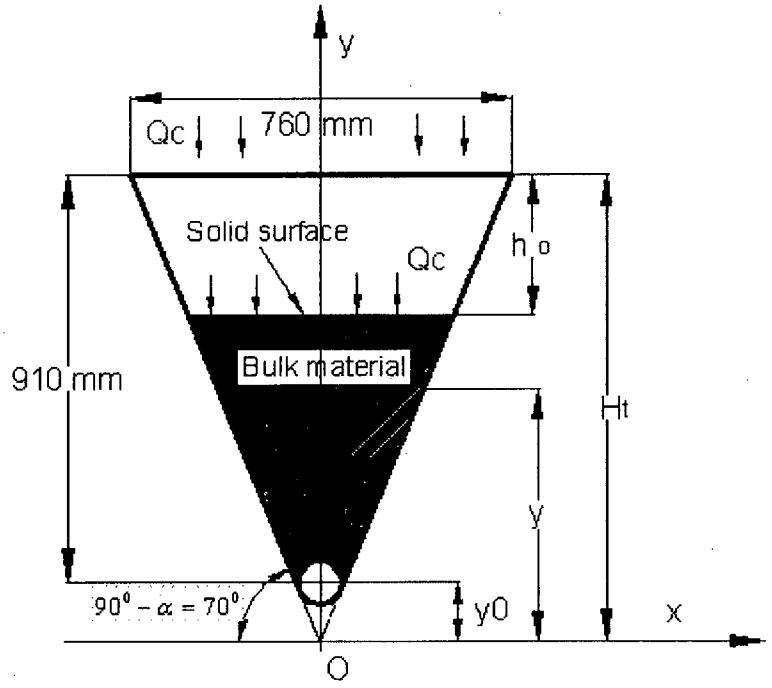


Figure 6-7. Coordinates of hopper.

$$q_i = \frac{1}{2\tan\alpha}\left(\frac{D}{B} - 1\right) \tag{6-28}$$

The vertical stress at the hopper outlet for initial conditions can be simplified to:

$$\sigma_{vi} = q_i \rho_b g B \tag{6-29}$$

For the hopper region, Jenike (1977) assumed a linear hydrostatic pressure gradient. In the present study, the upper surface of the bulk solids was flattened after the biomass was added to the hopper as indicated in Figure 6-7, where the coordinates are defined. The vertical stress at the hopper outlet can be expressed by

$$\sigma_{vi} = \rho_b g(H_t - h_0 - y_0) \tag{6-30}$$

Equations 6-29 and 6-30 are same, except that the former incorporated an initial dimensionless surcharge factor. Arnold et al. (1980) suggested that Equation 6-30 be used to calculate the filling stress providing that

$$2\alpha + 2\varepsilon_1 > \pi \tag{6-31}$$

The feeder load can be calculated from Equation 6-24, so that

$$Q_{vi} = \sigma_{vi} L_h B = q_i \rho_b g L_h B^2 = \rho_b g(H_t - h_0 - y_o) L_h B \tag{6-32}$$

where

$h_0$ = Distance between solids free surface and hopper top transition, see Figure 6-7, m.

$H_t$ = Distance between apex and top transition of hopper as shown in Figure 6-7, m.

$Q_{vi}$ = Initial feeder load exerted by bulk solids at hopper outlet, N.

$y$ = Vertical coordinate with apex of hopper as origin and upward direction as positive, m.

$y_0$ = Distance between apex of hopper and axis of screw as shown in Figure 6-7, m.

$\sigma_{vi}$ = Vertical stress due to bulk solids at hopper outlet for initial condition, Pa.

$\varepsilon_1 = \frac{\pi}{4} + \frac{\phi_w}{2} + \frac{1}{2}\cos^{-1}(\frac{\sin\phi_w}{\sin\delta})$, radians..

$\phi_w$ = Angle of kinetic friction between bulk solids and hopper wall, radians.

$\delta$ = Effective angle of internal friction of bulk solids, radians.

6.3.1.2 Flow condition

According to Mclean and Arnold (1979), Manjunnath and Roberts (1986), and Yu and Arnold (1996), the vertical stress at the hopper outlet for the flow condition can be calculated as

$$\sigma_v = q_f \rho_b g B \tag{6-33}$$

where

$q_f$ = Dimensionless surcharge factor for flow condition, dimensionless

$$q_f = \frac{1}{4\tan\alpha}\left(\frac{\pi}{3}\right)^m\left[\frac{Y(1+\sin\delta\cos 2\beta)(\tan\alpha+\tan\phi_w)}{(X-1)\sin\alpha}-\frac{1}{1+m}\right] \tag{6-34}$$

or alternatively

$$q_f = (\frac{\pi}{4})^m \frac{Y(1+\sin\delta)}{2(X-1)\sin\alpha} \tag{6-35}$$

$$X = \frac{\sin\delta}{1-\sin\delta}\left[\frac{\sin(2\beta+\alpha)}{\sin\alpha}+1\right] \tag{6-36}$$

$$Y = \frac{(\alpha+\beta)\sin\alpha+\sin\beta\sin(\alpha+\beta)}{(1-\sin\delta)\sin^2(\alpha+\beta)} \tag{6-37}$$

with $\alpha$ and $\beta$ in radians, and

$$\beta = \frac{1}{2}\left[\phi_w+\sin^{-1}(\frac{\sin\phi_w}{\sin\delta})\right], \text{ radians.} \tag{6-38}$$

Here m = 0 for plane flow or wedge-shaped hoppers, or 1 for axisymmetric or conical hoppers. The second expression for $q_f$ provides a better prediction of the flow surcharge factor according to Manjunnath and Roberts (1986). Hence we use Equation 6-35 in the present study.

By combining Equations 6-24 and 6-33, we obtain an expression for the feeder load,

$$Q_v = \sigma_v LB = q_f \rho_b g LB^2 \tag{6-39}$$

6.3.2 Forces, torque and power analysis in hopper feeding section

For the material within one pocket, forces are imposed on five boundary surfaces, i.e. the shear surface, driving side of the flight, trailing side of the flight, core shaft surface and trough surface (see Figure 6-2). In the choke section, a rigid upper casing surface limits the screw space instead of a shear surface (see Figure 6-8). There may or may not be bulk materials between the flight tips and the upper casing inside surface (i.e. upper clearance), depending on the feeding conditions. It is presumed that the forces on the individual surfaces within one pocket are

distributed uniformly or can be represented by average forces. The material element in a pocket is assumed to be at equilibrium, either static (initial filling condition) or moving at constant speed (flow condition) to simplify calculations through forces balances. Gravity, centrifugal force and cohesion are neglected. For comparison and convenience, we assume axial forces that push the material forward to be positive, whereas those that resist movement of the material are negative.

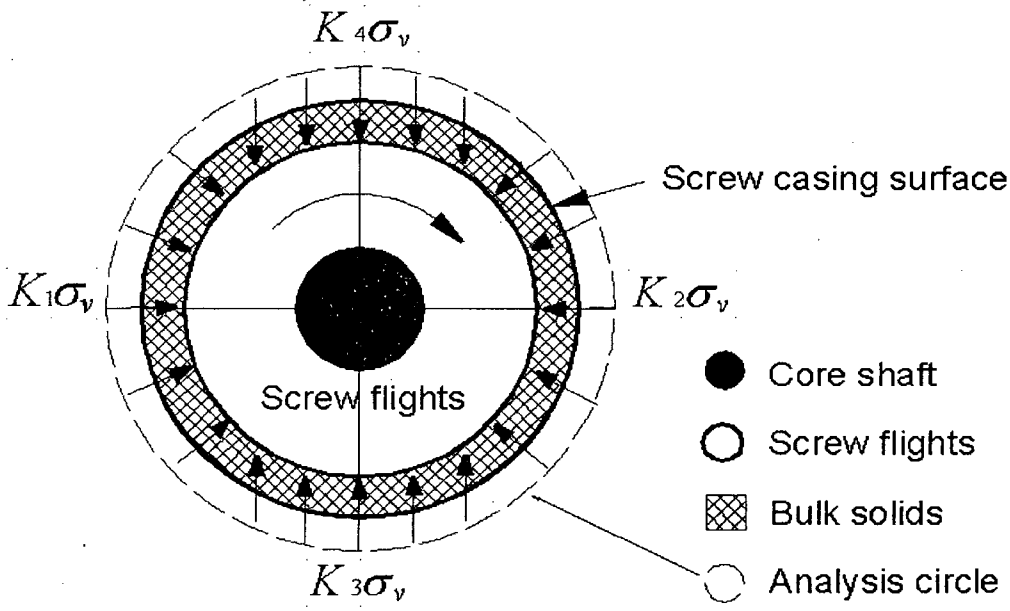


Figure 6-8. Stress around boundary in choke section.

6.3.2.1 Forces on shear surface

The bulk solid in the hopper exerts pressure at the hopper outlet, enhancing the shear strength of the material and making it difficult for the screw to rotate. Cohesion is ignored and only internal friction is considered. The axial resisting force on the material element within one pocket on the shear surface, shown in Figure 6-9, is

$$dF_{sa} = -\mu_e \sigma_v R_o P d\theta \cos(\alpha_o + \phi_f) \tag{6-40}$$

$$F_{sa} = -\mu_e \sigma_v R_o P \cos(\alpha_o + \phi_f) \int_0^{\pi} d\theta = -\frac{\pi}{2} \mu_e c_p \cos(\alpha_o + \phi_f) \sigma_v D_o^2 \quad (6\text{-}41)$$

or $$F_{sa} = -k_{sa} \sigma_v D_o^2 \quad (6\text{-}42)$$

with $$k_{sa} = \frac{\pi}{2} \mu_e c_p \cos(\alpha_o + \phi_f) \quad (6\text{-}43)$$

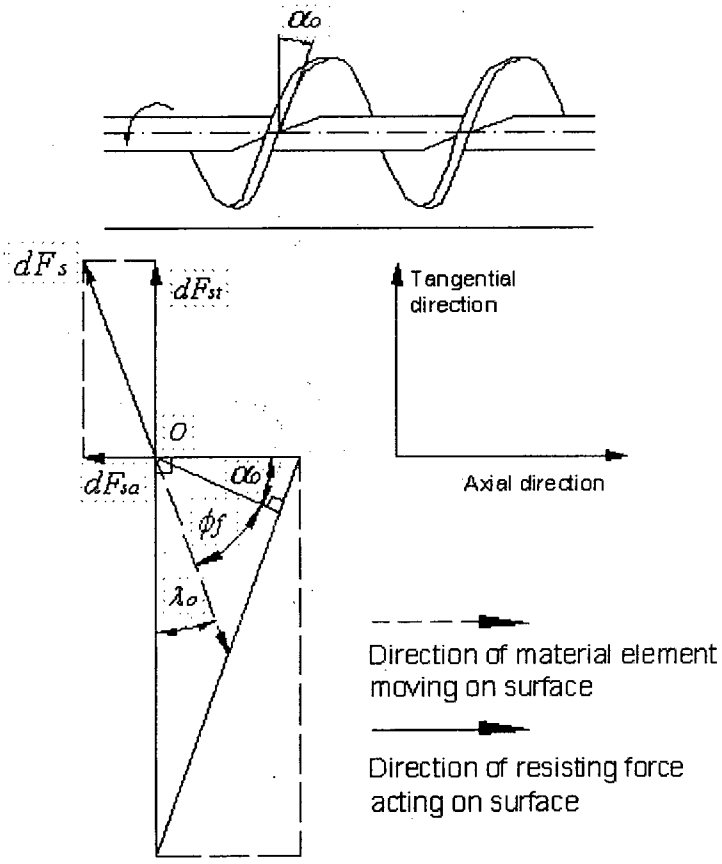


Figure 6-9. Forces on shear surface.

The tangential resisting force acting on the element on the shear surface in one pocket is

$$dF_{st} = -\mu_e \sigma_v R_o P d\theta \sin(\alpha_o + \phi_f) \quad (6\text{-}44)$$

so that $$F_{st} = -\mu_e \sigma_v R_o P \sin(\alpha_o + \phi_f) \int_0^{\pi} d\theta = -\frac{\pi}{2} \mu_e c_p \sin(\alpha_o + \phi_f) \sigma_v D_o^2 \quad (6\text{-}45)$$

Hence $$F_{st} = -k_{st} \sigma_v D_o^2 \quad (6\text{-}46)$$

with $$k_{st} = \frac{\pi}{2}\mu_e c_p \sin(\alpha_o + \phi_f) \quad (6\text{-}47)$$

where

$c_p$ = Ratio of pitch to screw flight diameter, $c_p = P/D_o$, -.

$\alpha_o$ = Screw flight helix angle at outside screw diameter, radians.

$\phi_f$ = Wall friction angle of bulk solids on screw surface, radians.

$\mu_e$ = Equivalent friction coefficient of bulk solids, with $\mu_e = (0.8 \sim 1)\sin\delta$ recommended by Roberts (1996).

6.3.2.2 Forces on core surface

The frictional force of the screw shaft contributes to turning the material inside the screw pockets, while, at the same time, preventing the material from moving forward. The axial resisting force acting on the element of bulk solid on the core surface, as shown in Figure 6-10, is

$$dF_{ca} = -2\pi R_c \sigma_{wa} \mu_{wc} dx \sin(\alpha_c) \quad (6\text{-}48)$$

$$F_{ca} = -2\pi R_c \sigma_{wa} \mu_{wc} \sin(\alpha_c) \int_0^P dx = -\pi c_d c_p \sigma_{wa} \mu_{wc} \sin(\alpha_c) \sigma_{wa} D_o^2 \quad (6\text{-}49)$$

When a moving element of material reaches steady states, there is equilibrium between the driving and resisting forces. Assuming that the axial and radial stresses are functions of x only, as shown in Figure 6-11, a force balance on the material element in a pocket gives

$$(R_t - R_c)\sigma_x = (R_t - R_c)(\sigma_x + d\sigma_x) + 2\tau_w dx \quad (6\text{-}50)$$

Let $$\lambda_s = \frac{\sigma_w}{\sigma_x} \quad (6\text{-}51)$$

so that $$\tau_w = \mu_w \sigma_w = \mu_w \lambda_s \sigma_x \quad (6\text{-}52)$$

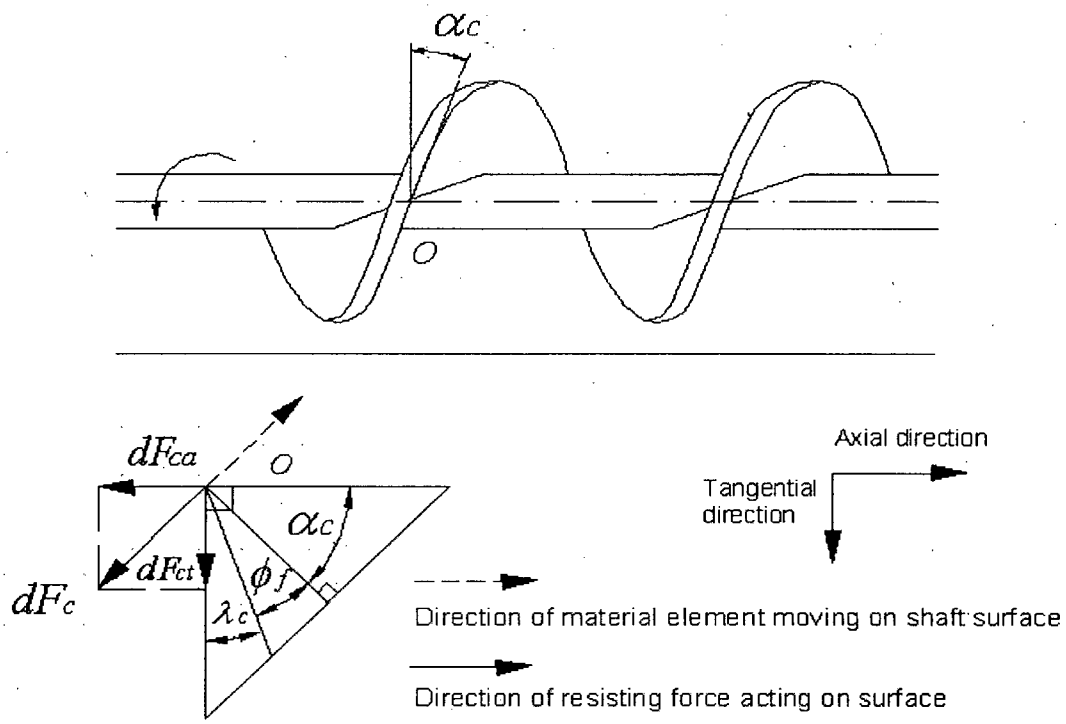


Figure 6-10. Forces on core shaft surface.

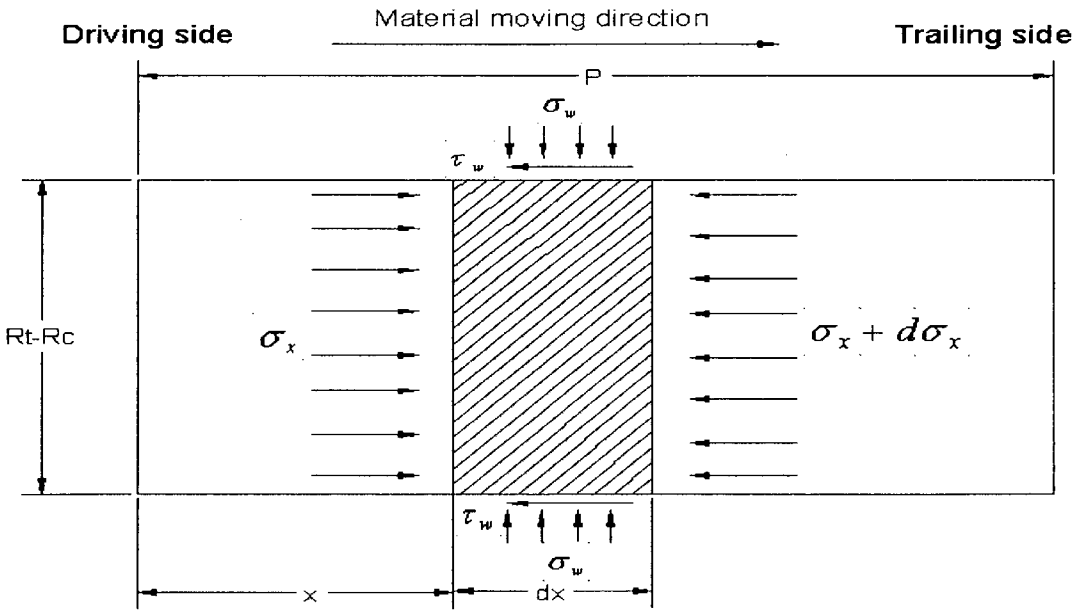


Figure 6-11. Stress on material element in a pocket.

Integrating Equation 6-50 with the boundary condition

$$\sigma_x = \sigma_v \text{ at } x = P \tag{6-53}$$

we obtain

$$\sigma_x = \sigma_v \exp\left[\frac{2\mu_w \lambda_s (P - x)}{R_t - R_c}\right] \tag{6-54}$$

The average normal wall stress can be obtained from

$$\sigma_{wa} = \frac{\lambda_s}{P} \int_0^P \sigma_x dx \tag{6-55}$$

After integration

$$\sigma_{wa} = \sigma_v \frac{(c_t - c_d)}{4\mu_w c_p}\left[\exp(\frac{4\mu_w \lambda_s c_p}{c_t - c_d}) - 1\right] \tag{6-56}$$

Hence Equation 6-49 can be expressed by

$$F_{ca} = -k_{ca}\sigma_v D_o^2 \tag{6-57}$$

$$\text{with } k_{ca} = \frac{\pi(c_t - c_d)c_d \sin\alpha_c}{4}\exp\left[\frac{4\mu_{wc}\lambda_s c_p}{(c_t - c_d)} - 1\right] = \frac{\pi(c_t - c_d)c_d c_p}{4\sqrt{c_p^2 + \pi^2 c_d^2}}\exp\left[\frac{4\mu_{wc}\lambda_s c_p}{(c_t - c_d)} - 1\right] \tag{6-58}$$

The tangential resistance force on the material element in a pocket on the core surface is

$$F_{ct} = k_{ct}\sigma_v D_o^2 \tag{6-59}$$

$$\text{where } k_{ct} = \frac{\pi(c_t - c_d)c_d \cos\alpha_c}{4}\exp\left[\frac{4\mu_{wc}\lambda_s c_p}{(c_t - c_d)} - 1\right] = \frac{\pi^2(c_t - c_d)c_d^2}{4\sqrt{c_p^2 + \pi^2 c_d^2}}\exp\left[\frac{4\mu_{wc}\lambda_s c_p}{(c_t - c_d)} - 1\right] \tag{6-60}$$

$$\frac{k_{ca}}{k_{ct}} = \frac{c_p}{\pi \times c_d} \tag{6-61}$$

with

$c_d$ = Ratio of core shaft diameter to screw flight diameter, $c_d = R_c / R_o = D_c / D_o$, -.

$c_p$ = Ratio of pitch to screw flight diameter, $c_p = P / D_o$, -.

$c_t$ = Ratio of trough or casing diameter to screw diameter, i.e. $c_t = 2R_t / D_o$, -.

$D_o$ = Screw flight diameter, m.

$R_t$ = Trough inside radius, $R_t = R_o + c$, m.

$\alpha_c$ = Screw flight helix angle at core shaft surface such that $\tan\alpha_c = P / 2\pi R_c$, radians.

$\mu_w$ = Wall friction coefficient between bulk solid and trough or core shaft surface, -.

$\mu_{wc}$ = Wall friction coefficient between bulk solid and core shaft surface, -.

$\mu_d$ = Effective coefficient of internal friction, $\mu_d = \tan\delta$, -.

$\sigma_w$ = Normal wall stress perpendicular to trough wall and core shaft surface, Pa.

$\sigma_{wa}$ = Average normal wall stress perpendicular to trough wall and core shaft, Pa.

$\sigma_x$ = Axial compression stress inside screw feeder, Pa.

$\tau_w$ = Shear stress on trough wall and core shaft surface, Pa.

$\lambda_s$ = Ratio of normal wall stress to axial compression stress on a confining surface as shown in Appendix C.

$$\lambda_s = \frac{\sigma_w}{\sigma_x} = \frac{\sin 2(\beta - \phi_w)\cos\phi_w}{\sin(2\beta - \phi_w) + \cos 2(\beta - \phi_w)\sin\phi_w} \tag{6-62}$$

where

$$\beta = \frac{1}{2}\left[\phi_w + \sin^{-1}\left(\frac{\sin\phi_w}{\sin\delta}\right)\right], \text{ radians.}$$

Equation 6-62 is based on the assumption that yield takes place on the wall as shown in Figure C-1.

6.3.2.3 Forces on trailing side of a flight

The frictional force due to the trailing side of a screw flight prevents the material from moving forward, while, at the same time, helping to turn the material inside the screw pockets if the wall friction angle of the bulk solid on the screw flight exceeds the helix angle of the trailing flight in Figure 6-12. Since the wall friction angle of biomass particles on screw flights is generally greater than the helix angle of the trailing flight, we begin by assuming that the tangential force on the trailing side helps the material inside the screw pockets rotate.

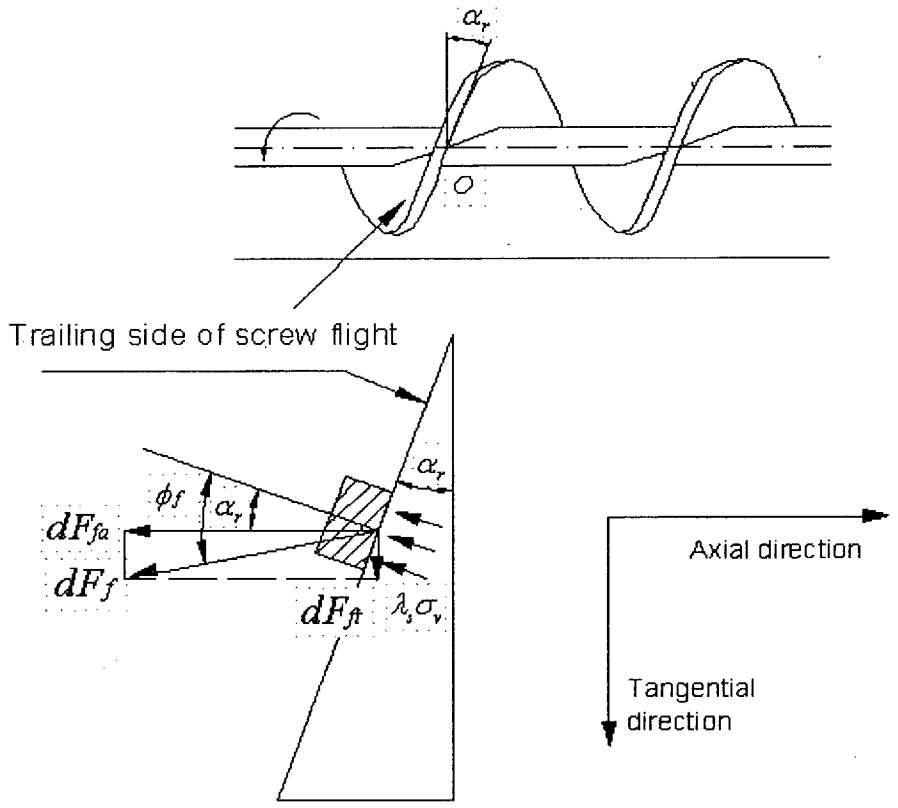


Figure 6-12. Forces on trailing side of flight.

The axial force acting on the material element in a pocket on the trailing side is

$$dF_{fa} = -\lambda_s \sigma_v \frac{\cos(\phi_f - \alpha_r)}{\cos\alpha_r \cos\phi_f} r dr d\theta = -\lambda_s \sigma_v r dr d\theta (1 + \tan\alpha_r \tan\phi_f) \qquad (6\text{-}63)$$

Substituting $\tan\alpha_r = P/2\pi r$ and $\tan\phi_f = \mu_f$ and integrating Equation 6-63 for $r$ from $R_c$ to $R_o$ and for $\theta$ from 0 to $2\pi$, we obtain

$$F_{fa} = -k_{fa}\sigma_v D_o^2 \tag{6-64}$$

with $$k_{fa} = \lambda_s\left[\frac{\pi}{4}(1-c_d^2) + \frac{c_p\mu_f}{2}(1-c_d)\right] \tag{6-65}$$

The tangential force acting on the material element on the trailing side is

$$dF_{ft} = \lambda_s\sigma_v \frac{r dr d\theta}{\cos\alpha_r \cos\phi_f}\sin(\phi_f - \alpha_r) \tag{6-66}$$

or $$F_{ft} = k_{ft}\sigma_v D_o^2 \tag{6-67}$$

with $$k_{ft} = \lambda_s\left[\frac{\pi\mu_f}{4}(1-c_d^2) - \frac{c_p}{2}(1-c_d)\right] \tag{6-68}$$

where

$\alpha_r$ = Screw flight helix angle at radius $r$, radians.

$\mu_f$ = Wall friction coefficient between bulk solids and screw flight surface, = $\tan\phi_f$, -.

6.3.2.4 Forces on trough surface

The frictional force exerted by the inside surface of the trough on the material element resists the material from moving forward and turning. We assume that particles in the vicinity of the trough surface move in the same manner as those in the vicinity of the flight tips.

Generally full wall slip is likely to take place when

$$\mu_{wt} < \mu_d \frac{R_o}{R_o + c} \tag{6-69}$$

where

$c$ = Clearance between screw flight tips and trough or casing inside surface, m.

$\mu_{wt}$ = Wall friction coefficient between bulk solids and trough surface, -.

$\mu_d$ = Effective coefficient of internal friction of bulk solids, -.

For some biomass particles when $\mu_{wt} < \mu_d R_o/(R_o + c)$, full wall slip may be assumed. When $\mu_{wt} > \mu_d R_o/(R_o + c)$, a coherent lining may form in the lower part of the screw in the hopper feeding section or in the choke section sheared by the flight tips.

The axial resisting force acting on a material element within a pocket on the trough surface indicated in Figure 6-13, is

$$dF_{ta} = -\pi R_t \mu_{wt} \sigma_{wa} dx \cos(\alpha_0 + \phi_f) \tag{6-70}$$

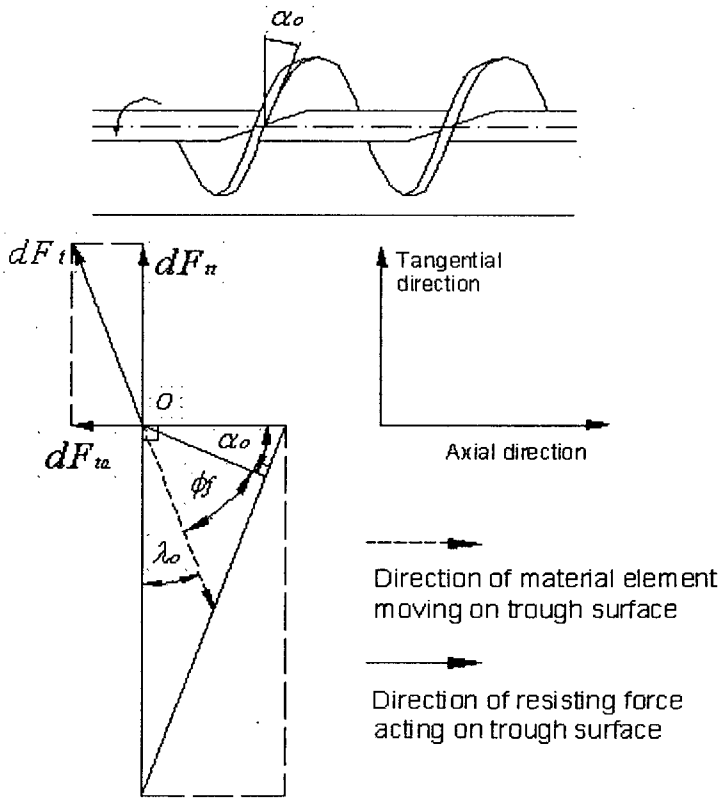


Figure 6-13. Forces on trough surface.

Substituting $\tan\alpha_o = P/2\pi R_o$ and $\tan\phi_f = \mu_f$ and integrating Equation 6-70 for $r$ from $R_c$ to $R_o$ and $\theta$ from 0 to $\pi$, we obtain

$$F_{ta} = -\frac{\pi c_t (c_t - c_d)}{8} \cos(\alpha_o + \phi_f) \exp\left[ \left( \frac{4\mu_{wt} \lambda_s c_p}{c_t - c_d} \right) - 1 \right] \sigma_v D_o^2 \tag{6-71}$$

$$F_{ta} = -k_{ta} \sigma_v D_o^2 \tag{6-72}$$

with $$k_{ta} = \frac{\pi c_t (c_t - c_d)}{8} \cos(\alpha_o + \phi_f) \exp\left[ \left( \frac{4\mu_{wt} \lambda_s c_p}{c_t - c_d} \right) - 1 \right] \tag{6-73}$$

The tangential force acting on the material element within a pocket on the trough surface is

$$dF_{tt} = -\pi R_t \mu_{wt} \sigma_{wa} dx \sin(\alpha_0 + \phi_f) \tag{6-74}$$

$$F_{tt} = -\frac{\pi c_t (c_t - c_d)}{8} \sin(\alpha_o + \phi_f) \exp\left[ \left( \frac{4\mu_{wt} \lambda_s c_p}{c_t - c_d} \right) - 1 \right] \sigma_v D_o^2 \tag{6-75}$$

or $$F_{tt} = -k_{tt} \sigma_v D_o^2 \tag{6-76}$$

where $$k_{tt} = \frac{\pi c_t (c_t - c_d)}{8} \sin(\alpha_o + \phi_f) \exp\left[ \left( \frac{4\mu_{wt} \lambda_s c_p}{c_t - c_d} \right) - 1 \right] \tag{6-77}$$

6.3.2.5 Forces and torque on driving side of a flight

The total axial force acting on the material element within a pocket transmitted by the driving side of the flight (see Figure 6-14) should equal the total resisting axial forces on the same material element due to the shear surface, core shaft surface, trailing side of flight and trough surface. It is assumed that the total force is applied uniformly to the surface of the driving side. The total force balance is

$$F_{da} + F_{sa} + F_{ca} + F_{fa} + F_{ta} = 0 \tag{6-78}$$

where $da$, $sa$, $ca$, $fa$, $ta$ denote axial forces on the driving side of the flight, shear surface, core shaft surface, trailing side of the flight and trough surface, respectively.

The resulting stress on the driving side of the flight is

$$\sigma_{da} = \frac{F_{da}}{\pi (R_o^2 - R_c^2)} = \frac{4(k_{sa} + k_{ca} + k_{fa} + k_{ta})}{\pi (1 - c_d^2)} \sigma_v = K_{da} \sigma_v \tag{6-79}$$

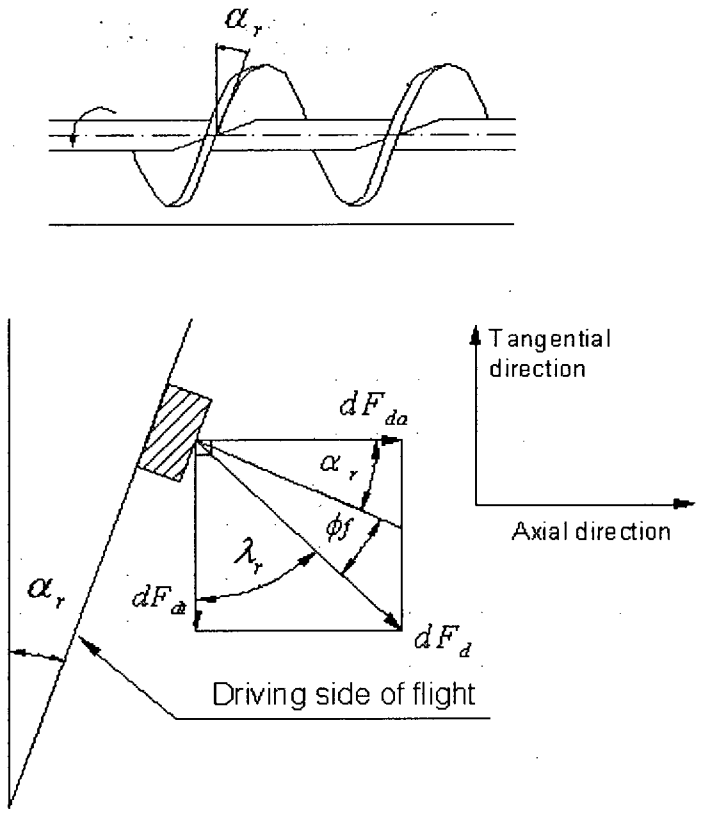


Figure 6-14. Forces on driving side of flight.

where $$K_{da} = \frac{4(k_{sa} + k_{ca} + k_{fa} + k_{ta})}{\pi(1 - c_d^2)} \tag{6-80}$$

The tangential force acting on the material element within a pocket transmitted by the driving flight is

$$dF_{dt} = \sigma_{da} r d\theta dr \tan(\alpha_r + \phi_f) \tag{6-81}$$

Substituting $\tan\alpha_r = P/2\pi r$ and $\tan\phi_f = \mu_f$ and integrating from $\theta$=0 to $2\pi$ leads to:

$$F_{dt} = 2\pi\sigma_{da}\int_{R_c}^{R_o} r\left(\frac{1 + \frac{2\pi\mu_f r}{P}}{\frac{2\pi r}{P} - \mu_f}\right)dr \tag{6-82}$$

Integrating Equation 6-82 from $R_c$ to $R_o$, we obtain (as derived in Appendix D)

$$F_{dt} = 2\pi\sigma_{da}D_o^2\left[\frac{\mu_f}{8}(1-c_d^2)+\frac{1+\mu_f^2}{4\pi}c_p(1-c_d)+\frac{\mu_f(1+\mu_f^2)c_p^2}{4\pi^2}\ln\left(\frac{\frac{\pi}{c_p}-\mu_f}{\frac{\pi c_d}{c_p}-\mu_f}\right)\right] \quad (6\text{-}83)$$

Note that the calculated stress on the driving side of a flight is not equal to the axial stress calculated from Equation 6-54 at $x=0$ (i.e. $\sigma_x=\sigma_v\exp[2\mu_w\lambda_s P/(R_t-R_c)]$). Instead, the calculated axial stress at $x=0$ in a pocket from Equation 6-54 is always larger than the stress on the driving side of the flight derived from Equation 6-79 for the boundary condition

$$\sigma_x = n\sigma_v \text{ at } x=P \ (n\geq 1) \quad (6\text{-}84)$$

This indicates that the maximum axial stress at $x=0$ in a pocket may not reach the theoretical maximum value, and that the axial stress distribution in a pocket may depend on flow conditions. The average axial stress is employed to reflect the magnitude of stress within a pocket. Equation 6-84 is the same as Equation 6-53 (i.e. $\sigma_x=\sigma_v$ at $x=P$) when $n=1$. Note that $n$ is introduced to adjust the boundary condition as discussed below. From Equations 6-51, 6-55, 6-56 and 6-84, the average axial stress ($\sigma_{xa}$) in a pocket can be expressed by

$$\sigma_{xa} = n\sigma_v\frac{(c_t-c_d)}{4\lambda_s\mu_w c_p}\left[\exp\left(\frac{4\mu_w\lambda_s c_p}{c_t-c_d}\right)-1\right] \quad (6\text{-}85)$$

The ratio of the average axial stress ($\sigma_{xa}$) to the stress on the driving side ($\sigma_{da}$) for a material element within a pocket changes as $n$ increases in Equation 6-84. Making the predicted starting torque equal to the measured starting torque leads to $\sigma_{xa}=0.85\sigma_{da}$ for wood pellets. This also works well for polyethylene particles (see Table 6-1). Since average axial stress in the screw pockets $\sigma_{xa}$ is not expected to be greater than the stress at the driving side of the flight, i.e. $\sigma_{da}$, we assume $\sigma_{xa}=0.99\sigma_{da}$ for relatively light and compressible materials, which provides reasonable predictions of starting torques (see Table 6-1).

Table 6-1. Comparison of predicted and measured torques for screw-1

| Name of specimen | Mean particle diameter (mm) | Bulk density ($kg/m^3$) | Friction angle on carbon steel (deg) | Internal friction angle (deg) | Measured average torque (N.m) | | Measured maximum torque (N.m) | | Measured Starting torque (N.m) | | Calculated average torque (N.m) | | Calculated starting torque (N.m) | |
|---|---|---|---|---|---|---|---|---|---|---|---|---|---|---|
| | | | | | 0.3 m | 0.45 m | 0.3 m | 0.45 m | 0.3 m | 0.45 m | 0.3 m | 0.45 m | 0.3 m | 0.45 m |
| Wood pellets | 9.8 | 630 | 31.4 | 32.0 | 52.8 | N/A | 72.6 | N/A | 29.4 | N/A | 58.3 | 75.9 | 30.0 | 44.9 |
| Ground wood pellets-1 | 4.05 | 485 | 30.2 | 33.2 | 31.3 | 55.4 | 38.0 | 64.9 | 15.6 | 15.9 | 39.5 | 56.4 | 13.8 | 20.8 |
| Ground wood pellets-2 | 0.55 | 423 | 30.4 | 38.0 | 27.7 | 43.5 | 32.6 | 51.6 | 13.1 | 14.7 | 32.6 | 48.4 | 11.4 | 17.1 |
| Sawdusts-1 | 0.45 | 210 | 31.8 | 38.0 | 16.5 | 21.7 | 19.9 | 25.8 | 8.9 | 9.0 | 16.3 | 23.6 | 6.3 | 9.4 |
| Hog fuel-1 | 0.72 | 200 | 31.5 | 39.0 | 13.0 | 21.7 | 25.2 | 33.1 | 10.5 | 11.8 | 15.5 | 23.0 | 5.5 | 8.2 |
| Ground hog fuel | 0.18 | 150 | 31.8 | 45.0 | 9.4 | 13.3 | 16.7 | 24.8 | 4.7 | 5.5 | 9.7 | 15.1 | 3.4 | 5.0 |
| Wood shavings-1 | 0.67 | 110 | 31.0 | 39.0 | 7.0 | 8.6 | 22.9 | 21.4 | 4.2 | 6.8 | 7.1 | 10.4 | 2.99 | 4.48 |
| Polyethylene particles | 4 | 610 | 21.5 | 26.2 | 11.8 | 22.8 | 15.8 | 27.4 | 8.7 | 14.9 | 18.1 | 23.6 | 11.8 | 17.7 |

We do not consider the $\sigma_{xa} > \sigma_{da}$ case in the present study, although this would make starting torque predictions better for some materials (e.g. hog fuel-1). $n$ is in the range of 1-1.5 for screw-1 in the present study. In other words, we set the boundary condition (see Equation 6-84) to make $\sigma_{xa} = 0.85\sigma_{da}$ and $\sigma_{xa} = 0.99\sigma_{da}$ for relatively incompressible and compressible materials, respectively. We do not consider $n < 1$ here since the minimum axial stress (on the trailing side of the flight, i.e. at $x = P$) for the material element is not expected to be less than the vertical stress at the hopper outlet (i.e. $\sigma_v$). A different strategy is employed for screw-2 due to different screw configurations, as discussed below. Once the boundary condition is determined, the forces and stresses for a material element within a pocket can be predicted using the above procedures. The reason for the different stress ratios (i.e. 0.85 and 0.99) for incompressible and compressible materials is probably that the stress distribution for compressible materials within a pocket is more uniform than for incompressible particles. A uniform stress distribution within a pocket is expected to make the average axial stress very close to the stress on the driving side of a flight for compressible materials. If $n = 1$ were to be employed (Yu and Arnold, 1997) for the torque predictions, the predicted results would be slightly smaller than for $n > 1$, as adopted here.

For compressible materials, the loose bulk density is first employed to calculate the vertical stress and torque requirements for both the initial and flow conditions. Once the vertical stress at the hopper outlet is determined, the compacted bulk density at the hopper outlet is estimated from the density-stress relation,

$$\rho_y = a(\sigma_y + b)^c \tag{6-86}$$

where $a$, $b$ and $c$ are constants, obtainable by curve fitting experimental data for the compacted bulk density and corresponding mean stress on the bulk solid surface. In this study, experiments were performed by adding weights to the top of biomass added to an initial depth of 0.12 m in a

cylinder of diameter 0.1 m. Least squares fitted values of $a$, $b$ and $c$ for various bulk materials are listed in Table 6-2. Although some researchers (e.g. Arnold et al., 1980) found that the bulk density could be well represented by equations of the form $\rho_y = a(1+\sigma_y)^b$ or $\rho_y = a\sigma_y^b$, the former leads to a mathematically awkward expression, while the latter cannot give satisfactory predictions as the stress approaches zero. Hence they are replaced by Equation 6-86 in the present study without significant deviation.

As an initial condition, $\sigma_y$ can be expressed by Equation 6-30, so that

$$\sigma_y = \rho_b g(H_t - h_0 - y_0) \tag{6-87}$$

In view of Equation 6-86, the average bulk density can then be estimated by

$$\rho_{ya} = \frac{1}{H_0}\int_{y_0}^{H_t-h_0} a\{\rho_{yb} g(H_t - h_0 - y) + b\}^c dy \tag{6-88}$$

where $\rho_{yb}$ is the compacted bulk density at $y$ and $H_0$ is the hopper level.

The average bulk density, which does not differ significantly from the loose bulk density in the present study, can be used to calculate the initial vertical stress. The average bulk density was calculated as an arithmetic mean of the loose bulk density and compacted bulk density at the hopper outlet for simplicity. Values are listed in Table 6-2. During flow, the passive stress is not a simple function of $y$. The average bulk density obtained from the initial condition is adopted when there is flow in the present study. However, for relatively incompressible materials (e.g. polyethylene and wood pellets), the loose bulk density is employed in the calculations.

The angle of kinetic wall friction and the effective angle of internal friction are used for both initial and flow conditions. Wall friction on the trough (carbon steel) and casing surfaces (carbon steel) are dominant compared to that on the stainless steel screw flight. Wall friction angles in the present study are based on slightly rusty carbon steel (see Chapter 4).

Table 6-2. Predicted initial feeder load and vertical stress for screw-1

| Name of specimen | Mean diameter (mm) [1] | Bulk density ($kg/m^3$) | a [2] | b | c | Ave. bulk density [3] ($kg/m^3$) | | Initial vertical stress (Pa) | | Initial feeder load (N) | | Weight of bulk solid in hopper (N) | |
|---|---|---|---|---|---|---|---|---|---|---|---|---|---|
| | | | | | | @ 0.3 [4]m | @ 0.45 m | @ 0.3 m | @ 0.45 m | @ 0.3 m | @ 0.45 m | @ 0.3 m | @ 0.45 m |
| Wood pellets | 9.8 | 630 | 630 | 0 | 0 | 630 | 630 | 1850 | 2780 | 173 | 259 | 378 | 694 |
| Ground wood pellets-1 | 4.05 | 485 | 485 | 0 | 0 | 485 | 485 | 1430 | 2140 | 133 | 199 | 291 | 534 |
| Ground wood pellets-2 | 0.55 | 423 | 157 | 17800 | 0.1 | 427 | 428 | 1260 | 1890 | 117 | 176 | 254 | 466 |
| Sawdusts-1 | 0.45 | 210 | 82 | 3297 | 0.12 | 212 | 213 | 624 | 941 | 58 | 88 | 126 | 231 |
| Hog fuel-1 | 0.72 | 200 | 158 | -359 | 0.05 | 199 | 202 | 584 | 892 | 55 | 83 | 120 | 220 |
| Ground hog fuel | 0.18 | 150 | 88 | 364 | 0.09 | 155 | 157 | 455 | 691 | 42 | 64 | 90 | 165 |
| Wood shavings-1 | 0.67 | 110 | 35 | 1932 | 0.16 | 114 | 114 | 334 | 504 | 31 | 47 | 66 | 121 |
| Polyethylene particles | 4 | 610 | 610 | 0 | 0 | 610 | 610 | 1790 | 2690 | 167 | 251 | 370 | 678 |

Notes: [1] Volume-equivalent diameters for wood pellets and polyethylene particles, Sauter mean particle diameters for the other materials.
[2] a, b and c constants for bulk density prediction, see Equation (6-86), R-square is 0.99 for ground hog fuel, 1.00 for Ground wood pellets-2, 0.99 for hog fuel-1, 1.00 for sawdust-1, 0.98 for wood shavings-1.
[3] average bulk density obtained by arithmetic mean of loose bulk density and compacted bulk density at hopper outlet.
[4] hopper level, 0.30 and 0.45 m in the present study.

The 0.30 m long cast acrylic tube at the discharge end of the screw feeder (used to assist visualization) is neglected. These simplifications are not expected to affect the predictions significantly.

The torque generated within one pocket is given by

$$T_i = T_d + T_c + T_f + T_{tip} \tag{6-89}$$

where

$T_c$ = Torque due to core shaft surface, N.m.

$T_d$ = Torque due to driving flight, N.m.

$T_f$ = Torque due to trailing flight, N.m.

$T_{tip}$ = Torque due to flight tip, N.m.

The torque generated by the driving side of the screw flight is

$$T_d = 2\pi\sigma_{da}\int_{R_c}^{R_o} r^2 \tan(\alpha_r + \phi_f)dr \tag{6-90}$$

Substituting $\tan\alpha_r = P/2\pi r$ and $\tan\phi_f = \mu_f$ and integrating Equation 6-90 from $r = R_c$ to $R_o$, we obtain:

$$T_d = K_s\sigma_{da}D_o^3 = K_s K_{da}\sigma_v D_o^3 \tag{6-91}$$

where

$$K_s = \frac{\pi\mu_f(1-c_d^3)}{12} + \frac{(1+\mu_f^2)(1-c_d^2)c_p}{8} + \frac{\mu_f(1+\mu_f^2)(1-c_d)c_p^2}{4\pi} + \frac{\mu_f^2(1+\mu_f^2)c_p^3}{4\pi^2}\ln\left\{\frac{\frac{\pi}{c_p}-\mu_f}{\frac{\pi c_d}{c_p}-\mu_f}\right\} \tag{6-92}$$

$K_{da}$ is calculated based on Equation 6-80. Equation 6-92 is derived in Appendix E.

The torque generated by the core shaft surface is given by

$$T_c = F_{ct} R_c = \frac{k_{ct} c_d}{2} \sigma_v D_o^3 = \frac{\pi c_d^2}{2 c_p} k_{ca} \sigma_v D_o^3 \tag{6-93}$$

Substitution of Equation 6-58 into Equation 6-93 leads to

$$T_c = \frac{\pi^2 (c_t - c_d) c_d^3}{8\sqrt{c_p^2 + \pi^2 c_d^2}} \exp\left[\frac{4\mu_{wc} \lambda_s c_p}{(c_t - c_d)} - 1\right] \sigma_v D_o^3 \tag{6-94}$$

The torque generated by the trailing side of the screw flight is calculated from

$$T_f = \lambda_s \sigma_v \int_{R_c}^{R_o} \frac{\sin(\phi_f - \alpha_r) r^2 dr}{\cos\alpha_r \cos\phi_f} \int_0^{2\pi} d\theta = 2\pi \lambda_s \sigma_v \int_{R_c}^{R_o} \frac{\sin(\phi_f - \alpha_r)}{\cos\alpha_r \cos\phi_f} r^2 dr \tag{6-95}$$

Integrating Equation 6-95 from $r = R_c$ to $r = R_o$, we obtain

$$T_f = \left[\frac{\pi \lambda_s \mu_f (1 - c_d^3)}{12} - \frac{\lambda_s c_p (1 - c_d^2)}{8}\right] \sigma_v D_o^3 \tag{6-96}$$

Equation 6-96 is derived in Appendix F. All of these equations can also be solved by numerical integration to confirm the results.

The torque required to overcome the flight tip surface resistance within a pocket is estimated by

$$T_{tip} = \frac{(\sigma_v + n\sigma_{wa}) \gamma P \mu_f R_o}{2 \sin\alpha_o} \tag{6-97}$$

Rearranging Equation 6-97, we obtain

$$T_{tip} = k_{tip} \sigma_v D_o^3 \tag{6-98}$$

$$k_{tip} = \frac{(\sigma_v + n\sigma_{wa}) c_b c_p \mu_f}{4\sigma_v \sin\alpha_o} \tag{6-99}$$

where

$c_b$ = Ratio of flight thickness to screw diameter, -.

The normal stresses on the flight tips are assumed to be $\sigma_v$ on the top and $n\sigma_{wa}$ on the bottom surfaces. The flight tip surface area in a pocket can be estimated by $A_{tip} = \gamma \times P / \sin\alpha_o$.

Note that the starting torque for the initial condition can be calculated if $\sigma_v$ is replaced by $\sigma_{vi}$ above. In the present study, the vertical stress for the flow condition $\sigma_v$ was replaced by the arithmetic mean of $\sigma_{vi}$ and $\sigma_v$, i.e. $(\sigma_{vi} + \sigma_v)/2$, considering the hopper level effects on the vertical stress at the hopper outlet. The influence of hopper level is generally neglected when there is flow in previous research, although some researchers (Arnold et al., 1980) considered the weight of a certain height of bulk solids above the hopper outlet as a feeder load. The hopper level is expected to have an insignificant effect on the vertical stress when there is flow if the hopper level exceeds twice the trough diameter, but higher hopper levels and refilling generally increase the fullness of screw pockets, including those in the choke section, leading to larger required torque, if bridging inside the hopper can be avoided during feeding.

The torque required to rotate the material element in a pocket in the hopper section, with consideration of the flight tip resistance, is

$$T_i = K_i \sigma_v D_o^3 \tag{6-100}$$

where

$$K_i = k_{sa}\left[\frac{4K_s}{\pi(1-c_d^2)}\right] + k_{ca}\left[\frac{4K_s}{\pi(1-c_d^2)} + \frac{\pi c_d^2}{2c_p}\right] + k_{ta}\left[\frac{4K_s}{\pi(1-c_d^2)}\right] + k_{fa}\left[\frac{4K_s}{\pi(1-c_d^2)}\right] + \left[\frac{\pi\lambda_s\mu_f(1-c_d^3)}{12} - \frac{\lambda_s c_p(1-c_d^2)}{8}\right] + k_{tip} \tag{6-101}$$

The first term reflects the contribution of the shear surface to torque requirements, the second the core shaft surface, the third the trough surface, the fourth and fifth the trailing side surface, and the final term reflects the flight tip surface contribution.

6.3.3 Forces, torque and power analysis in choke section

6.3.3.1 Straight casing in choke section

The choke section (i.e. conveying section) is adjacent to the hopper (Figures 4-2 and 4-3). For effective flow control, the choke section should extend at least two standard pitch lengths (Yu and Arnold, 1997). For biomass feeding, especially to pressurized reactors, this section should be even longer for effective plug sealing. We assume that the screw is operating 100% full. The shear surface in the hopper section does not exist in the choke section. There may or may not be bulk material between the screw flight tips and the upper casing inside surface (i.e. upper clearance) due to different feeding conditions.

For a cylindrical casing in the choke section, the above procedures apply, except that the shear surface must be replaced by a cylindrical sliding surface, giving.

$$T_i = K_i \sigma_v D_o^2 \tag{6-102}$$

$$K_i = k_{ca}\left[\frac{4K_s}{\pi(1-c_d^2)} + \frac{\pi c_d^2}{2c_p}\right] + 2k_{ta}\left[\frac{4K_s}{\pi(1-c_d^2)}\right] + k_{fa}\left[\frac{4K_s}{\pi(1-c_d^2)}\right] + \left[\frac{\pi\lambda_s\mu_f(1-c_d^3)}{12} - \frac{\lambda_s c_p(1-c_d^2)}{8}\right] + k_{tip} \tag{6-103}$$

or

$$K_i = k_{ca}\left[\frac{4K_s}{\pi(1-c_d^2)} + \frac{\pi c_d^2}{2c_p}\right] + k_{ta}\left[\frac{4K_s}{\pi(1-c_d^2)}\right] + k_{fa}\left[\frac{4K_s}{\pi(1-c_d^2)}\right] + \left[\frac{\pi\lambda_s\mu_f(1-c_d^3)}{12} - \frac{\lambda_s c_p(1-c_d^2)}{8}\right] + k_{tip} \tag{6-104}$$

Equation 6-103 is based on the assumption that the screw pockets are close to 100% full, whereas Equation 6-104 assumes that there is no material in the upper part of the screw casing,

i.e. in the upper clearance. The shear surface term is eliminated and the trough surface term adjusted in Equations 6-103 and 6-104 compared to Equation 6-101. Equation 6-103 works well for screw-2 which has a relatively large clearance, with insignificant compression in the choke section compared to screw-1. When feeding is aided by air (or inert gases), the gas path generally lies in the upper clearance due to the effects of bulk solids gravity. Equation 6-104 can then be used to estimate the torque required for smooth screw feeding. When gases assist in feeding, the required torque is generally reduced since the fullness of screw pockets decreases due to the gas paths. Torque requirements for screw-2 are discussed below.

Equations 6-103 and 6-104 underestimate torque requirements for the choke section for screw-1. The screw diameter of the screw feeder in the hopper section is 100 mm, so that the clearance is 1 mm, although the clearance in the choke section is higher (6-11 mm, as indicated in Figure 4-3). The increased clearance in the screw feeding direction for screw-1 is intended to release the axial and normal wall stresses at the discharge end of the screw feeder. Bulk solids are squeezed into the choke section when feeding is initiated. The accumulated solids in the choke section then make the axial stress even larger than in the hopper section, as shown in Table 6-3, and clearance effects are insignificant in the choke section.

Although complicated compression and dilation make analysis of the choke section very difficult, we can reasonably assume the stress conditions in the choke section to be as follows:

- The stress distribution within a pocket (i.e. in the space between adjacent flights) is of the same form as for the hopper section, but the boundary condition is now

$$\sigma_x = CF \times n\sigma_v \text{ at } x = P \ (CF > 1) \tag{6-105}$$

Here $CF$ denotes the compression factor, which depends on the length of the choke section, screw configurations and material properties.

Table 6-3. Predicted flow feeder load and stresses for screw-1

| Name of specimen | Wall friction angle on carbon steel (deg) | Internal friction angle (deg) | Vertical stress [1] (Pa) | | Feeder load (N) | | Axial stress in hopper [2] (Pa) | | Axial stress in choke section [3] (Pa) | |
|---|---|---|---|---|---|---|---|---|---|---|
| | | | @ 0.3 m | @ 0.45 m | @ 0.3 m | @ 0.45 m | @ 0.3 m | @ 0.45 m | @ 0.3 m | @ 0.45 m |
| Wood pellets | 31.4 | 32.0 | 1680 | 2150 | 157 | 200 | 5820 | 7410 | 9760 | 13200 |
| Ground wood pellets-1 | 30.2 | 33.2 | 1170 | 1530 | 109 | 143 | 2560 | 3340 | 11900 | 18300 |
| Ground wood pellets-2 | 30.4 | 38.0 | 945 | 1260 | 88 | 117 | 2250 | 3000 | 12600 | 20200 |
| Sawdusts-1 | 31.8 | 38.0 | 476 | 631 | 44 | 59 | 1180 | 1570 | 5450 | 8220 |
| Hog fuel-1 | 31.5 | 39.0 | 446 | 594 | 42 | 55 | 1030 | 1370 | 5810 | 9320 |
| Ground hog fuel | 31.8 | 45.0 | 324 | 438 | 30 | 41 | 599 | 809 | 5110 | 8700 |
| Wood shavings-1 | 31.0 | 39.0 | 251 | 334 | 23 | 31 | 573 | 764 | 2610 | 3960 |
| Polyethylene particles | 21.5 | 26.2 | 1570 | 2010 | 146 | 188 | 3270 | 421 | 4500 | 6000 |

Notes: [1] vertical stress at hopper outlet.
[2] [3] average axial stresses for a material element in a pocket.

From analysis of measured torques for different choke section lengths in the present study, it seems there is no significant change in $CF$ as the choke section length varies from 3 to 8 time the pitch. In the present study, the compression factor is expressed by

$$CF = \exp(\frac{2\mu_w \lambda_s P}{R_t - R_c} \times E) \tag{6-106}$$

where $E$ can be calculated by

$$E = C(\frac{q_f H_0 L_c}{c_t D_t^2})^{\frac{1}{5}} \tag{6-107}$$

with

$C$ = Constant dependant on material properties, -.

$c_t$ = Ratio of casing diameter to screw flight diameter, $c_t = (D_o + 2c)/D_o = 2R_t / D_o$, -.

$D_t$ = Casing inside diameter, m.

$H_0 = H_t - h_0 - y_0$, initial hopper level, m.

$L_c$ = Choke section length, m.

$q_f$ = Dimensionless surcharge factor for flow condition.

$\alpha$ = Hopper half-angle, radians.

Here $q_f$ reflects the fullness of screw pockets when there is flow. The larger the surcharge factor, the larger the fullness in the choke section and the larger the compression factor. Larger $H_0 / D_t$ and $L_c / D_t$, and smaller $c_t$ lead to a larger compression factor. Incompressible and compressible materials are expected to have different compression factors. $C$ is closely related to torque predictions. The following two conditions are met for each material when $C$ is determined:

- Minimum value $((T_{pre} - T_{\exp})_{0.3m} + (T_{pre} - T_{\exp})_{0.45m})$

- $T_{pre} \geq T_{\exp}$

where $T_{pre}$ is the predicted average torque and $T_{\exp}$ is the measured average torque for each material. $(T_{pre} - T_{\exp})_{0.3m}$ is the torque difference for a 0.30 m hopper level, and $(T_{pre} - T_{\exp})_{0.45m}$ represents the torque difference for a hopper level of 0.45 m. These two conditions indicate that $T_{pre}$ is equal to $T_{\exp}$ or slightly larger than $T_{\exp}$ ,and the difference between $T_{pre}$ and $T_{\exp}$ is minimized. $C$ and $CF$ are listed in Table 6-4. The minimum axial stress within a pocket in the choke section is expected to occur on the trailing side of the screw flight (i.e. at $x = P$ ) and can be expressed (see Equations 6-54, 6-105 and 6-106) by

$$\sigma_{\min x} = n\sigma_v \exp\left[\frac{2\mu_w \lambda_s PE}{R_t - R_c}\right] \tag{6-108}$$

Hence the average axial stress within a pocket in the choke section is obtained from

$$\sigma_{cxa} = \frac{1}{P}\int_0^P \sigma_{\min x} \exp\left[\frac{2\mu_w \lambda_s (P-x)}{R_t - R_c}\right] dx \tag{6-109}$$

Substituting and integrating yields the average axial stress that can be used to estimate the average compacted bulk density in the choke section based on Equation 6-86. The predicted average axial stress and compacted bulk density are listed in Tables 6-3 and 6-4. Due to compression in the choke section, compressible materials generally have larger volumetric efficiencies than incompressible materials.

The average normal stress within a pocket in the choke section can be expressed by

$$\sigma_{cwa} = \frac{\lambda_s}{P}\int_0^P \sigma_{\min x} \exp\left[\frac{2\mu_w \lambda_s (P-x)}{R_t - R_c}\right] dx \tag{6-110}$$

The torque generated within a pocket in the choke section can be estimated based on the above procedures. The total torque required to drive the screw feeder is then

Table 6-4. Parameters for stress and compression analysis for screw-1

| Name of specimen | Compression factor in choke section [1] | | Compacted bulk density in choke section [2] ($kg/m^3$) | | Density ratio [3] | | n [4] | | $\lambda_s$ [5] | C[6] |
|---|---|---|---|---|---|---|---|---|---|---|
| | @ 0.3 m | @ 0.45 m | @ 0.3 m | @ 0.45 m | @ 0.3 m | @ 0.3 m | @ 0.45 m | @ 0.45 m | | |
| Wood pellets | 1.65 | 1.72 | 630 | 630 | 1.00 | 1.38 | 1.38 | 1.00 | 0.48 | 0.15 |
| Ground wood pellets-1 | 4.43 | 5.03 | 485 | 485 | 1.00 | 1.09 | 1.09 | 1.00 | 0.39 | 0.60 |
| Ground wood pellets-2 | 5.67 | 6.57 | 452 | 461 | 1.07 | 1.45 | 1.45 | 1.09 | 0.28 | 1.00 |
| Sawdusts-1 | 4.59 | 5.22 | 236 | 243 | 1.12 | 1.45 | 1.45 | 1.16 | 0.29 | 0.80 |
| Hog fuel-1 | 5.69 | 6.59 | 225 | 229 | 1.13 | 1.41 | 1.41 | 1.15 | 0.27 | 1.00 |
| Ground hog fuel | 8.62 | 10.34 | 190 | 197 | 1.27 | 1.30 | 1.31 | 1.32 | 0.19 | 1.80 |
| Wood shavings-1 | 4.55 | 5.18 | 131 | 136 | 1.20 | 1.41 | 1.41 | 1.24 | 0.27 | 0.9 |
| Polyethylene particles | 1.37 | 1.40 | 610 | 610 | 1.00 | 1.20 | 1.20 | 1.00 | 0.47 | 0.15 |

Notes: [1] Compression factors are expressed by Equation (6-106).
[2] Compacted bulk density in choke section is calculated according to relation between bulk density and stress acting on the bulk solids surface.
[3] Density ratio is defined as the ratio of compacted bulk density in the choke section to the loose bulk density. This is used to describe compression in the choke section.
[4] Defined by Equation (6-84).
[5] Ratio of normal wall stress to axial stress for bulk solids sliding on surface, a function of wall friction angle and internal friction angle.
[6] Constant used for analysis of compression in choke section: see Equation (6-107).

$$T_{total} = \sum_{m} T_i \tag{6-111}$$

where m is the total number of pockets (each pocket being the space between adjacent flights) along the screw feeder, including the hopper section and the choke section. For special casing configurations (tapered and extended sections), further details are provided below.

The shaft power, $PW$, (not including bearing and drive losses) required to rotate the screw is

$$PW = T_{total} \times \omega = \frac{T_{total} \times 2\pi \times f}{60} \tag{6-112}$$

where $f$ is the rotational speed of the screw in rpm.

For torque and power readings, see Appendix G. For the computer program to predict the torque and power, see Appendix H.

6.3.3.2 Taper casing in choke section

Tapered sections of length 0.15 and 0.30 m at the discharge end of the screw feeder were tested in the present study. The outlet diameter of both tapered sections was 88 mm, so that there were different taper angles for the two tapered sections, as shown in Figure 6-15. Taking axial resistance forces caused by the tapered casings into account increases the torque requirements. Volume-reducing flow channels (i.e. converging tapered sections) block more readily for incompressible materials (such as polyethylene and wood pellets) unless the feeder is powerful enough to break the particles. For compressible bulk materials (e.g. sawdust and ground hog fuel), blockage is difficult to estimate. It depends on the material properties and flow conditions inside the screw casings. The geometry affecting the stress of a material element within a pocket in the tapered section is shown in Figure 6-16. Assuming steady state for a moving material element and equilibrium between the diving force and resisting force, the balance of forces acting on an element of length dx results in

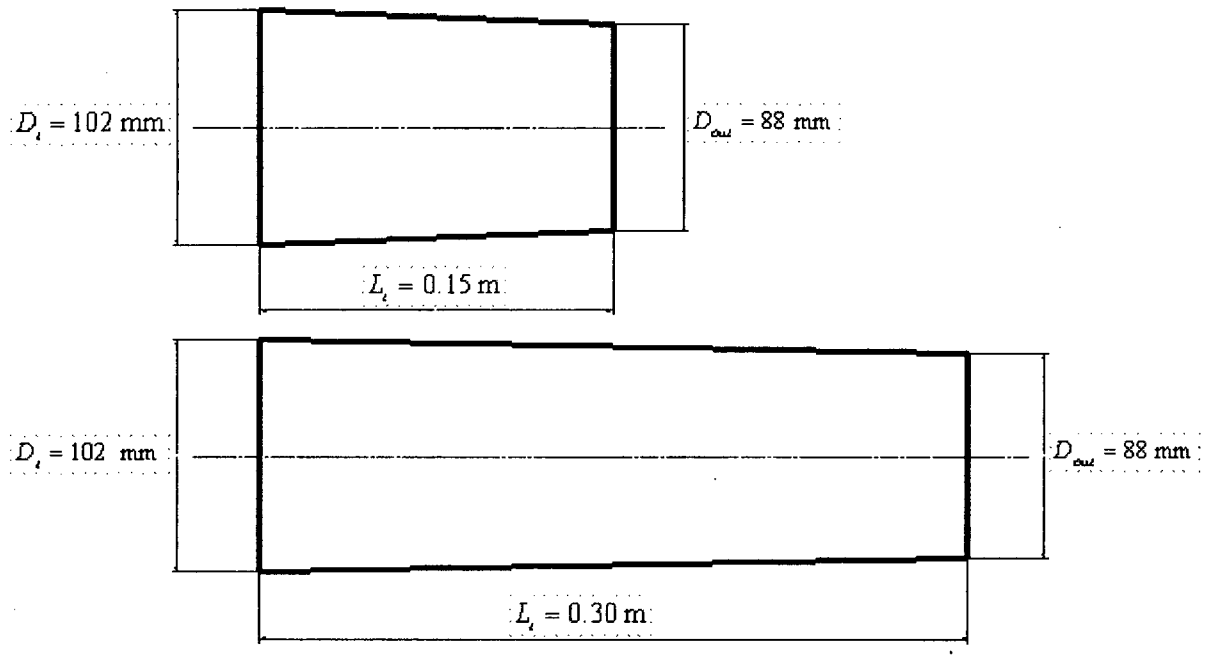


Figure 6-15. Schematics of the two tapered sections tested in this work.

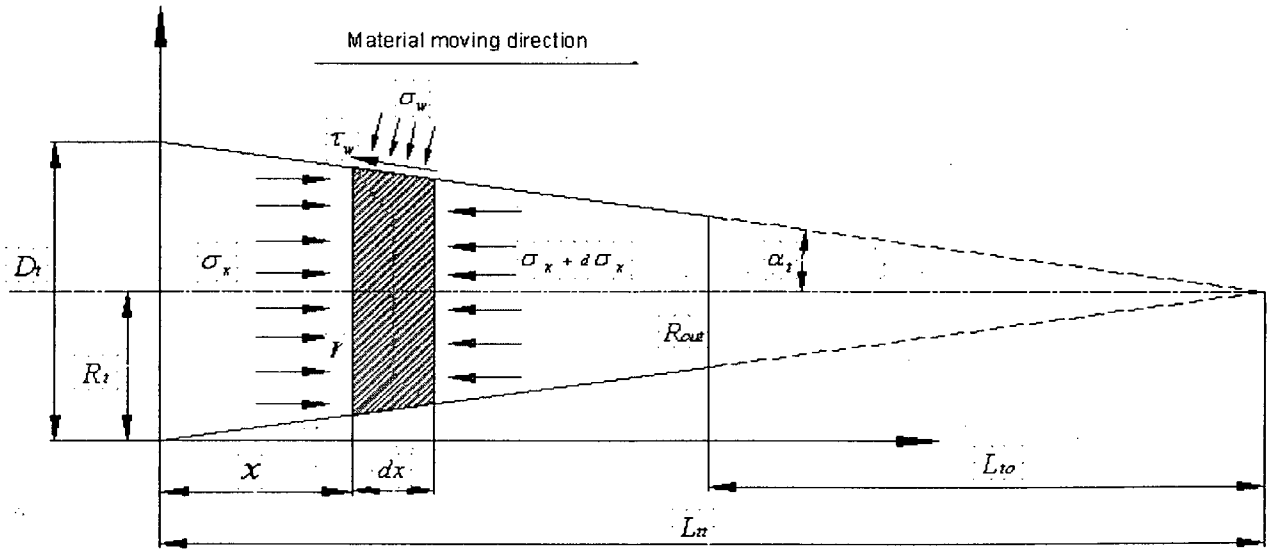


Figure 6-16. Stresses on material element in tapered section.

$$\sigma_x \pi r^2 = (\sigma_x + d\sigma_x)\pi(r - dx\tan\alpha_t)^2 + \tau_w\left[\frac{\pi r^2}{\tan\alpha} - \frac{\pi(r - dx\tan\alpha)^2}{\tan\alpha}\right] + \sigma_w\left[\pi r^2 - \pi(r - dx\tan\alpha)^2\right] \tag{6-113}$$

Elimination of second order terms yields

$$d\sigma_x - \frac{2\sigma_x \tan\alpha}{r}dx + \frac{2\tau_w}{r}dx + \frac{2\sigma_w \tan\alpha}{r}dx = 0 \tag{6-114}$$

Substituting $r = (D_t - 2x\tan\alpha_t)/2$ into Equation 6-114, we obtain

$$d\sigma_x + \frac{2\sigma_x}{r}dr - \frac{2\tau_w}{r\tan\alpha}dr - \frac{2\sigma_w}{r}dr = 0 \tag{6-115}$$

After substituting $\sigma_w / \sigma_x = \lambda_s$, $\tau_w = \mu_w \sigma_w$ and rearrangement, Equation 6-115 becomes

$$\frac{d\sigma_x}{\sigma_x} = -(2 - \frac{2\lambda_s \mu_w}{\tan\alpha} - 2\lambda_s)\frac{dr}{r} \tag{6-116}$$

Boundary conditions for the 0.30 m long tapered section ( $P$ = 0.1 m) are:

- first pocket: $\sigma_x = \sigma_{in}$ at $r = R_t$
- second pocket: $\sigma_x = \sigma_{in1}$ at $r = R_{t1}$
- third pocket: $\sigma_x = \sigma_{in2}$ at $r = R_{t2}$

Boundary condition for the 0.15 m long tapered section:

- first pocket: $\sigma_x = \sigma_{in}$ at $r = R_t$
- second half pocket: $\sigma_x = \sigma_{in1}$ at $r = R_{t1}$

Here $R_t$ is the inside radius of the casing at $x = 0$, $R_{t1}$ the inside radius of the casing at $x = P$, and $R_{t2}$ the inside radius of the casing at $x = 2P$ (only for 0.30 m long tapered section), as shown in Figure 6-16. $\sigma_{in}$, $\sigma_{in1}$, $\sigma_{in2}$ are axial stresses at the starting point of successive gaps in the tapered section. $R_t$ is used in the following sample calculations.

Integrating Equation 6-116 and substituting $r = (D_t - 2x\tan\alpha_t)/2$ yields

$$\sigma_x = \sigma_{in}(1 - \frac{x\tan\alpha_t}{R_t})^{-(2-\frac{2\lambda_s\mu_w}{\tan\alpha}-2\lambda_s)} \tag{6-117}$$

The average axial stress within a pocket is

$$\sigma_{xa} = \frac{1}{P}\int_0^P \sigma_{in}(1 - \frac{x\tan\alpha_t}{R_t})^{-(2-\frac{2\lambda_s\mu_w}{\tan\alpha}-2\lambda_s)} dx \tag{6-118}$$

Hence the average normal wall stress in a pocket is

$$\sigma_{wa} = \frac{\lambda_s}{P}\int_0^P \sigma_{in}(1 - \frac{x\tan\alpha_t}{R_t})^{-(2-\frac{2\lambda_s\mu_w}{\tan\alpha}-2\lambda_s)} dx \tag{6-119}$$

For both the 0.15 and 0.30 m long tapered sections, the compression can be estimated by stress analysis in the choke section and along the screw axis as the volume changes in the tapered sections. The ratios of compacted bulk densities in the choke section to loose bulk densities are listed in Table 6-4. For each pocket in a tapered section, the screw pocket volume can be calculated, and then used to estimate the compacted bulk density. Average axial stresses within each pocket in the taper section for various materials can be estimated by an axial stress-bulk density relation, i.e. Equation 6-86. The stress $\sigma_{in}$ can be obtained from Equation 6-118 by iteration until the calculated average axial stress $\sigma_{xa}$ matches the calculated compacted bulk density. It should be noted that $\sigma_{in}$ is not equal to the stress on the driving side calculated from the above equations, although they are similar. The stress on the driving side is employed for torque calculations. The torque requirement generated within each pocket in the tapered section can be estimated from the above procedures. The 0.15 m tapered section covers one-and-a-half pockets, whereas the 0.30 m tapered section includes three pockets. Total torque requirements for the tapered sections are obtained by summing the torque required for each pocket.

(1) 0.30 m long tapered section

The axial resistance acting on an element of bulk solid on the core surface can be expressed by Equation 6-49, i.e.

$$F_{ca} = -2\pi R_c \sigma_{wa} \mu_{wc} \sin(\alpha_c) \int_0^P dx = -\pi c_d c_p \sigma_{wa} \mu_{wc} \sin(\alpha_c) \sigma_{wa} D_o^2 \qquad (6\text{-}120)$$

The axial resistance force acting on the material element in a pocket on the trough surface is expressed by

$$F_{ta} = -(2\pi RP \mu_{wt} \sigma_{wa} + 2\pi RP \sigma_{wa} \tan\alpha_t) \qquad (6\text{-}121)$$

where $R$ is the inside radius of the taper section on the driving side of the flight, i.e. at the beginning of each pocket (at $x = 0$, $P$ and $2P$ for the 0.30 m long tapered section). $\sigma_{wa}$ is the average normal wall stress in each pocket in the taper section (see Equation 6-119).

The axial force acting on the material within a pocket on the trailing side is

$$F_{fa} = -2\pi\lambda_s \sigma_{xf} \int_{R_c}^{R_o} \frac{\cos(\phi_f - \alpha_r)}{\cos\alpha_r \cos\phi_f} r dr = -2\pi\lambda_s \sigma_{xf} \int_{R_c}^{R_o} (1 + \tan\alpha_r \tan\phi_f) r dr \qquad (6\text{-}122)$$

After substituting $\tan\alpha_r = P/2\pi R_r$ and $\tan\phi_f = \mu_f$, Equation 6-122 can be solved numerically or analytically.

The total axial force on the material element within a pocket caused by the driving side of a flight should equal the total resisting axial forces acting on the same material element due to the core shaft surface, trailing side of a flight and trough surface. It is again assumed that the total force is uniform on the surface of the driving side, so that

$$F_{da} + F_{ca} + F_{fa} + F_{ta} = 0 \qquad (6\text{-}123)$$

$$\sigma_{da} = \frac{F_{da}}{\pi(R_o^2 - R_c^2)} \qquad (6\text{-}124)$$

The torque generated in one pocket is

$$T_i = T_d + T_c + T_f + T_{tip} \qquad (6\text{-}125)$$

where

$T_d$ = Torque due to driving flight, N.m.

$T_c$ = Torque due to core shaft surface, N.m.

$T_f$ = Torque due to trailing flight, N.m.

$T_{tip}$ = Torque due to flight tip, N.m.

The torque generated by the driving side of the screw flight is

$$T_d = 2\pi\sigma_{da}\int_{R_c}^{R_o} r^2 \tan(\alpha_r + \phi_f)dr \tag{6-126}$$

After substituting $\tan\alpha_r = P/2\pi r$ and $\tan\phi_f = \mu_f$, Equation 6-126 can be integrated numerically.

The torque generated by the core shaft surface is

$$T_c = 2\pi R_c^2 P\mu_{wc}\sigma_{wa}\cos\alpha_c \tag{6-127}$$

The torque generated by the trailing side of the screw flight is

$$T_f = \lambda_s\sigma_{xf}\int_{R_c}^{R_o}\frac{\sin(\phi_f - \alpha_r)r^2 dr}{\cos\alpha_r\cos\phi_f}\int_0^{2\pi} d\theta = 2\pi\lambda_s\sigma_{xf}\int_{R_c}^{R_o}(\tan\phi_f - \tan\alpha_r)r^2 dr \tag{6-128}$$

Equation 6-128 can again be solved numerically.

The torque generated by the flight tip is

$$T_{tip} = \frac{\gamma\sigma_{wa}P\mu_f R_o}{\sin\alpha_o} \tag{6-129}$$

The normal stress on the flight tip surface is assumed to be $\sigma_{wa}$. The flight tip surface area within a pocket can be estimated by $A_{tip} = \gamma \times P/\sin\alpha_o$.

(2) 0.15 m long taper section

The 0.15 m long taper section includes one and a half pocket ( $P = 0.1$ m). The average axial stress in the second half-pocket is

$$\sigma_{xa} = \frac{2}{P}\int_0^{P/2} \sigma_{in}\left(1 - \frac{x\tan\alpha_t}{R_{t1}}\right)^{-\left(2-\frac{2\lambda_s\mu_w}{\tan\alpha}-2\lambda_s\right)} dx \tag{6-130}$$

Hence the average normal wall stress in a pocket is

$$\sigma_{wa} = \frac{2\lambda_s}{P}\int_0^{P/2} \sigma_{in}\left(1 - \frac{x\tan\alpha_t}{R_{t1}}\right)^{-\left(2-\frac{2\lambda_s\mu_w}{\tan\alpha}-2\lambda_s\right)} dx \tag{6-131}$$

The trailing side of the flight is absent in the second half-pocket for the 0.15 m tapered section. The force and torque calculations in this case are based on $P/2$ instead of $P$.

6.3.3.3 Extended section in choke section

In order to propel bulk materials forward in the extended section, the axial force exerted by the driving side of the screw flight must equal or exceed the resisting force, i.e.

$$\pi D_t L_e \sigma_{ewa} \mu_w \le \frac{\pi D_t^2}{4}\sigma_{exa} \tag{6-132}$$

where $\sigma_{exa}$ is the average axial stress, and $\sigma_{ewa}$ is the average normal wall stress in the extended section.

Substituting $\sigma_{ewa} = \lambda_s \sigma_{exa}$ yields

$$L_e \le L_{ct1} = \frac{D_t}{4\lambda_s\mu_w} \tag{6-133}$$

There is another critical length defined by

$$L_{ct2} = D_t \tan\delta \tag{6-134}$$

$L_{ct1}$ and $L_{ct2}$ are critical lengths for extended sections, and $\delta$ is the effective internal friction angle. Note that $D_t$ (casing diameter) is employed instead of $D_o$ (screw diameter) in these equations. When the length of the extended section exceeds the critical length, bulk materials

cannot be easily pushed out of the extended section since the force exerted by the screw flight is not transmitted forward effectively, but instead transmitted to the wall, tending to cause blockage for incompressible materials and significant compaction for compressible materials. The compression and blockage tendency for compressible materials in the extended section depends on the fullness of screw pockets and material properties. When

$$L_e > L_{ct1} = \frac{D_t}{4\lambda_s \mu_w} \tag{6-135}$$

or

$$L_e > L_{ct2} = D_t \tan\delta \tag{6-136}$$

particular attention should be paid to ensure effective compression and prevent unwanted blockage inside the extended section. The average axial stress in the extended section can be calculated based on the measured compacted bulk density in the extended section. Then the average normal stress in the extended section can be estimated by $\sigma_{ewa} = \lambda_s \sigma_{exa}$.

From a force balance at steady state (i.e. static state, as during blockage, or moving at a constant speed), the following expression can also be obtained

$$\pi D_t L_e \sigma_{ewa} \mu_w = \frac{\pi D_o^2}{4} \sigma_{da} \tag{6-137}$$

Rearrangement of Equation 6-137 gives the stress on the driving side of the screw flight

$$\sigma_{da} = \frac{4\pi D_t L_e \sigma_{ewa} \mu_w}{\pi D_o^2} \tag{6-138}$$

In Equation 6-138, $D_o$ is employed instead of $D_t$.

### 6.3.4 Comparison of model predictions with experimental measurements

#### 6.3.4.1 Straight casing in choke section for screw-1

The feeder load and vertical stress of initial and flow conditions at the hopper outlet for various materials for screw-1 are shown in Tables 6-1 and 6-2. Table 6-2 indicates that the initial feeder loads account for < 50% of the total initial weight of bulk materials in the hopper for a 0.30 m hopper level, whereas this ratio is reduced to < 40% for a 0.45 m hopper level. The initial feeder load can be calculated as the product of the initial vertical stress and the cross-sectional area (width of hopper outlet times length of hopper section) of the hopper outlet. The initial vertical stress can be estimated based on the hydrostatic pressure as noted above. This indicates that the initial vertical stress and initial feeder load are linearly proportional to the hopper level instead of the initial weight of bulk materials in the hopper. This is mainly attributable to partial support by the hopper wall. The feeder load when there is flow is slightly less than at the initial condition, mainly because a passive stress field is established when flow commences in the hopper, reducing the vertical stress at its outlet, as well as the feeder load. Although some researchers (e.g. Arnold et al., 1980) have approximated the feeder load during flow by taking the weight of a block of bulk material of a certain height (e.g. twice the outlet width) above the hopper outlet, calculations of the vertical stress and feeder load when there is flow (see Equation 6-33) generally do not consider the effects of hopper level. Here we use the initial vertical stress to calculate the initial feeder load, then an arithmetic mean of vertical stresses for the initial and flow conditions as vertical stresses for flow conditions listed in Table 6-3 in order to take the hopper level into consideration both initially and after the flow begins.

Axial stresses in hopper and choke sections for screw-1 for flow conditions appear in Table 6-3. These can be used to estimate compacted bulk densities in the choke section, and ratios of compacted bulk densities to loose bulk densities in the choke section for various materials, as

shown in Table 6-4. Ratios of calculated compacted bulk densities in the choke section to loose bulk densities approximately match the measured values during feeding experiments for the various materials tested. Parameters for stress and compression analysis ($C$ and $CF$) for screw-1 also appear in Table 6-4. Torque predictions and experimental measurements are compared in Table 6-1 and in Figures 6-17 to 6-24. Figure 6-25 plots predicted ratios of torque generated in the choke section to the overall torque. Figures 6-17 to 6-24 show that predicted torques, including average torques and starting torques, match the experimental results very well. Note that the average predicted and measured torques are the average values for the 0.30 and 0.45 m hopper levels in Figures 6-20 and 6-24.

Figure 6-25 shows that the torque requirements of the choke section account for more than 50% of the total torque for all biomass materials tested, especially for compressible biomasses, where it is more than 70%. This occurs even though the length of the choke section is less than that of the hopper section. We see that the choke section played a dominant role in determining the torque requirements for biomass fuels in the present study.

Table 6-5, Figures 6-26 and 6-27 compare experimental values with predicted efficiencies with and without allowance for compression in the choke section. Predicted efficiencies with allowance for compression in the choke section are obtained from products of predicted efficiencies without considering compression and corresponding density ratios (i.e. ratios of compacted to loose bulk density in the choke section). Figure 6-26 indicates that efficiencies are mostly in the 0.7-0.95 range in the present study, with the value depending on material properties and feeder configuration. Average measured efficiencies for the two hopper levels (0.30 and 0.45 m) are compared with predicted efficiencies in Figure 6-27.

The flow rate in each run is estimated by calculating the average flow rate in the first 2 minutes after stable feeding is established (see Appendix G). Feed rates, as well as torque

readings, are averaged from 2-5 repeat experiments for the same experimental conditions. Three initial hopper levels were tested: high (0.60 m), medium (0.45 m) and low (0.30 m). The effect of hopper level in this range on flow rate was found to be insignificant in the present study. Power predictions and experimental measurements for screw-1 are compared in Figures 6-28 to 6-29. The product of predicted average torques and corresponding angular velocities is taken as the predicted power, while the measured power is taken as the time-average torque times the corresponding angular velocity. We see from these figures that the predicted average powermatches experimental values much better than the predicted starting power. This indicates that starting power, like starting torque, is difficult to predict, due to uncertain packing conditions in the hopper and different material properties (e.g. size, shape and bulk density). For biomass feeding, the starting torque is less critical than the operating torque due to the large torque consumption in the choke section.

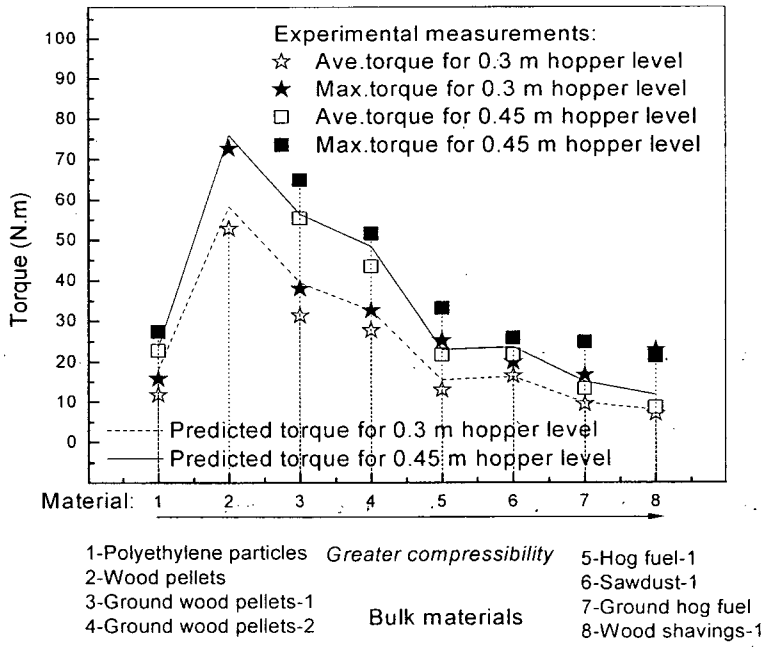


Figure 6-17. Comparison of predicted and measured torques for screw-1.

Table 6-5. Comparison of predicted and experimental efficiencies for screw-1

| Name of specimen | Wall friction angle on carbon steel (deg) | Internal friction angle (deg) | Density ratio [1] | | Average density ratio | Measured efficiency | | Average measured efficiency [2] | Incompressible predicted efficiency [3] | Predicted efficiency with compression [4] |
|---|---|---|---|---|---|---|---|---|---|---|
| | | | 0.3 | 0.45 | | 0.3 m | 0.45 m | | | |
| Wood pellets | 31.4 | 32.0 | 1.00 | 1.00 | 1.00 | 0.69 | | 0.69 | 0.74 | 0.74 |
| Ground wood pellets-1 | 30.2 | 33.2 | 1.00 | 1.00 | 1.00 | 0.80 | 0.74 | 0.77 | 0.74 | 0.74 |
| Ground wood pellets-2 | 30.4 | 38.0 | 1.07 | 1.09 | 1.08 | 0.81 | 0.78 | 0.80 | 0.74 | 0.80 |
| Sawdusts-1 | 31.8 | 38.0 | 1.12 | 1.16 | 1.14 | 0.81 | 0.83 | 0.82 | 0.73 | 0.84 |
| Hog fuel-1 | 31.5 | 39.0 | 1.13 | 1.15 | 1.14 | 0.87 | 0.86 | 0.87 | 0.74 | 0.84 |
| Ground hog fuel | 31.8 | 45.0 | 1.26 | 1.32 | 1.29 | 0.93 | 1.04 | 0.98 | 0.73 | 0.95 |
| Wood shavings-1 | 31.0 | 39.0 | 1.21 | 1.27 | 1.24 | 0.89 | 0.93 | 0.91 | 0.74 | 0.91 |
| Polyethylene particles | 21.5 | 26.2 | 1.00 | 1.00 | 1.00 | 0.84 | 0.86 | 0.85 | 0.79 | 0.79 |

Notes: [1] Density ratio is defined as the ratio of compacted bulk density in the choke section to loose bulk density. This is used to describe compression in the choke section.

[2] Average measured efficiency is obtained from arithmetic mean of measured efficiencies for 0.30 and 0.45 m hopper levels.

[3] Predicted efficiency without consideration of compression in the choke section.

[4] Predicted efficiency with consideration of compression in the choke section, i.e. density ratio times efficiency in [3].

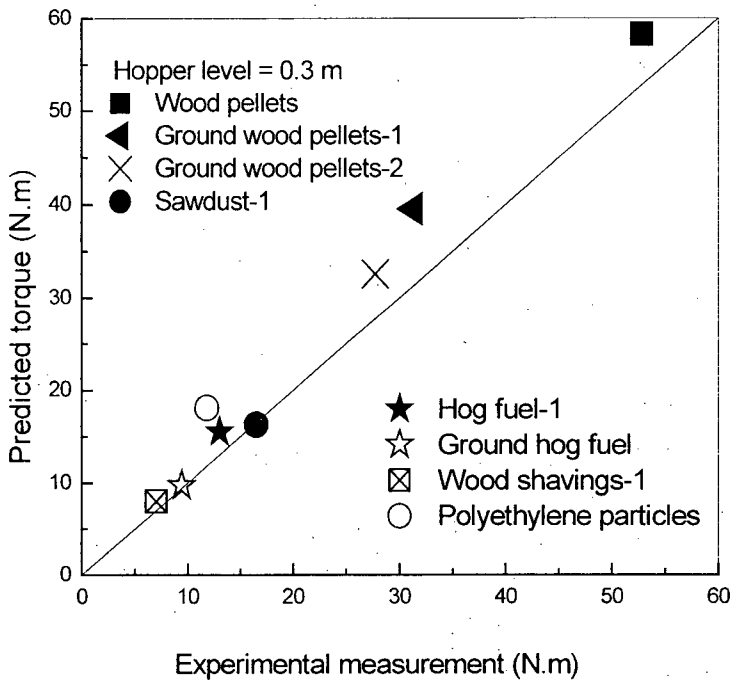


Figure 6-18. Comparison of predicted and measured average torques for 0.30 m hopper level and screw-1.

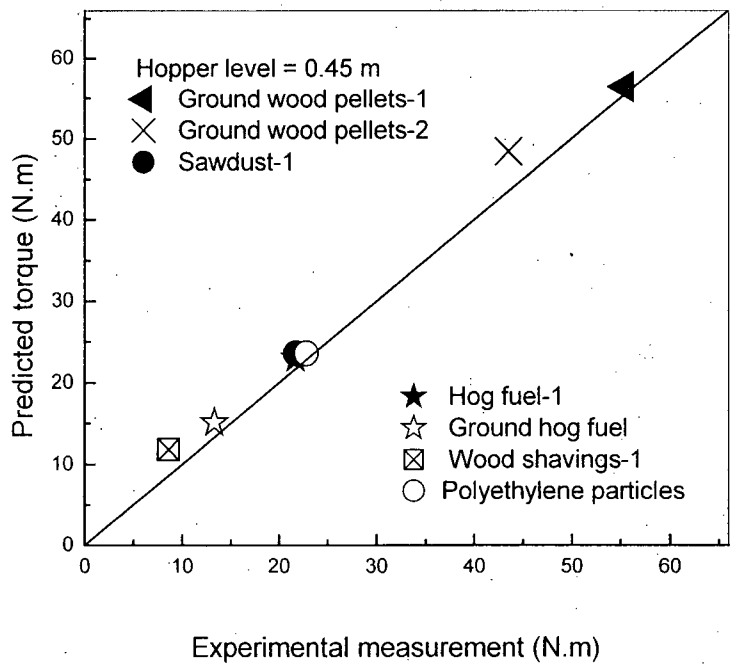


Figure 6-19. Comparison of predicted and measured average torques for 0.45 m hopper level and screw-1.

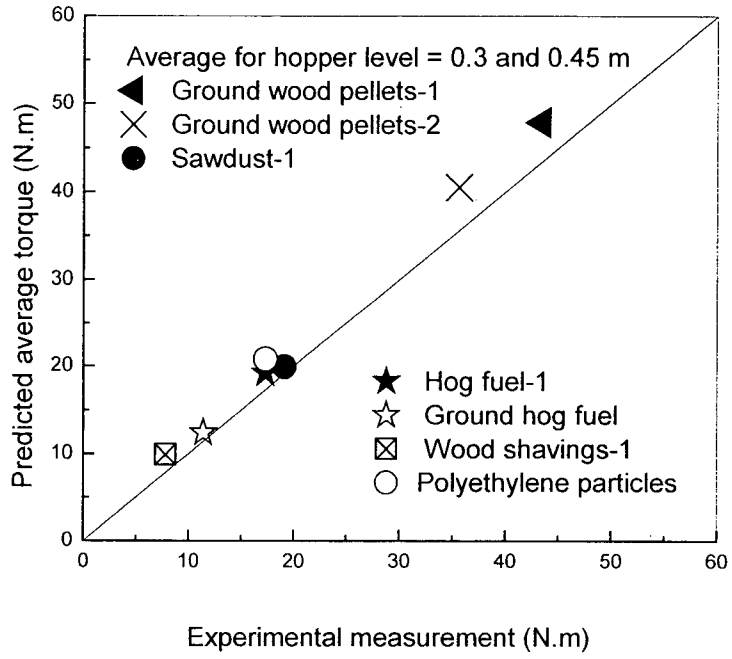


Figure 6-20. Comparison of average predicted and measured torques for 0.30 and 0.45 m hopper levels for screw-1.

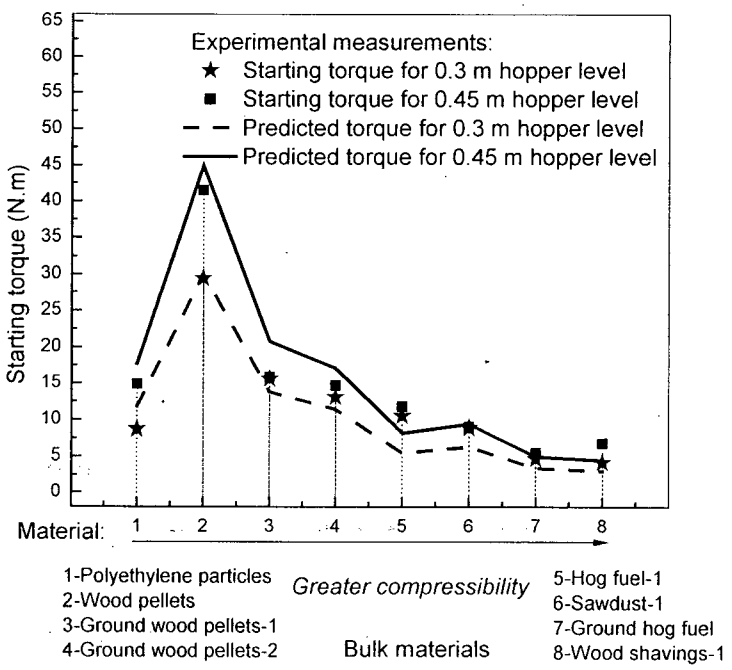


Figure 6-21. Comparison of predicted and measured starting torques for screw-1.

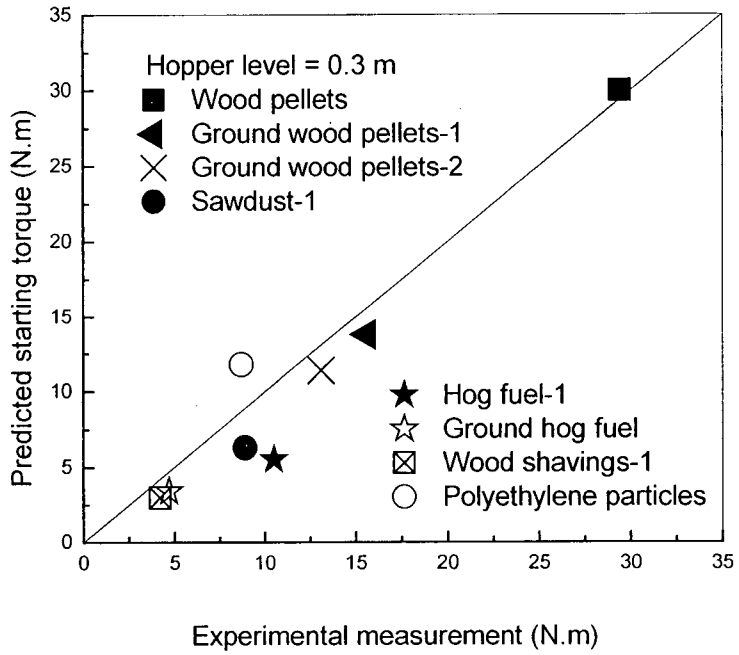


Figure 6-22. Comparison of predicted and measured starting torques for 0.30 m hopper level and screw-1.

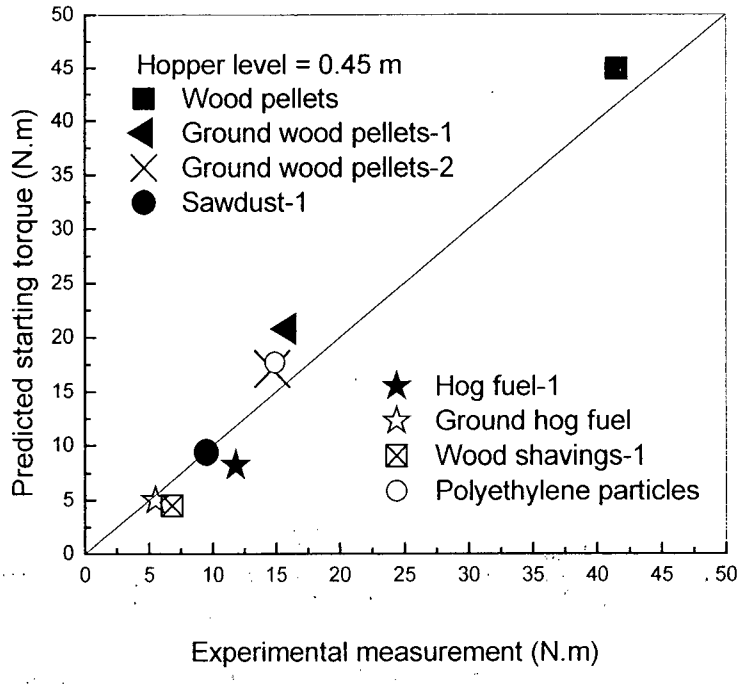


Figure 6-23. Comparison of predicted and measured starting torques for 0.45 m hopper level and screw-1.

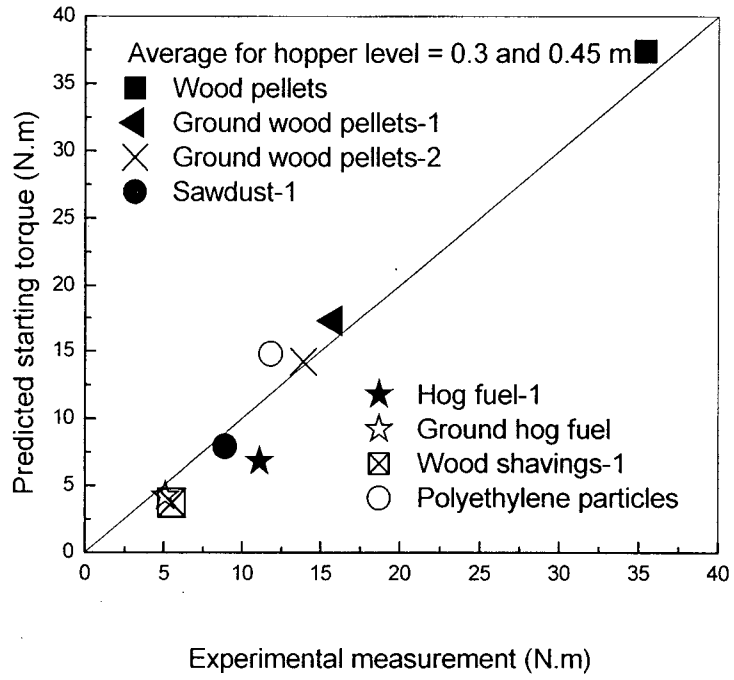


Figure 6-24. Comparison of average predicted and measured starting torques for 0.30 and 0.45 m hopper level and screw-1.

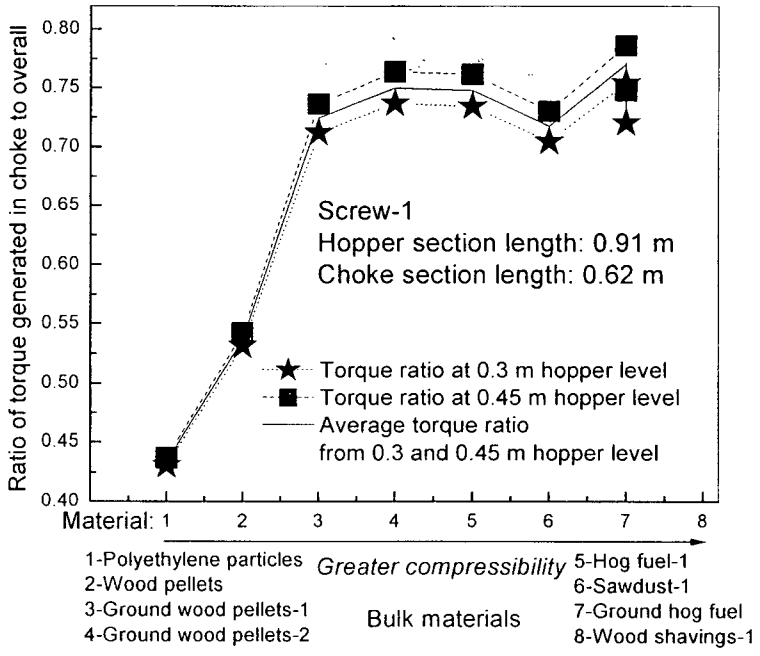


Figure 6-25. Predicted ratio of torque generated in choke section to overall torque for 0.30 and 0.45 m hopper level and screw-1.

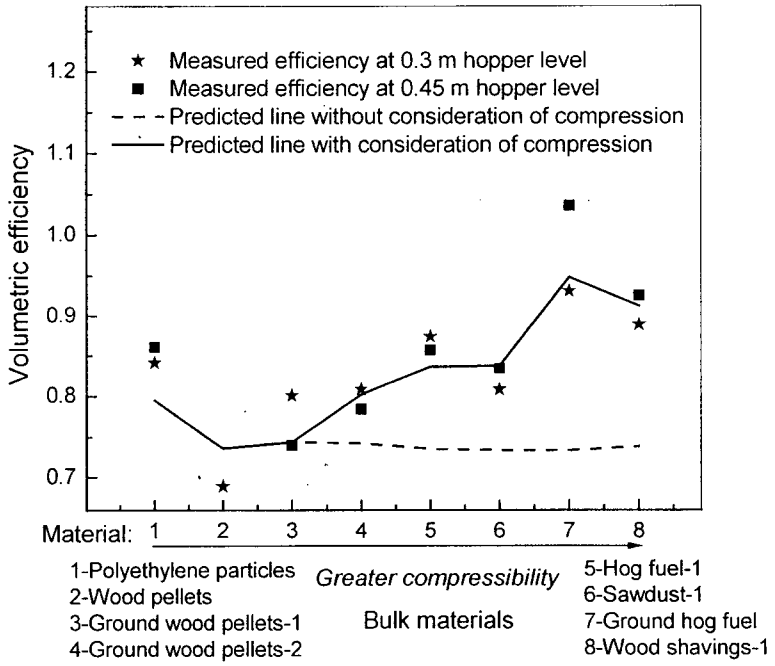


Figure 6-26. Comparison of predicted (with consideration of compression) and measured volumetric efficiencies for 0.30 and 0.45 m hopper level and screw-1.

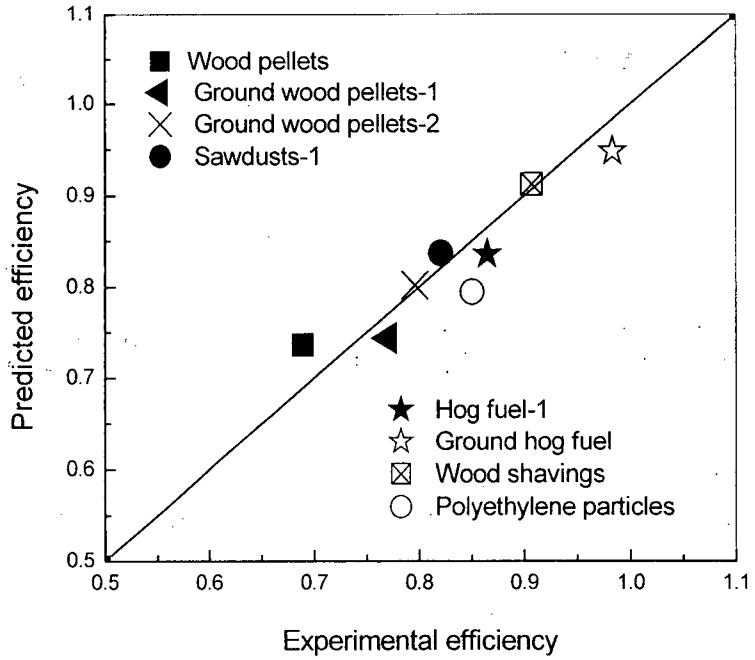


Figure 6-27. Comparison of predicted and averaged measured efficiencies for 0.30 and 0.45 m hopper level and screw-1.

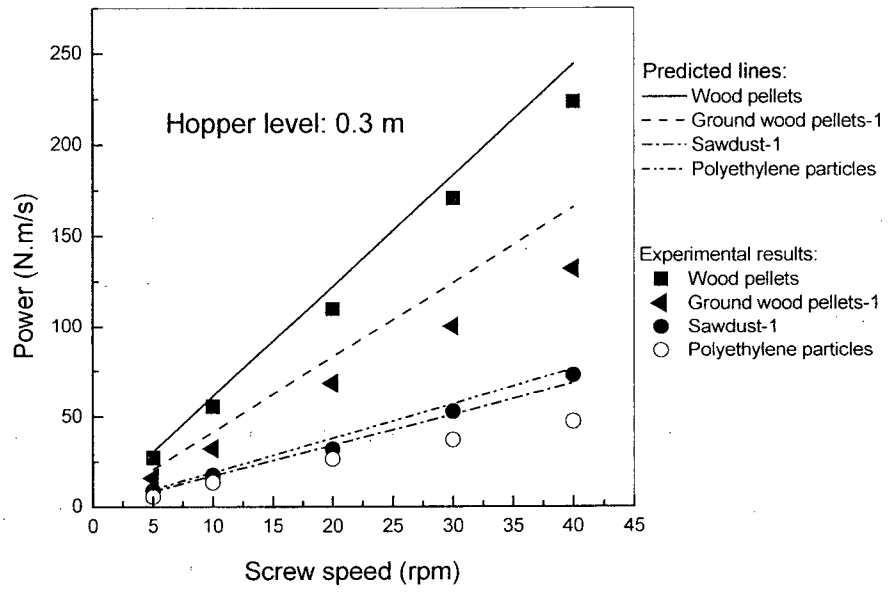


Figure 6-28. Comparison of predicted average power and measured average power for different screw speeds for 0.30 m initial hopper level and screw-1.

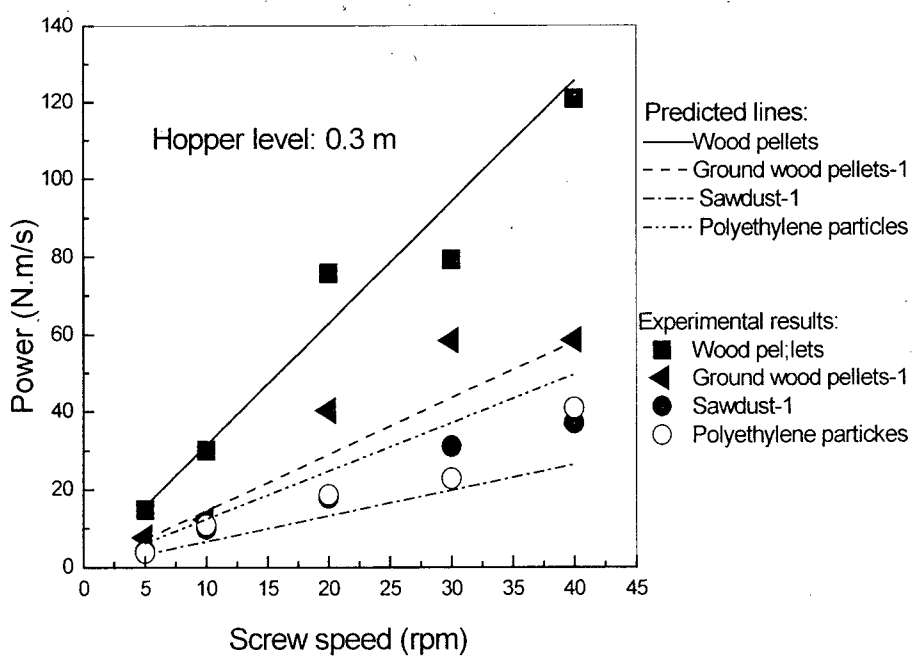


Figure 6-29. Comparison of predicted starting power and measured starting power for different screw speeds for 0.30 m hopper level and screw-1.

6.3.4.2 Taper casing in choke section for screw-1

Torque predictions and experimental measurements are compared in Figures 6-30 and 6-31. For sawdust and ground hog fuel, the predictions agree well with the experimental results, but the experimental results are much higher than the predictions for wood shavings. Blockage occurred for both the 0.15 and 0.30 m long taper sections for the wood shavings. The large deviations are probably due to the wide size distribution and wide range of particle strength for wood shavings. The torque predictions for hog fuel in the 0.15 and 0.30 m long tapered sections with a hopper level of 0.45 m are 276 and 419 N.m respectively, suggesting blockage (motor capacity < 100 N.m), although this could not be confirmed in the present experiments. For the 0.30 m long tapered section, blockage always occurred, whereas blockage sometimes, but not always, occurred for the 0.15 m long tapered section. The difference is attributed to the complicated flow patterns in the hopper and in the choke sections, leading to varying levels of fullness in the choke section. Higher fullness tended to cause blockage for both the 0.15 and 0.30 m long tapered section. Although the taper angle for the 0.15 m tapered section was larger than for the 0.30 m tapered section, the longer length made blockage more likely.

Screw rotational speeds affected the tendency to block in the tapered section. Higher screw speeds (e.g. 30 and 40 rpm) tended to transport more bulk materials into the tapered section per unit time, increasing the likelihood of blockage compared to lower screw speeds. The torque predictions neglect any effect of screw speed.

From observations on blockage of hog fuel during experiments, torque > 100 N.m is expected to disrupt blockage inside the tapered section and make feeding smoother. It should be noted that predictions for hog fuel and wood shavings are particularly uncertain for the tapered section cases due to the wide particle size distributions, wide ranges of particle strength and complex flow patterns in the hopper and choke sections.

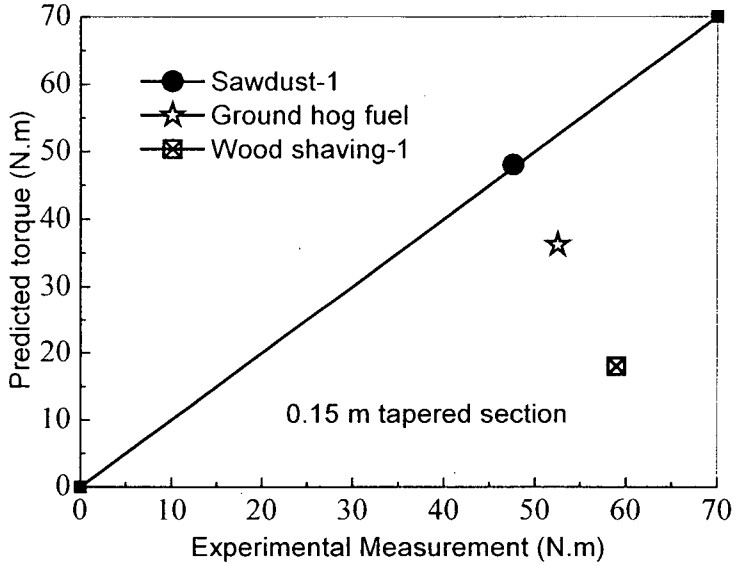


Figure 6-30. Comparison of torque predictions and experimental measurements with 0.15 m tapered sections and a 0.45 m hopper level.

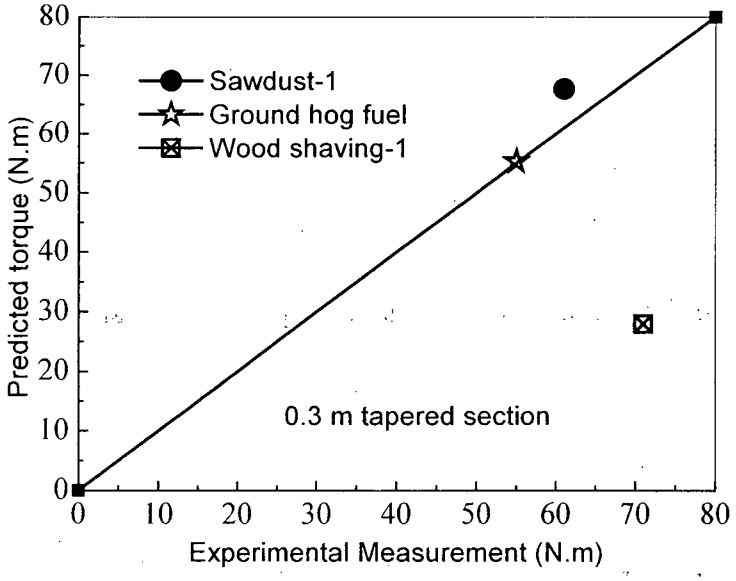


Figure 6-31. Comparison of torque predictions and experimental measurements with 0.30 m tapered sections and a 0.45 m hopper level.

6.3.4.3 Extended section in choke section for screw-1

Stresses on a material element in the extended section are shown in Figure 6-32. The torque generated by the extended section can be predicted by the above equations. The recommended critical lengths for various materials are listed in Table 6-6, while the predicted torques with extended sections appear in Table 6-7 and Figures 6-33 to 6-34. Although the predicted torques with a 0.15 m extended section for sawdust-1 do not match the experimental data very well, approximate estimates can be provided for biomass materials with consideration of torque fluctuations. Torque readings generally fluctuated in the range 10-30 N.m during the experimental tests. For blockage conditions, the predicted torques are those required to reach certain compression levels inside the extended sections, not those required to break up a blockage or to advance the plug inside the extended section. The plug formed in the extended section becomes even tighter when the axial stress exerted by the screw flight increases. A tighter plug also increases the resistance exerted by the casing wall, depending on the length of the extended section and the material properties. It is difficult to predict the required torque to expel the plug into the receiving vessel for different biomass materials. The critical length of the extended section is important if a screw feeder with extended sections is employed. It then acts like a piston feeder. Several plug formation regions (i.e. casings without screw flights) along the screw in the choke section are expected to provide better performance from a plug seal point of view (Bates, 2000).

6.3.4.4 Different choke section length for screw-1

The model developed above is intended for different choke section lengths, i.e. 0.30, 0.46 and 0.61 m in the present study, as shown in Figure 6-35. For the shortest length (0.30 m), the compression factor for torque predictions is the same as for the longest choke section (0.61 m) in the present experiments. Hence the torque requirements are reduced compared to the longer

section. Longer choke sections are expected to provide better plug sealing and a greater probability of blockage. For biomass feeding, 4–10 times the screw pitch is recommended for the choke section length.

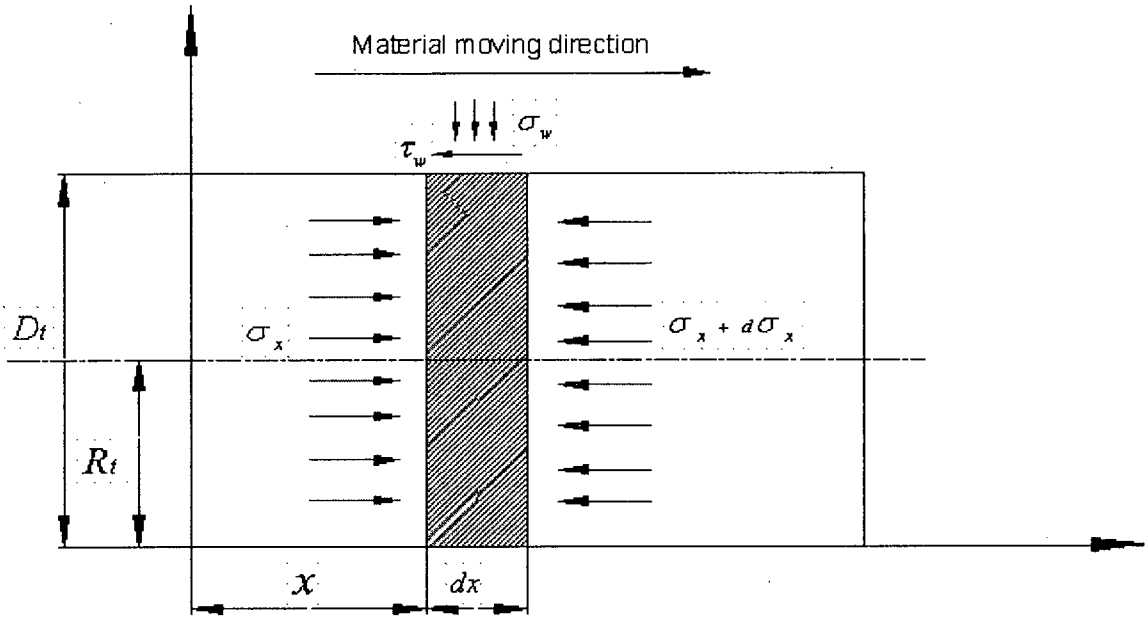


Figure 6-32. Stress on material element in extended section.

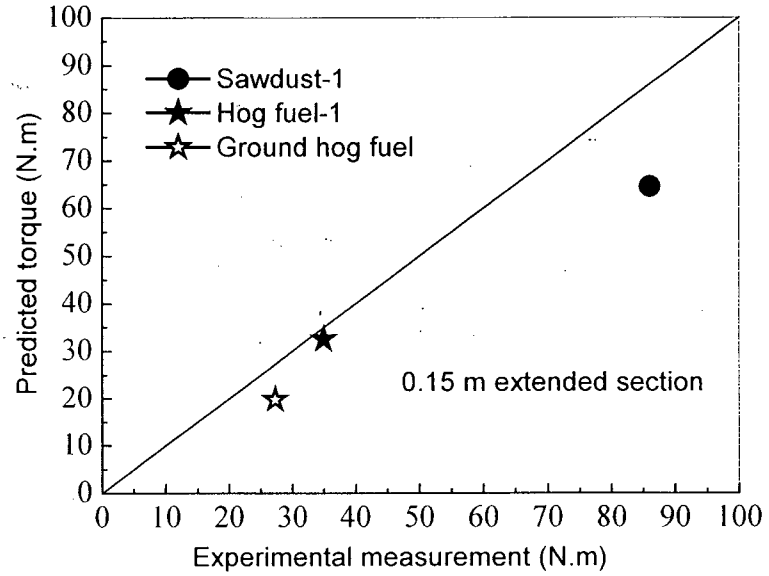


Figure 6-33. Comparison of torque predictions and experimental measurements for screw-1 with 0.15 m extended sections with a 0.45 m hopper level.

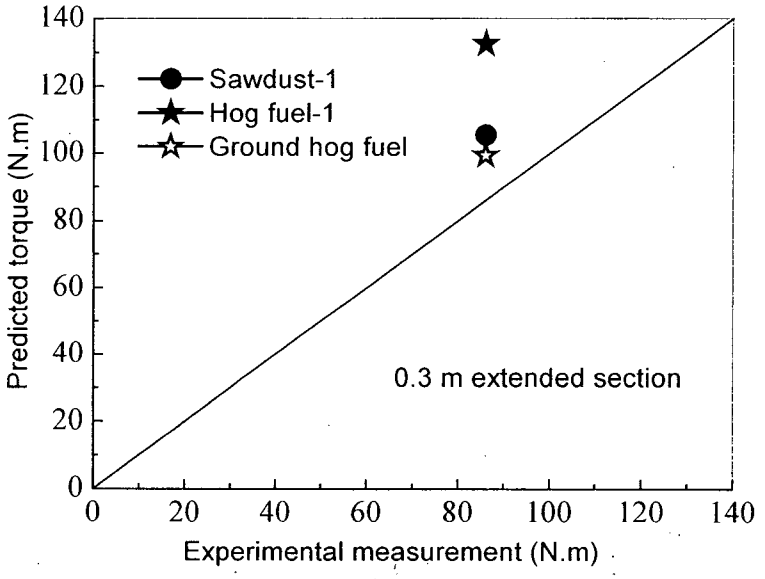


Figure 6-34. Comparison of torque predictions and experimental measurements for screw-1 with 0.30 m extended sections with a 0.45 m hopper level.

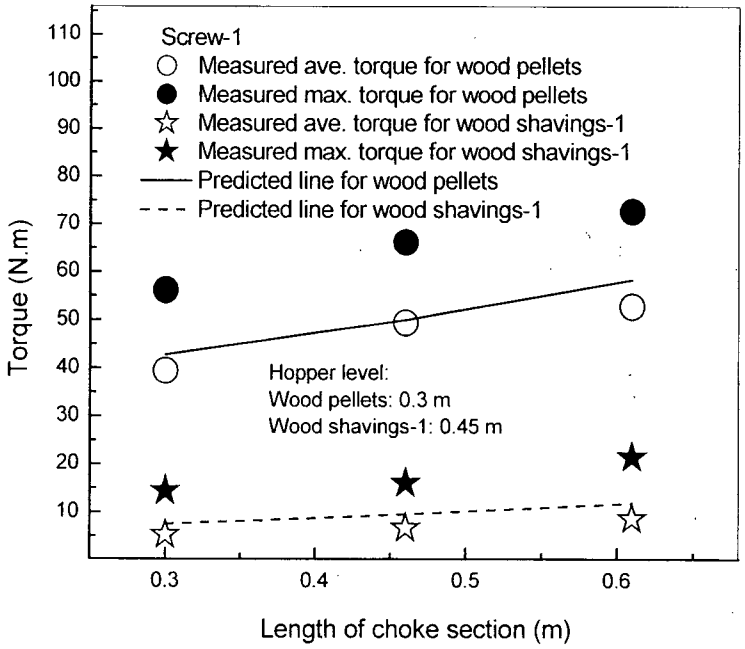


Figure 6-35. Comparison of torque predictions and experimental measurements for different choke section lengths.

Table 6-6. Recommended critical length of extended section (ID: 102 mm) for various materials

| Name of specimen | Wall friction angle on carbon steel (deg) | Internal friction angle (deg) | $L_{ct1}$ (m) | $L_{ct2}$ (m) |
|---|---|---|---|---|
| Wood pellets | 31.4 | 32.0 | 0.09 | 0.06 |
| Ground wood pellets-1 | 30.2 | 33.2 | 0.11 | 0.07 |
| Ground wood pellets-2 | 30.4 | 38.0 | 0.15 | 0.08 |
| Sawdusts-1 | 31.8 | 38.0 | 0.14 | 0.08 |
| Hog fuel-1 | 31.5 | 39.0 | 0.15 | 0.08 |
| Ground hog fuel | 31.8 | 45.0 | 0.21 | 0.10 |
| Wood shavings-1 | 31.0 | 39.0 | 0.16 | 0.08 |
| Polyethylene particles | 21.5 | 26.2 | 0.14 | 0.05 |

Table 6-7. Predicted torques with extended sections for 0.45 m hopper level and various biomass materials for screw-1

| Biomass Materials | Sawdusts-1 | Hog fuel | Ground hog fuel | Wood shavings-1 |
|---|---|---|---|---|
| Mean particle diameter (mm) | 0.45 | 0.72 | 0.18 | 0.67 |
| Bulk density (kg/m$^3$) | 210 | 200 | 150 | 110 |
| Bulk density in 0.15 m extended section (kg/ m$^3$) | 315 | 240 | 210 | 154 |
| Bulk density in 0.30 m extended section (kg/ m$^3$) | 378 | 270 | 270 | 231 |
| Axial stress in 0.15 m extended section (kPa) | 102 | 26 | 17.8 | 11.2 |
| Axial stress in 0.30 m extended section (kPa) | 508 | 330 | 299 | 178 |
| Measured ave. torque with 0.15 m extended section [1] (N.m) | Blocked [2] | 27.5 | 12.5 | 13.0 |
| Measured max. torque with 0.15 m extended section (N.m) | Blocked | 42.4 | 42 | 24.1 |
| Predicted torque with 0.15 m extended section [3] (N.m) | 64.6 | 32.5 | 19.8 | 15.7 |
| Measured ave. torque with 0.30 m extended section* (N.m) | Blocked | Blocked | Blocked | Blocked |
| Measured max. torque with 0.30 m extended section* (N.m) | Blocked | Blocked | Blocked | Blocked |
| Predicted torque with 0.30 m extended section (N.m) | 105.5 | 132.5 | 99.4 | 102.0 |

Note: [1] 0.45 m hopper level
[2] Max. torque reading < 100 N.m.
[3] Predicted torque should be predicted average torque

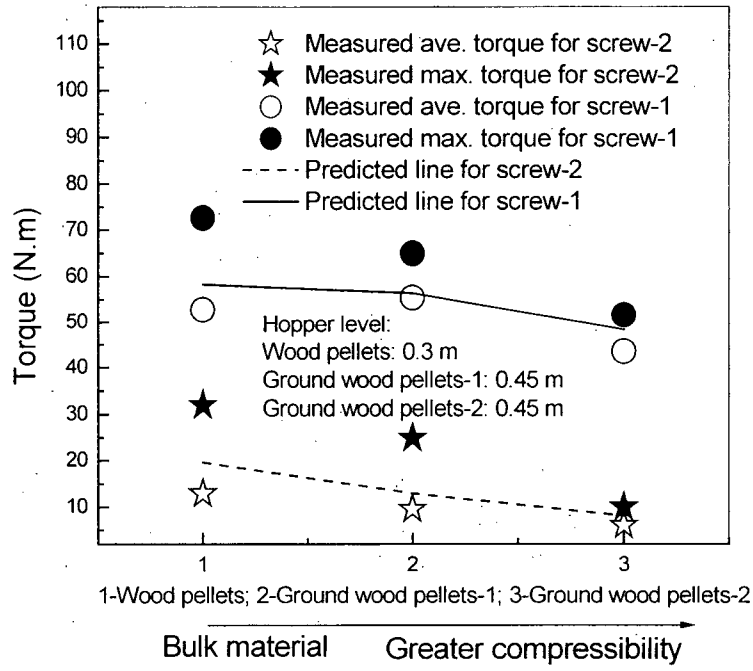


Figure 6-36. Comparison of torque predictions and experimental measurements for screw-1 and screw-2.

6.3.4.5 Comparison of predictions for screw-1 and screw-2

Screw-1 and screw-2 are compared in Figure 6-36. From this figure, we see that the torque requirements, as well as the torque predictions, are less for screw-2 than for screw-1. This is mainly due to the relatively large clearance (11 mm) and increased screw pocket space (increased pitch) for screw-2, as shown in Figure 4-3. The latter should lead to relatively uniform flow in the hopper and reduced torque requirements. In addition, the fullness of screw pockets in the choke section is lower due to the enlarged clearance for screw-2, which also reduced the torque requirements. Smaller clearance (1 mm for screw-1 in the hopper section) for given trough or casing diameter can increase the transport capacity and torque requirements, but may cause mechanical wear and increase the tendency to block. For screw-1, the clearance was greater, up to 5-11 mm in the choke section in order to reduce the blockage tendency in the

choke section. Special attention is required if reduced clearance is combined with tapered or extended sections in the choke section due to the tight plug formation and large blockage tendency. For biomass feeding, the clearance should be 2-11 mm for particles similar to those tested here. Note that $\sigma_{x\max} \approx \sigma_{da}$ when the boundary condition $\sigma_x = \sigma_v$ at $x = P$ is employed for Equation 6-50 in each pocket for screw-2 in the hopper section, where $\sigma_{da}$ is the stress on the driving side of the flight calculated from the above procedures, while $\sigma_{x\max}$ is the maximum stress in a pocket calculated from Equation 6-54, i.e. $\sigma_{x\max} = \sigma_v \exp[2\mu_w \lambda_s P/(R_t - R_c)]$. Using the boundary condition without consideration of $n$ (i.e. $\sigma_x = \sigma_v$ at $x = P$ ) and neglecting compression in the choke section can make the torque prediction match the experimental results very well for screw-2. The new model for screw-2 extended the model recommended by Yu and Arnold (1997), who analyzed axial forces with only the driving side of the screw flight considered for torque predictions, i.e. they neglected the effects of the core shaft surface, trailing side of the flight and flight tips on torque predictions. Note that the torque predicted from the driving side of a flight accounts for ~90% of the total torque requirements for screw-1 and ~80% for screw-2 for both compressible and incompressible materials in the present study. This indicates that the driving side of flight is dominant in determing the torque requirements. The contributions from the other terms appear in Table 6-8. The larger the screw diameter or the smaller the clearance (screw-1), the larger proportions the driving side of flight in total torque.

Table 6-8. Relative contributions of different surfaces to total torque (in % of total)

| Surfaces | Screw-1 | Screw-2 |
|---|---|---|
| Driving side of flight | 89.1-90.6 | 79.6-80.0 |
| Core shaft surface | 4.2-5.7 | 7.5-9.6 |
| Trailing side of flight | -0.13-1.1 | 2.5-2.6 |
| Flight tip | 4.1-5.4 | 7.9-10.3 |

## 6.4 Summary

(1) A new theoretical model for the torque requirement of a screw feeder is developed by applying principles of bulk solid mechanics to a material element moving within a pocket. The torque requirement is proportional to the vertical stress exerted on the hopper outlet by the bulk material in the hopper and approximately proportional to the third power of the screw diameter ($c_d, c_p, c_t, \mu_f$ are assumed constant) according to theoretical analysis. It is a function of screw configurations (e.g. screw diameter, shaft diameter, pitch, clearance), hopper configurations (e.g. hopper outlet width, half hopper angle) and flow properties of the bulk material (e.g. bulk density, wall friction and internal friction). Starting torque is also predicted, with reasonable accuracy, by stress analysis in the hopper section, which has also been neglected in previous studies.

(2) Consideration of the forces on the five confining surfaces surrounding the bulk material contained within a pocket between adjacent flights, and the stress distribution in the pocket, leads to better understanding of torque characteristics and to reasonable predictions of the torque requirement for a screw feeder. Incompressible and compressible materials are treated differently in the stress analysis within a pocket, including the hopper and choke sections, for different screw configurations. Predictions are mostly in good agreement with measurements.

(3) Effects of the driving side, trailing side, core shaft surface and flight tips, as well as trough/casing surface and shear surface, on torque predictions are considered in the new model. This approach differs from previous research.

(4) Consideration of compaction, especially in the choke section, is shown to be essential for successful torque predictions for screw feeding of compressible materials like biomass.

(5) Another novel feature of the work is that special casing configurations (e.g. tapered and extended sections) are considered, leading to better understanding of blockage in the choke

section and approximate prediction of torque requirements and volumetric efficiency for screw feeders of given geometry.

(6) For one of the two screws tested, the torque required for biomass feeding is determined mainly by the choke section, accounting for > 50% of the total torque requirement for biomass particles, especially for compressible materials (> 70%), even though the choke section is shorter than the hopper section. Different screw and choke section configurations cause different compression in the choke section, as well as different torque requirements. As a rule, smaller clearances and longer choke sections lead to greater compression and require larger torque for screw feeding.

# CHAPTER 7. CONCLUSIONS AND SUGGESTIONS FOR FURTHER WORK

## 7.1 Conclusions

### 7.1.1 Biomass feeding system

Biomass combustion and gasification are very promising clean energy options for reducing greenhouse gas emissions. In the present study, wood pellets, ground wood pellets, sawdust, hog fuel, ground hog fuel and wood shavings were tested with polyethylene particles as reference particles for comparison. The feeding system combined a wedge-shaped hopper, a lock hopper and a screw feeder to feed biomass. The diameter of the screw casing was 102 mm. Two screws were employed with clearance of 1-11 mm and pitch in the range of 40-100 mm. Tapered and extended sections, as well as hopper pressurization, were also tested. Screw speeds were from 5 to 40 rpm. The volumetric efficiencies of the screw feeder mainly ranged from 60-95%, while the volumetric flow rate varied from 0.09-1.2 $m^3/h$. The torque was mainly in the range of 7-60 N.m. When maximum torque readings exceeded ~70 N.m, blockage was likely to occur for the present motor drive system. The following conclusions can be drawn from this study:

(1) The level of solid in the hopper affected blockage inside the screw feeder. For wood pellets of uniform size, when the hopper level exceeded 0.35 m, blockage could occur, whereas no blockage occurred for hopper levels less than 0.3 m. For a hopper level exceeding 0.4 m, blockage occurred almost immediately after starting the screw feeder. Polyethylene particles never blocked for hopper levels < 0.6 m due to their regular shape and smooth surfaces.

(2) Larger particles, irregular particle shapes, rougher surfaces and larger bulk densities increase the tendency for wood pellets to block in the hopper. The larger torques required to

feed wood pellets compared to ground wood pellets are mainly attributable to the larger particle size of the wood pellets.

(3) Particle size distribution plays a significant role in determining bulk flow properties. Wood pellets containing fines blocked more frequently inside the screw feeder than wood pellets of uniform size, because fines decrease void fraction of bulk solids, increasing the contacting areas between bulk solids and screw. Moreover, fines tend to cause large cohesive resistance. Wider size distribution, especially large particles, required larger torque for hog fuel-1 compared to ground hog fuel and sawdust-1.

(4) High moisture content (e.g. 40 and 60%) caused larger cohesion and adhesion, making biomass fuels more likely to bridge in the hopper. Intermittent bridging in the hopper reduced the volumetric flow rate for wet biomass fuels. Wet biomass generally needed much more torque to achieve blockage-free feeding than dry biomass.

(5) Higher compressibility led to higher volumetric flow rates for screw feeding. Compressible biomass fuels passed through tapered sections more readily than incompressible materials. Plug formation inside the screw casing was also facilitated by increased compressibility.

(6) The choke section played an important role in biomass feeding. The choke section length and casing configurations (e.g. tapered and extended sections) were closely related to plug formation and plug sealing of the reactor, while also affecting the torque requirements.

(7) Pressurizing the hopper slightly (e.g. by 0.01 bar) relative to the receiving vessel generally increased the feed rate and decreased the torque requirement, while also preventing backflow of gases and bed materials.

(8) More compact materials (i.e. larger bulk density) and non-uniform moisture content tend to increase the torque requirements for feeding.

(9) Careful refilling need not disrupt feeding, especially for biomass fuels of low bulk density.

(10) Large clearance and increasing capacity along the length of the screw resulted in reduced torque for screw-2 relative to screw-1. Small clearance caused larger torque and more blockage, as well as better plug sealing, for screw-1.

(11) For biomass feeding, the choke section may need to be longer, e.g. 6-10 times the pitch, to promote plug formation and prevent backflow of hot gases and bed materials. Maximum torque instead of starting torque is critical for screw feeders with small clearance and long choke sections.

(12) Torque requirements are nearly independent of screw speeds, both for compressible and incompressible solid materials.

(13) Clearance and choke section length are critical factors affecting compression, torque requirements and blockage tendency, neglected in previous experimental work and modeling.

A new model based on stress analysis was developed to predict the torque requirements and efficiency for screw feeding. A new strategy was adopted in the stress analysis within a pocket (both in the hopper and choke sections), with incompressible and compressible materials treated differently. Yu and Arnold (1997) only used the force on the driving side of screw flights to estimate the torque requirements and neglected other boundaries (e.g. core shaft and trailing side of screw flights). The new model developed in this thesis extends previous models by considering the effects of all boundaries on torque, and allowing for compression in the choke section, as well as in the hopper section. Special casing configurations (e.g. tapered and extended sections) are also considered, leading to better understanding of blockage in the choke section and approximate prediction of torque requirements for screw feeders of given geometry. For the material element in a pocket, forces are imposed on five boundary surfaces, i.e. shear

surface, driving side of the flight, trailing side of the flight, core shaft surface and trough surface. In the choke section, a rigid upper casing surface limits the screw space, instead of a shear surface.

The torque requirement is proportional to the vertical stress exerted on the hopper outlet by the bulk material in the hopper and approximately proportional to the third power of the screw diameter ($c_d, c_p, c_t, \mu_f$ are assumed constant) according to theoretical analysis. Starting torque is also predicted, with reasonable accuracy, by stress analysis in the hopper section.

The new model predicts:

- Average torque requirements of screw feeding for various biomass materials, including screw feeders with tapered and extended discharge sections.
- Starting torque requirements for screw feeding of various biomass materials.
- Efficiency of biomass screw feeding with consideration of compression in the choke section.

### 7.1.2 Particulate flow loop

A Particulate Flow Loop was designed and fabricated to investigate the movement of clusters of particles of different regular shapes through narrow gaps or constrictions as they are conveyed by water. The work undertaken in this equipment was intended to provide background information and a better understanding of key hydrodynamic multiphase flow factors which cause, or contribute to, stalling and blockage in particulate feeding systems such as those used for feeding biomass to reactors.

The following conclusions can be drawn from the study:

(1) Spherical particles of small size and low density were easily transported and were unlikely to block the constriction, while irregular rubber and plastic particles of density greater

than water were difficult to convey. With increasing water mean velocity, the particles experienced creep, saltation and suspension.

(2) Large particles of high aspect ratio and density higher than water were difficult to transport. These particles were also more likely to block the constriction at high Reynolds number.

(3) The maximum particle dimension does not solely determine whether or not blockage occurs when the minimum dimension of the particles is less than the maximum gap dimension. However, large particles were more likely to cause blockage, and a lower particle concentration was required to block a constriction for larger than for smaller particles.

(4) Nearly neutrally buoyant conical particles were more likely to block a constriction at a high water mean velocity. This appears to be mainly because of the unbalanced shape, intense fluid-particle and particle-particle interactions, and a large ratio of maximum particle dimension to minimum constriction dimension.

(5) Particles with some compressibility were more likely to block constrictions than hard particles, because compressible particles tended to jam together instead of separating after colliding. However, soft particles did not form stable blockages due to their low hardness and high flexibility.

(6) The blockage probability depends on the interactions of the fluid, particles and constriction. Reynolds number affects particle motion and the blockage tendency. At small water mean velocity, non-spherical particles of density greater than water were difficult to transport because of sedimentation. As the water mean velocity increased, non-spherical particles were easier to transport, with some piling upstream of the constriction and others passing through the gap almost one by one. Blockage was unlikely for this case. For higher water mean velocities, more and more heavier non-spherical particles were transported and

lifted vigorously (saltation or suspension), increasing the probability of different particles passing through the constriction simultaneously, thereby increasing the probability of blockage. For the conditions of the present study, 3 to 10 non-spherical particles were sufficient to block the constriction if the ratio of particle maximum dimension to constriction minimum dimension > 0.4. As $U_m$ increased, blockage was less likely to occur and was more readily broken up because of increased particle inertia, increased drag and increased pressure gradient immediately upstream of the constriction.

(7) A wider slot which provided more space for particles to disperse laterally reduced the probability of blockage.

(8) The larger or heavier the particles, the greater the chance of them colliding with the wall and with each other because of inertial effects. Preliminary observations show that understanding the motion of a single particle is helpful to understand the motion of swarms of particles. However, blockage is related to swarms of particles and cannot occur without particle-particle and particle-wall interactions.

(9) The pressure drop needed to break a blockage was predicted based on horizontal packed bed assumption using a modified Ergun equation.

## 7.2 Recommendations for Further Work

Further research is required to examine a number of factors:

(1) Although the model works well in predicting the average and starting torques, it should be modified for different hopper and screw configurations. More screw configurations (e.g. different clearances and pitches), as well as different hopper configurations (e.g. hopper length and internals), should be tested to validate or modify the present model.

(2) Plug formation and plug seal are critical for screw feeding, especially for feeding to pressurized vessels. More screw configurations need to be tested for adverse pressure gradients in order to achieve better plug seals.

(3) Only internal and wall friction are considered in the model. Gravity, centrifugal force and cohesion are neglected in the present model. Their neglect should be reconsidered.

(4) A wider range of biomass materials with different mean sizes, size distributions, shapes and moisture contents should be tested. Data from industrial application are preferred.

(5) Innovative feeding systems are needed for reactor systems. Deep understanding of bulk solids properties, reactor types and operating conditions, feeder configurations, and diverse combinations of feeders, may be needed for successful feeder design and operation. A schematic of one conceptual design of biomass screw feeding to pressurized reactors is shown in Figure 7-1.

(6) Further study on blockage is still needed, typically cohesive blockage involving fine powders with certain moisture content (e.g. < 10% wet basis).

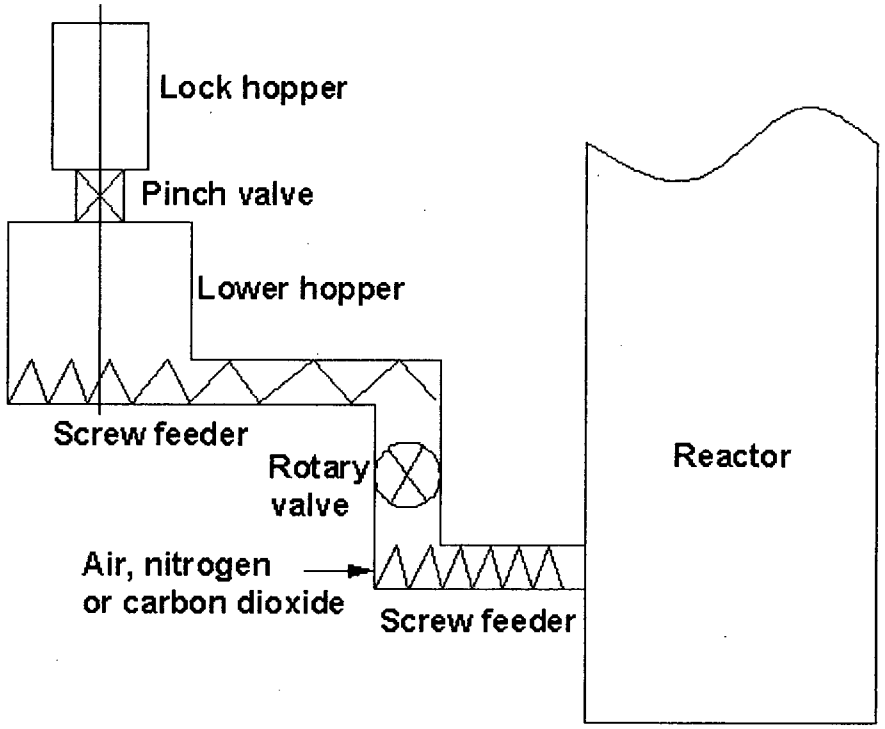


Figure 7-1. Schematic of conceptual design of biomass feeding to pressurized reactors

# NOMENCLATURE

| | |
|---|---|
| $a$ | Constant defined by Equation 6-86. |
| $A$ | Cross-sectional area of screw feeder, $A = \pi(D_s^2 - D_c^2)/4$, $m^2$ |
| $A$ | Blake–Kozeny–Carman constant in Equation 3-19, typically =150. |
| $A_c$ | Cross sectional area of vertical section of bin in Equation 6-26, $m^2$. |
| $b$ | Constant defined by Equation 6-86. |
| $B$ | Hopper outlet width in Equation 6-22, m |
| $B$ | Burke–Plummer constant in Equation 3-19, typically= 1.75. |
| $c$ | Clearance between screw flight tips and trough or casing inside surface, m. |
| $c$ | Constant defined by Equation 6-86. |
| $c_b$ | Ratio of flight thickness to screw diameter, -. |
| $c_d$ | Ratio of core shaft diameter to screw flight diameter, $= R_c / R_o = D_c / D_o$, -. |
| $c_p$ | Ratio of pitch to screw flight diameter, $= P / D_o$, -. |
| $c_t$ | Ratio of trough or casing diameter to screw flight diameter, $= 2R_t / D_o$, -. |
| $C$ | Factor defined by Equation 6-107. |
| $C_d$ | Drag coefficient, -. |
| $CF$ | Compression factor defined by Equation 6-106. |
| $d_i$ | Arithmetic mean sieve aperture, m |
| $d_m$ | Mean particle diameter, m |
| $d_p$ | Sieve aperture size, m |
| $d_s$ | Equivalent surface area diameter of particles, m. |
| $d_{sv}$ | Equivalent surface area-volume ratio diameter of particles, m |
| $d_v$ | Equivalent volume diameter of particles, m |
| $D$ | Width of long rectangular vertical section of bin or solid surface width in hopper defined by Equation 6-26, m. |
| $D_c$ | Core shaft diameter, m. |

$D_H$ Hydraulic diameter of duct, m.

$D_h$ Hydraulic diameter of flow channels in packed bed as shown in Equation 3-22, m.

$D_o$ Screw flight diameter, m.

$D_t$ Inside diameter of trough or casing in Table 4-1; m

$E$ Factor defined by Equation 6-107, $= C\left[q_f H_0 L_c /(c_t D_t^2)\right]^{1/5}$, -.

$E$ Elastic modulus defined in Equation 3-2, Pa.

$f$ Rotational speed of screw feeder, rpm.

$F$ Flexibility defined in Equation 3-1, 1/(Pa.m$^4$).

$F_c$ Force on core surface as shown in Figure 6-10, N.

$F_{ca}$ Axial force on core surface as shown in Figure 6-10, N.

$F_{ct}$ Tangential force on core surface as shown in Figure 6-10, N.

$F_d$ Force on driving side of flight in Figure 4-1, N

$F_{da}$ Axial force on driving side of flight in Figure 4-1, N

$F_{dt}$ Tangential force on driving side of flight in Figure 4-1, N

$F_f$ Force on trailing side as shown in Figure 6-12, N.

$F_{fa}$ Axial force on trailing side as shown in Figure 6-12, N.

$F_{ft}$ Tangential force on trailing side as shown in Figure 6-12, N.

$F_s$ Force on shear surface as shown in Figure 6-9, N.

$F_{sa}$ Axial force on shear surface as shown in Figure 6-9, N.

$F_{st}$ Tangential force on shear surface as shown in Figure 6-9, N.

$F_t$ Force on trough or casing surface as shown in Figure 6-13, N.

$F_{ta}$ Axial force on trough or casing surface as shown in Figure 6-13, N.

$F_{tt}$ Tangential force on trough or casing surface as shown in Figure 6-13, N.

$g$ Acceleration due to gravity, m/s$^2$

$h$ Height of cuboidal particle in Table 3-3, m.

$h_0$ Distance between bulk solids free surface and top transition of hopper in Figure 6-7, m.

$H$ Height of rectangular duct in Chapter 3, m.

| | |
|---|---|
| $H_b$ | Height of horizontal packed bed in Figure 3-24, m. |
| $H_0$ | Hopper level, m. |
| $H_t$ | Distance between apex of hopper and top transition of hopper, m. |
| $I$ | Area moment of inertia in Equation 3-3, $m^4$. |
| $I_h$ | Mass moment of inertia Equation 3-3, $kg.m^2$. |
| $k$ | Coefficient in Equation 6-1. |
| $K$ | Bulk modulus of compression, Pa. |
| $K_1$ | Empirical ratio in Figures 6-1 and 6-8, -. |
| $K_2$ | Empirical ratio in Figures 6-1 and 6-8, -. |
| $K_3$ | Empirical ratio in Figures 6-1 and 6-8, -. |
| $K_4$ | Empirical ratio in Figure 6-8, -. |
| $K_F$ | Ratio of drag in bounded fluid to that in infinite fluid defined in Equation 3-15, -. |
| $l$ | Particle length in Table 3-3, m |
| $L$ | Length (dimension along streamwise direction) of rectangular duct in Chapter 3, m. |
| $L_b$ | Length of horizontal packed bed in Figure 3-24, m. |
| $L_h$ | Hopper outlet length in Table 4-1, m |
| $L_c$ | Choke section length of screw in Table 4-1, m |
| $M_1$ | Mass of bulk solids and cylinder in Equation 4-1, kg |
| $M_2$ | Mass of empty cylinder in Equation 4-1, kg |
| m | Hopper shape factor; m=1 for axisymmetric flow or a conical hopper; m=0 for plane flow or a wedge-shaped hopper, dimensionless. |
| $M$ | Mass flow rate in Equation 6-2, kg/s. |
| $n$ | Factor defined by Equation 6-84, -. |
| $P$ | Consolidation pressure, Pa. |
| $P$ | Pitch of screw in Table 4-1, m |
| $PW$ | Shaft power required to rotate screw feeder defined by Equation 6-112, N.m/s. |
| $q$ | Dimensionless surcharge factor, -. |
| $q_f$ | Dimensionless surcharge factor for flow condition, -. |
| $q_i$ | Dimensionless initial surcharge factor, -. |

$Q_c$ Surcharge force at transition of vertical section of bin and hopper in Equation 6-26, N.

$Q_v$ Feeder load exerted by bulk solids at hopper outlet during flow, N.

$Q_{vi}$ Initial feeder load exerted by bulk solids at hopper outlet, N.

$R_c$ Screw core shaft radius, m.

$R_{av}$ Average screw flight radius defined by Equation 6-20, m.

Re Reynolds number based on hydraulic diameter of rectangular duct, $= D_H U_m \rho_w / \mu_w$, -.

$\mathrm{Re}_h$ Reynolds number based on half-height of rectangular duct, $= HU_m \rho_w /(2\mu_w)$, -.

$\mathrm{Re}_p$ Particle Reynolds number, -.

$R_m$ Mean screw radius defined by Equation 6-16.

$R_o$ Screw flight radius, m

$R_t$ Trough or casing inside radius, m.

$S$ Fibre stiffness in bending, $\mathrm{Pa.m}^4$.

$S_p$ Peripheral displacement of screw flight at radius $r$ per revolution in Figure 6-4, m

$S_p$ Particle surface area in Equation 3-19, $\mathrm{m}^2$.

$T_i$ Torque generated in one pocket, N.m.

$T_d$ Torque generated by driving flight, N.m.

$T_c$ Torque generated by core shaft surface, N.m.

$T_f$ Torque generated by trailing flight, N.m.

$T_{tip}$ Torque generated by flight tip, N.m.

$T_{\mathrm{exp}}$ Measured average torque, N.m.

$T_{pre}$ Predicted average torque, N.m.

$U_m$ Mean fluid velocity in Table 3-2, m/s.

$U_0$ Superficial fluid velocity in Equation 3-21, m/s.

$U_c$ Centerline fluid velocity, m/s.

$U_f$ Local fluid velocity, m/s.

$U_{fd}$ Fully developed local fluid velocity, m/s.

$U_{cfd}$ Fully developed centerline fluid velocity, m/s.

$u_p$ Particle velocity, m/s.

$V$ Internal volume of cylinder in Equation 4-1, $m^3$

$V$ Volumetric flow rate in Equation 6-1, $m^3/s$.

$V_{TM}$ Maximum theoretical throughput of screw feeder, $m^3/s$.

$v_a$ Absolute velocity of particle in Figure 4-1, m/s.

$v_h$ Axial velocity of particle in Figure 4-1, m/s.

$v_{Lh}$ Axial velocity of screw in Figure 4-1, m/s.

$v_s$ Tangential velocity of screw in Figure 4-1, m/s.

$v_r$ Relative velocity of particle with respect to screw surface in Figure 4-1, m/s.

$v_t$ Tangential velocity of particle in Figure 4-1, m/s.

$w$ Particle width in Table 3-3, m.

$W$ Width (dimension along spanwise direction) of rectangular duct in Figure 3-24, m.

$W_b$ Width of horizontal packed bed in Figure 3-24, m.

$x$ Coordinate in streamwise or horizontal direction, Figure 3-19 or 6-7, m.

$x_{fd}$ Development length in axial coordinate at which 99% of the centerline velocity is attained, m.

$x_i$ Mass fraction of particles of size i, -.

$X$ Factor defined by Equation 6-36, $= \sin\delta/(1-\sin\delta)[\sin(2\beta+\alpha)/\sin\alpha+1]$, -.

$Y$ Factor defined by Equation 6-37,

$= [(\alpha+\beta)\sin\alpha+\sin\beta\sin(\alpha+\beta)]/[(1-\sin\delta)\sin^2(\alpha+\beta)]$, -.

$y$ Vertical coordinate with apex of hopper as origin and upward direction as positive in Figure 6-7, m.

$y$ Coordinate in vertical direction in Figure 3-19, m.

$z$ Coordinate in spanwise direction in Figure 3-19, m.

## Greek letters

$\alpha$ Half-hopper angle, radians.

$\alpha$ Helical angle of screw flight in Figure 4-1, radians

| | |
|---|---|
| $\alpha$ | Angle in Figure C-1, radians. |
| $\alpha_c$ | Screw flight helical angle at core shaft surface, $= \arctan(P/2\pi R_c)$, radians. |
| $\alpha_m$ | Mean screw flight helical angle defined by Equation 6-17, radians. |
| $\alpha_o$ | Screw flight helical angle at outside radius, $= \arctan(P/2\pi R_o)$, radians. |
| $\alpha_r$ | Flight helical angle at screw radius $r$, radians. |
| $\beta$ | Factor defined by Equation 6-38, $= \lfloor \phi_w + \sin^{-1}(\sin\phi_w / \sin\delta) \rfloor / 2$, radians |
| $\beta$ | Ratio of short-to-long side dimension of duct in Chapter 3, $= W/H$, -. |
| $\delta$ | Effective angle of internal friction of bulk solids, radians. |
| $\varepsilon$ | Voidage, -. |
| $\varepsilon$ | Strain in Equation 3-2, -. |
| $\varepsilon_1$ | Angle defined by Equation 6-31, $\pi/4 + \phi_w/2 + 1/2 \times \cos^{-1}(\sin\phi_w / \sin\delta)$, radians |
| $\phi_f$ | Wall friction angle of bulk solids on flight surface, radians. |
| $\phi_w$ | Angle of kinetic friction between bulk solids and hopper wall, trough wall or casing surface, radians. |
| $\gamma$ | Screw flight thickness in Table 4-1, m. |
| $\Delta_A$ | Added mass coefficient in Equation 3-13, -. |
| $\eta_v$ | Volumetric efficiency, $= V/V_{TM}$, -. |
| $\eta_{vr}$ | Volumetric efficiency at screw radius $r$, -. |
| $\lambda$ | Angle between absolute velocity of particles and vertical direction to screw axis in Figure 4-1, radians. |
| $\lambda_r$ | Angle between absolute velocity of particles and vertical direction to screw axis at screw radius $r$ in Figure 6-2, radians. |
| $\lambda_s$ | Ratio of normal wall stress to axial stress for bulk solids sliding on surface, -. |
| $\mu_d$ | Effective coefficient of internal friction of bulk solids, $= \tan\delta$, -. |
| $\mu_f$ | Wall friction coefficient between bulk solids and screw flight surface, $= \tan\phi_f$, -. |
| $\mu_w$ | Wall friction coefficient between bulk solids and trough or core shaft surface, -. |
| $\mu_w$ | Dynamic viscosity of water, Pa.s. |
| $\mu_{wc}$ | Wall friction coefficient between bulk solids and core shaft surface, -. |
| $\mu_{wt}$ | Wall friction coefficient between bulk solids and trough surface or casing surface, -. |

$\mu_e$ Equivalent friction coefficient of bulk solids, $= (0.8-1)\sin\delta$, -.

$\rho_b$ Bulk density of bulk solids in hopper, kg/m$^3$

$\rho_p$ Particle density, kg/m$^3$

$\rho_f$ Fluid density, kg/m$^3$

$\rho_w$ Water density, kg/m$^3$

$\rho_{ya}$ Average bulk density in hopper defined by Equation 6-88.

$\rho_{yb}$ Compacted bulk density at $y$ defined by Equation 6-88.

$\sigma$ Stress in Equation 3-2, Pa.

$\sigma_{da}$ Stress on material element in a pocket due to driving flight side, Pa.

$\sigma_v$ Vertical stress exerted by bulk solids at hopper outlet, Pa.

$\sigma_{vi}$ Vertical stress exerted by bulk solids at hopper outlet for initial condition, Pa.

$\sigma_w$ Normal wall stress perpendicular to trough wall and core shaft surface, Pa.

$\sigma_{wa}$ Average normal wall stress perpendicular to trough wall and core shaft, Pa.

$\sigma_x$ Axial compression stress in a pocket inside screw feeder, Pa.

$\sigma_{xa}$ Average axial stress in a pocket, Pa.

$\sigma_{\min x}$ Minimum axial stress in a pocket in choke section, $= n\sigma_v \exp(2\mu_w \lambda_s PE/(R_t - R_c))$, Pa.

$\sigma_{cxa}$ Average axial stress in a pocket in choke section defined by Equation 6-109, Pa.

$\sigma_{cwa}$ Average normal stress in a pocket in choke section defined by Equation 6-110, Pa.

$\tau_w$ Shear stress on trough wall and core shaft, Pa.

$\omega$ Angular velocity of screw, 1/s

## Subscripts

a Axial direction

c Core shaft

d Driving side of flight

f Flow condition or trailing side of flight

fd Fully developed

| | |
|---|---|
| g | Gauge pressue |
| i | Initial filling condition |
| o | Outside diameter |
| s | Shear surface |
| t | Tangential direction or trough surface |
| w | Normal wall direction |

## Abbreviations

| | |
|---|---|
| ACFBG | Atmospheric circulating fluidized bed gasification/gasifier |
| BFBC | Bubbling fluidized bed combustion/combustor |
| CFBC | Circulating fluidized bed combustion/combustor |
| TPS | Termiska Processer AB of Sweden (TPS gasification process) |
| SRF | Short-rotation forest |
| RDF | Refuse-derived fuel |

# LITERATURE CITED

Abdullah, M. Z., Husain, Z. and Pong, S. L. Y., Analysis of cold flow fluidization test results for various biomass fuels, Biomass and Bioenergy. 24, 487-494 (2003).

Anderson, R. S., Saltation of sand: A qualitative review with biological analogy. Proc. R. Soc. Edin. B 96, 149-165 (1989).

Agarwal, A. K. and Agarwal, G. D., Recent technologies for the conversion of biomass into energy, fuels, and useful chemicals. Center for Energy Studies, Indian Institute of Technology, TERI Information Monitor on Environmental Science 4, 1–12 (1999).

Aghdam, M. M., Failure study of plug screw feeder of the MWPC complex: Part A—Stress and fatigue analysis. Report No. MAKU-02-02, Mech. Dept. of Amirkabir University, Tehran, Iran, 2002.

Aldred, D., Saunders, T. and Shirey, G., Continuous injection of solid fuels into advanced combustion and gasification system pressures. Gasification Technology Conference, October 12-15, 2003.

Arnold, P.C., Mclean, A.G and Roberts, A.W, Bulk solids: Storage, flow and handling (second edition). University of Newcastle Research Associates (TUNRA) Ltd., New South Wales, Australia, 1980.

Arnold, P.C., Some issues concerning the design of multi-screw feeders. Bulk Solids Handling 23 (4), 230-233 (2003).

Asadullah, M., Miyazawa, T., Ito, S., Kunimori, K. and Tomishige, K., Demonstration of real biomass gasification drastically promoted by effective catalyst. Applied Catalysis A: General 246, 103-116 (2003).

Asadullah, M., Miyazawa, T., Ito, S., Kunimori, K, Yamada, M. and Tomishige, K., Gasification of different biomasses in a dual-bed gasifier system combined with novel catalysts with high energy efficiency. Applied Catalysis A: General, 267, 95-102 (2004).

Ayhan, D., Fuel Characteristics of Olive Husk and Walnut, Hazelnut, Sunflower, and Almond Shells, Energy Sources, 24 (215–221), 2002.

Babu, S. P., Thermal gasification of biomass technology developments: End of task report for 1992 to 1994. Biomass and Bioenergy 9, 271-285 (1995).

Badger, P. C., Processing cost analysis for biomass feedstocks, General Bioenergy, Inc., Prepared for U.S. Department of Energy, Florence, Alabama, October 2002.

Bagnold, R. A., The Physics of Blown Sand and Desert Dunes, Methuen, 1941.

Bahillo, A., Cabanillas, A., Gayán, P., De Diego, L. and Adanez, J., Co-combustion of coal and biomass in FB boilers: model validation with experimental results from CFB pilot plant, 46th Int. Energy Agency- Fluidized Bed Conversion (IEA-FBC), Jacksonville, Florida, May, 2003.

Bates, L., Entrainment pattern of screw hopper dischargers, Transactions of ASME, Journal of Engineering for Industry 91B, 295-302 (1969).

Bates, L., Interfacing hoppers with screw feeders. Bulk Solid Handling 6, 66-78 (1986).

Bates, L., The storage, feed and collection of loose solids. Powder Handling and Processing 6, 215-221 (1994).

Bates, L., Guide to the design, selection and application of screw feeders. Professional Engineering Publishing, London, 2000.

Beavers, G. S., Sparrow, E. M., and Magnuson, R. A., Experiments on hydrodynamically developing flow in rectangular ducts of arbitrary aspect ratio, Int. J. Heat Mass Transfer 13, 689-702 (1970).

Beer, F. P., Johnston, Jr., E.R. and DeWolf, J. T., Mechanics of materials, Mc-Graw Hill, New York, 2002.

Bell, T. A., Couch, S. W., Krieger, T. L. and Feise, H. J., Screw feeders: A guide to selection and use. Chemical Engineering Progress 99, 44-51 (2003).

Bortolamasi, M. and Fottner, J., Design and sizing of screw feeders, International Congress for Particle Technology, Nuremberg, Germany, 2001.

Bridgwater, A. V., The future for biomass pyrolysis and gasification: status, opportunities and policies for Europe. Bio-Energy Research Group, Aston University, Birmingham, 2002.

Briggs, D. G., Forest products measurements and conversion factors: with special emphasis on the U.S. Pacific Northwest. University of Washington, Institute of Forest Resources, 1994.

Brodkey, Robert S. and Hershey, Harry C., Transport Phenomena: A Unified Approach, Mc-Graw Hill, New York, 1988.

Bundalli, N. and Martinez, O., Bin and silo design for biomass materials, Phase I. ENFOR project C-130, Ottawa, Ontario, 1982.

Bundalli, N., Morgan, D. and Martinez, O., Bin and silo design for biomass materials, Phase II. ENFOR project C-130, ENFOR Secretariat, Ottawa, Ontario, 1983.

Bundalli, N., Morgan, D. and Martinez, O., Bin and silo design for biomass materials, Phase III. ENFOR project C-130, B.C. Research project 6-06-245, B.C. Research, Vancouver, British Columbia, 1985.

Bundalli, N., Morgan, D. and Martinez, O., Bin-feeder design for reliable flow of hog fuel. Pulp and Paper Canada 87, 145-148 (1986).

Burkhardt, G. J., Effect of pitch radial clearance, hopper exposure and head on performance of screw feeders. Trans. ASAE 10, 685-690 (1967).

Carleton, A., Miles, J. and Valentin, F., A study of factors affecting the performance of screw conveyors and feeders. Trans. ASME, J. Eng. Ind., 91, 329-334 (1969).

Carpinlioglua, M. O. and Gundogdua, M. Y., An experimental approach for the determination of development length in particulate flows, International Journal of Multiphase Flow, 24, 347-353 (1998).

Carson, J. W., Designing efficient screw feeders. Powder and Bulk Engineering 12, 32-42 (1987).

CEMA Book No. 350, Screw conveyors, Conveyor Equipment Manufacturers' Association, Washington, DC, 1980.

Chattopadhyay, A., Rao, R. K. and Parameswaran, M. A., On the classification of bulk solids. Bulk Solids Handling 14, 339-344 (1994).

CIWMB, http://www.ciwmb.ca.gov/Organics/Conversion/AgForestRpt/Agriculture, 2007.

Cleary, P. W. and Sawley, M. L., DEM modeling of industrial granular flows: 3D case studies and the effect of particle shape on hopper discharge. Applied Mathematical Modeling 26(2), 89-111 (2002).

Clift, R., Grace, J. R. and Weber, M. E., Bubbles, Drops and Particles, Academic Press, New York, 1978.

Corella, J., Herguido, J. and Alday, F.J., Research in thermochemical biomass conversion. Edited by Bridgwater, A.V. and Kuester, J.L., Elsevier Applied Science, London, 1988.

CSIRO, http://www.det.csiro.au/cgi-bin/bfb-search, 2002

Cuenca, M. A. and Anthony, E. J., Pressurized fluidized bed combustion. Blackie Academic and Professional, London, 1995.

Cummer, K. R. and Brown, R. C., Ancillary equipment for biomass gasification. Biomass and Bioenergy 23, 113-128 (2002).

DOE, http://www.fossil.energy.gov/programs/powersystems/publications/Strategic_Plans/2001/mypp_2001_centsys.pdf, 2001.

Duran, J., Sands, powders, and grains: An introduction to the physics of granular materials, Springer-Verlag New York, Inc., New York, 2000

ECN Biomass – IEA Bioenergy Task 33 meeting, Vienna, May 3, 2004, http://www.gastechnology.org/webroot/downloads/en/IEA/vanderDriftIEAVienna030504syngas.pdf, www.ecn.nl/biomass.

Eckelmann, H., The structure of the viscous sublayer and the adjacent wall region in a turbulent channel flow. J.Fluid Mech. 65, 439-459 (1974).

Eckert, E. R. G and Irvine Jr, T. F., Incompressible friction factor, transition and hydrodynamic entrance length studies of ducts with triangular and rectangular cross sections, Fifth midwestern conference on fluid mechanics, 1957.

EERC (Energy & Environmental Research Center), Investigating the impacts of co-firing biomass with fossil fuels - developing effective and efficient strategies for co-firing biomass with coal in conventional power systems, 2000. http://www.eerc.und.nodak.edu/summaries/IICB.htm.

EERE (Energy Efficiency and Renewable Energy), http://www.eere.energy.gov/biomass/progs/search1.cgi, 2006

EERE (Energy & Environmental Research Center), Energy Efficiency and Renewable Energy, U.S. Department of Energy, http://www1.eere.energy.gov/biomass/feedstock_databases.html, 2006.

Eggels, J. G. M, Unger, F., Weiss, M. H., Westerweel, J., Adrian, R. J., Friedrich, R. and Nieuwstadt, F. T. M., Fully developed turbulent pipe flow: a comparison between direct numerical simulation and experiment, J. Fluid Mech. 268, 175-209 (1994).

Eisert, W. G. and Dennenloehr, M., Nozzle design for the generation of plane liquid surface, Cytometry 1, 249-253 (1981).

Elliott, T. C., Standard handbook of power plant engineering. McGraw-Hill, New York, 1989.

Ergun, S., Fluid flow through packed columns. Chemical Engineering Progress 48, 89-94 (1952).

Eriksson, G., Kjellströma, B., Lundqvista, B. and Paulrud, S., Combustion of wood hydrolysis residue in a 150 kW powder burner. Fuel 83, 1635-1641 (2004).

Eskin, D. and Kalman, H., A simple model of a cylindrical heavily laden gas-particle jet, Chemical Engineering Science 57, 449-455 (2002).

Fan, L. and Zhu, C., Principles of gas-solid flows, Cambridge University Press, New York, 1998.

Favier, J. F., Abbaspour-Fard, M. H. and Kremmer, M., Modeling non-spherical particles using multi-sphere discrete elements. Journal of Engineering Mechanics 127, 971-981 (2001).

FBT (Fluidized Bed Technologies), Inc. Fluidized bed combustion and gasification: a guide for biomass waste generators. Prepared for Southeastern Regional Biomass Energy Program, 1994.

Fitzpatrick, J.J., Barringer, S.A. and Iqbal, T., Flow property measurement of food powders and sensitivity of Jenike's hopper design methodology to the measured values. Journal of Food Engineering 61, 399–405 (2004).

Fleming, D. P. and Sparrow, E. M., Flow in the hydrodynamic entrance region of ducts of arbitrary cross section, Journal of Heat Transfer, Trans. ASME, 91, 345-354 (1969).

Forgacs, O. L. and Mason, S.G., Particle motions in sheared suspensions. 9. Spin and deformation of threadlike particles, J. Colloid Interface Sci. 14, 457–472 (1959a).

Fortes, A. F., Joseph, D. D and Lundgren, T. S., Nonlinear mechanics of fluidization of beds of spherical particles, Journal of Fluid Mechanics Digital Archive 177, 467-483 (1987).

Fukagata, K. Zahrai, S. and Bark, F. H., Force balance in a turbulent particulate channel flow, International Journal of Multiphase Flow 24, 867-887 (1998).

Furimsky, E., Gasification of oil sand coke: Review. Fuel Processing Technology 56, 263-290 (1998).

Gabra, M., Salman, H. and Kjellstrom, B., Development of a sugar cane residue feeding system for a cyclone gasifier. Biomass and Bioenergy 15, 143-153 (1998).

Garg, V. K., Computation of three-dimensional parabolic laminar flows, Applied Mechanics and Engineering 53, 207-221 (1985).

Garrison, R. P. and Byers, D. H., Static pressure, velocity, and noise characteristics of rectangular nozzle for high velocity/low volume exhaust ventilation, American Industrial Hygiene Association Journal, 855-863 (1980).

Gavrilakis, S., Numerical simulation of low-Reynolds-number turbulent flow through a straight square duct, J. Fluid Mech. 244, 101-129 (1992).

Geldart, D., Types of gas fluidization. Powder tech. 7, 285-292 (1973).

Gessner, F. B., The origin of secondary flow in turbulent flow along a corner, J. Fluid Mech. 58, 1-25 (1973).

Gessner, F.B. and Emery, A.F., The numerical prediction of developing turbulent flow in rectangular ducts, Journal of Fluids Engineering, Trans. ASME, 103, 445-455 (1981).

Gessner, F. B. and Po, J. K., A Reynolds stress model for turbulent corner flows-part II: comparisons between theory and experiment, Journal of Fluids Engineering, Trans. ASME, 269-276 (1976).

Ghaly, A., Taweel, A. and Ergudenler, A., Development and evaluation of a straw feeding system for fluidized bed gasifier. Canadian Bioenergy R&D seminar, 3017, 624, 7th 1989. Technical University of Nova Scotia Halifax, Nova Scotia, 297-303 (1989).

Goldsmith, H. L. and Mason, S. G., The microrheology of dispersions, Rheology, edited by F. Eirich (Academic, Oxford), 4, 85–201 (1967).

Goldstein, R.J. and Kreid, D.K., Measurement of laminar flow development in a square duct using a Laser-Doppler flowmeter, Journal of Applied Mechanics, 813-818 (1967).

Gotoh, K., Aoe, K. and Nishimura, T., Effect of nozzle shape and operating conditions on resuspension of single particles by an impinging air jet, J. Aerosol Sci. 31, S837-S838 (2000).

Granatstein, D. L, Case study on Biococomb biomass gasification project Zeltweg power station, Austria, for IEA Bioenergy agreement – Task 36, 2002.

Green, A. and van Ravenswaay, H., Wagner, J. and Green, B., Cherry, T. and Clauson, D., Co-feeding and co-firing biomass with non-hazardous waste and natural gas. Bioresource Technology 36 (3), 215-221 (1991).

Haaker, G., Van Poppelen, M. P., Jongejana, M. P. and Bechuis, J. H., In: Proc. Int. Symp. Reliable Flow of Particulate Solids II, 551–561 (1993).

Haaker, G., Van Poppelen, M. P., Jongejan, M. P. and Bekhuis, J. H., A method to optimize screw feeder geometry for equable draw-down performance. Powder Handling and Processing 6, 209-214 (1994).

Hagiwara, Y., Murata, T., Tanaka, M and Fukawa, T., Turbulence modification by clusters of settling particles in turbulent water flow in a horizontal duct, Powder Technology 125, 158-167 (2002).

Hall, D. O. and Rosillo-Calle, F., Evaluation environmental effects and carbon sources and sinks resulting from biomass production and use in developing countries, in Biomass energy: data, analysis and trends. IEA Conference Proceedings. Paris, France, 267-292, (1998).

Han, L. S., Hydrodynamics entrance lengths for incompressible laminar flow in rectangular ducts, Journal of Applied Mechanics 403-409 (1960).

Hansell, D., Kennedy, I. M. and Kollmann, W., A simulation of particle dispersion in a turbulent jet. Int. J. Multiphase Flow 18, 559-568 (1992).

Hao, X. H., Guo, L. J., Mao, X., Zhang, X. M. and Chen, X. J., Hydrogen production from glucose used as a model compound of biomass gasified in supercritical water. International Journal of Hydrogen Energy 28, 55-64 (2003).

Hartnett, J. P., Kou, J.C.Y. and McComas, S. T., A comparison of predicted and measured friction factors for turbulent flow through rectangular ducts, Transaction of the ASME, 82-88 (1962).

Henrich, E. and Weirich, F., Pressurized entrained flow gasifiers for biomass. Environmental Engineering Science 21, 53-64 (2004).

Henriksen, U., Ahrenfeldt, J., Jensen, T. K., Gøbel, B., Bentzen, J. D., Hindsgaul, C. and Sørensen, L. H., The design, construction and operation of a 75 kW two-stage gasifier. Energy, Article in Press, 2005.

Herrmann, H. J., Andrade Jr., J. S., Araujo, A. D., Almeida, M. P., Transport of particles in fluids. Physica A 372, 374-386 (2006).

Hislop, D and Hall, D. O., Biomass resources for gasification power plant. Energy For Sustainable Development Ltd., University of London, 1996.

Hu, H., Direct simulation of flows of solid-liquid mixtures, International Journal of Multiphase Flow, 22, 335-352 (1996).

Hu, H. H., Joseph, D. D., and Crochet, M. J., Direct simulation of fluid particle motions, Theoretical and Computational Fluid Dynamics 3, 285-306 (2004).

Huber, N. and Sommerfeld, M., Modeling and numerical calculation of dilute-phase pneumatic conveying in pipe systems, Powder Technology 99, 90-101 (1998).

Hughes, W. E. M. and Larson, E. D., Effect of fuel moisture content on biomass-IGCC performance. J. Eng. Gas Turb. Power 120, 455-459 (1998).

IS-8730: 1978: Classification of bulk materials handled by continuous handling equipment; Bureau of Indian standards, New Delhi, India.

Islam, M. S., Haga, K., Kaminaga, M., Hino, R. and Monde, M., Experimental analysis of turbulent flow structure in a fully developed rib-roughened rectangular channel with PIV, Experiments in Fluids 33, 296-306 (2002).

Jenike, A. W., Storage and flow of solids, Bulletin 123, Utah University, 1964.

Jenike, A. W., Load assumptions and distributions in silo design, Paper presented at Conference on Construction of Concrete Silos, Oslo, Norway, January 1977.

Jenike and Johanson, http://www.jenike.com/pages/services/test_equip/rst.html, 2006

Jensen, P. D., Mattssonb, J. E., Kofmana, P. D. and Klausnerc, A., Tendency of wood fuels from whole trees, logging residues and roundwood to bridge over openings. Biomass and Bioenergy 26, 107-113 (2004).

Jong, W., Ünal, O., Andries, J., Hein, K. R. G. and Spliethoff, H., Biomass and fossil fuel conversion by pressurized fluidized bed gasification using hot gas ceramic filters as gas cleaning. Biomass and Bioenergy 25 (1), 59-83 (2003).

Joppich, A. and Salman, H., Wood powder feeding, difficulties and solutions. Biomass and Bioenergy 16, 191-198 (1999).

Keyser, M.J., Conradie, M., Coertzen, M. and Van Dyk, J.C., Effect of coal particle size distribution on packed bed pressure drop and gas flow distribution, Fuel 85, 1439-1445 (2006).

Kerekes, R. J., Perspectives on fibre flocculation in papermaking, in Proceedings of the International Paper Physics Conference, Niagara-on-the-Lake, Ontario, Sept., 1995 (Canadian Pulp and Paper Association, Montreal), 23–31 (1995).

Kerekes, R. J. and Schell, C. J., Characterization of fiber flocculation regimes by a crowding factor, J. Pulp Pap. Sci. 18, J32–J38 (1992).

Kerekes, R. J., Soszynski, R. M. and Tam Doo, P. A., The flocculation of pulp fibers, in Transactions of the 8th Fundamental Research Symposium, Oxford, England, Sept. 1985, edited by V. Punton (Mechanical Engineering, London), 265–309 (1985).

Kim, J., Moin, P.and Moser, R., Turbulence statistics in fully developed channel flow at low Reynolds number, J. Fluid Mech. 177, 133-166 (1987).

Klausner, A., Handling characteristics of wood fuels—tendency to bridge over openings, Thesis, Fachhochschule Rottenburg, 2001.

Klein, A., Review: Turbulent developing pipe flow, J. Fluids Engineering 103, 243-249 (1981).

Koch, T., Winter, E. and Christensen, H., Feed preparation of straw. Prepared by ELKRAFT and the Danish Energy Agency for the IEA Biomass Thermal Gasification Activity, 1996.

Koch, T., http://listserv.repp.org/pipermail/gasification/2002-November/006823.html, 2002.

Kreplin, H and Eckelmann, H., Behavior of the three fluctuating velocity component in the wall region of a turbulent channel flow. Phys. Fluids 22, 1233-1239 (1979).

Kristoffersen, R. and Andersson, H. I., Direct simulation of low Reynolds number turbulent flow in a rotating channel, J. Fluid Mech. 256, 163-197 (1993).

Kumar, A., Passage of fibres through screen apertures, Ph.D. thesis, University of British Columbia, 1990.

Kwant, K. W., Status of Gasification in countries participating in the IEA Bioenergy gasification activity, IEA Bioenergy Gasification Country reports, Netherlands, March 2001.

Kwon, S.B., Kim, M.C., and Lee, K.W., Effects of jet configuration on the performance of multi-nozzle impactors, Aerosol Science 33, 859–869 (2002).

Lau, F. S., The Hawaiian project. Biomass and Bioenerg. 15, 233-238 (1998).

Launder, B. E. and Ying, W. M., Secondary flows in ducts of square cross section, J. Fluid Mech. 54, 289-295 (1972).

Leschziner, M. A. and Rodi, W., Calculation of annular and twin parallel jets using various discretization schemes and turbulence-model variations, Transaction of the ASME 103, 352-360 (1981).

Li, C., Mosyak, A. and Hetsroni, G., Direct numerical simulation of particle-turbulence interaction, International Journal of Multiphase Flow 25, 187-200 (1999).

Li, J., Li, Y., Kawano, H. and Yoder, R. E., Effects of double-rectangular-slot design on impact sprinkler nozzle performance, Transactions of the ASAE, 38, 1435-1441 (1995).

Li, X. T., Grace, J. R., Lim, C. J., Watkinson, A. P., Chen, H. P. and Kim, J. R., Biomass gasification in a circulating fluidized bed. Biomass and Bioenergy 26, 171-193 (2004).

Link Belt Co. (USA): Materials Handling and Processing Equipment-Catalog No. 1000; Chicago, 1959.

Lyons, S. L., Hanratty,T. J. and McLaughlin, J. B., Large-scale computer simulation of fully developed turbulent channel flow with heat heat transfer. Intl. J. Numer. Mech. Fluids 13, 999-1028 (1991).

Manjunath, K, S. and Roberts, A.W., Wall pressure-feeder load interactions in mass flow hopper/feeder combinations, Part I. Bulk Solids Handling 6, 769-775 (1986).

Marcus, R. D., Leung, L. S., Klinzing, G.. E. and Rizk, F., Pneumatic Conveying of Solids, a theoretical and practical approach, Chapman & Hall, New York, 1990.

Marghzar, Sh. H., Montazerin, N. and Rahimzadeh, H., Flow field, turbulence and critical condition at a horizontal water intake, Proc. Inst. Mech. Eng. Part A: J. Power and Energy, 217, 53-62 (2003).

Marinelli, J., All Hoppers Are Not Created Equal, http://www.powderandbulk.com/pb_services/ask_joe_archive/toc.htm, Sept. 1999.

Marinelli, J., How to Design a Volumetric Screw Feeder, Part 1, http://www.solidshandlingtech.com/ask_joe_articles/how_to_design_a_volumetric_screw_feeder.htm, April 1999.

Marinelli, J., Compressibility-What Is It? http://mail.powderandbulk.com/pb_services/ask_joe_archive/compressibility_what_is_it.htm, April, 2000.

Marinelli, J., Factors that impact a Bulk Solid's Flowability, http://www.powderandbulk.com/pb_services/ask_joe_archive/factors_that_impact_flowability.htm, Camber Southeast, Inc., 2004.

Mason, S. G., The flocculation of pulp suspensions and the formation of paper, Tappi J. 33, 440–444 (1950).

Massoudi, M., Constitutive relations for the interaction force in multi-component particulate flows, International Journal of Non-Linear Mechanics 38, 313-336 (2003).

Maton, A. E., Screw feeder design. Powder Handling and Processing 6, 87-89 (1994).

Mattsson, J.E., Basic handling characteristics of wood fuels: angle of repose, friction against surfaces and tendency to bridge for different assortments. Scandinavian Journal of Forest Research 5, 583-597 (1990).

Mattsson, J. E., Tendency to bridge over openings for chopped phalaris and straw of triticum mixed in different proportions with wood chips. Biomass and Bioenergy 12 (3), 199-210 (1997).

Mattsson, J.E and Kofman, P.D., Influence of cutting and storage method on bridging tendency in chips and chunks made from willow shoots. Manuscript. 2001.

Mattsson, J.E. and Kofman, P.D., Method and apparatus for measuring the tendency of solid biofuels to bridge over openings. Biomass and Bioenergy. 22 (3), 179-185 (2002).

Mattsson, J. E. and Kofman, Pieter D., Influence of particle size and moisture content on tendency to bridge in biofuels made from willow shoots. Biomass and Bioenergy. 24 (6), 429-435 (2003).

McComas, S.T., Hydrodynamic entrance lengths for ducts of arbitrary cross section, Journal of basic engineering 847-849 (1967).

McLellan, R., Design of a 2.5MW(e) biomass gasification power generation module, ETSU B/T1/00569/REP, Wellman Process Engineering Limited, 2000.

McLean, A.G. and Arnold, P.C., A simplified approach for the evaluation of feeder loads for mass-flow bins. Journal of Powder and Bulk Solids Technology 3, 25-28 (1979).

McLendona, T. R., Luib, A.P., Pineaulta, R.L., Beer, S.K. and Richardsona, S.W., High-pressure co-gasification of coal and biomass in a fluidized bed. Biomass and Bioenergy 26, 377-388 (2004).

Melling A. and Whitelaw, J. H., Turbulent flow in a rectangular duct, Fluid Mech. 78, 289-315 (1976).

Metcalf, J. R., The mechanics of the screw feeder. Proceedings Institution of Mechanical Engineering 180, 131-146 (1965-1966).

Miller, R. S., Madnia, C. K. and Givi, P. Numerical simulation of non-circular jets, Computers & Fluids 24, l-25 (1995).

Ming, J. Y., Beddow, J. K. and Vetter, A. F., Effects of particle shape on two-phase flow in pipes. Powder Technology 46, 53-60 (1986).

Mory, A. and Zotter, T., EU-demonstration project BioCoComb for biomass gasification and co-combustion of the product-gas in a coal-fired power plant in Austria. Biomass Bioenerg. 15, 239-244 (1998).

Murphy, M. L., Re-powering options: retrofit of coal-fired power boilers using fluidized bed biomass gasification, energy products of Idaho, 2001.

Nadeau, E., Stubly, G. D. and Burns, D. J., Prediction and role of abrasive velocity in abrasive water jet cutting, International Journal of water jet technology, 1, 109-116 (1991).

Nalpanis, P., Hunt, J. C. R. and Barrett, C. F., Saltating particles over flat beds, J. Fluid Mechanics 251, 661-685 (1993).

Nelson, D., Development of a screw feeder for hogged bark and other wood refuse. Pulp & Paper Canada 97, 63-67 (1996).

Nemeca, D. and Levecb, J., Flow through packed bed reactors: 1. Single-phase flow, Chemical Engineering Science 60, 6947-6957 (2005).

Nguyen, Nam-Trung and Wereley, Steven T., Fundamentals and applications of microfluidics, Artech House, Boston, 2002

Nieminen J. and Kivela M. R., Biomass CFB gasifier connected to a 350 MWth steam boiler fired with coal and natural gas - THERMIE demonstration project in Lahti in Finland. Biomass Bioenerg. 15, 251-257 (1998).

Nishimura, K. and Hunt, J. C. R., Saltation and incipient suspension abovea flat particle bed below a turbulent boundary layer, J. Fluid Mech. 417, 77-102 (2000).

Odar, F. and Hamilton, W. S., Forces on a sphere accelerating in a viscous fluid, J. Fluid Mech. 18, 302-310 (1964).

Ogg, J. C., Experimental and computational study of the break-up of laminar slurry jet, Ph.D thesis, Virginia Polytechnic Institute and State University, 1983.

Oka, S. N., Fluidized bed combustion. Technical editor: Anthony, E. J., Marcel Dekker, New York, 2004.

Ondik, Helen M., Christ, Bruce W.and Perloff, Alvin. etc., Construction materials for coal conversion : performance and properties data, prepared for Office of Fossil Energy, U.S. Department of Energy, Washington, D.C. : U.S. Dept. of Commerce, National Bureau of Standards, 1982.

Patel, V. C. and Head, M. R., Some observations on skin friction and velocity profile in fully developed pipe and channel flows, J. Fluid Mech. 38, 181-201 (1969).

Pitcher, K., Hilton, B., and Lundberg, H., The ARBRE project: Progress achieved. Biomass Bioenergy,. 15, 213-218 (1998).

Pletka, R., Brown, R. and Smeenk, J., Indectly heated fluidized bed biomass gasification using a latent heat ballast. BioEnergy '98: Expanding BioEnergy Partnerships, Center for Coal and the Environment, Iowa State University, USA.

Quaak, P., Knoef, H. and Stassen, H., Energy from biomass: a review of combustion and gasification technologies, World Bank Technical Paper No. 422, 1999

Rautenbach, R. and Schumacher, W., Theoretical and experimental analysis of screw feeders. Bulk Solids Handling 7, 675-680 (1987).

Rautalin, A., and Wilen, C., Feeding Biomass Into Pressure and Related Safety Engineering. VVT Research Notes No.1428, VVT Technical Research Center of Finland, Espoo, Finland.Task Study Report prepared for the IEA Biomass Thermal Gasification Activity (1992-1994). 1992.

Reed, T. B., Biomass gasification: principles and technology, energy technology review, Park Ridge, N.J.: Noyes Data Corp., 1981.

Rembold, B., Adams, N.A. and Kleiser, L., Direct numerical simulation of a transitional rectangular, International Journal of Heat and Fluid Flow 23, 547-553 (2002).

Richards, J. C., The storage and recovery of particulate solids, Inst. Chem. Engrs. Working Party Report, 1966.

Roberts, A. W., Determining screw geometry for specified hopper draw-down performance, Proc. Bulk 2000 Conference, Institution of Mechanical Engineers, London, 111–116, Oct. 1991.

Roberts, A. W., Basic principles of bulk solids storage, flow and handling, The Institute for Bulk Materials Handling Research, The University of Newcastle, 1992.

Roberts, A. W. and Manjunath, K.S., Volumetric and torque characteristics of screw feeders, Proc. Powder and Bulk Solids Conference, Rosemont, USA, 189-208, May 1994.

Roberts, A. W., Predicting the volumetric and torque characteristics of screw feeders. Bulk Solids Handling 16, 233-244 (1996).

Rudinger, G., Fundamentals of gas particle flow, Elsevier Scientific, Amsterdam, 1980.

Saffman, P., The lift on a small sphere in a low shear flow, Journal of Fluid Mechanics 22, 385-400 (1965).

Sattarifar, I., Failure study of plug screw feeder of the MWPC complex: Part B—material characterization and fractography. Repart No. MAKU-02-03, Mech. Dept. of Amirkabir University, Tehran, Iran, 2002.

Sattarifar, I., Failure study of connecting shafts of a plug screw feeder in a paper production plants. Engineering Failure Analysis 10, 1-9 (2003).

Savolainen, K., Co-firing of biomass in coal-fired utility boilers. Applied Energy 74 369-381 (2003).

Schmid, C. F., Switzer, L. H. and Klingenberg, D. G., Simulations of fiber flocculation: Effects of fiber properties and interfiber friction. J. Rheol. 44, 781-809 (2000).

Shieh, C. F., Numerical solutions of atmospheric flow over semielliptical simulated hills, Ph.D. thesis, University of Tennessee, 1980.

Soo, S. L., "Multiphase Fluid Dynamics", Beijing: Science Press; Brookfield, Vt.: Gower Technical, 1990.

Sovran, G. and Klomp, E., Experimentally determined optimum geometries for rectilinear diffuser with rectangular, conical or annular cross section, in Fluid Mechanics of Internal Flow (ed.: Sovran, G), Elsevier Publishing Company, Amsterdam, 1967.

Spalart, P. R., Direct simulation of a turbulent boundary layer up to Re=1410. J. Fluid Mech. 187, 61-98 (1988).

Sparrow, E. M., Hixon, C. W. and Shavit, G., Experiments on laminar flow development in rectangular ducts, Journal of Basic Engineering, Trans. ASME, 89, 116-124 (1967).

Su, M. D..and Friedrich, D., Investigation of fully developed turbulent flow in a straight duct with large eddy simulation, J. Fluids Engineering, Trans. ASME, 116, 677-684 (1994).

Tanida, Kei-Ich, Honda, Kouji, Kawano, Nobuaki, Kawaguchi, Toshihiro, Tanaka, Toshitsugu and Tsuji, Yutaka, Particle Motion in Screw Feeder Simulated by Discrete Element Method, International Conference on Digital Printing Technologies, 429-431 (1998).

Tardos, Gabriel I., Stress in Bins and Hoppers, http://www.erpt.org/992Q/tard-00.htm, 1999.

Tazibt, A. Q., Parsy, F. and Abriak, N., Theoretical Analysis of the Particle Acceleration Process in Abrasive Water Jet Cutting. Computational Material Science 5, 243-254 (1996).

Thomson, F. M., Handbook of Powder Science and Technology, 2nd edition, ed. Fayed, M. E. and Otten, L., Chapman and Hall, New York, 1997.

Tillman, D. A., Biomass cofiring: the technology, the experience, the combustion consequences. Biomass and Bioenergy 19, 365-384 (2000).

TK Energi, http://www.tke.dk/Sider/feeding+biomass.htm, 2006.

Tomas, J. and Schubert, H., Particle characterization. Partec 79, Nurnberg, Germany, 301-319 (1979).

Tsai, W. R. and Lin, C, I., On the mixing of granular materials in a screw feeder. Powder Technology 80, 119-126 (1994).

Turn, S., Demonstration-scale biomass gasification facility operates on bagasse, International cane energy news, 4-5 (1977).

Uchiyama T. and Naruse, M., Vortex simulation of slit nozzle gas-particle two-phase jet, Powder Technology 131, 156-165 (2003).

UONDEERC (University of North Dakota Energy and Environmental Research center) and GEI (Global Energy, Inc.) www.netl.doe.gov, 2001.

van den Enden, P. J. and Lora, E. S., Design approach for a biomass fed fluidized bed gasifier using the simulation software CSFB. Biomass and Bioenergy 26, 281-287 (2004).

van der Drift, A., de Kant, H. F., Rajani, J. B. and Hengelo, H., Commercialization of BIVKIN-Based gasification technology, Report, August 2000.

van der Drift, A., van Doorn, J. and Vermeulen, J. W., Ten residual biomass fuels for circulating fluidized-bed gasification. Biomass and Bioenergy 20, 45-56 (2001).

van der Drift A., Boerrigter, H., Coda, B., Cieplik, M. K. and Hemmes, K., Entrained flow gasification of biomass: ash behavior, feeding issues, and system analyses, ECN-C--04-039, 2004.

van der Kooi, Silo design: well begun is half done. Powder Handling Processing 9, 326-328 (1997).

Vriesman, P., Heginuz, E. and Sjostrom, K., Biomass gasification in a laboratory-scale AFBG: influence of the location of the feeding point on the fuel-N conversion. Fuel 79, 1371–1378 (2000).

Waldheim, L. and Carpentieri, E., Update on the progress of the Brazilian wood BIG-GT demonstration project. J. Eng. Gas Turb. Power 123, 525-536 (2001).

Wiginton, C. L. and Dalton, C., Incompressible laminar flow in the entrance region of a rectangular duct, Journal of applied mechanics, Trans.ASME, 854-856 (1970).

Wilén, C. and Rautalin, A., Handling and feeding of biomass to pressurized reactors: Safety engineering, Bioresource Technology, 46, 77-85 (1993).

Willeboer, W., The Amer demolition wood gasification project. Biomass Bioenerg. 15, 245-249 (1998).

Willetts, B.B., Rice, M.A., Intersaltation collisions. In: Barndorff-Nielsen, O.E. (Ed.), Proceedings of international workshop on the physics of blown sand 1, University of Aarhus, Denmark, 83-100 (1985).

Wilson, D. H., Feeding technology for plastic processing, Hanser/Gardner Publications, Cincinnati, 1998.

Wilson, D. H. and Dunnington, D. L., To avoid feeding problems. Chemical Engineering 72-81 (1991).

White, B. R., Schulz, J. C., Magnus effect in saltation, J. of Fluid Mechanics 81, 497−512 (1977).

White, Bruce R. and Tsoar, H., Slope effect on saltation over a climbing sand dune, Geomorphology 22, 159-180 (1998).

Ye, J., Swanson, T. R. and Richards, C. D., Particle transport and dispersion in the near field of a turbulent jet, American Society of Mechanical Engineers, Fluids Engineering Division, Gas-Particle Flows, 228, 89-94 (1995).

Ye, J. and Kovacevic, R., Turbulent solid-liquid flow through the nozzle of premixed abrasive water jet cutting systems, Proceedings of the Institution of Mechanical Engineers, Part B: Journal of Engineering Manufacture, 213, 59-67 (1999).

Yu, Y and Arnold, P. C., Estimate of the volumetric efficiency of a screw feeder, Proc. 5th International Conference on Bulk Material Storage, Handling and Transportation, Newcastle, Australia, 517-522, July 1995.

Yu, Y. and Arnold, P.C., On hopper geometry interfacing with a screw feeder to achieve uniform draw-down performance. Powder Handling & Processing 8, 321-328 (1996).

Yu, Y. and Arnold, P. C., Theoretical modeling of torque requirements for single screw feeders. Powder Technology 93, 151-162 (1997).

Zhang, W, Kang, J. H. and Lee, S. J., Tracking of saltating sand trajectories over a flat surface embedded in an atmospheric boundary layer, Geomorphology (2006).

Zhang, X. H., Wang H. T., Dong, Z. B., Ayrault, M., Experimental determination of the concentration Probability Density Function for a saltating particle layer, C. R. Mecanique 334 13–18 (2006).

Zheng, X. J., Xie, L.and Zhou, Y. H., Exploration of probability distribution of velocities of saltating sand particles based on the stochastic particle–bed collisions, Physics Letters A 341, 107–118 (2005).

# APPENDICES

## Appendix A Program Listings for Fourth-Order Runge-Kutta Method with Variable Stepsize for Particulate Flow Loop

File name: PFL_RK2.m
Function: rkfuncp, funnp, sovle_dupdt
Source code: see below

```
%-----------------------------------------------------------------------------------------------------------------------
% PFL_RK4.m
% Compute water velocity and particle velocity using Runge-Kutta RK4 algorithm
% with variable steps
clc
clear

n=600;          % iteration number
h=0.01;         % h is the time step
un=(n-1)*h;
t=[0:h:un];     % initialize time variable.

delta0=1e-6;
delta1=1;
hh=0;
guess=1;
x=zeros(1,n);     % intialize x, u, up
u=zeros(1,n);
up=zeros(1,n);
x(1)=0.0331;      % initial condition for x,u and up
u(1)=0.4663;
up(1)=0.2947;
w1=zeros(3,1);    % vector used to store K1 and L1 in RK4.
w2=zeros(3,1);    % vector used to store K2 and L2 in RK4.
w3=zeros(3,1);    % vector used to store K3 and L3 in RK4.
w4=zeros(3,1);    % vector used to store K4 and L4 in RK4.

for j=1:1:n-1
while delta1>1.01*delta0        % criterion to change time and recalculate
w1=h*rkfuncp(t(j),x(j),u(j),up(j),guess);      % w=[K,L];
w2=h*rkfuncp((t(j)+h./2),x(j)+w1(1)./2,u(j)+w1(2)./2,up(j)+w1(3)./2,guess);
w3=h*rkfuncp((t(j)+h./2),x(j)+w2(1)./2,u(j)+w2(2)./2,up(j)+w2(3)./2,guess);
w4=h*rkfuncp((t(j)+h),x(j)+w3(1),u(j)+w3(2),up(j)+w3(3),guess);
x(j+1)=x(j)+(w1(1)+2*(w2(1)+w3(1))+w4(1))./6;     % compute x,u and up at j+1
u(j+1)=u(j)+(w1(2)+2*(w2(2)+w3(2))+w4(2))./6;
up(j+1)=up(j)+(w1(3)+2*(w2(3)+w3(3))+w4(3))./6;
vv0=[x(j+1),u(j+1),up(j+1)];                  % store x,u,up in vv0
h=h./2;                                       % replace h by h/2
w1=h*rkfuncp(t(j),x(j),u(j),up(j),guess);      % w=[K,L];
w2=h*rkfuncp((t(j)+h./2),x(j)+w1(1)./2,u(j)+w1(2)./2,up(j)+w1(3)./2,guess);
w3=h*rkfuncp((t(j)+h./2),x(j)+w2(1)./2,u(j)+w2(2)./2,up(j)+w2(3)./2,guess);
w4=h*rkfuncp((t(j)+h),x(j)+w3(1),u(j)+w3(2),up(j)+w3(3),guess);
x1(j)=x(j)+(w1(1)+2*(w2(1)+w3(1))+w4(1))./6;      % value of x, u and up at h/2
u1(j)=u(j)+(w1(2)+2*(w2(2)+w3(2))+w4(2))./6;
up1(j)=up(j)+(w1(3)+2*(w2(3)+w3(3))+w4(3))./6;
w1=h*rkfuncp(t(j),x1(j),u1(j),up1(j),guess);          % w=[K,L];
w2=h*rkfuncp((t(j)+h./2),x1(j)+w1(1)./2,u1(j)+w1(2)./2,up1(j)+w1(3)./2,guess);
w3=h*rkfuncp((t(j)+h./2),x1(j)+w2(1)./2,u1(j)+w2(2)./2,up1(j)+w2(3)./2,guess);
```

```
w4=h*rkfuncp((t(j)+h),x(j)+w3(1),u(j)+w3(2),up(j)+w3(3),guess);
x(j+1)=x1(j)+(w1(1)+2*(w2(1)+w3(1))+w4(1))./6;     % value of x,u and up at h using h/2 method (j+1)
u(j+1)=u1(j)+(w1(2)+2*(w2(2)+w3(2))+w4(2))./6;
up(j+1)=up1(j)+(w1(3)+2*(w2(3)+w3(3))+w4(3))./6;
vv1=[x(j+1),u(j+1),up(j+1)];                    % store x,u,up in vv1
delta1=max(abs(vv1-vv0));                       % compute delta1 using vv1 and vv0
hh=2*h;
h0=2*h*((delta0./delta1).^0.2);                 % change h value
h=h0;
end
t(j+1)=t(j)+hh;
delta1=1;
t1=0.41;          % 0.4 s is the final time point for R-K with variable step

if t(j+1)>=t1
h2=t1-t(j);
w1=h*rkfuncp(t(j),x(j),u(j),up(j),guess);       % w=[K,L];
w2=h*rkfuncp((t(j)+h2./2),x(j)+w1(1)./2,u(j)+w1(2)./2,up(j)+w1(3)./2,guess);
w3=h*rkfuncp((t(j)+h2./2),x(j)+w2(1)./2,u(j)+w2(2)./2,up(j)+w2(3)./2,guess);
w4=h*rkfuncp((t(j)+h2),x(j)+w3(1),u(j)+w3(2),up(j)+w3(3),guess);
x(j+1)=x(j)+(w1(1)+2*(w2(1)+w3(1))+w4(1))./6;  % compute x,u and up at j+1
u(j+1)=u(j)+(w1(2)+2*(w2(2)+w3(2))+w4(2))./6;
up(j+1)=up(j)+(w1(3)+2*(w2(3)+w3(3))+w4(3))./6;
t(j+1)=t1;
break;
end
end

for i=1:j+1
   tp(i)=t(i);
end
for i=1:j+1
   uu(i)=u(i);
end
for i=1:j+1
   uup(i)=up(i);
end

tt=[0:0.0333:0.5667];  % This is the experimental data for particle velocity. But I only draw t=[0-0.4] in the figure.
e=[0.2974,0.2963,0.3048,0.3112,0.3112,0.3366,0.3588,0.3969,0.4699,0.6509,0.8020,0.7315,0.5459,0.3939,0.2858,
0.4128,0.4889,0.4667];
position=[0.0331, 0.0430, 0.0529, 0.0631, 0.0734, 0.0838, 0.0950, 0.1070, 0.1202, 0.1359, 0.1576, 0.1843, 0.2087,
0.2269,0.2400, 0.2496, 0.2633, 0.2796];

fprintf ('\n %10.6f\n ');      % plot the figute
fprintf ('\n    t     \n\n');
for i=1:j+1
fprintf('%12.6f  %12.6f  %12.6f\n', uup(i));
fprintf('\n');
end

plot(tp,uu,'.',tp,uup,'*');    % plot calculated water velocity and particle velocity.
axis([0,0.4,0,1.28]);
xlabel('time (s)');
ylabel('Water Velocity U and Particle Velocity Up');
title('Calculated Water Velocity U and Calculated Particle Velocity Up');
legend('Calculated Water Velocity U','Calculated Particle Velocity Up');
```

```
figure;

plot(tp,uup,'-',tt,e,'*', tt, position, 'o');    % plot experimental data and calculated data for particle velocity.
axis([0,0.4,0,1.28]);
xlabel('Time (s)');
ylabel('Particle velocity in horizontal direction (m/s)');
legend('Calculated particle velocity','Experimental data of particle velocity');
%-----------------------------------------------------------------------------------------------------------------------------------------
```

Functions for program
Function name: rkfuncp, funnp, sovle_dupdt
Source code: see below

```
%-----------------------------------------------------------------------------------------------------------------------------------------

function ff=rkfuncp(t,x,u,up,guess)
dxdt=u;
dudt=(-3313.2.*x^3+803.37.*x^2-19.54.*x+0.41).*u;
ff=[dxdt;dudt;sovle_dupdt(u,up,dudt,guess)];
%-----------------------------------------------------------------------------------------------------------------------------------------

function y=funnp(u,up,dudt,x1)

global dp Dh cdd Re Ret cddt j
dp=0.0115;
Dh=0.0367;
Re=dp*(u-up)*998/0.001;
cd0=21./Re+6/(Re.^0.5)+0.28;
KF=1/(1-1.6*(dp./Dh)^1.6);
cdd=cd0*KF;
Ret(j)=Re;
cddt(j)=cdd;
y=(0.125*3.14*dp^2*cdd*998*(u-up).^2+3.14*dp.^3*998/12*(dudt-
x1)).*6./((3.14*dp.^3).*1019)+998./1019*dudt;
%-----------------------------------------------------------------------------------------------------------------------------------------

function x=sovle_dupdt(u,up,dudt,x1)
% Successive Substitution for one-dimensional root finding
% find dup/dt
% x1 is guess for dup/dt, dudt is known value for relevant du/dt

   y1 = funnp(u,up,dudt,x1);
   while abs(y1-x1)>1e-8
      x1=y1;
      y1 = funnp(u,up,dudt,x1);
   end
   x=y1;
   return;
%-----------------------------------------------------------------------------------------------------------------------------------------
```

## Appendix B Materials Size Distributions

Table B-1. Size distribution of biomass materials (sieve analysis).

(1) Size distribution density

| $d_p$ | $f_i$, (%) | | | | |
|---|---|---|---|---|---|
| (mm) | Sawdusts-1 | Hog fuel | Ground hog fuel | Wood shavings-1 | Ground wood pellets-2 |
| 0.09[1] | 2.33 | 0.94 | 12.56 | 2.02 | 1.50 |
| 0.25 | 8.81 | 7.37 | 31.57 | 6.22 | 6.34 |
| 0.5 | 17.97 | 11.67 | 26.69 | 8.82 | 13.90 |
| 0.71 | 14.14 | 6.22 | 9.92 | 4.85 | 12.35 |
| 1 | 18.38 | 7.26 | 10.40 | 7.39 | 18.12 |
| 1.4 | 17.10 | 7.64 | 5.49 | 8.95 | 18.87 |
| 1.7 | 8.83 | 5.60 | 1.90 | 7.12 | 11.74 |
| 2 | 4.75 | 4.40 | 0.61 | 4.96 | 7.56 |
| 2.8 | 5.84 | 10.21 | 0.59 | 14.02 | 9.34 |
| 6.73 | 1.85 | 25.35 | 0.25 | 28.43 | 0.28 |
| 9.5 | 0 | 3.42 | 0 | 0 | 0 |
| 12.5 | 0 | 3.02 | 0 | 7.22 | 0 |
| 25 | 0 | 6.90 | 0 | 0 | 0 |
| mean $\overline{d}$ [2] | 0.45 | 0.72 | 0.18 | 0.67 | 0.55 |
| Initial mass (g) | 180 | 180 | 100 | 70 | 180 |

Notes: [1] upper limit of a sieve size range; [2] - See Chapter 4, Eq. (4-4) for definition.

(2) Cumulative size distribution (sieve analysis)

| $d_p$ | $\Sigma f_i$, (%) | | | | |
|---|---|---|---|---|---|
| (mm) | Sawdusts-1 | Hog fuel | Ground hog fuel | Wood shavings-1 | Ground wood pellets-2 |
| 0.09 | 33.2 | 0.94 | 12.56 | 2.02 | 1.50 |
| 0.25 | 11.15 | 8.31 | 44.13 | 8.24 | 7.84 |
| 0.5 | 29.11 | 19.98 | 70.82 | 17.06 | 21.74 |
| 0.71 | 43.26 | 26.20 | 80.75 | 21.91 | 34.08 |
| 1 | 61.63 | 33.45 | 91.14 | 29.30 | 52.21 |
| 1.4 | 78.74 | 41.10 | 96.63 | 38.25 | 71.08 |
| 1.7 | 87.56 | 46.70 | 98.54 | 45.37 | 82.82 |
| 2 | 92.31 | 51.10 | 99.15 | 50.33 | 90.38 |
| 2.8 | 98.15 | 61.30 | 99.75 | 64.36 | 99.72 |
| 6.73 | 100.00 | 86.66 | 100.00 | 92.78 | 100.00 |
| 9.5 | | 90.08 | | N/A | |
| 12.5 | | 93.10 | | 100 | |
| 25 | | 100.00 | | | |

## Appendix C Stress Ratio of Bulk Solid Sliding on Confined Surface

A Mohr circle diagram is shown in Figure C-1. This is used to represent the stress of a material element on a confining surface.

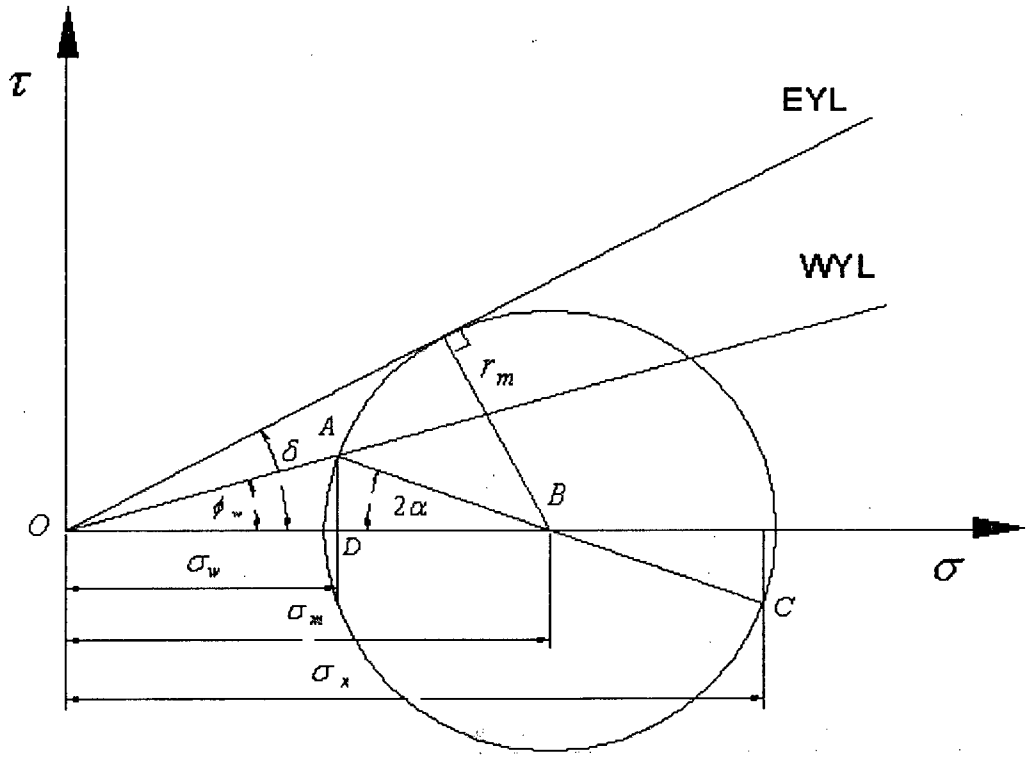


Figure C-1. Mohr circle representation of stress in a material element on a confining surface

Considering the geometry of the Mohr circle and using the sine rule in the triangle AOB in Figure C-1, we obtain:

$$\frac{r_m}{\sin\phi_w} = \frac{OD}{\cos\phi_w \sin 2\alpha} = \frac{OB}{\sin(180-(\phi_w+2\alpha))} \tag{C-1}$$

$$\frac{r_m}{\sin\phi_w} = \frac{r_m}{\sin\delta \sin(180-(\phi_w+2\alpha))} \tag{C-2}$$

From Equation C-1, we obtain

$$\frac{r_m \cos 2\alpha + OB}{\sin\phi_w \cos 2\alpha + \sin(\phi_w + 2\alpha)} = \frac{OD}{\cos\phi_w \sin 2\alpha} \quad \text{(C-3)}$$

The stress ratio of the bulk solid sliding on a confined surface can be written (see Equation 6-62) as

$$\lambda_s = \frac{\sigma_w}{\sigma_x} = \frac{OD}{r_m \cos 2\alpha + OB} = \frac{\cos\phi_w \sin 2\alpha}{\sin\phi_w \cos 2\alpha + \sin(\phi_w + 2\alpha)} \quad \text{(C-4)}$$

From Equation C-2, we obtain

$$\sin\phi_w = \sin\delta \sin(\phi_w + 2\alpha) \quad \text{(C-5)}$$

or

$$2\alpha = \arcsin(\frac{\sin\phi_w}{\sin\delta}) - \phi_w \quad \text{(C-6)}$$

We can get

$$2\alpha = 2\beta - 2\phi_w \quad \text{(C-7)}$$

where

$$\beta = \frac{1}{2}\left[\phi_w + \arcsin(\frac{\sin\phi_w}{\sin\delta})\right] \quad \text{(C-8)}$$

In Equation (C-6)-(C-8), $\phi_w$, $\delta$, $\alpha$ and $\beta$ are all in radians.

## Appendix D Tangential Force on Driving Flight

The tangential force acting on the material element in a pocket due to the driving flight (see Equation 6-83) is

$$dF_{dt} = \sigma_{da} r d\theta dr \tan(\alpha_r + \phi_f) \tag{D-1}$$

Substituting $\tan\alpha_r = P/2\pi r$ and $\tan\phi_f = \mu_f$ and integrating for $\theta$ from 0 to $2\pi$, the following equation is obtained:

$$F_{dt} = 2\pi\sigma_{da}\int_{R_c}^{R_o} r\left(\frac{1+\dfrac{2\pi\mu_f r}{P}}{\dfrac{2\pi r}{P}-\mu_f}\right)dr \tag{D-2}$$

let $x = r/P$, then

$dr = Pdx$

$x = R_c/P$ at $r = R_c$

$x = R_o/P$ at $r = R_o$

Equation D-2 becomes

$$F_{dt} = 2\pi P^2\sigma_{da}\int_{R_c/P}^{R_o/P}\left(\frac{x+2\pi\mu_f x^2}{2\pi x-\mu_f}\right)dx \tag{D-3}$$

let $y = 2\pi x - \mu_f$, then

$$dx = \frac{dy}{2\pi}$$

$$x = \frac{y+\mu_f}{2\pi}$$

Equation D-3 becomes

$$F_{dt} = 2\pi P^2 \sigma_{da} \int_{2\pi R_c / P - \mu_f}^{2\pi R_o / P - \mu_f} \left( \frac{1 + 2\mu_f^2}{4\pi^2} + \frac{\mu_f + \mu_f^3}{4\pi^2 y} + \frac{\mu_f y}{4\pi^2} \right) dy \tag{D-4}$$

The solution of Equation D-4 is

$$F_{dt} = 2\pi P^2 \sigma_{da} \left[ \frac{\mu_f}{2} \left( \frac{R_o^2}{P^2} - \frac{R_c^2}{P^2} \right) + \frac{1 + \mu_f^2}{2\pi} \left( \frac{R_o}{P} - \frac{R_c}{P} \right) + \frac{\mu_f (1 + \mu_f^2)}{4\pi^2} \ln \left( \frac{2\pi R_o - P\mu_f}{2\pi R_c - P\mu_f} \right) \right] \tag{D-5}$$

Employing non-dimensional parameters, i.e.

$$c_d = \frac{R_c}{R_o} = \frac{D_c}{D_o}$$

$$c_p = \frac{P}{D_o}$$

Equation D-5 becomes

$$F_{dt} = 2\pi \sigma_{da} D_o^2 \left[ \frac{\mu_f}{8} (1 - c_d^2) + \frac{1 + \mu_f^2}{4\pi} c_p (1 - c_d) + \frac{\mu_f (1 + \mu_f^2) c_p^2}{4\pi^2} \ln \left( \frac{\frac{\pi}{c_p} - \mu_f}{\frac{\pi c_d}{c_p} - \mu_f} \right) \right] \tag{D-6}$$

Equation D-2 can also be solved using numerical methods.

## Appendix E Torque Generated by Driving Side of Screw

The torque generated by driving side of the screw (see Equation 6-92) is

$$T_d = 2\pi\sigma_{da}\int_{R_c}^{R_o} r^2 \tan(\alpha_r + \phi_f)dr \tag{E-1}$$

Substituting $\tan\alpha_r = P/2\pi r$ and $\tan\phi_f = \mu_f$ and integrating for $\theta$ from 0 to $2\pi$, the following equation is obtained:

$$T_d = 2\pi\sigma_{da}\int_{R_c}^{R_o} r^2 \left( \frac{1+\dfrac{2\pi\mu_f r}{P}}{\dfrac{2\pi r}{P}-\mu_f} \right) dr \tag{E-2}$$

Let $x = r/P$, then

$dr = Pdx$

$x = R_c/P$ at $r = R_c$

$x = R_o/P$ at $r = R_o$

Hence

$$T_d = 2\pi P^3\sigma_{da}\int_{R_c/P}^{R_o/P} \left( \frac{x^2 + 2\pi\mu_f x^3}{2\pi x - \mu_f} \right) dx \tag{E-3}$$

Let $y = 2\pi x - \mu_f$, then

$$dx = \frac{dy}{2\pi}$$

$$x = \frac{y+\mu_f}{2\pi}$$

Equation E-3 becomes

$$T_d = 2\pi P^3 \sigma_{da} \int_{2\pi R_c / P - \mu_f}^{2\pi R_o / P - \mu_f} \left( \frac{(y+\mu_f)^2 + \mu_f (y+\mu_f)^3}{8\pi^3 y} \right) dy \qquad \text{(E-4)}$$

Employing non-dimensional parameters, i.e.

$$c_d = \frac{R_c}{R_o} = \frac{D_c}{D_o}$$

$$c_p = \frac{P}{D_o}$$

The solution of Equation E-4 is

$$T_d = D_o^3 \sigma_{da} \left[ \frac{\pi \mu_f (1-c_d^3)}{12} + \frac{(1+\mu_f^2)(1-c_d^2)c_p}{8} + \frac{\mu_f (1+\mu_f^2)(1-c_d)c_p^2}{4\pi} + \frac{\mu_f^2 (1+\mu_f^2)c_p^3}{4\pi^2} \ln\left( \frac{\frac{\pi}{c_p} - \mu_f}{\frac{\pi c_d}{c_p} - \mu_f} \right) \right]$$

(E-5)

Equation E-2 can also be solved using numerical methods.

## Appendix F Torque Generated by Trailing Side of Screw

The torque generated by the trailing side of the screw flight (see Equation 6-96) is

$$T_f = \lambda_s \sigma_v \int_{R_c}^{R_o} \frac{\sin(\phi_f - \alpha_r) r^2 dr}{\cos\alpha_r \cos\phi_f} \int_0^{2\pi} d\theta = 2\pi\lambda_s \sigma_v \int_{R_c}^{R_o} \frac{\sin(\phi_f - \alpha_r)}{\cos\alpha_r \cos\phi_f} r^2 dr \qquad \text{(F-1)}$$

where $\sin(\phi_f - \alpha_r) = \sin\phi_f \cos\alpha_r - \cos\phi_f \sin\alpha_r$.

Hence Equation F-1 becomes

$$T_f = 2\pi\lambda_s \sigma_v \int_{R_c}^{R_o} (\tan\phi_f - \tan\alpha_r) r^2 dr \qquad \text{(F-2)}$$

Substituting $\tan\alpha_r = P/2\pi r$ and $\tan\phi_f = \mu_f$ and integrating for $r$ from $R_c$ to $R_o$, the following equation is obtained:

$$T_f = 2\pi\lambda_s \sigma_v \int_{R_c}^{R_o} \left( \mu_f r^2 - \frac{P}{2\pi} r \right) dr \qquad \text{(F-3)}$$

Integrating Equation F-3 yields

$$T_f = \left[ \frac{\pi\lambda_s \mu_f (1 - c_d^3)}{12} - \frac{\lambda_s c_p (1 - c_d^2)}{8} \right] \sigma_v D_o^3 \qquad \text{(F-4)}$$

## Appendix G Listings of Experimental Data Samples

G-1. Torque and Power Readings

G-1-1. Hog fuel-1 (40 rpm for screw-1 at 0.45 m hopper level)

| Number | Time (s) | Time (min) | Torque reading (N. m) | Screw speed (rpm) | Power (N. m/s) |
|---|---|---|---|---|---|
| 1 | 0.000 | 0.000 | 2.429 | 0 | 0.000 |
| 2 | 0.021 | 0.000 | 2.542 | 0 | 0.000 |
| 3 | 0.043 | 0.001 | 2.711 | 0.85 | 0.000 |
| 4 | 0.066 | 0.001 | 2.937 | 0.85 | 0.257 |
| 5 | 0.090 | 0.001 | 3.107 | 1.7 | 0.543 |
| 6 | 0.114 | 0.002 | 3.333 | 3.4 | 0.860 |
| 7 | 0.138 | 0.002 | 3.558 | 5.1 | 1.207 |
| 8 | 0.161 | 0.003 | 3.784 | 6.8 | 2.359 |
| 9 | 0.186 | 0.003 | 4.067 | 8.5 | 3.214 |
| 10 | 0.255 | 0.004 | 4.914 | 14.45 | 6.760 |
| 11 | 0.280 | 0.005 | 5.253 | 17 | 7.967 |
| 12 | 0.303 | 0.005 | 5.592 | 19.55 | 10.844 |
| 13 | 0.329 | 0.005 | 5.931 | 21.25 | 12.434 |
| 14 | 0.353 | 0.006 | 6.270 | 23.8 | 14.666 |
| 15 | 0.447 | 0.007 | 7.795 | 30.6 | 23.941 |
| 16 | 0.515 | 0.009 | 9.094 | 34 | 30.601 |
| 17 | 0.539 | 0.009 | 9.546 | 34.85 | 32.794 |
| 18 | 0.563 | 0.009 | 9.941 | 34.85 | 36.088 |
| 19 | 0.588 | 0.010 | 10.280 | 35.7 | 38.025 |
| 20 | 0.611 | 0.010 | 10.506 | 36.55 | 38.870 |
| 21 | 0.635 | 0.011 | 10.675 | 36.55 | 40.444 |
| 22 | 0.662 | 0.011 | 10.845 | 37.4 | 42.491 |
| 23 | 0.686 | 0.011 | 10.958 | 37.4 | 42.934 |
| 24 | 0.709 | 0.012 | 11.071 | 38.25 | 43.155 |
| 25 | 0.779 | 0.013 | 11.353 | 38.25 | 45.041 |
| 26 | 0.804 | 0.013 | 11.410 | 39.1 | 46.736 |
| 27 | 0.828 | 0.014 | 11.523 | 39.1 | 46.967 |
| 28 | 0.852 | 0.014 | 11.579 | 39.1 | 47.431 |
| 29 | 0.876 | 0.015 | 11.692 | 39.1 | 47.662 |
| 30 | 0.900 | 0.015 | 11.805 | 39.1 | 48.356 |
| 31 | 0.926 | 0.015 | 11.918 | 39.1 | 48.819 |
| 32 | 0.949 | 0.016 | 12.031 | 39.1 | 49.050 |
| 33 | 0.973 | 0.016 | 12.144 | 39.1 | 49.513 |
| 34 | 1.041 | 0.017 | 12.483 | 39.1 | 51.132 |
| 35 | 1.066 | 0.018 | 12.652 | 39.1 | 51.595 |
| 36 | 1.090 | 0.018 | 12.765 | 39.1 | 52.058 |
| 37 | 1.114 | 0.019 | 12.935 | 39.95 | 52.752 |
| 38 | 1.139 | 0.019 | 13.161 | 39.95 | 54.371 |
| 39 | 1.164 | 0.019 | 13.387 | 39.95 | 55.790 |
| 40 | 1.188 | 0.020 | 13.669 | 39.95 | 56.736 |

| Number | Time (s) | Time (min) | Torque reading (N. m) | Screw speed (rpm) | Power (N. m/s) |
|---|---|---|---|---|---|
| 41 | 1.214 | 0.020 | 14.064 | 39.95 | 57.917 |
| 42 | 1.238 | 0.021 | 14.516 | 39.95 | 59.336 |
| 43 | 1.307 | 0.022 | 15.759 | 39.1 | 64.089 |
| 44 | 1.332 | 0.022 | 16.154 | 39.1 | 65.477 |
| 45 | 1.356 | 0.023 | 16.437 | 39.1 | 66.634 |
| 46 | 1.380 | 0.023 | 16.663 | 39.1 | 67.559 |
| 47 | 1.404 | 0.023 | 16.832 | 39.1 | 68.948 |
| 48 | 1.427 | 0.024 | 17.002 | 39.1 | 69.642 |
| 49 | 1.452 | 0.024 | 17.171 | 39.1 | 70.105 |
| 50 | 1.476 | 0.025 | 17.227 | 39.1 | 70.336 |
| 51 | 1.499 | 0.025 | 17.284 | 39.1 | 70.798 |
| 52 | 1.571 | 0.026 | 17.114 | 39.95 | 71.865 |
| 53 | 1.598 | 0.027 | 16.945 | 39.95 | 71.392 |
| 54 | 1.622 | 0.027 | 16.776 | 39.95 | 70.210 |
| 55 | 1.647 | 0.027 | 16.606 | 39.95 | 69.738 |
| 56 | 1.671 | 0.028 | 16.493 | 39.95 | 69.265 |
| 57 | 1.695 | 0.028 | 16.437 | 39.95 | 69.028 |
| 58 | 1.720 | 0.029 | 16.380 | 39.95 | 68.555 |
| 59 | 1.745 | 0.029 | 16.380 | 39.95 | 68.555 |
| 60 | 1.769 | 0.029 | 16.380 | 39.95 | 68.555 |
| 61 | 1.838 | 0.031 | 16.324 | 39.95 | 68.555 |
| 62 | 1.868 | 0.031 | 16.154 | 39.95 | 67.846 |
| 63 | 1.897 | 0.032 | 15.928 | 39.95 | 67.373 |
| 64 | 1.922 | 0.032 | 15.702 | 39.95 | 65.955 |
| 65 | 1.952 | 0.033 | 15.420 | 39.95 | 65.009 |
| 66 | 1.976 | 0.033 | 15.250 | 39.95 | 64.300 |
| 67 | 2.001 | 0.033 | 15.138 | 39.95 | 63.355 |
| 68 | 2.024 | 0.034 | 15.081 | 39.95 | 63.118 |
| 69 | 2.092 | 0.035 | 15.025 | 39.95 | 62.882 |
| 70 | 2.117 | 0.035 | 15.025 | 39.95 | 62.882 |
| 71 | 2.141 | 0.036 | 15.025 | 39.95 | 62.882 |
| 72 | 2.166 | 0.036 | 14.968 | 39.95 | 62.645 |
| 73 | 2.193 | 0.037 | 14.855 | 39.95 | 62.409 |
| 74 | 2.216 | 0.037 | 14.686 | 40.8 | 61.936 |
| 75 | 2.241 | 0.037 | 14.460 | 40.8 | 61.805 |
| 76 | 2.266 | 0.038 | 14.121 | 40.8 | 60.598 |
| 77 | 2.290 | 0.038 | 13.838 | 40.8 | 59.632 |
| 78 | 2.359 | 0.039 | 12.991 | 40.8 | 56.494 |
| 79 | 2.383 | 0.040 | 12.709 | 40.8 | 54.562 |
| 80 | 2.408 | 0.040 | 12.539 | 40.8 | 53.838 |
| 81 | 2.432 | 0.041 | 12.370 | 40.8 | 53.114 |
| 82 | 2.458 | 0.041 | 12.200 | 40.8 | 52.631 |
| 83 | 2.482 | 0.041 | 12.087 | 40.8 | 51.666 |
| 84 | 2.506 | 0.042 | 12.031 | 40.8 | 51.666 |
| 85 | 2.531 | 0.042 | 12.031 | 39.95 | 51.424 |
| 86 | 2.556 | 0.043 | 12.087 | 39.95 | 50.353 |
| 87 | 2.625 | 0.044 | 12.539 | 39.95 | 52.244 |

| Number | Time (s) | Time (min) | Torque reading (N. m) | Screw speed (rpm) | Power (N. m/s) |
|---|---|---|---|---|---|
| 88 | 2.650 | 0.044 | 12.822 | 39.95 | 53.190 |
| 89 | 2.674 | 0.045 | 13.048 | 39.95 | 53.899 |
| 90 | 2.698 | 0.045 | 13.161 | 39.95 | 54.608 |
| 91 | 2.725 | 0.045 | 13.161 | 39.95 | 55.317 |
| 92 | 2.748 | 0.046 | 13.104 | 39.95 | 55.081 |
| 93 | 2.777 | 0.046 | 12.935 | 40.8 | 54.608 |
| 94 | 2.801 | 0.047 | 12.709 | 40.8 | 54.321 |
| 95 | 2.827 | 0.047 | 12.426 | 40.8 | 53.355 |
| 96 | 2.894 | 0.048 | 11.805 | 40.8 | 50.941 |
| 97 | 2.919 | 0.049 | 11.636 | 40.8 | 50.217 |
| 98 | 2.943 | 0.049 | 11.523 | 40.8 | 49.251 |
| 99 | 2.970 | 0.049 | 11.523 | 39.95 | 49.251 |
| 100 | 2.996 | 0.050 | 11.579 | 39.95 | 48.225 |
| 101 | 3.019 | 0.050 | 11.636 | 39.95 | 48.462 |
| 102 | 3.044 | 0.051 | 11.805 | 39.95 | 49.170 |
| 103 | 3.068 | 0.051 | 11.974 | 39.95 | 49.880 |
| 104 | 3.093 | 0.052 | 12.200 | 39.95 | 50.589 |
| 105 | 3.162 | 0.053 | 12.991 | 39.95 | 54.135 |
| 106 | 3.188 | 0.053 | 13.274 | 39.95 | 55.317 |
| 107 | 3.213 | 0.054 | 13.556 | 39.95 | 56.263 |
| 108 | 3.236 | 0.054 | 13.782 | 39.95 | 56.972 |
| 109 | 3.262 | 0.054 | 14.008 | 39.95 | 58.627 |
| 110 | 3.286 | 0.055 | 14.177 | 39.95 | 59.100 |
| 111 | 3.310 | 0.055 | 14.290 | 39.95 | 59.573 |
| 112 | 3.334 | 0.056 | 14.347 | 39.95 | 59.808 |
| 113 | 3.357 | 0.056 | 14.347 | 39.95 | 60.045 |
| 114 | 3.426 | 0.057 | 14.121 | 39.95 | 59.336 |
| 115 | 3.452 | 0.058 | 14.008 | 39.95 | 58.863 |
| 116 | 3.475 | 0.058 | 13.838 | 39.95 | 58.390 |
| 117 | 3.500 | 0.058 | 13.669 | 39.95 | 57.917 |
| 118 | 3.527 | 0.059 | 13.500 | 39.95 | 56.736 |
| 119 | 3.551 | 0.059 | 13.330 | 39.95 | 56.263 |
| 120 | 3.576 | 0.060 | 13.217 | 39.95 | 55.553 |
| 121 | 3.604 | 0.060 | 12.991 | 39.95 | 54.608 |
| 122 | 3.627 | 0.060 | 12.878 | 40.8 | 54.135 |
| 123 | 3.702 | 0.062 | 12.370 | 40.8 | 52.873 |
| 124 | 3.728 | 0.062 | 12.200 | 40.8 | 52.390 |
| 125 | 3.754 | 0.063 | 12.031 | 40.8 | 51.907 |
| 126 | 3.779 | 0.063 | 11.918 | 40.8 | 51.424 |
| 127 | 3.803 | 0.063 | 11.805 | 40.8 | 50.459 |
| 128 | 3.827 | 0.064 | 11.692 | 40.8 | 49.975 |
| 129 | 3.852 | 0.064 | 11.579 | 40.8 | 49.734 |
| 130 | 3.878 | 0.065 | 11.523 | 40.8 | 49.493 |
| 131 | 3.902 | 0.065 | 11.466 | 40.8 | 49.010 |
| 132 | 3.973 | 0.066 | 11.410 | 40.8 | 48.768 |
| 133 | 3.998 | 0.067 | 11.410 | 40.8 | 48.768 |
| 134 | 4.024 | 0.067 | 11.523 | 40.8 | 49.251 |

| Number | Time (s) | Time (min) | Torque reading (N. m) | Screw speed (rpm) | Power (N. m/s) |
|---|---|---|---|---|---|
| 135 | 4.049 | 0.067 | 11.692 | 39.95 | 48.698 |
| 136 | 4.073 | 0.068 | 11.861 | 39.95 | 49.170 |
| 137 | 4.099 | 0.068 | 12.087 | 39.95 | 49.880 |
| 138 | 4.125 | 0.069 | 12.313 | 39.95 | 51.534 |
| 139 | 4.148 | 0.069 | 12.483 | 39.95 | 52.007 |
| 140 | 4.172 | 0.070 | 12.652 | 39.95 | 52.717 |
| 141 | 4.243 | 0.071 | 12.822 | 39.95 | 53.662 |
| 142 | 4.268 | 0.071 | 12.878 | 40.8 | 55.045 |
| 143 | 4.291 | 0.072 | 12.878 | 40.8 | 55.045 |
| 144 | 4.316 | 0.072 | 12.878 | 40.8 | 55.045 |
| 145 | 4.340 | 0.072 | 12.935 | 40.8 | 55.045 |
| 146 | 4.364 | 0.073 | 12.935 | 40.8 | 55.287 |
| 147 | 4.389 | 0.073 | 13.048 | 39.95 | 54.371 |
| 148 | 4.414 | 0.074 | 13.104 | 39.95 | 54.608 |
| 149 | 4.438 | 0.074 | 13.217 | 39.95 | 55.081 |
| 150 | 4.507 | 0.075 | 13.669 | 39.95 | 56.972 |
| 151 | 4.531 | 0.076 | 13.782 | 39.95 | 57.445 |
| 152 | 4.555 | 0.076 | 13.951 | 39.95 | 57.917 |
| 153 | 4.580 | 0.076 | 14.121 | 39.95 | 59.100 |
| 154 | 4.604 | 0.077 | 14.290 | 39.95 | 59.573 |
| 155 | 5.148 | 0.086 | 15.081 | 40.8 | 64.703 |
| 156 | 5.205 | 0.087 | 14.573 | 40.8 | 62.530 |
| 157 | 5.220 | 0.087 | 14.460 | 40.8 | 61.805 |
| 158 | 5.236 | 0.087 | 14.290 | 40.8 | 61.805 |
| 159 | 5.253 | 0.088 | 14.177 | 40.8 | 61.081 |
| 160 | 5.268 | 0.088 | 14.121 | 40.8 | 60.357 |
| 161 | 5.284 | 0.088 | 14.008 | 40.8 | 60.116 |
| 162 | 5.299 | 0.088 | 13.951 | 40.8 | 60.116 |
| 163 | 5.315 | 0.089 | 13.895 | 40.8 | 59.632 |
| 164 | 5.333 | 0.089 | 13.895 | 40.8 | 59.391 |
| 165 | 5.348 | 0.089 | 13.838 | 40.8 | 59.150 |
| 166 | 5.363 | 0.089 | 13.838 | 39.95 | 59.150 |
| 167 | 5.379 | 0.090 | 13.838 | 39.95 | 59.150 |
| 168 | 5.398 | 0.090 | 13.895 | 39.95 | 57.917 |
| 169 | 5.413 | 0.090 | 13.951 | 39.95 | 58.154 |
| 170 | 5.474 | 0.091 | 14.347 | 39.95 | 59.573 |
| 171 | 5.489 | 0.091 | 14.516 | 39.95 | 60.281 |
| 172 | 5.504 | 0.092 | 14.686 | 39.95 | 61.227 |
| 173 | 5.523 | 0.092 | 14.912 | 39.95 | 62.172 |
| 174 | 5.539 | 0.092 | 15.081 | 39.95 | 62.172 |
| 175 | 5.555 | 0.093 | 15.250 | 39.95 | 63.118 |
| 176 | 5.571 | 0.093 | 15.420 | 39.95 | 64.063 |
| 177 | 5.588 | 0.093 | 15.589 | 39.95 | 65.009 |
| 178 | 5.605 | 0.093 | 15.646 | 39.95 | 65.482 |
| 179 | 5.621 | 0.094 | 15.646 | 39.95 | 65.482 |
| 180 | 5.636 | 0.094 | 15.589 | 39.95 | 65.482 |
| 181 | 5.654 | 0.094 | 15.533 | 39.95 | 65.246 |

G-1-2. Sawdust-1 (20 rpm for screw-1 with 0.15 m tapered section at 0.45 m hopper level)

| Number | Time (s) | Time (min) | Torque reading (N. m) | Screw speed (rpm) | Power (N. m/s) |
|---|---|---|---|---|---|
| 1 | 0.000 | 0.000 | 1.864 | 0 | 0.000 |
| 2 | 0.068 | 0.001 | 2.090 | 0 | 0.000 |
| 3 | 0.087 | 0.001 | 2.203 | 0 | 0.000 |
| 4 | 0.109 | 0.002 | 2.372 | 0.85 | 0.201 |
| 5 | 0.132 | 0.002 | 2.485 | 1.7 | 0.442 |
| 6 | 0.156 | 0.003 | 2.655 | 2.55 | 0.694 |
| 7 | 0.181 | 0.003 | 2.824 | 4.25 | 0.985 |
| 8 | 0.204 | 0.003 | 2.994 | 5.1 | 1.282 |
| 9 | 0.228 | 0.004 | 3.163 | 6.8 | 1.902 |
| 10 | 0.253 | 0.004 | 3.333 | 7.65 | 2.671 |
| 11 | 0.326 | 0.005 | 3.841 | 11.05 | 3.984 |
| 12 | 0.350 | 0.006 | 4.010 | 11.9 | 4.512 |
| 13 | 0.377 | 0.006 | 4.236 | 12.75 | 5.583 |
| 14 | 0.401 | 0.007 | 4.406 | 13.6 | 5.809 |
| 15 | 0.425 | 0.007 | 4.575 | 14.45 | 6.357 |
| 16 | 0.451 | 0.008 | 4.745 | 14.45 | 7.182 |
| 17 | 0.475 | 0.008 | 4.971 | 15.3 | 7.876 |
| 18 | 0.499 | 0.008 | 5.140 | 16.15 | 8.148 |
| 19 | 0.524 | 0.009 | 5.309 | 16.15 | 8.792 |
| 20 | 0.593 | 0.010 | 5.874 | 17 | 10.361 |
| 21 | 0.615 | 0.010 | 6.044 | 17.85 | 10.663 |
| 22 | 0.640 | 0.011 | 6.213 | 17.85 | 11.513 |
| 23 | 0.666 | 0.011 | 6.439 | 17.85 | 11.830 |
| 24 | 0.690 | 0.011 | 6.609 | 17.85 | 12.041 |
| 25 | 0.716 | 0.012 | 6.778 | 18.7 | 13.168 |
| 26 | 0.739 | 0.012 | 6.947 | 18.7 | 13.500 |
| 27 | 0.763 | 0.013 | 7.117 | 18.7 | 13.721 |
| 28 | 0.788 | 0.013 | 7.286 | 18.7 | 14.053 |
| 29 | 0.856 | 0.014 | 7.738 | 19.55 | 15.733 |
| 30 | 0.881 | 0.015 | 7.908 | 19.55 | 16.080 |
| 31 | 0.905 | 0.015 | 8.021 | 19.55 | 16.311 |
| 32 | 0.929 | 0.015 | 8.190 | 19.55 | 16.543 |
| 33 | 0.953 | 0.016 | 8.303 | 19.55 | 17.006 |
| 34 | 0.981 | 0.016 | 8.473 | 19.55 | 17.237 |
| 35 | 1.008 | 0.017 | 8.585 | 19.55 | 17.353 |
| 36 | 1.033 | 0.017 | 8.698 | 19.55 | 17.815 |
| 37 | 1.059 | 0.018 | 8.811 | 19.55 | 17.931 |
| 38 | 1.128 | 0.019 | 9.037 | 19.55 | 18.394 |
| 39 | 1.151 | 0.019 | 9.150 | 20.4 | 19.556 |
| 40 | 1.176 | 0.020 | 9.263 | 20.4 | 19.676 |
| 41 | 1.200 | 0.020 | 9.320 | 20.4 | 19.917 |
| 42 | 1.224 | 0.020 | 9.433 | 20.4 | 20.038 |
| 43 | 1.249 | 0.021 | 9.546 | 20.4 | 20.280 |
| 44 | 1.273 | 0.021 | 9.659 | 20.4 | 20.642 |
| 45 | 1.296 | 0.022 | 9.828 | 20.4 | 20.884 |
| 46 | 1.322 | 0.022 | 9.941 | 20.4 | 21.125 |
| 47 | 1.390 | 0.023 | 10.336 | 20.4 | 21.849 |
| 48 | 1.414 | 0.024 | 10.449 | 20.4 | 22.332 |

| Number | Time (s) | Time (min) | Torque reading (N. m) | Screw speed (rpm) | Power (N. m/s) |
|---|---|---|---|---|---|
| 49 | 1.439 | 0.024 | 10.562 | 20.4 | 22.453 |
| 50 | 1.462 | 0.024 | 10.675 | 20.4 | 22.694 |
| 51 | 1.487 | 0.025 | 10.788 | 20.4 | 22.936 |
| 52 | 1.512 | 0.025 | 10.845 | 20.4 | 23.177 |
| 53 | 1.537 | 0.026 | 10.958 | 20.4 | 23.298 |
| 54 | 1.560 | 0.026 | 11.014 | 20.4 | 23.418 |
| 55 | 1.585 | 0.026 | 11.071 | 20.4 | 23.539 |
| 56 | 1.655 | 0.028 | 11.240 | 20.4 | 24.022 |
| 57 | 1.679 | 0.028 | 11.297 | 20.4 | 24.143 |
| 58 | 1.703 | 0.028 | 11.353 | 20.4 | 24.143 |
| 59 | 1.728 | 0.029 | 11.353 | 20.4 | 24.264 |
| 60 | 1.752 | 0.029 | 11.353 | 20.4 | 24.264 |
| 61 | 1.778 | 0.030 | 11.353 | 20.4 | 24.264 |
| 62 | 1.802 | 0.030 | 11.353 | 20.4 | 24.264 |
| 63 | 1.826 | 0.030 | 11.353 | 20.4 | 24.264 |
| 64 | 1.851 | 0.031 | 11.297 | 20.4 | 24.143 |
| 65 | 1.919 | 0.032 | 11.184 | 21.25 | 25.023 |
| 66 | 1.943 | 0.032 | 11.127 | 21.25 | 24.897 |
| 67 | 1.968 | 0.033 | 11.127 | 21.25 | 24.772 |
| 68 | 1.993 | 0.033 | 11.071 | 21.25 | 24.646 |
| 69 | 2.017 | 0.034 | 11.014 | 21.25 | 24.520 |
| 70 | 2.042 | 0.034 | 10.958 | 21.25 | 24.394 |
| 71 | 2.066 | 0.034 | 10.901 | 21.25 | 24.394 |
| 72 | 2.092 | 0.035 | 10.901 | 21.25 | 24.268 |
| 73 | 2.117 | 0.035 | 10.845 | 21.25 | 24.143 |
| 74 | 2.184 | 0.036 | 10.788 | 20.4 | 23.057 |
| 75 | 2.211 | 0.037 | 10.788 | 20.4 | 23.057 |
| 76 | 2.236 | 0.037 | 10.788 | 20.4 | 23.057 |
| 77 | 2.261 | 0.038 | 10.788 | 20.4 | 23.057 |
| 78 | 2.284 | 0.038 | 10.788 | 20.4 | 23.057 |
| 79 | 2.310 | 0.039 | 10.788 | 20.4 | 23.057 |
| 80 | 2.335 | 0.039 | 10.788 | 20.4 | 23.057 |
| 81 | 2.358 | 0.039 | 10.845 | 21.25 | 24.143 |
| 82 | 2.385 | 0.040 | 10.845 | 21.25 | 24.143 |
| 83 | 2.455 | 0.041 | 10.958 | 21.25 | 24.394 |
| 84 | 2.479 | 0.041 | 10.958 | 21.25 | 24.394 |
| 85 | 2.503 | 0.042 | 10.958 | 21.25 | 24.394 |
| 86 | 2.529 | 0.042 | 10.958 | 21.25 | 24.394 |
| 87 | 2.552 | 0.043 | 10.901 | 21.25 | 24.268 |
| 88 | 2.577 | 0.043 | 10.901 | 21.25 | 24.268 |
| 89 | 2.601 | 0.043 | 10.845 | 21.25 | 24.143 |
| 90 | 2.628 | 0.044 | 10.788 | 21.25 | 24.143 |
| 91 | 2.653 | 0.044 | 10.788 | 21.25 | 24.017 |
| 92 | 2.720 | 0.045 | 10.788 | 21.25 | 24.017 |
| 93 | 2.745 | 0.046 | 10.845 | 21.25 | 24.143 |
| 94 | 2.770 | 0.046 | 10.845 | 21.25 | 24.143 |
| 95 | 2.794 | 0.047 | 10.845 | 21.25 | 24.143 |
| 96 | 2.818 | 0.047 | 10.845 | 21.25 | 24.143 |
| 97 | 2.844 | 0.047 | 10.845 | 21.25 | 24.143 |
| 98 | 2.868 | 0.048 | 10.788 | 21.25 | 24.143 |
| 99 | 2.891 | 0.048 | 10.788 | 21.25 | 24.017 |

| Number | Time (s) | Time (min) | Torque reading (N. m) | Screw speed (rpm) | Power (N. m/s) |
|---|---|---|---|---|---|
| 100 | 2.917 | 0.049 | 10.675 | 21.25 | 23.891 |
| 101 | 2.985 | 0.050 | 10.506 | 21.25 | 23.514 |
| 102 | 3.009 | 0.050 | 10.449 | 21.25 | 23.389 |
| 103 | 3.033 | 0.051 | 10.336 | 21.25 | 23.011 |
| 104 | 3.058 | 0.051 | 10.223 | 21.25 | 22.885 |
| 105 | 3.081 | 0.051 | 10.167 | 21.25 | 22.760 |
| 106 | 3.109 | 0.052 | 10.054 | 21.25 | 22.508 |
| 107 | 3.132 | 0.052 | 9.998 | 21.25 | 22.257 |
| 108 | 3.157 | 0.053 | 9.941 | 21.25 | 22.131 |
| 109 | 3.184 | 0.053 | 9.885 | 21.25 | 22.005 |
| 110 | 3.252 | 0.054 | 9.772 | 21.25 | 21.753 |
| 111 | 3.275 | 0.055 | 9.715 | 21.25 | 21.628 |
| 112 | 3.301 | 0.055 | 9.715 | 21.25 | 21.628 |
| 113 | 3.326 | 0.055 | 9.715 | 21.25 | 21.628 |
| 114 | 3.350 | 0.056 | 9.715 | 21.25 | 21.628 |
| 115 | 3.377 | 0.056 | 9.715 | 21.25 | 21.628 |
| 116 | 3.400 | 0.057 | 9.715 | 21.25 | 21.628 |
| 117 | 3.425 | 0.057 | 9.715 | 21.25 | 21.628 |
| 118 | 3.450 | 0.057 | 9.772 | 21.25 | 21.753 |
| 119 | 3.517 | 0.059 | 9.885 | 21.25 | 22.005 |
| 120 | 3.542 | 0.059 | 9.941 | 21.25 | 22.005 |
| 121 | 3.567 | 0.059 | 9.941 | 21.25 | 22.131 |
| 122 | 3.593 | 0.060 | 9.998 | 21.25 | 22.257 |
| 123 | 3.617 | 0.060 | 10.054 | 21.25 | 22.382 |
| 124 | 3.644 | 0.061 | 10.111 | 21.25 | 22.508 |
| 125 | 3.668 | 0.061 | 10.223 | 21.25 | 22.634 |
| 126 | 3.693 | 0.062 | 10.280 | 21.25 | 22.885 |
| 127 | 3.722 | 0.062 | 10.393 | 21.25 | 23.011 |
| 128 | 3.789 | 0.063 | 10.732 | 21.25 | 23.640 |
| 129 | 3.813 | 0.064 | 10.901 | 21.25 | 24.268 |
| 130 | 3.838 | 0.064 | 11.071 | 21.25 | 24.520 |
| 131 | 3.863 | 0.064 | 11.184 | 21.25 | 24.772 |
| 132 | 3.887 | 0.065 | 11.353 | 21.25 | 25.023 |
| 133 | 3.913 | 0.065 | 11.466 | 21.25 | 25.526 |
| 134 | 3.936 | 0.066 | 11.579 | 21.25 | 25.777 |
| 135 | 3.961 | 0.066 | 11.749 | 21.25 | 26.029 |
| 136 | 3.987 | 0.066 | 11.861 | 21.25 | 26.280 |
| 137 | 4.057 | 0.068 | 12.257 | 20.4 | 26.074 |
| 138 | 4.083 | 0.068 | 12.426 | 20.4 | 26.316 |
| 139 | 4.109 | 0.068 | 12.539 | 20.4 | 26.678 |
| 140 | 4.132 | 0.069 | 12.709 | 20.4 | 27.160 |
| 141 | 4.157 | 0.069 | 12.878 | 20.4 | 27.402 |
| 142 | 4.182 | 0.070 | 12.991 | 20.4 | 27.644 |
| 143 | 4.205 | 0.070 | 13.161 | 20.4 | 27.885 |
| 144 | 4.229 | 0.070 | 13.274 | 20.4 | 28.126 |
| 145 | 4.255 | 0.071 | 13.387 | 20.4 | 28.609 |
| 146 | 4.325 | 0.072 | 13.726 | 20.4 | 29.213 |
| 147 | 4.348 | 0.072 | 13.782 | 20.4 | 29.333 |
| 148 | 4.372 | 0.073 | 13.838 | 20.4 | 29.575 |
| 149 | 4.396 | 0.073 | 13.838 | 20.4 | 29.575 |
| 150 | 4.419 | 0.074 | 13.838 | 20.4 | 29.575 |

| Number | Time (s) | Time (min) | Torque reading (N. m) | Screw speed (rpm) | Power (N. m/s) |
|---|---|---|---|---|---|
| 151 | 4.444 | 0.074 | 13.838 | 21.25 | 29.575 |
| 152 | 4.470 | 0.074 | 13.782 | 21.25 | 30.807 |
| 153 | 4.493 | 0.075 | 13.726 | 21.25 | 30.555 |
| 154 | 4.519 | 0.075 | 13.613 | 21.25 | 30.430 |
| 155 | 4.588 | 0.076 | 13.330 | 21.25 | 29.801 |
| 156 | 4.612 | 0.077 | 13.161 | 21.25 | 29.298 |
| 157 | 4.637 | 0.077 | 13.048 | 21.25 | 29.172 |
| 158 | 4.662 | 0.078 | 12.878 | 21.25 | 28.921 |
| 159 | 4.685 | 0.078 | 12.765 | 21.25 | 28.670 |
| 160 | 4.711 | 0.079 | 12.596 | 21.25 | 28.041 |
| 161 | 4.736 | 0.079 | 12.483 | 21.25 | 27.789 |
| 162 | 4.760 | 0.079 | 12.313 | 21.25 | 27.538 |
| 163 | 4.784 | 0.080 | 12.200 | 21.25 | 27.286 |
| 164 | 4.855 | 0.081 | 11.805 | 21.25 | 26.280 |
| 165 | 4.880 | 0.081 | 11.692 | 21.25 | 26.155 |
| 166 | 4.906 | 0.082 | 11.579 | 21.25 | 25.903 |
| 167 | 4.930 | 0.082 | 11.466 | 21.25 | 25.777 |
| 168 | 4.954 | 0.083 | 11.410 | 21.25 | 25.400 |
| 169 | 4.979 | 0.083 | 11.353 | 21.25 | 25.274 |
| 170 | 5.003 | 0.083 | 11.297 | 21.25 | 25.274 |
| 171 | 5.028 | 0.084 | 11.240 | 21.25 | 25.148 |
| 172 | 5.051 | 0.084 | 11.240 | 21.25 | 25.023 |
| 173 | 5.119 | 0.085 | 11.184 | 20.4 | 23.901 |
| 174 | 5.143 | 0.086 | 11.184 | 20.4 | 23.901 |
| 175 | 5.167 | 0.086 | 11.240 | 21.25 | 23.901 |
| 176 | 5.192 | 0.087 | 11.240 | 21.25 | 25.023 |
| 177 | 5.216 | 0.087 | 11.297 | 21.25 | 25.148 |
| 178 | 5.242 | 0.087 | 11.353 | 21.25 | 25.274 |
| 179 | 5.266 | 0.088 | 11.410 | 21.25 | 25.274 |
| 180 | 5.290 | 0.088 | 11.466 | 21.25 | 25.400 |
| 181 | 5.316 | 0.089 | 11.523 | 21.25 | 25.652 |
| 182 | 5.386 | 0.090 | 11.579 | 21.25 | 25.777 |
| 183 | 5.410 | 0.090 | 11.636 | 21.25 | 25.777 |
| 184 | 5.435 | 0.091 | 11.692 | 21.25 | 25.903 |
| 185 | 5.460 | 0.091 | 11.692 | 21.25 | 26.029 |
| 186 | 5.484 | 0.091 | 11.749 | 21.25 | 26.155 |
| 187 | 5.510 | 0.092 | 11.805 | 21.25 | 26.280 |
| 188 | 5.533 | 0.092 | 11.861 | 21.25 | 26.406 |
| 189 | 5.558 | 0.093 | 11.918 | 21.25 | 26.532 |
| 190 | 5.583 | 0.093 | 11.974 | 21.25 | 26.658 |
| 191 | 5.652 | 0.094 | 12.087 | 21.25 | 26.909 |
| 192 | 5.678 | 0.095 | 12.087 | 21.25 | 26.909 |
| 193 | 5.703 | 0.095 | 12.087 | 21.25 | 26.909 |
| 194 | 5.727 | 0.095 | 12.087 | 21.25 | 26.909 |
| 195 | 5.752 | 0.096 | 12.087 | 21.25 | 26.909 |
| 196 | 5.776 | 0.096 | 12.031 | 21.25 | 26.784 |
| 197 | 5.801 | 0.097 | 11.974 | 21.25 | 26.784 |
| 198 | 5.827 | 0.097 | 11.918 | 21.25 | 26.658 |
| 199 | 5.852 | 0.098 | 11.861 | 21.25 | 26.406 |
| 200 | 5.923 | 0.099 | 11.636 | 21.25 | 26.029 |
| 201 | 5.953 | 0.099 | 11.523 | 21.25 | 25.777 |

G-1-3. Ground wood pellets-2 (20 rpm for screw-1 at 0.45 m hopper level with 1500 Pa pressurization in hopper)

| Number | Time (s) | Time (min) | Torque reading (N. m) | Screw speed (rpm) | Power (N. m) |
|---|---|---|---|---|---|
| 1 | 0.000 | 0.000 | 2.090 | 0 | 0.000 |
| 2 | 0.034 | 0.001 | 2.542 | 0.85 | 0.000 |
| 3 | 0.068 | 0.001 | 2.994 | 1.7 | 0.513 |
| 4 | 0.086 | 0.001 | 3.276 | 2.55 | 0.860 |
| 5 | 0.149 | 0.002 | 4.293 | 5.95 | 2.203 |
| 6 | 0.193 | 0.003 | 4.914 | 7.65 | 3.802 |
| 7 | 0.223 | 0.004 | 5.309 | 9.35 | 5.145 |
| 8 | 0.239 | 0.004 | 5.535 | 10.2 | 5.145 |
| 9 | 0.255 | 0.004 | 5.705 | 11.05 | 5.915 |
| 10 | 0.271 | 0.005 | 5.874 | 11.9 | 6.669 |
| 11 | 0.287 | 0.005 | 6.044 | 11.9 | 7.464 |
| 12 | 0.304 | 0.005 | 6.213 | 12.75 | 8.224 |
| 13 | 0.338 | 0.006 | 6.496 | 13.6 | 9.094 |
| 14 | 0.419 | 0.007 | 7.060 | 16.15 | 11.136 |
| 15 | 0.441 | 0.007 | 7.173 | 16.15 | 12.137 |
| 16 | 0.457 | 0.008 | 7.286 | 16.15 | 12.137 |
| 17 | 0.473 | 0.008 | 7.343 | 17 | 12.328 |
| 18 | 0.493 | 0.008 | 7.456 | 17 | 13.178 |
| 19 | 0.528 | 0.009 | 7.625 | 17.85 | 13.479 |
| 20 | 0.568 | 0.009 | 7.795 | 17.85 | 14.576 |
| 21 | 0.584 | 0.010 | 7.908 | 17.85 | 14.682 |
| 22 | 0.604 | 0.010 | 7.964 | 17.85 | 14.893 |
| 23 | 0.703 | 0.012 | 8.416 | 18.7 | 16.487 |
| 24 | 0.729 | 0.012 | 8.585 | 18.7 | 16.709 |
| 25 | 0.745 | 0.012 | 8.642 | 19.55 | 17.584 |
| 26 | 0.766 | 0.013 | 8.698 | 19.55 | 17.815 |
| 27 | 0.782 | 0.013 | 8.811 | 19.55 | 17.931 |
| 28 | 0.798 | 0.013 | 8.868 | 19.55 | 17.931 |
| 29 | 0.843 | 0.014 | 9.037 | 19.55 | 18.510 |
| 30 | 0.873 | 0.015 | 9.207 | 19.55 | 18.741 |
| 31 | 0.938 | 0.016 | 9.489 | 19.55 | 19.204 |
| 32 | 0.954 | 0.016 | 9.546 | 19.55 | 19.435 |
| 33 | 0.970 | 0.016 | 9.659 | 19.55 | 19.666 |
| 34 | 1.003 | 0.017 | 9.772 | 20.4 | 20.884 |
| 35 | 1.046 | 0.017 | 9.998 | 20.4 | 21.245 |
| 36 | 1.061 | 0.018 | 10.054 | 20.4 | 21.487 |
| 37 | 1.077 | 0.018 | 10.111 | 20.4 | 21.487 |
| 38 | 1.099 | 0.018 | 10.167 | 20.4 | 21.608 |
| 39 | 1.115 | 0.019 | 10.223 | 20.4 | 21.849 |
| 40 | 1.130 | 0.019 | 10.280 | 20.4 | 21.970 |
| 41 | 1.237 | 0.021 | 10.675 | 20.4 | 22.573 |
| 42 | 1.256 | 0.021 | 10.732 | 20.4 | 22.815 |
| 43 | 1.272 | 0.021 | 10.788 | 20.4 | 22.936 |
| 44 | 1.289 | 0.021 | 10.845 | 20.4 | 23.057 |

| Number | Time (s) | Time (min) | Torque reading (N. m) | Screw speed (rpm) | Power (N. m) |
|---|---|---|---|---|---|
| 45 | 1.305 | 0.022 | 10.901 | 20.4 | 23.298 |
| 46 | 1.348 | 0.022 | 11.071 | 20.4 | 23.539 |
| 47 | 1.382 | 0.023 | 11.184 | 20.4 | 23.901 |
| 48 | 1.449 | 0.024 | 11.410 | 20.4 | 24.264 |
| 49 | 1.465 | 0.024 | 11.410 | 20.4 | 24.385 |
| 50 | 1.492 | 0.025 | 11.466 | 20.4 | 24.505 |
| 51 | 1.541 | 0.026 | 11.579 | 20.4 | 24.746 |
| 52 | 1.557 | 0.026 | 11.636 | 20.4 | 24.746 |
| 53 | 1.572 | 0.026 | 11.636 | 20.4 | 24.867 |
| 54 | 1.594 | 0.027 | 11.692 | 20.4 | 24.867 |
| 55 | 1.609 | 0.027 | 11.692 | 20.4 | 24.988 |
| 56 | 1.627 | 0.027 | 11.749 | 20.4 | 25.108 |
| 57 | 1.658 | 0.028 | 11.805 | 20.4 | 25.108 |
| 58 | 1.746 | 0.029 | 11.918 | 20.4 | 25.350 |
| 59 | 1.763 | 0.029 | 11.918 | 20.4 | 25.471 |
| 60 | 1.778 | 0.030 | 11.918 | 20.4 | 25.471 |
| 61 | 1.794 | 0.030 | 11.974 | 20.4 | 25.592 |
| 62 | 1.815 | 0.030 | 12.031 | 20.4 | 25.592 |
| 63 | 1.852 | 0.031 | 12.087 | 20.4 | 25.832 |
| 64 | 1.886 | 0.031 | 12.200 | 20.4 | 25.953 |
| 65 | 1.901 | 0.032 | 12.200 | 20.4 | 26.074 |
| 66 | 1.921 | 0.032 | 12.313 | 20.4 | 26.316 |
| 67 | 2.023 | 0.034 | 12.709 | 20.4 | 27.040 |
| 68 | 2.041 | 0.034 | 12.765 | 20.4 | 27.281 |
| 69 | 2.056 | 0.034 | 12.822 | 20.4 | 27.281 |
| 70 | 2.071 | 0.035 | 12.878 | 20.4 | 27.402 |
| 71 | 2.095 | 0.035 | 12.935 | 20.4 | 27.523 |
| 72 | 2.110 | 0.035 | 12.935 | 20.4 | 27.644 |
| 73 | 2.126 | 0.035 | 12.991 | 20.4 | 27.764 |
| 74 | 2.184 | 0.036 | 13.104 | 20.4 | 28.006 |
| 75 | 2.243 | 0.037 | 13.104 | 21.25 | 29.172 |
| 76 | 2.262 | 0.038 | 13.104 | 21.25 | 29.172 |
| 77 | 2.278 | 0.038 | 13.048 | 21.25 | 29.172 |
| 78 | 2.295 | 0.038 | 13.048 | 21.25 | 29.047 |
| 79 | 2.327 | 0.039 | 12.991 | 21.25 | 28.921 |
| 80 | 2.362 | 0.039 | 12.935 | 21.25 | 28.796 |
| 81 | 2.389 | 0.040 | 12.878 | 21.25 | 28.670 |
| 82 | 2.404 | 0.040 | 12.822 | 21.25 | 28.670 |
| 83 | 2.420 | 0.040 | 12.822 | 21.25 | 28.543 |
| 84 | 2.437 | 0.041 | 12.765 | 21.25 | 28.543 |
| 85 | 2.541 | 0.042 | 12.539 | 21.25 | 27.915 |
| 86 | 2.557 | 0.043 | 12.539 | 21.25 | 27.915 |
| 87 | 2.577 | 0.043 | 12.483 | 21.25 | 27.915 |
| 88 | 2.593 | 0.043 | 12.426 | 21.25 | 27.789 |
| 89 | 2.609 | 0.043 | 12.426 | 21.25 | 27.664 |
| 90 | 2.626 | 0.044 | 12.370 | 21.25 | 27.538 |
| 91 | 2.659 | 0.044 | 12.257 | 21.25 | 27.412 |

| Number | Time (s) | Time (min) | Torque reading (N. m) | Screw speed (rpm) | Power (N. m) |
|---|---|---|---|---|---|
| 92 | 2.698 | 0.045 | 12.144 | 21.25 | 27.160 |
| 93 | 2.767 | 0.046 | 11.974 | 21.25 | 26.658 |
| 94 | 2.783 | 0.046 | 11.918 | 21.25 | 26.658 |
| 95 | 2.818 | 0.047 | 11.861 | 21.25 | 26.532 |
| 96 | 2.857 | 0.048 | 11.749 | 21.25 | 26.280 |
| 97 | 2.874 | 0.048 | 11.692 | 21.25 | 26.155 |
| 98 | 2.889 | 0.048 | 11.692 | 21.25 | 26.029 |
| 99 | 2.905 | 0.048 | 11.636 | 21.25 | 25.903 |
| 100 | 2.921 | 0.049 | 11.579 | 21.25 | 25.903 |
| 101 | 2.938 | 0.049 | 11.579 | 21.25 | 25.903 |
| 102 | 2.955 | 0.049 | 11.523 | 21.25 | 25.777 |
| 103 | 3.036 | 0.051 | 11.353 | 21.25 | 25.400 |
| 104 | 3.079 | 0.051 | 11.297 | 21.25 | 25.274 |
| 105 | 3.096 | 0.052 | 11.297 | 21.25 | 25.148 |
| 106 | 3.112 | 0.052 | 11.240 | 21.25 | 25.148 |
| 107 | 3.128 | 0.052 | 11.240 | 21.25 | 25.023 |
| 108 | 3.144 | 0.052 | 11.240 | 21.25 | 25.023 |
| 109 | 3.162 | 0.053 | 11.240 | 21.25 | 25.023 |
| 110 | 3.180 | 0.053 | 11.184 | 21.25 | 24.897 |
| 111 | 3.213 | 0.054 | 11.184 | 21.25 | 24.897 |
| 112 | 3.292 | 0.055 | 11.071 | 21.25 | 24.646 |
| 113 | 3.321 | 0.055 | 11.014 | 21.25 | 24.520 |
| 114 | 3.340 | 0.056 | 11.014 | 21.25 | 24.520 |
| 115 | 3.355 | 0.056 | 10.958 | 21.25 | 24.394 |
| 116 | 3.377 | 0.056 | 10.901 | 21.25 | 24.394 |
| 117 | 3.393 | 0.057 | 10.901 | 21.25 | 24.268 |
| 118 | 3.409 | 0.057 | 10.845 | 21.25 | 24.268 |
| 119 | 3.427 | 0.057 | 10.845 | 21.25 | 24.143 |
| 120 | 3.443 | 0.057 | 10.788 | 21.25 | 24.017 |
| 121 | 3.479 | 0.058 | 10.732 | 21.25 | 23.891 |
| 122 | 3.574 | 0.060 | 10.562 | 21.25 | 23.514 |
| 123 | 3.590 | 0.060 | 10.562 | 21.25 | 23.514 |
| 124 | 3.605 | 0.060 | 10.506 | 21.25 | 23.389 |
| 125 | 3.643 | 0.061 | 10.506 | 21.25 | 23.389 |
| 126 | 3.683 | 0.061 | 10.506 | 21.25 | 23.389 |
| 127 | 3.700 | 0.062 | 10.506 | 21.25 | 23.389 |
| 128 | 3.716 | 0.062 | 10.562 | 21.25 | 23.389 |
| 129 | 3.732 | 0.062 | 10.562 | 21.25 | 23.514 |
| 130 | 3.813 | 0.064 | 10.619 | 21.25 | 23.640 |
| 131 | 3.849 | 0.064 | 10.619 | 21.25 | 23.640 |
| 132 | 3.867 | 0.064 | 10.619 | 21.25 | 23.640 |
| 133 | 3.882 | 0.065 | 10.619 | 21.25 | 23.640 |
| 134 | 3.899 | 0.065 | 10.619 | 21.25 | 23.640 |
| 135 | 3.915 | 0.065 | 10.619 | 21.25 | 23.640 |
| 136 | 3.930 | 0.066 | 10.619 | 21.25 | 23.640 |
| 137 | 3.968 | 0.066 | 10.562 | 21.25 | 23.514 |
| 138 | 4.004 | 0.067 | 10.562 | 21.25 | 23.514 |

| Number | Time (s) | Time (min) | Torque reading (N. m) | Screw speed (rpm) | Power (N. m) |
|---|---|---|---|---|---|
| 139 | 4.064 | 0.068 | 10.449 | 21.25 | 23.263 |
| 140 | 4.081 | 0.068 | 10.449 | 21.25 | 23.263 |
| 141 | 4.118 | 0.069 | 10.449 | 21.25 | 23.263 |
| 142 | 4.152 | 0.069 | 10.393 | 21.25 | 23.136 |
| 143 | 4.174 | 0.070 | 10.393 | 21.25 | 23.136 |
| 144 | 4.190 | 0.070 | 10.393 | 21.25 | 23.136 |
| 145 | 4.206 | 0.070 | 10.393 | 21.25 | 23.136 |
| 146 | 4.224 | 0.070 | 10.393 | 21.25 | 23.136 |
| 147 | 4.246 | 0.071 | 10.393 | 21.25 | 23.136 |
| 148 | 4.261 | 0.071 | 10.449 | 21.25 | 23.263 |
| 149 | 4.366 | 0.073 | 10.506 | 21.25 | 23.389 |
| 150 | 4.382 | 0.073 | 10.562 | 21.25 | 23.514 |
| 151 | 4.411 | 0.074 | 10.562 | 21.25 | 23.514 |
| 152 | 4.466 | 0.074 | 10.675 | 21.25 | 23.765 |
| 153 | 4.505 | 0.075 | 10.788 | 21.25 | 24.017 |
| 154 | 4.959 | 0.083 | 13.669 | 20.4 | 28.851 |
| 155 | 5.031 | 0.084 | 14.008 | 20.4 | 29.816 |
| 156 | 5.082 | 0.085 | 14.234 | 21.25 | 31.687 |
| 157 | 5.123 | 0.085 | 14.290 | 21.25 | 31.813 |
| 158 | 5.152 | 0.086 | 14.347 | 21.25 | 31.938 |
| 159 | 5.176 | 0.086 | 14.347 | 21.25 | 31.938 |
| 160 | 5.200 | 0.087 | 14.290 | 21.25 | 31.938 |
| 161 | 5.243 | 0.087 | 14.234 | 21.25 | 31.687 |
| 162 | 5.334 | 0.089 | 13.895 | 21.25 | 31.059 |
| 163 | 5.363 | 0.089 | 13.726 | 21.25 | 30.681 |
| 164 | 5.393 | 0.090 | 13.556 | 21.25 | 30.430 |
| 165 | 5.419 | 0.090 | 13.443 | 21.25 | 30.179 |
| 166 | 5.445 | 0.091 | 13.274 | 21.25 | 29.550 |
| 167 | 5.469 | 0.091 | 13.161 | 21.25 | 29.298 |
| 168 | 5.535 | 0.092 | 12.878 | 21.25 | 28.796 |
| 169 | 5.609 | 0.093 | 12.596 | 21.25 | 28.167 |
| 170 | 5.633 | 0.094 | 12.539 | 21.25 | 28.041 |
| 171 | 5.658 | 0.094 | 12.370 | 21.25 | 27.789 |
| 172 | 5.682 | 0.095 | 12.257 | 21.25 | 27.286 |
| 173 | 5.707 | 0.095 | 12.144 | 21.25 | 27.160 |
| 174 | 5.762 | 0.096 | 11.861 | 21.25 | 26.532 |
| 175 | 5.786 | 0.096 | 11.805 | 21.25 | 26.280 |
| 176 | 5.916 | 0.099 | 11.466 | 21.25 | 25.526 |
| 177 | 5.940 | 0.099 | 11.410 | 21.25 | 25.526 |
| 178 | 5.965 | 0.099 | 11.410 | 21.25 | 25.400 |
| 179 | 5.992 | 0.100 | 11.353 | 21.25 | 25.274 |
| 180 | 6.016 | 0.100 | 11.353 | 21.25 | 25.274 |
| 181 | 6.041 | 0.101 | 11.297 | 21.25 | 25.148 |
| 182 | 6.147 | 0.102 | 11.184 | 21.25 | 24.897 |
| 183 | 6.175 | 0.103 | 11.127 | 21.25 | 24.772 |
| 184 | 6.199 | 0.103 | 11.071 | 21.25 | 24.772 |

*G-1-4. Ground wood pellets-1 (20 rpm for screw-2 at 0.45 m hopper level)*

| Number | Time (s) | Time (min) | Torque reading (N. m) | Screw speed (rpm) | Power (N. m/s) |
|---|---|---|---|---|---|
| 1 | 0.000 | 0.000 | 6.383 | 0 | 0.000 |
| 2 | 0.021 | 0.000 | 6.496 | 0 | 0.000 |
| 3 | 0.042 | 0.001 | 6.665 | 0 | 0.000 |
| 4 | 0.063 | 0.001 | 6.947 | 0 | 0.000 |
| 5 | 0.084 | 0.001 | 7.230 | 0 | 0.000 |
| 6 | 0.153 | 0.003 | 8.585 | 0.85 | 0.734 |
| 7 | 0.177 | 0.003 | 9.094 | 2.55 | 1.549 |
| 8 | 0.200 | 0.003 | 9.546 | 3.4 | 3.380 |
| 9 | 0.225 | 0.004 | 9.998 | 4.25 | 4.401 |
| 10 | 0.249 | 0.004 | 10.449 | 5.95 | 5.462 |
| 11 | 0.274 | 0.005 | 10.788 | 6.8 | 6.584 |
| 12 | 0.299 | 0.005 | 11.127 | 8.5 | 9.908 |
| 13 | 0.323 | 0.005 | 11.410 | 9.35 | 11.121 |
| 14 | 0.347 | 0.006 | 11.636 | 11.05 | 12.313 |
| 15 | 0.416 | 0.007 | 12.031 | 13.6 | 15.994 |
| 16 | 0.442 | 0.007 | 12.087 | 13.6 | 17.222 |
| 17 | 0.466 | 0.008 | 12.144 | 14.45 | 18.384 |
| 18 | 0.492 | 0.008 | 12.200 | 15.3 | 19.556 |
| 19 | 0.516 | 0.009 | 12.200 | 16.15 | 19.556 |
| 20 | 0.540 | 0.009 | 12.257 | 16.15 | 20.737 |
| 21 | 0.566 | 0.009 | 12.313 | 17 | 20.737 |
| 22 | 0.589 | 0.010 | 12.313 | 17 | 21.929 |
| 23 | 0.613 | 0.010 | 12.370 | 17 | 21.929 |
| 24 | 0.683 | 0.011 | 12.426 | 17.85 | 23.237 |
| 25 | 0.708 | 0.012 | 12.426 | 18.7 | 24.344 |
| 26 | 0.732 | 0.012 | 12.426 | 18.7 | 24.344 |
| 27 | 0.757 | 0.013 | 12.483 | 18.7 | 24.344 |
| 28 | 0.780 | 0.013 | 12.539 | 18.7 | 24.565 |
| 29 | 0.804 | 0.013 | 12.596 | 18.7 | 24.565 |
| 30 | 0.829 | 0.014 | 12.652 | 19.55 | 25.797 |
| 31 | 0.852 | 0.014 | 12.709 | 19.55 | 25.913 |
| 32 | 0.878 | 0.015 | 12.765 | 19.55 | 26.144 |
| 33 | 0.947 | 0.016 | 12.991 | 19.55 | 26.492 |
| 34 | 0.972 | 0.016 | 13.048 | 19.55 | 26.608 |
| 35 | 0.996 | 0.017 | 13.104 | 20.4 | 26.723 |
| 36 | 1.021 | 0.017 | 13.161 | 20.4 | 28.126 |
| 37 | 1.046 | 0.017 | 13.161 | 20.4 | 28.126 |
| 38 | 1.069 | 0.018 | 13.161 | 20.4 | 28.126 |
| 39 | 1.095 | 0.018 | 13.161 | 20.4 | 28.126 |
| 40 | 1.119 | 0.019 | 13.104 | 20.4 | 28.006 |
| 41 | 1.143 | 0.019 | 13.048 | 20.4 | 27.885 |
| 42 | 1.215 | 0.020 | 12.709 | 20.4 | 27.402 |
| 43 | 1.240 | 0.021 | 12.539 | 20.4 | 26.799 |
| 44 | 1.264 | 0.021 | 12.370 | 21.25 | 26.557 |
| 45 | 1.289 | 0.021 | 12.200 | 21.25 | 27.412 |

| Number | Time (s) | Time (min) | Torque reading (N. m) | Screw speed (rpm) | Power (N. m/s) |
|---|---|---|---|---|---|
| 46 | 1.313 | 0.022 | 12.031 | 21.25 | 27.035 |
| 47 | 1.337 | 0.022 | 11.861 | 21.25 | 26.784 |
| 48 | 1.361 | 0.023 | 11.692 | 21.25 | 26.155 |
| 49 | 1.385 | 0.023 | 11.579 | 21.25 | 25.903 |
| 50 | 1.409 | 0.023 | 11.410 | 21.25 | 25.526 |
| 51 | 1.477 | 0.025 | 11.127 | 21.25 | 24.897 |
| 52 | 1.503 | 0.025 | 11.127 | 21.25 | 24.772 |
| 53 | 1.528 | 0.025 | 11.071 | 21.25 | 24.646 |
| 54 | 1.553 | 0.026 | 11.071 | 21.25 | 24.646 |
| 55 | 1.578 | 0.026 | 11.071 | 21.25 | 24.646 |
| 56 | 1.602 | 0.027 | 11.071 | 21.25 | 24.646 |
| 57 | 1.628 | 0.027 | 11.071 | 21.25 | 24.646 |
| 58 | 1.651 | 0.028 | 11.071 | 21.25 | 24.646 |
| 59 | 1.676 | 0.028 | 11.071 | 21.25 | 24.646 |
| 60 | 1.743 | 0.029 | 11.014 | 21.25 | 24.520 |
| 61 | 1.770 | 0.030 | 11.014 | 21.25 | 24.520 |
| 62 | 1.794 | 0.030 | 10.958 | 21.25 | 24.394 |
| 63 | 1.819 | 0.030 | 10.958 | 21.25 | 24.394 |
| 64 | 1.843 | 0.031 | 10.958 | 21.25 | 24.394 |
| 65 | 1.867 | 0.031 | 10.901 | 21.25 | 24.268 |
| 66 | 1.890 | 0.032 | 10.901 | 21.25 | 24.268 |
| 67 | 1.916 | 0.032 | 10.845 | 21.25 | 24.268 |
| 68 | 1.940 | 0.032 | 10.845 | 21.25 | 24.143 |
| 69 | 2.008 | 0.033 | 10.675 | 21.25 | 23.891 |
| 70 | 2.034 | 0.034 | 10.619 | 21.25 | 23.765 |
| 71 | 2.058 | 0.034 | 10.506 | 21.25 | 23.389 |
| 72 | 2.084 | 0.035 | 10.449 | 21.25 | 23.263 |
| 73 | 2.109 | 0.035 | 10.336 | 21.25 | 23.136 |
| 74 | 2.133 | 0.036 | 10.280 | 21.25 | 23.011 |
| 75 | 2.159 | 0.036 | 10.167 | 21.25 | 22.634 |
| 76 | 2.182 | 0.036 | 10.054 | 21.25 | 22.382 |
| 77 | 2.207 | 0.037 | 9.941 | 21.25 | 22.257 |
| 78 | 2.274 | 0.038 | 9.659 | 21.25 | 21.628 |
| 79 | 2.300 | 0.038 | 9.602 | 21.25 | 21.377 |
| 80 | 2.324 | 0.039 | 9.546 | 21.25 | 21.251 |
| 81 | 2.350 | 0.039 | 9.546 | 21.25 | 21.251 |
| 82 | 2.373 | 0.040 | 9.546 | 21.25 | 21.251 |
| 83 | 2.398 | 0.040 | 9.659 | 21.25 | 21.502 |
| 84 | 2.423 | 0.040 | 9.715 | 21.25 | 21.502 |
| 85 | 2.448 | 0.041 | 9.772 | 21.25 | 21.753 |
| 86 | 2.472 | 0.041 | 9.885 | 21.25 | 21.879 |
| 87 | 2.540 | 0.042 | 10.054 | 21.25 | 22.382 |
| 88 | 2.566 | 0.043 | 10.167 | 21.25 | 22.508 |
| 89 | 2.590 | 0.043 | 10.223 | 21.25 | 22.634 |
| 90 | 2.615 | 0.044 | 10.280 | 21.25 | 22.760 |
| 91 | 2.639 | 0.044 | 10.336 | 21.25 | 23.011 |
| 92 | 2.664 | 0.044 | 10.393 | 21.25 | 23.136 |

| Number | Time (s) | Time (min) | Torque reading (N. m) | Screw speed (rpm) | Power (N. m/s) |
|---|---|---|---|---|---|
| 93 | 2.691 | 0.045 | 10.449 | 21.25 | 23.136 |
| 94 | 2.715 | 0.045 | 10.506 | 21.25 | 23.263 |
| 95 | 2.739 | 0.046 | 10.562 | 21.25 | 23.514 |
| 96 | 2.807 | 0.047 | 10.732 | 21.25 | 23.765 |
| 97 | 2.833 | 0.047 | 10.788 | 21.25 | 23.891 |
| 98 | 2.857 | 0.048 | 10.788 | 21.25 | 24.017 |
| 99 | 2.882 | 0.048 | 10.845 | 21.25 | 24.143 |
| 100 | 2.908 | 0.048 | 10.845 | 21.25 | 24.143 |
| 101 | 2.932 | 0.049 | 10.901 | 21.25 | 24.268 |
| 102 | 2.960 | 0.049 | 10.958 | 21.25 | 24.394 |
| 103 | 2.984 | 0.050 | 11.014 | 21.25 | 24.394 |
| 104 | 3.008 | 0.050 | 11.014 | 21.25 | 24.520 |
| 105 | 3.075 | 0.051 | 11.071 | 21.25 | 24.646 |
| 106 | 3.100 | 0.052 | 11.071 | 21.25 | 24.646 |
| 107 | 3.124 | 0.052 | 11.071 | 21.25 | 24.646 |
| 108 | 3.149 | 0.052 | 11.014 | 21.25 | 24.520 |
| 109 | 3.174 | 0.053 | 10.958 | 21.25 | 24.520 |
| 110 | 3.198 | 0.053 | 10.901 | 21.25 | 24.268 |
| 111 | 3.224 | 0.054 | 10.788 | 21.25 | 24.143 |
| 112 | 3.248 | 0.054 | 10.732 | 21.25 | 23.891 |
| 113 | 3.273 | 0.055 | 10.675 | 21.25 | 23.765 |
| 114 | 3.340 | 0.056 | 10.562 | 21.25 | 23.514 |
| 115 | 3.365 | 0.056 | 10.562 | 21.25 | 23.514 |
| 116 | 3.389 | 0.056 | 10.562 | 21.25 | 23.514 |
| 117 | 3.412 | 0.057 | 10.619 | 21.25 | 23.514 |
| 118 | 3.436 | 0.057 | 10.619 | 21.25 | 23.640 |
| 119 | 3.460 | 0.058 | 10.675 | 21.25 | 23.765 |
| 120 | 3.488 | 0.058 | 10.732 | 21.25 | 23.891 |
| 121 | 3.513 | 0.059 | 10.788 | 21.25 | 23.891 |
| 122 | 3.536 | 0.059 | 10.901 | 21.25 | 24.143 |
| 123 | 3.605 | 0.060 | 11.127 | 21.25 | 24.646 |
| 124 | 3.629 | 0.060 | 11.184 | 21.25 | 24.897 |
| 125 | 3.655 | 0.061 | 11.297 | 21.25 | 25.023 |
| 126 | 3.679 | 0.061 | 11.353 | 21.25 | 25.274 |
| 127 | 3.704 | 0.062 | 11.353 | 21.25 | 25.274 |
| 128 | 3.727 | 0.062 | 11.410 | 21.25 | 25.400 |
| 129 | 3.754 | 0.063 | 11.466 | 21.25 | 25.400 |
| 130 | 3.778 | 0.063 | 11.466 | 21.25 | 25.526 |
| 131 | 3.802 | 0.063 | 11.466 | 21.25 | 25.526 |
| 132 | 3.871 | 0.065 | 11.466 | 21.25 | 25.526 |
| 133 | 3.897 | 0.065 | 11.466 | 21.25 | 25.526 |
| 134 | 3.921 | 0.065 | 11.466 | 21.25 | 25.526 |
| 135 | 3.946 | 0.066 | 11.466 | 21.25 | 25.526 |
| 136 | 3.970 | 0.066 | 11.466 | 21.25 | 25.526 |
| 137 | 3.994 | 0.067 | 11.410 | 21.25 | 25.526 |
| 138 | 4.023 | 0.067 | 11.410 | 21.25 | 25.400 |
| 139 | 4.046 | 0.067 | 11.353 | 21.25 | 25.274 |

| Number | Time (s) | Time (min) | Torque reading (N. m) | Screw speed (rpm) | Power (N. m/s) |
|---|---|---|---|---|---|
| 140 | 4.071 | 0.068 | 11.297 | 21.25 | 25.274 |
| 141 | 4.137 | 0.069 | 11.297 | 21.25 | 25.148 |
| 142 | 4.161 | 0.069 | 11.240 | 21.25 | 25.023 |
| 143 | 4.187 | 0.070 | 11.240 | 21.25 | 25.023 |
| 144 | 4.212 | 0.070 | 11.184 | 21.25 | 25.023 |
| 145 | 4.236 | 0.071 | 11.127 | 21.25 | 24.897 |
| 146 | 4.260 | 0.071 | 11.071 | 21.25 | 24.646 |
| 147 | 4.287 | 0.071 | 11.014 | 21.25 | 24.646 |
| 148 | 4.311 | 0.072 | 10.958 | 21.25 | 24.520 |
| 149 | 4.335 | 0.072 | 10.901 | 21.25 | 24.394 |
| 150 | 4.403 | 0.073 | 10.845 | 21.25 | 24.143 |
| 151 | 4.429 | 0.074 | 10.901 | 21.25 | 24.143 |
| 152 | 4.453 | 0.074 | 10.901 | 21.25 | 24.268 |
| 153 | 4.478 | 0.075 | 10.901 | 21.25 | 24.268 |
| 154 | 4.503 | 0.075 | 10.901 | 21.25 | 24.268 |
| 155 | 4.528 | 0.075 | 10.958 | 21.25 | 24.268 |
| 156 | 4.554 | 0.076 | 10.958 | 21.25 | 24.394 |
| 157 | 4.580 | 0.076 | 10.958 | 21.25 | 24.394 |
| 158 | 4.604 | 0.077 | 10.958 | 21.25 | 24.394 |
| 159 | 4.672 | 0.078 | 10.901 | 21.25 | 24.268 |
| 160 | 4.698 | 0.078 | 10.788 | 21.25 | 24.143 |
| 161 | 4.721 | 0.079 | 10.732 | 21.25 | 23.891 |
| 162 | 4.746 | 0.079 | 10.675 | 21.25 | 23.765 |
| 163 | 4.772 | 0.080 | 10.562 | 21.25 | 23.640 |
| 164 | 4.796 | 0.080 | 10.506 | 21.25 | 23.514 |
| 165 | 4.822 | 0.080 | 10.393 | 21.25 | 23.136 |
| 166 | 4.846 | 0.081 | 10.280 | 21.25 | 23.011 |
| 167 | 4.870 | 0.081 | 10.167 | 21.25 | 22.760 |
| 168 | 4.938 | 0.082 | 9.941 | 21.25 | 22.131 |
| 169 | 4.964 | 0.083 | 9.828 | 21.25 | 22.005 |
| 170 | 4.988 | 0.083 | 9.772 | 21.25 | 21.879 |
| 171 | 5.013 | 0.084 | 9.715 | 21.25 | 21.753 |
| 172 | 5.038 | 0.084 | 9.659 | 21.25 | 21.502 |
| 173 | 5.063 | 0.084 | 9.602 | 21.25 | 21.502 |
| 174 | 5.088 | 0.085 | 9.602 | 21.25 | 21.377 |
| 175 | 5.115 | 0.085 | 9.602 | 21.25 | 21.377 |
| 176 | 5.139 | 0.086 | 9.546 | 21.25 | 21.251 |
| 177 | 5.208 | 0.087 | 9.546 | 21.25 | 21.251 |
| 178 | 5.233 | 0.087 | 9.602 | 21.25 | 21.377 |
| 179 | 5.258 | 0.088 | 9.602 | 21.25 | 21.377 |
| 180 | 5.283 | 0.088 | 9.546 | 21.25 | 21.251 |
| 181 | 5.307 | 0.088 | 9.546 | 21.25 | 21.251 |
| 182 | 5.331 | 0.089 | 9.546 | 21.25 | 21.251 |
| 183 | 5.356 | 0.089 | 9.489 | 21.25 | 21.251 |
| 184 | 5.381 | 0.090 | 9.489 | 21.25 | 21.125 |

G-2. Weight Readings and Flow Rate Calculations for Sawdust-1 at 30 rpm

| Time (s) | Time (min) | Time interval (s) | Weight (kg) | Weight increment (kg) | Mass flow rate (kg/h) |
|---|---|---|---|---|---|
| 0.00 | 0.00 | 2.03 | 0.00 | 0.08 | 141.87 |
| 2.03 | 0.03 | 2.04 | 0.08 | 0.08 | 141.18 |
| 4.07 | 0.07 | 2.08 | 0.16 | 0.10 | 173.08 |
| 6.15 | 0.10 | 2.04 | 0.26 | 0.08 | 141.18 |
| 8.19 | 0.14 | 2.03 | 0.34 | 0.10 | 177.34 |
| 10.22 | 0.17 | 2.09 | 0.44 | 0.08 | 137.80 |
| 12.31 | 0.21 | 2.03 | 0.52 | 0.10 | 177.34 |
| 14.34 | 0.24 | 4.12 | 0.62 | 0.18 | 157.28 |
| 18.46 | 0.31 | 2.08 | 0.80 | 0.10 | 173.08 |
| 20.54 | 0.34 | 2.04 | 0.90 | 0.10 | 176.47 |
| 22.58 | 0.38 | 2.03 | 1.00 | 0.08 | 141.87 |
| 24.61 | 0.41 | 2.14 | 1.08 | 0.10 | 168.22 |
| 26.75 | 0.45 | 2.03 | 1.18 | 0.10 | 177.34 |
| 28.78 | 0.48 | 2.09 | 1.28 | 0.10 | 172.25 |
| 30.87 | 0.51 | 2.03 | 1.38 | 0.08 | 141.87 |
| 32.90 | 0.55 | 4.12 | 1.46 | 0.20 | 174.76 |
| 37.02 | 0.62 | 2.03 | 1.66 | 0.10 | 177.34 |
| 39.05 | 0.65 | 2.04 | 1.76 | 0.08 | 141.18 |
| 41.09 | 0.68 | 2.03 | 1.84 | 0.10 | 177.34 |
| 43.12 | 0.72 | 2.09 | 1.94 | 0.10 | 172.25 |
| 45.21 | 0.75 | 2.03 | 2.04 | 0.10 | 177.34 |
| 47.24 | 0.79 | 2.03 | 2.14 | 0.08 | 141.87 |
| 49.27 | 0.82 | 2.03 | 2.22 | 0.10 | 177.34 |
| 51.30 | 0.86 | 2.09 | 2.32 | 0.10 | 172.25 |
| 53.39 | 0.89 | 2.03 | 2.42 | 0.10 | 177.34 |
| 55.42 | 0.92 | 2.03 | 2.52 | 0.10 | 177.34 |
| 57.45 | 0.96 | 2.04 | 2.62 | 0.10 | 176.47 |
| 59.49 | 0.99 | 2.14 | 2.72 | 0.08 | 134.58 |
| 61.63 | 1.03 | 2.03 | 2.80 | 0.10 | 177.34 |
| 63.66 | 1.06 | 2.09 | 2.90 | 0.10 | 172.25 |
| 65.75 | 1.10 | 2.09 | 3.00 | 0.10 | 172.25 |
| 67.84 | 1.13 | 2.08 | 3.10 | 0.10 | 173.08 |
| 69.92 | 1.17 | 2.03 | 3.20 | 0.10 | 177.34 |
| 71.95 | 1.20 | 2.04 | 3.30 | 0.10 | 176.47 |
| 73.99 | 1.23 | 2.03 | 3.40 | 0.10 | 177.34 |
| 76.02 | 1.27 | 6.21 | 3.50 | 0.30 | 173.91 |
| 82.23 | 1.37 | 2.03 | 3.80 | 0.10 | 177.34 |
| 84.26 | 1.40 | 2.09 | 3.90 | 0.10 | 172.25 |
| 86.35 | 1.44 | 2.03 | 4.00 | 0.08 | 141.87 |
| 88.38 | 1.47 | 2.08 | 4.08 | 0.10 | 173.08 |
| 90.46 | 1.51 | 2.09 | 4.18 | 0.10 | 172.25 |
| 92.55 | 1.54 | 2.03 | 4.28 | 0.10 | 177.34 |
| 94.58 | 1.58 | 2.09 | 4.38 | 0.10 | 172.25 |
| 96.67 | 1.61 | 2.03 | 4.48 | 0.10 | 177.34 |
| 98.70 | 1.64 | 2.09 | 4.58 | 0.08 | 137.80 |
| 100.79 | 1.68 | 2.03 | 4.66 | 0.10 | 177.34 |

## Appendix H Program Listings of Model Predicting Torque Requirements

H-1: Torque prediction for wood pellets

File name: Torque_Woodpellets.m
Function: taoxave1, taoxh, trailing, integrnd_Td and integrnd_Tf
Source code: see below

```
% Hopper-screw feeder load and torque calculation for static and dynamic conditions.
% Screw speeds, gravity and centrifugal forces are neglected in screw torque analysis
clc
clear
%-----------------------------------------------------------------------------------------------------------------------
% fixed parameters for screw feeder and hopper

global P taof_v muf muwt muwh lamdas Rt Rc alphas phi phif lamdas_a CCC
rou_bulk=630;            % bulk density of bulk solid, kg/m^3.
H0=0.3;                  % initial bed height in the hopper, m
P=0.1;                   % pitch,m
Do=0.1;                  % screw diameter, m
Ro=Do/2;                 % screw radius, m.
Dc=0.030;                % screw core shaft diameter, m
Rc=Dc/2;                 % screw core shaft radius, m
Dt=0.102;                % trough diameter,m
Rt=Dt/2;                 % trough radius, m
cp=P/Do;                 % ratio of pitch to screw diameter.
ct=Dt/Do;                % ratio of trough diameter to screw diameter.
cd=Dc/Do;                % ratio of core shaft diameter to screw diameter.
Lh=0.914;                % hopper outlet length,m
L=0.8;                   % length of screw with .1 m screw diameter, a little shorter than outlet length (.914 m).
Lc=0.62;                 % choke section length, m
B=0.102;                 % width of the trough,m
A_cross=pi*(Ro^2-Rc^2)   % Effective cross section area of screw casing, m^2.
alpha=20/180*pi;         % half hopper angle, radian
g=9.8;                   % gravitational acceleration, m/s^2.
alphao=atan(P/(2*pi*Ro));          % helical angle at outside screw diameter, radian.
alphac=atan(P/(2*pi*Rc));          % helical angle at core shaft surface, radian.
alphao_deg=atan(P/(2*pi*Ro))/pi*180;   % helical angle at outside screw diameter, degree.
alphac_deg=atan(P/(2*pi*Rc))/pi*180;   % helical angle at core shaft surface, degree.
%-----------------------------------------------------------------------------------------------------------------------

% variable parameters for biomass fuels and hopper-screw feeder
% initial vertical stress and initial feeder load
m=1;
delta1_deg=32;                  % set effective internal friction angle, degree
delta2_deg=32;
delta_deg=[delta1_deg:m:delta2_deg];   % effective internal friction angle, degree.
n=(delta2_deg-delta1_deg)./m+1;
delta=[delta1_deg/180*pi:m/180*pi:delta2_deg/180*pi];
phi=31.4/180*pi;   % angle of friction between bulk solids and hopper wall (or casing surface), radian.
phif=31.4/180*pi;  % angle of friction between bulk solids and screw flight, radian.
muf=tan(phif);              % coefficient of friction between solids and flight surface
muwc=muf;                   % friction coefficient of bulk solid on core surface
muwh=tan(phi);              % friction coefficient of bulk solid on hopper surface.
muwt=muwh;                  % friction coefficient of bulk solid on trough surface.

D=2*(H0+B./2*cot(alpha))*tan(alpha);
```

```
                                % compute width of bulk solid free surface in hopper (flate surface), m
qi=1/(2*tan(alpha))*(D/B-1); % compute non-dimensional surcharge factor for initial condition.
taoi_v=qi*rou_bulk*g*B;      % compute vertical stress at hopper outlet for initial condition
Fv_i=taoi_v*Lh*B;            % compute feeder load at hopper outlet for initial condition
%-----------------------------------------------------------------------------------------------------------------------------------

% vertical stress and feeder load for flow condition
for i=1:1:n
mud(i)=tan(delta(i));        % effective coefficient of internal friction.
mue(i)=sin(delta(i));        % equivalent friction coefficient of bulk solid,.from Roberts
alpha_Mohr(i)=(asin(sin(phi)/sin(delta(i)))-phi)/2;
lamdas(i)=cos(phi)*sin(2*alpha_Mohr(i))/(sin(phi)*cos(2*alpha_Mohr(i))+sin(phi+2*alpha_Mohr(i)));
                        % stress ratio of normal stress acting perpendicularly to wall
                        % of trough and core shaft surfaces to axial compression stress
                        % derived from Mohr circle
beta(i)=0.5*(phi+asin(sin(phi)/sin(delta(i))));                    % compute beta(i), constant
X(i)=sin(delta(i))/(1-sin(delta(i)))*(sin(2*beta(i)+alpha)/sin(alpha)+1); % constant to compute feeder load
Y(i)=((alpha+beta(i))*sin(alpha)+sin(beta(i))*sin(alpha+beta(i)))./((1-sin(delta(i)))*sin(alpha+beta(i))^2);
qf(i)=Y(i)*(1+sin(delta(i)))/(2*(X(i)-1)*sin(alpha));              % surcharge factor for flow conditions
% qf1(i)=1/4*(1/tan(alpha))*(Y(i)*(1+sin(delta(i))*cos(2*beta(i)))*(tan(alpha)+tan(phi))/sin(alpha)/(X(i)-1)-1);
taof_v0(i)=qf(i)*rou_bulk*g*B;  % use loose bulk density for incompressible solids in the present study
Fv_f0(i)=taof_v0(i).*Lh.*B;     % vertical stress and feeder load for flow condition
taof_v(i)=(taof_v0(i)+taoi_v)./2;  % average vertical stress for flow condition
Fv_f(i)=taof_v(i).*Lh.*B;       % average feeder load for flow condition
end
%-----------------------------------------------------------------------------------------------------------------------------------

% hopper section, for a material element in a pitch first then entire hopper section
t=1.0;                  % factor used to modify boundary condition at trailing side of flight
eps=0.0001;             % one small number
a=0;                    % set initial value for a, a is ratio, i.e. taoxa(i)/tao_daf(i)
while abs(0.85-a) > eps
for i=1:1:n
taoxamax(i)=t*taof_v(i)*(exp(2*tan(phi)*lamdas(i)*P/(Rt-Rc)));
                        % maximum stress at driving side of flight according to stress analysis
taoxamin(i)=t*taof_v(i);        % minimum stress at trailing side of flight according to stress analysis
lamdas_a=lamdas(i);             % stress ratio of normal wall stress to axial stress on confined surface
taoxa(i)=1/P*t*taof_v(i)*quadl(@taoxh, 0,P);  % average axial stress in a pitch for flow condition
taoxai(i)=1/P*t*taoi_v*quadl(@taoxh, 0,P);    % average axial stress in a pitch for initial condition
taowa(i)=lamdas(i)*taoxa(i);            % average normal wall stress in a pitch for flow condition
taowai(i)=lamdas(i)*taoxai(i);          % average normal wall stress in a pitch for initial condition

%-1. shear surface
ksa(i)=pi*mue(i)*cp*cos(alphao+phif)./2;   % parameter for axial force calculations on shear surface
Fsaf(i)=-ksa(i).*taof_v(i).*Do.^2;         % axial force on shear surface for flow condition
Fsai(i)=-ksa(i)*taoi_v*Do^2;               % axial force on shear surface for initial condition
kst(i)=pi*mue(i)*cp*sin(alphao+phif)./2;   % parameter for tangential force calculations on shear surface
Fstf(i)=-kst(i).*taof_v(i)*Do^2;           % tangential force on shear surface for flow condition
Fsti(i)=-kst(i)*taoi_v*Do^2;               % tangential force on shear surface for initial condition
Fstfp_try(i)=1/2*(taof_v(i)+taowa(i))*0.00635*P/sin(alphao)*tan(phif);
                        % tangential force from flight tips for flow condition
Fstip_try(i)=1/2*(taoi_v+taowai(i))*0.00635*P/sin(alphao)*tan(phif);
                        % tangential force from flight tips for initial condition

Tstfp(i)=Fstfp_try(i)*Ro;       % torque from flight tips for flow condition
Tstip(i)=Fstip_try(i)*Ro;       % torque from flight tips for initial condition
```

```
%-2. core shaft
kca(i)=t*pi*(ct-cd)*cd*cp*(exp(4*muwc*lamdas(i)*cp/(ct-cd))-1)/4/(cp^2+pi^2*cd^2)^0.5;
                        % parameter for axial force calculations on core shaft surface
Fcaf(i)=-kca(i)*taof_v(i)*Do^2;    % axial force on core surface for flow condition
Fcai(i)=-kca(i)*taoi_v*Do^2;       % axial force on core surface for initial condition
Fca1_try(i)=2*pi*Rc*P*tan(phif)*taowa(i)*sin(alphac); % axial force on core surface for flow condition
kct(i)=t*pi^2*(ct-cd)*cd^2*(exp(4*muwc*lamdas(i)*cp/(ct-cd))-1)/4/(cp^2+pi^2*cd^2)^0.5;
                        % parameter for tangential force calculations on core shaft surface
Fctf(i)=kct(i)*taof_v(i)*Do^2;     % tangential force on core surface for flow condition
Fcti(i)=kct(i)*taoi_v*Do^2;        % tangential force on core surface for initial condition

%-3. trailing flight side
kfa(i)=t*lamdas(i)*(pi*(1-cd^2)/4+cp*muf*(1-cd)/2);
                        % parameter for axial force calculations on trailing side surface
Ffaf(i)=-kfa(i)*taof_v(i)*Do^2;    % axial force on trailing side surface for flow condition
Ffai(i)=-kfa(i)*taoi_v*Do^2;       % axial force on trailing side surface for initial condition
Ffaf1_try(i)=2.*pi.*lamdas(i).*taoxamin(i).*quadl(@trailing, Rc, Ro);
                        % axial force on trailing side surface for flow condition
kft(i)=t*lamdas(i)*(pi*muf*(1-cd^2)/4-cp*(1-cd)/2);
                        % parameter for tangential force calculations on trailing side surface
Fftf(i)=kft(i)*taof_v(i)*Do^2;     % tangential force on trailing side surface for flow condition
Ffti(i)=kft(i)*taoi_v*Do^2;        % tangential force on trailing side surface for initial condition

%-4. trough surface
kta(i)=t*pi*(ct-cd)*ct*cos(alphao+phif)/8*(exp(4*muwt*lamdas(i)*cp/(ct-cd))-1);
                        % parameter for axial force calculations on trough surface
Ftaf(i)=-kta(i).*taof_v(i).*Do.^2;  % axial force on trough surface for flow condition
Ftai(i)=-kta(i)*taoi_v*Do^2;       % axial force on trough surface for initial condition
ktt(i)=t*pi*(ct-cd)*ct*sin(alphao+phif)/8*(exp(4*muwt*lamdas(i)*cp/(ct-cd))-1);
                        % parameter for tangential force calculations on trough surface
Fttf(i)=-ktt(i)*taof_v(i)*Do^2;     % tangential force on trough surface for flow condition
Ftti(i)=-ktt(i)*taoi_v*Do^2;        % tangential force on trough surface for initial condition

%-5. stress on driving side
Kda(i)=4*(ksa(i)+kca(i)+kfa(i)+kta(i))/pi/(1-cd^2);
                        % parameter for axial force calculations on driving side surface
tao_daf(i)=Kda(i)*taof_v(i);       % compute axial stress on driving surface for flow condition
tao_dai(i)=Kda(i)*taoi_v;          % compute axial stress on driving surface for initial condition
Ftao_daf(i)=tao_daf(i)*A_cross;        % compute axial force on driving surface for flow condition
Ftao_dai(i)=tao_dai(i)*A_cross;        % compute axial force on driving surface for initial condition

% torque calculation
Tdf(i)=2*pi*tao_daf(i)*quadl(@integrnd_Td, Rc, Ro);
                        % compute torque generated by driving side of screw for flow condition
Tdi(i)=2*pi*tao_dai(i)*quadl(@integrnd_Td, Rc, Ro);
                        % compute torque generated by driving side of screw for initial condition
Tcf(i)=2*pi*Rc*P*taowa(i)*tan(phif)*cos(alphac)*Rc;;
                        % compute torque generated by core shaft surface for flow condition
Tci(i)=2*pi*Rc*P*taowai(i)*tan(phif)*cos(alphac)*Rc;
                        % compute torque generated by core shaft surface for initial condition
Tff(i)=2*pi*lamdas(i)*t*taof_v(i)*quadl(@integrnd_Tf, Rc, Ro);
                        % compute torque from trough surface for flow condition
Tfi(i)=2*pi*lamdas(i)*t*taoi_v*quadl(@integrnd_Tf, Rc, Ro);
                        % compute torque from trough surface for initial condition

T_hopperf(i)=Lh/P*(Tdf(i)+Tcf(i)+Tff(i)+Tstfp(i));  % compute total torque in hopper section for flow condition
T_hopperi(i)=Lh/P*(Tdi(i)+Tci(i)+Tfi(i)+Tstip(i));  % compute total torque in hopper section for initial condition
```

```
ratio01(i)=tao_daf(i)/taoxamax(i);  % ratio of stress on driving side to theoretical maximum stress in a pitch
ratio02(i)=taoxa(i)/tao_daf(i);     % ratio of average axial stress to stress on driving side in a pitch
end

a=ratio02(1);                % ratio of average axial stress to stress on driving side
t=t+0.0001;                  % 0.0001 as increment for t
end
t=t-0.0001;
%-------------------------------------------------------------------------------------------------------------------------------

% Choke section-0.9 m screw diameter
P=0.1;                % pitch,m
Do=0.09;              % screw diameter, m
Ro=Do/2;              % screw radius, m.
Dc=0.030;             % screw core shaft diameter, m
Rc=Dc/2;              % screw core shaft radius, m
Dt=0.102;             % trough diameter,m
Rt=Dt/2;              % trough radius, m
cp=P/Do;              % ratio of pitch to screw diameter.
ct=Dt/Do;             % ratio of trough diameter to screw diameter.
cd=Dc/Do;             % ratio of core shaft diameter to screw diameter.
A_cross=pi*(Ro^2-Rc^2)      % Effective cross section area of the screw casing
L1=0.2;               % length of screw with 0.09 m screw diameter.
alphao=atan(P/(2*pi*Ro));          % helical angle at the outside screw diameter, radian.
alphac=atan(P/(2*pi*Rc));          % helical angle at the core shaft surface, radian.
alphao_deg=atan(P/(2*pi*Ro))/pi*180;    % helical angle at the outside screw diameter, degree.
alphac_deg=atan(P/(2*pi*Rc))/pi*180;    % helical angle at the core shaft surface, degree.

% torque calculation
for i=1:1:n
con=0.15;                    % constant for estimating the axial stress in choke section
e=0.2;
CC1(i)=con*(qf(i)*H0/Dt*Lc/Dt/ct)^(e);  % exponent to estimate the axial stress on trailing side of flight
taoxam1(i)=t*taof_v(i)*(exp(2*tan(phi)*lamdas(i)*P/(Rt-Rc))).^(CC1(i)+1);
                        % theoretical maximum stress on driving side of flight
taoxam11(i)=t*taof_v(i)*(exp(2*tan(phi)*lamdas(i)*P/(Rt-Rc))).^(CC1(i));
                        % theoretical minimum stress on trailing side of flight
EE1(i)=(exp(2*tan(phi)*lamdas(i)*P/(Rt-Rc))).^(CC1(i));
                        % how many times for stress on trailing side compared to vertical stress taof_v
                        % for flow condition, compression factor in choke section
lamdas_a=lamdas(i);          % compute lamdas for function taoxave1
CCC=CC1(i);                  % compute CC1 for function taoxave1
taox1_a(i)=1/P*t*taof_v(i)*quadl(@taoxave1, 0,P);  % average axial stress in choke section
taowa1(i)=lamdas(i)*taox1_a(i);          % average normal wall stress in choke section

Fca1(i)=2*pi*Rc*P*tan(phif)*taowa1(i)*sin(alphac);
                        % axial force on core surface in choke section
Ffaf1(i)=2.*pi.*lamdas(i).*taoxam11(i).*quadl(@trailing, Rc, Ro);
                        % axial force on trailing side surface in choke section
Ftaf1(i)=2*pi*tan(phi)*taowa1(i)*Rt*P*cos(alphao+phif);    % axial force on trough surface in choke section

Fdaf1(i)=Fca1(i)+Ffaf1(i)+Ftaf1(i);
                        % axial force on driving side surface in choke section
tao_daf1(i)=Fdaf1(i)./pi./(Ro^2-Rc^2);
                        % compute axial stress on driving surface for flow condition in choke section
Tdf1(i)=2*pi*tao_daf1(i)*quadl(@integrnd_Td, Rc, Ro);
                        % compute torque generated by driving side surface for choke section
```

```
Tcf1(i)=taowa1(i)*2*pi*Rc*P*tan(phif)*Rc*cos(alphac);
                                        % compute torque generated by trailing side surface for choke section
Tff1(i)=2*pi*lamdas(i)*taoxam11(i)*quadl(@integrnd_Tf, Rc, Ro);
                                        % compute torque generated by trough side surface for choke section
Ttip1(i)=taowa1(i)*0.00635*P./sin(alphao)*tan(phif)*Ro;
                                        % compute torque generated by flight tips for choke section
T_choke1(i)=L1/P*(Tdf1(i)+Tcf1(i)+Tff1(i)+Ttip1(i));
                                        % compute total torque in choke section 1 for flow condition
end
%-----------------------------------------------------------------------------------------------------------------------

% Choke section-0.8 m screw diameter
P=0.1;              % pitch,m
Do=0.08;            % screw diameter, m
Ro=Do/2;            % screw radius, m.
Dc=0.030;           % screw core shaft diameter, m
Rc=Dc/2;            % screw core shaft radius, m
Dt=0.102;           % trough diameter,m
Rt=Dt/2;            % trough radius, m
cp=P/Do;            % ratio of pitch to screw diameter.
ct=Dt/Do;           % ratio of trough diameter to screw diameter.
cd=Dc/Do;           % ratio of core shaft diameter to screw diameter.
A_cross=pi*(Ro^2-Rc^2)      % Effective cross section area of the screw casing
L2=0.42;            % length of screw with 0.08 m screw diameter.
alphao=atan(P/(2*pi*Ro));          % helical angle at outside screw diameter, radian.
alphac=atan(P/(2*pi*Rc));          % helical angle at core shaft surface, radian.
alphao_deg=atan(P/(2*pi*Ro))/pi*180;    % helical angle at outside screw diameter, degree.
alphac_deg=atan(P/(2*pi*Rc))/pi*180;    % helical angle at core shaft surface, degree.

% torque calculation
for i=1:1:n
CC2(i)=con*(qf(i)*H0/Dt*Lc/Dt/ct)^(e);
                % exponent to estimate axial stress on trailing side of a flight
taoxam2(i)=t*taof_v(i)*(exp(2*tan(phi)*lamdas(i)*P/(Rt-Rc)))^(CC2(i)+1);
                % theoretical maximum stress on driving side of flight
taoxam22(i)=t*taof_v(i)*exp(2*tan(phi)*lamdas(i)*P/(Rt-Rc))^(CC2(i));
                % theoretical minimum stress on trailing side of flight
EE2(i)=(exp(2*tan(phi)*lamdas(i)*P/(Rt-Rc))).^(CC2(i));
                % how many times for stress on trailing side compared to vertical stress taof_v
                % for flow condition, compression factor in choke section
lamdas_a=lamdas(i);       % compute lamdas for function taoxave1
CCC=CC2(i);               % compute CC2 for function taoxave1
taox2_a(i)=1/P*t*taof_v(i)*quadl(@taoxave1, 0,P);   % average axial stress in choke section
taowa2(i)=lamdas(i)*taox2_a(i);                     % average normal wall stress in choke section
Fca2(i)=2*pi*Rc*P*tan(phi)*taowa2(i)*sin(alphac);
                % axial force on core surface in choke section
Ffaf2(i)=2*pi*lamdas(i)*taoxam22(i)*quadl(@trailing, Rc, Ro);
                % axial force on trailing side surface in choke section
Ftaf2(i)=2*pi*tan(phi)*taowa2(i)*Rt*P*cos(alphao+phif);
                % axial force on trough surface in choke section
Fdaf2(i)=Fca2(i)+Ffaf2(i)+Ftaf2(i);       % axial force on driving side surface in choke section
tao_daf2(i)=Fdaf2(i)./pi./(Ro^2-Rc^2);;   % compute axial stress on driving surface in choke section
Tdf2(i)=2*pi*tao_daf2(i)*quadl(@integrnd_Td, Rc, Ro);
                        % compute torque generated by driving side surface for choke section 2
Tcf2(i)=taowa2(i)*2*pi*Rc*P*tan(phif)*Rc*cos(alphac);
                        % compute torque generated by trailing side surface for choke section 2
Tff2(i)=2*pi*lamdas(i)*taoxam22(i)*quadl(@integrnd_Tf, Rc, Ro);
```

```
                        % compute torque generated by trough surface for choke section 2
Ttip2(i)=taowa2(i)*0.00635*P./sin(alphao)*tan(phif)*Ro;
                        % compute torque generated by flight tips for choke section
T_choke2(i)=L2/P*(Tdf2(i)+Tcf2(i)+Tff2(i)+Ttip2(i));
                        % compute total torque in choke section 2 for flow condition
end
Tor_totalf=(T_choke1+T_choke2)+T_hopperf;    % compute total torque for flow condition
Tor_initial=T_hopperi;                       % compute initial torque for hopper section
tao_dft=[tao_daf tao_daf1 tao_daf2];         % axial stress in hopper, choke 1 and choke 2
%-------------------------------------------------------------------------------------------------------------------------
% power estimation

screwspeed=[5 10 20 30 40];
for j=1:1:5
power(j)=Tor_totalf(1)*2*pi*screwspeed(j)/60;
end

result=[taoxa(1) taox1_a(1) taox2_a(1) taoi_v Fv_i taof_v0(1) Fv_f0(1) taof_v(1) Fv_f(1) Tor_initial(1)
T_hopperf(1)  T_choke1(1) T_choke2(1) Tor_totalf(1)];

fprintf('The solution is \n')
fprintf('axial stress in hopper=%8.4f \n',result(1))
fprintf('axial stress1=%8.4f \n',result(2))
fprintf('axial stress2=%8.4f \n',result(3))
fprintf('initial vertical stress=%8.4f \n',result(4))
fprintf('initial feeder load=%8.4f \n',result(5))
fprintf('vertical stress for flow condition=%8.4f \n',result(6))
fprintf('feeder load for flow condition=%8.4f \n',result(7))
fprintf('modified vertical stress for flow condition=%8.4f \n',result(8))
fprintf('modified feeder load for flow condition=%8.4f \n',result(9))
fprintf('torque requirement for hopper in initial condition=%8.4f \n',result(10))
fprintf('torque requirement for hopper in flow condition=%8.4f \n',result(11))
fprintf('torque requirement for choke 1 in flow condition=%8.4f \n',result(12))
fprintf('torque requirement for choke 2 in flow condition=%8.4f \n',result(13))
fprintf('torque requirement for flow condition=%8.4f \n',result(14))

x=[5 10 20 30 40];
power2=zeros(5,2);

for i=1:1:5
   power2(i,1)=x(i);
   power2(i,2) =power(i);
end
fprintf('\n Power requirements for 5, 10, 20 ,30 ,40 rpm is \n');
```

H-2: Torque prediction for sawdust-1 for 0.15 m tapered section

File name: Torque_sawdust_taper6inch.m
Function: taoxave1, taoxh, trailing, integrnd_Td, integrnd_Tf, taotaper
Source code: see below

```
% Hopper-screw feeder load and torque calculation for static and dynamic conditions with taper section
% Screw speeds, gravity and centrifugal forces are neglected in screw torque analysis
clc
clear
%-----------------------------------------------------------------------------------------------------------------------
% fixed parameters for screw feeder and hopper
global P taof_v muf muwt lamdas Rt Rc alphas muwh phi phif lamdas_a CCC
rou_bulk=212;      % bulk density of bulk solid, kg/m^3.
H0=0.45;           % initial bed height in hopper, m
P=0.1;             % pitch,m
Do=0.1;            % screw diameter, m
Ro=Do/2;           % screw radius, m.
Dc=0.030;          % screw core shaft diameter, m
Rc=Dc/2;           % screw core shaft radius, m
Dt=0.102;          % trough diameter,m
Rt=Dt/2;           % trough radius, m
cp=P/Do;           % ratio of pitch to screw diameter.
ct=Dt/Do;          % ratio of trough diameter to screw diameter.
cd=Dc/Do;          % ratio of core shaft diameter to screw diameter.
Lh=0.914;          % hopper outlet length,m
L=0.8;             % length of screw with 0.1 m screw diameter, a little shorter than outlet length, i.e. 0.914 m.
Lc=0.62;
B=0.102;           % width of trough,m
t=0.00635;         % flight thickness,m
A_cross=pi*(Ro^2-Rc^2);    % effective cross section area of the screw casing
alpha=20/180*pi;           % half hopper angle, radian
g=9.8;             % gravitational acceleration, m/s^2.
alphao=atan(P/(2*pi*Ro));          % helical angle at outside screw diameter, radian.
alphac=atan(P/(2*pi*Rc));          % helical angle at core shaft surface, radian.
alphao_deg=atan(P/(2*pi*Ro))/pi*180;     % helical angle at outside screw diameter, degree.
alphac_deg=atan(P/(2*pi*Rc))/pi*180;     % helical angle at core shaft surface, degree.
%-----------------------------------------------------------------------------------------------------------------------

% variable parameters for biomass fuels and hopper-screw feeder; initial vertical stress and initial feeder load
m=1;
delta1_deg=38;                     % set effective internal friction angle, degree
delta2_deg=38;
delta_deg=[delta1_deg:m:delta2_deg];     % effective internal friction angle, degree.
nn=(delta2_deg-delta1_deg)./m+1;
delta=[delta1_deg/180*pi:m/180*pi:delta2_deg/180*pi];
phi=31.8/180*pi;           % angle of friction between bulk solids and hopper wall (or casing surface), radian
phif=31.8/180*pi;          % angle of friction between bulk solids and screw flight, radian.PE
muf=tan(phif);             % coefficient of friction between solids and screw flight surface
muwc=muf;                  % friction coefficient of bulk solid on core surface
muwh=tan(phi);             % friction coefficient of bulk solid on hopper surface.
muwt=muwh;                 % friction coefficient of bulk solid on trough surface.
D=2*(H0+B./2*cot(alpha))*tan(alpha);  % compute width of bulk solid free surface in hopper (flate surface), m
qi=1/(2*tan(alpha))*(D/B-1);       % compute non-dimensional surcharge factor for initial condition
taoi_v=qi*rou_bulk*g*B;            % compute vertical stress at hopper outlet for initial condition
Fv_i=taoi_v*Lh*B;                  % compute feeder load at hopper outlet for initial condition
%-----------------------------------------------------------------------------------------------------------------------
```

```
% vertical stress and feeder load for flow condition
for i=1:1:nn
mud(i)=tan(delta(i));              % effective coefficient of internal friction.
mue(i)=sin(delta(i));              % equivalent friction coefficient of bulk solid,.from Roberts
%lamdas(i)=1/(1+2*mud(i)^2+2*((1+mud(i)^2)*(mud(i)^2-muwt^2))^0.5);  % stress ratio of normal stress acting
perpendicularly to wall
                    % of trough and core shaft surfaces to axial compression stress
                    % derived from Mohr circle
alpha_Mohr(i)=(asin(sin(phi)/sin(delta(i)))-phi)/2;
lamdas(i)=cos(phi)*sin(2*alpha_Mohr(i))/(sin(phi)*cos(2*alpha_Mohr(i))+sin(phi+2*alpha_Mohr(i)));
                          % stress ratio of normal stress acting perpendicularly to wall
                          % of trough and core shaft surfaces to axial compression stress
                          % derived from Mohr circle
beta(i)=0.5*(phi+asin(sin(phi)/sin(delta(i))));       % compute beta(i), constant
X(i)=sin(delta(i))/(1-sin(delta(i)))*(sin(2*beta(i)+alpha)/sin(alpha)+1);
                          % constant to compute feeder load
Y(i)=((alpha+beta(i))*sin(alpha)+sin(beta(i))*sin(alpha+beta(i)))./((1-sin(delta(i)))*sin(alpha+beta(i)).^2);
                          % constant to compute feeder load
qf(i)=Y(i)*(1+sin(delta(i)))/(2*(X(i)-1)*sin(alpha));      % surcharge factor for flow conditions
taof_v0(i)=qf(i)*rou_bulk*g*B;      % use average bulk density for compressible solids in the present study
Fv_f0(i)=taof_v0(i).*Lh.*B;          % vertical stress and feeder load for flow condition
taof_v(i)=(taof_v0(i)+taoi_v)./2;    % average vertical stress for flow condition
Fv_f(i)=taof_v(i).*Lh.*B;            % average feeder load for flow condition
end

%-------------------------------------------------------------------------------------------------------------------------

% hopper section, for a material element in a pitch first then entire hopper section
n=1.0;
eps=1e-4;
a=0;
while abs(0.99-a) > eps
for i=1:1:nn
taoxamax(i)=n*taof_v(i)*(exp(2*tan(phi)*lamdas(i)*P/(Rt-Rc)));
                          % maximum stress at driving side of flight according to stress analysis
taoxamin(i)=n*taof_v(i);          % minimum stress at trailing side of flight according to stress analysis
lamdas_a=lamdas(i);               % stress ratio of normal wall stress to axial stress on confined surface
taoxa(i)=1/P*n*taof_v(i)*quadl(@taoxh, 0,P);     % average axial stress in a pitch for flow condition
taoxai(i)=1/P*n*taoi_v*quadl(@taoxh, 0,P);     % average axial stress in a pitch for initial condition
taowa(i)=lamdas(i)*taoxa(i);          % average normal wall stress in a pitch for flow condition
taowai(i)=lamdas(i)*taoxai(i);        % average normal wall stress in a pitch for initial condition

%-1. shear surface
ksa(i)=pi*mue(i)*cp*cos(alphao+phif)./2;   % parameter for axial force calculations on shear surface
Fsaf(i)=-ksa(i).*taof_v(i).*Do.^2;          % axial force on shear surface for flow condition
Fsai(i)=-ksa(i)*taoi_v*Do^2;              % axial force on shear surface for initial condition
kst(i)=pi*mue(i)*cp*sin(alphao+phif)./2;     % parameter for tangential force calculations on shear surface
Fstf(i)=-kst(i).*taof_v(i)*Do^2;          % tangential force on shear surface for flow condition
Fsti(i)=-kst(i)*taoi_v*Do^2;              % tangential force on shear surface for initial condition
Fstfp_try(i)=1/2*(taof_v(i)+taowa(i))*t*P/sin(alphao)*tan(phif);
                          % tangential force from flight tips for flow condition
Fstip_try(i)=1/2*(taoi_v(i)+taowai(i))*t*P/sin(alphao)*tan(phif);
                          % tangential force from flight tips for initial condition
Tstfp(i)=Fstfp_try(i)*Ro;          % torque from flight tips for flow condition
Tstip(i)=Fstip_try(i)*Ro;          % torque from flight tips for initial condition
%-2. core shaft
```

```
kca(i)=n*pi*(ct-cd)*cd*cp*(exp(4*muwc*lamdas(i)*cp/(ct-cd))-1)/4/(cp^2+pi^2*cd^2)^0.5;
                        % parameter for axial force calculations on core shaft surface
Fcaf(i)=-kca(i)*taof_v(i)*Do^2;          % axial force on core surface for flow condition
Fcai(i)=-kca(i)*taoi_v*Do^2;             % axial force on core surface for initial condition
Fca1_try(i)=2*pi*Rc*P*tan(phif)*taowa(i)*sin(alphac);  % axial force on core surface for flow condition
kct(i)=n*pi^2*(ct-cd)*cd^2*(exp(4*muwc*lamdas(i)*cp/(ct-cd))-1)/4/(cp^2+pi^2*cd^2)^0.5;
                        % parameter for tangential force calculations on core shaft surface
Fctf(i)=kct(i)*taof_v(i)*Do^2;           % tangential force on core surface for flow condition
Fcti(i)=kct(i)*taoi_v*Do^2;              % tangential force on core surface for initial condition
Fct1_try(i)=2*pi*Rc*P*tan(phif)*taowa(i)*cos(alphac);
                                         % tangential force on core surface for flow condition
%-3. trailing flight side
kfa(i)=n*lamdas(i)*(pi*(1-cd^2)/4+cp*muf*(1-cd)/2);
                                % parameter for axial force calculations on trailing side surface
Ffaf(i)=-kfa(i)*taof_v(i)*Do^2;          % axial force on trailing side surface for flow condition
Ffai(i)=-kfa(i)*taoi_v*Do^2;             % axial force on trailing side surface for initial condition
Ffaf1_try(i)=2.*pi.*lamdas(i).*taoxamin(i).*quadl(@trailing, Rc, Ro);
kft(i)=n*lamdas(i)*(pi*muf*(1-cd^2)/4-cp*(1-cd)/2);  % parameter for tangential force calculations on trailing
side surface
Fftf(i)=kft(i)*taof_v(i)*Do^2;           % tangential force on trailing side surface for flow condition
Ffti(i)=kft(i)*taoi_v*Do^2;              % tangential force on trailing side surface for initial condition

%-4. trough surface
kta(i)=n*pi*(ct-cd)*ct*cos(alphao+phif)/8*(exp(4*muwt*lamdas(i)*cp/(ct-cd))-1);
                                % parameter for axial force calculations on trough surface
Ftaf(i)=-kta(i).*taof_v(i).*Do.^2;        % axial force on trough surface for flow condition
Ftai(i)=-kta(i)*taoi_v*Do^2;              % axial force on trough surface for initial condition
Ftaf_try(i)=pi*Rt*P*tan(phi)*cos(alphao+phif)*taowa(i);
                                % axial force on trough surface for flow condition
ktt(i)=n*pi*(ct-cd)*ct*sin(alphao+phif)/8*(exp(4*muwt*lamdas(i)*cp/(ct-cd))-1);
                                % parameter for tangential force calculations on trough surface
Fttf(i)=-ktt(i)*taof_v(i)*Do^2;           % tangential force on trough surface for flow condition
Ftti(i)=-ktt(i)*taoi_v*Do^2;              % tangential force on trough surface for initial condition

%-5. stress on driving side
Kda(i)=4*(ksa(i)+kca(i)+kfa(i)+kta(i))/pi/(1-cd^2);
                                % parameter for axial force calculations on driving side surface
tao_daf(i)=Kda(i)*taof_v(i);             % compute axial stress on driving surface for flow condition
tao_dai(i)=Kda(i)*taoi_v;                % compute axial stress on driving surface for initial condition
Ftao_daf(i)=tao_daf(i)*A_cross;          % compute axial force on driving surface for flow condition
Ftao_dai(i)=tao_dai(i)*A_cross;          % compute axial force on driving surface for initial condition

% torque calculation
Tdf(i)=2*pi*tao_daf(i)*quadl(@integrnd_Td, Rc, Ro);
                        % compute torque generated by driving side of screw for flow condition
Tdi(i)=2*pi*tao_dai(i)*quadl(@integrnd_Td, Rc, Ro);
                        % compute torque generated by driving side of screw for initial condition
Tcf(i)=2*pi*Rc*P*taowa(i)*tan(phif)*cos(alphac)*Rc;;
                        % compute torque generated by core shaft surface for flow condition
Tci(i)=2*pi*Rc*P*taowai(i)*tan(phif)*cos(alphac)*Rc;
                        % compute torque generated by core shaft surface for initial condition
Tff(i)=2*pi*lamdas(i)*n*taof_v(i)*quadl(@integrnd_Tf, Rc, Ro);
                        % compute torque from trough surface for flow condition
Tfi(i)=2*pi*lamdas(i)*n*taoi_v*quadl(@integrnd_Tf, Rc, Ro);
                        % compute torque from trough surface for initial condition
T_hopperf(i)=Lh/P*(Tdf(i)+Tcf(i)+Tff(i)+Tstfp(i));
                        % compute total torque in hopper section for flow condition
```

```
T_hopperi(i)=Lh/P*(Tdi(i)+Tci(i)+Tfi(i)+Tstip(i));
                        % compute total torque in hopper section for initial condition
ratio01(i)=tao_daf(i)/taoxamax(i);
                        % ratio of stress on driving side to theoretical maximum stress in a pitch
ratio02(i)=taoxa(i)/tao_daf(i);
                        % ratio of average axial stress to stress on driving side in a pitch
end
a=ratio02(1);           % ratio of average axial stress to stress on driving side

n=n+0.0001;             % 0.0001 as increment for t
end
n=n-0.0001;
%-----------------------------------------------------------------------------------------------------------------------

% Choke section-0.9 m screw diameter
P=0.1;                  % pitch,m
Do=0.09;                % screw diameter, m
Ro=Do/2;                % screw radius, m.
Dc=0.030;               % screw core shaft diameter, m
Rc=Dc/2;                % screw core shaft radius, m
Dt=0.102;               % trough diameter,m
Rt=Dt/2;                % trough radius, m
cp=P/Do;                % ratio of pitch to screw diameter.
ct=Dt/Do;               % ratio of trough diameter to screw diameter.
cd=Dc/Do;               % ratio of core shaft diameter to screw diameter.
A_cross=pi*(Ro^2-Rc^2)  % effective cross section area of the screw casing
L1=0.2;                 % length of the screw with 0.1 m screw diameter.
alphao=atan(P/(2*pi*Ro));       % helical angle at the outside screw diameter, radian.
alphac=atan(P/(2*pi*Rc));       % helical angle at the core shaft surface, radian.
alphao_deg=atan(P/(2*pi*Ro))/pi*180;    % helical angle at the outside screw diameter, degree.
alphac_deg=atan(P/(2*pi*Rc))/pi*180;    % helical angle at the core shaft surface, degree.

% torque calculation
for i=1:1:nn
con=0.8;                        % constant for estimating axial stress in choke section
e=0.2
CC1(i)=con*(qf(i)*H0/Dt*Lc/Dt/ct)^(e);
                                % exponent to estimate axial stress on trailing side of a flight
taoxam1(i)=n*taof_v(i)*(exp(2*tan(phi)*lamdas(i)*P/(Rt-Rc))).^(CC1(i)+1);
                        % stress on driving side of a flight
taoxam11(i)=n*taof_v(i)*(exp(2*tan(phi)*lamdas(i)*P/(Rt-Rc))).^(CC1(i));
                        % stress on trailing side of a flight
EE1(i)=(exp(2*tan(phi)*lamdas(i)*P/(Rt-Rc))).^(CC1(i));
                        % how many times for stress on trailing side compared to vertical stress
                        % for flow condition, compaction ration in choke section
lamdas_a=lamdas(i);   % compute lamdas for function taoxave1
CCC=CC1(i);           % compute CC1 for function taoxave1
taox1_a(i)=1/P*n*taof_v(i)*quadl(@taoxave1, 0,P); % average axial stress in choke section
taowa1(i)=lamdas(i)*taox1_a(i);         % average normal wall stress in choke section
Fca1(i)=2*pi*Rc*P*tan(phif)*taowa1(i)*sin(alphac);  % axial force on core surface in choke section
Ffaf1(i)=2.*pi.*lamdas(i).*taoxam11(i).*quadl(@trailing, Rc, Ro);
                        % axial force on trailing side surface in choke section
Ftaf1(i)=2*pi*tan(phi)*taowa1(i)*Rt*P*cos(alphao+phif);
                        % axial force on trough surface in choke section
Fdaf1(i)=Fca1(i)+Ffaf1(i)+Ftaf1(i);     % axial force on driving side surface in choke section
tao_daf1(i)=Fdaf1(i)./pi./(Ro^2-Rc^2);
                        % compute axial stress on the driving surface for flow condition in choke section
```

```
Tdf1(i)=2*pi*tao_daf1(i)*quadl(@integrnd_Td, Rc, Ro);
                    % compute the torque generated by driving side surface for choke section 1
Tcf1(i)=taowa1(i)*2*pi*Rc*P*tan(phif)*Rc*cos(alphac);
                    % compute the torque generated by trailing side surface for choke section 1
Tff1(i)=2*pi*lamdas(i)*taoxam11(i)*quadl(@integrnd_Tf, Rc, Ro);
                    % compute the torque generated by trough side surface for choke section 1
Ttip1(i)=taowa1(i)*0.00635*P./sin(alphao)*tan(phif)*Ro;
ratio_choke1(i)=taox1_a(i)/tao_daf1(i);
T_choke1(i)=L1/P*(Tdf1(i)+Tcf1(i)+Tff1(i)+Ttip1(i));
                    % compute total torque in choke section 1 for flow condition
end
%-----------------------------------------------------------------------------------------------------------------------

% Choke section-taper section and 0.8 m screw diameter
P=0.1;              % pitch,m
Do=0.08;            % screw diameter, m
Ro=Do/2;            % screw radius, m.
Dc=0.030;           % screw core shaft diameter, m
Rc=Dc/2;            % screw core shaft radius, m
Dt=0.102;           % trough diameter,m
Rt=Dt/2;            % trough radius, m
cp=P/Do;            % ratio of pitch to screw diameter.
ct=Dt/Do;           % ratio of trough diameter to screw diameter.
cd=Dc/Do;           % ratio of core shaft diameter to screw diameter.
A_cross=pi*(Ro^2-Rc^2)      % effective cross section area of the screw casing
alphao=atan(P/(2*pi*Ro));          % helic angle at the outside screw diameter, radian.
alphac=atan(P/(2*pi*Rc));          % helic angle at the core shaft surface, radian.
alphao_deg=atan(P/(2*pi*Ro))/pi*180;  % helic angle at the outside screw diameter, degree.
alphac_deg=atan(P/(2*pi*Rc))/pi*180;  % helic angle at the core shaft surface, degree.
%-----------------------------------------------------------------------------------------------------------------------

% taper section
global Ef Httf taoinf
Taperinch=6;                % length of taper section, inch

LLt=Taperinch*0.0254;          % length of taper section, m
alphat=atan((Rt-0.044)/LLt)    % half angle of taper section, radian
Ht0=0.044/tan(alphat);         % length from apex of taper section to discharge outlet of screw feeder
Htt=Rt/tan(alphat);            % length from apex of taper section to starting point of taper section
mm=0.01;                       % incremental distance along screw axis from Ht0 to Htt
xt=[Ht0:mm:Htt];               % array of distance along screw axis
number=floor((Htt-Ht0)/mm+1);    % number of array data

for i=1:1:nn
EE(i)=-2*(1-lamdas(i)-lamdas(i)*tan(phi)./tan(alphat));
                    % exponent in relation of axial stress and axial position in choke section;
T_choke_tapersum=0;            % set T_choke_tapersum equal to 0
v=ceil(Taperinch/4);           % number of pitch (including the second half pitch)
h = zeros(1,v);                % iteration times
taoxt_aa=80000;                % initial stress value
s=[22000 81000];
                % stress calculated from stress-bulk density relation for pitch-1 and half pitch-2 in taper section
for j=1:v-1
taoin(j)=s(j)*2.8;   % initial stress value for stress at the beginning of each pitch in taper section
Ht01(j)=Htt-j*P;   % axial position of trailing side of flight for each pitch in taper section
Htt1(j)=Ht01(j)+P;   % axial position of driving side of flight for each pitch in taper section
```

```
while abs(taoxt_aa-s(j))>50
Ef=EE(i);          % exponent in relation of axial stress and axial position in choke section;
Httf=Htt1(j);      % axial position of driving side of flight for each pitch in taper section
taoinf=taoin(j);   % initial stress value for stress at the beginning (driving side) of each pitch in taper section
taoxt_a(i,j)=1./P*quadl(@taotaper, Ht01(j), Htt1(j));  % average axial stress in each pitch in taper section
taowt_a(i,j)=lamdas(i)*taoxt_a(i,j);   % average normal stress in each pitch in taper section
taoxt_aa=taoxt_a(i,j);       % adjust initial stress
taoin(j)=taoin(j)-5;         % adjust maximum stress in the second half pitch
h(j)=h(j)+1;                 % iteration times
end
taoxt_aa=80000;              % restore initial value
end

for j=1:v-1
xt1=[Ht01(j):mm:Htt1(j)];  % array of distance along screw axis
number1(j)=floor((Htt1(j)-Ht01(j))/mm+1);      % number of array data
for m=1:1: number1(j)
  taoxt(j,m)=(xt1(m)./Htt1(j)).^(Ef)*taoin(j);     % stress distribution in a pitch
end
end
%-----------------------------------------------------------------------------------------------------------------------------------------

% torque calculation for taper section
for j=1:v-1
Fcataper1(i,j)=2*pi*Rc*P*tan(phi)*taowt_a(i,j)*sin(alphac);
                                % axial force on core surface in choke section
Ffaftaper1(i,j)=2*pi*lamdas(i)*taoxt(j,1)*quadl(@trailing, Rc, Ro);
                                % axial force on trailing side surface in choke section
Ftaftaper1(i,j)=tan(phi)*taowt_a(i,j)*2*pi*Rt*P+taowt_a(i,j)*2*pi*Rt*P*tan(alphat);
                                % axial force on trough surface in choke section
Fdaftaper1(i,j)=Fcataper1(i,j)+Ffaftaper1(i,j)+Ftaftaper1(i,j);
                                % axial force on driving side surface in choke section
tao_daftaper1(i,j)=Fdaftaper1(i,j)./pi./(Ro^2-Rc^2);;
                                % compute axial stress on the driving surface in choke section
Tdtaper1(i,j)=2*pi*tao_daftaper1(i,j)*quadl(@integrnd_Td, Rc, Ro);
                    % compute torque generated by driving side of screw for flow condition
Tcftaper1(i,j)=2*pi*tan(phi)*taowt_a(i,j)*Rc*Rc*P*cos(alphac);
                    % compute torque generated by core shaft surface for flow condition
Tfftaper1(i,j)=2*pi*lamdas(i)*taoxt(j,1)*quadl(@integrnd_Tf, Rc, Ro);
                    % compute torque generated by core shaft surface for flow condition
Ttiptaper1(i,j)=taowt_a(i,j)*0.00635*P/sin(alphao)*tan(phif)*Ro;
                    % compute torque generated by flight tips for flow condition
T_choke_taper1(i,j)=(Tdtaper1(i,j)+Tcftaper1(i,j)+Tfftaper1(i,j)+Ttiptaper1(i,j));
                    % compute total torque in hopper section for flow condition
T_choke_tapersum=T_choke_tapersum+T_choke_taper1(i,j);
                    % torque generated by each pitch in taper section
end
T_choke_tapertt1(i)=T_choke_tapersum;
%-----------------------------------------------------------------------------------------------------------------------------------------

% for 0.15 m taper section-second half pitch taper section
Ht01(v)=Htt-(v-0.5)*P;      % axial position of taper section outlet
Htt1(v)=Ht01(v)+(0.5)*P;    % axial position of the last second half pitch in taper section
taoin(v)=s(v)*3.8;     % initial stress value for stress at the beginning of each pitch in taper section
taoxt_aa=80000;        % initial stress value
while abs(taoxt_aa-s(v))>50
Ef=EE(i);              % exponent in relation of axial stress and axial position in choke section;
```

```
Httf=Htt1(v);            % axial position of the last second half pitch in taper section
taoinf=taoin(v);
taoxt_a(i,v)=2./P*quadl(@taotaper, Ht01(v), Htt1(v));  % average axial stress in the second half pitch
taowt_a(i,v)=lamdas(i)*taoxt_a(i,v);   % average normal wall stress in the second half pitch
taoxt_aa=taoxt_a(i,v);      % adjust initial stress
taoin(v)=taoin(v)-5;      % adjust maximum stress in the second half pitch
h(v)=h(v)+1;            % iteration times
end
Fcataper1(i,v)=2*pi*Rc*P/2*tan(phi)*taowt_a(i,v)*sin(alphac);
                        % axial force on core surface in choke section
Ftaftaper1(i,v)=tan(phi)*taowt_a(i,v)*2*pi*Rt*P/2+taowt_a(i,v)*2*pi*Rt*P/2*tan(alphat);
                        % axial force on trough surface in choke section
Fdaftaper1(i,v)=Fcataper1(i,v)+Ftaftaper1(i,v);
                        % axial force on driving side surface in choke section
tao_daftaper1(i,v)=Fdaftaper1(i,v)./pi./(Ro^2-Rc^2);;
                        % compute axial stress on driving surface in choke section
Tdtaper1(i,v)=2*pi*tao_daftaper1(i,v)*quadl(@integrnd_Td, Rc, Ro);
                        % compute torque generated by driving side of screw for flow condition
Tcftaper1(i,v)=2*pi*tan(phi)*taowt_a(i,v)*Rc*Rc*P/2*cos(alphac);
                        % compute torque generated by core shaft surface for flow condition
Ttiptaper1(i,v)=taowt_a(i,v)*0.00635*P/2/sin(alphao)*tan(phif)*Ro;
                        % compute torque generated by flight tips for flow condition
T_choke_taper1(i,v)=(Tdtaper1(i,v)+Tcftaper1(i,v)+Ttiptaper1(i,v));
                        % compute total torque in hopper section for flow condition
T_choke_tapertt2(i)=T_choke_taper1(i,v);        % torque generated by the second half pitch
T_choke_tapert(i)=T_choke_tapertt1(i)+T_choke_tapertt2(i);
                        % torque generated by taper section
end
%-----------------------------------------------------------------------------------------------------------------------------------

% Choke section-0.8 m screw diameter
L2=0.42-LLt;    % the length of the screw with 0.1 m screw diameter.
% torque calculation
for i=1:1:nn
CC2(i)=con*(qf(i)*H0/Dt*Lc/Dt/ct)^(e);
            % exponent to estimate axial stress on trailing side of a flight
taoxam2(i)=n*taof_v(i)*(exp(2*tan(phi)*lamdas(i)*P/(Rt-Rc)))^(CC2(i)+1);
            % theoretical maximum stress in a pitch
taoxam22(i)=n*taof_v(i)*exp(2*tan(phi)*lamdas(i)*P/(Rt-Rc))^(CC2(i));
            % theoretical minimum stress in a pitch
EE2(i)=(exp(2*tan(phi)*lamdas(i)*P/(Rt-Rc))).^(CC2(i));
            % how many times for stress on trailing side compared to vertical stress in hopper
            % for flow condition, compression factor in choke section
lamdas_a=lamdas(i);        % compute lamdas for function taoxave1
CCC=CC2(i);              % compute CC2 for function taoxave1
taox2_a(i)=1/P*n*taof_v(i)*quadl(@taoxave1, 0,P);
                        % average axial stress in choke section
taowa2(i)=lamdas(i)*taox2_a(i);   % average normal wall stress in choke section
Fca2(i)=2*pi*Rc*P*tan(phi)*taowa2(i)*sin(alphac);
                        % axial force on core surface in choke section
Ffaf2(i)=2*pi*lamdas(i)*taoxam22(i)*quadl(@trailing, Rc, Ro);
                        % axial force on trailing side surface in choke section
Ftaf2(i)=2*pi*tan(phi)*taowa2(i)*Rt*P*cos(alphao+phif);
                        % axial force on trough surface in choke section
Fdaf2(i)=Fca2(i)+Ffaf2(i)+Ftaf2(i);       % axial force on driving side surface in choke section
tao_daf2(i)=Fdaf2(i)./pi./(Ro^2-Rc^2);;   % compute axial stress on driving surface in choke section
Tdf2(i)=2*pi*tao_daf2(i)*quadl(@integrnd_Td, Rc, Ro);
```

```
                                % compute torque generated by driving side surface for choke section 2
Tcf2(i)=taowa2(i)*2*pi*Rc*P*tan(phif)*Rc*cos(alphac);
                                % compute torque generated by core shaft surface for choke section 2
Tff2(i)=2*pi*lamdas(i)*taoxam22(i)*quadl(@integrnd_Tf, Rc, Ro);
                                % compute torque generated by trailing side surface for choke section 2
Ttip2(i)=taowa2(i)*0.00635*P/sin(alphao)*tan(phif)*Ro;
                                % compute torque generated by flight tips surface for choke section 2
ratio_choke2(i)=taox2_a(i)/tao_daf2(i);
                                % ratio of average stress to stress on the driving side of flight
T_choke2(i)=L2/P*(Tdf2(i)+Tcf2(i)+Tff2(i)+Ttip2(i));
                                % compute total torque in choke section 2 for flow condition
end
%-----------------------------------------------------------------------------------------------------------------------------

Tor_totalf=T_choke1+T_choke2+T_hopperf+T_choke_tapert;    % compute total torque for flow condition
Tor_initial=T_hopperi;                                    % compute initial torque for hopper section

% power estimation
screwspeed=[5 10 20 30 40];
for j=1:1:5
power(j)=Tor_totalf(1)*2*pi*screwspeed(j)/60;
end

result=[taoxa(1) taox1_a(1) taox2_a(1) taoi_v Fv_i taof_v0(1) Fv_f0(1) taof_v(1) Fv_f(1) Tor_initial(1)
T_hopperf(1)  T_choke1(1) T_choke2(1) T_choke_tapert(1) Tor_totalf(1)];

fprintf('The solution is \n')
fprintf('axial stress in hopper=%8.4f \n',result(1))
fprintf('axial stress1=%8.4f \n',result(2))
fprintf('axial stress2=%8.4f \n',result(3))
fprintf('initial vertical stress=%8.4f \n',result(4))
fprintf('initial feeder load=%8.4f \n',result(5))
fprintf('vertical stress for flow condition=%8.4f \n',result(6))
fprintf('feeder load for flow condition=%8.4f \n',result(7))
fprintf('modified vertical stress for flow condition=%8.4f \n',result(8))
fprintf('modified feeder load for flow condition=%8.4f \n',result(9))
fprintf('torque requirement for hopper in initial condition=%8.4f \n',result(10))
fprintf('torque requirement for hopper in flow condition=%8.4f \n',result(11))
fprintf('torque requirement for choke 1 in flow condition=%8.4f \n',result(12))
fprintf('torque requirement for choke 2 in flow condition=%8.4f \n',result(13))
fprintf('torque requirement for 12" taper section=%8.4f \n',result(14));
fprintf('torque requirement for flow condition=%8.4f \n',result(15))
```

H-3: Torque prediction for sawdust-1 for 0.3 m tapered section

File name: Torque_sawdust_taper12inch.m
Function: taoxave1, taoxh, trailing, integrnd_Td, integrnd_Tf, taotaper
Source code: see below

```
% Hopper-screw feeder load and torque calculation for static and dynamic conditions with taper section
% Screw speeds, gravity and centrifugal forces are neglected in screw torque analysis
clc
clear
%-----------------------------------------------------------------------------------------------------------------------
% fixed parameters for screw feeder and hopper
global P taof_v muf muwt lamdas Rt Rc alphas muwh phi phif lamdas_a CCC
rou_bulk=212;              % bulk density of bulk solid, kg/m^3.
H0=0.45;                   % initial bed height in hopper, m
P=0.1;                     % pitch,m
Do=0.1;                    % screw diameter, m
Ro=Do/2;                   % screw radius, m.
Dc=0.030;                  % screw core shaft diameter, m
Rc=Dc/2;                   % screw core shaft radius, m
Dt=0.102;                  % trough diameter,m
Rt=Dt/2;                   % trough radius, m
cp=P/Do;                   % ratio of pitch to screw diameter.
ct=Dt/Do;                  % ratio of trough diameter to screw diameter.
cd=Dc/Do;                  % ratio of core shaft diameter to screw diameter.
Lh=0.914;                  % hopper outlet length,m
L=0.8;                     % length of screw with 0.1 m screw diameter, a little shorter than outlet length, i.e. 0.914 m.
Lc=0.62;
B=0.102;                   % width of trough,m
t=0.00635;                 % flight thickness,m
A_cross=pi*(Ro^2-Rc^2);    % effective cross section area of the screw casing
alpha=20/180*pi;           % half hopper angle, radian
g=9.8;                     % gravitational acceleration, m/s^2.
alphao=atan(P/(2*pi*Ro));          % helical angle at outside screw diameter, radian.
alphac=atan(P/(2*pi*Rc));          % helical angle at core shaft surface, radian.
alphao_deg=atan(P/(2*pi*Ro))/pi*180;    % helical angle at outside screw diameter, degree.
alphac_deg=atan(P/(2*pi*Rc))/pi*180;    % helical angle at core shaft surface, degree.
%-----------------------------------------------------------------------------------------------------------------------

% variable parameters for biomass fuels and hopper-screw feeder; initial vertical stress and initial feeder load
m=1;
delta1_deg=38;                     % set effective internal friction angle, degree
delta2_deg=38;
delta_deg=[delta1_deg:m:delta2_deg];     % effective internal friction angle, degree.
nn=(delta2_deg-delta1_deg)./m+1;
delta=[delta1_deg/180*pi:m/180*pi:delta2_deg/180*pi];
phi=31.8/180*pi;           % angle of friction between bulk solids and hopper wall (or casing surface), radian
phif=31.8/180*pi;          % angle of friction between bulk solids and screw flight, radian.PE
muf=tan(phif);             % coefficient of friction between solids and screw flight surface
muwc=muf;                  % friction coefficient of bulk solid on core surface
muwh=tan(phi);             % friction coefficient of bulk solid on hopper surface.
muwt=muwh;                 % friction coefficient of bulk solid on trough surface.
D=2*(H0+B./2*cot(alpha))*tan(alpha);  % compute width of bulk solid free surface in hopper (flate surface), m
qi=1/(2*tan(alpha))*(D/B-1);       % compute non-dimensional surcharge factor for initial condition
taoi_v=qi*rou_bulk*g*B;            % compute vertical stress at hopper outlet for initial condition
Fv_i=taoi_v*Lh*B;                  % compute feeder load at hopper outlet for initial condition
%-----------------------------------------------------------------------------------------------------------------------
```

```
% vertical stress and feeder load for flow condition
for i=1:1:nn
mud(i)=tan(delta(i));              % effective coefficient of internal friction.
mue(i)=sin(delta(i));              % equivalent friction coefficient of bulk solid,.from Roberts
%lamdas(i)=1/(1+2*mud(i)^2+2*((1+mud(i)^2)*(mud(i)^2-muwt^2))^0.5);
                    % stress ratio of normal stress acting perpendicularly to wall
                    % of trough and core shaft surfaces to axial compression stress, derived from Mohr circle
alpha_Mohr(i)=(asin(sin(phi)/sin(delta(i)))-phi)/2;
lamdas(i)=cos(phi)*sin(2*alpha_Mohr(i))/(sin(phi)*cos(2*alpha_Mohr(i))+sin(phi+2*alpha_Mohr(i)));
                          % stress ratio of normal stress acting perpendicularly to wall
                          % of trough and core shaft surfaces to axial compression stress
                          % derived from Mohr circle
beta(i)=0.5*(phi+asin(sin(phi)/sin(delta(i))));                    % compute beta(i), constant
X(i)=sin(delta(i))/(1-sin(delta(i)))*(sin(2*beta(i)+alpha)/sin(alpha)+1);
                          % constant to compute feeder load
Y(i)=((alpha+beta(i))*sin(alpha)+sin(beta(i))*sin(alpha+beta(i)))./((1-sin(delta(i)))*sin(alpha+beta(i)).^2);
                                        % constant to compute feeder load
qf(i)=Y(i)*(1+sin(delta(i)))/(2*(X(i)-1)*sin(alpha));      % surcharge factor for flow conditions
%qf1(i)=1/4*(1/tan(alpha))*(Y(i)*(1+sin(delta(i))*cos(2*beta(i)))*(tan(alpha)+tan(phi))/sin(alpha)/(X(i)-1)-1);
                          % smaller than the above one
taof_v0(i)=qf(i)*rou_bulk*g*B;     % use average bulk density for compressible solids in the present study
Fv_f0(i)=taof_v0(i).*Lh.*B;        % vertical stress and feeder load for flow condition
taof_v(i)=(taof_v0(i)+taoi_v)./2;  % average vertical stress for flow condition
Fv_f(i)=taof_v(i).*Lh.*B;          % average feeder load for flow condition
end
%-------------------------------------------------------------------------------------------------------------------------------------------

% hopper section, for a material element in a pitch first then entire hopper section
n=1.0;
eps=1e-4;
a=0;
while abs(0.99-a) > eps

for i=1:1:nn
taoxamax(i)=n*taof_v(i)*(exp(2*tan(phi)*lamdas(i)*P/(Rt-Rc)));
                          % maximum stress at driving side of flight according to stress analysis
taoxamin(i)=n*taof_v(i);          % minimum stress at trailing side of flight according to stress analysis
lamdas_a=lamdas(i);               % stress ratio of normal wall stress to axial stress on confined surface
taoxa(i)=1/P*n*taof_v(i)*quadl(@taoxh, 0,P);   % average axial stress in a pitch for flow condition
taoxai(i)=1/P*n*taoi_v*quadl(@taoxh, 0,P);     % average axial stress in a pitch for initial condition
taowa(i)=lamdas(i)*taoxa(i);                   % average normal wall stress in a pitch for flow condition
taowai(i)=lamdas(i)*taoxai(i);                 % average normal wall stress in a pitch for initial condition

%-1. shear surface
ksa(i)=pi*mue(i)*cp*cos(alphao+phif)./2;   % parameter for axial force calculations on shear surface
Fsaf(i)=-ksa(i).*taof_v(i).*Do.^2;         % axial force on shear surface for flow condition
Fsai(i)=-ksa(i)*taoi_v*Do^2;               % axial force on shear surface for initial condition
kst(i)=pi*mue(i)*cp*sin(alphao+phif)./2;   % parameter for tangential force calculations on shear surface
Fstf(i)=-kst(i).*taof_v(i)*Do^2;           % tangential force on shear surface for flow condition
Fsti(i)=-kst(i)*taoi_v*Do^2;               % tangential force on shear surface for initial condition
Fstfp_try(i)=1/2*(taof_v(i)+taowa(i))*t*P/sin(alphao)*tan(phif);
                          % tangential force from flight tips for flow condition
Fstip_try(i)=1/2*(taoi_v(i)+taowai(i))*t*P/sin(alphao)*tan(phif);
                          % tangential force from flight tips for initial condition
Tstfp(i)=Fstfp_try(i)*Ro;                  % torque from flight tips for flow condition
Tstip(i)=Fstip_try(i)*Ro;                  % torque from flight tips for initial condition
```

```
%-2. core shaft
kca(i)=n*pi*(ct-cd)*cd*cp*(exp(4*muwc*lamdas(i)*cp/(ct-cd))-1)/4/(cp^2+pi^2*cd^2)^0.5;
                                % parameter for axial force calculations on core shaft surface
Fcaf(i)=-kca(i)*taof_v(i)*Do^2;          % axial force on core surface for flow condition
Fcai(i)=-kca(i)*taoi_v*Do^2;             % axial force on core surface for initial condition
Fca1_try(i)=2*pi*Rc*P*tan(phif)*taowa(i)*sin(alphac);  % axial force on core surface for flow condition
kct(i)=n*pi^2*(ct-cd)*cd^2*(exp(4*muwc*lamdas(i)*cp/(ct-cd))-1)/4/(cp^2+pi^2*cd^2)^0.5;
                                % parameter for tangential force calculations on core shaft surface
Fctf(i)=kct(i)*taof_v(i)*Do^2;           % tangential force on core surface for flow condition
Fcti(i)=kct(i)*taoi_v*Do^2;              % tangential force on core surface for initial condition
Fct1_try(i)=2*pi*Rc*P*tan(phif)*taowa(i)*cos(alphac); % tangential force on core surface for flow condition

%-3. trailing flight side
kfa(i)=n*lamdas(i)*(pi*(1-cd^2)/4+cp*muf*(1-cd)/2);  % parameter for axial force calculations on trailing side
surface
Ffaf(i)=-kfa(i)*taof_v(i)*Do^2;          % axial force on trailing side surface for flow condition
Ffai(i)=-kfa(i)*taoi_v*Do^2;             % axial force on trailing side surface for initial condition
Ffaf1_try(i)=2.*pi.*lamdas(i).*taoxamin(i).*quadl(@trailing, Rc, Ro);
kft(i)=n*lamdas(i)*(pi*muf*(1-cd^2)/4-cp*(1-cd)/2);  % parameter for tangential force calculations on trailing
side surface
Fftf(i)=kft(i)*taof_v(i)*Do^2;           % tangential force on trailing side surface for flow condition
Ffti(i)=kft(i)*taoi_v*Do^2;              % tangential force on trailing side surface for initial condition

%-4. trough surface
kta(i)=n*pi*(ct-cd)*ct*cos(alphao+phif)/8*(exp(4*muwt*lamdas(i)*cp/(ct-cd))-1);
                                % parameter for axial force calculations on trough surface
Ftaf(i)=-kta(i).*taof_v(i).*Do.^2;   % axial force on trough surface for flow condition
Ftai(i)=-kta(i)*taoi_v*Do^2;             % axial force on trough surface for initial condition
Ftaf_try(i)=pi*Rt*P*tan(phi)*cos(alphao+phif)*taowa(i); % axial force on trough surface for flow condition
ktt(i)=n*pi*(ct-cd)*ct*sin(alphao+phif)/8*(exp(4*muwt*lamdas(i)*cp/(ct-cd))-1);
                                % parameter for tangential force calculations on trough surface
Fttf(i)=-ktt(i)*taof_v(i)*Do^2;          % tangential force on trough surface for flow condition
Ftti(i)=-ktt(i)*taoi_v*Do^2;             % tangential force on trough surface for initial condition

%-5. stress on driving side
Kda(i)=4*(ksa(i)+kca(i)+kfa(i)+kta(i))/pi/(1-cd^2);  % parameter for axial force calculations on driving side
surface
tao_daf(i)=Kda(i)*taof_v(i);             % compute axial stress on driving surface for flow condition
tao_dai(i)=Kda(i)*taoi_v;                % compute axial stress on driving surface for initial condition
Ftao_daf(i)=tao_daf(i)*A_cross;          % compute axial force on driving surface for flow condition
Ftao_dai(i)=tao_dai(i)*A_cross;          % compute axial force on driving surface for initial condition

% torque calculation
Tdf(i)=2*pi*tao_daf(i)*quadl(@integrnd_Td, Rc, Ro);
                                % compute torque generated by driving side of screw for flow condition
Tdi(i)=2*pi*tao_dai(i)*quadl(@integrnd_Td, Rc, Ro);
                                % compute torque generated by driving side of screw for initial condition
Tcf(i)=2*pi*Rc*P*taowa(i)*tan(phif)*cos(alphac)*Rc;;
                                % compute torque generated by core shaft surface for flow condition
Tci(i)=2*pi*Rc*P*taowai(i)*tan(phif)*cos(alphac)*Rc;
                                % compute torque generated by core shaft surface for initial condition
Tff(i)=2*pi*lamdas(i)*n*taof_v(i)*quadl(@integrnd_Tf, Rc, Ro);
                                % compute torque from trough surface for flow condition
Tfi(i)=2*pi*lamdas(i)*n*taoi_v*quadl(@integrnd_Tf, Rc, Ro);
                                % compute torque from trough surface for initial condition
T_hopperf(i)=Lh/P*(Tdf(i)+Tcf(i)+Tff(i)+Tstfp(i));
```

```
                                % compute total torque in hopper section for flow condition
T_hopperi(i)=Lh/P*(Tdi(i)+Tci(i)+Tfi(i)+Tstip(i));
                                % compute total torque in hopper section for initial condition
ratio01(i)=tao_daf(i)/taoxamax(i);  % ratio of stress on driving side to theoretical maximum stress in a pitch
ratio02(i)=taoxa(i)/tao_daf(i);     % ratio of average axial stress to stress on driving side in a pitch
end
a=ratio02(1);              % ratio of average axial stress to stress on driving side
n=n+0.0001;                % 0.0001 as increment for t
end
n=n-0.0001;
%-------------------------------------------------------------------------------------------------------------------------

% Choke section-0.9 m screw diameter
P=0.1;                  % pitch,m
Do=0.09;                % screw diameter, m
Ro=Do/2;                % screw radius, m.
Dc=0.030;               % screw core shaft diameter, m
Rc=Dc/2;                % screw core shaft radius, m
Dt=0.102;               % trough diameter,m
Rt=Dt/2;                % trough radius, m
cp=P/Do;                % ratio of pitch to screw diameter.
ct=Dt/Do;               % ratio of trough diameter to screw diameter.
cd=Dc/Do;               % ratio of core shaft diameter to screw diameter.
A_cross=pi*(Ro^2-Rc^2); % effective cross section area of the screw casing
L1=0.2;                 % length of the screw with 0.1 m screw diameter.
alphao=atan(P/(2*pi*Ro));           % helical angle at the outside screw diameter, radian.
alphac=atan(P/(2*pi*Rc));           % helical angle at the core shaft surface, radian.
alphao_deg=atan(P/(2*pi*Ro))/pi*180;    % helical angle at the outside screw diameter, degree.
alphac_deg=atan(P/(2*pi*Rc))/pi*180;    % helical angle at the core shaft surface, degree.

% torque calculation
for i=1:1:nn
con=0.8;                        % constant for estimating axial stress in choke section
e=0.2
CC1(i)=con*(qf(i)*H0/Dt*Lc/Dt/ct)^(e);    % exponent to estimate axial stress on trailing side of a flight
taoxam1(i)=n*taof_v(i)*(exp(2*tan(phi)*lamdas(i)*P/(Rt-Rc))).^(CC1(i)+1);
                                % stress on driving side of a flight
taoxam11(i)=n*taof_v(i)*(exp(2*tan(phi)*lamdas(i)*P/(Rt-Rc))).^(CC1(i));
                                % stress on trailing side of a flight
EE1(i)=(exp(2*tan(phi)*lamdas(i)*P/(Rt-Rc))).^(CC1(i));
                                % how many times for stress on trailing side compared to vertical stress
                                % for flow condition, compaction ration in choke section
lamdas_a=lamdas(i);  % compute lamdas for function taoxave1
CCC=CC1(i);          % compute CC1 for function taoxave1
taox1_a(i)=1/P*n*taof_v(i)*quadl(@taoxave1, 0,P); % average axial stress in choke section
taowa1(i)=lamdas(i)*taox1_a(i);             % average normal wall stress in choke section
Fca1(i)=2*pi*Rc*P*tan(phif)*taowa1(i)*sin(alphac);  % axial force on core surface in choke section
Ffaf1(i)=2.*pi.*lamdas(i).*taoxam11(i).*quadl(@trailing, Rc, Ro);
                    % axial force on trailing side surface in choke section
Ftaf1(i)=2*pi*tan(phi)*taowa1(i)*Rt*P*cos(alphao+phif);      % axial force on trough surface in choke section
Fdaf1(i)=Fca1(i)+Ffaf1(i)+Ftaf1(i);     % axial force on driving side surface in choke section
tao_daf1(i)=Fdaf1(i)./pi./(Ro^2-Rc^2);
                                % compute axial stress on the driving surface for flow condition in choke section

Tdf1(i)=2*pi*tao_daf1(i)*quadl(@integrnd_Td, Rc, Ro);
                    % compute the torque generated by driving side surface for choke section 1
Tcf1(i)=taowa1(i)*2*pi*Rc*P*tan(phif)*Rc*cos(alphac);
```

```
                % compute the torque generated by trailing side surface for choke section 1
Tff1(i)=2*pi*lamdas(i)*taoxam11(i)*quadl(@integrnd_Tf, Rc, Ro);
                % compute the torque generated by trough side surface for choke section 1
Ttip1(i)=taowa1(i)*0.00635*P./sin(alphao)*tan(phif)*Ro;
ratio_choke1(i)=taox1_a(i)/tao_daf1(i);
T_choke1(i)=L1/P*(Tdf1(i)+Tcf1(i)+Tff1(i)+Ttip1(i));
                % compute total torque in choke section 1 for flow condition
end
%-----------------------------------------------------------------------------------------------------------------------

% Choke section-taper section and 0.8 m screw diameter
P=0.1;              % pitch,m
Do=0.08;            % screw diameter, m
Ro=Do/2;            % screw radius, m.
Dc=0.030;           % screw core shaft diameter, m
Rc=Dc/2;            % screw core shaft radius, m
Dt=0.102;           % trough diameter,m
Rt=Dt/2;            % trough radius, m
cp=P/Do;            % ratio of pitch to screw diameter.
ct=Dt/Do;           % ratio of trough diameter to screw diameter.
cd=Dc/Do;           % ratio of core shaft diameter to screw diameter.
A_cross=pi*(Ro^2-Rc^2) % effective cross section area of the screw casing
alphao=atan(P/(2*pi*Ro));          % helical angle at the outside screw diameter, radian.
alphac=atan(P/(2*pi*Rc));          % helical angle at the core shaft surface, radian.
alphao_deg=atan(P/(2*pi*Ro))/pi*180;    % helical angle at the outside screw diameter, degree.
alphac_deg=atan(P/(2*pi*Rc))/pi*180;    % helical angle at the core shaft surface, degree.
%-----------------------------------------------------------------------------------------------------------------------

% taper section
global Ef Httf taoinf
Taperinch=12;              % length of taper section, inch
LLt=Taperinch*0.0254;      % length of taper section, m
alphat=atan((Rt-0.044)/LLt)    % half angle of taper section
Ht0=0.044/tan(alphat);     % length from apex of taper section to discharge outlet of screw feeder
Htt=Rt/tan(alphat);        % length from apex of taper section to starting point of taper section
mm=0.01;                   % incremental distance along screw axis from Ht0 to Htt
xt=[Ht0:mm:Htt];           % array of distance along screw axis
number=floor((Htt-Ht0)/mm+1);  % number of array data
for i=1:1:nn
EE(i)=-2*(1-lamdas(i)-lamdas(i)*tan(phi)./tan(alphat));
                           % exponent in relation of axial stress and axial position in choke section
T_choke_tapersum=0;        % set T_choke_tapersum equal to 0
v=ceil(Taperinch/4);       % number of pitch
h = zeros(1,v);            % iteration times
taoxt_aa=80000;            % initial stress value
s=[13800 33600 81000];     % stress calculated from stress-bulk density relation for pitch-1 and half pitch-2 in
taper section
for j=1:v
taoin(j)=s(j)*1.8;         % initial stress value for stress at the beginning of each pitch in taper section
Ht01(j)=Htt-j*P;           % axial position of trailing side of flight for each pitch in taper section
Htt1(j)=Ht01(j)+P;         % axial position of driving side of flight for each pitch in taper section
while abs(taoxt_aa-s(j))>50
Ef=EE(i);                  % exponent in relation of axial stress and axial position in choke section;
Httf=Htt1(j);              % axial position of driving side of flight for each pitch in taper section
taoinf=taoin(j);           % initial stress value for stress at the beginning (driving side) of each pitch in taper section
taoxt_a(i,j)=1./P*quadl(@taotaper, Ht01(j), Htt1(j)); % average axial stress in each pitch in taper section
taowt_a(i,j)=lamdas(i)*taoxt_a(i,j);     % average normal stress in each pitch in taper section
```

```
taoxt_aa=taoxt_a(i,j);      % adjust initial stress
taoin(j)=taoin(j)-5;        % adjust maximum stress in the second half pitch
h(j)=h(j)+1;                % iteration times
end
taoxt_aa=80000;             % restore initial value
end
number1=floor(number/v);
for j=1:v
xt1=[Ht01(j):mm:Htt1(j)];                  % array of distance along screw axis
number1(j)=floor((Htt1(j)-Ht01(j))/mm+1);  % number of array data
for m=1:1: number1(j)
  taoxt(j,m)=(xt1(m)./Htt1(j)).^(Ef)*taoin(j); % stress distribution in a pitch
end
end
for j=1:v
Fcataper1(i,j)=2*pi*Rc*P*tan(phi)*taowt_a(i,j)*sin(alphac);        % axial force on core surface in choke section
Ffaftaper1(i,j)=2*pi*lamdas(i)*taoxt(j,1)*quadl(@trailing, Rc, Ro);
                                    % axial force on trailing side surface in choke section
Ftaftaper1(i,j)=tan(phi)*taowt_a(i,j)*2*pi*Rt*P+taowt_a(i,j)*2*pi*Rt*P*tan(alphat);
Fdaftaper1(i,j)=Fcataper1(i,j)+Ffaftaper1(i,j)+Ftaftaper1(i,j);
                                    % axial force on driving side surface in choke section
tao_daftaper1(i,j)=Fdaftaper1(i,j)./pi./(Ro^2-Rc^2);;
                                    % compute axial stress on driving surface in choke section
Tdtaper1(i,j)=2*pi*tao_daftaper1(i,j)*quadl(@integrnd_Td, Rc, Ro);
                                    % compute torque generated by driving side of screw for flow condition
Tcftaper1(i,j)=2*pi*tan(phi)*taowt_a(i,j)*Rc*Rc*P*cos(alphac);
                                    % compute torque generated by core shaft surface for flow condition
Tfftaper1(i,j)=2*pi*lamdas(i)*taoxt(j,1)*quadl(@integrnd_Tf, Rc, Ro);
                                    % compute torque generated by core shaft surface for flow condition
Ttiptaper1(i,j)=taowt_a(i,j)*0.00635*P/sin(alphao)*tan(phif)*Ro;
                                    % compute torque generated by flight tips for flow condition
T_choke_taper1(i,j)=(Tdtaper1(i,j)+Tcftaper1(i,j)+Tfftaper1(i,j)+Ttiptaper1(i,j));
                                    % compute torque in taper ection for flow condition
T_choke_tapersum=T_choke_tapersum+T_choke_taper1(i,j);
                                    % compute total torque in taper section for flow condition
end
T_choke_tapert(i)=T_choke_tapersum;    % compute total torque in taper section for flow condition
end
%-----------------------------------------------------------------------------------------------------------------------------------

% Choke section-0.8 m screw diameter
L2=0.42-LLt;    % length of the screw with 0.1 m screw diameter.
% torque calculation
for i=1:1:nn
CC2(i)=con*(qf(i)*H0/Dt*Lc/Dt/ct)^(e);      % exponent to estimate axial stress on trailing side of a flight
taoxam2(i)=n*taof_v(i)*(exp(2*tan(phi)*lamdas(i)*P/(Rt-Rc)))^(CC2(i)+1);
                                    % theoretical maximum stress in a pitch
taoxam22(i)=n*taof_v(i)*exp(2*tan(phi)*lamdas(i)*P/(Rt-Rc))^(CC2(i));
                                    % theoretical minimum stress in a pitch
EE2(i)=(exp(2*tan(phi)*lamdas(i)*P/(Rt-Rc))).^(CC2(i));
                        % how many times for stress on trailing side compared to vertical stress in hoppper
                        % for flow condition, compression factor in choke section
lamdas_a=lamdas(i);     % compute lamdas for function taoxave1
CCC=CC2(i);             % compute CC2 for function taoxave1
taox2_a(i)=1/P*n*taof_v(i)*quadl(@taoxave1, 0,P);  % average axial stress in choke section
taowa2(i)=lamdas(i)*taox2_a(i);                    % average normal wall stress in choke section
Fca2(i)=2*pi*Rc*P*tan(phi)*taowa2(i)*sin(alphac);  % axial force on core surface in choke section
```

```
Ffaf2(i)=2*pi*lamdas(i)*taoxam22(i)*quadl(@trailing, Rc, Ro);
                                        % axial force on trailing side surface in choke section
Ftaf2(i)=2*pi*tan(phi)*taowa2(i)*Rt*P*cos(alphao+phif);      % axial force on trough surface in choke section
Fdaf2(i)=Fca2(i)+Ffaf2(i)+Ftaf2(i);          % axial force on driving side surface in choke section
tao_daf2(i)=Fdaf2(i)./pi./(Ro^2-Rc^2);;      % compute axial stress on the driving surface in choke section
Tdf2(i)=2*pi*tao_daf2(i)*quadl(@integrnd_Td, Rc, Ro);
                                        % compute the torque generated by driving side surface for choke section 2
Tcf2(i)=taowa2(i)*2*pi*Rc*P*tan(phif)*Rc*cos(alphac);
                                        % compute the torque generated by trailing side surface for choke section 2
Tff2(i)=2*pi*lamdas(i)*taoxam22(i)*quadl(@integrnd_Tf, Rc, Ro);
                                        % compute the torque generated by trough surface for choke section 2
Ttip2(i)=taowa2(i)*0.00635*P/sin(alphao)*tan(phif)*Ro;
                                        % compute the torque generated by flight tips for choke section 2
ratio_choke2(i)=taox2_a(i)/tao_daf2(i);   % ratio of axial stress to stress on driving side of flight
T_choke2(i)=L2/P*(Tdf2(i)+Tcf2(i)+Tff2(i)+Ttip2(i));
                                        % compute total torque in choke section 2 for flow condition
end
%-------------------------------------------------------------------------------------------------------------------
Tor_totalf=T_choke1+T_choke2+T_hopperf+T_choke_tapert;    % compute total torque for flow condition
Tor_initial=T_hopperi;          % compute initial torque for hopper section
%-------------------------------------------------------------------------------------------------------------------

result=[taoxa(1) taox1_a(1) taox2_a(1) taoi_v Fv_i taof_v0(1) Fv_f0(1) taof_v(1) Fv_f(1) Tor_initial(1)
T_hopperf(1)  T_choke1(1) T_choke2(1) T_choke_tapert(1) Tor_totalf(1)];

fprintf('The solution is \n')
fprintf('axial stress in hopper=%8.4f \n',result(1))
fprintf('axial stress1=%8.4f \n',result(2))
fprintf('axial stress2=%8.4f \n',result(3))
fprintf('initial vertical stress=%8.4f \n',result(4))
fprintf('initial feeder load=%8.4f \n',result(5))
fprintf('vertical stress for flow condition=%8.4f \n',result(6))
fprintf('feeder load for flow condition=%8.4f \n',result(7))
fprintf('modified vertical stress for flow condition=%8.4f \n',result(8))
fprintf('modified feeder load for flow condition=%8.4f \n',result(9))
fprintf('torque requirement for hopper in initial condition=%8.4f \n',result(10))
fprintf('torque requirement for hopper in flow condition=%8.4f \n',result(11))
fprintf('torque requirement for choke 1 in flow condition=%8.4f \n',result(12))
fprintf('torque requirement for choke 2 in flow condition=%8.4f \n',result(13))
fprintf('torque requirement for 12" taper section=%8.4f \n',result(14));
fprintf('torque requirement for flow condition=%8.4f \n',result(15))
```

## H-4: Torque prediction for hog fuel-1 with extended sections

File name: Torque_hogfuel_extendedsection
Function: taoxave1, taoxh, trailing, integrnd_Td and integrnd_Tf
Source code: see below

```
% Hopper-screw feeder load and torque calculation for static and dynamic conditions.
% Screw speeds, gravity and centrifugal forces are neglected in screw torque analysis
clc
clear
%-----------------------------------------------------------------------------------------------------------------------
% fixed parameters for screw feeder and hopper
global P taof_v muf muwt lamdas Rt Rc alphas muwh phi phif lamdas_a CCC
rou_bulk=202;            % bulk density of bulk solid, kg/m^3.
H0=0.45;                 % initial bed height in hopper, m
P=0.1;                   % pitch,m
Do=0.1;                  % screw diameter, m
Ro=Do/2;                 % screw radius, m.
Dc=0.030;                % screw core shaft diameter, m
Rc=Dc/2;                 % screw core shaft radius, m
Dt=0.102;                % trough diameter,m
Rt=Dt/2;                 % trough radius, m
cp=P/Do;                 % ratio of pitch to screw diameter.
ct=Dt/Do;                % ratio of trough diameter to screw diameter.
cd=Dc/Do;                % ratio of core shaft diameter to screw diameter.
Lh=0.914;                % hopper outlet length,m
L=0.8;                   % length of the screw with 0.1 m screw diameter, a little shorter than outlet length, i.e. 0.914
m.
Lc=0.62;                 % choke section length, m
B=0.102;                 % width of the trough,m
A_cross=pi*(Ro^2-Rc^2);  % Effective cross section area of screw casing, m^2.
alpha=20/180*pi;         % half hopper angle, radian
g=9.8;                   % gravitational acceleration, m/s^2.
alphao=atan(P/(2*pi*Ro));              % helical angle at outside screw diameter, radian.
alphac=atan(P/(2*pi*Rc));              % helical angle at core shaft surface, radian.
alphao_deg=atan(P/(2*pi*Ro))/pi*180;   % helical angle at outside screw diameter, degree.
alphac_deg=atan(P/(2*pi*Rc))/pi*180;   % helical angle at core shaft surface, degree.
%-----------------------------------------------------------------------------------------------------------------------

% variable parameters for biomass fuels and hopper-screw feeder
% initial vertical stress and initial feeder load
m=1;
delta1_deg=39;                  % set effective internal friction angle, degree
delta2_deg=39;
delta_deg=[delta1_deg:m:delta2_deg];  % effective internal friction angle, degree.
n=(delta2_deg-delta1_deg)./m+1;
delta=[delta1_deg/180*pi:m/180*pi:delta2_deg/180*pi];
phi=31.5/180*pi;     % angle of friction between bulk solids and hopper wall (or casing surface), radian.
phif=31.5/180*pi;    % angle of friction between bulk solids and screw flight, radian.
muf=tan(phif);               % coefficient of friction between solids and flight surface
muwc=muf;                    % friction coefficient of bulk solid on core surface
muwh=tan(phi);               % friction coefficient of bulk solid on hopper surface.
muwt=muwh;                   % friction coefficient of bulk solid on trough surface.
D=2*(H0+B./2*cot(alpha))*tan(alpha); % compute width of bulk solid free surface in hopper (flate surface), m
qi=1/(2*tan(alpha))*(D/B-1);         % compute non-dimensional surcharge factor for initial condition.
taoi_v=qi*rou_bulk*g*B;              % compute vertical stress at hopper outlet for initial condition
Fv_i=taoi_v*Lh*B;                    % compute feeder load at hopper outlet for initial condition
```

```
%-----------------------------------------------------------------------------------------------------------------------------

% vertical stress and feeder load for flow condition
for i=1:1:n
mud(i)=tan(delta(i));          % effective coefficient of internal friction.
mue(i)=sin(delta(i));          % equivalent friction coefficient of bulk solid,.from Roberts
alpha_Mohr(i)=(asin(sin(phi)/sin(delta(i)))-phi)/2;
lamdas(i)=cos(phi)*sin(2*alpha_Mohr(i))/(sin(phi)*cos(2*alpha_Mohr(i))+sin(phi+2*alpha_Mohr(i)));
                    % stress ratio of normal stress acting perpendicularly to wall
                    % of trough and core shaft surfaces to axial compression stress
                    % derived from Mohr circle
beta(i)=0.5*(phi+asin(sin(phi)/sin(delta(i))));                    % compute beta(i), constant
X(i)=sin(delta(i))/(1-sin(delta(i)))*(sin(2*beta(i)+alpha)/sin(alpha)+1);    % constant to compute feeder load
Y(i)=((alpha+beta(i))*sin(alpha)+sin(beta(i))*sin(alpha+beta(i)))./((1-sin(delta(i)))*sin(alpha+beta(i))^2);
qf(i)=Y(i)*(1+sin(delta(i)))/(2*(X(i)-1)*sin(alpha));              % surcharge factor for flow conditions
% qf1(i)=1/4*(1/tan(alpha))*(Y(i)*(1+sin(delta(i))*cos(2*beta(i)))*(tan(alpha)+tan(phi))/sin(alpha)/(X(i)-1)-1);
taof_v0(i)=qf(i)*rou_bulk*g*B;     % use loose bulk density for incompressible solids in the present study
Fv_f0(i)=taof_v0(i).*Lh.*B;        % vertical stress and feeder load for flow condition
taof_v(i)=(taof_v0(i)+taoi_v)./2;  % average vertical stress for flow condition
Fv_f(i)=taof_v(i).*Lh.*B;          % average feeder load for flow condition
end
%-----------------------------------------------------------------------------------------------------------------------------
% hopper section, for a material element in a pitch first then entire hopper section
t=1.0;                  % factor used to modify boundary condition at trailing side of flight
eps=0.0001;             % one small number
a=0;                    % set initial value for a, a is ratio, i.e. taoxa(i)/tao_daf(i)
while abs(0.99-a) > eps
for i=1:1:n
taoxamax(i)=t*taof_v(i)*(exp(2*tan(phi)*lamdas(i)*P/(Rt-Rc)));
                    % maximum stress at driving side of flight according to stress analysis
taoxamin(i)=t*taof_v(i);        % minimum stress at trailing side of flight according to stress analysis
lamdas_a=lamdas(i);             % stress ratio of normal wall stress to axial stress on confined surface
taoxa(i)=1/P*t*taof_v(i)*quadl(@taoxh, 0,P);   % average axial stress in a pitch for flow condition
taoxai(i)=1/P*t*taoi_v*quadl(@taoxh, 0,P);     % average axial stress in a pitch for initial condition
taowa(i)=lamdas(i)*taoxa(i);                   % average normal wall stress in a pitch for flow condition
taowai(i)=lamdas(i)*taoxai(i);                 % average normal wall stress in a pitch for initial condition
%-1. shear surface
ksa(i)=pi*mue(i)*cp*cos(alphao+phif)./2;       % parameter for axial force calculations on shear surface
Fsaf(i)=-ksa(i).*taof_v(i).*Do.^2;             % axial force on shear surface for flow condition
Fsai(i)=-ksa(i)*taoi_v*Do^2;                   % axial force on shear surface for initial condition
kst(i)=pi*mue(i)*cp*sin(alphao+phif)./2;       % parameter for tangential force calculations on shear surface
Fstf(i)=-kst(i).*taof_v(i)*Do^2;               % tangential force on shear surface for flow condition
Fsti(i)=-kst(i)*taoi_v*Do^2;                   % tangential force on shear surface for initial condition
Fstfp_try(i)=1/2*(taof_v(i)+taowa(i))*0.00635*P/sin(alphao)*tan(phif);
                    % tangential force from flight tips for flow condition
Fstip_try(i)=1/2*(taoi_v+taowai(i))*0.00635*P/sin(alphao)*tan(phif);
                    % tangential force from flight tips for initial condition
Tstfp(i)=Fstfp_try(i)*Ro;                      % torque from flight tips for flow condition
Tstip(i)=Fstip_try(i)*Ro;                      % torque from flight tips for initial condition
%-2. core shaft
kca(i)=t*pi*(ct-cd)*cd*cp*(exp(4*muwc*lamdas(i)*cp/(ct-cd))-1)/4/(cp^2+pi^2*cd^2)^0.5;
                    % parameter for axial force calculations on core shaft surface
Fcaf(i)=-kca(i)*taof_v(i)*Do^2;                 % axial force on core surface for flow condition
Fcai(i)=-kca(i)*taoi_v*Do^2;                    % axial force on core surface for initial condition
Fca1_try(i)=2*pi*Rc*P*tan(phif)*taowa(i)*sin(alphac); % axial force on core surface for flow condition
kct(i)=t*pi^2*(ct-cd)*cd^2*(exp(4*muwc*lamdas(i)*cp/(ct-cd))-1)/4/(cp^2+pi^2*cd^2)^0.5;
                    % parameter for tangential force calculations on core shaft surface
```

```
Fctf(i)=kct(i)*taof_v(i)*Do^2;          % tangential force on core surface for flow condition
Fcti(i)=kct(i)*taoi_v*Do^2;             % tangential force on core surface for initial condition

%-3. trailing flight side
kfa(i)=t*lamdas(i)*(pi*(1-cd^2)/4+cp*muf*(1-cd)/2);
                        % parameter for axial force calculations on trailing side surface
Ffaf(i)=-kfa(i)*taof_v(i)*Do^2;         % axial force on trailing side surface for flow condition
Ffai(i)=-kfa(i)*taoi_v*Do^2;            % axial force on trailing side surface for initial condition
Ffaf1_try(i)=2.*pi.*lamdas(i).*taoxamin(i).*quadl(@trailing, Rc, Ro);
                        % axial force on trailing side surface for flow condition
kft(i)=t*lamdas(i)*(pi*muf*(1-cd^2)/4-cp*(1-cd)/2);
                        % parameter for tangential force calculations on trailing side surface
Fftf(i)=kft(i)*taof_v(i)*Do^2;          % tangential force on trailing side surface for flow condition
Ffti(i)=kft(i)*taoi_v*Do^2;             % tangential force on trailing side surface for initial condition
%-4. trough surface
kta(i)=t*pi*(ct-cd)*ct*cos(alphao+phif)/8*(exp(4*muwt*lamdas(i)*cp/(ct-cd))-1);
                        % parameter for axial force calculations on trough surface
Ftaf(i)=-kta(i).*taof_v(i).*Do.^2;      % axial force on trough surface for flow condition
Ftai(i)=-kta(i)*taoi_v*Do^2;            % axial force on trough surface for initial condition
ktt(i)=t*pi*(ct-cd)*ct*sin(alphao+phif)/8*(exp(4*muwt*lamdas(i)*cp/(ct-cd))-1);
                        % parameter for tangential force calculations on trough surface
Fttf(i)=-ktt(i)*taof_v(i)*Do^2;         % tangential force on trough surface for flow condition
Ftti(i)=-ktt(i)*taoi_v*Do^2;            % tangential force on trough surface for initial condition
%-5. stress on driving side
Kda(i)=4*(ksa(i)+kca(i)+kfa(i)+kta(i))/pi/(1-cd^2);
                        % parameter for axial force calculations on driving side surface
tao_daf(i)=Kda(i)*taof_v(i);            % compute axial stress on driving surface for flow condition
tao_dai(i)=Kda(i)*taoi_v;               % compute axial stress on driving surface for initial condition
Ftao_daf(i)=tao_daf(i)*A_cross;         % compute axial force on driving surface for flow condition
Ftao_dai(i)=tao_dai(i)*A_cross;         % compute axial force on driving surface for initial condition
% torque calculation
Tdf(i)=2*pi*tao_daf(i)*quadl(@integrnd_Td, Rc, Ro);
                        % compute torque generated by driving side of screw for flow condition
Tdi(i)=2*pi*tao_dai(i)*quadl(@integrnd_Td, Rc, Ro);
                        % compute torque generated by driving side of screw for initial condition
Tcf(i)=2*pi*Rc*P*taowa(i)*tan(phif)*cos(alphac)*Rc;;
                        % compute torque generated by core shaft surface for flow condition
Tci(i)=2*pi*Rc*P*taowai(i)*tan(phif)*cos(alphac)*Rc;
                        % compute torque generated by core shaft surface for initial condition
Tff(i)=2*pi*lamdas(i)*t*taof_v(i)*quadl(@integrnd_Tf, Rc, Ro);  % compute torque from trough surface for flow
condition
Tfi(i)=2*pi*lamdas(i)*t*taoi_v*quadl(@integrnd_Tf, Rc, Ro);     % compute torque from trough surface for initial
condition
T_hopperf(i)=Lh/P*(Tdf(i)+Tcf(i)+Tff(i)+Tstfp(i));  % compute total torque in hopper section for flow condition
T_hopperi(i)=Lh/P*(Tdi(i)+Tci(i)+Tfi(i)+Tstip(i));  % compute total torque in hopper section for initial condition
ratio01(i)=tao_daf(i)/taoxamax(i);   % ratio of stress on driving side to theoretical maximum stress in a pitch
ratio02(i)=taoxa(i)/tao_daf(i);      % ratio of average axial stress to stress on driving side in a pitch
end
a=ratio02(1);                   % ratio of average axial stress to stress on driving side
t=t+0.0001;                     % 0.0001 as increment for t
end
t=t-0.0001;
%-------------------------------------------------------------------------------------------------------------------------------

% Choke section-0.9 m screw diameter
P=0.1;                  % pitch,m
Do=0.09;                % screw diameter, m
```

```
Ro=Do/2;            % screw radius, m.
Dc=0.030;           % screw core shaft diameter, m
Rc=Dc/2;            % screw core shaft radius, m
Dt=0.102;           % trough diameter,m
Rt=Dt/2;            % trough radius, m
cp=P/Do;           % ratio of pitch to screw diameter.
ct=Dt/Do;           % ratio of trough diameter to screw diameter.
cd=Dc/Do;           % ratio of core shaft diameter to screw diameter.
A_cross=pi*(Ro^2-Rc^2)    % Effective cross section area of the screw casing
L1=0.2;             % length of screw with 0.09 m screw diameter.
alphao=atan(P/(2*pi*Ro));          % helical angle at the outside screw diameter, radian.
alphac=atan(P/(2*pi*Rc));          % helical angle at the core shaft surface, radian.
alphao_deg=atan(P/(2*pi*Ro))/pi*180;    % helical angle at the outside screw diameter, degree.
alphac_deg=atan(P/(2*pi*Rc))/pi*180;    % helical angle at the core shaft surface, degree.
% torque calculation
for i=1:1:n
con=1;                  % constant for estimating the axial stress in choke section
e=0.2;
CC1(i)=con*(qf(i)*H0/Dt*Lc/Dt/ct)^(e); % exponent to estimate the axial stress on trailing side of flight
taoxam1(i)=t*taof_v(i)*(exp(2*tan(phi)*lamdas(i)*P/(Rt-Rc))).^(CC1(i)+1);
                        % theoretical maximum stress on driving side of flight
taoxam11(i)=t*taof_v(i)*(exp(2*tan(phi)*lamdas(i)*P/(Rt-Rc))).^(CC1(i));
                        % theoretical minimum stress on trailing side of flight
EE1(i)=(exp(2*tan(phi)*lamdas(i)*P/(Rt-Rc))).^(CC1(i));
                        % how many times for stress on trailing side compared to vertical stress taof_v
                        % for flow condition, compression factor in choke section
lamdas_a=lamdas(i);         % compute lamdas for function taoxave1
CCC=CC1(i);                 % compute CC1 for function taoxave1
taox1_a(i)=1/P*t*taof_v(i)*quadl(@taoxave1, 0,P);  % average axial stress in choke section
taowa1(i)=lamdas(i)*taox1_a(i);          % average normal wall stress in choke section
Fca1(i)=2*pi*Rc*P*tan(phif)*taowa1(i)*sin(alphac);          % axial force on core surface in choke section
Ffaf1(i)=2.*pi.*lamdas(i).*taoxam11(i).*quadl(@trailing, Rc, Ro);
                                        % axial force on trailing side surface in choke section
Ftaf1(i)=2*pi*tan(phi)*taowa1(i)*Rt*P*cos(alphao+phif);      % axial force on trough surface in choke section
Fdaf1(i)=Fca1(i)+Ffaf1(i)+Ftaf1(i); % axial force on driving side surface in choke section
tao_daf1(i)=Fdaf1(i)./pi./(Ro^2-Rc^2);
                                % compute axial stress on driving surface for flow condition in choke section
Tdf1(i)=2*pi*tao_daf1(i)*quadl(@integrnd_Td, Rc, Ro); % compute torque generated by driving side surface for
choke section
Tcf1(i)=taowa1(i)*2*pi*Rc*P*tan(phif)*Rc*cos(alphac); % compute torque generated by trailing side surface for
choke section
Tff1(i)=2*pi*lamdas(i)*taoxam11(i)*quadl(@integrnd_Tf, Rc, Ro);
                                % compute torque generated by trough side surface for choke section
Ttip1(i)=taowa1(i)*0.00635*P./sin(alphao)*tan(phif)*Ro; % compute torque generated by flight tips for choke
section
T_choke1(i)=L1/P*(Tdf1(i)+Tcf1(i)+Tff1(i)+Ttip1(i));   % compute total torque in choke section 1 for flow
condition
end
%-----------------------------------------------------------------------------------------------------------------------

% Choke section-0.8 m screw diameter
P=0.1;              % pitch,m
Do=0.08;            % screw diameter, m
Ro=Do/2;            % screw radius, m.
Dc=0.030;           % screw core shaft diameter, m
Rc=Dc/2;            % screw core shaft radius, m
Dt=0.102;           % trough diameter,m
```

```
Rt=Dt/2;            % trough radius, m
cp=P/Do;            % ratio of pitch to screw diameter.
ct=Dt/Do;           % ratio of trough diameter to screw diameter.
cd=Dc/Do;           % ratio of core shaft diameter to screw diameter.
A_cross=pi*(Ro^2-Rc^2); % Effective cross section area of the screw casing
L2=0.42;            % length of screw with 0.08 m screw diameter.
alphao=atan(P/(2*pi*Ro));          % helical angle at outside screw diameter, radian.
alphac=atan(P/(2*pi*Rc));          % helical angle at core shaft surface, radian.
alphao_deg=atan(P/(2*pi*Ro))/pi*180;  % helical angle at outside screw diameter, degree.
alphac_deg=atan(P/(2*pi*Rc))/pi*180;    % helical angle at core shaft surface, degree.
% torque calculation
for i=1:1:n
CC2(i)=con*(qf(i)*H0/Dt*Lc/Dt/ct)^(e);
                % exponent to estimate axial stress on trailing side of a flight
taoxam2(i)=t*taof_v(i)*(exp(2*tan(phi)*lamdas(i)*P/(Rt-Rc)))^(CC2(i)+1);
                % theoretical maximum stress on driving side of flight
taoxam22(i)=t*taof_v(i)*exp(2*tan(phi)*lamdas(i)*P/(Rt-Rc))^(CC2(i));
                % theoretical minimum stress on trailing side of flight
EE2(i)=(exp(2*tan(phi)*lamdas(i)*P/(Rt-Rc))).^(CC2(i));
                % how many times for stress on trailing side compared to vertical stress taof_v
                % for flow condition, compression factor in choke section
lamdas_a=lamdas(i);      % compute lamdas for function taoxave1
CCC=CC2(i);              % compute CC2 for function taoxave1
taox2_a(i)=1/P*t*taof_v(i)*quadl(@taoxave1, 0,P); % average axial stress in choke section
taowa2(i)=lamdas(i)*taox2_a(i);          % average normal wall stress in choke section
Fca2(i)=2*pi*Rc*P*tan(phi)*taowa2(i)*sin(alphac);
                % axial force on core surface in choke section
Ffaf2(i)=2*pi*lamdas(i)*taoxam22(i)*quadl(@trailing, Rc, Ro);
                % axial force on trailing side surface in choke section
Ftaf2(i)=2*pi*tan(phi)*taowa2(i)*Rt*P*cos(alphao+phif);    % axial force on trough surface in choke section
Fdaf2(i)=Fca2(i)+Ffaf2(i)+Ftaf2(i);      % axial force on driving side surface in choke section
tao_daf2(i)=Fdaf2(i)./pi./(Ro^2-Rc^2);  % compute axial stress on driving surface in choke section
Tdf2(i)=2*pi*tao_daf2(i)*quadl(@integrnd_Td, Rc, Ro);
                % compute torque generated by driving side surface for choke section 2
Tcf2(i)=taowa2(i)*2*pi*Rc*P*tan(phif)*Rc*cos(alphac);
                % compute torque generated by trailing side surface for choke section 2
Tff2(i)=2*pi*lamdas(i)*taoxam22(i)*quadl(@integrnd_Tf, Rc, Ro);
                % compute torque generated by trough surface for choke section 2
Ttip2(i)=taowa2(i)*0.00635*P./sin(alphao)*tan(phif)*Ro;
                % compute torque generated by flight tips for choke section
T_choke2(i)=L2/P*(Tdf2(i)+Tcf2(i)+Tff2(i)+Ttip2(i));
                % compute total torque in choke section 2 for flow condition
end
%-----------------------------------------------------------------------------------------------------------------------

tao_daf3=239256.2904;  % axial stress from compacted bulk density in extended section
Tdf3=2*pi*tao_daf3*quadl(@integrnd_Td, Rc, Ro);   % compute torque generated by last driving side surface
Tor_totalf=(T_choke1+T_choke2)+T_hopperf+Tdf3;    % compute total torque for flow condition
Tor_initial=T_hopperi;                % compute initial torque for hopper section
%-----------------------------------------------------------------------------------------------------------------------

result=[taoxa(1) taox1_a(1) taox2_a(1) taoi_v Fv_i taof_v0(1) Fv_f0(1) taof_v(1) Fv_f(1) Tor_initial(1)
T_hopperf(1)  T_choke1(1) T_choke2(1) Tor_totalf(1)];
```

H-5: Torque prediction for ground wood pellets-1 for screw-2

File name: Torque_GWP34_newscrew
Function: taoxave1, taoxh, trailing, integrnd_Td and integrnd_Tf
Source code: see below

```
% Hopper-screw feeder load and torque calculation for static and dynamic conditions.
% Flight thickness, screw speeds, gravity and centrifugal forces are neglected in screw torque analysis
clc
clear
%-----------------------------------------------------------------------------------------------------------------------
% fixed parameters for screw feeder and hopper
global P taof_v muf muwt lamdas Rt Rc alphas muwh phi phif lamdas_a CCC
rou_bulk=485;          % bulk density of bulk solid, kg/m^3.
H0=0.45;               % initial bed height in hopper, m
P=0.04;                % pitch,m
Do=0.08;               % screw diameter, m
Ro=Do/2;               % screw radius, m.
Dc=0.056;              % screw core shaft diameter, m
Rc=Dc/2;               % screw core shaft radius, m
Dt=0.102;              % trough diameter,m
Rt=Dt/2;               % trough radius, m
cp=P/Do;               % ratio of pitch to screw diameter.
ct=Dt/Do;              % ratio of trough diameter to screw diameter.
cd=Dc/Do;              % ratio of core shaft diameter to screw diameter.
Lh=0.914;              % hopper outlet length,m
L1=0.1;                % length of the screw with P=0.04 m and Dc=0.056 m
Lc=0.62
B=0.102;               % width of trough,m
A_cross=pi*(Ro^2-Rc^2)     % effective cross section area of screw casing
alpha=20/180*pi;       % half hopper angle, radian
g=9.8;                 % gravitational acceleration, m/s^2.
alphao=atan(P/(2*pi*Ro));          % helical angle at outside screw diameter, radian.
alphac=atan(P/(2*pi*Rc));          % helical angle at core shaft surface, radian.
alphao_deg=atan(P/(2*pi*Ro))/pi*180;   % helical angle at outside screw diameter, degree.
alphac_deg=atan(P/(2*pi*Rc))/pi*180;   % helical angle at core shaft surface, degree.
%-----------------------------------------------------------------------------------------------------------------------

% variable parameters for biomass fuels and hopper-screw feeder; initial vertical stress and initial feeder load
m=1;
delta1_deg=33.2;                       % set effective internal friction angle, degree
delta2_deg=33.2;
delta_deg=[delta1_deg:m:delta2_deg];   % effective internal friction angle, degree.
n=(delta2_deg-delta1_deg)./m+1;
delta=[delta1_deg/180*pi:m/180*pi:delta2_deg/180*pi];
phi=30.2/180*pi;       % angle of friction between bulk solids and hopper wall (or casing surface),radian
phif=30.2/180*pi;      % angle of friction between bulk solids and screw flight, radian.
muf=tan(phif);         % coefficient of friction between solids and screw flight surface
muwc=muf;              % friction coefficient of bulk solid on core surface
muwh=tan(phi);         % friction coefficient of bulk solid on hopper surface.
muwt=muwh;             % friction coefficient of bulk solid on trough surface.
D=2*(H0+B./2*cot(alpha))*tan(alpha);  % compute width of bulk solid free surface in hopper (flate surface), m
qi=1/(2*tan(alpha))*(D/B-1);          % compute non-dimensional surcharge factor for initial condition
taoi_v=qi*rou_bulk*g*B;               % compute vertical stress at hopper outlet for initial condition
Fv_i=taoi_v*Lh*B;                     % compute feeder load at hopper outlet for initial condition
%-----------------------------------------------------------------------------------------------------------------------
```

```
% vertical stress and feeder load for flow condition
for i=1:1:n
mud(i)=tan(delta(i));                % effective coefficient of internal friction.
mue(i)=sin(delta(i));                % equivalent friction coefficient of bulk solid,.from Roberts
alpha_Mohr(i)=(asin(sin(phi)/sin(delta(i)))-phi)/2;
lamdas(i)=cos(phi)*sin(2*alpha_Mohr(i))/(sin(phi)*cos(2*alpha_Mohr(i))+sin(phi+2*alpha_Mohr(i)));
                        % stress ratio of normal stress acting perpendicularly to the wall
                        % of trough and core shaft surfaces to axial compression stress
                        % derived from Mohr circle
beta(i)=0.5*(phi+asin(sin(phi)/sin(delta(i))));                    % compute beta(i), constant
X(i)=sin(delta(i))/(1-sin(delta(i)))*(sin(2*beta(i)+alpha)/sin(alpha)+1);   % constant to compute feeder load
Y(i)=((alpha+beta(i))*sin(alpha)+sin(beta(i))*sin(alpha+beta(i)))./((1-sin(delta(i)))*sin(alpha+beta(i))^2);
                        % constant to compute feeder load
qf(i)=Y(i)*(1+sin(delta(i)))/(2*(X(i)-1)*sin(alpha));    % surcharge factor for flow conditions
%qf1(i)=1/4*(1/tan(alpha))*(Y(i)*(1+sin(delta(i))*cos(2*beta(i)))*(tan(alpha)+tan(phi))/sin(alpha)/(X(i)-1)-1);
                        % smaller than the above one
taof_v0(i)=qf(i)*rou_bulk*g*B;    % use loose bulk density, even for compressible solids in the present study
Fv_f0(i)=taof_v0(i).*Lh.*B;       % vertical stress and feeder load for flow condition
taof_v(i)=(taof_v0(i)+taoi_v)./2;  % average vertical stress for flow condition
Fv_f(i)=taof_v(i).*Lh.*B;          % average feeder load for flow condition
end
%-------------------------------------------------------------------------------------------------------------------------------

% hopper section, for a material element in a pitch first and entire hopper section
t=1.0;
for i=1:1:n
taoxamax1(i)=t*taof_v(i)*(exp(2*tan(phi)*lamdas(i)*P/(Rt-Rc)));
                        % maximum stress at driving side of flight according to stress analysis
taoxamin1(i)=t*taof_v(i);          % minimum stress at trailing side of flight according to stress analysis
lamdas_a=lamdas(i);                % stress ratio of normal wall stress to axial stress on confined surface
taoxa1(i)=1/P*t*taof_v(i)*quadl(@taoxh, 0,P);  % average axial stress in a pitch for flow condition
taoxai1(i)=1/P*t*taoi_v*quadl(@taoxh, 0,P);    % average axial stress in a pitch for initial condition
taowa1(i)=lamdas(i)*taoxa1(i);     % average normal wall stress in a pitch for flow condition
taowai1(i)=lamdas(i)*taoxai1(i);   % average normal wall stress in a pitch for initial condition
%-1. shear surface
ksa1(i)=pi*mue(i)*cp*cos(alphao+phif)./2;    % parameter for axial force calculations on shear surface
Fsaf1(i)=-ksa1(i).*taof_v(i).*Do.^2;         % axial force on shear surface for flow condition
Fsai1(i)=-ksa1(i)*taoi_v*Do^2;               % axial force on shear surface for initial condition
kst1(i)=pi*mue(i)*cp*sin(alphao+phif)./2;    % parameter for tangential force calculations on shear surface
Fstf1(i)=-kst1(i).*taof_v(i)*Do^2;           % tangential force on shear surface for flow condition
Fsti1(i)=-kst1(i)*taoi_v*Do^2;               % tangential force on shear surface for initial condition
Fstfp_try1(i)=1/2*(taof_v(i)+taowa1(i))*0.00635*P/sin(alphao)*tan(phif);  % tangential force from flight tips for
flow condition
Fstip_try1(i)=1/2*(taoi_v+taowai1(i))*0.00635*P/sin(alphao)*tan(phif);
                                % tangential force from flight tips for initial condition
Tstfp1(i)=Fstfp_try1(i)*Ro;        % torque from flight tips for flow condition
Tstip1(i)=Fstip_try1(i)*Ro;        % torque from flight tips for initial condition
%-2. core shaft
kca1(i)=t*pi*(ct-cd)*cd*cp*(exp(4*muwc*lamdas(i)*cp/(ct-cd))-1)/4/(cp^2+pi^2*cd^2)^0.5;
                        % parameter for axial force calculations on core shaft surface
Fcaf1(i)=-kca1(i)*taof_v(i)*Do^2;     % axial force on core surface for flow condition
Fcai1(i)=-kca1(i)*taoi_v*Do^2;        % axial force on core surface for initial condition
Fca1_try1(i)=2*pi*Rc*P*tan(phif)*taowa1(i)*sin(alphac);
kct1(i)=t*pi^2*(ct-cd)*cd^2*(exp(4*muwc*lamdas(i)*cp/(ct-cd))-1)/4/(cp^2+pi^2*cd^2)^0.5; % parameter for
tangential force calculations on core shaft surface
Fctf1(i)=kct1(i)*taof_v(i)*Do^2;      % tangential force on core surface for flow condition
Fcti1(i)=kct1(i)*taoi_v*Do^2;         % tangential force on core surface for initial condition
```

```
%-3. trailing flight side
kfa1(i)=t*lamdas(i)*(pi*(1-cd^2)/4+cp*muf*(1-cd)/2);      % parameter for axial force calculations on trailing
side surface
Ffaf1(i)=-kfa1(i)*taof_v(i)*Do^2;                  % axial force on trailing side surface for flow condition
Ffai1(i)=-kfa1(i)*taoi_v*Do^2;                     % axial force on trailing side surface for initial condition
Ffaf1_try1(i)=2.*pi.*lamdas(i).*taoxamin1(i).*quadl(@trailing, Rc, Ro);
                                % axial force on core surface for flow condition
kft1(i)=t*lamdas(i)*(pi*muf*(1-cd^2)/4-cp*(1-cd)/2);
                                % parameter for tangential force calculations on trailing side surface
Fftf1(i)=kft1(i)*taof_v(i)*Do^2;   % tangential force on trailing side surface for flow condition
Ffti1(i)=kft1(i)*taoi_v*Do^2;      % tangential force on trailing side surface for initial condition
%-4. trough surface
kta1(i)=t*pi*(ct-cd)*ct*cos(alphao+phif)/8*(exp(4*muwt*lamdas(i)*cp/(ct-cd))-1);
                        % parameter for axial force calculations on trough surface
Ftaf1(i)=-kta1(i).*taof_v(i).*Do.^2;          % axial force on trough surface for flow condition
Ftai1(i)=-kta1(i)*taoi_v*Do^2;                % axial force on trough surface for initial condition
ktt1(i)=t*pi*(ct-cd)*ct*sin(alphao+phif)/8*(exp(4*muwt*lamdas(i)*cp/(ct-cd))-1);
                        % parameter for tangential force calculations on trough surface
Fttf1(i)=-ktt1(i)*taof_v(i)*Do^2;             % tangential force on trough surface for flow condition
Ftti1(i)=-ktt1(i)*taoi_v*Do^2;                % tangential force on trough surface for initial condition
%-5. stress on driving side
Kda1(i)=4*(ksa1(i)+kca1(i)+kfa1(i)+kta1(i))/pi/(1-cd^2);  % parameter for axial force calculations on driving side
surface
tao_daf1(i)=Kda1(i)*taof_v(i);            % compute axial stress on driving surface for flow condition
tao_dai1(i)=Kda1(i)*taoi_v;               % compute axial stress on driving surface for initial condition
Ftao_daf1(i)=tao_daf1(i)*A_cross;         % compute axial force on driving surface for flow condition
Ftao_dai1(i)=tao_dai1(i)*A_cross;         % compute axial force on driving surface for initial condition
% torque calculation
Tdf1(i)=2*pi*tao_daf1(i)*quadl(@integrnd_Td, Rc, Ro);
                                % compute torque generated by driving side of the screw for flow condition
Tdi1(i)=2*pi*tao_dai1(i)*quadl(@integrnd_Td, Rc, Ro);
                                % compute torque generated by driving side of the screw for initial condition
Tcf1(i)=2*pi*Rc*P*taowa1(i)*tan(phif)*cos(alphac)*Rc;
                                % compute torque generated by core shaft surface for flow condition
Tci1(i)=2*pi*Rc*P*taowai1(i)*tan(phif)*cos(alphac)*Rc;
                                % compute torque generated by core shaft surface for initial condition
Tff1(i)=2*pi*lamdas(i)*t*taof_v(i)*quadl(@integrnd_Tf, Rc, Ro);
                                % compute torque from trailing surface for flow condition
Tfi1(i)=2*pi*lamdas(i)*t*taoi_v*quadl(@integrnd_Tf, Rc, Ro);
                                % compute torque from trailing surface for initial condition
T_hopperf1(i)=L1/P*(Tdf1(i)+Tcf1(i)+Tff1(i)+Tstfp1(i));
                                % compute total torque in hopper section 1 for flow condition
T_hopperi1(i)=L1/P*(Tdi1(i)+Tci1(i)+Tfi1(i)+Tstip1(i));
                                % compute total torque in hopper section 1 for initial condition
ratio01(i)=tao_daf1(i)/taoxamax1(i);   % ratio of stress on driving side to theoretical maximum stress in a pitch
ratio02(i)=taoxa1(i)/tao_daf1(i);      % ratio of average axial stress to stress on driving side in a pitch
end
%-----------------------------------------------------------------------------------------------------------------------

% the second stage along the screw
P=0.056;              % pitch,m
Do=0.08;              % screw diameter, m
Ro=Do/2;              % screw radius, m.
Dc=0.043;             % screw core shaft diameter, m
Rc=Dc/2;              % screw core shaft radius, m
Dt=0.102;             % trough diameter,m
Rt=Dt/2;              % trough radius, m
```

```
cp=P/Do;              % ratio of pitch to screw diameter.
ct=Dt/Do;             % ratio of trough diameter to screw diameter.
cd=Dc/Do;             % ratio of core shaft diameter to screw diameter.
Lh=0.914;             % hopper outlet length,m
L2=0.31;              % length of the screw with P=0.056 m and Dc=0.043 m.
Lc=0.62
B=0.102;              % width of the trough,m
A_cross=pi*(Ro^2-Rc^2)  % effective cross section area of the screw casing
alpha=20/180*pi;          % half hopper angle, radian
g=9.8;              % gravitational acceleration, m/s^2.
alphao=atan(P/(2*pi*Ro));         % helical angle at the outside screw diameter, radian.
alphac=atan(P/(2*pi*Rc));           % helical angle at the core shaft surface, radian.
alphao_deg=atan(P/(2*pi*Ro))/pi*180;  % helical angle at the outside screw diameter, degree.
alphac_deg=atan(P/(2*pi*Rc))/pi*180;       % helical angle at the core shaft surface, degree.
%-----------------------------------------------------------------------------------------------------------------------------

% variable parameters for biomass fuels and hopper-screw feeder; initial vertical stress and initial feeder load
for i=1:1:n
taoxamax2(i)=t*taof_v(i)*(exp(2*tan(phi)*lamdas(i)*P/(Rt-Rc)));
                % maximum stress at driving side of flight according to stress analysis
taoxamin2(i)=t*taof_v(i);  % minimum stress at driving side of flight according to stress analysis
lamdas_a=lamdas(i);       % stress ratio of normal wall stress to axial stress on confined surface
taoxa2(i)=1/P*t*taof_v(i)*quadl(@taoxh, 0,P);  % average axial stress in a pitch for flow condition
taoxai2(i)=1/P*t*taoi_v*quadl(@taoxh, 0,P);     % average axial stress in a pitch for initial condition
taowa2(i)=lamdas(i)*taoxa2(i);        % average normal wall stress in a pitch for flow condition
taowai2(i)=lamdas(i)*taoxai2(i);      % average normal wall stress in a pitch for initial condition
%-1. shear surface
ksa2(i)=pi*mue(i)*cp*cos(alphao+phif)./2;  % parameter for axial force calculations on shear surface
Fsaf2(i)=-ksa2(i).*taof_v(i).*Do.^2;      % axial force on shear surface for flow condition
Fsai2(i)=-ksa2(i)*taoi_v*Do^2;            % axial force on shear surface for initial condition
kst2(i)=pi*mue(i)*cp*sin(alphao+phif)./2;     % parameter for tangential force calculations on shear surface
Fstf2(i)=-kst2(i).*taof_v(i)*Do^2;              % tangential force on shear surface for flow condition
Fsti2(i)=-kst2(i)*taoi_v*Do^2;                  % tangential force on shear surface for initial condition
Fstfp_try2(i)=1/2*(taof_v(i)+taowa2(i))*0.00635*P/sin(alphao)*tan(phif);
                                        % tangential force from flight tips for flow condition
Fstip_try2(i)=1/2*(taoi_v+taowai2(i))*0.00635*P/sin(alphao)*tan(phif);
                                        % tangential force from flight tips for initial condition

Tstfp2(i)=Fstfp_try2(i)*Ro;      % torque from flight tips for flow condition
Tstip2(i)=Fstip_try2(i)*Ro;      % torque from flight tips for initial condition
%-2. core shaft
kca2(i)=t*pi*(ct-cd)*cd*cp*(exp(4*muwc*lamdas(i)*cp/(ct-cd))-1)/4/(cp^2+pi^2*cd^2)^0.5;
                % parameter for axial force calculations on core shaft surface
Fcaf2(i)=-kca2(i)*taof_v(i)*Do^2;    % axial force on core surface for flow condition
Fcai2(i)=-kca2(i)*taoi_v*Do^2;       % axial force on core surface for initial condition
Fca1_try2(i)=2*pi*Rc*P*tan(phif)*taowa2(i)*sin(alphac); % axial force on core surface for flow condition
kct2(i)=t*pi^2*(ct-cd)*cd^2*(exp(4*muwc*lamdas(i)*cp/(ct-cd))-1)/4/(cp^2+pi^2*cd^2)^0.5;
                % parameter for tangential force calculations on core shaft surface
Fctf2(i)=kct2(i)*taof_v(i)*Do^2;    % tangential force on core surface for flow condition
Fcti2(i)=kct2(i)*taoi_v*Do^2;       % tangential force on core surface for initial condition
%-3. trailing flight side
kfa2(i)=t*lamdas(i)*(pi*(1-cd^2)/4+cp*muf*(1-cd)/2); % parameter for axial force calculations on trailing side
surface
Ffaf2(i)=-kfa2(i)*taof_v(i)*Do^2;           % axial force on trailing side surface for flow condition
Ffai2(i)=-kfa2(i)*taoi_v*Do^2;              % axial force on trailing side surface for initial condition
Ffaf1_try2(i)=2.*pi.*lamdas(i).*taoxamin2(i).*quadl(@trailing, Rc, Ro);
kft2(i)=t*lamdas(i)*(pi*muf*(1-cd^2)/4-cp*(1-cd)/2);
```

```
                                        % parameter for tangential force calculations on trailing side surface
Fftf2(i)=kft2(i)*taof_v(i)*Do^2;        % tangential force on trailing side surface for flow condition
Ffti2(i)=kft2(i)*taoi_v*Do^2;           % tangential force on trailing side surface for initial condition
%-4. trough surface
kta2(i)=t*pi*(ct-cd)*ct*cos(alphao+phif)/8*(exp(4*muwt*lamdas(i)*cp/(ct-cd))-1);
                                % parameter for axial force calculations on trough surface
Ftaf2(i)=-kta2(i).*taof_v(i).*Do.^2;    % axial force on trough surface for flow condition
Ftai2(i)=-kta2(i)*taoi_v*Do^2;          % axial force on trough surface for initial condition
ktt2(i)=t*pi*(ct-cd)*ct*sin(alphao+phif)/8*(exp(4*muwt*lamdas(i)*cp/(ct-cd))-1);
                                % parameter for tangential force calculations on trough surface
Fttf2(i)=-ktt2(i)*taof_v(i)*Do^2;       % tangential force on trough surface for flow condition
Ftti2(i)=-ktt2(i)*taoi_v*Do^2;          % tangential force on trough surface for initial condition
%-5. stress on driving side
Kda2(i)=4*(ksa2(i)+kca2(i)+kfa2(i)+kta2(i))/pi/(1-cd^2);   % parameter for axial force calculations on driving
side surface
tao_daf2(i)=Kda2(i)*taof_v(i);          % compute axial stress on driving surface for flow condition
tao_dai2(i)=Kda2(i)*taoi_v;             % compute axial stress on driving surface for initial condition
Ftao_daf2(i)=tao_daf2(i)*A_cross;       % compute axial force on driving surface for flow condition
Ftao_dai2(i)=tao_dai2(i)*A_cross;       % compute axial force on driving surface for initial condition
% torque calculation
Tdf2(i)=2*pi*tao_daf2(i)*quadl(@integrnd_Td, Rc, Ro);
                                % compute torque generated by driving side of screw for flow condition
Tdi2(i)=2*pi*tao_dai2(i)*quadl(@integrnd_Td, Rc, Ro);
                                % compute torque generated by driving side of screw for initial condition
Tcf2(i)=2*pi*Rc*P*taowa2(i)*tan(phif)*cos(alphac)*Rc;
                                % compute torque generated by core shaft surface for flow condition
Tci2(i)=2*pi*Rc*P*taowai2(i)*tan(phif)*cos(alphac)*Rc;
                                % compute torque generated by core shaft surface for initial condition
Tff2(i)=2*pi*lamdas(i)*t*taof_v(i)*quadl(@integrnd_Tf, Rc, Ro);
                                % compute torque from trough surface for flow condition
Tfi2(i)=2*pi*lamdas(i)*t*taoi_v*quadl(@integrnd_Tf, Rc, Ro);
                                % compute torque from trough surface for initial condition
T_hopperf2(i)=L2/P*(Tdf2(i)+Tcf2(i)+Tff2(i)+Tstfp2(i));
                                % compute total torque in hopper section for flow condition
T_hopperi2(i)=L2/P*(Tdi2(i)+Tci2(i)+Tfi2(i)+Tstip2(i));
                                % compute total torque in hopper section for initial condition
ratio012(i)=tao_daf2(i)/taoxamax2(i);  % ratio of stress on driving side to theoretical maximum stress in a pitch
ratio022(i)=taoxa2(i)/tao_daf2(i);     % ratio of average axial stress to stress on driving side in a pitch
end
%-------------------------------------------------------------------------------------------------------------------------

% the third stage of the screw
P=0.071;                % pitch,m
Do=0.08;                % screw diameter, m
Ro=Do/2;                % screw radius, m.
Dc=0.0305;              % screw core shaft diameter, m
Rc=Dc/2;                % screw core shaft radius, m
Dt=0.102;               % trough diameter,m
Rt=Dt/2;                % trough radius, m
cp=P/Do;                % ratio of pitch to screw diameter.
ct=Dt/Do;               % ratio of trough diameter to screw diameter.
cd=Dc/Do;               % ratio of core shaft diameter to screw diameter.
Lh=0.914;               % hopper outlet length,m
L3=0.31;                % length of the screw with P=0.071 m and Dc=0.0305 m.
Lc=0.62
B=0.102;                % width of the trough,m
A_cross=pi*(Ro^2-Rc^2)      % effective cross section area of the screw casing
```

```
alpha=20/180*pi;                % half hopper angle, radian
g=9.8;                  % gravitational acceleration, m/s^2.
for i=1:1:n
taoxamax3(i)=t*taof_v(i)*(exp(2*tan(phi)*lamdas(i)*P/(Rt-Rc)));
                % maximum stress at driving side of flight according to stress analysis
taoxamin3(i)=t*taof_v(i);  % minimum stress at driving side of flight according to stress analysis
lamdas_a=lamdas(i);        % stress ratio of normal wall stress to axial stress on confined surface
taoxa3(i)=1/P*t*taof_v(i)*quadl(@taoxh, 0,P);  % average axial stress in a pitch for flow condition
taoxai3(i)=1/P*t*taoi_v*quadl(@taoxh, 0,P);     % average axial stress in a pitch for initial condition
taowa3(i)=lamdas(i)*taoxa3(i);     % average normal wall stress in a pitch for flow condition
taowai3(i)=lamdas(i)*taoxai3(i);   % average normal wall in a pitch for initial condition
%-1. shear surface
ksa3(i)=pi*mue(i)*cp*cos(alphao+phif)./2;  % parameter for axial force calculations on shear surface
Fsaf3(i)=-ksa3(i).*taof_v(i).*Do.^2;         % axial force on shear surface for flow condition
Fsai3(i)=-ksa3(i)*taoi_v*Do^2;              % axial force on shear surface for initial condition
kst3(i)=pi*mue(i)*cp*sin(alphao+phif)./2;   % parameter for tangential force calculations on shear surface
Fstf3(i)=-kst3(i).*taof_v(i)*Do^2;          % tangential force on shear surface for flow condition
Fsti3(i)=-kst3(i)*taoi_v*Do^2;              % tangential force on shear surface for initial condition
Fstfp_try3(i)=1/2*(taof_v(i)+taowa3(i))*0.00635*P/sin(alphao)*tan(phif);
                                        % tangential force from flight tips for flow condition
Fstip_try3(i)=1/2*(taoi_v+taowai3(i))*0.00635*P/sin(alphao)*tan(phif);
                                        % tangential force from flight tips for initial condition
Tstfp3(i)=Fstfp_try3(i)*Ro;         % torque from flight tips for flow condition
Tstip3(i)=Fstip_try3(i)*Ro;         % torque from flight tips for initial condition
%-2. core shaft
kca3(i)=t*pi*(ct-cd)*cd*cp*(exp(4*muwc*lamdas(i)*cp/(ct-cd))-1)/4/(cp^2+pi^2*cd^2)^0.5;
                        % parameter for axial force calculations on core shaft surface
Fcaf3(i)=-kca3(i)*taof_v(i)*Do^2;          % axial force on core surface for flow condition
Fcai3(i)=-kca3(i)*taoi_v*Do^2;             % axial force on core surface for initial condition
Fca1_try3(i)=2*pi*Rc*P*tan(phif)*taowa3(i)*sin(alphac);
kct3(i)=t*pi^2*(ct-cd)*cd^2*(exp(4*muwc*lamdas(i)*cp/(ct-cd))-1)/4/(cp^2+pi^2*cd^2)^0.5;
                        % parameter for tangential force calculations on core shaft surface
Fctf3(i)=kct3(i)*taof_v(i)*Do^2;          % tangential force on core surface for flow condition
Fcti3(i)=kct3(i)*taoi_v*Do^2;             % tangential force on core surface for initial condition
%-3. trailing flight side
kfa3(i)=t*lamdas(i)*(pi*(1-cd^2)/4+cp*muf*(1-cd)/2);
                                        % parameter for axial force calculations on trailing side surface
Ffaf3(i)=-kfa3(i)*taof_v(i)*Do^2;           % axial force on trailing side surface for flow condition
Ffai3(i)=-kfa3(i)*taoi_v*Do^2;              % axial force on trailing side surface for initial condition
Ffaf1_try3(i)=2.*pi.*lamdas(i).*taoxamin3(i).*quadl(@trailing, Rc, Ro);
                        % axial force on core surface for flow condition
kft3(i)=t*lamdas(i)*(pi*muf*(1-cd^2)/4-cp*(1-cd)/2);
                        % parameter for tangential force calculations on trailing side surface
Fftf3(i)=kft3(i)*taof_v(i)*Do^2;          % tangential force on trailing side surface for flow condition
Ffti3(i)=kft3(i)*taoi_v*Do^2;             % tangential force on trailing side surface for initial condition
%-4. trough surface
kta3(i)=t*pi*(ct-cd)*ct*cos(alphao+phif)/8*(exp(4*muwt*lamdas(i)*cp/(ct-cd))-1);
                        % parameter for axial force calculations on trough surface
Ftaf3(i)=-kta3(i).*taof_v(i).*Do.^2;       % axial force on trough surface for flow condition
Ftai3(i)=-kta3(i)*taoi_v*Do^2;             % axial force on trough surface for initial condition
ktt3(i)=t*pi*(ct-cd)*ct*sin(alphao+phif)/8*(exp(4*muwt*lamdas(i)*cp/(ct-cd))-1);
                        % parameter for tangential force calculations on trough surface
Fttf3(i)=-ktt3(i)*taof_v(i)*Do^2;          % tangential force on trough surface for flow condition
Ftti3(i)=-ktt3(i)*taoi_v*Do^2;             % tangential force on trough surface for initial condition
%-5. stress on driving side
Kda3(i)=4*(ksa3(i)+kca3(i)+kfa3(i)+kta3(i))/pi/(1-cd^2);
                                        % parameter for axial force calculations on driving side surface
```

```
tao_daf3(i)=Kda3(i)*taof_v(i);                % compute axial stress on driving surface for flow condition
tao_dai3(i)=Kda3(i)*taoi_v;                   % compute axial stress on driving surface for initial condition
Ftao_daf3(i)=tao_daf3(i)*A_cross;             % compute axial force on driving surface for flow condition
Ftao_dai3(i)=tao_dai3(i)*A_cross;             % compute axial force on driving surface for initial condition
% torque calculation
Tdf3(i)=2*pi*tao_daf3(i)*quadl(@integrnd_Td, Rc, Ro);
                        % compute torque generated by driving side of screw for flow condition
Tdi3(i)=2*pi*tao_dai3(i)*quadl(@integrnd_Td, Rc, Ro);
                        % compute the torque generated by the driving side of the screw for initial condition
Tcf3(i)=2*pi*Rc*P*taowa3(i)*tan(phif)*cos(alphac)*Rc;
                        % compute torque generated by core shaft surface for flow condition
Tci3(i)=2*pi*Rc*P*taowai3(i)*tan(phif)*cos(alphac)*Rc;
                        % compute torque generated by core shaft surface for initial condition
Tff3(i)=2*pi*lamdas(i)*t*taof_v(i)*quadl(@integrnd_Tf, Rc, Ro);
                        % compute torque from trailing surface for flow condition
Tfi3(i)=2*pi*lamdas(i)*t*taoi_v*quadl(@integrnd_Tf, Rc, Ro);
                        % compute torque from trailing surface for initial condition
T_hopperf3(i)=L3/P*(Tdf3(i)+Tcf3(i)+Tff3(i)+Tstfp3(i));
                        % compute total torque in hopper section for flow condition
T_hopperi3(i)=L3/P*(Tdi3(i)+Tci3(i)+Tfi3(i)+Tstip3(i));
                        % compute total torque in hopper section for initial condition
ratio013(i)=tao_daf3(i)/taoxamax3(i);   % ratio of stress on driving side to theoretical maximum stress in a pitch
ratio023(i)=taoxa3(i)/tao_daf3(i);      % ratio of average axial stress to stress on driving side in a pitch
end
%-----------------------------------------------------------------------------------------------------------------------------------

% the fourth- in the hopper
P=0.08;                 % pitch,m
Do=0.08;                % screw diameter, m
Ro=Do/2;                % screw radius, m.
Dc=0.0203;              % screw core shaft diameter, m
Rc=Dc/2;                % screw core shaft radius, m
Dt=0.102;               % trough diameter,m
Rt=Dt/2;                % trough radius, m
cp=P/Do;                % ratio of pitch to screw diameter.
ct=Dt/Do;               % ratio of trough diameter to screw diameter.
cd=Dc/Do;               % ratio of core shaft diameter to screw diameter.
Lh=0.914;               % hopper outlet length,m
L4=0.019;               % length of the screw with P=0.08 m and Dc=0.0203 m.
Lc=0.62
B=0.102;                % width of the trough,m
A_cross=pi*(Ro^2-Rc^2)  % effective cross section area of the screw casing
alpha=20/180*pi;        % half hopper angle, radian
g=9.8;                  % gravitational acceleration, m/s^2.
for i=1:1:n
taoxamax4(i)=t*taof_v(i)*(exp(2*tan(phi)*lamdas(i)*P/(Rt-Rc))); % maximum stress at driving side of flight
according to stress analysis
taoxamin4(i)=t*taof_v(i);   % minimum stress at driving side of flight according to stress analysis
lamdas_a=lamdas(i);     % stress ratio of normal wall stress to axial stress on confined surface
taoxa4(i)=1/P*t*taof_v(i)*quadl(@taoxh, 0,P);  % average axial stress in a pitch for flow condition
taoxai4(i)=1/P*t*taoi_v*quadl(@taoxh, 0,P);    % average axial stress in a pitch for initial condition
taowa4(i)=lamdas(i)*taoxa4(i);    % average normal wall stress in a pitch for flow condition
taowai4(i)=lamdas(i)*taoxai4(i);  % average normal wall in a pitch for initial condition
%-1. shear surface
ksa4(i)=pi*mue(i)*cp*cos(alphao+phif)./2;      % parameter for axial force calculations on shear surface
Fsaf4(i)=-ksa4(i).*taof_v(i).*Do.^2;           % axial force on shear surface for flow condition
Fsai4(i)=-ksa4(i)*taoi_v*Do^2;                 % axial force on shear surface for initial condition
```

```
kst4(i)=pi*mue(i)*cp*sin(alphao+phif)./2;   % parameter for tangential force calculations on shear surface
Fstf4(i)=-kst4(i).*taof_v(i)*Do^2;          % tangential force on shear surface for flow condition
Fsti4(i)=-kst4(i)*taoi_v*Do^2;              % tangential force on shear surface for initial condition
Fstfp_try4(i)=1/2*(taof_v(i)+taowa4(i))*0.00635*P/sin(alphao)*tan(phif);
                                % tangential force from flight tips for flow condition
Fstip_try4(i)=1/2*(taoi_v+taowai4(i))*0.00635*P/sin(alphao)*tan(phif);
                                % tangential force from flight tips for initial condition
Tstfp4(i)=Fstfp_try4(i)*Ro; % torque from flight tips for flow condition
Tstip4(i)=Fstip_try4(i)*Ro; % torque from flight tips for initial condition
%-2. core shaft
kca4(i)=t*pi*(ct-cd)*cd*cp*(exp(4*muwc*lamdas(i)*cp/(ct-cd))-1)/4/(cp^2+pi^2*cd^2)^0.5;
                        % parameter for axial force calculations on core shaft surface
Fcaf4(i)=-kca4(i)*taof_v(i)*Do^2;           % axial force on core surface for flow condition
Fcai4(i)=-kca4(i)*taoi_v*Do^2;              % axial force on core surface for initial condition
Fca1_try4(i)=2*pi*Rc*P*tan(phif)*taowa4(i)*sin(alphac);
kct4(i)=t*pi^2*(ct-cd)*cd^2*(exp(4*muwc*lamdas(i)*cp/(ct-cd))-1)/4/(cp^2+pi^2*cd^2)^0.5;
                        % parameter for tangential force calculations on core shaft surface
Fctf4(i)=kct4(i)*taof_v(i)*Do^2;            % tangential force on core surface for flow condition
Fcti4(i)=kct4(i)*taoi_v*Do^2;               % tangential force on core surface for initial condition
%-3. trailing flight side
kfa4(i)=t*lamdas(i)*(pi*(1-cd^2)/4+cp*muf*(1-cd)/2);
                                % parameter for axial force calculations on trailing side surface
Ffaf4(i)=-kfa4(i)*taof_v(i)*Do^2;           % axial force on trailing side surface for flow condition
Ffai4(i)=-kfa4(i)*taoi_v*Do^2;              % axial force on trailing side surface for initial condition
Ffaf1_try4(i)=2.*pi.*lamdas(i).*taoxamin4(i).*quadl(@trailing, Rc, Ro);
                                % axial force on trailing side surface for flow condition
kft4(i)=t*lamdas(i)*(pi*muf*(1-cd^2)/4-cp*(1-cd)/2);
                                % parameter for tangential force calculations on trailing side surface
Fftf4(i)=kft4(i)*taof_v(i)*Do^2;            % tangential force on trailing side surface for flow condition
Ffti4(i)=kft4(i)*taoi_v*Do^2;               % tangential force on trailing side surface for initial condition
%-4. trough surface
kta4(i)=t*pi*(ct-cd)*ct*cos(alphao+phif)/8*(exp(4*muwt*lamdas(i)*cp/(ct-cd))-1);
                                % parameter for axial force calculations on trough surface
Ftaf4(i)=-kta4(i).*taof_v(i).*Do.^2;        % axial force on trough surface for flow condition
Ftai4(i)=-kta4(i)*taoi_v*Do^2;              % axial force on trough surface for initial condition
ktt4(i)=t*pi*(ct-cd)*ct*sin(alphao+phif)/8*(exp(4*muwt*lamdas(i)*cp/(ct-cd))-1);
                                % parameter for tangential force calculations on trough surface
Fttf4(i)=-ktt4(i)*taof_v(i)*Do^2;           % tangential force on trough surface for flow condition
Ftti4(i)=-ktt4(i)*taoi_v*Do^2;              % tangential force on trough surface for initial condition
%-5. stress on driving side
Kda4(i)=4*(ksa4(i)+kca4(i)+kfa4(i)+kta4(i))/pi/(1-cd^2);
                                % parameter for axial force calculations on driving side surface
tao_daf4(i)=Kda4(i)*taof_v(i);              % compute axial stress on driving surface for flow condition
tao_dai4(i)=Kda4(i)*taoi_v;                 % compute axial stress on driving surface for initial condition
Ftao_daf4(i)=tao_daf4(i)*A_cross;           % compute axial force on driving surface for flow condition
Ftao_dai4(i)=tao_dai4(i)*A_cross;           % compute axial force on driving surface for initial condition
% torque calculation
Tdf4(i)=2*pi*tao_daf4(i)*quadl(@integrnd_Td, Rc, Ro);
                                % compute torque generated by driving side of screw for flow condition
Tdi4(i)=2*pi*tao_dai4(i)*quadl(@integrnd_Td, Rc, Ro);
                                % compute torque generated by driving side of screw for initial condition
Tcf4(i)=2*pi*Rc*P*taowa4(i)*tan(phif)*cos(alphac)*Rc;
                                % compute torque generated by core shaft surface for flow condition
Tci4(i)=2*pi*Rc*P*taowai4(i)*tan(phif)*cos(alphac)*Rc;
                                % compute torque generated by core shaft surface for initial condition
Tff4(i)=2*pi*lamdas(i)*t*taof_v(i)*quadl(@integrnd_Tf, Rc, Ro);
                                % compute torque from trailing surface for flow condition
```

```
Tfi4(i)=2*pi*lamdas(i)*t*taoi_v*quadl(@integrnd_Tf, Rc, Ro);
                                % compute torque from trailing surface for initial condition
T_hopperf4(i)=L4/P*(Tdf4(i)+Tcf4(i)+Tff4(i)+Tstfp4(i));
                                % compute total torque in hopper section for flow condition
T_hopperi4(i)=L4/P*(Tdi4(i)+Tci4(i)+Tfi4(i)+Tstip4(i));
                                % compute total torque in hopper section for initial condition
ratio014(i)=tao_daf4(i)/taoxamax4(i);  % ratio of stress on driving side to theoretical maximum stress in a pitch
ratio024(i)=taoxa4(i)/tao_daf4(i);     % ratio of average axial stress to stress on driving side in a pitch
end
%-----------------------------------------------------------------------------------------------------------------------

% hopper total
T_hopperf=T_hopperf1+T_hopperf2+T_hopperf3+T_hopperf4;
                                % compute total torque in hopper section for flow condition
T_hopperi=T_hopperi1+T_hopperi2+T_hopperi3+T_hopperi4;
                                % compute total torque in hopper section for initial condition
%-----------------------------------------------------------------------------------------------------------------------
% the fifth-in choke section
P=0.08;             % pitch,m
Do=0.08;            % screw diameter, m
Ro=Do/2;            % screw radius, m.
Dc=0.0203;          % screw core shaft diameter, m
Rc=Dc/2;            % screw core shaft radius, m
Dt=0.102;           % trough diameter,m
Rt=Dt/2;            % trough radius, m
cp=P/Do;            % ratio of pitch to screw diameter.
ct=Dt/Do;           % ratio of trough diameter to screw diameter.
cd=Dc/Do;           % ratio of core shaft diameter to screw diameter.
Lh=0.914;           % hopper outlet length,m
L5=0.305;           % length of the screw with P=0.08 m and Dc=0.0203 m in choke section
Lc=0.62
B=0.102;            % width of trough,m
A_cross=pi*(Ro^2-Rc^2); % effective cross section area of the screw casing
alpha=20/180*pi;        % half hopper angle, radian
g=9.8;              % gravitational acceleration, m/s^2.
for i=1:1:n
taoxamax5(i)=t*taof_v(i)*(exp(2*tan(phi)*lamdas(i)*P/(Rt-Rc)));
                        % maximum stress at driving side of flight according to stress analysis
taoxamin5(i)=t*taof_v(i);  % minimum stress at driving side of flight according to stress analysis
lamdas_a=lamdas(i);     % stress ratio of normal wall stress to axial stress on confined surface
taoxa5(i)=1/P*t*taof_v(i)*quadl(@taoxh, 0,P);
                        % average axial stress in a pitch for flow condition
taowa5(i)=lamdas(i)*taoxa5(i);  % average normal wall stress in a pitch for flow condition
%-1. shear surface
ksa5(i)=pi*mue(i)*cp*cos(alphao+phif)./2;  % parameter for axial force calculations on shear surface
Fsaf5(i)=-ksa5(i).*taof_v(i).*Do.^2;       % axial force on shear surface for flow condition
kst5(i)=pi*mue(i)*cp*sin(alphao+phif)./2;  % parameter for tangential force calculations on shear surface
Fstf5(i)=-kst5(i).*taof_v(i)*Do^2;         % tangential force on shear surface for flow condition
Fstfp_try5(i)=1/2*(taof_v(i)+taowa5(i))*0.00635*P/sin(alphao)*tan(phif);
                                % tangential force from flight tips for flow condition
Tstfp5(i)=Fstfp_try5(i)*Ro; % torque from flight tips for flow condition
%-2. core shaft
kca5(i)=t*pi*(ct-cd)*cd*cp*(exp(4*muwc*lamdas(i)*cp/(ct-cd))-1)/4/(cp^2+pi^2*cd^2)^0.5;
                        % parameter for axial force calculations on core shaft surface
Fcaf5(i)=-kca5(i)*taof_v(i)*Do^2;          % axial force on core surface for flow condition
Fca1_try5(i)=2*pi*Rc*P*tan(phif)*taowa5(i)*sin(alphac);
kct5(i)=t*pi^2*(ct-cd)*cd^2*(exp(4*muwc*lamdas(i)*cp/(ct-cd))-1)/4/(cp^2+pi^2*cd^2)^0.5;
```

```
                                % parameter for tangential force calculations on core shaft surface
Fctf5(i)=kct5(i)*taof_v(i)*Do^2;    % tangential force on core surface for flow condition
%-3. trailing flight side
kfa5(i)=t*lamdas(i)*(pi*(1-cd^2)/4+cp*muf*(1-cd)/2);
                                % parameter for axial force calculations on trailing side surface
Ffaf5(i)=-kfa5(i)*taof_v(i)*Do^2;          % axial force on trailing side surface for flow condition
Ffaf1_try5(i)=2.*pi.*lamdas(i).*taoxamin5(i).*quadl(@trailing, Rc, Ro);
                                % axial force on trailing side surface for flow condition
kft5(i)=t*lamdas(i)*(pi*muf*(1-cd^2)/4-cp*(1-cd)/2);
                                % parameter for tangential force calculations on trailing side surface
Fftf5(i)=kft5(i)*taof_v(i)*Do^2;           % tangential force on trailing side surface for flow condition
%-4. trough surface
kta5(i)=t*pi*(ct-cd)*ct*cos(alphao+phif)/8*(exp(4*muwt*lamdas(i)*cp/(ct-cd))-1); % parameter for axial force
calculations on trough surface
Ftaf5(i)=-kta5(i).*taof_v(i).*Do.^2;          % axial force on trough surface for flow condition
ktt5(i)=t*pi*(ct-cd)*ct*sin(alphao+phif)/8*(exp(4*muwt*lamdas(i)*cp/(ct-cd))-1); % parameter for tangential
force calculations on trough surface
Fttf5(i)=-ktt5(i)*taof_v(i)*Do^2;          % tangential force on trough surface for flow condition
%-5. stress on driving side
Kda5(i)=4*(kca5(i)+kfa5(i)+2*kta5(i))/pi/(1-cd^2);
                                % parameter for axial force calculations on driving side surface
tao_daf5(i)=Kda5(i)*taof_v(i);             % compute axial stress on driving surface for flow condition
Ftao_daf5(i)=tao_daf5(i)*A_cross;          % compute axial force on driving surface for flow condition
% torque calculation
Tdf5(i)=2*pi*tao_daf5(i)*quadl(@integrnd_Td, Rc, Ro);
                                % compute torque generated by driving side of the screw for flow condition
Tcf5(i)=2*pi*Rc*P*taowa5(i)*tan(phif)*cos(alphac)*Rc;
                                % compute torque generated by core shaft surface for flow condition
Tff5(i)=2*pi*lamdas(i)*t*taof_v(i)*quadl(@integrnd_Tf, Rc, Ro);
                                % compute torque from trailing surface for flow condition
T_chokef5(i)=L5/P*(Tdf5(i)+Tcf5(i)+Tff5(i)+Tstfp5(i));
                                % compute total torque in choke section5 for flow condition
ratio015(i)=tao_daf5(i)/taoxamax5(i);  % ratio of stress on driving side to theoretical maximum stress in a pitch
ratio025(i)=taoxa5(i)/tao_daf5(i);     % ratio of average axial stress to stress on driving side in a pitch
end
%-------------------------------------------------------------------------------------------------------------------------------------------

% sixth stage of the screw-choke section
P=0.07;          % pitch,m
Do=0.08;         % screw diameter, m
Ro=Do/2;         % screw radius, m.
Dc=0.0203;       % screw core shaft diameter, m
Rc=Dc/2;         % screw core shaft radius, m
Dt=0.102;        % trough diameter,m
Rt=Dt/2;         % trough radius, m
cp=P/Do;         % ratio of pitch to screw diameter.
ct=Dt/Do;        % ratio of trough diameter to screw diameter.
cd=Dc/Do;        % ratio of core shaft diameter to screw diameter.
Lh=0.914;        % hopper outlet length,m
L6=0.305;        % length of the screw with 0.1 m screw diameter, a little shorter than outlet length, i.e. 0.914 m.
Lc=0.62
B=0.102;         % width of the trough,m
A_cross=pi*(Ro^2-Rc^2)      % effective cross section area of screw casing
alpha=20/180*pi;            % half hopper angle, radian
g=9.8;                      % gravitational acceleration, m/s^2.
for i=1:1:n
taoxamax6(i)=t*taof_v(i)*(exp(2*tan(phi)*lamdas(i)*P/(Rt-Rc)));
```

```
                                % maximum stress at driving side of flight according to stress analysis
taoxamin6(i)=t*taof_v(i);
                                % minimum stress at driving side of flight according to stress analysis
lamdas_a=lamdas(i);          % stress ratio of normal wall stress to axial stress on confined surface
taoxa6(i)=1/P*t*taof_v(i)*quadl(@taoxh, 0,P);    % average axial stress in a pitch for flow condition
taowa6(i)=lamdas(i)*taoxa6(i);        % average normal wall stress in a pitch for flow condition
%-1. shear surface
ksa6(i)=pi*mue(i)*cp*cos(alphao+phif)./2;       % parameter for axial force calculations on shear surface
Fsaf6(i)=-ksa6(i).*taof_v(i).*Do.^2;             % axial force on shear surface for flow condition
kst6(i)=pi*mue(i)*cp*sin(alphao+phif)./2;    % parameter for tangential force calculations on shear surface
Fstf6(i)=-kst6(i).*taof_v(i)*Do^2;            % tangential force on shear surface for flow condition
Fstfp_try6(i)=1/2*(taof_v(i)+taowa6(i))*0.00635*P/sin(alphao)*tan(phif);
                                % tangential force from flight tips for flow condition
Tstfp6(i)=Fstfp_try6(i)*Ro; % torque from flight tips for flow condition
%-2. core shaft
kca6(i)=t*pi*(ct-cd)*cd*cp*(exp(4*muwc*lamdas(i)*cp/(ct-cd))-1)/4/(cp^2+pi^2*cd^2)^0.5;
                                % parameter for axial force calculations on core shaft surface
Fcaf6(i)=-kca6(i)*taof_v(i)*Do^2;             % axial force on core surface for flow condition
kct6(i)=t*pi^2*(ct-cd)*cd^2*(exp(4*muwc*lamdas(i)*cp/(ct-cd))-1)/4/(cp^2+pi^2*cd^2)^0.5;
                        % parameter for tangential force calculations on core shaft surface
Fctf6(i)=kct6(i)*taof_v(i)*Do^2;              % tangential force on core surface for flow condition
%-3. trailing flight side
kfa6(i)=t*lamdas(i)*(pi*(1-cd^2)/4+cp*muf*(1-cd)/2);
                                % parameter for axial force calculations on trailing side surface
Ffaf6(i)=-kfa6(i)*taof_v(i)*Do^2;             % axial force on trailing side surface for flow condition
Ffaf1_try6(i)=2.*pi.*lamdas(i).*taoxamin6(i).*quadl(@trailing, Rc, Ro);
kft6(i)=t*lamdas(i)*(pi*muf*(1-cd^2)/4-cp*(1-cd)/2);
                                % parameter for tangential force calculations on trailing side surface
Fftf6(i)=kft6(i)*taof_v(i)*Do^2;              % tangential force on trailing side surface for flow condition
%-4. trough surface
kta6(i)=t*pi*(ct-cd)*ct*cos(alphao+phif)/8*(exp(4*muwt*lamdas(i)*cp/(ct-cd))-1);
                                % parameter for axial force calculations on trough surface
Ftaf6(i)=-kta6(i).*taof_v(i).*Do.^2;          % axial force on trough surface for flow condition
ktt6(i)=t*pi*(ct-cd)*ct*sin(alphao+phif)/8*(exp(4*muwt*lamdas(i)*cp/(ct-cd))-1);
                                % parameter for tangential force calculations on trough surface
Fttf6(i)=-ktt6(i)*taof_v(i)*Do^2;             % tangential force on trough surface for flow condition
%-5. stress on driving side
Kda6(i)=4*(kca6(i)+kfa6(i)+2*kta6(i))/pi/(1-cd^2);    % parameter for axial force calculations on driving side
surface
tao_daf6(i)=Kda6(i)*taof_v(i);                % compute axial stress on the driving surface for flow condition
Ftao_daf6(i)=tao_daf6(i)*A_cross;             % compute axial force on driving surface for flow condition
% torque calculation
Tdf6(i)=2*pi*tao_daf6(i)*quadl(@integrnd_Td, Rc, Ro);
                                % compute torque generated by driving side of the screw for flow condition
Tcf6(i)=2*pi*Rc*P*taowa6(i)*tan(phif)*cos(alphac)*Rc;
                                % compute torque generated by core shaft surface for flow condition
Tff6(i)=2*pi*lamdas(i)*t*taof_v(i)*quadl(@integrnd_Tf, Rc, Ro);
                                % compute torque from trailing surface for flow condition
T_chokef6(i)=L6/P*(Tdf6(i)+Tcf6(i)+Tff6(i)+Tstfp6(i));
                                % compute total torque in choke section6 for flow condition
ratio016(i)=tao_daf6(i)/taoxamax6(i);  % ratio of stress on driving side to theoretical maximum stress in a pitch
ratio026(i)=taoxa6(i)/tao_daf6(i);        % ratio of average axial stress to stress on driving side in a pitch
end
%-------------------------------------------------------------------------------------------------------------------
Tor_totalf=T_hopperf+T_chokef5+T_chokef6;  % compute total torque for flow condition
Tor_initial=T_hopperi;                % compute total torque for initial condition
%-------------------------------------------------------------------------------------------------------------------
```

```
ratio1=[ratio01 ratio012 ratio013 ratio014 ratio015 ratio016]; % ratios of stress on driving side to theoretical maximum stress in a pitch
ratio2=[ratio02 ratio022 ratio023 ratio024 ratio025 ratio026]; % ratio of average axial stress to stress on driving side in a pitch
tao_dft=[tao_daf1 tao_daf2 tao_daf3 tao_daf4 tao_daf5 tao_daf6];   % stresses on the driving side

result=[taoi_v Fv_i taof_v0(1) Fv_f0(1) taof_v(1) Fv_f(1) Tor_initial(1) T_hopperf(1)  T_chokef5(1) T_chokef6(1) Tor_totalf(1)];
```

## H-6: Functions for program

Function: taoxave1, taoxh, trailing, integrnd_Td, integrnd_Tf and taotaper
Source code: see below

### H-6-1:

```
% compute average axial stress
function y=taoxave1(x)
global muwt lamdas_a P Rt Rc CCC
y=(exp(2*muwt *lamdas_a*P/(Rt-Rc)))^CCC*exp(2*muwt*lamdas_a*(P-x)/(Rt-Rc));
```

### H-6-2:

```
% compute average axial stress
function y=taoxh(x)
global muwt lamdas_a P Rt Rc
y=exp(2*muwt*lamdas_a*(P-x)/(Rt-Rc));
```

### H-6-3:

```
% computer force on trailing side
function y=trailing(x)
global phif P
y=x.*cos(phif-atan(P./(2.*pi.*x))./cos(atan(P./2./pi./x))./cos(phif);
```

### H-6-4:

```
% compute torque on driving side
function y=integrnd_Td(x)
global P phif
y=x.^2.*tan(atan(P./2./pi./x)+phif);
%y=x.^2.*(1+2.*pi.*muf.*x./P)./(2.*pi.*x./P-muf);
```

### H-6-5:

```
% computer torque on trailing side
function y=integrnd_Tf(x)
global P muf phif

y=x.^2.*sin(phif-atan(P./(2.*pi.*x)))./cos(atan(P./2./pi./x))./cos(phif);
%y=x.^2.*sin(atan(muf)-atan(P./2./pi./x))./cos(atan(P./.2./pi./x))./cos(atan(muf));
```

### H-6-6:

```
% computer torque for taper section
function y=taotaper(x)
global Httf Ef taoinf

y=(x./Httf).^(Ef).*taoinf;
```